Agronomy Research

Established in 2003 by the Faculty of Agronomy, Estonian Agricultural University

Aims and Scope:

Agronomy Research is a peer-reviewed international Journal intended for publication of broad-spectrum original articles, reviews and short communications on actual problems of modern biosystems engineering incl. crop and animal science, genetics, economics, farm- and production engineering, environmental aspects, agro-ecology, renewable energy and bioenergy etc. in the temperate regions of the world.

Copyright:

***Agronomy Research* online:**

Agronomy Research is available online at: http://agronomy.emu.ee/

Acknowledgement to Referees:

The Editors of *Agronomy Research* would like to thank the many scientists who gave so generously of their time and expertise to referee papers submitted to the Journal.

Abstracted and indexed:

SCOPUS, EBSCO, CABI Full Paper and Thompson Scientific database: (Zoological Records, Biological Abstracts and Biosis Previews, AGRIS, ISPI, CAB Abstracts, AGRICOLA (NAL; USA), VINITI, INIST-PASCAL.)

Subscription information:

Institute of Technology, EULS
St. Kreutzwaldi 56, 51014 Tartu, ESTONIA
E-mail: timo.kikas@emu.ee

Journal Policies:

CONTENTS

Development and testing results of IoT based air temperature and humidity measurement system for industrial greenhouse

A. Avotins[1,*], P. Apse-Apsitis[1], J. Bicāns[1] and J. Gruduls[2]

[1]Riga Technical University, Institute of Industrial Electronics and Electrical Engineering, Azenes 12, LV-1048 Riga, Latvia
[2]SIA "Latgales darzenu logistika" greenhouse, "Kloneshniki", Mezvidi parish, LV-5725 Karsava region, Latvia
*Correspondence: ansis.avotins@rtu.lv

Abstract. Industrial greenhouse control systems are changing and getting new capabilities, due to the evolution of the Internet of Things (IoT) technologies, allowing wirelessly integrate various sensor technologies and create a cloud-based database and analytic solutions. Greenhouse systems typically are controlled by consuming single temperature and humidity measurement unit data (treated as an average value), this raises a question about the precision of such approach for application in a large industrial greenhouse. In this article IoT based temperature and humidity measurement system uMOL architecture is described and first measurement results of multi-point data collection with high resolution compared to existing single-point measurements.

Key words: Temperature, humidity, wireless data, IoT, Greenhouse automation systems.

INTRODUCTION

It is well known, that energy efficiency is one of Europe's and Latvia's economy actual problem, where electricity and heat energy costs are a significant components also in the industrial greenhouse sector, for main consumers like lighting, irrigation and climate control systems. For greenhouse illumination high pressure sodium lamps are widely used, having high electricity consumption and extra heat losses, and during plant growth process this heat can 'burn' top part of the plants stalk. As greenhouse environment control systems play an important role (Salazar et al., 2010) in tomato plant and crop growth, thus even small changes to their parameters can influence and result in undesired changes after a week, as the growth process is relatively slow and effect isn't noticeable immediately.

Existing industrial greenhouses are designed and their lighting systems are built to use high-pressure sodium vapour lamps, but nowadays due to recent LED technology advancement, they are replaced by LED luminaries to get electrical energy savings, at the same time increasing need for additional heating energy. Impact of LED lighting on crop quality can be investigated by calculating fluctuating asymmetry (Rakutko et al., 2017), as it is known to be minimal only under optimal environmental conditions, but it increases under any stress conditions, that is caused by electronic ballasts of RGB LED lighting sources (Tetervenoks & Galkin, 2012). The height of greenhouse is around 6 m,

therefore temperature and humidity levels vary across greenhouse. Accordingly having an impact on plants and their crop growth rate. To determine the exact effect, more detailed studies must be carried out for relatively long period of time, by measuring temperature, humidity and crop growth rate, and analysing outdoor weather conditions impact on plants growth and tomato production. Furthermore, such study may play important role to notice changes in temperature and humidity readings in upper height levels of a greenhouse, in case if existing sodium vapour top-lighting is changed to LED technology. The freezing effect can happen, as with lower temperature and higher humidity, ventilation system opens the ventilation windows, letting inside the cool air, which in winter can damage upper plants stalk.

Greenhouse environment, in general, is determined by inside temperature, humidity and CO_2 levels, which are affected by sunlight, outside parameters, inside heat sources (heating, lighting). Energy and environmental parameters can be measured in real time using wireless IoT solutions like (Kondratjevs et al., 2016), and by adding parameters of crop measurements, can used to calculate cost function $J(u)$ as given in formula (1), where $\Phi(x,t)$ is the final cost determined by the crop dry weight parameters (2), and $L(x,u,t)$ is penalties costs for temperature, relative humidity and energy consumption (3), where t_f and t_0 are time domain period. Example of such calculation approach is given research done by (Van Ooteghem et al., 2003).

$$J(u) = -\Phi(x,t) + \int_{t_0}^{t_f} L(x,u,t)dt \tag{1}$$

$$L(x,u,t) = L_{Ta}(x,u,t) + L_{RHa}(x,u,t) + L_Q(x,u,t) \tag{2}$$

$$\Phi(x,t) = C_{Wf} \times (t_f - t_0) \times (W_f(t_f) - W_f(t_0)) \tag{3}$$

This study demonstrates the importance of temperature and humidity parameter measurements, and question raises how detailed the measurements should be in a time domain, and geographically in the greenhouse. Research done by (Chung et al., 2012), shows that greenhouse of 650 m² growing cherry tomatoes, has temperature variates from 2.12 °C to 6.20 °C in various greenhouse sectors at the same time, and humidity variates from 11.18% to 19.27%. As greenhouse systems typically are controlled by single temperature and humidity measurement point data (treated as an average value), this raises a question about the precision of such approach for control and prediction algorithm application in a large scale industrial greenhouse.

MATERIALS AND METHODS

Description of experimental place
IoT based temperature and humidity measurement system with detailed data resolution is created and installed at an industrial greenhouse, to monitor climate readings throughout a year. The industrial greenhouse grows several sorts of tomatoes and can be treated as a complex environment, as it has a relatively large growing area (5,062 sq. meters), same time having a height of 6 meters, 40 sections of tomato growing rows top-lighted by 1,760 pieces of Hellight Helturn 400 W high-pressure sodium vapour lamps. Total installed electrical power is around 809 kW including ballast losses,

and in same time these electrical losses can be treated also as heat energy gains with same power affecting inside temperature and humidity levels. Clear horticultural glass of 3.8–4.2 mm thickness is used for greenhouse, inner temperature level is set from +19 °C in night and +21 °C, but in reality temperature varies from +16 °C to +24 °C, and relative humidity level around 60–92%. Outside the greenhouse is a meteorological data measurement system and, in order to collect readings of inside temperature, humidity and CO_2 levels, one measurement unit is placed in the centre of the greenhouse, collecting data every 5 minutes.

uMOL temperature and humidity measurement system

The developed IoT based air temperature and air humidity measurement system 'uMOL' consists of eight sensor poles, distributed evenly at greenhouse growing area, where each pole (A-G) has six sensors, measuring temperature and humidity values every 30 seconds (see Fig. 1). The vertical distance between each sensor is one meter, and the one sensor measures parameters above light curtains (see Fig. 2). With such approach, detailed data about greenhouse environment is obtained, analysed and correlated with other parameters from a photobiological perspective, crop yield and quality. Furthermore, data correlation between outside weather conditions can create necessary inputs in order to adjust greenhouse lighting, climate, irrigation and power system, more suited to local geographical conditions, enabling the creation of new greenhouse control system program and control algorithms.
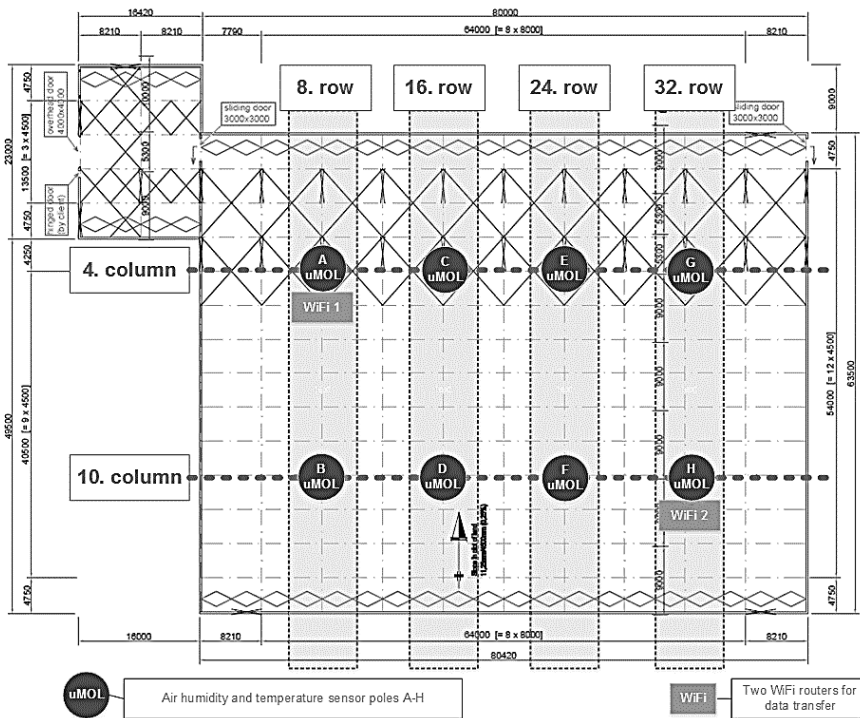
Figure 1. Typical industrial greenhouse layout and uMOL sensor pole A−H placement.
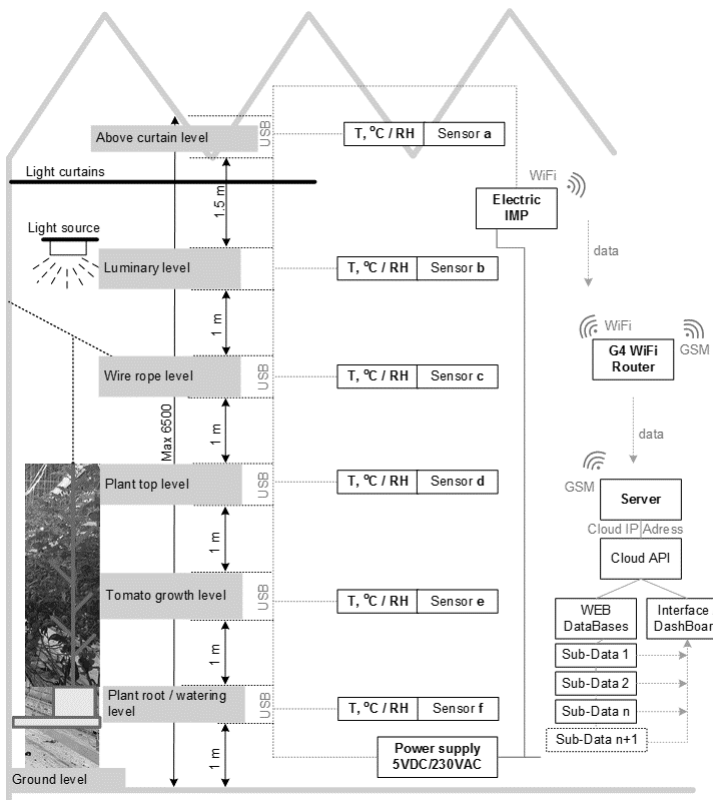
Figure 2. uMOL data system and temperature and humidity sensor pole schematic.

uMOL data system and temperature and humidity sensor pole schematic is shown in Fig. 2, where for each sensor pole A−H, six measurement levels (a-f) are selected to be observed in details. In this way 48 measurement points are placed around greenhouse, at different altitude and location. Each sensor measures both temperature and humidity. Sensor F is placed on level of plant roots and irrigation height, the next sensor E is placed at tomato growth level, then next sensor D is at plant top level. The next sensor C observes wire rope level, where tomato plant wire is attached and thus its top part is periodically moved further (length of tomato plant after 10-month vegetation period is around 14 m). Sensor B measures parameters at luminary mounting level and upper heating pipe level, but sensor (see Fig. 4) A gets readings above light curtains, used during nights to decrease heat losses through greenhouse glass and decrease solar radiation in summer during daytime. For sensor module development Sensiron SHT21S integral circuit is used (see Table 1).

Table 1. Technical parameters of temperature and humidity sensor Sensiron SHT21S

Parameter	Range	Accuracy	Resolution	Long Term Drift
Temperature sensor	-40 … +125 °C	+/- 0.3 °C	14 bit	< 0.04 °C per yr
Humidity sensor	0..100% RH	+/- 2% RH	12 bit	< 0.5% RH per yr

Temperature and humidity data are read by the ATtiny85 microcontroller and by means of multiplexing circuit sent to Electric Imp module Cortex micro-controller. Development imp001 module is used, where raw (binary) temperature and humidity data are converted to real values, that are wirelessly (WiFi) sent to logging file on the server. Electric Imp Platform is the first IoT platform to be independently certified to UL® 2900-2-2 (Standard for Software Cybersecurity for Network-Connectable Devices, Part 2-2: Particular Requirements for Industrial Control Systems). Thus we gain additional data security in addition to server side security means.
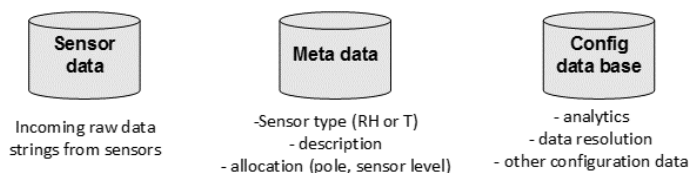
Figure 3. uMOL system data base main structure and functions.

Figure 4. uMOL sensors in Mezvidi greenhouse.

Sensors a-f are connected through USB cable and attached to data transmission and post-processing module (Electric Imp) with integrated WiFi transceiver, which is located at each Sensor pole (A-H). The obtained raw data strings are sent to Cloud based server using two 4G mobile network WiFi routers (4 poles (24 data points) are connected to one router), where they are stored in raw format in Sensor database (see Fig. 3), then deciphered in Metadata database, adding additional information, and then processed for data analysis in a Configuration data base. The software architecture uses Microsoft technologies and platform products, the development environment is Visual Studio, but its components are done in C#, XAML, JS, HTML5, CSS3 programming languages and stored on Microsoft Azure cloud computing platform server in Ireland datacentre. Data storage uses is stored in SQL relational databases.

RESULTS AND DISCUSSION

System setup was activated at industrial greenhouse at the end of September 2017. In September 2017 – January 2018 period sensors have generated over 5 million entries of sensor data readings. Along with the uMOL sensors system contains sensor data readings from Mezvidi greenhouse management system. We use both system sensor data

to identify and illustrate differences in the measurements. As previously described, the sensor measurements are captured at various locations and altitudes in the greenhouse compare to a single sensor unit (at fixed height) that is used for greenhouse management system.

As uMOL system gets readings each 30 seconds, and existing single point measurement is done once per 5 minutes, temperature data post-processing is needed for comparison, and to get new temperature value (T) for new period (in this case 5 minutes), simple averaging formula (1) is applied:

$$T_{period} = \frac{1}{n} \sum_{i=1}^{n} t_i \qquad (4)$$

where n – data-set extent for 5min period; t_i – variable at the i index of a data-set, n.

This approach allowed us to compare uMOL system sensor data reading with the ones captured by greenhouse native system. We choose for detailed discussion analysis 24 hours of 7th of January 2018. Temperature sensor data readings (see Fig. 5) demonstrates measured Max, Min and Average temperature values from all 48 uMOL sensors. Bolded line shows greenhouse single-point sensor data reading and it is mostly close with calculated average temperature across all uMOL temperature sensors. Largest deviations can be observed during high sun activity (12:00) period differing up to 10 degrees and up to 5 degrees during the night period (22:00 till 2:00). The figure shows, wide ranges in temperatures changes in all greenhouse levels.
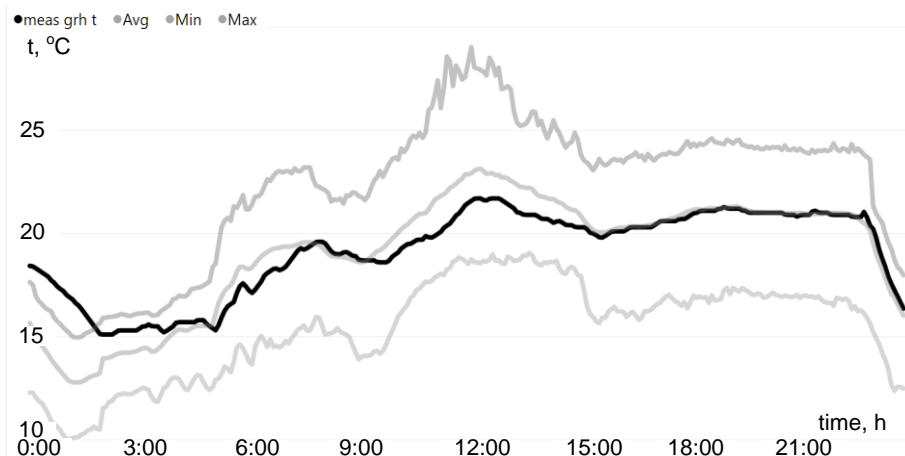
Figure 5. uMOL system and greenhouse system temperature data comparison using all levels.

Due to fact that heat is moving upwards, we could analyse the temperature sensor data readings same way as in Fig. 5, using only C, D and E levels to be compared against greenhouse single point sensor readings, thus obtaining results, shown in Fig. 6. The difference during high sun activity period (see Fig. 7) vary up to 5 degrees and up to 3 degrees during the night period. The greenhouse system value is more close to uMOL readings of E level.

Both figures clearly indicate best average temperature stability when artificial light is turned ON, but most differences when lights are turned OFF and sunlight is present. This effect can be taken into account, to create more precise heat and ventilation system control algorithms, and even more − it brings the idea, that highest (A,B) and lowest (F) level sensor data can be used to predict middle-level temperatures for next time periods.
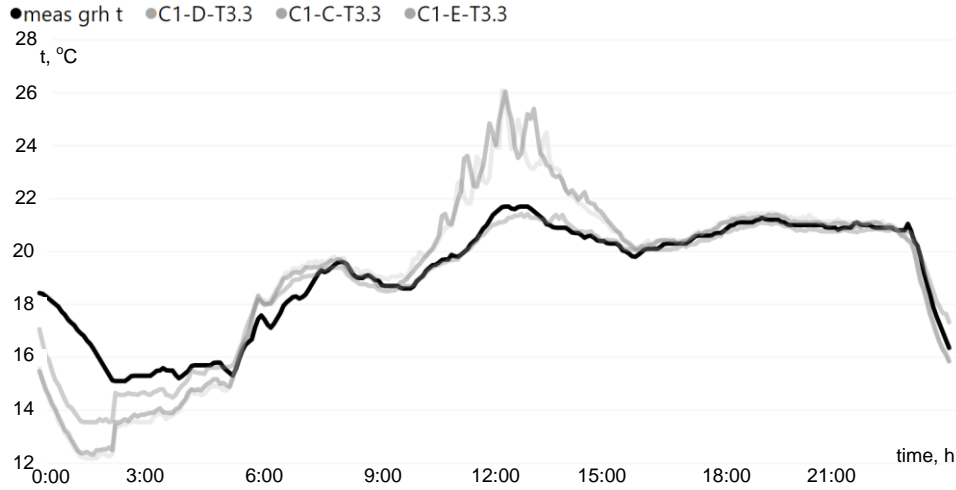
Figure 6. uMOL system and greenhouse temperature data comparison using only levels C,D,E (plant area).
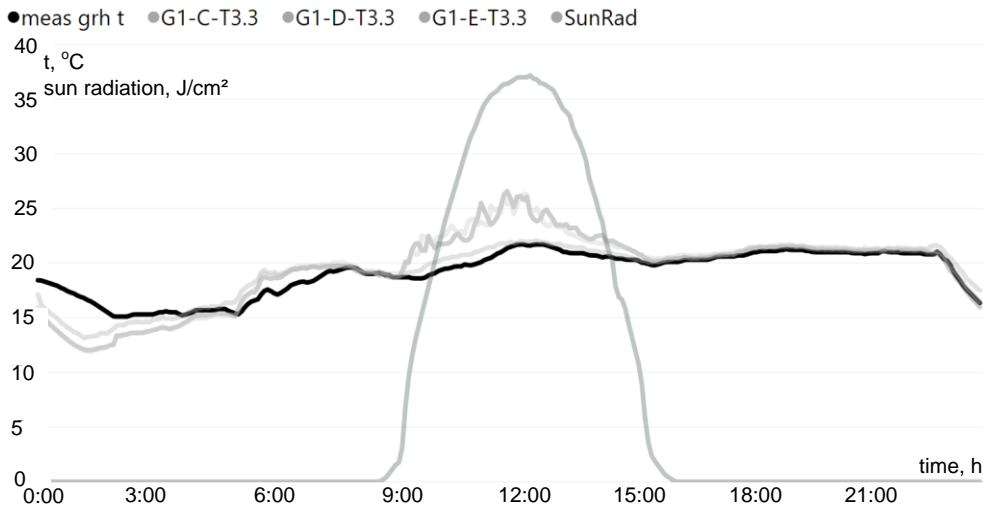
Figure 7. uMOL system G pole C,D,E sensor level, greenhouse temperatures (M=1:1) and sun radiation readings (M=1:20).

As the greenhouse measures humidity deficit value (see Fig. 8), it looks very stable (amplitude is 2.5%) but variation between values is 58%, same time all pole D level relative humidity readings (%) look more dynamic (amplitude 14%−28%), and giving variations between readings around 65.7%. If looking on average monthly readings of relative humidity and temperature (see Fig. 9), in both cases it shows difference between the various greenhouse zones (around A-H poles).
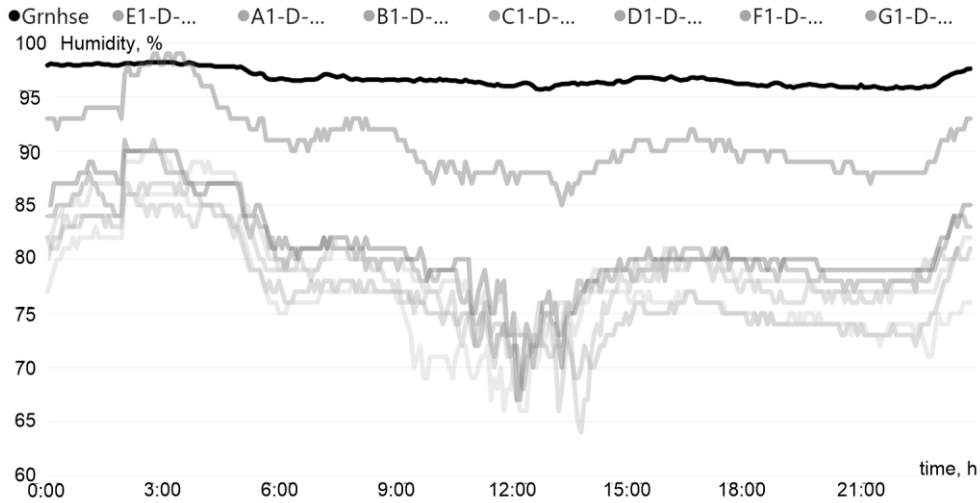
Figure 8. uMOL system D level relative humidity readings per poles A-H comparing to humidity deficit values (bold).
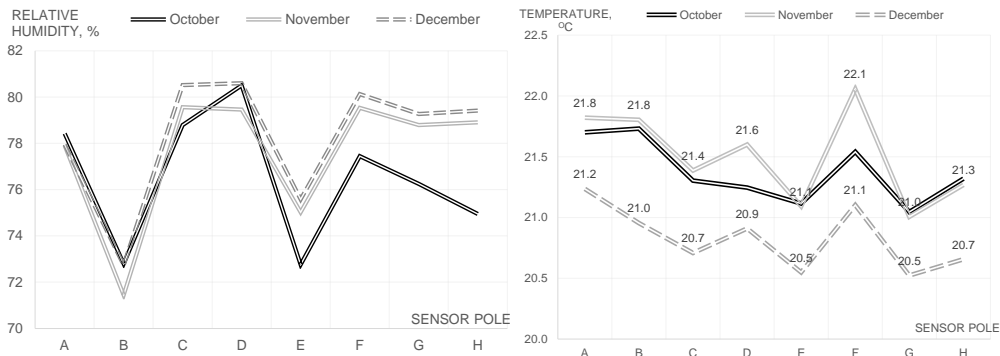
Figure 9. uMOL system monthly average relative humidity (left) and temperature (right) readings per sensor poles A-H.

CONCLUSIONS

Research clearly shows that industrial greenhouse zones/areas have a noticeable difference in climate conditions, showing a detectable impact of solar radiation on inside temperature and relative humidity. uMOL system architecture works properly in heavy humidity conditions. Further studies are needed, to analyse climate differences impact

on tomato crop yield and biological growth parameters. uMOL multi-point measurement system joint with pre-emptive control of heat and ventilation systems climate system management may improve greenhouse environment stability and have impact on the tomato plant performance.

REFERENCES

Salazar, R., Rojano, A., Lopez, I. & Schmidt, U., 2010. A Model for the Combine Description of the Temperature and Relative Humidity Regime in the Greenhouse. In: *Ninth Mexican International Conference on Artificial Intelligence*, Pachuca, 2010, pp. 113–117.

Kondratjevs, K., Kunicina, N., Patlins, A., Zabasta, A. & Galkina, A., 2016. Vehicle weight detection sensor development for data collecting in sustainable city transport system. In: *57th International Scientific Conference RTUCON*, Riga, 2016, pp. 1–5.

Rakutko, S., Rakutko, E., Kaposhko, D., Vaskin, A. & Tranchuk, A., 2017. Influence of light quality on fluctuating asymmetry of bilateral traits of forced parsley leaves. In: *16th International Scientific Conference Engineering for Rural Development*, Jelgava, Latvia, 2017. Volume **16**, 2017, Pages 42–47.

Tetervenoks, O. & Galkin, I., 2012. Evaluation of efficacy of light sources combined of different color LEDs. In: *13th Biennial Baltic Electronics Conference*, Tallinn, 2012, pp. 231–234.

Chung, S., Kim, K., Huh, Y., Hur, S., Ha, S., Ryu, M., Kim, H & Han, K., 2012. Determination of Sensor Locations for Monitoring of Greenhouse Ambient Environment. In: *11th International conference on Precision Agriculture.* Indianapolis, Indiana, U.S.A.

Van Ooteghem, R.J.C., Stigter, J.D., Van Willigenburg, L.G. & Van Straten, G., 2003. Optimal control of a solar greenhouse. In: 2003 European Control Conference, Pages 2739–2746.

Crop weight measurement sensor for IoT based industrial greenhouse systems

A. Avotins[1,*], A. Potapovs[1], P. Apse-Apsitis[1] and J. Gruduls[2]

[1]Riga Technical University, Institute of Industrial Electronics and Electrical Engineering, Azenes 12, LV-1048 Riga, Latvia
[2]SIA 'Latgales darzenu logistika' greenhouse, "Kloneshniki", Mezvidi parish, LV-5725 Karsava region, Latvia
*Correspondence: ansis.avotins@rtu.lv

Abstract. Nowadays the industrial management systems are changing by means of implementing various Internet of Things (IoT) technologies, allowing a simple integration of sensor technologies with wireless communications and development of cloud based database solutions. The industrial greenhouse management systems are not the exception in this regard, as they are becoming more and more popular with the use of various sensors for the automation of the vegetable and other crop cultivation process.The general aim they have is to raise the level of process automation, quality, energy efficiency and other important parameters. The implemented technologies and environment of industrial greenhouse can be different fir the research type laboratories, as they are focused on production, therefore this research is conducted in cooperation with tomato producing industrial greenhouse of SIA 'Latgales darzenu logistika' focusing on IoT based crop weight measurement.

Key words: Crop, Weight measurement, IoT, Greenhouse systems.

INTRODUCTION

Each automation system obtains a control signal from feedback loop, typically gained from some physical sensor, controlling in that way the irrigation process of tomatoes. It is necessary to monitor the weight of tomato plants and its soil pod (Van Straten et al., 2011; Chen et al., 2016). Weight measurements show the tendency of water (fertilizer) consumption and give a precise timing when irrigation must be started and stopped (the changing in moisture level between start and the end of watering is about 7 to 13%). Furthermore, it helps to show the tendency of crops biomass increasing, plants overall health, balance between parts of the plant according to the programmed greenhouse climate values (Ehret, 2001).

One of the most important factors hindering wider implementation of weighting system in greenhouse is their high price, where the largest costs are related to the weighing sensors themselves. In addition to the price factor, the weight sensor systems are often characterized on the market by known structural and functional limitations, which can be solved if developing a new weighting system (Paskal, 2018).

The initial studies show that in the existing industrial greenhouse weighing systems and their prototypes, mostly S-type weighting sensors are used, that simplifies the measurements of the weight of hanged objects. In this case, weight sensors of high-precision with temperature compensation and high output signal linearity are in use for obtaining the accurate measurement data, increasing also the costs of the sensor (Carrasquilla-Batista et al., 2016; Alberta, 2018).

The authors assume that the price of a high-quality sensor cost system can be reduced by using considerably cheaper sensor solutions, embedding electronics that automatically processes the readings of this sensor. The adapting of it to the variations of the ambient temperature meets the requirements of temperature compensation and non-linearity of the weight sensor in all possible operating modes (De Koning & Bakker, 1992). This fact raises a number of scientific research tasks related to the digitization of high-resolution analogue signal of the weight sensors, obtaining of the data filtering post-processing, and subsequently data transmission to the server database.

MATERIALS AND METHODS

In order to obtain the data of the periodic crop weight measurements, an IoT based crop measurement system shown in Fig. 1 is used. The main block is the Load Sensor Module (LSM) with such elements:
- LSM – Load Sensor Module;
- L – Load;
- WS – Weight Sensor;
- ADC – Analog-to-Digital Converter;
- MC – Microcontroller with Built in Wi-fi Module;
- R – Wi-Fi Router;
- S – Data Server (IoT Cloud).
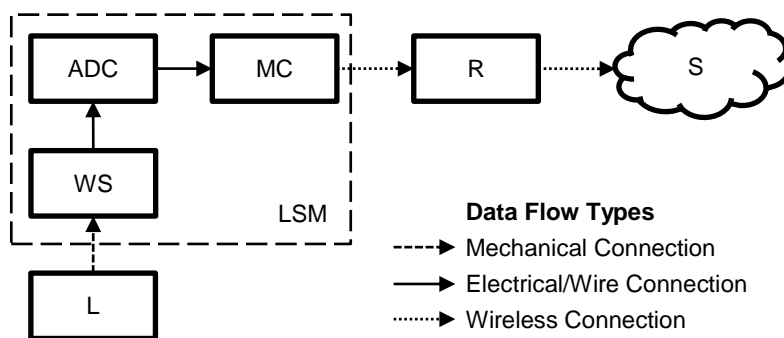
Figure 1. Block diagram of Load Sensor Module (LSM) for IoT application.

LSM uses a microcontroller (MC) with embedded Wi-Fi module (similar to ElectricImp, ESP8266, etc); and two main aspects determine such approach:
• Using the existing 2.4 GHz WiFi network (with the latest ElectricImp and ESP microcontroller versions also 5 GHz) within LSM working zone, the selected MC allows measurement data transmission to cloud based server S (in this case MS Azure based platform), but any other wireless system can also exist, like described by K. Kondratjevs

et al. (2016), where data is stored and post-processed without any hardware element of external wireless communication.

• Selected MC also has a distant reprogramming and status monitoring function, which is very useful for the IoT solutions, especially at research and development stages, as it allows a distant changing of control, calculation algorithms, calibration coefficients and other LSM working parameters by means of Internet (mobile or wireless network).

In this case, separate WiFi router R can ensure a stable Wi-Fi network for the experiments.

The output signal of the Weight Sensor (WS) is processed with 24-bit analogue-to-digital converter (ADC) module. The reason to select such high precision is a relatively low working range of WS output signal (2–5 mV at rated regime of LSM). Furthermore, this ADC module has integrated a signal pre-amplifier, which allows the simplification of LSM circuitry, decreasing of the elements and costs, obtaining at the same time the measurement resolution with precision of 0.02 grams.

The first LSM prototype has been tested and verified under the laboratory conditions, where the experimental testing is based on the continuous weighing of a mass object under different external temperature conditions. These experiments clarified that temperature changes of the WS itself affect the measurement readings of WS. After the analysis of the results of the measurements, a hypothesis can state , that if the data of the weight and temperature measurements are post-processed in real-time, the precision of the load weight will be increased. In this case, formula (1) describes the transfer function of measurement data post-processing:

$$m_C = m_M + (T_i - T_C) \cdot K \tag{1}$$

where m_C – calculated weight (true weight from LSM); m_M – measured weight (raw data from WS); T_i – current WS temperature; T_C – WS temperature at LSM calibration; K – linear calculating coefficient.

The linear calculating coefficient is obtained for each LSM, according to the first testing results. The assumption is that in future coefficient K will be more precise due to self-learning algorithms, using various calibration weights.

Various temperature impact tests (sunlight, extra heat, etc.) were carried out within the laboratory environment; and the most characteristic measurements are shown in Fig. 2, where $m_{measured}$ – raw data from WS, g; $m_{calculated}$ – calculated weight (true weight from LSM), g; m_{real} – real weight of the object, g; T_{sensor} – WS temperature.

The horizontal axis represents serial number of a measurement. For all the experiments the measurement interval was 15 seconds.

According to the obtained results at the dynamic WS temperature reading changes, two important factors of the chosen WS exist:

• Transition processes within WS temperature changes cause significant fluctuations in the weight readings and opposite to the temperature process direction (see Fig. 2). This effect can be reduced by using filtration of WS signal, and creating more stable environment inside the WS sensor casing.

• At rapid temperature changes WS sensor readings have a significant reaction delay, which could be reduced by means of actual WS measurement data and historical temperature data use in formula (1).
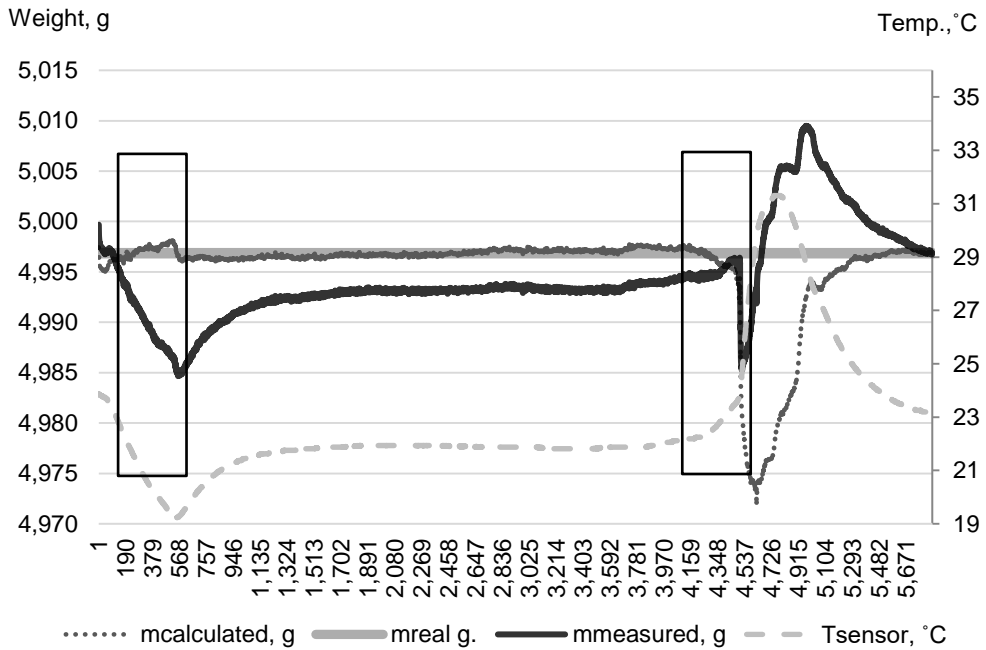
Figure 2. LSM reading stability experiment (impact of temperature test result).

Experiments at slow WS temperature changes (much closer to a real greenhouse environment), show, that in comparison to the the real load weight the calculated weight absolute error does not exceed 0.5%.

RESULTS AND DISCUSSION

Currently the first three LSM prototypes are installed in real industrial greenhouse environment at Mezvidi from 15.12.2017 (see Fig. 3.), thus collecting 179732 measurement points in IoT database by 30.01.2018., with 1 min resolution.
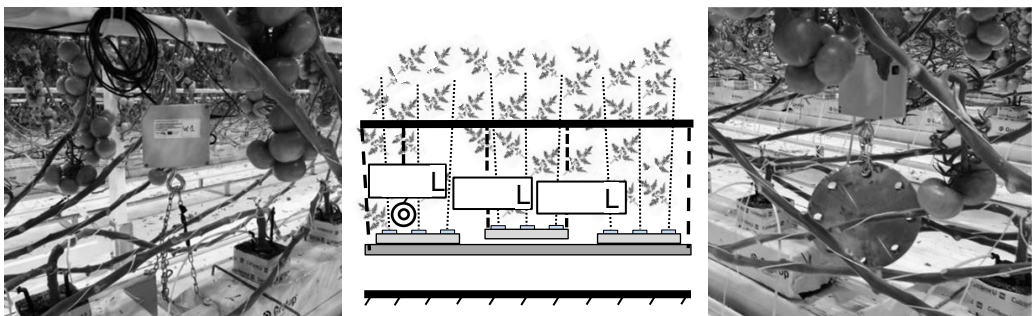
Figure 3. LSM testing in real greenhouse environment, LSM$_3$ for constant weight (right).

Two sensors (LSM_1 and LSM_2) are used to weight base with three tomato plants (see Fig. 3.), but the third weight sensor (LSM_3) is equipped with a reference weight of 5,770 g, to evaluate LSM measurement precision in industrial greenhouse environment, obtaining long term data. As all measurement data are stored in IoT cloud database, weight changes during twenty-four hour period, can be observed in Fig. 4.
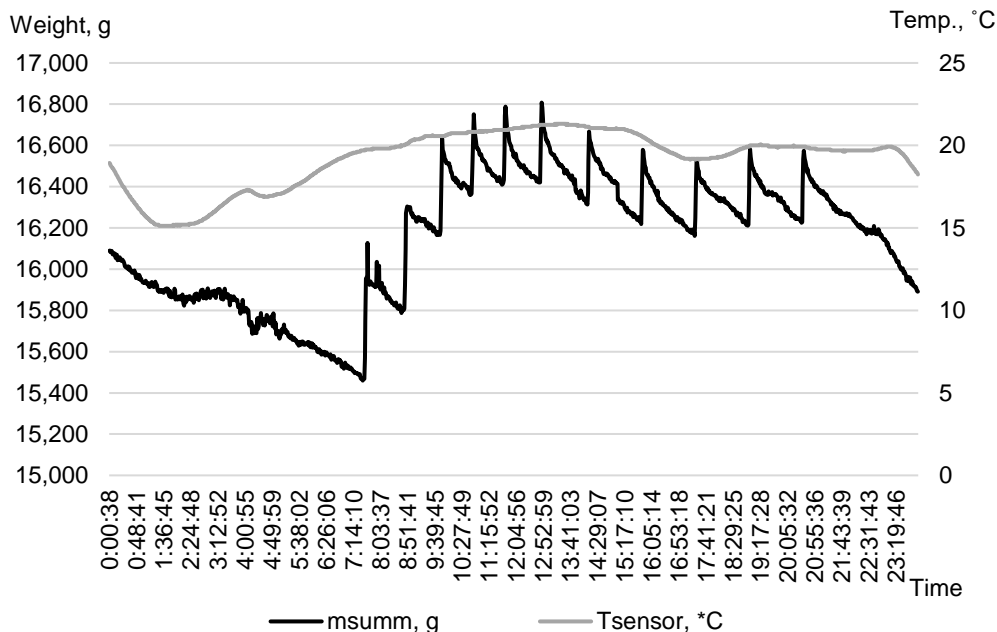
Figure 4. LSM_1 and LSM_2 calculated weight.

As it can be seen in Fig. 4., from LSM_1 and LSM_2 measurements, it is possible to determine the trend in water consumption and accurately detect the time to start and stop watering system. It is also obvious that the water weight changes between watering system start and stop are about 8%, that meets the rules of the greenhouse irrigation system.

LSM_3 measurements give an opportunity to analyse LSM measurement precision under real working conditions, to evaluate LSM construction parameters and efficiency of WS data post-processing algorithm, where the error of measurements in this case does not exceed 0.1% (see Fig. 5).

Both laboratory and industrial greenhouse experimental measurement results show, that LSM weight precision can be increased if WS working temperature is stable. As the dynamic temperature changes have a great impact on readings, thus the previous or historic WS temperature readings could be used in data post-processing algorithms.

Measurement experiments of 30 h using constant weight of 5 kg show that, the use of linear data post-processing method (temperature changed 18–32 °C with max raise of 2 °C h^{-1}) gives the measurement errors from 0 to 0.6% (in average 0.1%). In its turn the use of the second and the third grade polynomial data post-processing (temperature changed 19–42 °C with max raise of 10 °C h^{-1}) gives the measurement errors from 0 to

1.5% (in average 0.9%). During calibration process, a transition process takes place, and 'stretching' effect must be taken into account at the first moment after applying calibration load, to avoid 'floating' readings later in the working regime.
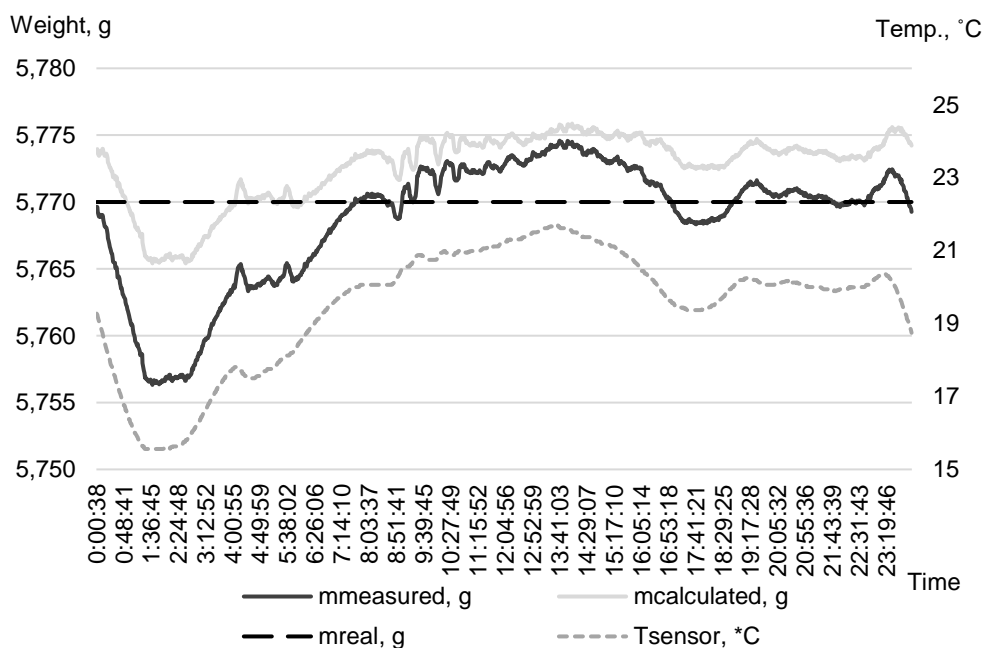
Figure 5. LSM$_3$ output data.

At this stage LSM testing results prove their ability to work in industrial greenhouse environment (high humidity, voltage drops, etc). The obtained data can be used to improve greenhouse irrigation control systems and to enable the high accuracy detection of crop biomass growth.

CONCLUSIONS

Experimental measurements show, that both electrical and mechanical design properties of the sensor must be taken into account to get stable thermal operating mode and other operating conditions. Furthermore, the first testing results show that theuse of a S-type sensor of medium precision, it is possible to make post-processing of their raw output data, that results in the required resolution and sampling level of weight measurement data. As a result the logging of the measured weight data and subsequent statistical processing can be carried out with the aim to apply them for the energy efficient control of the total greenhouse management system.

REFERENCES

Alberta Agriculture and Forestry *http://www1.agric.gov.ab.ca/$department/deptdocs.nsf/all/ green14532*. Accessed 30.1.2018.

Ehret, D.L., Lau, A., Bittman, S., Lin, W. & Shelford, T. 2001. Automated monitoring of greenhouse crops. In: *INRA, EDP Sciences*, pp. 403–414.

Carrasquilla-Batista, A., Chacon-Rodriguez, A. & Solorzano-Quintana, M. 2016. *Using IoT resources to enhance the accuracy of overdrain measurements in greenhouse horticulture.* CONCAPAN.2016.7942345. 5pp.

Chen, W.T., Yeh, Y.H., Liu, T.Y. & Lin, T.T. 2016. *An Automated and Continuous Plant Weight Measurement System for Plant Factory*. Frontiers in Plant Science vol **7**, 392.

De Koning, A.N.M. & Bakker, J.C. 1992. In situ plant weight measurement of tomato with an electronic force gauge. *Acta Hort.* 304., pp. 183–186.

Kondratjevs, K., Kunicina, N., Patlins, A. Zabasta, A. & Galkina, A. 2016. Vehicle weight detection sensor development for data collecting in sustainable city transport system. In: *57th International Scientific Conference RTUCON*, Riga, 2016, pp. 1–5.

Paskal Monitoring Solutions *https://www.paskal-systems.com/about.* Accessed 30.1.2018.

Van Straten, G., Van Willigenburg, G., Van Helten, E. & Van Ooteghem, R. 2011. Optimal Control of Greenhouse Cultivation. *Taylor & Francis Group*, 318p.

Investigation into the performance characteristics of electric automobiles by means of a data logger

D. Berjoza[1,*], V. Pīrs[1] and I. Jurgena[2,*]

[1]Latvia University of Life Sciences and Technologies, Technical Faculty, Institute of Motor Vehicles, 5 J. Cakstes boulevard, LV-3001 Jelgava, Latvia
[2]Latvia University of Life Sciences and Technologies, Faculty of Economics and Social Development, Institute of Business and Management Science, 18 Svetes street LV-3001 Jelgava, Latvia
[*]Correspondence: dainis.berjoza@llu.lv; inara.jurgena@llu.lv

Abstract. Fossil fuel deposits are constrained in the world. Various alternative energy sources are introduced in vehicles to limit the depletion of fossil fuel reserves and to reduce environmental pollution. One of the alternative energy sources is electricity. The use of electric automobiles has begun in the Baltic States too, yet accurate performance parameters of the automobiles, which could sometimes differ from the technical characteristics specified, are not always known. Road testing an electric automobile was performed using a data logger that recorded the battery's voltage, current, temperature and the automobile's speed. These parameters allowed computing changes in the electric automobile's power output under various driving regimes, e.g. acceleration or braking. Road testing the electric automobile was done under two driving regimes – urban and non-urban – on a certain route. The experiment represented a full cycle road test, with the batteries fully charged, that lasted until the batteries were discharged to a minimum level, which was limited by the battery management system (BMS). The experiment identified the maximum current as well as the effectiveness of the regenerative braking system.

Key words: electric vehicle, energy consumption, current, voltage, driving regime, cruising.

INTRODUCTION

In the world, electric vehicle (EV) progress began along with internal combustion vehicle progress. Electric vehicles were equipped with lead-acid batteries that could not provide a sufficient driving range, and the electric vehicles could not compete with internal combustion vehicles. Even though historical electric automobiles had a lot of advantages in comparison with internal combustion automobiles, e.g. quiet operation, an easy startup and an easy movement startup, the electric automobiles were not widespread until the 21st century (Berjoza & Jurgena, 2013). Nowadays a problem with electric automobiles is the same as it was long ago – a small driving range per charge. This relates to the low weight-to-energy capacity ratio for batteries, compared with that for liquid fuel.

The key electric parameters of electric automobiles – voltage, current and power consumed – recorded during driving depend very much on the driving regime. The parameters can be, to a smaller extent, affected by other powerful electrical devices, e.g. an air conditioner or an interior heater. The energy consumed by the mentioned devices is usually quite constant, whereas the energy consumed by the electrical motor can change several times within a very short moment. The standard driving regimes of an electric automobile, like those of an internal combustion automobiles, are as follows: acceleration, cruising, smooth deceleration or coasting and braking.

Vehicle movement simulations by means of computer tools began in the late 1990s. Various hybrid electric vehicle (HEV) and electric vehicle models were researched by using the Matlab-Based Modelling and Simulation software. The simulation results were obtained during both simple driving regimes – acceleration, cruising and braking – and more complicated driving cycles, e.g. the FTP−75, a federal highway drive cycle. The research investigations analysed various vehicle driving strategies after determining CH, NOX and CO emissions and fuel consumption (Butler et al., 1999) and compared electric vehicle current changes, simulating the selected driving cycles. The research investigations did not consider emissions, assuming that no emissions were produced, yet the latest research investigations provide data on indirect emissions produced by electric vehicles (Berjoza & Jurgena, 2016) from electricity production. In Latvia, for example, average CO_2 emissions from the production of a kWh of electricity equal 115 g $(kWh)^{-1}$. The planned research intends to analyse changes in current and voltage at diverse driving regimes, and an electric vehicle is going to be road tested.

American Control Conference researchers have published their research findings on plug-in hybrid electric vehicle (PHEV) control strategies. The research object was a Toyota Prius, and a Control Strategy and a Proposed Strategy for the car was examined by means a mathematical model. The Proposed Strategy achieved a 16% longer driving range of the PHEV than the standard one did. The mentioned research examined current and torque changes under both strategies. A comparative examination was performed in UDDS and EPA driving cycles. The research also found an optimum PHEV control strategy model that could yield the best economic and performance characteristics (Banvait et al., 2009).

An analysis of the literature revealed that most of the research investigations focused on HEVs, optimising the inter-related operation of the electric motor and the internal combustion engine and designing algorithms aimed at reducing fuel consumption and impacts on the environment (Musardo et al., 2005). An investigation produced motor torque curves and sought optimum HEV operation regimes by using Simuling modelling software. It also developed a mathematical model for fuel consumption reduction. The investigation compared the Dynamic Programming and the Equivalent Consumption Minimization Strategy in six various driving cycles, yet the results did not differ by more than 0.4% (Musardo et al., 2005).

Chilean scientists have developed an energy management system for a hybrid electric vehicle. The system exploits ultracapacitors that allow reducing energy consumption and using various energy sources, e.g. fuel cells, microturbines and zinc-air batteries. The energy could be also generated by the regenerative braking system. The research developed and analysed a mathematical model and performed road tests in a 14.2 km driving cycle. The lowest energy consumption was achieved under the Optimal Neural Network Control System with regenerative braking, which performed 28.7%

better than the standard system did. The road tests measured momentary vehicle speed, voltage and current (Moreno et al., 2006). The planned road tests intend to identify the effect of the regenerative braking system with the controller set to 45%.

Chinese scientists have done research on a plug-in hybrid electric vehicle with a Fuzzy Logic System. The system allows optimally using batteries depending on the charge level and temperature of the batteries. The scientists developed vehicle, motor-controller, engine-generator and vehicle drive mathematical models. They performed a simulation, producing current-voltage curves, in the USA Urban Dynamometer Driving Schedule (UDDS) and the New European Driving Cycle (NEDC). The research found that the Fuzzy Logic System was effective in preventing a battery from being overcharged as well as enhanced the capability of the motor control system to provide optimum motor operation (Li et al., 2011).

The literature provides a few research studies on EV road tests. There are more research studies focusing on a system analysis of hybrid electric vehicles and plug-in hybrid electric vehicles, the development of mathematical models for various systems and the enhancement of control system algorithms. For this reason, it is useful to do research on the effect of electric vehicle driving regimes on the electric parameters of the electric vehicle in urban and non-urban driving, which is the key aim of the research.

MATERIALS AND METHODS

The experimental research was performed using an electric car Renault Clio. This car was converted from an internal combustion car equipped with a 1.2 l engine into an electric car. The car was equipped with a 30 kW electric motor with a maximum power of 50 kW as well as 30 lithium-iron hybrid batteries with a capacity of 100 Ah. The battery system was controlled by the battery management system (BMS). The BMS was set to prevent the batteries from being discharged by more than 2.4 V or from being overcharged by more 3.8 V. The total battery voltage was 96 V. The distance covered per charge was 60 km, while the maximum speed was 120 km h^{-1}.

The road tests were done on several road sections that are presented in Fig. 1.

Two diverse routes were chosen for the road tests: Jelgava city for the urban driving regime and general road P97 between Jelgava city and Dobele town for the non-urban driving regime. In non-urban driving, the road test was done back and forth, while in urban driving it was done on a circle route (Fig. 1). The length of a full urban circle route was 14.7 km, while the length of a non-urban route in one direction was 25.1 km.

The road surface on both routes was in good condition; the average rolling resistance coefficient was 0.010−0.012. In accordance with the Road Safety Rules, the road tests used LED lamps with a total power of 15 W. Each road test was replicated five times (Fig. 2). The electric data were registered and stored by a logger Graphtec midi Logger GL220. The road test was conducted with fully charged batteries until the battery charge level reached 5−6% of the total battery capacity. The batteries were recharged after every road test, and the data on the five replications were stored in the logger Graphtec midi Logger GL220. After the batteries were fully recharged, the next road test was performed. The driving regime was changed during every replication, which means that a road test started in the city was continued outside the city, and then again in the city. In this way, the weather factor was excluded. The road tests were done in October and November 2017 at an ambient temperature from +5 to +10 °C. After the

road tests, the data were processed and represented graphically. The car's interior heating system – an Eberspacher heater – running on ethanol was used during the road tests. An electric heater would consume too much energy, and an examination of it was not intended in the present research.

a)

b)
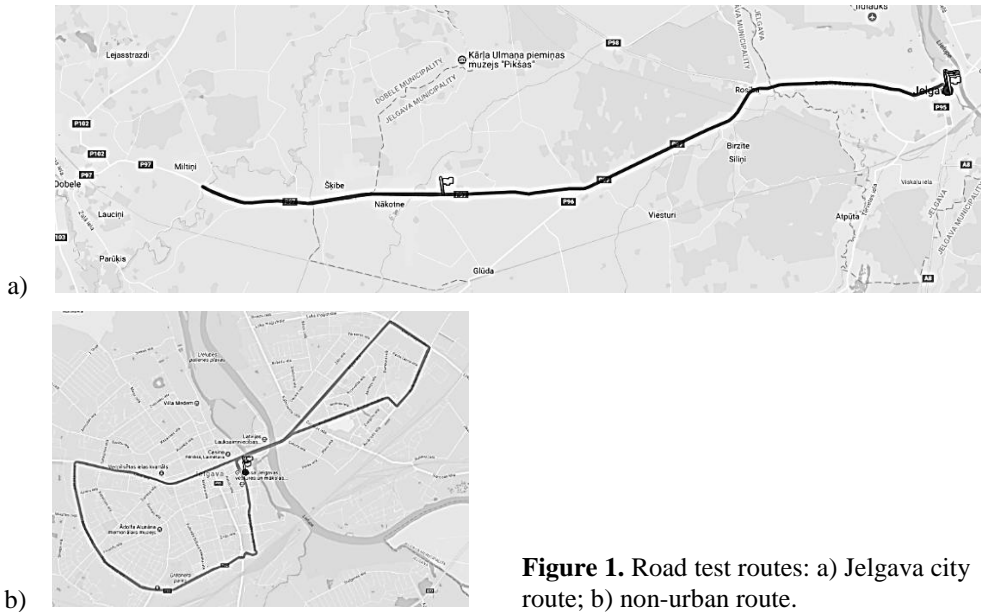
Figure 1. Road test routes: a) Jelgava city route; b) non-urban route.
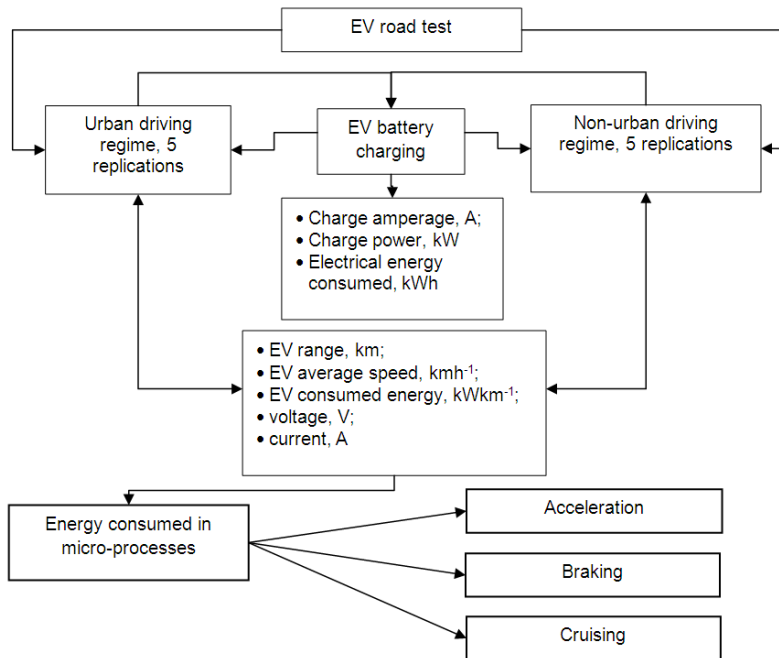
Figure 2. Road test scheme.

A logger HOLUX GP Sport 245 was used to store the route data. The logger had a 512 kB memory and the capacity of its batteries was sufficient for a 28 h operation. The logger could store 200,000 waypoints, measure speed, time, distance and store the route data. The logger could operate in a temperature range from -10 °C to +50 °C. The scheme for connecting a data logger to the electric automobile is presented in Fig. 3.
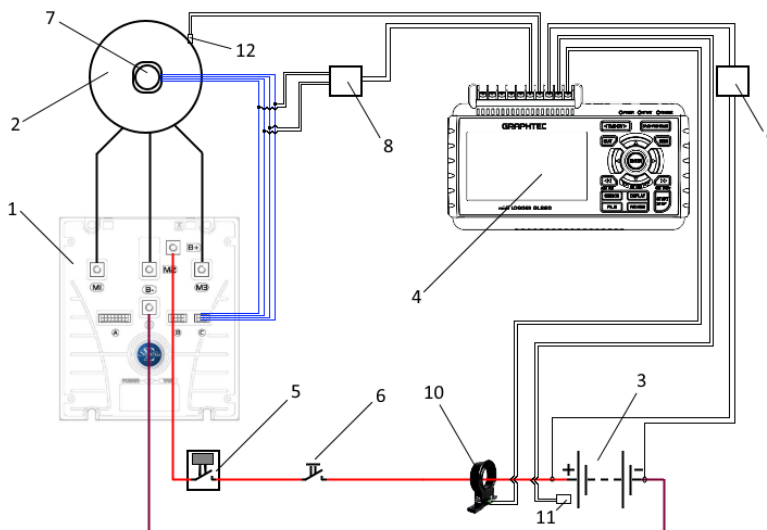
Figure 3. Scheme for connecting experimental equipment: 1 – motor controller; 2 – electromotor; 3-96 V accumulator; 4 – data logger; 5 – electromagnetic safety switch; 6 – mechanical safety switch; 7 – electromotor speed sensor; 8 – frequency-voltage converter; 9 – voltage divider; 10 – current sensor; 11 – accumulator temperature sensor; 12 – electromotor temperature sensor.

A data logger Graphtec midi Logger GL220 was used to record the electric car's electric parameters. The logger's sampling interval ranged from 10 ms to 24 h, a time scale was from 1 s to 24 h. This device was equipped with a 4.3 inch TFT LCD display, a 8.5–24 V power supply and 10 analogue input channels.

RESULTS AND DISCUSSION

After the road tests, the logger data were transferred to a computer and processed, interpreted and analysed.

A GPS data logger recorded speed in urban and non-urban driving. Changes in speed in both driving regimes are shown in Fig. 4. Urban driving involves frequent acceleration and braking, and the speed is very volatile. The average speed in urban driving during the road tests was 31.15 km h^{-1}. In non-urban driving, the beginning and the end of a road test was in Jelgava city, therefore, it was urban driving. The average speed in non-urban driving was 57.71 km h^{-1}.

To analyse various electric parameters of the electric car under various driving regimes, the recorded data were aggregated to produce synchronised graphs v = f(t), U = f(t), I = f(t) and P = f(t). A graph for urban driving is shown in Fig. 3. In the road test, the speed in urban driving is very volatile due to all the regimes: acceleration,

braking, cruising and coasting. Urban driving is appropriate for the structure of the electric car, as electrical energy is consumed by only on-board devices when stopping at intersections, whereas it is generated when braking.

a)

b)
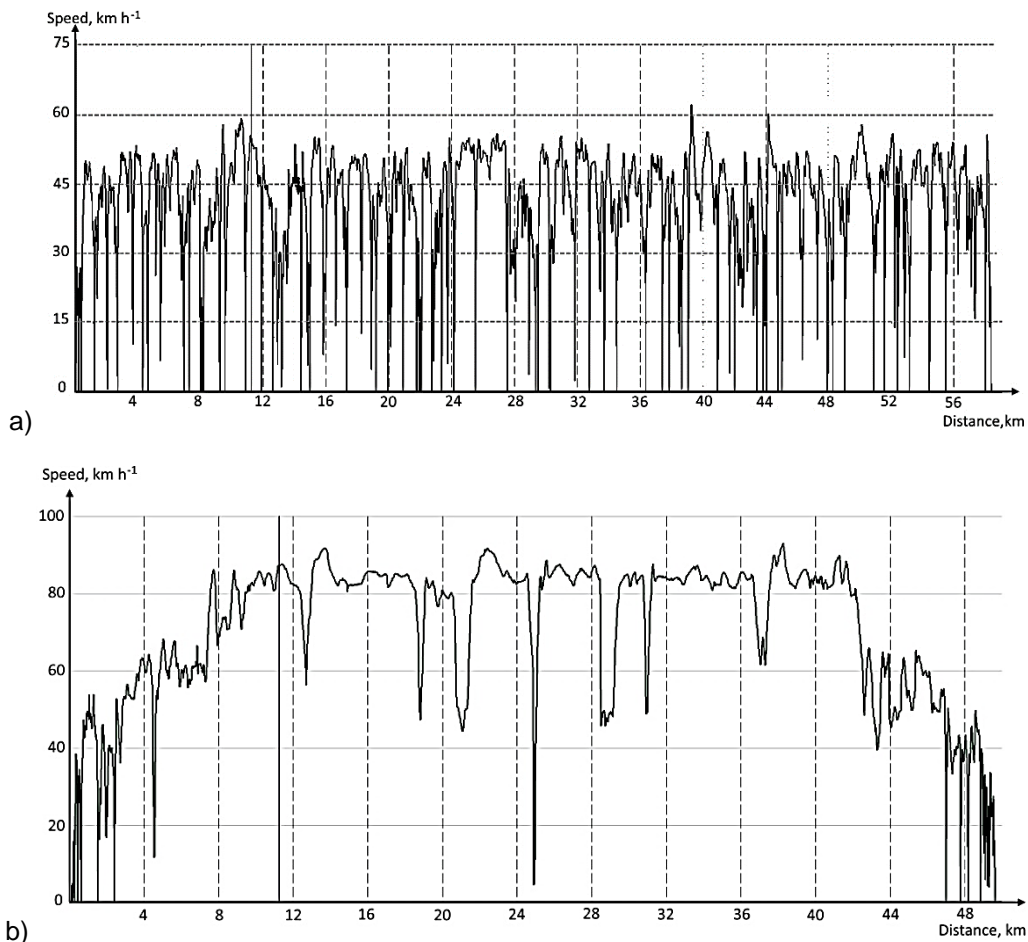
Figure 4. Speed on road test routes: a) Jelgava city route; b) non-urban route.

In view of the fact that the electric car had a 96 V battery system, in the driving regimes when a lot of current was drawn from the batteries, e.g. when accelerating, the voltage considerably decreased. The nominal voltage of every battery was 3.2 V. The BMS was set to stop the charging process if the voltage of some battery had reached 3.8 V. During charging, the total voltage of the battery pack reached 113−114 V. Immediately after the charging, the voltage decreased to 100−101.5 V. At the beginning of the road test in urban driving, the voltage decreased to 95 V during medium-intense acceleration. During very intense acceleration, the voltage of a fully charged battery-pack decreased to 87 V. At the beginning of the road test, the voltage returned to the previous level when stopping at intersections. After covering half of the road test route, the voltage did not exceed 96.3 V when stopping, yet it decreased to, on average, 87.5 V when accelerating and to 86 V when intensively accelerating (Fig. 5). When cruising at

50 km h^{-1}, the voltage, on average, decreased to 92.6 V. At the end of the road test, when no electrical energy was consumed or when stopping, the voltage did not exceed 92.1 V; when accelerating, the voltage could decrease to 82.7 V. One can conclude after completing the road tests that if taking into account only the voltage of the batteries, a voltage of 92 V in the stopping regime was the lowest level, and the batteries needed to be immediately recharged. After driving only 1−2 km more, the batteries were almost fully discharged, reaching the minimum allowable discharge level. After driving on average 50 km in urban driving, the BMS often started giving warnings; it was activated when the momentary voltage of some battery element had decreased to 2.5 V (the critical level was 2.4 V).
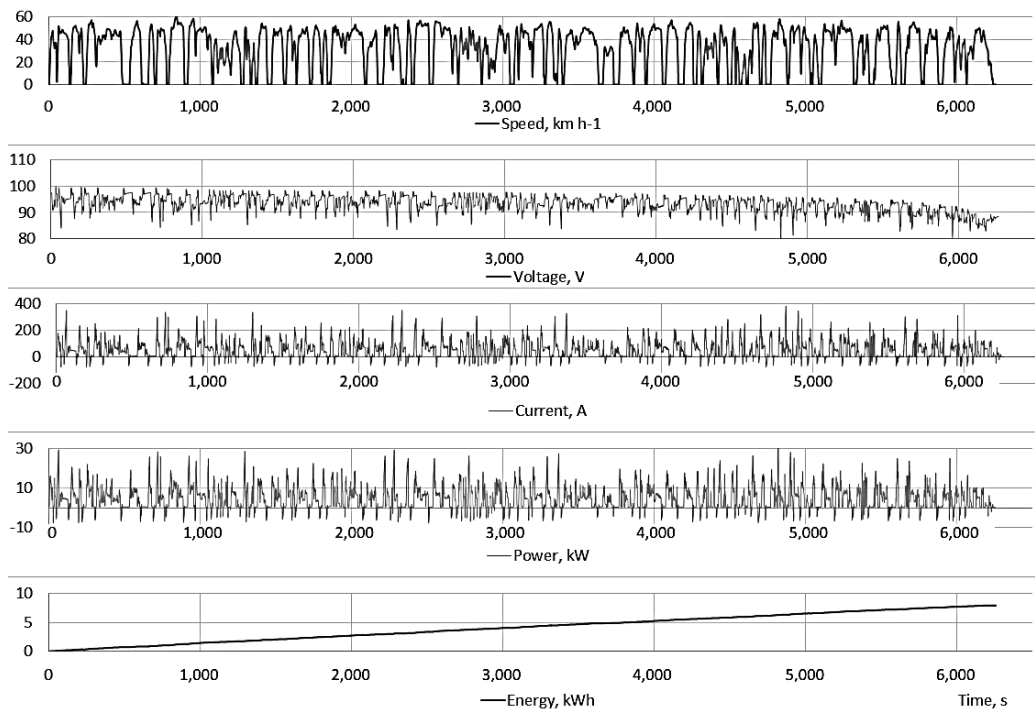
Figure 5. Electric car parameters in urban driving.

In urban driving, current and power changes were proportionally related to speed (Fig. 5). At the beginning of the road tests, the current reached 240–250 A during smooth acceleration, while the motor power output was 20−21 kW. During fast acceleration, the current could reach 350 A. The maximum power output at the mentioned peaks was 30 kW. The regenerative braking of the electric car Renault Clio was activated by pushing the brake pedal, while in the casting regime the regenerative braking was not activated. In the braking regime, the regenerative current reached 75 A, while the power – 7.5 kW. Compared with non-urban driving, this regime increased the electric car's range in urban driving. The regenerative level of the electric car Renault Clio was controllable, and it was set at 45% for the road tests. A regenerative level of above 50% creates an inadequate increase in braking force caused by the regenerative braking system before the main brakes have been activated. This results in a braking force

964

increase to be difficult to control by means of the braking pedal. When stopping, the electric car consumed an current of 4.8−5.0 A. With the batteries being partially discharged, no significant changes in current and power were observed under various driving regimes. When cruising at 50 km h⁻¹, the current reached 67−70 A. When accelerating fast during the final part of the road tests, the current reached 385 A, while the motor output power was 31 kW. The increase in current might be explained by a lower voltage of the battery pack, and a higher current is requited to ensure the necessary motor output power.

Road testing the electric car in non-urban driving was started as well as finished in the centre of Jelgava city. For this reason, the initial section of the route 6.5 km in length and the final one (6.5 km) are typical of urban traffic, and no electric parameter analysis was performed for the mentioned route sections (Fig. 6).
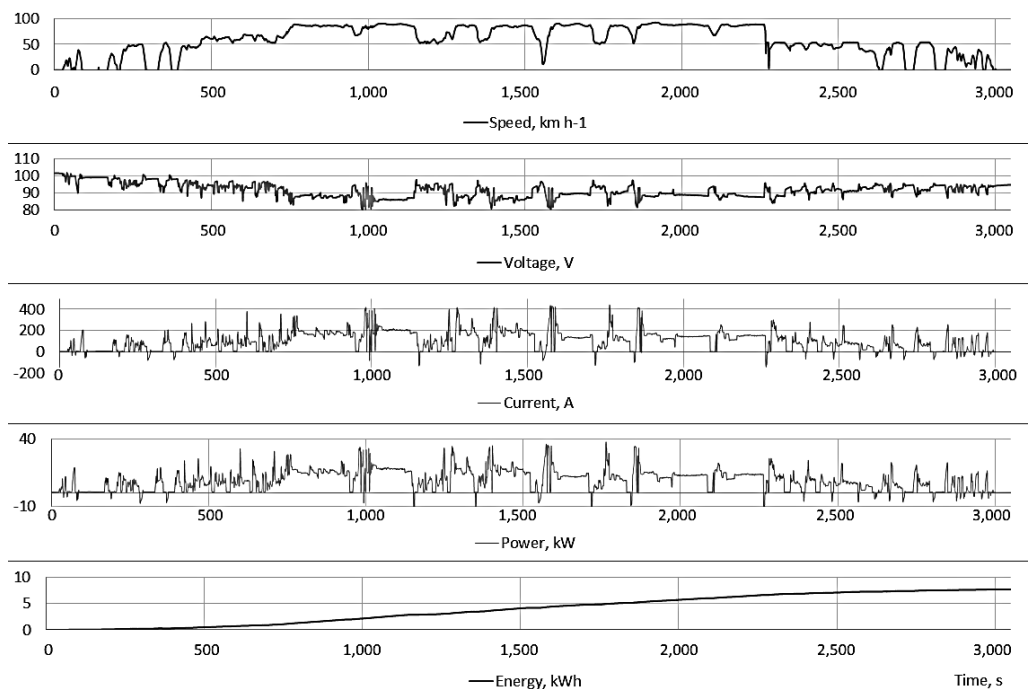
Figure 6. Electric car parameters in non-urban driving.

When starting the non-urban route section, the average voltage was 96.5 V. When accelerating, e.g. from 73.5 to 87.1 km h⁻¹, the voltage of the batteries decreased to 87.9 V. In the cruising regime at 87 km h⁻¹, the voltage of the batteries equalled 91.5 V, while the current reached 353 A. When accelerating fast, the maximum current reached 450 A, which was the highest value set for the motor controller. The motor output power at the maximum points reached 38.6 kW. A careful examination of the power and current curves reveals that the average values of these parameters were higher when driving away from the start than driving back down the route. This could be explained by a small average road slope angle of $\alpha = 0.6°$, which increases road resistance when driving away from the start and decreases it by the same value when driving back. Regenerative

965

braking application in non-urban driving was less frequent, yet the values of electric parameters were much higher in non-urban driving than in urban driving. Braking from a speed of 86.3 km h^{-1} to 50.5 km h^{-1}, the batteries were charged at an current of 140 A or a power of 13.2−13.4 kW. Cruising at 85 km h^{-1} consumed a 149−150 A current, which ensured a motor output power of 13.2−13.4 kW. It has to be noted that these parameters were measured right after the batteries were recharged, which means that the power supplied to the motor was lower than the value of the efficiency factor of the wiring-inverter-motor system, while the power transmitted to wheels was lower than the value of the efficiency factor of the motor-transmission system.

Due to higher average battery discharge current values when driving the last 10 kilometres of the route, the BMS tended to give warnings more often in non-urban driving than in urban driving, which indicated the negative effect of fast acceleration on the battery lifetime.

Based on the road test results, it is intended to do road tests with a 6.4 V higher voltage of the battery pack, which is within the allowable limits for the motor and the control system.

An excessive voltage drop in the battery pack during acceleration indicates a decrease in the working capacity of some battery cells. It is required to control the voltage of every individual battery pack cell during acceleration and, in necessary, change the defective battery cell. An alternative option for the cell change is to set the controller Sigmadrive to limit the maximum current to less than 400 A, which would allow saving the batteries. An expected decrease in the dynamics of the electric automobile should be minimum.

If converting a vehicle to electric power in next projects, it is necessary to choose a system with higher voltage, e.g. 144 V. Such a system decreases the maximum current during fast acceleration and ensures a safer mode for the batteries and a longer lifespan of the batteries.

CONCLUSIONS

1. A methodology for electric vehicle road tests in urban and non-urban driving was developed and approbated by means of a data logger for measuring electric parameters.

2. After recharging, the voltage of the battery pack was within a range of 113−114 V. Upon starting the road test immediately after the batteries were charged, the battery voltage was 100−100.5 V. After starting driving, the battery voltage decreased to 97−98 V in the no-load regime.

3. During the road tests, the battery voltage tended to decrease, which could be observed most explicitly at a no-load voltage. After the voltage has decreased to 92 V, the electric car batteries have to be recharged, as a full battery discharge occurs after driving as many as 1−2 km.

4. The maximum current of 450 A was reached in non-urban driving. The corresponding maximum motor output power was 38.6 kW. In urban driving, the maximum current was 350 A and the corresponding power was 30 kW.

5. When smoothly accelerating in urban driving, the current did not exceed 240−250 A. When cruising at 50 km h^{-1}, the current reached 70−75 A.

6. When braking in urban driving, the regenerative current reached 75 A, while the power – 7.5 kW at the regenerative level of 45%. A regenerative level of above 50% creates an inadequate increase in braking force caused by the regenerative braking system before the main brakes have been activated.

7. The regenerative braking system performed more effectively in non-urban driving, generating an current of 140 A; however, its proportion in the energy balance was insignificant and could not considerably increase the non-urban distance travelled.

8. After driving a distance equal to 70% of the total distance covered, the BMS started giving warnings when accelerating the electric car, which indicated that the voltage of the weakest battery element had decreased to 2.5 V and the no-overload driving regime was activated. This driving regime does not allow exceeding the pre-set speed.

9. More energy was consumed in non-urban driving before the route turnaround point was reached (25 ± 0.1 km), as the average road slope angle in this route section was $\alpha=0.6°$. The road slope angle allowed saving energy on the way back.

10. Due to a decrease in the voltage of the battery pack when accelerating, it is intended to increase the voltage by 6.4 V, which is within the allowable limits for the motor and the control system.

11. Due to the fast voltage drop in acceleration regimes, it is necessary to do a battery test for the electric automobile or set the controller to limit the maximum current to less than 400 A.

12. If converting a vehicle to electric power, it is required to choose a system with higher voltage that ensures a lower peak current and a safer way of exploitation of the batteries.

REFERENCES

Banvait, H., Anwar, S. & Chen, Y. 2009. A Rule-Based Energy Management Strategy for Plugin Hybrid Electric Vehicle (PHEV). In *American Control Conference*. Hyatt Regency Riverfront, St. Louis, MO, USA, pp. 3938−3943.

Berjoza, D. & Jurgena, I. 2016. Ecological effect of electric vehicles on CO_2 emissions in Latvia. In *Engineering for rural development*. Latvia University of Agriculture, Faculty of Engineering. Jelgava, Latvia. Vol. **15**, pp. 1199−1205.

Berjoza, D. & Jurgena, I. 2013. *Research of the exploitational and infrastructural parameters of electric vehicles* : monograph. Latvia University of Agriculture. Faculty of Engineering. Jelgava : Latvijas Lauksaimniecības universitāte, 1 CD, pp.163.

Butler, K.L., Ehsani, M. & Kamath, P. 1999. A Matlab-Based Modeling and Simulation Package for Electric and Hybrid Electric Vehicle Design. *IEEE Transactions on Vehicular Technology* **48**(6), November 1999, pp. 1770−1778.

Li, S.G., Sharkh, S.M., Walsh, F.C. & Zhang, C.N. 2011. Energy and Battery Management of a Plug-In Series Hybrid Electric Vehicle Using Fuzzy Logic. *IEEE Transactions on Vehicular Technology* **60**(8), October 2011, pp. 3571−3585.

Moreno, J., Ortuzar, M.E. & Dixon, J.W. 2006. Energy-Management System for a Hybrid Electric Vehicle, Using Ultracapacitors and Neural Networks. *IEEE Transactions on Industrial Electronics* **53**(2), April 2006, pp.614−623.

Musardo, C., Rizzoni, G., Guezennec, Y. & Staccia, B. 2005. A-ECMS: An Adaptive Algorithm for Hybrid Electric Vehicle Energy Management. *European Journal of Control* **11**, pp. 509–523.

Experimental research on compatibility of mineral and biobased hydraulic oils

A. Birkavs[*] and R. Smigins

Latvia University of Life Sciences and Technologies, Faculty of Engineering, Motor Vehicle Institute, 5 J.Cakstes blvd, LV3001 Jelgava, Latvia
[*]Correspondence: aivars.birkavs@llu.lv

Abstract. The use of biobased hydraulic oils becomes more popular in the different industries, but especially in agriculture machinery. This is stimulated by the fact that significant amount of hydraulic oils effluence in the environment and therefore leaves a negative impact to the ecosystem. Besides of that, the part of sold hydraulic oils grows and now forms approximately 15% of total oil consumption amounts worldwide (Nagendramma & Kaul, 2012).
The aim of this research was to study the compatibility of the comercially produced mineral and biobased hydraulic oils, identify viscosity of a different mixtures in the entire work temperature range, as also changes of anti-frictional properties. Two different oils and three mixtures were tested. Special hydraulic experimental apparatus was established for visual observation of fluid properties. Sliding friction bench was used for the comparision of friction properties.
The results showed that change of the working pressure and temperature of the hydraulic oil in the various mixtures of mineral and biological hydraulic oils do not change its original appearance. It was observed that the highest viscosity 71 mm^2 s^{-1} and worst anti-friction properties is for the 50% mix of mineral and biologial hydraulic oil at 20 °C ambient temperature.

Key words: biobased, mineral, hydraulic oil, compatibility.

INTRODUCTION

Nowadays hydraulic systems are found in a variety applications realizing most significant work converting mechanical power in hydraulic power. The modern aviation, heavy industry and agricultural machinery is no longer inconceivable without the built-in hydraulic systems. The main advantages of modern hydraulic systems are simple structure, light weight and easy maintenance and installation. One of the main component of such systems is hydraulic fluid the aim of which is transmit and distribute forces based on its main advantage over other materials – incompressibility. The importance of hydraulic fluids is very essential as they play a key role in operation and protection of main components of hydraulic system, which is working on high temperatures and pressures. Insufficient protection could lead to a shorter maintenance intervals and expensive problems due to an increased wear, tear, cavitation and corrosion. Manufacturers of such systems usually specify the type of hydraulic liquid based on characteristics of equipment operation, necessary pressure, and expected temperatures in the system and outside of it. Therefore hydraulic liquids have many

properties and characteristics, which should be known to ensure correct system operation.

Most popular hydraulic liquids are mineral based oils due to its lower costs and availability, as also synthetic lubricants mainly developed to perform high temperature ranges in aviation and military equipment (Paredes et al., 2014). Although synthetic oils have eco-friendly characteristics and have better impact on environment compared to mineral based oils, the main disadvantage of all oils is effluence in environment mainly due to a damaged hydraulic systems. It results with effluence of about 20–30% of all sold amount of hydraulic oil. This is the quantity of oil, which poses a serious threat to the ecosystem, especially if the oil is used in protected nature areas. Besides of that, professional mechanics and also other technical specialists are exposed to these oils mainly by dermal contact promoting irritation of skin. As some researches have shown that mineral based oils have possible carcinogenic effect, than substitution of such oils would be valuable for those people who have a risk to be in contact with it practically every day. Such replacement could be done by biological or renewable oils. In that case there exists a term – 'Green Tribology', which discusses a concept of this area and its relation to the other ones formulating 12 principles, where one of them is biodegradable lubrication, connected with the use of biodegradable and environment friendly lubricants (Nosonovsky & Bhushan, 2010). Lubricants, which are based on different renewable oils (corn, soybean, etc.) usually have an excellent lubricity compared to mineral based oils, but they have also insufficient thermal and oxidative stability which makes oil polymerization to a plastic-like consistency (Mannekote & Kailas, 2009). This problem could be resolved by different chemical modifications of oil or usage of additives.

Biobased oil is a lubricant, containing of at least 95% (by weight) base fluid and not more than 5% (by weight) additives and having derived carbon ratio at least 70% from renewable materials. It cannot contain mineral oil, as well as toxic, carcinogenic, mutagenic, teratogenic or environmentally hazardous additives. In general 62% of the total exploitable renewable natural resources which are used for the production of oil are plants containing oil (rape, sunflower seeds, palm trees, etc.), 33% of the total renewable raw materials used by wood waste, but 5% is algae, bacteria and genetically modified plants (Bart et al., 2013). Biobased hydraulic oil can be used both in stationary and mobile equipment. The total share of it is growing rapidly and these oils starting to replace mineral based hydraulic oils. Although it is not mandatory to use organic oils separate vehicle users have already tried and understood the opportunities it offers, thus preserving the environment from pollution.

Studies done before do not confirm any negative impact of biobased hydraulic oil on hydraulic system. The experiments did not show any signs of increased wear of the oil pump that might indicate on the poor anti-friction properties of the hydraulic oil. There was not found aeration or cavitation due to a high viscosity (Bart et al., 2013).

For example, Kassfeldta (Kassfeldta & Daveb, 1997) was tested one mineral based hydraulic oil and three environmentally adapted hydraulic oils, from which there were two mixtures of vegetable base oil and synthetic esters, and the last was based on synthetic esters only. Researchers determined lubricant capability properties by measurements of the capability of each oil to build a film in an elastohydrodynamic contact. The results showed that environmentally adapted oils at 40 °C give a thicker film than the mineral oil, but at 80 °C there is no significant difference between the

different types of oil in their capability to build a lubricating film (Kassfeldta & Daveb, 1997).

Other researchers (Silva et al., 2015) conducted the study, the purpose of which was to develop new hydraulic biolubricants based on vegetable oils and to investigate their tribological behavior under conditions of boundary lubrication. The tribological performance of the developed lubricants was analysed in an HFRR apparatus. Researchers have found that biobased oils have satisfactory tribological properties, which were considered as a potential hydraulic oils for replacing mineral based hydraulic oils (Silva et al., 2015).

Another study (Paredes et al., 2014), which was realized to analyse potential industrial applicability of vegetable bases, realizing research with two mineral and two biobased hydraulic oils. Viscosity measurements have been carried out at three temperatures: 313.15 K, 343.15 K and 363.15 K and a pressure up to 250 MPa. In case of behaviours of the four liquid oils, they have found that the oils with a vegetable base should offer better energy efficiency due to the thinner protective layer they grant specially at low temperatures therefore extending life cycle of hydraulic systems (Paredes et al., 2014).

Based on the literature, the choice of hydraulic oil is dependent on the type of hydraulic system, operating temperature range, working and natural conditions, as well as the pump type, working pressure and environmental considerations. In case of the use of hydraulic oil, the oil viscosity is important to the specified temperature range. The lower viscosity means the system is less inert throughout the operation. On the other hand, the viscosity must be sufficiently large to ensure safety and lubrication of the lubrication pump and other moving parts. Knowing the range of operating temperature and changes of the viscosity depending on the temperature of the proposed oil, it is possible to choose exact oil for the hydraulic system.

The aim of this research was to carry out a practical study on the compatibility of the mineral and biobased hydraulic oils in hydraulic systems of tractors, as also trying to understand if there will be any advantages or disadvantages in case of mineral oil change to biobased oil. In that case it is important to understand if the hydraulic system must be cleaned before biobased oil use, identify viscosity changes of a different oil mixtures in the entire work temperature, detect how fast each oil is heated at the same working conditions, as also identify changes of anti-frictional properties. All these issues have a direct impact on productivity of tractor units, as also on different operations: loading, lifting, floating, etc.

MATERIALS AND METHODS

Experiments were realized using two different oil types and three mixtures. There was used a mineral based *46 HLP* hydraulic oil produced by LIQUI MOLY and characterized as a high performance hydraulic oil with optimal anti-wear properties and excellent oxidation resistance and operating intervals. As a biobased hydraulic oil was chosen *Agra Utto Bio* produced by AVIATICON. This oil is characterised as universal tractor transmission oil, contains ester and additive, and it confirm to the API GL4 class. The main parameters of both oils are reflected in the Table 1.

Table 1. Main parameters of the used oils

Parameters	HLP 46	Agra Utto Bio
Density, 15 °C	0.880 g mL^{-1}	0.903 g mL^{-1}
Viscosity, 40 °C	46 mm^2 s^{-1}	46.50 mm^2 s^{-1}
Viscosity, 100 °C	6.7 mm^2 s^{-1}	10.00 mm^2 s^{-1}
Viscosity index	97	211
Flash point, °C	226	230
Pour point, °C	-25	-41
Neutralisation number, mg KOH g^{-1}	0.5	4.7
Solubility	Insoluble in water	NA
Degradability	Not readily biodegradable	Biodegradable

*NA – not available.

All used oils and mixtures prepared for the tests are as follows: 1 – mineral based hydraulic oil with 0% addition of biobased hydraulic oil (marked as 'M + 0% Bio'); 2 – mineral based hydraulic oil + 25% addition of biobased hydraulic oil (marked as 'M + 25% Bio'); 3 – mineral based hydraulic oil + 50% addition of biobased hydraulic oil (marked as 'M + 50% Bio'); 4 – mineral based hydraulic oil + 75% addition of biobased hydraulic oil (marked as 'M + 75% Bio'); 5 – biobased hydraulic oil with 0% addition of mineral based hydraulic oil (marked as 'Bio + 0% M'). Prepared mixtures can be seen in Fig. 1.
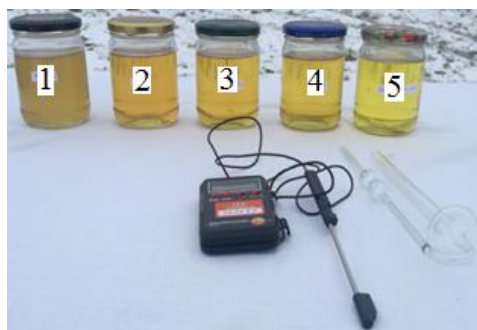
Figure 1. Samples of tested oils and created mixtures.

Oil heating measurements

Special hydraulic experimental apparatus was established by the authors for the visual observation of mixtures of mineral and biobased hydraulic oils at different operating temperatures (Fig. 2.).

Figure 2. Special hydraulic experimental apparatus established for the tests.

It consists from all necessary units to perform a pressure in the system as it would be in real working conditions. The main components of the system could be seen in Fig. 3. Electric motor, with rotation frequency 1,480 rpm^{-1}, was used to drive a pump. In addition, the safety valve was used operating a little before the maximum pressure of the pump (240 bar) is reached.

The procedure to determine condition of the oil is as follows. After switching of electric motor, it is verified if the hydraulic line is fully filled up with oil and if there is no any leakage. The next step – reduction of adjustable throttle aperture have been started activating stopwatch and registering and controlling pressure and temperature of the oil, as also looking for visual changes. Once the oil is warmed up to 65 °C, the square of the aperture of adjustable throttle is increased and control of the pressure, temperature and visual changes is continued. After an hour of such operation the aperture of adjustable throttle is fully opened and all necessary parameters have been registered once more.
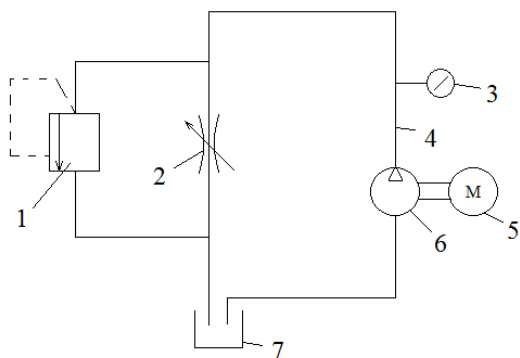
Figure 3. Technical scheme of special hydraulic experimental apparatus established for the tests: 1 – safety valve; 2 – adjustable opening throttle; 3 – gauge; 4 – hydraulic line; 5 – electric motor for hydraulic station operation; 6 – oil pump; 7 – return reservoir.

Based on the operation principles of established hydraulic experimental apparatus, it is possible to regulate operation pressure in hydraulic system till 240 bars and assure the hydraulic oil temperature changes from -10 °C to 100 °C. Besides the visual observations, the temperature measurements were realized in order to find out the mixture, which heats faster at the same operation conditions. The tests were performed at ambient temperature 0 °C and air relative humidity 80%.

Viscosity measurements

Viscosity measurements of oils and their mixtures were realized using glass capillary viscometer VPZ – 4, which is intended for the determination of kinematic viscosity of liquids. Preparation for experimental work (washing and drying of viscometer) based on standard procedures. For the realization of experiment was used also manual air baster, stopwatch, thermometer, calibrated flask. Viscosity measurements were performed under field conditions in the temperature range from – 15 °C to +20 °C.

Friction measurements

Sliding friction bench was used for the comparison of friction properties (Fig. 4.). In order to ensure the full functioning of the bench, in addition there was used multimeter, torque wrench, stopwatch. Experiments were carried out under laboratory conditions at ambient temperature (+19 °C). For the operation of the bench there were used a 12 V battery and multimeter switched in electric circuit for the control of the

amperage (A). Unused friction bricks and the roller was prepared for the tests. Friction block was changed after the usage of each oil mixture. Bricks and the roller was cleaned before check of each oil sample. In order to determine the anti-friction characteristics, 10 Nm load was applied to torque wrench and amperage was controlled. The aim was to determine the changes of the amperage at the same load and then measure the size of the wear on the block.

Figure 4. Side view of sliding friction test bench with friction blocks used in the tests: 1 – friction block; 2 – steel disc; 3 – oil reservoir.

RESULTS AND DISCUSSION

During testing conditions realized in hydraulic experimental apparatus, similar to those which is possible to get in hydraulic system of agricultural machinery, was observed that mineral and biobased hydraulic oils are practically compatible. There was not observed any visual changes in the oil mixtures during regulation of operation pressure of hydraulic experimental apparatus and the temperature of the oil mix in it. Besides of that there was not also observed any changes in its original appearance.

Tests have showed that mineral based oil warms faster than biobased oil. For example, biobased hydraulic oil achieved maximal testing temperature about 60 second later than the mineral one. Oil mixtures have very similar results to mineral oil with small difference based on the amount of added biobased additive. This could be connected with the molecular structure of biobased oil, which is slightly different from the mineral oil. Mineral oil molecules have tendency to radically change its size based on the impact of temperature. While the biobased oil molecules does not change its size so radically, and therefore biobased oil viscosity under temperature influence don't change so quickly (Nathan et al., 2012). Heating curves of hydraulic oils and its mixtures could be seen in Fig. 5.

Technical characteristics of both oils shows that pour point of mineral based oil is -25 °C, but for biobased oil – only at -41 °C (Table 1). Based on these characteristics can be deduced that the results of the experiments carried out at the -10 °C will show a drastic difference, but obtained data showed that biobased oil viscosity at this temperature is 206.1 $mm^2 s^{-1}$, but mineral oil viscosity is 190.0 $mm^2 s^{-1}$, but other oil mixtures based on the growing of organic oils impurity showed viscosity gradually reduction till the biobased oil viscosity.
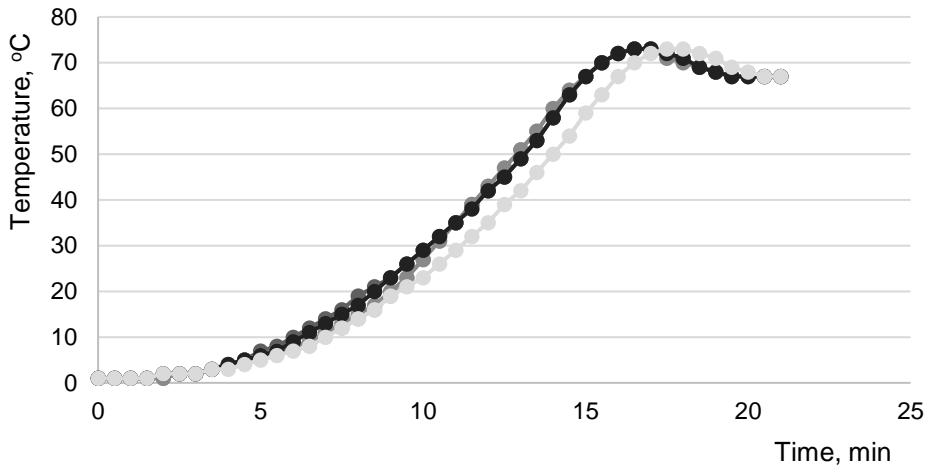
Figure 5. Heating curves of hydraulic oils and its mixtures: M + 0% Bio – ━●━; M +25% Bio – ━●━; M +50% Bio – ━●━; M +75% Bio – ━●━; Bio + 0% M – ━●━.

The increase in temperature showed decrease of distinction. The measurements taken at 20 °C showed mineral oil viscosity about 71.84 mm^2 s^{-1}, but the biobased oil viscosity at 65.86 mm^2 s^{-1}. Comparison of the viscosities of the hydraulic oil and its mixtures can be seen in Fig. 6.
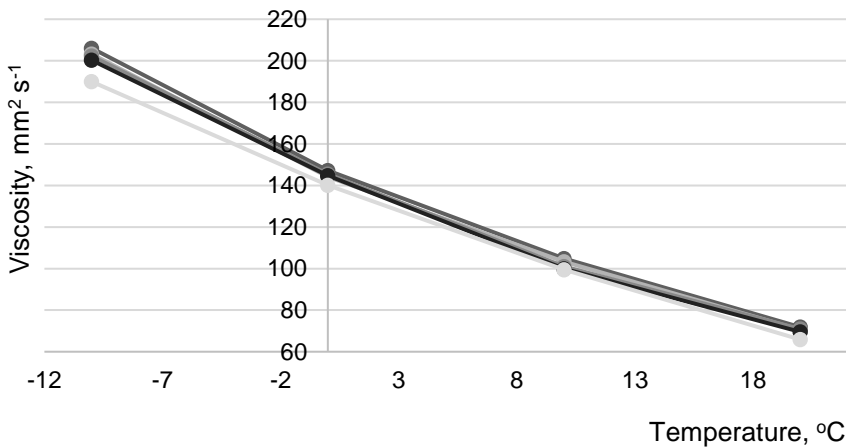
Figure 6. Viscosity curves of hydraulic oils and its mixtures: M + 0% Bio – ━●━; M +25% Bio – ━●━; M +50% Bio – ━●━; M +75% Bio – ━●━; Bio + 0% M – ━●━.

It should be noted that oil specification indicates that hydraulic fluid contains anti-abrasive additives, but it does not guarantee that the oil will protect parts from the increased wear. This parameter is important as due to a bad anti-friction properties there is possible increased wearing of all devices involved in hydraulic system. Experimental results of the mixtures using sliding friction bench is showed in Fig. 7. Data showed that biobased hydraulic oil have the best protection of hydraulic system from wearing, but

50% mixture with mineral based oil have the worst antifriction characteristics. It could be explained by chemical reaction between main components of oils, which are not compatible and therefore such mixture has shown largest wear zone. As it is seen, such situation is mainly observed for mixtures, where biobased oil concentration is larger than 50%. Wear zone for separate oils – weather it mineral or biobased – is very similar.
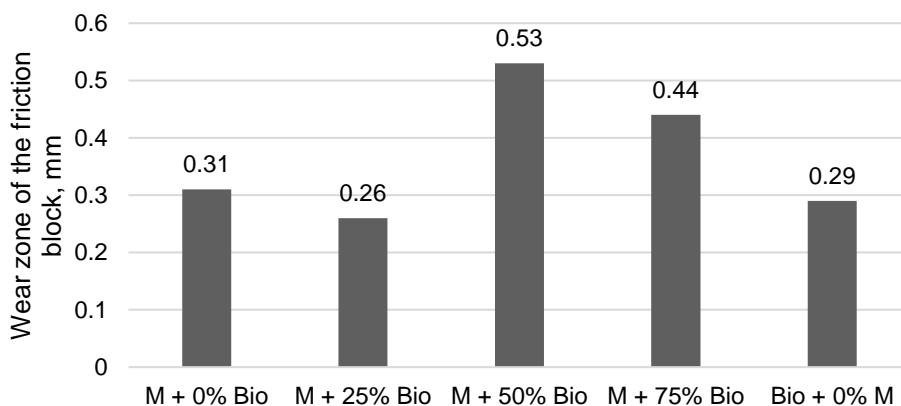
Figure 7. Graph of the wear zone of friction blocks for different oil types and their mixtures.

In general, the characteristics of the biobased hydraulic oils is good enough for use in hydraulic systems of the vehicles, as also oil mixture (M + 25% Bio), as has been shown, can ensure normal operation of hydraulic systems.

CONCLUSIONS

Based on the research of all oil mixtures it could be concluded that mineral based and biobased hydraulic oils are compatible as there was not observed any visual changes in the oil mixtures during regulation of operation pressure and simulating of real working conditions in the hydraulic system. Research on the viscosities of hydraulic oils at one and the same temperature did not show rapid changes based on the different percentage of admixture of biobased oil. Largest difference of viscosities of mineral based oil over biobased oil was observed only at –10 °C. Increasing the percentage of biobased hydraulic oil, viscosity of a mixture decreased. Besides of that, experimental results using the sliding friction bench showed that the worst anti-friction properties and the largest wear occurred using mineral based hydraulic oil by 50% and 75% biobased oil addition, but the smallest wear occurred using hydraulic oil with 25% organic additive. Therefore only small amount of biobased oil addition can ensure acceptable wear and a positive impact on environment. Usage of large mixtures are not recommended.

REFERENCES

Bart, J.C.J., Gucciardi, E. & Cavallaro, S. 2013. *Biolubricants: science and technology.* Woodhead Publishing Limited, 944 pp.

Kassfeldta, E. & Daveb, G. Environmentally adapted hydraulic oils. *Wear* **207**, Issue 1–2, 41–45. DOI:10.1016/S0043-1648(96)07466-2

Mannekote, J.K. & Kailas, S.V. 2009. Performance evaluation of vegetable oils as lubricant in a four stroke engine. In: *Proc. 4th World Tribology Congress*. Kyoto, Japan, 6–11 September, pp. 331.

Nagendramma, P. & Kaul, S. 2012. Development of ecofriendly/biodegradable lubricants: An overview. *Renewable and Sustainable Energy Reviews* **16**, 764–774.

Nathan, S. Mosier, M. & Ladisch, R. 2012. *Modern Biotechnology.* United States of America: Willey, 433 pp.

Nosonovsky, M. & Bhushan, B. 2010. Green tribology: principles, research areas and challanges. *Phil. Trans. R. Soc. A* **368**, 4677–4694. DOI: 10.1098/rsta.2010.0200

Paredes, X., Comunas, M.J.P., Pensado, A.S., Bazile, J.P., Boned, C. & Fernandez, J. 2014. High pressure viscosity characterization of four vegetable and mineral hydraulic oils. *Industrial Crops and Products* **54**, 281–290.

Silva, M.S., Foletto, E.L., Alves, S.M., Dantas, T.N.C. & Dantas Neto, A.A. 2015. New hydraulic biolubricants based on passion fruit and moringa oils and their epoxy. *Industrial Crops and Products* **69**, 362–370. DOI: 10.1016/j.indcrop.2015.02.037

An assessment of stratification of exhaust gases from gasoline and diesel engine

A. Birkavs[*] and R. Smigins

Latvia University of Life Sciences and Technologies, Faculty of Engineering, Motor Vehicle Institute, 5 J.Cakstes blvd, LV3001 Jelgava, Latvia
[*]Correspondence: aivars.birkavs@llu.lv

Abstract. Research the aim of which was to find out stratification of main exhaust components outside the tailpipe of the vehicle was realized in Alternative Fuels Research Laboratory of Latvia University of Agriculture using two commercially produced testing vehicles (diesel and gasoline) and exhaust gas analytical system AVL SESAM FTIR. Additionally there was created a gas testing camera allowing to measure concentration of exhaust gas components in different heights and windless conditions. Regulated and unregulated emissions from gasoline and diesel engines were measured and discussed. Results obtained during the measurements showed main stratification of toxic components from both engine types from 0.6 to 1.1 m from the ground making a risk to get some health problems by inhalation, especially for children. Main components (NOx, CO, HC) of exhaust gases of gasoline engines stay in the air for about 15 minutes in height of 1.0 m from the ground level, while methane and acetylene stay in the air for a 15 minutes in height of 0.6 m from the ground level.

Key words: exhaust gases, stratification, diesel, gasoline, engine.

INTRODUCTION

Internal combustion (IC) engines are widely used in transport sector for a long time leaving a positive impact on almost any sector globally as any other invention. In addition IC engines leave also an important impact on environmental conditions as they have been considered as main contributors to environmental pollution based on the amount and consistence of emitted components. Main part of those components is the result of various processes taking part during the combustion of fuel in the cylinders of the engine – incomplete combustion, combustion of non-carbon components, different reactions between components under complicated conditions, etc. The main air quality affecting componets from diesel and gasoline engines, which are also regulated by EURO emission standards, are nitrogen oxides, carbon monoxide, hydracarbons and particulate matters. The concentration of those components are strongly connected with driving conditions, vehicle technology, maintenance of the vehicles, etc. Despite the fact that engine technology all the time is under improvement to meet more stringent emission standards, possibility to develop more efficient and low cost emission control systems becomes more complicated.

Despite to all improvements, growth in global road emissions are expected mainly due to a prognosed increase in growth of vehicle owners worldwide reaching 2 billion vehicles till 2050 (Rothengatter et al., 2011). Additional problem is also a gap between official and real-world emission results, which was intensively analyzed by researchers due to diesel emission scandal in recent years. The research realized by International Council on Clean Transportation (ICCT), analyzing 11 data sources covering 14 years and 6 countries, and almost 600,000 vehicles, have found that the gap between official vehicle CO_2 emissions and real-world CO_2 emissions continues to grow – from 8% in 2001 to 38% in 2014 (Tietge et al., 2015). It is expected that the widening gap will add 1.5bn additional tonnes of CO_2 for 2030 increasing the prospects of dangerous and uncontrollable climate changes (Mind the gap, 2015). Another research done due to a diesel emissions scandal discovered that diesel cars in EU meet official limit for NO_x mainly in laboratory conditions, but emit far more pollution in real driving on the roads and therefore the global human health impact from NO_x excess in exhaust emissions could result in at least 38,000 premature deaths due to heart and lung disease and strokes (Anenberg et al., 2017). Additionaly breathing of fuel fumes can affect human health causing irritation of eyes or respiratory tract. Despite to the fact that these effects could be experienced in short term, regular or prolonged exposure could be the reason for coughing, chestiness or even the risk of lung cancer or asthma.

Besides the direct impact of exhaust gas components emitted directly from fuel combustion there exists also synthesis of them in the atmosphere based on different chemical reactions. One of such examples is ozone, which is noxious pollutant at the ground level and is significant contributor of global warming (Johnson, 2017). Main ozone precursors are man-made and emitted mostly by transport, especially diesel engines, which are leading source of NO_x (Johnson, 2017). Formation of ozone is over a day, starting in the morning, when NO, HC and CO is emitted from tailpipes of the vehices till mid-afternoon, when NO_x in the presence of sunlight form ozone together with VOCs. The formation of ozone and secondary organic aerosols from gaseous organic compounds emitted by diesel and gasoline are confirmed by laboratory experiments (Harrison & Hester, 2017).

Based on background knowledge, this study is designed to identify concentration level of the main exhaust gas components in the air in current conditions from two general transport groups (diesel and gasoline vehicles) to highlight potential risks for public health. It is important also due to a fact that Latvia has one of the oldest car fleet in the EU – average age is about 12.5 years (Smigins & Shipkovs, 2014). And the structure of the fleet shows rapid increase in the number of diesel vehicles. Besides of that it was observed that the largest, slow-moving traffic flow usually forms at the entrance doors of shops, near kindergardens, near sidewalks during congestions. where usually is possible to meet a lots of people and children. This research gives possibility to understand movement of exhaust gas components in such places and explain why it is necessary to avoid prolonged stay in it.

MATERIALS AND METHODS

To achieve the objectives of this study, evaluation of exhaust gases were conducted in laboratory environment using two vehicles – one with diesel engine (*Volvo V70 2.5TDI*) and another with gasoline engine (*Audi A6 2.6*). *Volvo V70* engine is a five-

cylinder, four stroke, OHC, water cooled, with effective power of 103 kW. *Audi A6* engine is a six-cylinder, four stroke, OHC, water cooled engine with effective power of 110 kW. Both engines are with industrial application and they have catalytic converters. Diesel fuel used in tests is based on standard EN590:2014 and gasoline based on standard EN228:2013.

Air sampling was realized in the Alternative Fuels Research Laboratory of the Latvia University of Agriculture in the laboratory controlled environment provided by gas testing camera and AVL SESAM FTIR multicomponent exhaust gas measurement system, which allows to measure up to 25 gases simultaneously and some components can be calculated from this process.

Gas camera with height of 2 m and a diameter of 0.6 m was prepared specially for experimental work. Gas supply valve was built-in 40 cm from the ground level for the regulation of gas inlet, as also gas exhaust valve was built in the top of gas camera. This allowed to measure concentration of exhaust gas components in different heights and windless conditions. Four different positions were chosen for measurements: 0.1 m, 0.6 m, 1.1 and 1.8 m. Measurements were started only when the engine was turned-off and camera was completely filled with exhaust gases realizing 0.5 min record for each position. Such measurements were realized 4 times with time interval 3 min. Overall, there is possible to highlight such measurement times: 0–2 min, 5–7 min, 10–12 min and 15–17 min. After each test gas camera was fully aired from exhaust gases. Filling of the camera with exhaust gases was realized in 5 minutes. During the tests each engine was operated in idle mode, following to the corresponding working temperature. Each vehicle was tested based on such methodology.

The schematic diagram of the experimental setup used for studying engine emission characteristics is shown in Fig. 1.
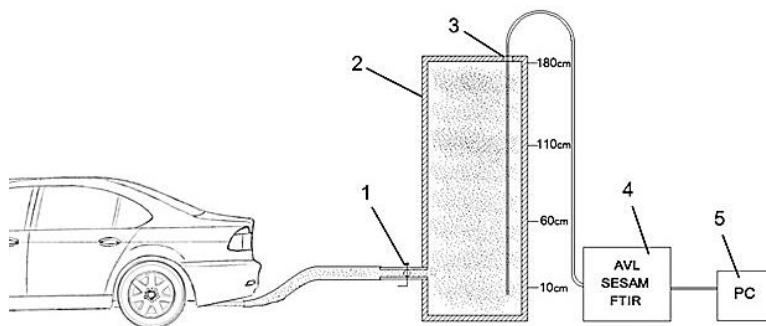
Figure 1. Schematic diagram of experimental setup: 1 – inlet valve; 2 – gas storage tank; 3 – probe loading aperture; 4 – multicomponent exhaust gas measurement system AVL SESAM FTIR; 5 – data recording PC.

During the research all gases were fixed, but detailed analysis were done only for the most essential regulated exhaust gas components: nitrogen oxides (NO_x), carbon monoxide (CO), carbon dioxide (CO_2) and unburned hydrocarbons (HC), sulphur dioxide (SO_2), as also unregulated exhaust gas components: ammonia (NH_3), methane (CH_4), acetylene (C_2H_2) and ethane (C_2H_6). The detected level of each component was averaged as the result of three replications to decrease the uncertainty. Each replication was the real time record with an interval of 1 sec.

Besides of that it was taken into account that stratification of gases was affected by the density of gas at defined pressure and temperature, which depends on its molecular weight.

RESULTS AND DISCUSSION

The experimental data, which characterizes the variation of different emissions for diesel engine based on time and height can be seen in figures below (Fig. 2). Results shows that main part of NO_x, CO and CO_2 emissions do not move in height for more than 0.6 m for a first 2 minutes after the blurring from tailpipe in environment. More substantial movement has been observed during next time period (5–7 min), when the gases divided evenly in all camera. After that it is possible to observe that all mentioned gases gradually settles and retains a significant concentration in next two measurements (10–17 min) in height up to 1.1 m. This is a height, which is freely accessible to children, pets and poses a significant health risk.
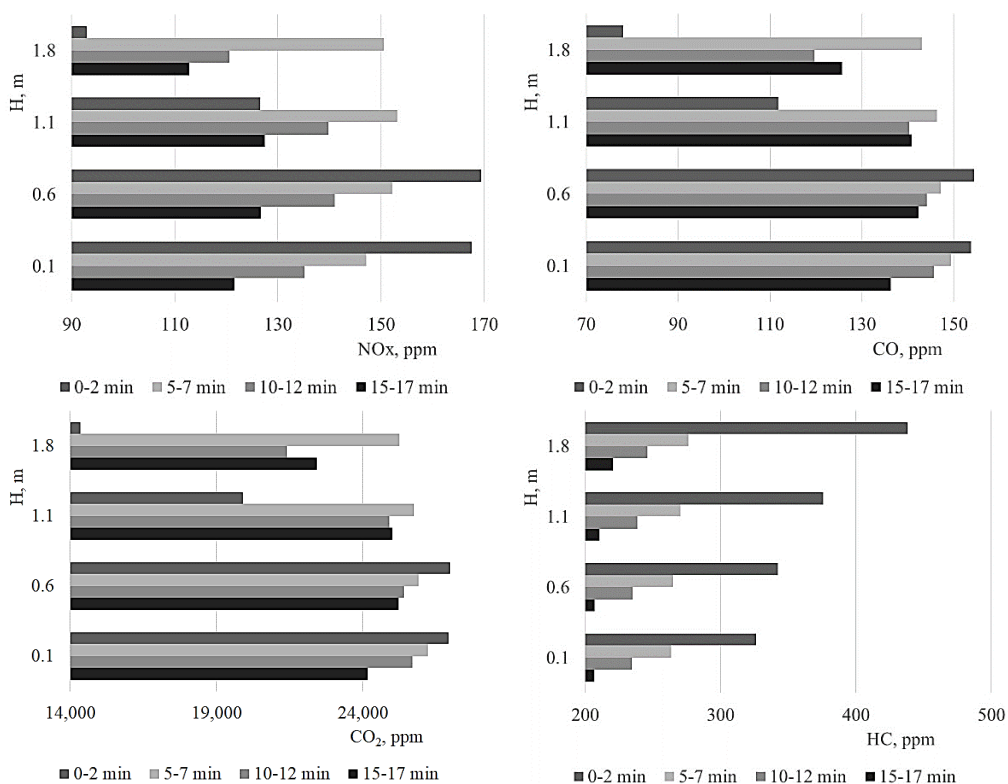
Figure 2. Variation of main regulated emissions (NOx, CO, CO_2 and HC) for diesel engine (Volvo V70 2.5TDI).

The situation is completely different for HC emissions, where the largest concentration in first two minutes after blurring from tailpipe in environment was registered in height of 1.8 m reaching 438 ppm. Significant HC concentration reduction till 206–220 ppm was observed in the next time periods with increasing of a time, but

the gas was evenly spaced around the camera. It means that HC emissions also increase the risk to reach a human respiratory tract.

Very similar results with small derogations were observed in case of gasoline vehicle. The main difference is expressed in the big gap in concentration of the main components compared to the diesel emissions. Fig. 3 summarizes main results obtained during the tests. As presented in Fig. 3, that main part of NO_x, CO and CO_2 emissions concentrate in height of 0.1–1.1 m for a first 2 minutes after the blurring from tailpipe in environment. Gradually all mentioned gas component concentration decreases reaching the highest level of around 1.1 m in height during the next 15 minutes (431 ppm for NO_x, 26598 ppm for CO).
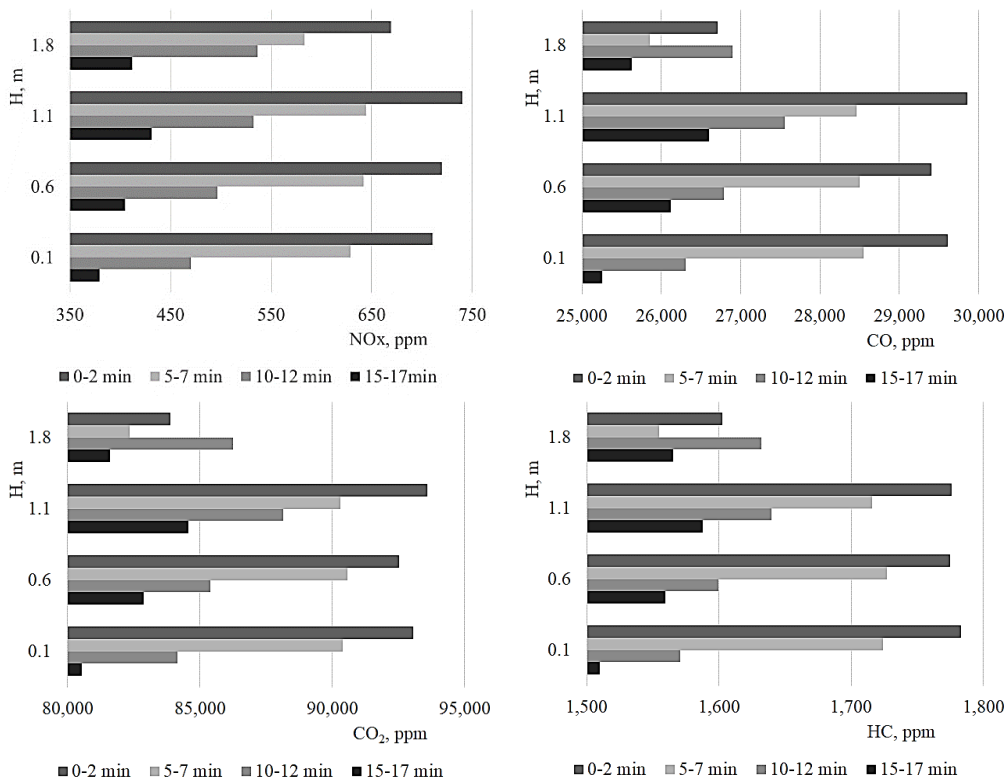
Figure 3. Variation of main regulated emissions (NO_x, CO, CO_2 and HC) for gasoline engine (Audi A6 2.6).

HC emissions are more pronounced in height of 0.1 m in a first 2 minutes gradually increasing concentration till 1.1 m in the next 10–15 min. Among all the pollutants, HC has the highest concentration in the air after defined period (10–15 min).

Differences in the amount of emitted components from gasoline and diesel engines could be explained by the difference in carbon (C) and hydrogen (H) content in fuel, which combine with oxygen (O) during combustion. This difference can vary in a couple of percentage between both fuels and therefore it is possible to observe variation of the produced emissions (especially, CO_2) during combustion.

Besides of those components, there was decided to turn attention on main unregulated emissions, like NH_3, C_2H_6 and others. Ammonia is one of the most abundant nitrogen compounds in the atmosphere and actively reacts with other compounds – in reaction with nitric acid it generates ammonium nitrate (NH_4NO_3), but in the reaction with sulphuric acid (($NH_4)_2SO_4$) in the gas phase it generates particulate matters (Borsari & Assuncao, 2017). There was not found correlation between NH_3 and other emissions, but possible values of this compound could be lower if the catalyst is not used, because results in literature claims formation of this compound within the automotive catalyst (Borsari & Assuncao, 2017). Current research showed that reduction of NH_3 in different time periods is not as drastic as in case of other regulated compounds and it remains stable throughout the volume of test camera in different time periods for both fuel types (Figs 4, 5). Reduction level do not exceed 5–7% after first 5 minutes from the start of tests.
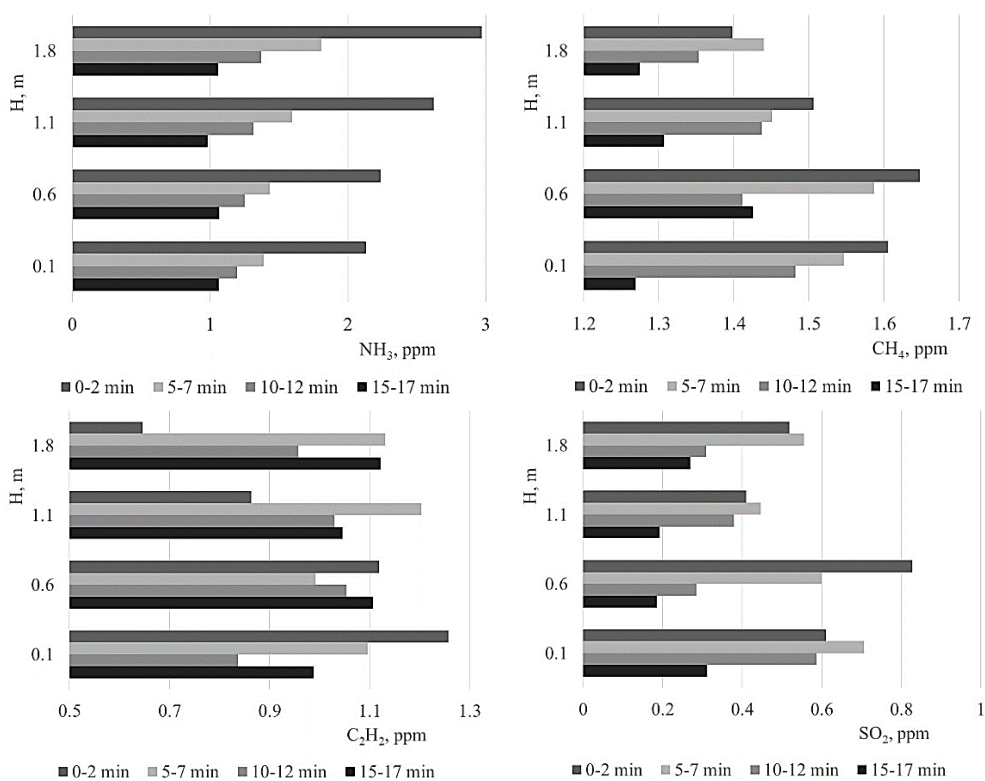
Figure 4. Variation of main unregulated emissions (NH_3, CH_4, C_2H_2 and SO_2) for diesel engine (Volvo V70 2.5TDI).

CH_4 is another important component, which participates in formation of GHG. This component cannot be estimated based on fuel carbon and usually are determined by combustion system type and control technology (Lipman & Delucchi, 2002). Methane emissions usually occur due to incomplete combustion along with unburned hydrocarbons (Lipman & Delucchi, 2002). In any case CH_4 emission level for gasoline engine is higher than for diesel and stratification nature is quiet similar – 15 minutes

after the start of the test largest concentration of methane emission is at 0.6–1.1 m (Figs 4, 5). As it was mentioned before, this is a height, which is freely accessible to children and poses a significant health risk.
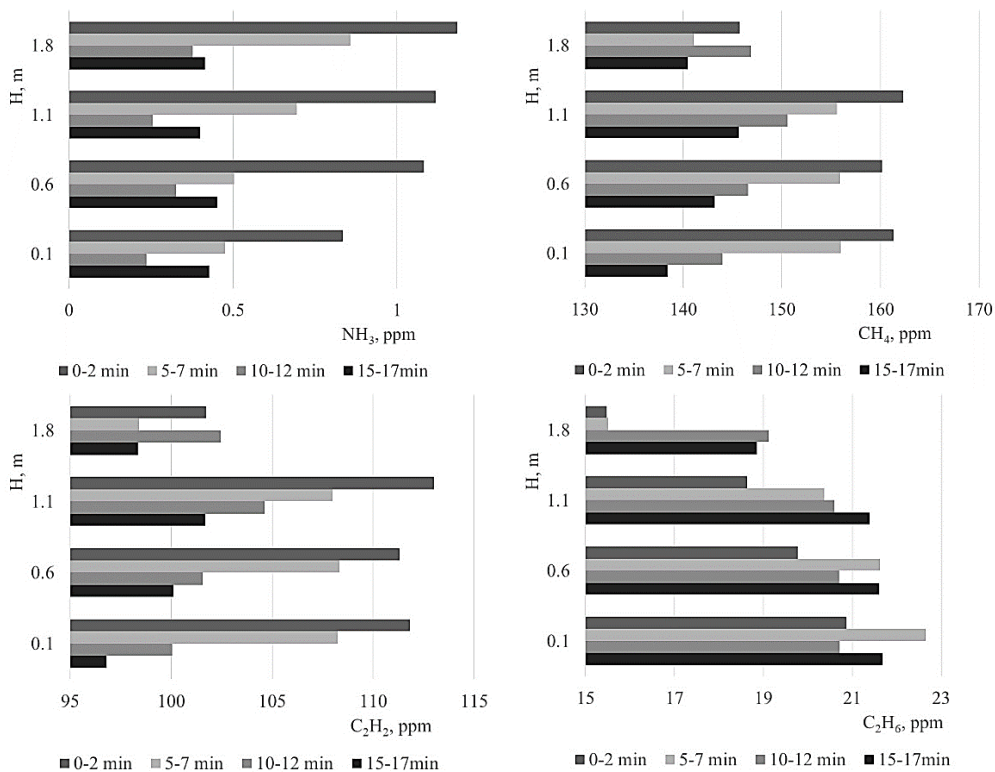
Figure 5. Variation of main unregulated emissions (NH_3, CH_4, C_2H_2 and C_2H_6) for gasoline engine (Audi A6 2.6).

Acetylene (C_2H_2) is another combustible gas, which could be found in engine emissions in negligible concentration. It is highly combustible and unstable gas, which produces high flame temperatures from 3,000 °C to 5,400 °C in combination with oxygen (Basha et al., 2016). Results on acetylene obtained during the tests did not show some united patterns as it was in case of other compounds, but it showed the similarity with methane – both of these gases reached maximal concentration in height of 0.6–1.1 m at the end of the test.

Sulphur dioxide (see Fig. 4), which is more characteristic for diesel engines did not show large concentration in air (max 0.82 ppm) and was mainly stratified in the height of the vehicle tailpipe (0.1–0.6 m). As it is known, presence of sulphur increase the risk of acid rain caused by SO_2, as also a fraction of this oxide can be converted in sulphuric acid, which is a particulate.

Ethane (C_2H_6) is another greenhouse gas, which is more characteristic for gasoline engines showed increase in concentration in the next time periods starting from 5th minute and almost in all volume of gas camera till 20–21 ppm (Fig. 5). This could be

explained by different chemical reactions taking participation in the presence of other compounds in the exhaust emissions.

CONCLUSIONS

Results showed that the concentration of main regulated components (NOx, CO, HC) stratify in the height close to the height of children (0.6 – 1.1 m), but some of them also in height close to adult (about 1.8 m), while others (C_2H_2, C_2H_6) did not show clear reduction tendencies. In overall, it can leave an important impact on health in the long term, if it is necessary to be in such environment each day. The problematic could be age and technical condition of the vehicles, as also the place where the concentration of vehicles is constantly high (like, congestions, parking lots, etc.). Therefore it is desirable to avoid a subsistence in the following locations for a long time, especially with children. In addition, each of the gases can stay in atmosphere for a long time to become well mixed making unfavorable conditions also globally and contributing development of smog.

Results could be different, if the research would be realised in conditions close to the real, taking in account different temperature, pressure and wind flow regimes. Therefore further investigations must be done to determine such information.

REFERENCES

Anenberg, S.C., Miller, J., Minjares, R., Du, L., Henze, D.K., Lacey, F., Malley, C.S., Emberson, L., Franco, V., Klimont, Z. & Heyes, C. 2017. Impacts and mitigation of excess diesel-related NOx emissions in 11 major vehicle markets. *Nature* **545**, 467–471. DOI:10.1038/nature22086

Basha, S.K., Rao, P.S. & Gopal, K.R. 2016. Experimental Investigation of Performance of Acetylene Fuel Based Diesel Engine. *Int. J. Adv. Technol.* **7**(1), 151. DOI: 10.4172/0976-4860.1000151

Borsari, V. & Assuncao, J.V. 2017. Ammonia emissions from a light-duty vehicle. *Transportation Research* **Part D 51**, 53–61.

Harrison, R.M. & Hester, R.E. 2017. *Environmental Impacts of Road Vehicles: Past, Present and Future.* Royal Society of Chemistry, 264 pp.

Johnson, E. 2017. Cars and ground-level ozone: how do fuels compare? *Eur. Transp. Res. Rev*. 13 pp. https://link.springer.com/content/pdf/10.1007%2Fs12544-017-0263-7.pdf

Lipman, T. & Delucchi, M. 2002. Emissions of Nitrous Oxide and Methane from Conventional and Alternative Fuel Motor Vehicles. *Climatic Change* **53**, 477–516.

Mind the gap. *European Federation for Transport and Environment* AISBL, 2015. 18 pp. https://www.transportenvironment.org/sites/te/files/publications/TE_Mind_the_Gap_2015_FINAL.pdf

Rothengatter, W., Hayashi, Y. & Schade, W. 2011. *Transport Moving to Climate Intelligence: New Chances for Controlling Climate Impacts of Transport after the Economic Crisis*. Springer Science & Business Media, 316 pp.

Smigins, R. & Shipkovs, P. 2014. Biofuels in transport sector of Latvia: experience, current status and barriers. *Latvian Journal of Physics and Technical Sciences* **51**, 32–43. ISSN 0868-8257. DOI: 10.2478/lpts-2014-0004

Tietge, U., Zacharof, N., Mock, P., Franco, V., German, J., Bandivadekar, A., Ligterink, N. & Lambrecht, U. 2015. *From laboratory to road: A 2015 update of official and 'real-world' fuel consumption and CO_2 values for passenger cars in Europe.* International Council on Clean Transportation Europe, 56 pp.

Effect of sunflower and rapeseed oil on production of solid particles and performance of diesel engine

J. Čedík[1,*], M. Pexa[1], M. Holůbek[1], D. Mader[1] and R. Pražan[2]

[1]Czech University of Life Sciences Prague, Faculty of Engineering, Department for Quality and Dependability of Machines, Kamýcká 129, CZ165 21 Prague 6, Czech Republic
[2]Research Institute of Agriculture Engineering, Drnovská 507, CZ161 01 Prague 6, Czech Republic
*Correspondence: cedikj@tf.czu.cz

Abstract. The development of biofuels for compression ignition engines is heading primarily to utilization of vegetable oils. Combusting of 100% vegetable oil in unmodified CI engine is usually not possible due to higher viscosity of the vegetable oil. In order to use 100% vegetable oil in CI engine the oil needs to be preheated, esterified or hydrotreated. Alternatively, in order to use raw vegetable oil in CI engine without preheating it is possible to use vegetable oil – diesel fuel blends or vegetable oil – butanol – diesel fuel blends in order to lower the viscosity of the fuel. The contribution focuses on comparison of the effect of sunflower and rapeseed vegetable oils on operational parameters of the turbocharged compression ignition engine, especially on production of solid particles. The measurement was carried out according to standardized NRSC test cycle. 5% and 20% concentration of vegetable oils in diesel fuel were used as a test fuels for the measurement while the diesel fuel was used as a reference. The count and size of solid particles were measured by means of EEPS particle analyser. Based on the measured values it can be stated that the slight increase of performance parameters occurred with strong effect on emissions production, especially on production of solid particles.

Key words: Combustion engine, biofuels, diesel fuel, particulate matter, vegetable oil, fuel blend.

INTRODUCTION

The biofuels in the combustion engines are used to reduce the impact of combustion of fossil fuels on the atmosphere and to reduce dependency on fossil fuel products. The biofuels based on vegetable oils or alcohols are most commonly used for CI (Compression Ignition) engine (Jindra et al., 2016; Kumar et al., 2016; Kumar & Saravanan, 2016; Gailis et al., 2017; How et al., 2018). For this purpose the edible and non-edible oils from a variety of plants with suitable oil characteristics can be used (Vanichseni et al., 2003; Sidibé et al., 2010; No, 2011; Mat et al., 2018; Shah et al., 2018).

In comparison with the diesel fuel the vegetable oil is denser and has a higher viscosity, higher flash point, lower calorific value, higher surface tension, higher oxygen content and lower carbon content (Franco & Nguyen, 2011; Esteban et al., 2012).

Utilization of the 100% vegetable oil as a fuel for compression ignition engine requires modification of the fuel system because it is necessary to preheat the oil in order to reduce the viscosity (Pexa et al., 2014). The recommended temperature for oil preheating varies significantly, the values, published by other authors, are in the range from 70 °C (Kumar et al., 2005) to 135 °C (Pugazhvadivu & Jeyachandran, 2005). Vegetable oil may be also used as an admixture to the diesel fuel or other fuel blends (Franco & Nguyen, 2011). Raw vegetable oil can be added into the diesel fuel in ratio 20% oil and 80% diesel fuel and it can be burned without modification of the engine or preheating of the fuel (Elango & Senthilkumar, 2011; Yilmaz & Morton, 2011; Gad et al., 2017; Mat et al., 2018), some sources state 30% of oil (Masjuki et al., 2001).

According to review, made by Mat et al. (2018), authors found that under the concentration of 50% of vegetable oil in the diesel fuel the smoke of the engine is reduced. Shah & Ganesh (2016) and Shah et al. (2018) found increased cylinder pressure and reduced smoke of the engine, especially at high engine load, when using filtered vegetable oil as a fuel for CI engine. Rakopoulos et al. (2006) and Hazar & Aydin (2010) found increased smoke density when using not preheated vegetable oil-diesel fuel blends, especially at low engine speed. Sathiyamoorthi & Sankaranarayanan (2017) found increased opacity at low and moderate engine loads and decreased opacity at high engine load.

Particulate matter (PM) produced by combustion engines means serious danger to human health (Kotek et al., 2017). The carbon particles absorb other substances (i.e. hydrocarbons or heavy metals, ect.) on their surface. The harmfulness of the solid particles rapidly increases with their decreasing size and the smallest particles can even enter into the blood stream (Dockery et al., 1992; Mohankumar & Senthilkumar, 2017; Soleimani et al., 2018). The particles with a diameter of 20 nm was found to have the highest deposition efficiency in the alveolar region of the lungs (Warnatz et al., 2006).

The aim of the paper is to experimentally verify the effect of rapeseed and sunflower oil as a fuel admixture on performance parameters and solid particles production of compression ignition engine.

MATERIALS AND METHODS

The measurement was performed using turbocharged compression ignition engine Zetor 1204 placed in the tractor Zetor Forterra 8641 (Fig. 1). The displacement of the engine is 4.156 L, the rated power is 60 kW (53.4 kW on PTO (Power Take Off) according to Deutsche Landwirtschafts-Gesellschaft). The basic parameters of the engine are listed in Table 1. The engine is unmodified and its operating time does not exceed 150 operating hours.

The engine was loaded trough the PTO using mobile dynamometer MAHA ZW 500 (Fig. 1).

Figure 1. The tractor Zetor 8641 with mobile dynamometer MAHA ZW 500.

The dynamometer has maximum torque of 6,800 Nm, maximum braked power of 500 kW and maximum rotation speed of 2,500 rpm. The data from the dynamometer were stored using data acquisition unit, provided by manufacturer, to the hard drive of PC with frequency of 10 Hz. The exhaust gas temperature sensor, fuel temperature sensor and ambient conditions sensors (atmospheric pressure, temperature and humidity) were also connected to the MAHA data acquisition unit. The losses in the gearbox have no effect on the comparative measurement of the influence of fuel on the operational parameters of the engine and therefore they are not taken into consideration.

Table 1. The engine parameters

Manufacturer and type	Zetor 1204
No. and arrangement of cylinders	4, in-line
Air flow	Turbocharged
Rated power	60 kW at 2,200 min^{-1} (53.4 kW on PTO)
Maximum torque	351 Nm (312 Nm on PTO)
Engine displacement volume	4.156 L
Cylinder bore X stroke	105 x 120 mm
Compression ratio	17
Fuel system	Mechanical in-line injection pump
Injection type	Direct injection
Combustion chamber	Bowl-in-piston
Injector noozle	Multihole
Start of injection (SOI)	12° before top dead center
Injection pressure	22 MPa
Valve mechanism	OHV
Valves per cylinder	2

The production of solid particles was measured using the Engine Exhaust Particle Sizer 3090 (EEPS) made by TSI Inc. The particles are evaluated as the count of particles in 1 cm^3. The basic operational parameters of the EEPS particle analyser is shown in Table 2. Before entering the particle analyser the exhaust gas is diluted (dilution factor 99.2667, dilution ratio 0.01007) and cooled down to temperature approx. 23 °C. The pressure of the measured gas is kept at approx. 90 kPa. Data from the particle analyser were stored to the hard drive of PC with the frequency of 1 Hz.

Table 2. The basic parameters of the EEPS

Particle Size Range	5.6–560 nm
Particle Size Resolution	16 channels per decade (32 total)
Electrometer Channels	22
Charger Mode of Operation	Unipolar diffusion charger
Inlet Cyclone 50% Cutpoint	1 μm
Time Resolution	10 size distributions s^{-1}

As a test fuels the diesel fuel blended with vegetable oils were used. As a reference fuel the diesel fuel with no bio-components was used. The following fuel blends were used for the measurement:

- 5% sunflower oil / 95% diesel fuel
- 20% sunflower oil / 80% diesel fuel

- 5% rapeseed oil / 95% diesel fuel
- 20% rapeseed oil / 80% diesel fuel
- 100% diesel fuel according to the regulation EN 590 (Diesel - EN 590) – with no bio-component

The viscosity and density of the tested fuels are shown in Table 3. The values in Table 3 were measured by means of Stabinger Viscometer SVM 3000 made by Anton Paar GmbH (measuring accuracy < 1%, repeatibilty 0.1%).

Table 3. Viscosity and density of the tested fuels

Fuel	Temperature °C	Dynamic Viscosity mPa s	Kinematic Viscosity mm² s⁻¹	Density kg m⁻³
Diesel fuel	40	1.444	1.801	801.65
	15	2.329	2.843	819.1
20% rapeseed oil	40	2.443	2.984	818.75
	15	4.216	5.042	836.1
5% rapeseed oil	40	1.627	2.022	804.4
	15	2.65	3.224	821.9
20% sunflower oil	40	2.54	3.088	822.45
	15	4.426	5.27	839.85
5% sunflower oil	40	1.647	2.041	806.9
	15	2.726	3.307	824.35
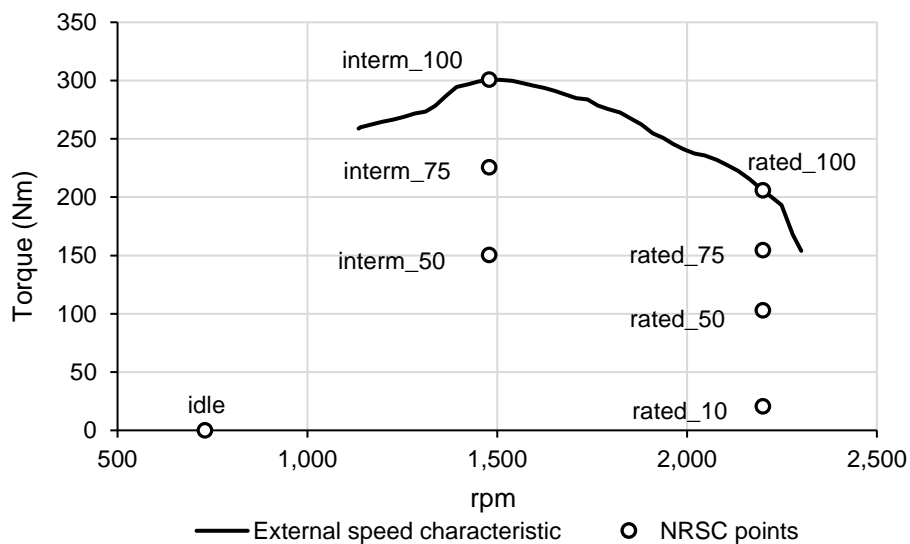
Figure 2. The example of the measurement points for NRSC test for diesel fuel.

The measurement was carried out according to 8-point NRSC (Non-Road Steady cycle) test (ISO 8178-4, type C1). For each tested fuel the torque curve was measured. Then, based on the torque curve, the points for the NRSC cycle was determined for each fuel. Points are defined by rotation speed (idle, at max. torque and rated) and torque (10%, 50%, 75% and 100%). The example of the points for the NRSC test are shown in

the Fig. 2. At each measurement point the engine operational parameters are stabilized and then the data are recorded for approx. 80 seconds. The software MS Excel was used for data evaluation.

RESULTS AND DISCUSSION

In the Fig. 3 the torque curves for all tested fuels can be seen. From the figure it is evident that the all tested blends of vegetable oil with diesel fuel caused an increase of the engine torque and power. The higher torque and power could be a result of combinations of different physical properties, such as viscosity and bulk modulus of vegetable oils in comparison with diesel fuel. According to Shah & Ganesh (2016) the different physical properties of fuel could affect injection timing and rate of fuel delivery. Also, the different chemical properties of vegetable oils in comparison with diesel fuel could affect the combustion process and may lead to higher cylinder pressure (Shah et al., 2018). The Table 4 shows the maximal reached values of torque and power for all tested fuels. The increase of torque and power between approx. 2–3% can be seen for all tested blended fuels in comparison with diesel fuel.
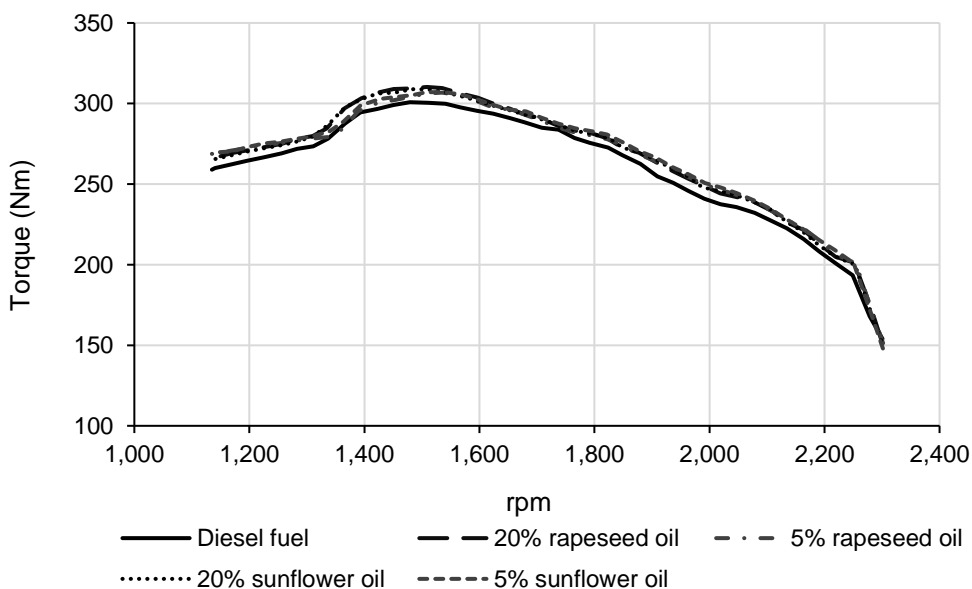
Figure 3. The torque curves, reached with the tested fuels.

Table 4. The maximum reached values of torque and power for all tested fuels

Fuel	Max. torque		Max. power	
	Nm	%	kW	%
Diesel fuel	300.82	100	52.05	100
20% rapeseed oil	310.27	103.14	53.11	102.03
5% rapeseed oil	306.75	101.97	53.07	101.94
20% sunflower oil	308.89	102.68	53.22	102.23
5% sunflower oil	307.11	102.09	53.57	102.92

In the Fig. 4 the results for all 8 points of the NRSC test for diesel fuel are shown. It can be seen that the engine reaches the highest concentration of solid particles at point rated_10, the size of most produced particles is in range of 45.3–69.8 nm.
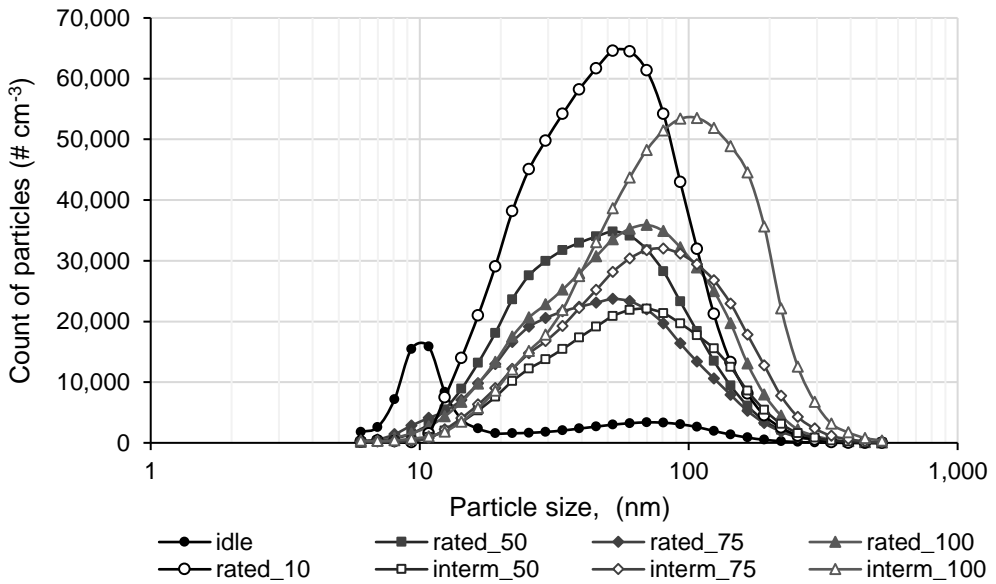
Figure 4. The results of particles analysis for diesel fuel.
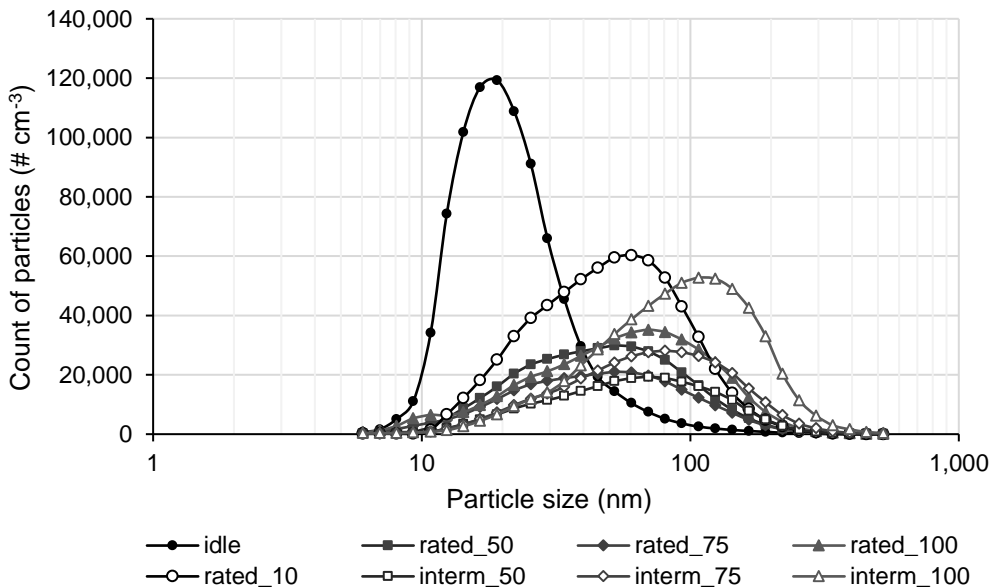
Figure 5. The results of particles analysis for the fuel containing 20% of rapeseed oil.

In the Fig. 5 the results of particle analysis for the blended fuel with 20% rapeseed oil are shown. It can be seen that the main difference in comparison with the diesel fuel

is reached at idle. In comparison with the diesel fuel the substantial increase can be seen in production of the very small particles. Rakopoulos et al. (2006) and Hazar & Aydin (2010) also found the increase smoke density for vegetable oil-diesel fuel blends, particularly at low engine speed. This may be caused by the combination of higher viscosity of the fuel, containing 20% of rapeseed oil, and therefore worse atomization of the fuel, and worse evaporation, caused by worse evaporation ability of the vegetable oils in comparison with diesel fuel. Since in idle the substantial part of the combustion is premixed combustion, the effect of worse evaporation is increased. Also, it can be seen that in the case of fuel with 20% of rapeseed oil the maximum concentration of produced particles while engine idle is in the range of approx. 14.3–22.1 nm, while in case of diesel fuel it is in the range of 9.31–10.8 nm. However, the maximum concentration of produced particles at idle is more than 6.5 times higher in the case of fuel with 20% of rapeseed oil in comparison with diesel fuel. In other measurement points the engine, running on blended fuel with 20% of rapeseed oil, produced lower concentrations of particles with slightly bigger sizes in comparison with the diesel fuel.

In the Fig. 6 the results of particle analysis for the fuel blended with 5% of rapeseed oil are shown. From the figure it is evident that at idle the amount of produced solid particles in the small sizes is substantially lower than in the case of fuel with 20% of rapeseed oil, but their size is also lower. The most particles, produced while idle, has size of 10.8 nm. In other points of the NRSC test the engine tends to produce less amount of solid particles in comparison with the diesel fuel or fuel, containing 20% of rapeseed oil. The sizes of particles are approximately the same as in the case of fuel with 20% of rapeseed oil (except idle).
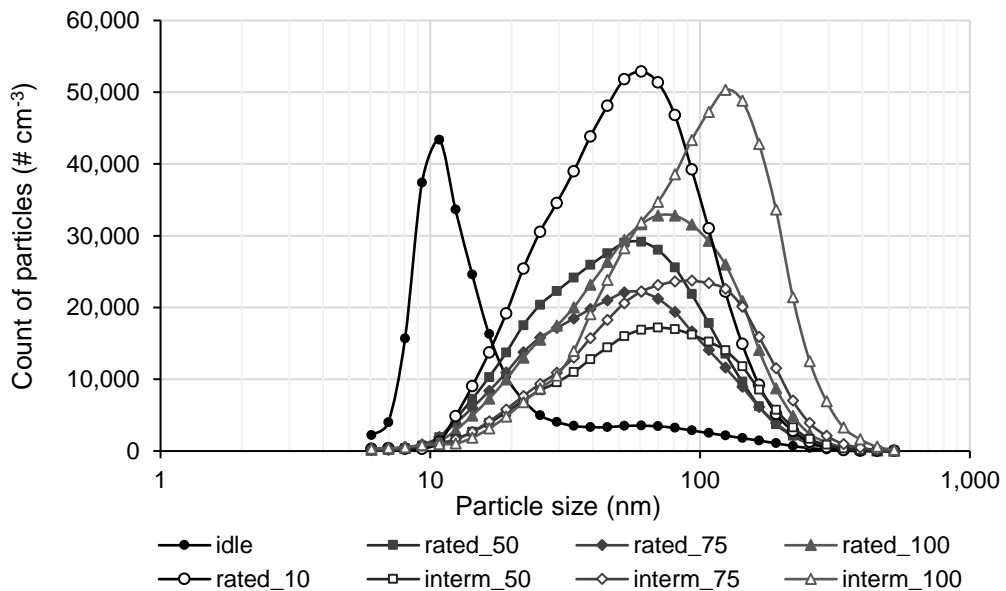
Figure 6. The results of particles analysis for fuel containing 5% of rapeseed oil.

In the Fig. 7 the results of particle analysis for the fuel blended with 20% of sunflower oil are shown. In comparison with diesel fuel, similar trend as in the case of

991

20% rapeseed oil can be seen, except of idle, less particles are created and their size is slightly bigger. At idle the substantial increase in production of small solid particles (14.3–19.1 nm) in comparison with diesel fuel occurred, similarly to fuel containing 20% rapeseed oil. In comparison with the results obtained with 20% rapeseed oil the lower number of particles are created while their size remains approximatelly the same.
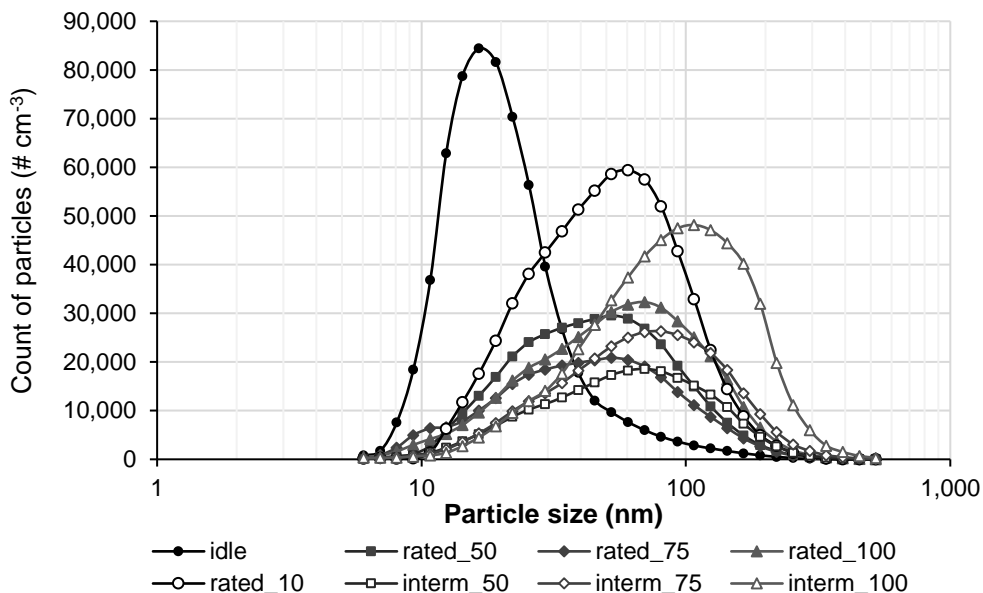
Figure 7. The results of particles analysis for fuel containing 20% of sunflower oil.
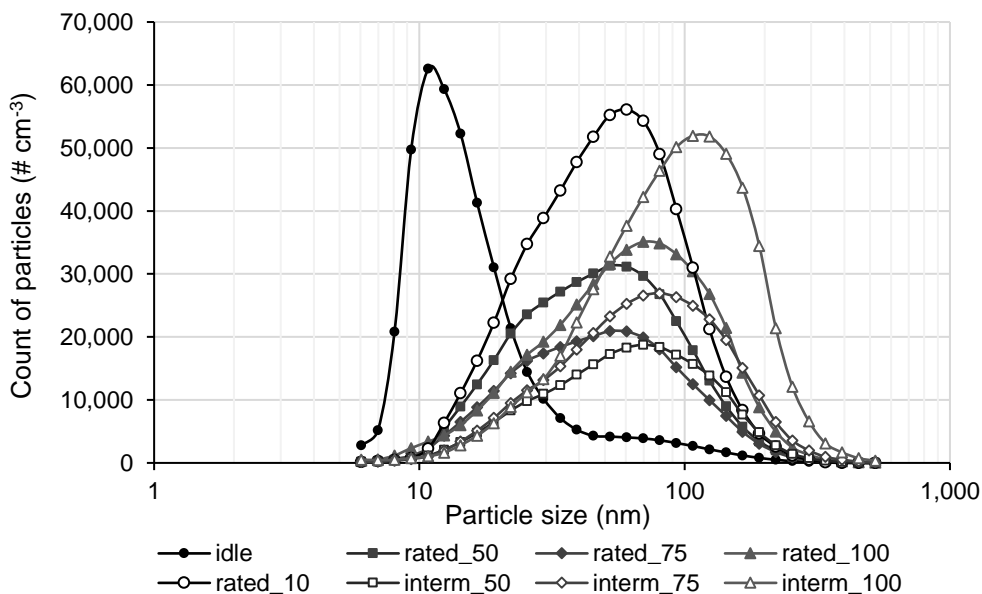
Figure 8. The results of particles analysis for fuel containing 5% of sunflower oil.

In the Fig. 8 the results of particle analysis for the fuel blended with 5% of sunflower oil are shown. In comparison with the rapeseed oil the the results obtained with sunflower oil does not follow the same trend. At points idle, rated_10, rated_75, interm_50 and interm_75 the production of solid particles is lower compared with 20% concentration of sunflower oil. At points rated_50, rated_100 and interm_100 the number of produced solid particles is higher than in case of 20% sunflower oil. From this result it is evident that at high engine load the higher percentage (20%) of sunflower oil reached better results, at moderate engine load the results of 5% and 20% sunflower oil are comparable and at low engine loads the 5% sunflower oil reached better results. At idle the decrease of amount of produced small solid particles can be seen, but compared to the fuel blend with 5% rapeseed oil the amount of particles is still approx. by 44.3% higher (at size 10.8 nm).
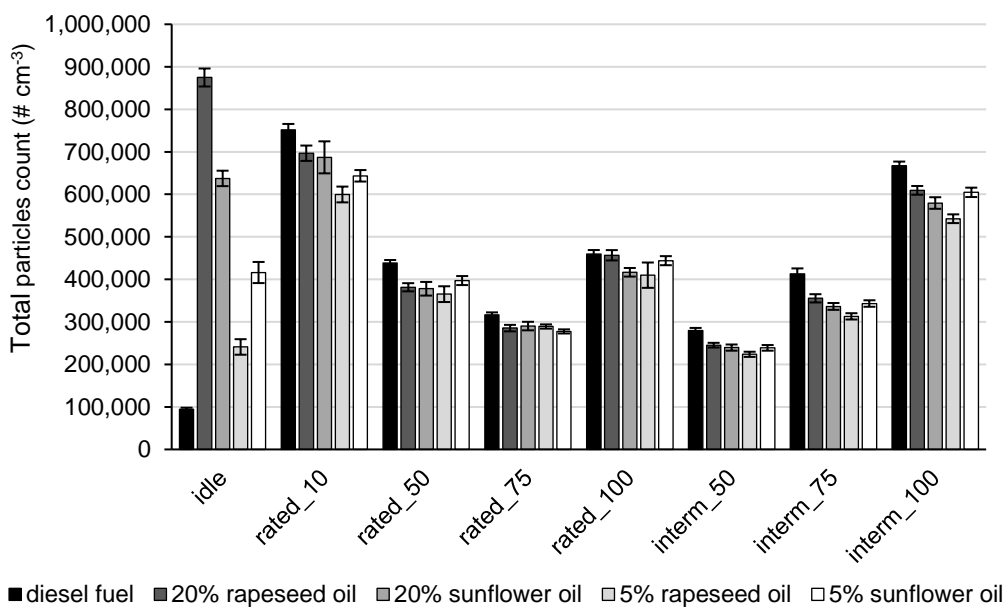
Figure 9. The total particles count for all tested fuels (error bars represents the standard deviation of the measured data).

In the Fig. 9 the total count of produced solid particles for all tested fuels is shown. Except of idle the highest amount of solid particles was produced by engine operating on diesel fuel. However, the vegetable oils caused substantial increase of production of solid particles at idle where the smallest particles that can be detected by the measuring device are produced. In the Table 5 the comparison of total count of produced particles in percentage is shown. From the table it is evident that, except of idle, all tested blended fuels achieved better results than diesel fuel. According to Shah & Ganesh (2016) this can be explained by higher oxygen content and lower carbon content in vegetable oils in comparison with diesel fuel.

It may be also noted that from the blended fuels the best result was achieved with fuel, containing 5% rapeseed oil (except rated_75). In comparison with diesel fuel the

fuel with 5% of rapeseed oil decreased the total solid particles count by 8.7–24.2% (except idle).

Table 5. Comparison of total particles count in 1 cm^3 for all tested fuels

Measurement point	Diesel fuel	20% rapeseed oil	20% sunflower oil	5% rapeseed oil	5% sunflower oil
-	%	%	%	%	%
idle	100	922.08	671.91	254.02	438.61
rated_10	100	92.66	91.37	79.75	85.59
rated_50	100	87.00	86.20	83.30	90.59
rated_75	100	90.16	91.69	91.35	87.70
rated_100	100	99.33	90.63	89.14	96.56
interm_50	100	87.57	85.56	79.90	85.31
interm_75	100	86.06	81.44	75.79	83.11
interm_100	100	91.37	86.90	81.36	90.65

CONCLUSIONS

From the results of measurement the following conclusions were made:

- The addition of both rapeseed and sunflower oil in concentration of 5% and 20% resulted in increased torque and power of the engine. The torque and power increase was between approx. 2–3%.
- When operating on 5% and 20% sunflower or rapeseed oil the engine tends to create slightly bigger particles in comparison with diesel fuel.
- Addition of rapeseed and sunflower oil in concentration of 5 and 20% resulted in decreased production of solid particles by approx. 0.7–24.2% in 7 from 8 measured points.
- The substantial increase of production of solid particles occurred when engine idling. The cause may be the combination of low temperature, insufficient atomization of the fuel with high viscosity and poor evaporation of the vegetable oil before premixed combustion. The increase of injection pressure may help to solve the problem.
- From tested fuel blends the fuel with 5% rapeseed oil and 95% diesel fuel showed the best result in terms of solid particles production.

From the obtained results it can be claimed that in comparison with diesel fuel the addition of rapeseed or sunflower oil in the concentration up to 20% into the diesel fuel decreases the production of particulate matter in most of tested engine mods despite increased viscosity of the blended fuels. The substantially increased production of very small particles while engine idle could be possibly solved by increased injection pressure, addition of butanol (Atmanli et al., 2015; Hönig et al., 2015; Pexa et al. 2016) or preheating of the fuel in order to improve atomization of the fuel.

REFERENCES

Atmanli, A., Ileri, E. & Yüksel, B. 2015. Effects of higher ratios of n-butanol addition to diesel-vegetable oil blends on performance and exhaust emissions of a diesel engine. *Journal of the Energy Institute* **88**(3), 209–220.

Dockery, D.W., Schwartz, J. & Spengler, J.D. 1992. Air pollution and daily mortality: Associations with particulates and acid aerosols. *Environmental Research* **59**(2), 362–373.

Elango, T. & Senthilkumar, T. 2011. Performance and emission characteristics of CI engine fuelled with non edible vegetable oil and diesel blends. *Journal of Engineering Science and Technology* **6**(2), 252–262.

EN 590 Automotive fuels. Diesel. Requirements and test methods. 2013

Esteban, B., Riba, J.-R., Baquero, G., Rius, A. & Puig, R. 2012. Temperature dependence of density and viscosity of vegetable oils. *Biomass and Bioenergy* **42**, 164–171.

Franco, Z. & Nguyen, Q.D. 2011. Flow properties of vegetable oil-diesel fuel blends. *Fuel* **90**, 838–843.

Gad, M.S., El-Araby, R., Abed, K.A., El-Ibiari, N.N., El Morsi, A.K. & El-Diwani, G.I. 2017. Performance and emissions characteristics of C.I. engine fueled with palm oil/palm oil methyl ester blended with diesel fuel. *Egyptian Journal of Petroleum*, Article in press

Gailis, M., Rudzitis, J., Kreicbergs, J. & Zalcmanis, G. 2017. Experimental analysis of hydrotreated vegetable oil (HVO) and commercial diesel fuel blend characteristics using modified CFR engine. *Agronomy Research* **15**(4), 1582–1601.

Hazar, H. & Aydin, H. 2010. Performance and emission evaluation of a CI engine fueled with preheated raw rapeseed oil (RRO)–diesel blends. *Applied Energy* **87**, 786–790.

Hönig, V., Smrčka, L., Ilves, R. & Küüt, A. 2015. Adding biobutanol to diesel fuel and impact on fuel blend parametres. *Agronomy Research* **13**(5), 1227–1233.

How, H.G., Masjuki, H.H., Kalam, M.A. & Teoh, Y.H. 2018. Influence of injection timing and split injection strategies on performance, emissions, and combustion characteristics of diesel engine fueled with biodiesel blended fuels. *Fuel* **213**, 106–114.

ISO 8178-4 Reciprocating internal combustion engines-Exhaust emission measurement-Part 4: Steady-state test cycles for different engine applications. 2007.

Jindra, P., Kotek, M., Mařík, J. & Vojtíšek, M. 2016. Effect of different biofuels to particulate matters production. *Agronomy Research* **14**(3), 783–789.

Kotek, M., Jindra, P., Prikner, P. & Mařík, J. 2017. Comparison of PM production in gasoline and diesel engine exhaust gases. *Agronomy Research* **15**(S1), 1041–1049.

Kumar, M.S., Kerihuel, A., Bellettre, J. & Tazerout, M. 2005. Experimental investigations on the use of preheated animal fat as fuel in a compression ignition engine. *Renewable Energy* **30**(9), 1443–1456.

Kumar, R.B. & Saravanan, S. 2016. Use of higher alcohol biofuels in diesel engines: A review. *Renewable and Sustainable Energy Reviews* **60**, 84–115.

Kumar, R.B., Saravanan, S., Rana, D. & Nagendran, A. 2016. Use of some advanced biofuels for overcoming smoke/NO x trade-off in a light-duty DI diesel engine. *Renewable Energy* **96**, 687–699.

Masjuki, H.H., Kalam, M.A., Maleque, M.A., Kubo, A. & Nonaka, T. 2001. Performance, emissions and wear characteristics of an indirect injection diesel engine using coconut oil blended fuel. In: *Proceedings of the Institution of Mechanical Engineers, Part D: Journal of Automobile Engineering* **215**(3), 393–404.

Mat, S.C., Idroas, M.Y., Hamid, M.F. & Zainal, Z.A. 2018. Performance and emissions of straight vegetable oils and its blends as a fuel in diesel engine: A review. *Renewable and Sustainable Energy Reviews* **82**(2018), 808–823.

Mohankumar, S. & Senthilkumar, P. 2017. Particulate matter formation and its control methodologies for diesel engine: A comprehensive review. *Renewable and Sustainable Energy Reviews* **80**, 1227–1238.

No, S.-Y. 2011. Inedible vegetable oils and their derivatives for alternative diesel fuels in CI engines: A review. *Renewable and Sustainable Energy Review* **15**(1), 131–149.

Pexa, M., Čedík, J. & Pražan, R. 2016. Smoke and NOx emissions of combustion engine using biofuels. *Agronomy Research* **14**(2), 547–555.

Pexa, M., Mařík, J., Čedík, J., Aleš, Z. & Valášek, P. 2014. Mixture of oil and diesel as fuel for internal combustion engine. In: *2nd International Conference on Materials, Transportation and Environmental Engineering*. CMTEE, Kunming, pp. 1197–1200.

Pugazhvadivu, M. & Jeyachandran, K. 2005. Investigations on the performance and exhaust emissions of a diesel engine using preheated waste frying oil as fuel. *Renewable Energy* **30**(14), 2189–2202.

Rakopoulos, C.D., Antonopoulos, K.A., Rakopoulos, D.C., Hountalas, D.T. & Giakoumis, E.G. 2006. Comparative performance and emissions study of a direct injection Diesel engine using blends of Diesel fuel with vegetable oils or bio-diesels of various origins. *Energy Conversion and Management* **47**, 3272–3287.

Sathiyamoorthi, R. & Sankaranarayanan, G. 2017. The effects of using ethanol as additive on the combustion and emissions of a direct injection diesel engine fuelled with neat lemongrass oil-diesel fuel blend. *Renewable Energy* **101**, 747–756.

Shah, P.R. & Ganesh, A. 2016. A comparative study on influence of fuel additives with edible and non-edible vegetable oil based on fuel characterization and engine characteristics of diesel engine. *Applied Thermal Engineering* **102**, 800–812.

Shah, P.R., Gaitonde, U.N. & Ganesh, A. 2018. Influence of soy-lecithin as bio-additive with straight vegetable oil on CI engine characteristics. *Renewable Energy* **115**, 685–696.

Sidibé, S.S., Blin, J., Vaitilingom, G. & Azoumah, Y. Use of crude filtered vegetable oil as a fuel in diesel engines state of the art: Literature review. *Renewable and Sustainable Energy Reviews* **14**(9), 2748–2759.

Soleimani, M., Amini, N., Sadeghian, B., Wang, D. & Fang, L. 2018. Heavy metals and their source identification in particulate matter (PM2.5) in Isfahan City, Iran. *Journal of Environmental Science*. Article in press

Vanichseni, T., Saitthiti, B., Intaravichai, S. & Kiatiwat, T. 2003. An Energy Modeling Analysis of the Integrated Commercial Biodiesel Production from Palm Oil for Thailand. *AMA, Agricultural Mechanization in Asia, Africa and Latin America* **34**(3), 67–74.

Warnatz, J., Maas, U. & Dibble, R.W. 2006. *Combustion: physical and chemical fundamentals, modelling and simulation, experiments, pollutant formation.* Springer, Berlin, 378 pp.

Yilmaz, N. & Morton, B. 2011. Effects of preheating vegetable oils on performance and emission characteristics of two diesel engines.*Biomass and Bioenergy* **35**(5), 2028–2033.

A comparative case study of the efficiency of collection systems for paper and biodegradable municipal solid waste

O. Chotovinský[*] and V. Altmann

Department of Machinery Utilisation, Faculty of Engineering, Czech University of Life Sciences in Prague, Kamycká 129, CZ165 21 Prague 6 – Suchdol, Czech Republic
[*]Correspondence: chotovinsky@tf.czu.cz

Abstract. The need to increase municipal solid waste recycling rates has led to the study and analysis of recycling schemes from the perspective of the technical issues that may be involved. This paper compares two waste collection systems, which are operating in the Vysočina region of the Czech Republic: a municipal solid waste collection system for paper (including cardboard) and a biodegradable municipal solid waste collection system. Both collection systems were introduced at different times to cover one selected urban area. The emphasis has been placed on an evaluation of the development of individual, separate collections between 2014 and 2016. Analysis of the technological operation and performance of the collections are observed and evaluated by measuring a range of waste collection system indicators. Efficiency levels, especially when it comes to separate collections of both types of municipal solid waste, are compared to their relative representation in the remaining bulk of municipal solid waste. The changes in representation of these types of waste against those in the rest of the municipal solid waste shows which collection systems are more successful from the perspective of the implementation of the directive which covers landfill usage. The results also describe why systems could be more successful within the view of well-chosen or inappropriately-selected technological parameters for materials separation. The possibly statistically significant impact of paper waste production in terms of the relative amount of paper waste across the rest of the municipal solid waste has also been shown.

Key words: municipal solid waste, rest municipal solid waste, biodegradable municipal solid waste, biodegradable municipal solid waste collection, paper and cardboard waste collection, material compositions.

INTRODUCTION

In the Czech Republic, the mean production per capita of municipal solid waste (MSW) is about 339 kg per year and, typically, 50% of the total mass is bio-waste, eg. food waste, and paper (PCMSW) and biodegradable municipal solid waste from parks and gardens (BMSW). PCMSW and BMSW which is produced within a municipal area is a quantitatively highly important category of waste, and the way in which it is treated can both positively and negatively influence environmental components. PCMSW and BMSW contributes to the accumulation of the anthropogenic greenhouse effect and planetary climate change. The greenhouse gases which are produced during the process of bio-waste decay at landfill sites contributes to global greenhouse gas emissions by

approximately 4% (Papageorgiou et al., 2009). A directive which has a crucial value from this perspective and which is fully integrated with Czech legislation is referred to as the Council Directive on Landfill 1999/31/EC (known familiarly as the 'Landfill Directive'). Landfill Directive 1999/31/EC establishes targets which should result in a decrease in the quantity of bio-waste that is disposed in landfill. In 2010, around 75% of the total bio-waste mass produced in 1995 should be stored in landfill sites, while in 2013 the figure should be 50% of this amount, and by 2020 only 35% of bio-waste from 1995 should remain in landfill sites. In the Czech Republic, a total of 1,530,000 tons of bio-waste was produced in 1995, and in 2010 there were 1.5 million tons of bio-waste being stored in landfill sites instead of the admissible 1.15 million tons. The precautions set out by the directive should take care of the materials and energy-related use of the waste from the perspective of a solid waste management system (Vehlow et al., 2007). Waste collections form one of the most visible activities in a waste solid management system, and it is one that the public highly perceives. Although the goal of waste collection is to keep a city clean, the activity needs to deal with budgetary challenges, logistical constraints, public acceptance, and a reduction of environmental and health impacts, as well as being capable of reaching collection and recycling targets which have been set by Landfill Directive 1999/31/EC (Rogge & De Jaeger, 2013; Usón et al., 2013; Williams & Cole, 2013).

The services for PCMSW and BMSW collection are defined as being a combination of a certain form of technology and human labour (Bilitewsky et al., 1997). This action corresponds not only to waste collection from certain types of source, but also includes the transportation of this waste to locations at which waste management lorries are loaded up (Tchobanoglous & Kreith, 2002). PCMSW and BMSW collection systems which are applied within the Czech Republic can form a kerbside collection, where recyclables are placed by members of the public on the kerbside outside their houses for collection by a lorry on an appointed day, or by means of a drop-off collection, where recyclables are taken by members of the public to drop-off points at various localities in their vicinity and then are picked up by lorry at an identified frequency. Both kerbside and drop-off systems are characterised by a diversity of implementation technologies (sometimes including especially-designed collection vehicles), and different collection frequencies and logistics are needed to support them. The way in which each region operates its PCMSW and BMSW collection depends upon socio-economic conditions, available infrastructure, and service provision (Timlett & Williams, 2011; Martinho et al., 2017).

More studies of waste collection systems are needed to generate a greater knowledge base of such collection systems and to understand how they should be adapted in order to be more successful. Waste collection services which separate the PCMSW and BMSW parts from municipal solid waste could be analysed according to their performance in terms of cost (Teerioja et al., 2012; Rogge & De Jaeger, 2013), environmental impact (Powell, 1996; Maimoun et al., 2013; Teixeira et al., 2014; Yildiz-Geyhan et al., 2016), recycling/collection rates (Wilson & Williams, 2007), and public participation and behaviour (Oskamp et al., 1996; Wang et al., 1997; Bolaane, 2006; Martin et al., 2006; Shaw et al., 2006). When focusing on operations, Huang et al. (2011), for example, developed key performance indicators in order to assess the efficiency of the MSW collection.

The main aim of this paper consists of a basic description of a better collection strategy, taking into account the analysis of two selected collection schemes for sorted BMSW and PCMSW waste from the perspective of its diversion from landfill. In the first stage data is collected, treated, and statistically analysed, based on some selected variables and performance indicators from one selected urban area in the Czech Republic. It provides conclusive information regarding whether selective waste collection behaviours and trends follow the same direction for all type of sorted waste collected under each collection scheme. The second stage focuses on a more detailed analysis and comparisons between possibly significant impacts which may be caused by the increased production of selected sorted waste on its relative volume in the rest of the MSW stream (RMSW), which is sent to landfill sites.

MATERIALS AND METHODS

Collection area

The methodology was applied to two selected kerbside collection services for paper and biodegradable waste in a medium-sized city in the Vysočina region. The collection area consisted of a typical city centre, mainly one with apartment buildings or residences with a rather high population density. The total surface area occupied by the city is 56 km^2. By the year 2016, it had grown to include 36,630 inhabitants, who are permanently domiciled in 5,304 houses and 14,779 flats. This corresponds to a mean spatial distribution of about 704 inhabitants per km^2 and they are distributed throughout seventeen different city districts. Ten of them are located directly in the urban area and the other seven are in the vicinity of the integrated village. Gas is the most common heating medium.

Economic activities for this population include industry (50%), trade and business (46%), and agriculture (4%). MSW production per capita is only about 2.3 kg per day. Most of the municipal solid waste production is deposited in landfill sites.

Separate collection of PCMSW and BMSW can be considered to be fully developed, with good access throughout the whole of the urban area. The collection BMSW here is applied as a combination of drop-off and kerbside systems. The situation regarding a separate collection of PCMWS also includes the kerbside system and drop-off system.

Data collection

Data collection was carried out in order to obtain a representative sample which was able to produce accurate generalisations about the performance of both of the kerbside collection systems. Data was collected through measurements from the urban area which were taken by the local collection company (ESKO-T s.r.o.) over the course of three years (2014–2016 inclusive). Above all, data related to production, the number of containers, and the volume of each container, describing the frequency of the collection within the selected reference period. The total volume of BMSW and PCMSW is shown in Table 1. For the other purposes of this paper these total amounts were calculated on a monthly basis during each year of the survey. This conversion also took into account the available volume of containers by frequency of collection.

The values given in Table 2 were provided by the collection company which carried out regular RMSW analysis at monthly intervals within the city being surveyed. A substance analysis of RMSW has been carried out since 2012. For the purposes of evaluation, use was made of the total volumes of BMSW (20 02 01) and PCMSW (20 01 01) in RMSW data from January to December in the years 2014–2016.

Table 1. Waste production in 2014–2016 in the urban area under study

Year	Total volume of waste, t	Amount of MSW, t	Amount of RMSW, t	Amount of BMSW, t	Amount of PCMSW, t
2014	192,200	31,074	16,239	149	580
2015	193,693	31,169	16,230	274	591
2016	235,374	31,484	16,676	545	620

Source: research ESKO-T s.r.o.

Table 2. Rest municipal solid waste composition – average mass fraction in 2014–2016

Type no	Waste component	Mass fraction, kg
20 01 01	Paper and cardboard (PCMSW)	12.17
20 01 08	Food waste	12.71
20 01 39	Plastics	10.31
20 01 10	Clothes	1.75
20 01 11	Textiles	2.09
20 01 38	Wood	1.18
20 02 01	Biodegradable waste (BMSW)	5.62
20 03 01	Glass	1.03
20 03 02	Metals	1.28
20 03 07	Other	43.60

Note: type no – the code for each type of waste in the Czech Republic's waste catalogue; Source: research ESKO-T s.r.o.

The density of the waste was evaluated by measuring any increase in weight for empty containers of a size of 1.1m^3 and 0.66m^3 once they had been filled with PCMSW and BMSW (Table 3). The identified density was used to determine the total capacity utilisation of the containers.

Table 3 Results of our own measurements of density for both kinds of segregated municipal solid waste in the collection containers

Waste	Density*, kg m^{-3}
BMSW	300
PCMSW	50

* average.

Statistics methods
In this work we present a methodology which aims to support the assessment of waste collection performance. The determination of the volume of BMSW and PCMSW in RMSW is based on the results of composition analysis which was carried out by the local collection company. Average values of the content of individual RMSW components are calculated by derived relation (1), where the formula for the arithmetic mean is adjusted from progressively-performed RMSW analysis in 2014 and 2016. For the calculations being considered, the methodology also allows for the relation (2), which determines the relative volume of PCMSW and BMSW in RMSW.

Average relative content of type of waste in RMSW, %

$$\overline{p}_D = \frac{\sum_{i=1}^{n}\left(\frac{m_{Di}}{m_{Ci}}\right)}{n} \cdot 100 \tag{1}$$

where $\overline{p}_D$ – average relative content of the type of waste in RMSW, %; m_{Di} – content mass of the type of waste in one RMSW sample, kg; m_{Ci} – one whole RMSW sample mass, kg; n – number of performed RMSW analyses, (-).

Relative amount of PCMSW and BMSW in RMSW, %

$$P_{PCMSW/BMSW} = \frac{m_{PCMSW/BMSW}}{m_{sample}} \cdot 100 \tag{2}$$

where $p_{PCMSW/RCMSW}$ – relative amount of PCMSW and BMSW in RMSW, %; $m_{PCMSW/RCMSW}$ – content mass of the type of waste in one RMSW sample, kg; m_{sample} – one whole RMSW sample mass, kg.

In addition, a methodology for producing descriptive statistics was used to process the RMSW composition results, involving standard deviation, dispersion, maximum and minimum averages, an error allowance for the 95% base file of reliability, and a variation coefficient.

The methodology for determining the total capacity utilisation of PCMSW and BMSW containers was based on relations 3, 4, and 5.

Total available volume of PCMSW and BMSW containers, dm³ year⁻¹

$$TAVc_{PCMSW/BMSW} = nc_{PCMSW/BMSW} \cdot nj_{PCMSW/BMSW} \cdot Vc_{PCMSW/BMSW} \tag{3}$$

where $TAVc_{PCMSW/BMSW}$ – total available volume of PCMSW and BMSW containers, dm³ year⁻¹; $nc_{PCMSW/BMSW}$ – the number of PCMSW and BMSW containers, (number); $nj_{PCMSW/BMSW}$ – the number of rides to empty the PCMSW and BMSW containers, (number); $Vc_{PCMSW/BMSW}$ – volume of PCMSW and BMSW containers, dm³.

Total capacity of PCMSW and BMSW containers, kg year⁻¹

$$TCc_{PCMSW/BMSW} = \frac{TAVc_{PCMSW/BMSW}}{\rho_{PCMSW/BMSW}} \cdot 100 \tag{4}$$

where $TCc_{PCMSW/BMSW}$ – total capacity of PCMSW and BMSW containers, kg year⁻¹; $TAVc_{PCMSW/BMSW}$ – total available volume of PCMSW and BMSW containers, dm³ year⁻¹; $\rho_{PCMSW/BMSW}$ – identified density of PCMSW and BMSW, kg m³.

Utilisation of the total capacity of PCMSW and BMSW containers, %

$$UCc_{PCMSW/BMSW} = \frac{Q_{PCMSW/BMSW}}{TCc_{PCMSW/BMSW}} \cdot 100 \tag{5}$$

where $UCc_{PCMSW/BMSW}$ – utilisation of the total capacity of PCMSW and BMSW containers, %; $TCc_{PCMSW/BMSW}$ – total capacity of PCMSW and BMSW containers, kg year⁻¹; $Q_{PCMSW/BMSW}$ – total volume of PCMSW and BMSW, kg year⁻¹.

The STATISTICA 8 program was used to analyse the data and obtain the necessary characteristics of simple regression and analyses of variances (F-test in regression). These statistical methods were used to describe the dependence between the relative monthly volume of sorted waste in RMSW and its average monthly productions.

RESULTS AND DISCUSSION

The totals for PCMSW and BMSW production were shown on a monthly basis for each year of the survey. These monthly production values were completed by adding in values for the total available volume of PCMSW and BMSW containers. Figs 1 and 2 reflect the same trend regarding how the total available volume corresponds with the production of both kind of waste.
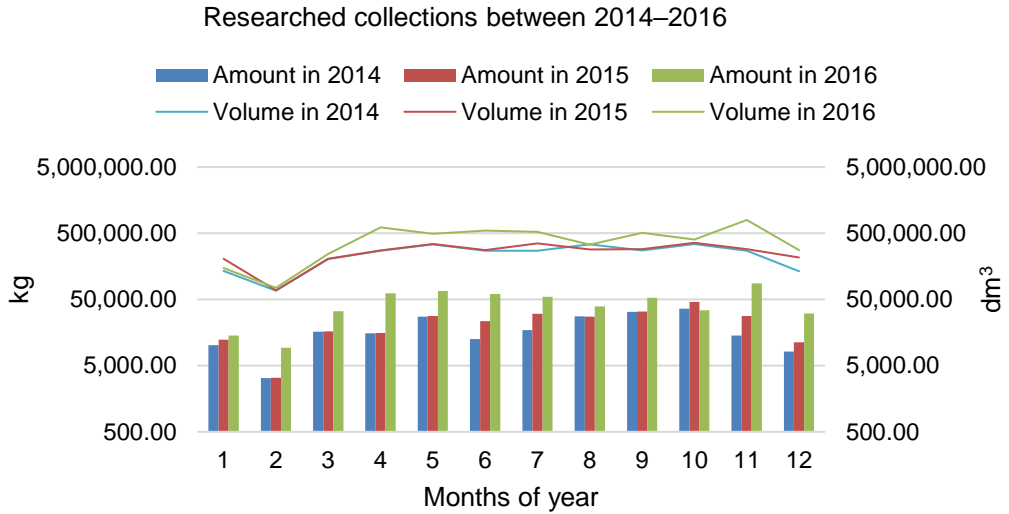
Figure 1. BMSW production and total available volume of BMSW containers.
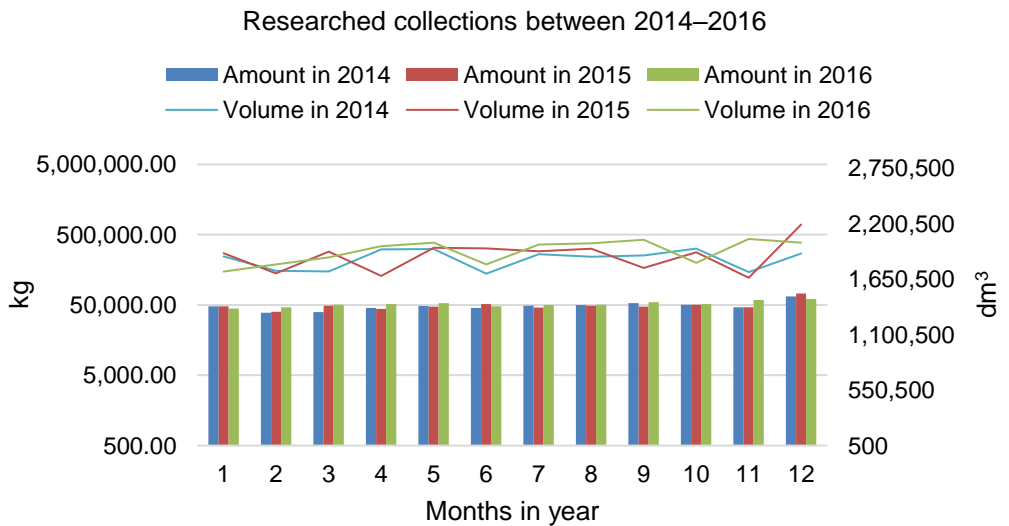
Figure 2. PCMSW production and total available volume of PCMSW containers.

The percentages calculated for PCMSW and BMSW collections by methodology for determining the total capacity utilisation of containers used are presented in Fig. 3. For BMSW, the percentage of use is very low. This is caused by too-frequent a waste collection. From the perspective of PCMSW the percentages are slightly higher, but overall these are also low. In the PCMSW containers, distributed packaging boxes often appear, and they then fill a large proportion of the container.
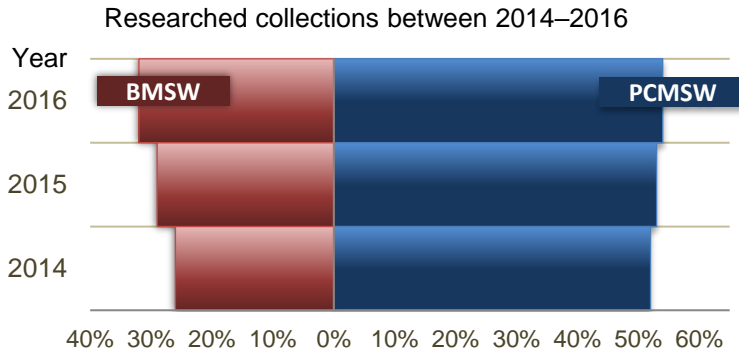
Figure 3. Utilisation of the total capacity of BMSW and PCMSW containers.

The successful evaluation of PCMSW and BMSW collections by means of the results of the composition analysis of RMSW is shown in Fig. 4. This figure shows that, in the area being researched, the percentage of BMSW in RMSW is increasing, and the percentage of PCMSW in RMSW has a tendency to decline. Table 4 shows the value of individual calculations of descriptive statistics relating to the average checked values of PCMSW and BMSW in RMSW.
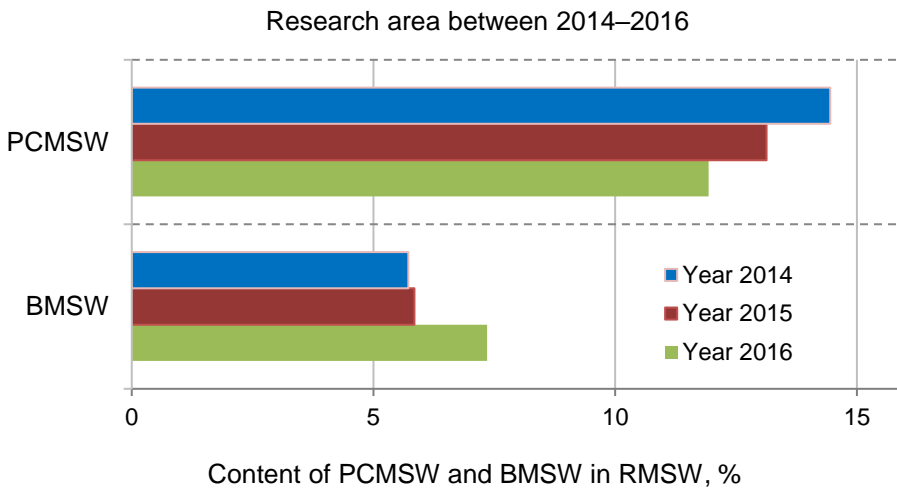
Figure 4. Relative amount of PCMSW and BMSW in RMSW between 2014–2016.

Table 4. Overview of descriptive statistics (PCMSW and BMSW values)

Year	Dispersion, (-)	Standard deviation, (-)	Coefficient of variation, (-)	Δ*, %	Minimum average, %	Maximum average, %
2014	9.71	3.12	55.94	1.98	3.59	7.55
2015	6.21	2.49	34.43	1.58	5.66	8.82
2016	6.21	2.49	34.43	1.58	5.66	8.82

* error for 95% base file of reliability.

The sites which had a separate collection for BMSW placed four types of BMSW containers in the built-up area. Their usage is as follows:
- containers measuring 0.66 m^3, 0.44 m^3, and 1.1 m^3 – BMSW from residences,
- containers measuring 14 m^3 – BMSW from public green areas.

The situation regarding separate collection of PCMWS placed only one type of container with an available volume of 1.1 m^3 alongside all collections points.

The year-by-year development of the number of PCMSW and BMSW containers and their collection inside the surveyed area is presented in Table 5, below.

The increasing numbers of PCMSW containers (and the associated increase of the number of collections) influenced the total amount of collected PCMSW between 2014 and 2016 during kerbside collections with effective separation procedures taking place. The summarised values also show that collections especially tend to increase with a small number of collection containers. The increasing numbers of collection containers and collections can be seen from the perspective of BMSW collections with the same level of influence between 2014–2016. However, non-effective separation also exists in the comparison of relative volumes of BMSW in RMSW. This is due to the fact

Table 5. Average number of collections and the average number of collected containers per month

Year/Volume	0.66 m^3	0.77 m^3	1.1 m^3	14 m
PCMSW				
2014	-	-	9/1,681	-
2015	-	-	11/1,709	-
2016	-	-	13/1,750	-
BMSW				
2014	-	2/206	-	-
2015	-	4/341	-	-
2016	3/9	4/331	3/9	7/10

*average number of collections/average collected containers per month (PCMSW and BMSW containers).

that the increasing number of collection containers is not gradual on the kerbside in relation to apartment buildings or houses. A large increase is only seen in relation to large-volume containers which are collected from public green areas. The collection company has deployed these containers primarily in marginal areas (which can be labelled using the phrase 'gardening colonies') within the urban area, where there is no large-scale RMSW production.

Therefore only one more effective separation has been used for the next calculation (which covers the average number of collections per month).

The first of result of the analysis by STATISTICA 8 focuses on the simple regression summary that is presented in Table 6. The determination coefficient R^2 can be considered as a percentage of the total variability of the response variable, as explained by the regression model. However, use of the adjusted determination coefficient R^2 is recommended (Šmilaur, 2007).

Table 6. Results of regression for the average number of collections per month

	Regression Summary for dependent variable: [%] (waste composition) $R = 0.67521326$ $R^2 = 0.45591294$ Adjusted $R^2 = 0.43991038$ $F(1.34) = 28.790$ $p < 0.00001$ Std.Error of estimate: 2.3979					
$N = 36$	Beta	Std.Err. of Beta	B	Std.Err. of B	$t(14)$	p level
Intercept,			23.10718	2.086260	11.07589	0.000000
%	-0.675213	0.126501	-0.97875	0.183369	-5.33760	0.000006

Notes: The R field contains the correlation coefficient, which is the positive square root of R-squared. The R^2 field contains the determination coefficient, which measures the reduction in the total variation of the dependent variable due to the independent variables; the adjusted R^2 is interpreted similarly to the R^2 value except that the adjusted R^2 takes into consideration the number of degrees of freedom.
The F value, df, and the resultant p value are used as an overall F test for the relationship between the dependent variable and the set out independent variables. The standard estimate error measures the dispersion of the observed values about the regression line.
The intercept field contains the intercept value if a choice was made to include the intercept in the model on the 'Model Definition - Advanced'.
The 'Std.Error' field contains the standard error for the intercept. The t value with the resulting p value are used to test the hypothesis that the intercept is equal to zero.
The beta coefficients are the regression coefficients which would have been obtained had all of the variables first been standardised to a mean of zero and a standard deviation of one.
The N is the total number of observations.

'F statistics' which result from the analysis of the variance regression model were carried out as an intermediate step of the selected regression function (Table 7).

Table 7. ANOVA results

	Variance analysis; DV: % (waste composition)				
$N = 36$	Sums of Squares	df	Mean Squares	F	p level
Regress	163.8105	1	163.8105	28.49000	0.000006
Residual	195.4917	34	5.7498		
Total	359.3022				

Note: The N is the total number of observations.

The values for mean squares in Table 7 were used for testing the significance of the regression model, whereas the key value used was the ratio of the model mean square and the residual mean square. In the case of the null hypothesis, the value of this ratio should be relatively close to one (ie. the explained and unexplained variability should be of a similar size). More precisely (for this particular model), it should originate from the F disturbance with a parameter value of 1.34 (for the model being presented). Nevertheless, the probability that the true value of this ratio, ie. the F statistic (with a value of 28.4900), originates from this F disturbance is less than 0.000001 or equal to 0[6], as confirmed by the values in the 'p level' column. Hence H_0 can be rejected with this probability of a Type I error (at the concerned level of significance).

We present below a graphical representation of the regression line (Fig. 5).
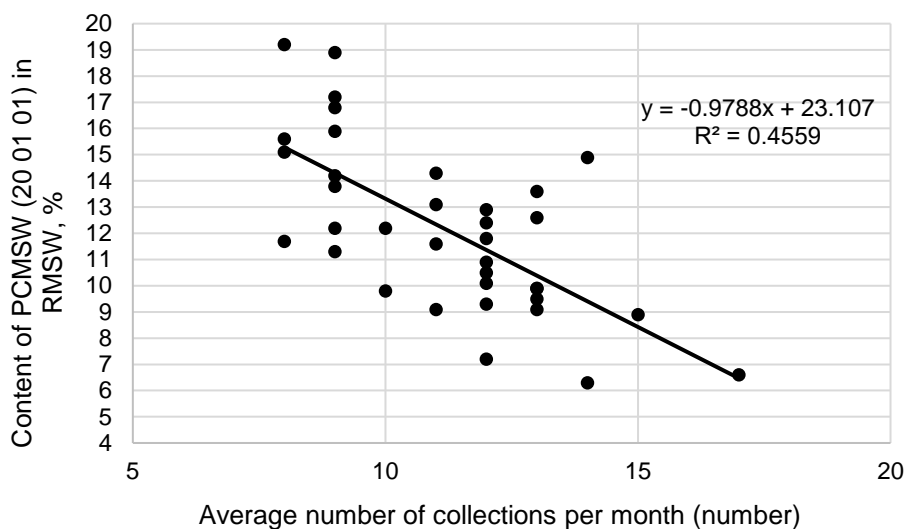
Figure 5. Graphical representation of regression.

According to Fig. 4 but in more detail, there is a decrease in the relative content of PCWSW (20 01 01) in RMSW, from approximately 14.45% to 11.93% here in the years being monitored, 2014–2016. This corresponds to the opposite course of utilisation of the total capacity of PCMSW containers. There utilisation rose to 54% from 51%. However, the percentages calculated for paper are evaluated as being unsatisfactory. This state is achieved by a lack of discipline during the disposal of waste by members of the public. It is stated that the paper volume after pressing is only 20% of the total volume. In this example, it may be possible to achieve substantial savings in logistics costs for these processes by consistent deformation. The role of the public is fundamental in achieving this goal. In fact, the correct source separation of PCMSW is at the basis of any successful collection scheme (Dhokhikah et al., 2015). For example, members of the public can be interviewed to assess their willingness to pay as a function of the separate collection services, in order to work out which socio-demographic characteristics influence the production of waste as well as the identification of proposals for the promotion of recycling (Challcharoenwattana & Pharino, 2016; Giovanni et al., 2017). On the other hand, there was no reflection of any separate BMSW collection in RMSW composition. The representation of BMSW in RMSW is still rising, from 5.72% to 7.35% in the period being monitored. The utilisation of the total capacity rose too. Values have increased from 26% to 32% but they are lower than those for paper. The BMSW collection is carried out once a week. It is therefore possible to reduce the frequency of collections without there being a risk of overfilling the containers or damaging the efficiency of separation.

In view of a comparison between both of these areas, a collection through the use indicator of waste generation per capita per year (Teixeira et al., 2014, and CML et al., 2014) also evidences a difference in the achieved value of 16.2 kg per person^{-1} year^{-1} (PCMSW collection) and 8.3 kg per person^{-1} year^{-1} (BMSW collection) in the last year

of measurement – 2016 – from the perspective of production from apartment buildings or houses.

An assessment of the mean values of input data (regarding the PCMSW collection) further proves a statistically significant relation that the relative volume of PCMSW in RMSW depends upon the average number of collections per month by settings of collection parameters, from the perspective of the overall size of this site. The positive relationship was furthermore enriched by regression analysis; however this does not necessarily reflect a causal relation (in fact, only non-manipulated areas were observed). Therefore, the relative volume of PCMSW in RMSW is influenced by non-measured factors. Furthermore, as the distribution of regression residuals around the x axis shows, there exist some differences between the real (observed) and predicted (fitted by the regression model) values of the variables in the regression equation. These differences could have been caused by increasing numbers of collections with a small number of collected containers.

CONCLUSIONS

The principal objective of the present study was to conduct a comparison of PCMSW and BMSW collections in one selected urban area from the perspective of its diversion from landfill (during the 2014–2016 period). The authors also studied the influence of the average number of PCMSW collections per month, it corresponds to increasing PCMSW production in terms of the relative volume of this form of waste in RMSW for kerbside paper collections.

The study proves that the average number of PCMSW collections per month influences the relative amount of PCMSW in RMSW, and mathematically defines this dependence. Available data for individual quarters of 2014–2016 confirm the following regression compensation straight line of the average monthly PCMSW production **p** and the relative amount of PCMSW in RMSW **T** for kerbside paper collections A: T = 23.107–0.9788.p.

The decrease of PCMSW in RMSW for on-site paper collection indicates that the directive on landfills can be followed with well-chosen technological parameters in regard to a separate BMSW collection. It confirms the statistically significant relation. Improperly adjusted technological parameters for on-site BMSW collections indicate that this site has total monitored results which are parallel to areas without any separate collection. It means then that the collection has only an increase in costs for BMSW disposal without any of the concrete positive effects of a separate BMSW collection or any equivalent benefit towards the environment.

Hence it is necessary to continually analyse the collection data, rigorously evaluate and carry out immediate remedial measures, and optimise the technological parameters at the given site with both separate forms of collection.

REFERENCES

Bilitewsky, B., Hardtle, G. & Marek, K. 1997. *Waste Manegement*. 1st ed. Verlag Berlin Heidelberg, DEA, Springer, 430 pp.

Bolaane, B. 2006. Constraints to promoting people centred approaches in recycling. *Habit. Int.* **30**, 731–740.

Challcharoenwattana, A. & Pharino, C. 2016. Wishing to finance a recycling program? Willingness-to-pay study for enhancing municipal solid waste recycling in urban settlements in Thailand. *Habitat Int.* **51***,* 23–30.

CML, FCT-UNL, ISCTE-UL, Valorsul, Lipor. 2014. *Guide of municipal solid waste indicators* (*Guia de indicadores de Resíduos Urbanos*)*.* Report of project financed by Sociedade Ponto Verde. (in Portuguese).

Dhokhikah, Y., Trihadiningrum, Y. & Sunaryo, S. 2015. Community participation inhousehold solid waste reduction in Surabaya. *Resour. Conserv. Recycl.* **102**, 153–162.

Giovanni, D.F., Polito, R.A., Ferrara, C. & Zamballetti, I. 2017. Evaluating opinions, behaviours and motivations of the users of a MSW separate collection centre in the town of Baronissi, Southern Italy. *Waste Management* **68**, 742–751.

Huang, Y.T., Pan, T.C. & Kao, J. J. 2011. Performance assessment for municipal solid waste collection in Taiwan. *J. Environ Manage.* **92**, 1277–1283.

Maimoun, M.A., Reinhart, D.R., Gammoh, F.T. & Bush, P.M. 2013. Emissions from US waste collection vehicles. *Waste Management* **33**, 1079–1089.

Martin, M., Williams, I.D. & Clark, M. 2006. Social, cultural and structural influences on household waste recycling: a case study. *Resour. Conserv. Recycl*. **48**, 357–395.

Martinho, G., Gomes, A., Santos, P., Ramos, M., Cardoso, J., Silveira, A., Pires, A. 2017. A case study of packaging waste collection systems in Portugal – Part I: Performance and operation analysis. *Waste Management* **61**, 96–107. http://dx.doi.org/10.1016/j.wasman.2017.01.030

Oskamp, S., Zelezny, L., Schultz, P.W., Hurin, S. & Burkhardt, R. 1996. Commingled versus separated curbside recycling: does sorting matter? *Environ. Behav.* **28**, 73–91.

Papageorgiou, A., Barton, J. R. & Karagiaannidis, A. 2009. Assessment of the greenhouse effect impact of technologies used for energy recovery from municipal waste. *Journal of environmental management* **90**, 2999–3012.

Powell, J.C. 1996. A lifecyle assessment and economic valuation of recycling. *J. Environ. Plan. Manage*. **39**, 97–112.

Rogge, N. & De Jarger, S. 2013. Measuring and explaining the cost efficiency of municipal solid waste collection and processing services. *Omega 41* **4**, 653–664.

Shaw, P.J., Lyas, J.K. & Hudson, M.D. 2006. Quantitative analysis of recyclable materials composition: tools to support decision making in curbside recycling. *Resour. Conserv. Recycl*. **48**, 263–279.

Šmilauer, P. 2007. *Moderní regresní metody. [Modern Regression Methods]*. České Budějovice, Biologická fakulta JU, 168 pp.

Tchobanoglous, G. & Kreith., F. 2002. *Handbook of solidwaste management.* 2nd ed. New York, USA, McGraw-Hill, 505 pp.

Teerioja, N., Moliis, K., Kuvaja, E., Ollikainen, M., Punkkinenm, H. & Merta, E. 2012. Pneumatic vs. door-to-door waste collection systems in existing urban areas: a comparison of economic performance. *Waste Management* **32**, 1782–1791.

Teixeira, C.A., Russo, M., Matos, C. & Bentes, I. 2014. Evaluation of operational, economic, and environmental performance of mixed and selective collection of municipal solid waste: Porto case study. *Waste Manage. Res.* **32**, 1210–1218.

Timlett, R. & Williams, I.D. 2011. The ISB model (infrastructure, service, behaviour): a tool for waste practitioners. *Waste Management* **31**, 1381–1392.

Usón, A.A., Ferreira, G., Vásquez, D.Z., Bribián, I.Z. & Sastresa, E.L. 2013. Environmental benefit analysis of two urban waste collection systems. *Sci. Total Environ* **463–464**, 72–77.

Vehlow, J. 2007. Union waste management strategy and the importance of biogenic waste. *Journal of Material Cycles and Waste Management* **9**, 130–139.

Wang, F.S., Richardson, A.J. & Roddick, F.A. 1997. Relationships between set-out rate, participation rate and set-out quantity in recycling programs. *Resour. Conserv. Recycl.* **20**, 1–17.

Williams, I.D. & Cole, C. 2013. The impact of alternate weekly collections on waste arisings. *Sci. Total Environ.* **445-446**, 29–14.

Wilson, C.D.H. & Williams, I.D. 2007. Curbside collection: a case study from the north-west of England. *Resour. Conserv. Recycl.* **52**, 381–394.

Yildiz-Geyhan, E., Yilan-Çiftçi, G., Altun-Çiftçioglu, G.A. & Kadirgan, M.A.N. 2016. Environmental analysis of different packaging waste collection systems for Istanbul – Turkey case study. *Resour. Conserv. Recycl.* **107**, 27–37.

Detection reliability for passive infrared detectors in intrusion and hold-up alarm systems and their ergonomics

J. Hart[1,*] and V. Hartová[2]

[1]Czech University of Life Sciences Prague, Faculty of Engineering, Department of Technological Equipment of Buildings, Kamýcká 129, CZ165 00 Prague, Czech Republic
[2]Czech University of Life Sciences Prague, Faculty of Engineering, Department of Vehicles and Ground Transport, Kamýcká 129, CZ165 00 Prague, Czech Republic
*Correspondence: janhart77@gmail.com

Abstract. Currently it is highly important for detectors to be able to achieve efficiency, reliability, and faultless operation, and to be ergonomic thanks to their assembly and being easy-to-fit. In the case of a proposal for the placement of detectors it is naturally important to determine position of the detector and the type of detector being used, but also to guarantee their capability to be able to detect anything when in use and their user and installation-friendliness. The problem of passive infrared (PIR) detectors affects a large proportion of intrusion and hold-up alarm systems (I&HAS). In a time of increasing property crime, it is highly important for PIR detector to actually be able to detect break-in attempts within the guarded area on a reliable basis and free of error. In the case of the installation of PIR detectors, it is naturally important not only to ensure correct installation, to gauge the external influences which may impact upon the detector and to ensure proper maintenance, but also to guarantee the capability of detection under more arduous conditions. The tests and comparisons which have been conducted examine both the normal operation of the PIR detectors and the ergonomics of these detectors. These tests are important both from an informative perspective and due to the opportunities to be able to develop potential counter-measures which could lead to their improvement.

Key words: security risks, ergonomic, intrusion and hold-up alarm systems, passive infrared detector.

INTRODUCTION

At a time of increasing property crime, it is very important for detectors to achieve efficiency, reliability, faultlessness, and ergonomic ease of assembly and assembly. Passive infrared detectors, known as PIR detectors, are the most commonly used space protection elements in alarm systems for intrusion and retention. They can, however, be used in many other applications than simply to provide space protection. PIR detectors are, as the name suggests, passive non-emitting motion detectors. For proper operation, these detectors are typically DC powered (using a low voltage). Movement is detected by a pyro element which detects a change in temperature with a pyroelectric effect in the background of the space that is under surveillance. In the case of installing PIR detectors, it is of course not only important to ensure proper installation, to measure external influences on the detector and to ensure proper maintenance, but also to ensure their

detection capability in more demanding conditions (Cumming, 1994; Capel, 1999; Hart & Hartová, 2016).

PIR detectors are highly prone to poor installation and, as a result, it is very important to pay attention to these detectors. PIR detectors have in general the highest number of false alarms from all detectors. This high error rate is due mainly to incorrect installation. This is why we've defined a problem which should serve to compare the properties and parameters of the PIR detector with its suitability for installation (Staff & Honey, 1999; Powell & Shim, 2012; Malaťák et al., 2016; Choubisa et al., 2017).

MATERIALS AND METHODS

Measurements were made in order to determine the response of the PIR sensor (Fig. 1) in various situations. The PIR sensor is a basic feature of the PIR detector. These are sensors that are sensitive to infrared light irradiation. These are semiconductor devices and are made of crystalline materials such as tantalum and lithium compounds. They can respond to irradiation with infrared light. In the case of irradiation, an electrical charge occurs on the crystals. It works as a gradient drive, ie. it only detects changes of incident radiation on the sensor. In the case of usually more expensive and better quality sensors, two and four pyroelements are used.

Since the pyroelectric sensor is sensitive to the large wavelength range of electromagnetic waves, a radiation filter is inserted in front of the sensor. The purpose of the filter is to pass through only infrared radiation. The PIR sensor is a so-called pyroelectric phenomenon (the effect of temperature on the crystalline lattice -> electrical potential, electrical charge difference -> triggering of an alarm) (Petruzzellis, 1993; Upadrashta et al., 2015; Drga et al., 2016; Hart et al., 2016; Luo et al., 2016).
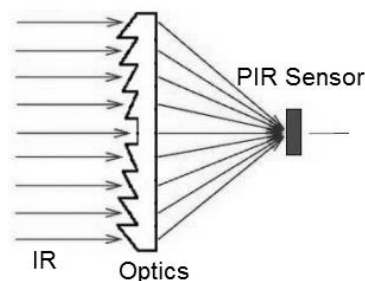
Figure 1. Schematic showing the PIR sensor function.

For testing and comparison, digital PIR detectors were selected (see Fig. 2). These were detectors from Bosch, PARADOX, Satel, and Pyronix-Hikvision. PET Immunity detectors with the largest representation in the Czech Republic were selected. These detectors have met Security Level 2 standards (a low-to-medium risk). From each type of detector, five samples were tested and average values of all of the measured results were reported.

Figure 2. PIR detectors (from the left: ISC-BPR2-WP12; NV5; AQUA PET; KX10DP).

The following tests were carried out:

- Slow test passage
    - Walking speed – 1.5 km an hour^{-1} (simulating offender movement)
    - Distance from detector – 7 m.
- Range test (max)
    - Walking speed – 5 km an hour^{-1} (standard motion simulation)
    - Testing started at the maximum distance indicated by the manufacturer
    - The measurement is repeated cyclically ten times in succession
    - After a successful measurement, the distance of the drive was extended by half a metre
    - The alarm should have been triggered at least nine times out of ten attempts. If this did not happen then the test was unsuccessful and the test distance was defined as being the maximum distance.
- Detection angle test (max)
    - Walking speed – 5 km an hour^{-1} (standard motion simulation)
    - Distance from detector – 7 m
    - PIR sensors were monitored during the passage
    - The measurement is repeated cyclically ten times in succession
    - During these cycles, the subject's position and the first 'reliable' pulse were monitored
    - A reliable pulse was defined and these pulses had to occur so that at least eight out of ten cycles were triggered, otherwise the angle is defined as being the maximum permitted.
- Sampling Test (max)
    - During the activation of the detector (placing it in its alarm state) its current consumption was measured against the data provided by the manufacturer.

In addition, thirteen independent firms were approached. These companies had all of the selected detectors in their installation portfolio. All of these companies filled out a questionnaire, describing which of these detectors best suited their needs. They were to assign three points to the best of the detectors, two to their second choice, one to their third choice, and zero to the worst detector in their view.

The selection of the most appropriate (compromise) variant was carried out using a multi-criteria analysis. The difference in the price of the PIR detectors being compared is insignificant and therefore has not been counted. The difference between the cheapest and most expensive PIR detectors is only 2 €, which is not particularly crucial when investing in the security feature. For this reason, in the case of these particular detectors, their technical parameters are preferred over their cost. Table 1 shows the value of the judged criteria for individual PIR detectors (Hart et al., 2016).

Table 1. An average expression of detected PIR detector parameters

Type	Slow passage-triggered alarms	Range (max) [m]	Detection angle [°]	Current consumption [mA]	Installation friendliness
Bosch ISC-BPR2-WP12	48	13.5	98.0	10.5	21
Paradox NV5	46	13.5	92.0	11.2	17
Satel AQUA PET	50	16.0	90.5	10.5	16
Pyronix-Hikvision KX10DP	39	11.0	88.5	12.9	24

The priority of each parameter was expressed by means of weights. Weights were determined according to Table 2. The points assigned to the parameters of each PIR detector, the weights, the overall rating, and the PIR detector variant that was selected as the most appropriate are listed in Table 3 (Hart et al., 2016).

Table 2. Determination of weights for PIR detectors

Parameters	Scoring	Scales
Slow passage-triggered alarms	6	0.167
Range (max)	10	0.278
Detection angle	9	0.250
Current consumption	4	0.111
Installation friendliness	7	0.194
Total	36	1

Table 3. A selection of the most suitable PIR detector by multi-criteria analysis

Type	Slow passage-triggered alarms	Range (max) [m]	Detection angle [°]	Current consumption [mA]	Installation friendliness	**Points**
Bosch	6	8	10	9	8	**8.277**
Paradox	7	8	9	8	5	**7.501**
Satel	5	10	8	10	4	**7.501**
Pyronix	10	7	7	7	10	**8.083**
Scales	**0.167**	**0.278**	**0.250**	**0.111**	**0.194**	

RESULTS AND DISCUSSION

Of all four PIR detectors being compared, the Bosch ISC-BPR2-WP12 detector was selected as the best option, with a total score of 8.277 points. This means that the required criteria satisfied approximately 83% of the total possible score. The Pyronix-Hikvision KX10DP detector was placed in second position with 8.083 points (81%), and the Paradox NV5 and Satel AQUA PET detectors were placed in last position, both with 7.501 points (75%). The final order is shown in Fig. 3.
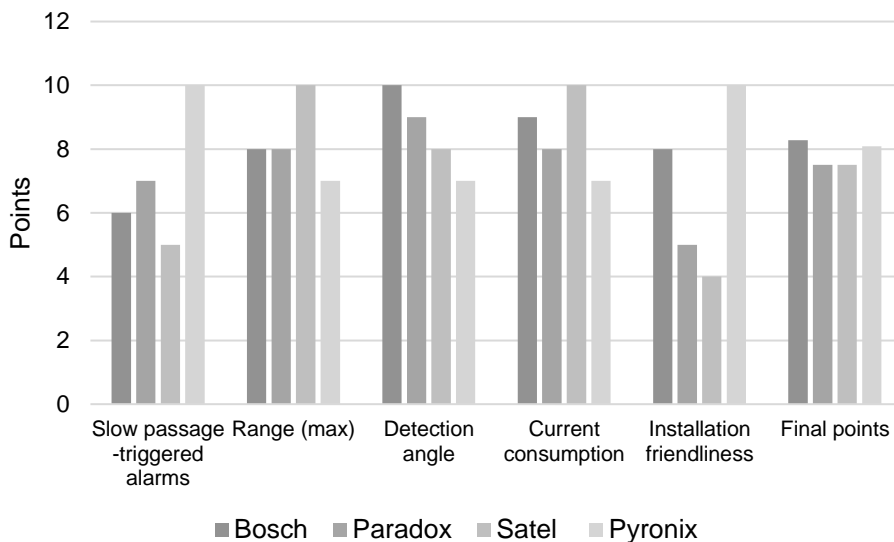
Figure 4. Overall standings for PIR detectors.

Until all of the systems have been tested, it is possible only to ask how many detectors and systems are at all secure. A further question is whether any system exists which could provide reliable protection for a reasonable price.

Although manufacturers are constantly attempting to develop systems, the majority copy old errors in the technical design into new products of a higher class, even despite the endeavours of customers to ensure manufacture is modified. Without innovative approaches and user feedback, this array will career into a blind alley (Upadrashta et al., 2015; Hart & Hartová, 2016; Drga et al., 2016; Luo et al., 2016; Choubisa et al., 2017).

This testing is also appropriate because PIR sensors are beginning to be used to monitor the movement of persons in the smarthome, as reported by authors in these articles: 'An Optical-Camera Complement to a PIR Sensor Array for Intrusion Detection and Classification in an Outdoor Environment' (Choubisa et al., 2017); 'ALPAS: Analogue-PIR-sensor-based Activity Recognition System in the Smarthome' (Kashimoto et al., 2017); 'Health Checking System Using a Wearable Health Device and PIR Sensors' (Miyazaki et al., 2016); 'Machine-to-machine Communication-Based Smart Home Security System by NFC, Fingerprint, and PIR Sensor with Mobile Android Application' (Morsalin et al., 2016); and 'Human Daily Activity Recognition Using Ceiling Mounted PIR Sensors' (Luo et al., 2016).

CONCLUSIONS

The technical design of security systems is unique for the majority of manufacturers. In the case of every manufacturer it is possible to find some degree of poor technical design which requires modification. This deficiency can be resolved through the technical development of the given product and adaptation to customer requirements.

The practical tests which have been conducted on PIR detectors delivered a level of insight into their functionality and usability in practice. Using multi-criteria analysis of variants, an optimal PIR detector was selected. In the research, the measured values of the PIR detector and installation convenience were compared. The PIR detector, ISC-BPR2-WP12 from the manufacturer Bosch, has emerged as being the best choice out of the comparison detectors.

The other detectors did not fare much worse than the ISC-BPR2-WP12. The second-placed one was the Pyronix-Hikvision KX10DP detector. In joint third position, the Paradox NV5 and Satel AQUA PET ended up with the same number of points. The difference between worst placed and best placed detector was only 10%.

REFERENCES

Capel, V. 1999. *Security Systems & Intruder Alarms*. Elsevier Science, 301 pp. ISBN-13: 9780750642361.

Choubisa, T., Mohanty, S.B., Kashyap, M., Ganlbhir, S., Chaitanya, K.K., Sridhar, A. & Kumar, P.V. 2017. An Optical-Camera Complement to a PIR Sensor Array for Intrusion Detection and Classification in an Outdoor Environment. In: *2017 IEEE 42nd Conference on Local Computer Networks Workshops (LCN WORKSHOPS)*, pp. 44–52.

Cumming, N. 1994. Security: *A. Guide to Security System Design and Equipment Selection and Installation.* Elsevier Science, 338 pp. ISBN-13: 9780750642361.

Drga, R., Janacova, D. & Charvatova, H. 2016. Simulation of the PIR detector active function. In: *20th International Conference On Circuits, Systems, Communications and Computers (CSCC 2016)*, vol. **76**, UNSP 04036.

Hart, J. & Hartová, V. 2016. Risks of vibration detectors in intrusion and hold-up alarm systems. In: *15th International scientific conference on engineering for rural development*, pp. 529–535.

Hart, J., Hartová, V. & Bradna, J. 2016. Intrusion and hold-up alarm systems and their reliability glass break detection. In: *Proceeding of 6th International Conference on Trends in Agricultural Engineering 2016*, pp. 171–174.

Kashimoto, Y., Fujiwara, M., Fujimoto, M., Suwa, H., Arakawa, Y. & Yasumoto, K. 2017. ALPAS: Analog-PIR-sensor-based Activity Recognition System in Smarthome. In: *2017 IEEE 31st International Conference on Advanced Information Networking and Applications (AINA)*, pp. 880–885.

Luo, X.M., Liu, T., Shen, B.H., Hong, J.M., Chen, Q.Q. & Chen, H. 2016. Human Daily Activity Recognition Using Ceiling Mounted PIR Sensors. In: *Proceedings Of The 2nd International Conference on Advances In Mechanical Engineering and Industrial Informatics (AMEII 2016)*, vol. 73, pp. 872–877.

Malat'ak, J., Bradna, J., Hrabe, P. & Kucera, M. 2016. Energy Utiliztion of By-Products from Mechanical Recycling Process of Electronic Waste. In: *6th International Conference on Trends in Agricultural*, CULS, Prague, pp. 385–390.

Miyazaki, T., Shinohara, F., Horiuchi, T., Ohira, Y., Yamamoto, H. & Nishi, M. 2016. Health Checking System Using Wearable Health Devise and PIR Sensors. In: *Sensors and Electronic Instrumentation Advances (SEIA)*, pp. 85–86.

Morsalin, S., Islam, A.M.J., Rahat, G.R., Pidim, S.R.H., Rahman, A. & Siddiqe, M.A.B. 2016. Machine-to-machine Communication Based Smart Home Security System by NFC, Fingerprint, and PIR Sensor with Mobile Android Application. In: *2016 3rd International Conference on Electrical Engineering and Information & Communication Technology (ICEEICT)*, art. num. 7873048.

Petruzzellis, T. 1993. Alarm Sensor and Security. McGraw-Hill Professional Publishing, 256 pp. ISBN-13: 9780830643141.

Powell, S. & Shim, J.P. 2012. *Wireless Technology: Applications, Management, and Security*. Springer-Verlag New York, LLC, 276 pp. ISBN-13: 9781461429364.

Staff, H. & Honey, G. 1999. *Electronic Security Systems Pocket Book*. Elsevier Science, 226 pp. ISBN-13: 9780750639910.

Upadrashta, R., Choubisa, T., Aswath, V.S., Praneeth, A., Prabhu, A., Raman, S., Gracious, T., Kumar, P.V., Kowshik, S., Iyer, M.S. & Prabhakar, T.V. 2015. An Animation-and-Chirplet Based Approach to Intruder Classification using PIR Sensing. In: *2015 IEEE Tenth International Conference on Intelligent Sensors, Sensor Networks and Information Processing (ISSNIP)*, art. num. 7106914.

Testing of ISM band at remotes for unlocking vehicles

J. Hart[1,*] and V. Hartová[2]

[1]Czech University of Life Sciences Prague, Faculty of Engineering, Department of Technological Equipment of Buildings, Kamýcká 129, CZ165 00 Prague, Czech Republic
[2]Czech University of Life Sciences Prague, Faculty of Engineering, Department of Vehicles and Ground Transport, Kamýcká 129, CZ165 00 Prague, Czech Republic
*Correspondence: janhart77@gmail.com

Abstract. Every modern car has a remote control for wireless unlocking. Wireless drivers for unlocking the vehicle using frequency in the ISM bands. ISM bands are unlicensed bands. They are usually used for industrial, medical and scientific purposes. The question is whether wireless transmission parameters are sufficient and do not violate defined range of ISM band. Another important aspect is the security of the wireless transmissions and any other signal interference. The problem of interference plays an important role in ensuring the quality and safety of wireless communications, especially when wireless networks can be found everywhere. The issues of remote control vehicles is very important due to the resulting security of a guarded vehicle. One of the major risks that may occur are data transmission that the signal is blocked by another signal and the end user does not notice. In this case, does not lock the vehicle nor ensuring its securing security system. Tests which were performed accurately determined the bandwidth of broadcast remote control for each vehicle. Vehicles for which the tests were conducted are standard vehicles used to frequent occurrence. These are the following types: Alfa Romeo, Hyundai, Mercedes, Škoda and Toyota. Subsequently, the analysis was performed of transmission compared with standard broadcast of jammers. All test drivers worked in the band ISM433. These tests clearly demonstrated that not every manufacturer strictly observes ranges of ISM band. This may affect traffic on surrounding licensed bands.

Key words: Remotes, vehicle, wireless transmission, interference, measuring.

INTRODUCTION

Currently, the issue of electromagnetic interference is growing steadily and much attention is focused on it from both scientists and the general public. Electromagnetic interference is increasing almost every day, and disseminators include seemingly risk-free parts of everyday life such as home appliances, machinery and devices, urban environments and high-voltage lines that supply electricity in both areas near and far away (hereinafter common electromagnetic interference). It has been shown that it also arises, for example, in the thermal treatment of materials. It is not possible to state that this is directly a natural disaster, but it does have a major impact on both the environment, and the functionality of various communication technologies (Mpitziopoulos et al., 2007; Commander et al., 2008; Altman et al., 2011; Bradna & Malaťák, 2016).

Electromagnetic interference is also increased with the boom in wireless technologies, which has led to a large increase in the use of wireless devices. Through their broadcasts, these devices gradually overload individual frequencies, which leads not only to transmission errors, but sometimes also to their disabling. Electromagnetic interference overloading of 433 MHz and 868 MHz frequencies, through which the wireless component of wireless transmissions with remotes for unlocking vehicles communicates, strongly affects their reliability, usability (Commander et al., 2008; Tahir & Shah, 2008; Pelechrinis et al., 2009; Hart & Hartová, 2014).

Although common electromagnetic interference for wireless transmission with remotes for unlocking vehicles is very risky, it is not the greatest risk. The greatest risks are becoming low-frequency jammers that are able to jam ongoing communication between a remotes and vehicles, thus disabling the alarm (Staff & Honey, 1999; Mpitziopoulos et al., 2007; Siddhabathula et al., 2012; Hartová & Hart, 2017).

Many research has shown that not every transmitter meets the ISM band. These bands are free of charge and are specified by the telecommunication authorities. It was therefore a question of whether wireless communications with remotes for unlocking vehicles meet the necessary requirements of telecommunication authorities. If these requirements were not met, it would have had a major impact on the production engineering of these remotes (Hart & Hartová, 2014; Hartová & Hart, 2017).

MATERIALS AND METHODS

Tests which were performed accurately determined the bandwidth of broadcast remote control for each vehicle. Vehicles for which the tests were conducted are standard vehicles used to frequent occurrence. These are the following types: Alfa Romeo, Hyundai, Mercedes, Škoda and Toyota.

SPECTRAN HF-6060 spectrum analyser (Fig. 1) was used, which investigated the strength of the broadcasting remotes for unlocking vehicles at frequencies of 433 MHz (ISM 433). ISM 433 is only standard for ITU 1 (EMEA), not for Asia and therefore the cars distributed in ITU1 area were selected. The manufacturer must adhere to the wireless transmission standards of countries where he distributes his products.

Figure 1. Spectrum analyser SPECTRAN HF-6060 with an antenna.

The ISM (industrial, scientific and medical) bands that were measure are bands for radio broadcasts, which are used, for example, in industry, and for health and scientific purposes. They are of course also used in the commercial sector, where we most often encounter them with RC models and intruder and hold-up alarm systems. They are unlicensed (free) bands, which means that they are allowed to operate without license fees if they use homologated (approved) devices. Although a commercial company may save money by using them, but their one big disadvantage is that these frequencies do not guarantee against interference (Cumming, 1994; Capel, 1999; Powell & Shim, 2012).

Within the measurement the following values were set on the SPECTRAN HF-6060 spectrum analyser:

- Sampletime – 50 ms
- Samples – 500
- Bandwidth – 1 MHz

For each car, two identical controls were tested in five cycles. For all charts, top line shows wireless transmission and lower default values for natural interference. In the following figures (Figs 2–5) are an evident intensity of the wireless transmission vehicles: Hyundai i30, Mercedes-Benz CLK, Alfa Romeo 159 and Toyota Verso in the scope of ISM 433.
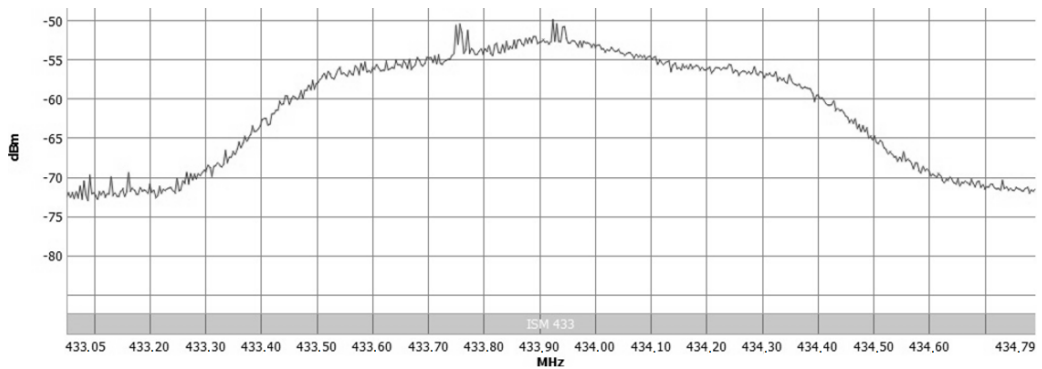
Figure 2. Transmission characteristics of Hyundai i30.
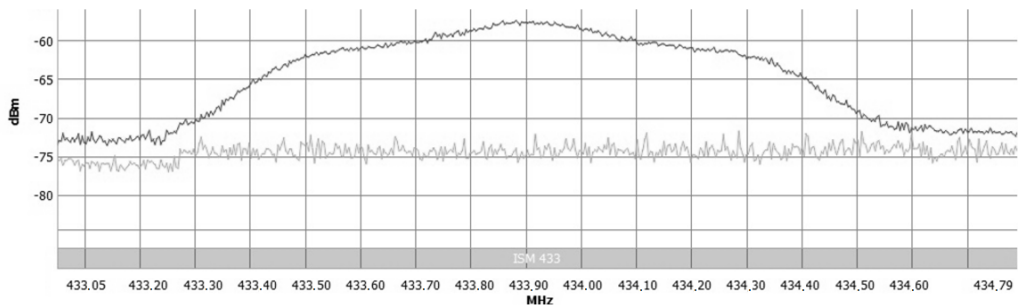
Figure 3. Transmission characteristics of Mercedes Benz CLK.
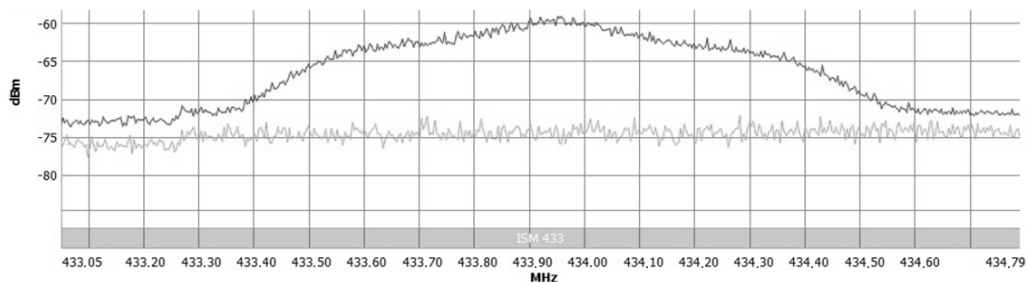
Figure 4. Transmission characteristics of Alfa Romeo 159.
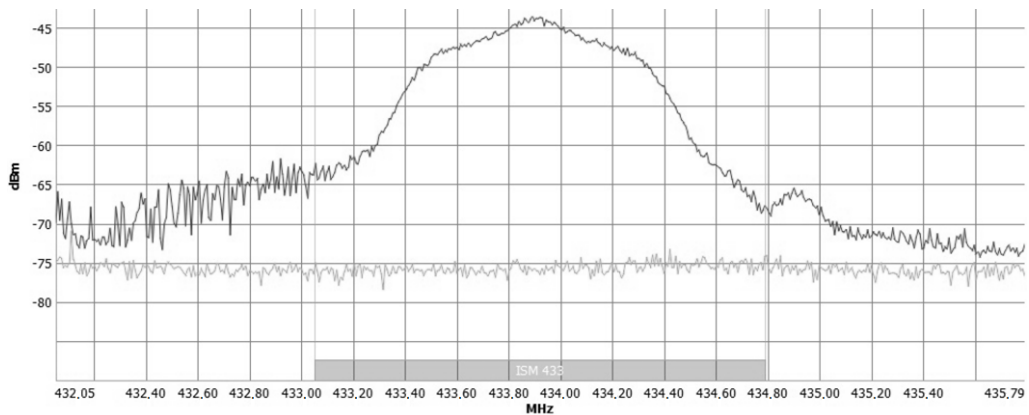
Figure 5. Transmission characteristics of Toyota Verso.

In the following figures (Figs 6–9) are an evident intensity of the wireless transmission vehicles: Škoda Fabia III, Škoda Octavia II, Škoda Superb II and Škoda Octavia III RS in the scope of ISM 433.
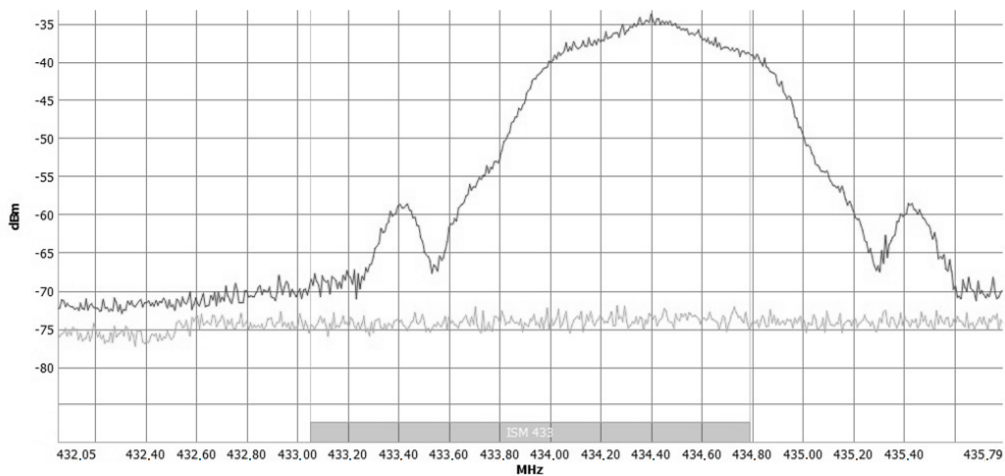
Figure 6. Transmission characteristics of Škoda Fabia III.
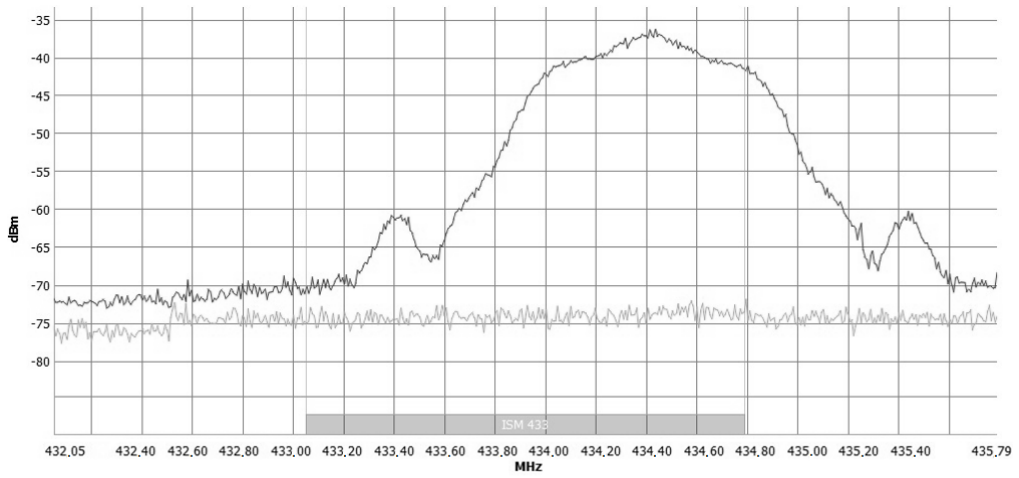
Figure 7. Transmission characteristics of Škoda Octavia II.
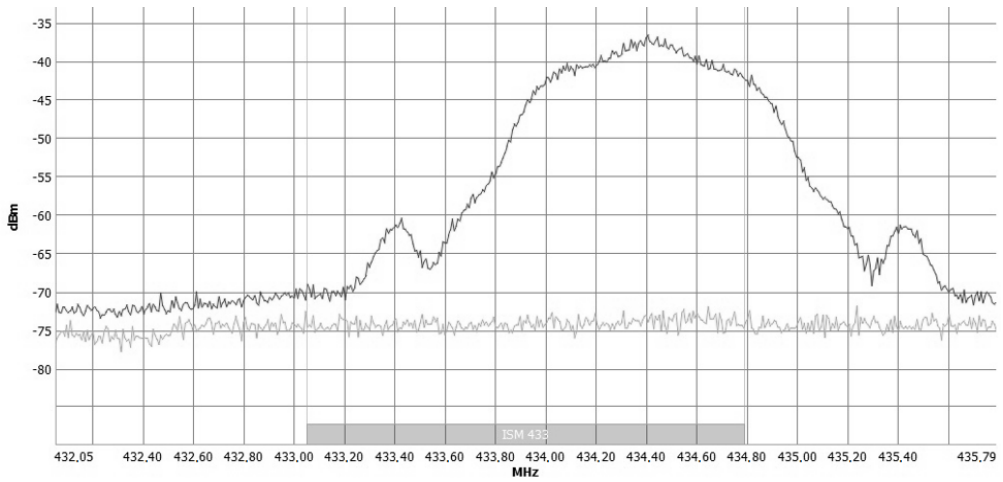
Figure 8. Transmission characteristics of Škoda Superb II.
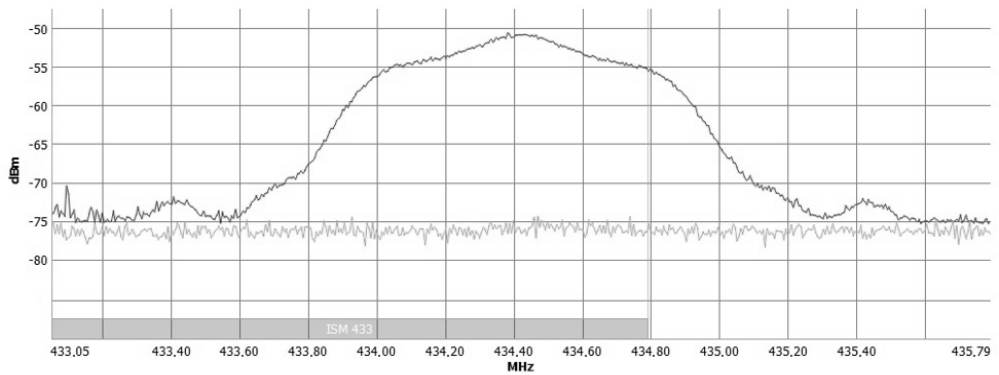
Figure 9. Transmission characteristics of Škoda Octavia III RS.

In the last figure (Fig. 10) is an evident intensity of the wireless transmission of vehicle Toyota Auris in the scope of ISM 433.
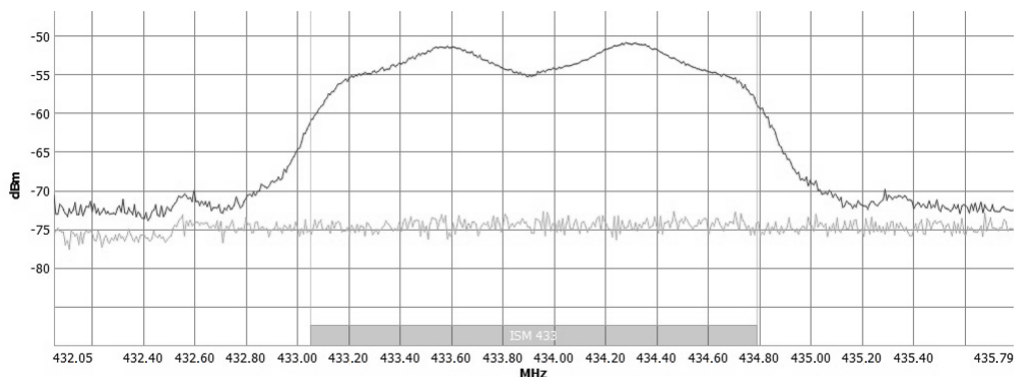
Figure 10. Transmission characteristics of Toyota Auris.

RESULTS AND DISCUSSION

From the measured results of wireless transmissions using the remote control to unlock the vehicle based on best provided wireless transmissions shown in Figs 2, 5 and 10 respectively.

They have the power in their broadcasts and do not depart from prescribed ISM band. At the same time wireless transmissions in the results in Fig. 10 and implemented in parallel in two bands, thereby reducing the likelihood jamming. Wireless transmissions in Figs 3 and 4 while also do not interfere outside ISM bands, but their broadcasts is weaker over the previous variants. It may give rise to a situation that, due to natural electromagnetic interference is not successfully transmitted. The remaining transmissions, shown in Figs 6–9, although they have great power, but failed to comply with specified range of transmission for the ISM band, so should officially not used at all. A comparison of different wireless transmissions can be seen in Fig. 11, based on the above parameters. This figure shows the percentage of transmission quality for each measured vehicle.
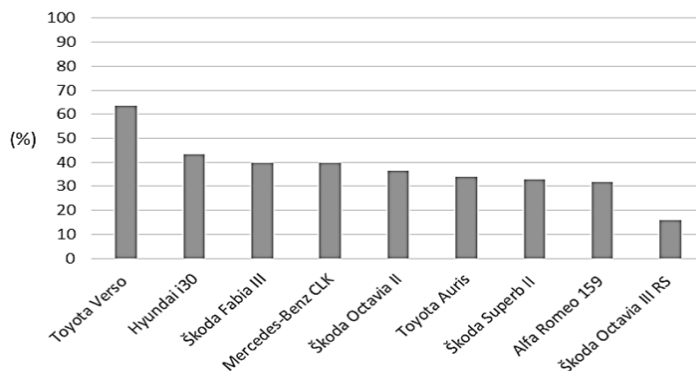
Figure 11. Evaluation of individual criteria through a multi-criteria scoring options.

1022

Since the first public demonstration of radio and radio communication in 1893 by Nikola Tesla, people have been trying to find a way to communicate with each other without such communication being interfered with. One of the biggest booms in this research began during the Vietnam War, as described by the author of the article 'The Progress of Tactical Radios from Legacy Systems to Cognitive Radios.' (Elmasry, 2013). Many years of research have passed since this historic turning point, but this also includes jamming devices as described in the article 'Responsive Communications Jamming Against Radio-Controlled Improvised Explosive Devices' (Mietzner et al., 2012), where the author focused mainly on protective jammers used to protect against 'radio-controlled improvised explosive devices (RCIEDs)'.

According to recent research and gradual overloading of ISM bands, it is necessary to further develop the possibilities of unlicensed bands, as described in the article 'Complex radio frequency (RF) communications with virtual pulses' (Maina et al., 2008), which describes the use of virtual pulses for communication. It also includes protection against interference. It is also advisable to constantly explore other options, thanks to which new wireless sensor networks could develop, as described by the authors in the article 'UWB wireless sensor networks: UWEN – A practical example' (Opperman et al., 2004), where they favour the use of Impulse-radio-based UWB technology for WSN development.

CONCLUSIONS

Wireless transmissions with remotes for unlocing vehicles are very susceptible to interference – both interference caused by the environment, and interference caused by a targeted jammer.

The measured values clearly show that not every wireless transmissions with remotes for unlocing vehicles has effective intensity against band interference. In order to ensure the vehicle system, guarded vahicle and property, it is important that the band interference control is flawless.

It is important to have an overview of the reliability and functionality of each wireless transmissions. When using wireless transmissions, it is also important for remotes to have bidirectional communication, which increases the system's chances to detect band interference, and also allows the transmission to be switched to a free zone. The only problem would then be if the perpetrator used a smart jammer with detection of used frequencies.

Vehicles Škoda Fabia III, Škoda Octavia II, Škoda Superb II and Škoda Octavia III RS detected overlapping outside ISM bands. It is therefore recommended that the wireless technology of these vehicles be changed. It is recommended that this change be made due to a weak signal even for vehicles Mercedes Benz CLK and Alfa Romeo 159, even though their transmission is within the ISM bandwidth.

All of the measured data are also important for manufacturers of vehicle systems as feedback on their products. In the future, there will be efforts to expand similar tests to other I&HAS manufacturers, as the reliability of these systems is very important, and it will be necessary to check them after deficiencies in the tested systems are ascertained.

REFERENCES

Altman, E., Avrachenkov, K. & Garnaev, A. 2011. Jamming in wireless networks under uncertainty. *Mobile Networks & Applications* **16**, 246–254.

Bradna, J. & Malaťák, J. 2016. Flue gases thermal emission concentration during waste biomass combustion in small combustion device with manual fuel supply. *Research in Agricultural Engineering* 1–7.

Capel, V. 1999. *Security Systems & Intruder Alarms*. Elsevier Science, 301 pp.

Commander, C.V., Pardalos, P.M., Ryabchenko, V., Shylo, O., Uryasev, S. & Zrazhevsky, G. 2008. Jamming communication networks under complete uncertainty. *Optimization Letters* **2**, 53–70.

Elmasry, G.F. 2013. The Progress of Tactical Radios from Legacy Systems to Cognitive Radios. *IEEE Communications Magazine* 51, 50–56.

Hart, J. & Hartová, V. 2014. The risks of data transmissions in intrusion and hold-up alarm systems and solutions thereto. In: *3rd International Conference on Applied Materials and Electronics Engineering*, pp. 570–574.

Hartová, V. & Hart, J. 2017. Livestock monitoring system using bluetooth technology. In: *Agronomy Research* **15**(3), 707–712.

Maina, J.Y., Mickle, M.H., Lovell, M.R. & Schaefer, L.A. 2008. Complex radio frequency (RF) communications with virtual pulses. *Computers & Electrical Engineering* **34**, 423–437.

Mietzner, J., Nickel, P., Meusling, A., Loos, P. & Bauch, G. 2012. Responsive Communications Jamming Against Radio-Controlled Improvised Explosive Devices. *IEEE Communications Magazine* **50**, 38–46.

Mpitziopoulos, A., Gavalas, D., Pantziou, G. & Konstantopoulos, C. 2007. Defending wireless sensor networks from jamming attacks. *IEEE 18th International Symposium on Personal, Indoor and Mobile Radio Communications* **1–9**, 81–85.

Oppermann, I., Stoica, L., Rabbachin, A., Shelby, Z. & Haapola, J. 2004. UWB wireless sensor networks: UWEN – A practical example. *IEEE Communications Magazine* **42**, S27–S32.

Pelechrinis, K., Koutsopoulos, I., Broustis, I. & Krishnamurthy, S.V. 2009. Lightweight Jammer Localization in Wireless Networks: System Design and Implementation. *IEEE Global Telecommunications Conference* **1–8**, 1301–1306.

Powell, S. & Shim, J.P. 2012. Wireless Technology: Applications, Management, and Security. Springer-Verlag, New York, 276 pp.

Siddhabathula, K., Dong, Q., Liu, D.G. & Wright, M. 2012. Fast Jamming Detection in Sensor Networks. *IEEE International Conference on Communications (ICC)*, pp. 934–938.

Staff, H. & Honey, G. 1999. Electronic Security Systems Pocket Book. Elsevier Science, 226 pp.

Tahir, H. & Shah, S.A.A. 2008. Wireless Sensor Networks – A Security Perspective. In: *INMIC: 2008 International Multitopic Conference*, pp. 189–193.

Influence of face lighting on the reliability of biometric facial readers

V. Hartová[1,*], J. Hart[2] and P. Prikner[1]

[1]Czech University of Life Sciences Prague, Faculty of Engineering, Department of Vehicles and Ground Transport, Kamýcká 129, CZ165 00 Prague, Czech Republic
[2]Czech University of Life Sciences Prague, Faculty of Engineering, Department of Technological Equipment of Buildings, Kamýcká 129, CZ165 00 Prague, Czech Republic
[*]Correspondence: nverca@seznam.cz

Abstract. At present, there is an increasing need to protect workplace entry and specially guarded premises. In addition to standard access systems on a chip cards are getting to the fore of biometric identification systems such as readers for fingerprint, biometric scans faces and others. Biometric readers face still improve, but still have a lot of blind spots, thanks to which their reliability and user-friendliness decreases. One such problem is the light intensity in the room where the reading device is located. The varying intensity of the light in the room causes a different illumination of the person's face. It emphasizes or suppresses the main points of the face that needed for user authorization, and the whole identification process is prolonged and difficult. The reliability value is significantly different from the value given by the manufacturers. It is very important to highlight on this problem and begin to address it by altering the current production engineering.

Key words: light intensity, measuring, False Acceptance Rate, identification, facial features.

INTRODUCTION

In today's world, an increasing emphasis is placed on securing objects. Quality security is not only about detectors for perimeter and indoor protection, but it is also very important to take care of the security of access systems. At first it used a very simple devices that operate on the principle of a password or pin, then began to use access cards and in recent years the industry has developed so much that for access to protected objects using biometric identification systems. Such systems are many (Jazzaret & Muhammad, 2013).

Most commonly used are systems that use fingerprints to identify people. These systems are quite good enough, but there is still a high chance of their sabotage. In second place are identifying systems based on the geometry of the face. Such systems are financially acceptable, but their reliability is quite a problem. (Di Martino et al., 2016) The first problem is that imitating one's appearance is not difficult, and another problem is that the identification depends on the environment in which the reader works. Although the manufacturer makes recommendations, where he writes about the lighting conditions, the spatial location of the reader, temperature and humidity conditions, etc.,

but the device is usually installed already in the original space and therefore it is not always possible to fulfill all the recommendations of the equipment manufacturer.

This paper focuses on the issue of the illumination intensity of the room in which the reader is located. It has been found that too high or low light intensity increases the wrong user denial and possible confusion of these users. Appropriate system innovation was needed to increase reliability to an acceptable level (Zou et al., 2010¸ Vinay et al., 2015). By testing, this problem was largely suppressed by adding an additional ice strip to individual biometric identification devices. It is very important to emphasize this problem and begin to address it by changing the current manufacturing engineering. The development of innovation in this area is of great importance. The emphasis is on the implementation of measures that will improve their ability to identify flawless (Ashbourn, 2000; Zhang, 2000; Jain & Feng et al., 2009).

To determine the reliability values of biometric identification systems, the formula for False Acceptance Rate (FAR) and False Rejection Rate (FRR) was used.

MATERIALS AND METHODS

The measurements build upon the previous research which was carried out with 80 participants using the readers MultiBio 700 and iFace 302.

A cohort of 30 participants was chosen for measurements which were repeated 20times. Regarding the face scan it was necessary to observe laboratory conditions, in particular lighting (the lighting required by the manufacturer is in the range of 0–800 lux) for the first measurement, which served as a model standard. A further 20 repeat measurements were performed with the original participants, the room lighting was provided by a dimming reflector. The tests were performed on AFT-500, AccuFACE® EFR-T1, MultiBio 700 and iFace 302 readers, represented in Figs 1 and 2. The light dimmable reflector has been attached to a classical illumination. Testing ranged from 0 Lux values of light intensity up to 1,700 lux value.

Figure 1. AFT-500 and AccuFACE® EFR-T1.   **Figure 2.** MultiBio 700 and iFace 302.

The measurement was primarily focused on false user acceptance. False acceptance of a user means that an unauthorized person is admitted to a particular premises. The admittance of an unauthorized person can happen in two ways, namely through a reading device error, when a person in question has no intention of criminal activity, while the other way consists in intentionally causing the door to open with certain intents in mind (trespassing, theft and other offenses. The offender has more than one possibility of outsmarting the biometric identification system. One of them is to cause a shortcircuit

of the reading device without subsequent alarm activation (most of the identification systems are connected to the switchboard of Intrusion and Hold-up Alarm Systems.) Another way is to adjust your visage in a way that is as close as possible to one of the eligible users (Rak, et al., 2012; Jazzar & Muhammad, 2013).

$$FAR = \frac{N_{FA}}{N_{IIA}} \cdot 100 \ (\%) \qquad (1)$$

FAR – False Acceptance Rate; N_{FA} – Number of False Rejection; N_{IIA} – Number of attempts by unauthorized persons to identify.

In addition, testing was aimed at a false denial of the user, and in the case of these readers a threshold for user denial was set for 2 seconds. Facial-identifying readers can not reject the user, only the user can accept, so it is necessary to set a limit. This limit is the value the manufacturer gives as the value at which the identification is to take place.

$$FRR = \frac{N_{FR}}{N_{EIA}} \cdot 100 \ (\%) \qquad (2)$$

FRR – False Rejection Rate; NFR – Number of false rejection; NEIA – Number of Enrolle Identification Attemps.

A measurement panel was set up and all the measured readers were attached to it – see Fig. 3. First it was necessary to download individual users to each biometric system. All the tested readers have the same software and downloading was carried out in the same manner. First, each user was assigned his/her ID (identification number), next their fingerprints were taken (scanning the same finger 3times) and after that a 3D face model example was downloaded. The readers' voice application gave the users instructions on how to turn their heads (Abateet al., 2005, Stroica & Vladescu, 2012).

Figure 3. Measuring panel.

The readers are equipped with two cameras scanning the user's face at a specific angle. If the cameras get the required values, they will create a picture and store it. Already during the scanning of the model/template it is necessary for the scans to reach minimally 95% correspondence with the first scan. This means a match at the points which developers determined to be the points of reference (tip of the nose, nose width, distance between eyes, facial bones, mouth shape, chin and more). It was the matching of the individual snaps which were scanned in gradual steps, which extended the time needed for creating of example models.

When testing the readers, a series of measurements was performed at each light intensity. The individual luminous intensities were 0 lux, 45 lux, 160 lux, 400 lux, 725 lux, 1,150 lux and 1,700 lux.

After that LED lighting was attached to the measurement board, made up of six rows of LED tape which contained 270 LEDs.

These additional LEDs have been used to increase the reliability of biometric identification systems. Again, a set of tests was performed on the same counts as the previous measurements, except that the reader had an additional white LED light.

RESULTS AND DISCUSSION

First, measurements were made of the number of received users by each biometric systems. A total of 600 measurements were made for each light intensity and for each biometric identification system. Seven different luminous intensities were determined. These intensities were set from 0 lux to 1,700 lux. These values correspond to the values measured in individual rooms in different businesses that did not want to be published for security reasons. The graphs in Figs 4 to 7 show the measured values, where at each luminous intensity there are 4 levels of acceptance / rejection of the user. According to the legend of the chart, it is obvious that it is a borderline and so identification within 3 seconds, within 5 seconds, within 10 seconds and over 10 seconds. 10 seconds have been set limit for user identification. Anything over 10 seconds has already been taken as a wrong user denial. The first two readers AccuFace and AFT 500 are modern biometric identification systems that are in the middle price range. According to distributors and manufacturers are statistically one of the most used in Europe. The first two levels of the chart are decisive for the system owner. Both the AccuFace reader and the AFT reader make it clear that they are encircling the gaus curve. Highest reliability have systems from 1,150 lux up to 160 lux. If the intensity is too high or too low, there is a significant decrease in reliability. At values of 45–0 lux, it is clear that the integrated illumination with red LEDs is inadequate.
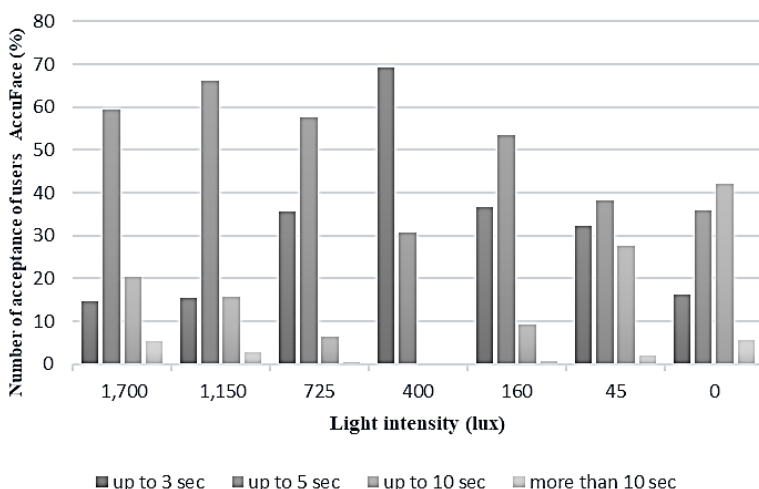
Figure 4. False Rejection Rate AccuFace.
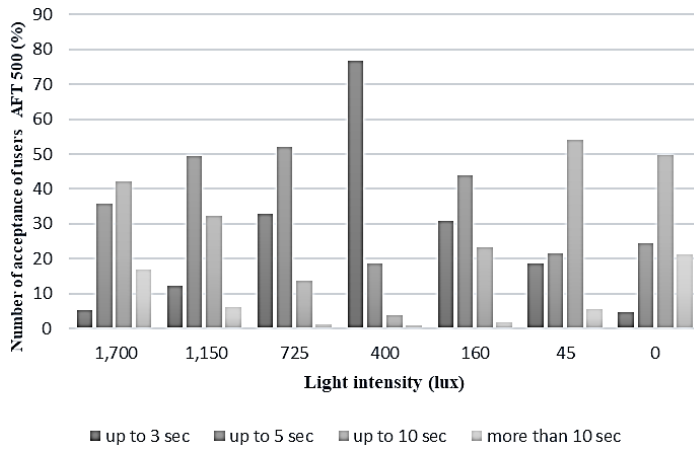
Figure 5. False Rejection Rate ATF 500.
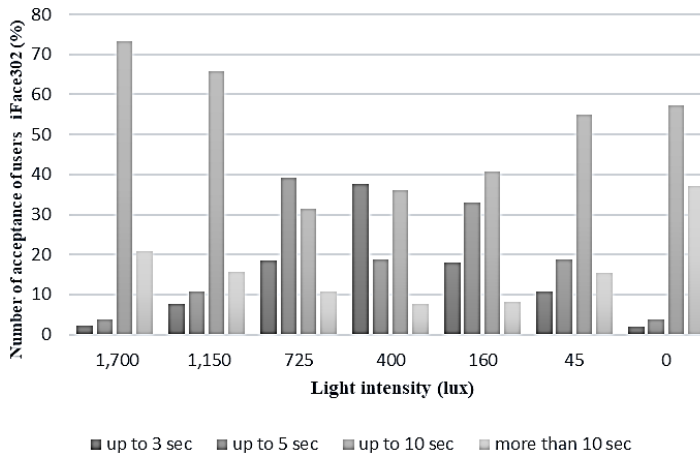
Figure 6. False Rejection Rate IFace302.
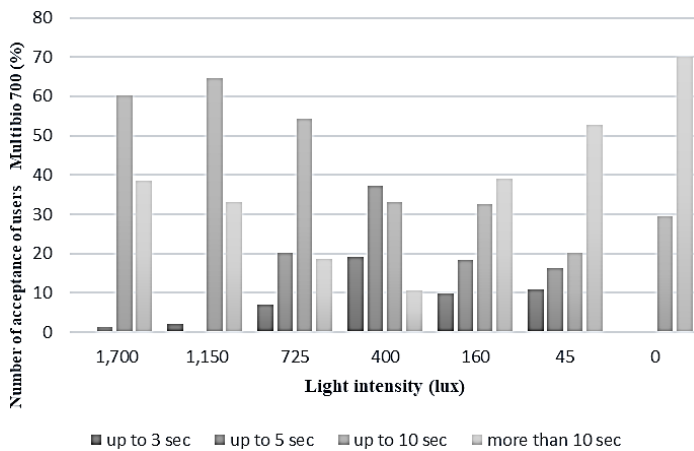
Figure 7. False Rejection Rate Multibio 700.

The IFace 302 and Multibio 700 readers have charts with the same waveform, with worse measured values. These readers are most commonly used in the Czech Republic. It belongs to a lower price category and is gradually changing for newer technologies. The graphs show that the technology of biometric face readers is still evolving and improving.

The second step was measured incorrect user acceptance. Fig. 8 shows that the highest error rate was achieved at luminous intensities of 1,150 lux and above and 46 lux and below. The optimum luminous intensity was 400 lux for all readers.
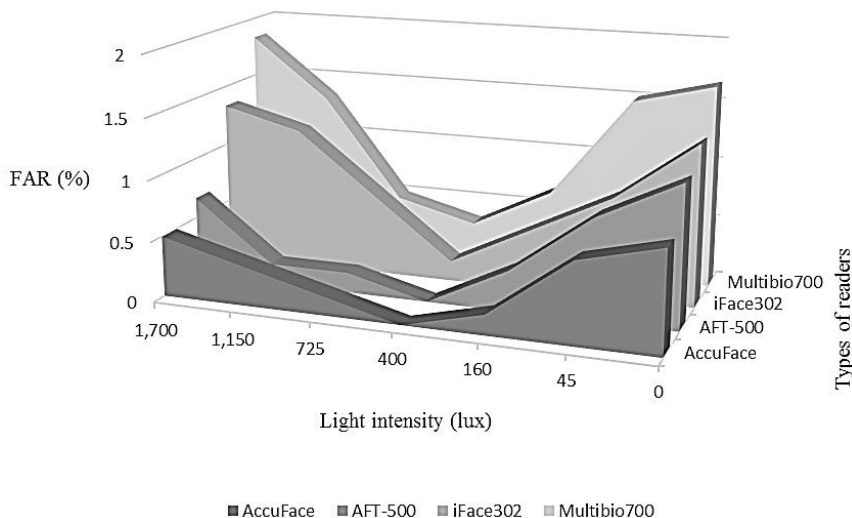
Figure 8. False Acceptance Rate.

As a countermeasure to increase reliability, another series of measurements was made, but this time with an additional panel LED white light. In all cases, the values have improved almost by half. And so the reliability reached an acceptable level. The question of the intensity of the room has not yet been dealt with by anyone else.

The authors Bourlai, T. and Hornak, L.A. in their article Face recognition outside the visible spectrum, highlight the issue of exposure, examining the reliability of systems in low light conditions or at night. Where they point to the different wavelengths and functionality of the systems in the balance sheets.

CONCLUSIONS

Measurement has shown that the intensity of light in the room in which biometric identification systems are located is very important. Too high and low light intensity values reduce the reliability of these systems. Manufacturers declare that the reliability values should be up to 1%, but the graphs could even see values around 30%, which is very unacceptable to the user. It was important to make countermeasures to increase the value of reliability for individual readers to a user-friendly value. This was aided by an additional white LED LED strip. Erroneous acceptance and false rejection values improved by an average of half by adding this additional device. This development area

needs to be further deepened and addressing new innovations in these systems. Accesses to protected objects should not be underestimated.

REFERENCES

Abate, A.F., Ricciardi, S., Sabatino, G. & Tucci, M. 2005, Beard tolerant face recognition based on 3D geometry and color texture, In: *11th International Conference on Distributed Multimedia Systems,* pp. 202–207.

Ashbourn, J. 2000, Biometrics. Advanced Identity Verification, In: *Springer-Verlag*, London, pp. 266–268.

Di Martino, L., Preciozzi, J., Lecumberry, F. & Fernández, A. 2016. Face matching with an a contrariofalse detection control, vol. **173**. pp. 64–71.

Jain, A.K. & Feng, J.J. 2009. Latent Palmprint Matching, In: *IEEE Transactions on pattern analysis and machine intelligence,* pp. 1032–1047.

Jazzar, M.M. & Muhammad, G. 2013. Feature Selection Based Verification/Identification System Using Fingerprints and Palm Print. In: *Arabian journal for science and engineering* pp. 849–857.

Rak, R., Matyáš, V., Říha, Z. 2012. Biometrics and identity of man in forensic and commercial applications. Praha: Grada Publishing, a.s. (in Czech).

Stroica, P. & Vladescu, M. 2012. Implementation of a multiple biometric identification system based on face, fingerprints and iris recognition. In: *Advanced topics in optoelectronics, microelectronics, and nanotechnologies VI.*

Vinay, A., Vinay, S. & Shekhar, K.N., Balasubramanya, M. & Natarajan, S. 2015, Face Recognition Using Gabor Wavelet Features with PCA and KPCA - A Comparative Study. In: *Procedia Computer Science* **57**, 650–659.

Zhang, D.A. 2000. Automated Biometrics. Technologies and Systems, In: *Kluwer Academic Publishers*, Boston, pp. 137–158.

Zou, W., Pong, C. & Yuen 2010. Discriminability and reliability indexes: Two new measures to enhance multi-image face recognition. In: *Pattern Recognition* **43**, 3483–3493.

Combustion property analyses with variable liquid marine fuels in combustion research unit

M. Hissa[*], S. Niemi and K. Sirviö

University of Vaasa, School of Technology and Innovations, Department of Energy Technology, P.O. Box 700, FI-65101 Vaasa, Finland
[*]Correspondence: Michaela.Hissa@uva.fi

Abstract. The quality of ignition and combustion of four marine and power plant fuels were studied in a Combustion Research Unit, CRU. The fuels were low-sulphur Light Fuel Oil (LFO, baseline), Marine Gas Oil (MGO), kerosene and renewable wood-based naphtha. To meet climate change requirements and sustainability goals, combustion systems needs to be able to operate with a variety of renewable and 'net-zero-carbon' fuels. Due to the variations in the chemical and physical properties of the fuels, they generally cannot simply be dropped into existing systems. The aim of this research project was to understand how changes in fuel composition affect engine operation. The focus was on how various properties of the fuels impact on the combustion process – especially ignition delay and in-cylinder combustion. The goal of the research project was to allow broad fuel flexibility without any or only minor changes to engine hardware. Before the engine tests, the CRU forms an easy and cost-effective device to find out the engine suitability of the fuel. The results showed that the ignition delay decreased expectedly with all fuels when the in-cylinder pressure and temperature increased. The differences in the maximum heat release rates between fuels decreased in high-pressure conditions. MGO had the shortest ignition delay under both pressure and temperature conditions. Based on the CRU results MGO and kerosene are suitable to use in compression-ignited engines like the reference fuel LFO. In contrast renewable naphtha had a long ignition delay. If naphtha is used in a CI engine, the engine must be started and stopped with, e.g. LFO or MGO.

Key words: Diesel engines, alternative fuels, ignition delay, heat release rate.

INTRODUCTION

In compression ignition (CI) engines the combustion process starts when liquid fuel is injected as one or more jets into the cylinder fulfilled with hot high-pressured air near the top dead centre (TDC) position of the piston. The ignition delay (ID) is a period when injected fuel entrains to cylinder, atomizes and mixes with existing air. Chemical reactions start slowly and ignition occurs after the ID. Good atomization provides rapid air-fuel mixing decreasing the ID. The ignition of air-fuel mixture prepared during the ID causes a rapid pressure rise that is called as rapid uncontrolled or premixed combustion. Controlled combustion follows and is the part where preparation of fresh air-fuel mixture determines the rate of combustion. Combustion continues until all the fuel or air is utilized. This last phase is called as final combustion.

Due to variations in the chemical and physical properties of the fuels, they generally can not simply be dropped into existing systems. The aim of this research project was to understand how changes in fuel composition affect engine operation. The fuel properties have a significant effect on the ignition and combustion as well as pressure, temperature and mechanical issues (e.g. nozzles and their hole diameters). The viscosity, density, heating value and cetane number have a major effect on good atomization and ignition delay especially under low pressure conditions (Heywood, 1988; Bae & Kim, 2016). Too rapid a chamber pressure increase may cause engine damage and also increase NO_x emissions (Steenberg & Forget, 2007). Buchholz (2013) and Chang et al. (2013) even states that current diesel fuel ignites too easily causing poor mixing with oxygen, which leads to increasing levels of soot and NOx emissions. As a solution they suggest that one way to cut down number of aftertreatment devices and high injection pressure, is to use less processed fuel.

Currently most of the energy sources rely on fossil fuels which have limited resources. That is why alternative energies are necessary. Based on Bae & Kim (2016) significance of using alternative fuels can be defined as followes:

'(1) pursuing energy sustainability through the extended usage of those alternative fuels derived from renewable energy sources and mitigating the concerns of limited fossil fuel energy

(2) improving engine efficiency and engine-out emissions with the aid of superior physical or chemical properties of alternative fuels compared to those of conventional fuels

(3) relieving the unbalanced usage of conventional petroleum-based fossil fuels'.

In this study, the ignition characteristics of four marine and power plant fuels were studied in a Combustion Research Unit, CRU. The fuels were low-sulphur Light Fuel Oil (LFO, baseline), Marine Gas Oil (MGO), kerosene and renewable wood-based naphtha. MGO represents recycled fuels cause it is produced from used lubricant oils. LFO and kerosene may be called as heavier fuels and naphtha represents lighter fractions, which is generally the product of the initial distillation of crude oil. In this study, used naphtha was renewable wood-based naphtha.

Studies (Chang et al., 2013; Wang et al., 2013; Bae & Kim, 2016) have shown that crude oil-based naphtha, run in compression ignition engines, had a high efficiency with good transient operation and acceptable noise levels, while achieving NOx emissions below the EURO6 levels, lower particulate matter (PM) emissions and lower smoke levels than with diesel fuel. However, the low CN and viscosity of naphtha may cause increased NOx emissions due to the retarded start of combustion and prolonged ignition delay (Subramanian et al., 2018).

Kerosene is primarily used in the aviator sector particularly in gas turbine engines. Behind the kerosene usage in diesel engines is North Atlantic Treaty Organization (NATO) military's intending to use JP-8 fuel for all their automobiles and equipments, based on their Single Fuel Concept (SFC), due to logistical benefits. Another reason to study kerosene in diesel engine is adulteration of diesel by mixing it with kerosene, which is big problem in some parts of world. JP-8 has very similar chemical composition compared to the present Jet-A fuel despite some additives (Yadav et al., 2005; Lee et al., 2012). Based on the research of Vasu et al. (2007), JP-8 and Jet-A have very similar ignition delay times. Although, low lubrication may cause problems in the fuel pump system (Anastopoulos et al., 2002; Bae & Kim, 2016).

MGO is commonly known as shipping fuel. The ship owners have been driven to examine how to comply the forthcoming sulphur emission regulations (IMO, 2008), and MGO is promising alternative besides sulphur scrubbers and alternative fuels. MGO is required in a vessel by existing and upcoming regulations depending on time and location. For example a vessel uses MGO when it is inside Emission Controlled Area (ECA) or within EU ports. Outside the ECA, HFO is used. However, by 2020 low-sulphur heavy fuel oil (LSFO) is required outside of the ECA (Germanischer Lloyd and MAN, 2012). Jiang et al. (2014) calculated that it is more beneficial to use MGO in a old ships compared to use scrubber retrofits.

However, MGO has a higher viscosity and density compared to diesel fuel which may lead to poor atomization resulting in incomplete combustion with higher soot emissions (Nabi et al., 2012). However, the studied MGO had a significantly higher CN (68), compared to other studied fuels, which may count as a compensatory property to higher viscosity and density. In literature (i.e. Karavalakis et al., 2008; Nabi et al., 2012; Ushakov et al., 2013) the CN of MGO is generally around 47−55.

Due to the variations in the chemical and physical properties of the fuels, they generally cannot simply be dropped into existing systems. Proper fuel analysis is necessary before engine use to observe suitability of the fuel. Ensured fuel flexibility of IC engine is needed to manage with fuel availability and fuel price fluctuation, and to meet emission regulations set for industrial engines and end-users. The goal of the research project was to allow broad fuel flexibility without any or only minor changes to engine hardware. Before the engine tests, the CRU forms an easy and cost-effective device to find out engine suitability of the fuel.

MATERIALS AND METHODS

Fuels

The studied fuels were selected to enlarge the choice of fuel alternatives of marine engines. The fuels were Light Fuel Oil (LFO), Jet A-1 -type aviation fuel (100% kerosene), Marine Gas Oil (MGO) produced from used lubricant oils and wood-based naphtha that was a side-product of wood-based biodiesel production. Chemically, all the fuels contained several hydrocarbon compounds; that is why no simple chemical formulas could not be given.

The research started by analysing the basic fuel properties (Table 1). The kinematic viscosity has an important role in fuel injection and droplet formation. Too high or too low viscosity causes poor fuel injection and increases fuel consumption. Too high viscosity leads to poor atomization resulting in incomplete combustion. However, too low fuel viscosity may cause mechanical problems in engine use as leaking from the nozzle sealing and the fuel pump system. All selected fuels had a relatively low viscosity. At a temperature of 40 °C wood based-naphtha had the lowest viscosity (0.50 mm^2 s^{-1}) and MGO (8 mm^2 s^{-1}) the highest. Kerosene (0.94 mm^2 s^{-1}) and the reference fuel LFO (3.0 mm^2 s^{-1}) were between the values of naphtha and MGO. The lower viscosity of naphtha and kerosene, compared to diesel, could improve the fuel atomization, evaporation and air/fuel mixing process (Subramanian et al., 2018).

A high fuel density may indicate higher energy content and minimize fuel losses. Too high a density correlates with higher viscosity and it has a negative effect on the formation of the fuel spray incurring poor burning process and high emissions. Among the studied fuels, the correlation between kinematic viscosity and fuel density was correct. Wood-based naphtha had the lowest viscosity and the lowest density (722 kg m^{-3} at 15 °C). MGO had the highest viscosity and the highest density (843 kg m^{-3}). Kerosene (787 kg m^{-3}) and LFO (836 kg m^{-3}) were between the values of naphtha and MGO.

The cetane number (CN) indicates how quickly fuel auto-ignites under compression. A low CN increases ignition delay causing problems for engine starting and running, e.g. unstable engine running leads to noise and smoke. MGO had a relatively high CN, 68, probably caused by used lubricants that formed the feedstock. The calculated cetane index of LFO (EN ISO 4264) was 54. The CN of kerosene (41) and wood-based naphtha (34) were lower, most likely resulting in a longer ignition delay.

A high lower heating value (LHV) implicates good heat release rate during the burning process improving the engine performance. The level of LHV of alternative fuels must meet the level of that of conventional fuels, other way there will be problems in volumetric fuel consumption (Bae & Kim, 2016). Unexpectedly the highest LHV was with wood-based naphtha (44 MJ kg^{-1}). However, the LHV of wood-based naphtha equated to earlier studied values of crude oil-based naphtha (Chang et al., 2013; Bae & Kim, 2016). All the other studied fuels had the same LHV, 43 MJ kg^{-1}.

Table 1. Studied fuel properties

		LFO	MGO	naphtha	kerosene
C	wt.%	87	83	81	89
H	wt.%	14	14	15	15
N	wt.%	< 0.1	0	0	0
S	wt.%	0	0	0	0
Pour point	°C	-42	Max. -6	< -50	
Flash point	°C	64	110	10	Min. 38
Boiling point	°C			20−220	170−300
Density at 15 °C	kg m^3	836	843	722	787
Kinematic viscosity at 40 °C	mm^2 s^{-1}	3.0	8.0	0.5	0.94
Surface tension at 20 °C	mN m^{-1}		29	20	25
HHV	MJ kg^{-1}		46	47	46
LHV	MJ kg^{-1}	43	43	44	43
Cetane number		54*	68	34	41
Sulphur	wt.%	< 0.01	Max. 0.1		0.1
Ash cotent	wt.%	< 0.01	< 0.001	0.005	0.001
Water content	mg kg^{-1}	< 100	22		35
Lubricity	μm	345	491		

*calculated cetane index (EN ISO 4264).

Combustion Research Unit

The Combustion Research Unit, CRU, is a constant volume combustion chamber based instrument designed to resemble engine conditions. In the CRU there are no moving parts and the starting conditions of the fuel injections are controlled more precisely than in a real compression ignition (CI) engine. Fuel is injected in a fixed injection period (250–3000 µs) through a twin nozzle injection system into a chamber with fixed dimensions (500 cm^3 ± 2%). In the injection system the first nozzle is the main injector and the second is a pilot injector, which can be activated or de-activated. In this study the pilot injector was de-activated. The used injector was a BOSCH CR injector which has electronic control of timing, opening period and pressure. The combustion and fuel pressures were observed with piezoelectric pressure sensors. Air was heated by heating the chamber wall. Fig. 1 illustrates the CRU used in this study.

To meet broad fuel flexibility without any or only minor changes to engine hardware, the fuel injection duration was assigned to be 1,000 µs with all fuels despite the differences in kinematic viscosity between the fuels. The pilot injector was de-activated and research was conducted under two different pressure and temperature conditions, 50 bar; 550°C and 70 bar; 590 °C. The results showed, however, that with MGO the injection duration had been 1,025 µs instead of 1,000 µs. Due to this slight difference, MGO is not completely comparable with other studied fuels. Based on Heywood (1988), under normal operation conditions, increasing the quantity of injected fuel has no significant effect on delay period. However, under engine starting conditions, the delay increases due to the larger drop sizes which are associated with evaporating and heating the increased amount of fuel.

All fuels were first centrifuged and then hot filtrated through a 10 µm filter before the CRU measurements. The fuels were at room temperature when injected into the fuel injection system. Measurements were performed two to three times under the both measurement conditions. Information about the set-up configurations of the CRU can be found in Table 2.

Table 2. Research set-up configurations of the CRU

		High pressure	Low pressure
Temperature at fuel injection (theoretical)	°C	590	550
Pressure at fuel injection	bar	70	55
Max. chamber pressure	bar	70	55
Max, pressure	bar	81.2	65.9
Injector period, main (LFO, naphtha, kerosene)	µs	1,000	1,000
Injector period, main (MGO)	µs	1,025	1,025

It should be noted that the actual engine conditions differ from conditions in the CRU. The major difference is the cylinder pressure that in 4-stroke engines reaches even more than 200 bar while the pressure in the CRU was max. 81 bar. Other differences are the fuel injection process and injection timing. In the CRU fuel is injected in a fixed period (1,000 µs), in this study, all fuel was injected before ignition, since all fuels had

an ignition delay of longer than 1 ms. In engines, especially at high loads, the fuel injection overlaps ignition and combustion (Steernberg & Forget, 2007). This means that in an engine large amount of the fuel (max. 80%) is injected into a space with a flame. Despite the differences between the CRU and actual engine conditions, the CRU is fast, easy and cost-effective device to find out the engine suitability of the fuel.
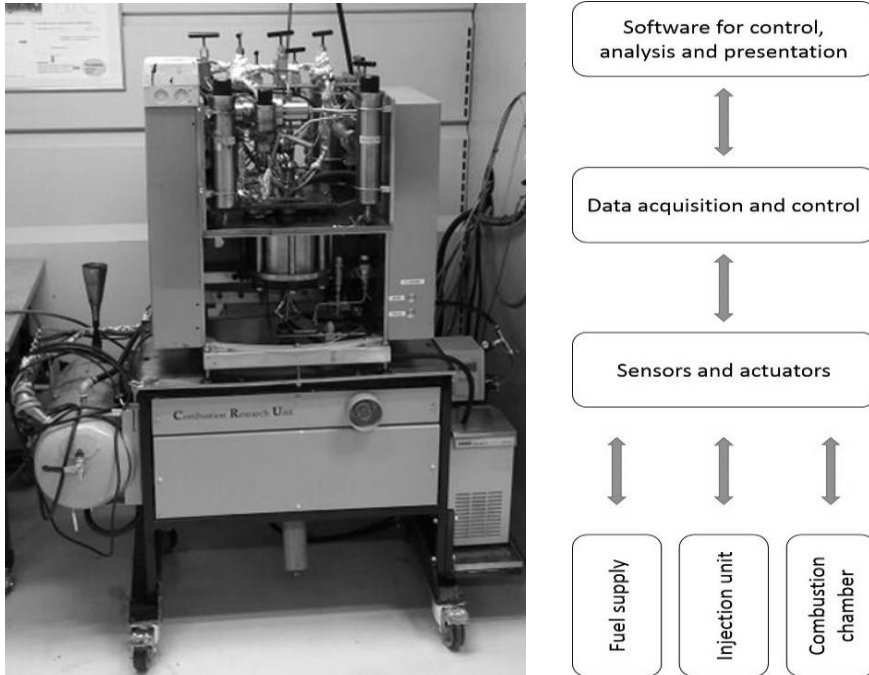
Figure 1. Combustion Research Unit and its modules. (Modules based on Fueltech AS, 2005).

CRU measures the Ignition Delay (ID) from the start of injection (t = 0) until the pressure in the chamber increases 0.1 bar. The following phases are determined:
– Pre Combustion Period (PCP) starts at the point where pressure is increased by 0.1 bar and ends when pressure is 1% of maximum pressure increase.
– Main Reaction Delay (MRD) is considered when pressure is increased 10% of the maximum pressure increase.
– The time between fuel ignition until 10% of the maximum pressure increase is achieved is called as Pre Combustion Period (PRP).
– Main Combustion Period (MCP) is measured from the MRD until 85% of the maximum pressure increase is reached.
– After the main combustion period, After Burning Period (ABP) starts, which continues until 95% of the maximum pressure increase is reached. At the end point of ABP, the combustion is considered end (EC).

In the next chapter, Fig. 2 shows these above-mentioned parameters in a pressure diagram with LFO.

RESULTS AND DISCUSSION

Based on the obtained results in the CRU, the ignition delays, complete combustion periods, maximum chamber pressure increases, and maximum rate of heat release rates of the fuels are examined in this chapter. The CRU chamber pressure results are presented as a function of time at high and low initial chamber pressures. The heat release curves are converted to pressure rises versus time in the combustion chamber. The effects of the measured fuel properties on the above-mentioned combustion parameters are considered.

High pressure

Fig. 2 presents the CRU chamber pressure results as a function of time for the studied fuels at high initial chamber pressure. All the variables were calculated from the raw data of one measurement and the results of LFO are marked in Fig. 2. The injection duration of the fuels was identical, despite the MGO (+2.5%), but the amount of the fuel during injection varied due to the different densities of the fuels. The results of MGO are only directional due to the slightly longer main injector period. The results determined from Fig. 2 are listed in Table 3.
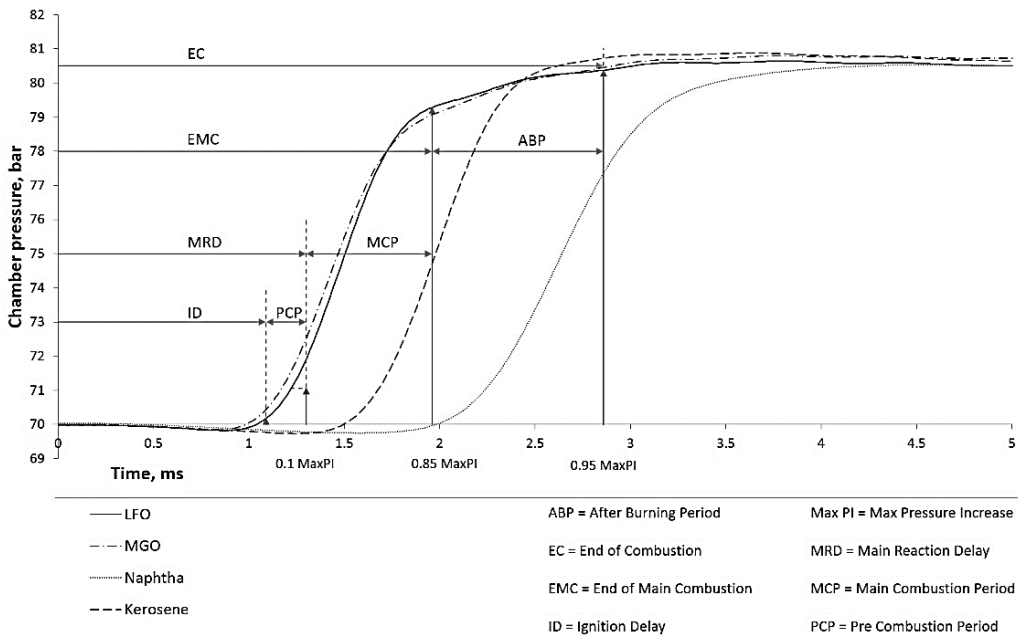
Figure 2. Chamber pressure diagram of LFO, MGO, naphtha and kerosene at high pressure.

Fig. 2 and Table 3 show that MGO had the shortest ignition delay (1.04 ms), perhaps partly due to slightly longer main injector period (MGO 1.025 ms versus other fuels' 1 ms) and significantly higher CN, as Grab-Rogalinski & Szwaja (2016) also noticed. Among other studied fuels, LFO had the shortest ID (1.08 ms), kerosene was the second (1.54 ms) and the longest ID was detected with naphtha (2.04 ms). The difference between ID of MGO and naphtha was 1.0 ms. In engine use the longer ignition

delay allows more fuel to be injected which once ignited gives a stronger pressure peak. Steenberg & Forget (2007) suggests that too strong a pressure peak may lead not only to engine damage but also to increased NOx emissions. The ignition delay period can be shortened by increasing the fuel injection pressure (Chen et al., 2013). On the other hand, Agrawal et al. (2013) noticed that too high a fuel injection pressure may lead even into too short an ignition delay. In that case, homogenous mixing may decrease and combustion efficiency reduce. Gnanasekaran et al. (2016) even noticed that the prolonged ignition delay may also be exhibited as lower smoke levels because the better mixture formation.

Table 3. CRU measurement results at high pressure

High pressure conditions		LFO	MGO	naphtha	kerosene
Ignition Delay (ID)	ms	1.08	1.04	2.04	1.54
Pre Combustion Period (PCP)	ms	0.16	0.14	0.22	0.16
Main Reaction Delay (MRD)	ms	1.24	1.18	2.26	1.7
Main Combustion Period (MCP)	ms	0.74	0.98	0.78	0.6
End of Main Combustion (EMC)	ms	1.98	2.16	3.04	2.3
After Burning Period (ABP)	ms	0.9	0.86	0.26	0.26
End of Combustion (EC)	ms	2.88	3.02	3.3	2.56
Max. Pressure Increase	bar	80.9 at 10.5 ms	81.2 at 10.3 ms	80.2 at 47.7 ms	80.9 at 10.9 ms
Max. Rate of Heat Release (MaxROHR)	bar ms^{-1}	16.3	15.2	11.7	16.2
Position of MaxROHR (PMR)	ms	1.5	1.44	2.62	2

Naphtha had a slightly higher LHV but it required more time to ignite than other fuels. Kerosene, MGO and LFO had a very similar LHV, but MGO had the shortest ID.

Despite the longer ID of kerosene, the complete combustion period (EC) of kerosene (2.56 ms) was shorter than that of LFO (2.88 ms), MGO (3.02 ms) or naphtha (3.3 ms). This can be assumed to relate to light components of kerosene that burns more rapidly than the heavier compounds of other fuels. Kerosene's lower viscosity and surface tension, compared to LFO and MGO, leads to a more rapid EC due to better fuel-air-mixing caused by smaller droplet sizes and faster vaporization characteristics (Lee et al., 2012; Agarwal et al., 2013; Chen et al., 2013). Based on Steenberg & Forget (2007) the EC may give information on the formation of combustion products and unburned or burned fuel components that affect emission, and may also relate to the formation of engine deposits and wear. The studies of Gnanasekaran et al. (2016) and Nabi et al. (2012) concerning a DI diesel engine showed that a shorter ignition delay and combustion duration results in lower heat release rate, peak pressure and rate of pressure rise.

The maximum pressure increase (Max.PI) of MGO (81.2 bar at 10.3 ms) was a slightly higher than Max.PI of kerosene (80.9 bar at 10.7 ms) and LFO (80.9 bar at 10.5 ms) but the peaks were almost equal. Naphtha had a long ID and that caused delay in the position of the peak of Max.PI (80.2 bar at 47.7 ms). Naphtha also included more heavier compounds that take time to burn and evaporate. Grab-Rogalinski & Szwaja (2016) also noticed a correlation between an ID and pressure increase.

Fig. 3 shows the heat release curves as converted to pressure rises versus time in the combustion chamber. The heat release (bar msec^{-1}) was the fastest with LFO (16.3 bar msec^{-1}) and kerosene (16.2 bar msec^{-1}). The placement of the curve against time depends on the fuel ID. The MaxROHR of naphtha was the lowest (11.7 bar msec^{-1}) and the position was delayed due to its long ID. The shape of MaxROHR curve shows that naphtha burned more slowly and the curve was not as spiky as with other fuels.
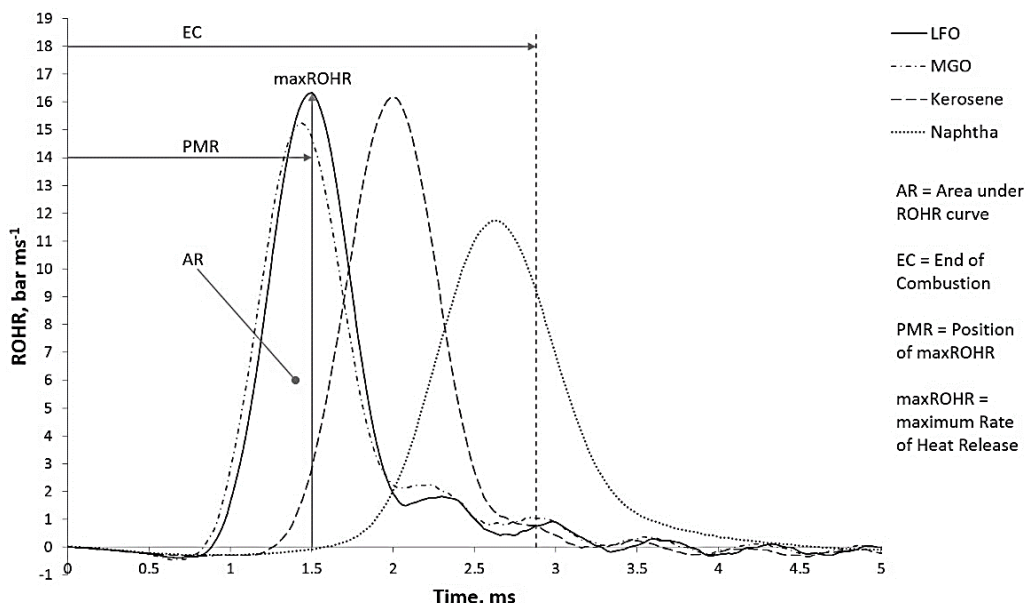
Figure 3. Rate of heat release curve of LFO, MGO, naphtha and kerosene at high pressure.

Low pressure

Fig. 4 presents the CRU chamber pressure results as a function of time for the studied fuels at low chamber pressure that was adjust at 55 bar. All the variables were calculated from the raw data of one measurement, and the results of LFO are marked in Fig. 4. The injection duration of the fuels were identical, despite the MGO (+2.5%), but the amount of the fuel during injection varied due to the different densities of the fuels.

The lower pressure conditions set higher demands for the used fuels and the differences between the research fuels were clearer. The injection temperature of the fuels was also dropped from 590 °C to 550 °C. Based on the CRU results, the fuels can roughly be divided into two groups; LFO and MGO, kerosene and naphtha.

Wood-based naphtha had almost twice as long an ID (3.20 ms) as LFO (1.76 ms) and MGO (1.74 ms). Figs 4−5 and Table 4 show that a long ID also reflected to the position of MaxROHR and the position of Max.PI. The Max.PI of naphtha (64.6 bar) was near the values of other studied fuels (LFO 65.9 bar, MGO 66.0 bar and kerosene 65.0 bar), but the slow ignition is shown in the position of Max.PI of naphtha (35.8 ms). The position of Max.PI of naphtha occurred 9.1 times later than that of LFO (3.92 ms) or MGO (3.94 ms). The study of Grab-Rogalinski & Szwaja (2016) also showed that a lower initial chamber temperature and pressure lead to worse atomization and evaporation and delayed ignition. With constant volume vessel, Bae & Kim (2016)

observed that the ID of the kerosene type JP-8 fuel (CN 38) was 25% to 50% higher compared to diesel fuel (CN 48). It was also noticed that when the CNs of the fuels meet, the difference in the ID's is no longer detected.
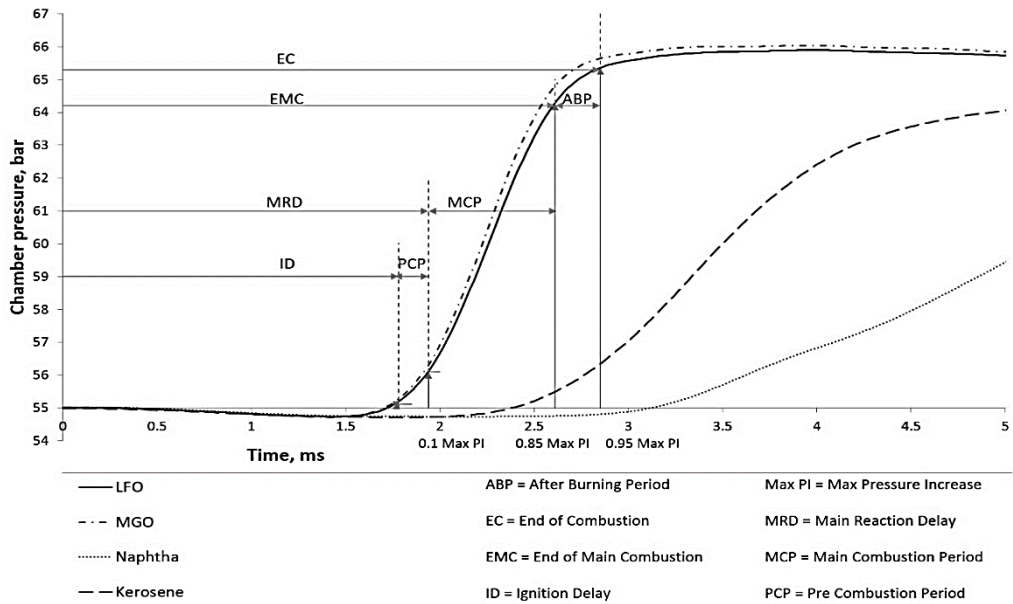
Figure 4. Chamber pressure diagram of LFO, MGO, naphtha and kerosene at low pressure.
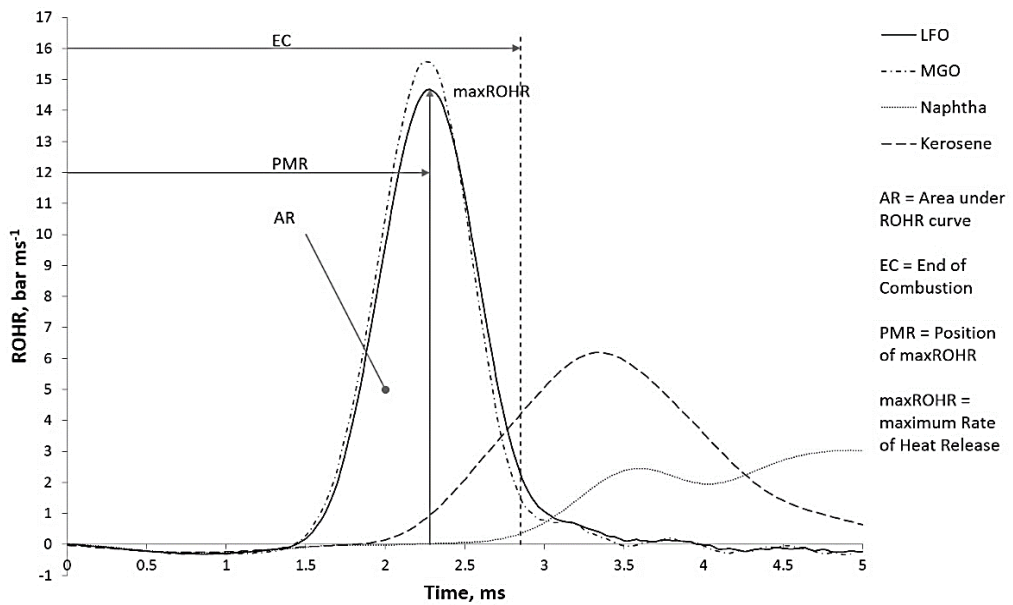
Figure 5. Rate of heat release curve of LFO, MGO, naphtha and kerosene at low pressure.

The whole combustion period (EC) was the fastest with MGO. The fast ignition and good combustion of MGO under low pressure conditions may be related to the high CN (68). In high pressure conditions, kerosene had the fastest combustion (EC), maybe due to the major amount of the light compounds in the fuel. Now, it can be assumed that the chamber pressure and the injection temperature were too low to burn the light compounds of kerosene well enough.

The MaxROHR varied more under the low than the high pressure conditions, Fig. 5. LFO and MGO burned almost similarly in both pressure conditions. MGO released heat even faster at the low (15.6 bar ms^{-1}) than high pressure (15.2 bar ms^{-1}). The MaxROHR curves of kerosene and naphtha differed considerably. The combustion was slow and the peak of the MaxROHR curve was low. The MaxROHR curve of naphtha also had a little drop at time of 4 ms. The reason might be that the light components of naphtha burned first and heavier compounds needed more time to ignite. Once the heavier compounds were also ignited, the MaxROHR reached its highest peak at 4.92 ms (3.03 bar ms^{-1}). According to Bergeron & Hallett (1989) higher mass components of a fuel have also higher ignition delay times.

Table 4. CRU measurement results at low pressure

Low pressure conditions		LFO	MGO	naphtha	kerosene
Ignition Delay (ID)	ms	1.76	1.74	3.20	2.46
Pre Combustion Period (PCP)	ms	0.18	0.18	0.42	0.32
Main Reaction Delay (MRD)	ms	1.94	1.92	3.62	2.78
Main Combustion Period (MCP)	ms	0.68	0.64	4.26	1.72
End of Main Combustion (EMC)	ms	2.62	2.56	7.88	4.50
After Burning Period (ABP)	ms	0.24	0.22	3.92	3.84
End of Combustion (EC)	ms	2.86	2.78	11.8	8.34
Max. Pressure	bar	65.9 at 3.92 ms	66.0 at 3.94 ms	64.6 at 35.8 ms	65.0 at 12.5 ms
Max. Rate of Heat Release (MaxROHR)	bar ms^{-1}	14.7	15.6	3.03	6.19
Position of MaxROHR (PMR)	ms	2.28	2.26	4.92	3.34

Based on the received results of the CRU measurements, kerosene can be used in CI engines without or with only minor changes. The possible modifications could be starting and stopping an engine with other fuel (e.g. LFO) or the change of the nozzles to have smaller diameter holes. Based on Heywood (1988) the nozzles with smaller diameter holes improves droplet formation and may promote better combustion with a shorter ID. The low lubricity of kerosene may result in malfunction of the injection system. Lubricity improvers and additives may be required in engine use (Bae & Kim, 2016).

Naphtha in CI engine use needs other fuel for starting and stopping engine. The lower CN and lower viscosity may limit the use of naphtha as a drop-in fuel to a diesel in CI engines because the retarded start of combustion and prolonged ignition delay may cause increased NOx emissions. Fuel additives may be needed to improve the ignition i characteristics and decrease NOx emissions. (Subramanian et al., 2018).

Due to the very similar results of MGO and LFO, MGO can be used in a CI engine like LFO without any modifications to engine or injection system.

Continue of the research

The research continues with engine measurements to validate the engine operation with each fuel. At the same time, the correlation between combustion parameters from the CRU (e.g. EC, EMC, ID) and engine parameters are studied. Only few similar studies have been performed. One is the study of Steenberg & Forget (2007) where the correspondence of the Fuel Ignition Analyzer (FIA) parameters and engine parameters was examined. Good results of the correlation between the FIA and the engine combustion parameters were achieved at high loads. At low loads, poor correlation between the FIA and the engine combustion parameters was detected. It might be partly due to the differences in the test conditions between the FIA and the engine. The fuel injection in the engine was also very different and strongly affected the combustion process.

CONCLUSIONS

The quality of ignition and combustion of four marine and power plant fuels were studied in a Combustion Research Unit, CRU. The fuels were low-sulphur Light Fuel Oil (LFO, baseline), Marine Gas Oil (MGO), kerosene and renewable wood-based naphtha. The research fuels were selected to broaden the choice of alternatives of marine and power plant engine fuels.

Based on the results obtained in the study, the following conclusions could be drawn:

Under the high pressure conditions:
– MGO had the shortest ID that indicated good atomization and high CN. A good atomization provides rapid fuel-air mixing decreasing ID.
– Naphtha had the longest ID, maybe due to the high amount of heavy components of naphtha. Heavy components also affects atomization and the whole combustion process.
– Kerosene burned quickly due to its light components, lower viscosity and surface tension, and showed a short EC period. Naphtha had the longest EC which may in engine use lead to higher emissions and engine damages.
– Under the higher pressure conditions, the combustion parameters of the fuels were closer to each other than under the lower pressure conditions.

Under the low pressure conditions:
– The lower chamber pressure and the lower fuel injection temperature affected clearly the combustion performance of the fuels.
– Fuels could be roughly divided into two groups:
1) Straightly usable in engine without any modifications: LFO & MGO
2) Fuels that require some minor modifications (e.g. starting and stopping the engine with another fuel): kerosene and naphtha.
– The long ID of naphtha and kerosene affected the positions of Max.PI curve and MaxROHR curve.
– Kerosene was competitive under high pressure conditions but fell behind when the chamber pressure and injection temperature were lowered.

REFERENCES

Agarwal, A., Srivastava, D., Dhar, A., Maurya, R., Shukla, P. & Singh, A. 2013. Effect of fuel injection timing and pressure on combustion, emissions and performance characteristics of a single cylinder diesel engine. *Fuel*, Volume 111, pp. 374−383.

Anastopoulos, G., Lois, E., Zannikos, F., Kalligeros S. & Teas, C. 2002. HFRR lubricity response of an additized aviation kerosene for use in CI engines. *Tribology International* **35**, 599−604.

Bae, C. & Kim, J., 2016. Alternative fuels for internal combustion engines, *Proceedings of the Combustion Institute 0000*, pp. 1−25.

Bergeron, C.A. & Hallett, W.L.H., 1989. Ignition characteristics of liquid hydrocarbon fuels as single droplets, *Can J Chem Eng.* **67**, 142−149.

Buchholz, K. 2013. Naphtha-fueled research car meets emissions, other targets. *AEI* **121**(4), 6–8. ISSN: 1543-849X.

Chang, J., Kalghatgi, G., Amer, A., Adomeit, P., Rohs, H. & Heuser, B., 2013. Vehicle Demonstration of Naphtha Fuel Achieving Both High Efficiency and Drivability with EURO6 Engine-Out NOx Emission. *SAE Int. J. Engines,* Volume **6**(1), 101−119.

Chen, P-C, Wang, W-C., Roberts, W. & Fang, T., 2013. Spray and atomization of diesel fuel and its alternatives from a single-hole injector using a common rail fuel injection system. *Fuel* **103**, 850−861.

EN ISO 4264:2007 standard, *International Organization for Starsdization (ISO)*. 2007.

Fueltech AS, Combustion Research Unit - CRU, specification. 2005.

Germanischer Lloyd & MAN, Costs and Benefits of LNG as Ship Fuel for Container Vessels, Key results from a GL and MAN joint study, Germanischer Lloyd, Hamburg. 2012.

Gnanasekaran, S., Saravanan, N. & Ilangkumaran, M., 2016. Influence of injection timing on performance, emission and combustion characteristics of a DI diesel engine running on fish oil biodiesel. *Energy* **116**(1), 1218−1229.

Grab-Rogalinski, K & Szwaja, S., 2016. The combustion properties analysis of various liquid fuels based on crude oil and renewables. In *IOP Conference Series: Materials Science and Engineering*, Volume **148**(1) DOI: 10.1088/1757-899X/148/1/012066.

Heywood, J. 1988. *Internal Combustion Engine Fundamentals*, pp. 541−562. ISBN: 0-07-100499-8.

IMO 2008. MARPOL Annex VI: Regulations for the prevention of air pollution from ships and NOx. *IMO Marine Environmental Protection Committee (MEPC)*.

Jiang, L., Kronbak, J. & Christensen, L., 2014. The costs and benefits of sulphur reduction measures: Sulphur scrubbers versus marine gas oil. *Transportation Research Part D: Transport and Environment*, Vol. **28**, pp. 19–24.

Karavalakis, G., Tzirakis, E., Mattheou, L., Stournas, S., Zannikos, F. & Karonis, D., 2008. The impact of using biodiesel/marine gas oil blends on exhaust emissions from a stationary diesel engine. *Journal of Environmental Science and Health, Part A*, **43:14**, 1663–1672.

Lee, J., Oh, H. & Bae, C. 2012. Combustion process of JP-8 and fossil Diesel fuel in a heavy duty diesel engine using two-color thermometry. *Fuel* **102**, 264−273.

Nabi, Md.N., Brown, R., Ristovski, Z. & Hustad, J. 2012. A comparative study of the number and mass of fine particles emitted with diesel fuel and marine gas oil (MGO). *Atmospheric Environment* **57**, 22–28.

Steernberg, K. & Forget, S. 2007. The effects of a changing oil industry on marine fuel quality and how new and old analytical techniques can be used to ensure predictable performance in marine diesel engines. In *25th CIMAC Congress*, Vienna. Paper no. 198.

Subramanian, T., Varuvel, E., Ganapathy, S., Vedharaj, S. & Vallinayagam, R. 2018. Role of fuel additives on reduction of NOx emission from a diesel engine powered by camphor oil biofuel. In *Environmental Science and Pollution Research*, pp. 1−10.

Ushakov, S., Halvorsen, N., Valland, H., Williksen, D. & Æsøy, V. 2013. Emission characteristics of GTL fuel as an alternative to conventional marine gas oil. *Transportation Research Part D: Transport and Environment* **18**, 31–38.

Vasu, S., Davidson, D. & Hanson, R. 2007. Jet fuel ignition times: Shock tube experiments over wide conditions and surrogate model predictions. *Combustion and Flame* **152**, 125−143.

Wang, B., Yang, H., Shuai, S., Wang, Z., He, X. & Xu, H. 2013. Numerical Resolution of Multiple Premixed Compression Ignition (MPCI) Mode and Partially Premixed Compression Ignition (PPCI) Mode for Low Octane Gasoline, *SAE Technical Paper*, No. 2013-01-2631.

Yadav, S., Murthy, K., Mishra, D. & Baral, B. 2005. Estimation of petrol and diesel adulteration with kerosene and assessment of usefulness of selected automobile fuel quality test parameters. *International Journal of Environmental Science & Technology* **1**(4), 253−255.

Mechanical behaviour of Sugar palm (*Arenga pinnata*) fibres

P. Hrabě[1,*], Č. Mizera[2], D. Herák[2] and A. Kabutey[2]

[1]Czech University of Life Sciences, Faculty of Engineering, Department of Material Science and Manufacturing Technology, Kamýcká 129, CZ165 21 Prague, Czech Republic
[2]Czech University of Life Sciences, Faculty of Engineering, Department of Mechanical Engineering, Kamýcká 129, CZ165 21 Prague, Czech Republic
*Correspondence: hrabe@tf.czu.cz

Abstract. The tensile strength of Sugar palm (*Arenga pinnata*) fibres was examined. Fibre samples were prepared and tested up to the point of rupture with a deformation rate of 0.05 min^{-1}. The tensile device (Labortech, MPTest 5.050, Czech Republic) were used to determine the tensile force. The aim of the paper was to describe a mechanical behaviour of Sugar palm (*Arenga pinnata*) fibres. Measured values can be used as a basis for further research on the application of Sugar palm fibres.

Key words: tensile force, agriculture material, deformation energy.

INTRODUCTION

Environmental and economic concerns are stimulating research in the design of new materials for construction, furniture, packaging and automotive industries. Particularly attractive are the new materials in which a good part is based on natural renewable resources, preventing further stress on the environment. However, it is important to know that renewable resources depend on a balance, in which their harvests should be lower than its growth. Renewable, non-timber based materials could reduce the use of traditional materials such as wood, minerals and plastics for some applications (Leão et al., 1998). Vegetable fibres offer several advantages in comparison with synthetic fibres. They are biodegradable (crucial at the end of life of products), non-abrasive to processing equipment, are CO_2 neutral and can be used as acoustic and thermal insulators. Furthermore, they are an important source of income for agricultural societies (Alves et al., 2010).

Arenga pinnata (syn. Arenga saccharifera) is an economically important feather palm native to tropical Asia, from eastern India east to Malaysia, Indonesia, and the Philippines in the east. Common names include sugar palm, arenga palm, areng palm, black-fiber palm, gomuti palm, aren, enau, irok, and kaong.

Another important product of the sugar palm is its fibres. It has several names such as Aren, gomuti, and black and locally it is known as the ijuk fibres. The commercialization of sugar palm fibres can be tracked back as early as 1416 during the Malacca Sultanate era. Later in 1800, sugar palm was planted by British East India

Company in Penang to produce high durability rope made from its fibres (Othman & Haron, 1992). These multipurpose fibres can be used to make a number of products such as ropes, filters, brushers, brooms, mats, cushions and shelters for fish breeding (Mogea et al., 1991). Other than that, the preparation for sugar palm fibres is effortless as the fibres do not require any secondary processes such as water retting or mechanical decorticating process to yield the fibre. This is due to the fact that the fibres, originally wrapped around the sugar palm trunk from the bottom to the upper part of the tree, are in the form of natural woven fibre (Ishak et al., 2012; Ishak et al., 2013).

The tree begins to produce fibre before flowering approximately after five years of plantation. The fibre is black and its length is up to 1.19 m. Its diameter ranges between 94 and 370 μm and its density is 1.26 kg m^{-3} (Bachtiar et al., 2010). Bachtiar et al. (2010) reported the tensile strength, tensile modulus and elongation at break of sugar palm fibre to be 190.29 MPa, 3.69 GPa, and 19.6%, respectively.

Further characterisation of tensile properties of sugar palm fibres was conducted by Ishak (2011). The fibres were obtained from different heights of sugar palm tree (1, 3, 5, 7, 9, 11, 13, and 15 m) and tested for single fibre tensile test. The results showed that the fibres obtained from bottom part demonstrated inferior properties of tensile strength, modulus, elongation at break and toughness compared to fibres obtained in the area of a live palm frond.

This experiment aims to describe the mechanical behavior of Sugar palm (*Arenga pinnata*) fiber under tension loading.

MATERIALS AND METHODS

Sample

Samples of fibres produced from Sugar palm (*Arenga pinnata*), obtained from Balige, province of North Sumatra, Indonesia, were used for the experiment. The moisture content Mc = 11.12 ± 0.81% (d.b.) of the samples was determined using standard oven method, ASAE method (ASAE S410.1 DEC97), (ASAE, 1998). Samples of 500 g mass from a batch of Sugar palm (*Arenga pinnata*) were randomly selected for the moisture content determination. The mass of each sample m_s (g) was determined using an electronic balance (Kern 440–35, Kern & Sohn GmbH, Balingen, Germany). For determining mechanical properties were produced five sets (set 1 – set 5) and each set was 5 fibres.

Tension test

To determine the relationship between tension force and deformation, a device (Labortech, MPTest 5.050, Czech Republic) was used to record the course of deformation function. The fibres of Sugar palm (Fig. 1) were glued into a paper to precisely fix gauge length $L_0 = 20$ mm (Fig. 1) and subsequently were inserted into grips of testing machines. The carrier paper was cut before starting the tensile test. The fibres were tested up to the rupture with a tension speed of 0.5 mm.min^{-1} under temperature of 20 °C. The experiment was repeated five times with randomly selected fibres. The microscope (Zeiss Jenavert, Carl Zeiss, Jena, Germany) was used to measure of fibre diameter. The dimensions were determined in 5 places at gauge length for each fibre.
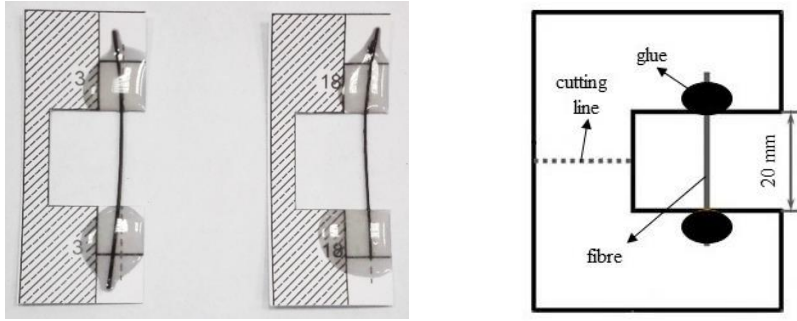
Figure 1. Method of fasting of the fibres to the tensile test.

The fibre cross-section area (S) was calculated by Eq. (1)

$$S = \frac{\pi D^2}{4}$$ (1)

where D (mm) is the outer diameter of fibre.

Stress–strain curve

Determined amounts of tension force were transformed into stress by Eq. (2) and the amounts of deformation were transformed into strain by Eq. (3)

$$\sigma = \frac{F}{S}$$ (2)

$$\varepsilon = \frac{x}{L_0}$$ (3)

where σ (MPa) is stress in fibre; F (N) is tension force; S (mm^2) is appropriate cross section area of fibre; ε (-) is strain; x (mm) is the elongation of fibre, and L_0 (mm) is gauge length.

Volume energy

Volume energy is the area under the stress–strain curve from the zero strain to maximum strain and it was calculated by Eq. (4)

$$\lambda = \sum_{n=0}^{n=i-1} \left[\left(\frac{\sigma_{n+1} + \sigma_n}{2} \right) \cdot (\varepsilon_{n+1} - \varepsilon_n) \right]$$ (4)

where λ (J m^{-3}) is the volume energy; i indicates the additional amount of strain in which the stress was determined (step of measurement was 0.001 mm); σ_n (MPa) is tension stress at appropriate strain; σ_{n+1} (MPa) is tension stress at the sequential strain. ε_n is strain, and ε_{n+1} is the sequential strain.

RESULTS AND DISCUSSION

For each of the five fibres the cross sectional area was determined by the equation Eq. 1 and its results are shown in Table 1 with additional information. The measurements show that all the specified geometrical properties of each fibre have similar properties throughout its length and it is given by the amount of variation coefficient less than 6%,

which is usually the quantity determined in biological materials (Mohsenin 1970; Stroshine 2000; Blahovec 2008; Mizera et al., 2016). The average values for each set are shown in Fig. 2 as the dependence between the tensile force and the elongation.

Table 1. Geometric and mechanical properties of Sugar palm (*Arenga pinnata*) fibres

Set	Tension force, N	Fibre diameter, μm	Tension stress, MPa	Deformation, mm	Deformation energy, J
I	29.43 ± 6.39	734.73 ± 41.37	31.20 ± 7.60	3.99 ± 0.98	70.99 ± 37.24
II	35.38 ± 8.25	813.93 ± 52.76	37.15 ± 6.37	4.25 ± 1.12	94.98 ± 55.00
III	32.26 ± 7.84	701.09 ± 39.54	28.43 ± 5.87	3.61 ± 0.89	41.19 ± 33.65
IV	31.20 ± 7.61	715.49 ± 40.23	35.26 ± 6.58	3.94 ± 0.95	57.09 ± 39.42
V	28.89 ± 6.27	722.69 ± 41.65	33.83 ± 7.56	4.19 ± 1.03	74.39 ± 42.54
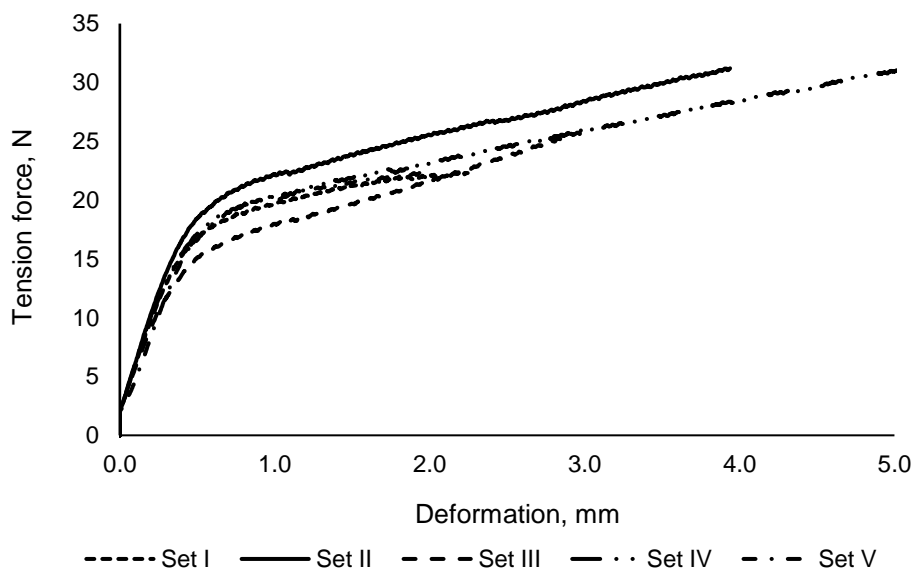
Figure 2. Dependency between tension force and deformation.

From already published studies is evident that Sugar palm fibre has very similar rupture stress as other fibres produced from other natural materials such as bamboo, vakka, coconut, banana, pineapple, hemp, abaca or sisal (Mogea et al., 1991; Bachtiar et al., 2010; Ishak et al., 2012).

Each measured relationship of tension force versus elongation was transformed using Eq. (2) and Eq. (3) into the stress–strain curve. For transformation, the individual cross-section areas (Table 1) were used.

Sahari, et al. (2012) studied tensile properties of Sugar palm (ijuk) fibre and compared it with fibres obtained from different parts of sugar palm tree namely the frond, trunk and bunch fibres. The results showed that the highest tensile properties (tensile strength, tensile modulus and elongation at break) were obtained at frond fibre followed by bunch fibre, ijuk fibre and lastly at trunk fibre. These results are in good agreement with their chemical compositions in the same study since the mechanical properties of

natural fibres are strongly influenced by their cellulose content (Habibi, et al., 2008) that provides strength and stability to the cell walls of fibres (Reddy & Yang, 2005).

From already published studies is evident that sugar palm fibre has very similar rupture stress as other fibres produced from other natural materials such as bamboo, vakka, coconut, banana, pineapple, hemp, abaca or sisal (Othman & Haron, 1992; Leão, et al., 1998; Reddy & Yang, 2005; Bachtiar, et al., 2010; Ishak, et al., 2011; Ishak, et al., 2012; Mizera, et al., 2016). In terms of elongation, the sisal and date show similar deformation properties as sugar palm.

From the point of view of classical construction materials, the mechanical behaviour of sugar palm fibre under tension loading can be also compared with standard materials such as aluminium or magnesium metal (Howard 2007). From the conducted study and previously published information about sugar palm (Alves, et al., 2010; Ishak, et al., 2011; Sahari et al., 2012), it follows that sugar palm fibre is environmentally friendly, biodegradable, and recyclable material and due to its mechanical behaviour under tension loading. In this study, the determined results of the mechanical behaviour could be applied as background for further research focused on the sugar palm fibre application.

CONCLUSIONS

The mechanical behaviour of Sugar palm fibre was determined. The fibre with its desirable properties, has great potential to be used. Not only is the fibre highly durable. On top of it, it is readily available in the form of woven fibres, making it easy to process. Since sugar palm remains largely unknown by many people and very little information is available about it, more research needs to be conducted to unveil its significance and to promote its usefulness for the benefits of the public.

From an analysis of determined mechanical and physical properties determined in this study, it follows that the fibre produced by sugar palm shows high strength, stiffness and exhibits exceptional structural properties. With regard to its biodegradability and recyclability as well as its mechanical behaviour, the fibre produced from sugar palm could be used as a construction material of the future.

REFERENCES

Alves, C., Ferrão, P.M.C., Silva, A., Reis, L.G., Freitas, M., Rodrigues, L.B. & Alves, D.E. 2010. Ecodesign of automotive components making use of natural jute fiber composites. *Journal of Cleaner Production* **4**, 313–327.

ASAE Standards 1998. *ASAE S410.1 DEC97 Moisture Measurement of Peanut* 45th Ed. American Society of Agricultural Engineers, St. Joseph.

Bachtiar, D., Sapuan, S.M., Zainudin, E.S., Khalina, A. & Dahlan, K.Z.M. 2010. The tensile properties of single sugar palm (Arenga pinnata) fibre. *IOP Conference Series: Materials Science and Engineering* **11**, 12–18.

Blahovec, J. 2008. Agromaterials: Study guide. Prague: Czech University of Life Sciences Prague, 102 pp.

Habibi, Y., El-Zawawy, W., Ibrahim, M.M. & Dufresne, A. 2008. Processing and characterization of reinforced polyethylene composites made with lignocellulosic fibres from Egyptian agro-industrial residues. *Composite Science and Technology* **68**, 1877–1885.

Howard, A.K. 2007. *Overview of mechanical properties and testing for design.* ASM Handbook. Mechanical Testing and Evaluation. Johnstown, PA: Concurrent Technologies, 959 pp.

Ishak, M.R., Sapuan, S.M., Leman, Z., Rahman, M.Z.A. & Anwar, U.M.K. 2012. Characterization of sugar palm (Arenga pinnata) fibres: Tensile and thermal properties. *Journal of Thermal Analysis and Calorimetry* **109**, 981–989.

Ishak, M.R., Sapuan, S.M., Leman, Z., Rahman, M.Z.A., Anwar, U.M.K. & Siregar, J.P. 2013. Sugar palm (Arenga pinnata): Its fibres, polymers and composites. *Carbohydrate Polymers* **91**, 699–710.

Ishak, M.R., Leman, Z., Sapuan, S.M., Rahman, M.Z.A. & Anwar, U.M.K. 2011. Effects of impregnation pressure on physical and tensile properties of impregnated sugar palm (Arenga pinnata) fibres. *Key Engineering Materials*, pp. 471–472.

Leão, A.L., Rowell, R. & Tavares, N. 1998. Applications of natural fibers in automotive industry in Brazil – thermoforming process. P.N. Prasad, *et al.* (Eds.), *Science and Technology of Polymers and Advanced Materials*, Plenum Press, New York, pp. 755–761.

Mizera, C., Herak, D., Hrabe, P., Muller, M. & Kabutey, A. 2016. Mechanical Behavior of Ensete ventricosum Fiber Under Tension Loading. *Journal of Natural Fibers* **14**, 287–296.

Mogea, J., Seibert, B. & Smits, W. 1991. Multipurpose palms: The sugar palm. *Agroforestry System* **13**, 111–129.

Mohsenin, N.N. 1970. Physical properties of plant and animal materials. New York: Gordon and Breach, 891 pp.

Othman, A.R. & Haron, N.H. 1992. In Nik, A.R. (Ed.), *Potensi industri kecil tanaman enau*. FRIM report No. 60. FRIM Press: Kepong, Malaysia. pp. 7–18 (in Indonesian).

Reddy, N. & Yang, Y. 2005. Biofibres from agricultural by products for industrial applications. *Trends in Biotechnology* **23**, 22–27.

Sahari, J., Sapuan, S.M., Ismarrubie, Z.N. & Rahman, M.Z.A. 2012. Physio-chemical properties of different parts of sugar palm fibre. *Fibers and Textile in Eastern Europe* **20**, 23–26.

Stroshine, R.L. 2000. Physical properties of agricultural materials and products. West Lafayette: Purdue University, 296 pp.

Stabilization of persistent organic pollutants (POP) in flue gases in a biological waste incinerating facility

P. Jirsa[*] and J. Malaťák

Czech University of Life Sciences Prague, Faculty of Engineering, Department of Technological Equipment of Buildings, Kamýcká 129, CZ165 21 Praha-Suchdol, Czech Republic
[*]Correspondence: pjirsa@tf.czu.cz

Abstract. The article focuses on a technology of flue gases stabilization in biological and hospital waste incinerating facility. Hazardous particles and compounds formed in flue gas during the process of thermal waste degradation need to be stabilized according to an enacted legislation. The aim of the research is to examine technological process of polychlorinated dibenzodioxins and polychlorinated dibenzofurans (PCDD/F) elimination in flue gas. PCDD/F is group of persistent organic pollutants which are resistant to environmental degradation and are highly toxic for the environment in very small amounts. Experiments were performed in semi operation hospital waste incinerating plant with heating power 1.5 MW and capacity 250 kg h^{-1} of incinerating material. It was observed that formation of PCDD/F exponentially grows with increasing concentration of chlorides in the flue gas, but formation varies based on type of congener. The highest concentration was measured for HxDF, 17,522 pg Nm^{-3} and HpDF, 16,334 pg Nm^{-3} at chloride concentration of 867 mg Nm^{-3}. However, concentration of PCDD congeners didn´t exceeded 4,000 pg Nm^{-3} for the same level of chlorides in flue gas. Two types of activated carbon Chezacarb and NORIT were tested for capability to stabilize PCDD/F in flue gas. Results show that refining effect for both sorbent are very similar. It was observed that 0.1 g of activated carbon should be applied per 1 Nm^3 of flue gas in regard to reduce 3–4 ng Nm^{-3} PCDD/F under required emission limit.

Key words: PCDD, PCDF, hospital waste, activated carbon.

INTRODUCTION

Elimination of hazardous particles and compounds in flue gas can be done by several methods such as a wet, semi-dry and dry process (Wey et al., 2001). Dry refining technology is based on a sorbent injection that is in a form of finely crushed dry powder. The agent is sprayed directly into the flue gas flow (Allen et al., 2001) or mixed with waste going into the reactor (Cunill et al., 1991). Neutral compounds are formed after reaction with injected sorbent and captured on solid particles separator subsequently. There is a vast range of commercially produced sorbents that can be used for stabilization of different particles with different efficiency. Sodium and calcium based sorbents can effectively eliminate sulphur dioxide and hydrogen chloride (Jirsa & Malaťák, 2017), but for activated carbon based sorbent seems to be effective agent for persistent organic pollutants stabilization (Gunes et al., 2015).

Hydrogen chloride and small amount of chlorinated radicals can form during incineration of material that contains chemically bonded chlorine (Phan et al., 2014). The combustion runs in oxidation atmosphere in presence of catalytically active particles of ash such as Cu^{2+}. It is known as a Deacon´s process (Hisham & Benson, 1995). Under such condition, hydrogen chloride can transform to chlorine that can reacts with organic radicals and persistent Polychlorinated dibenzodioxins (PCDD) and Polychlorinated dibenzofurans (PCDF) can form (Phan et al., 2014).

PCDD/F occurs while incineration of substances that contain chlorine (Zhou et al., 2015). It is highly toxic for the environment in very small amounts. Production of PCDD/F in flue gases grows with increasing amount of hydrogen chloride and other chlorine element in flue gas (Van Caneghem et al., 2012). Its formation occurs at temperature range from 250 to 600 °C (Stanmore, 2004). Emission limits for PCDD/F is 0.1 ng I-TEF m^{-3} at standard conditions.

This paper follows up on research of the dry sorption refining technology in small biological and medical waste incinerating plant with heating power under 5 MW (Jirsa & Malaťák, 2017). The aim of this study is to determine a formation of PCDD/F in flue gas during medical waste incineration in relation with concentration of chlorides. Further task of the study is to examine the effect of calcium hydroxide on PCDD/F elimination. Above all, it is determination of sorption efficiency of activated carbon-based sorbents Chezacarb and NORIT to reduce PCDD/F concentration in flue gas.

MATERIALS AND METHODS

Experimental unit and technology

All experimental tests were conducted in semi-operation conditions of incinerating plant for hospital waste degradation in Strakonice, Czech Republic. It is a small-scale facility with output of approximately 1,400–1,500 t processed waste annually. The facility consists of a pyrolysis furnace Hoval – Schiestl GG 24, thermo-reactor TR 24 and a steam boiler THD IV 0580 with heating power 1,508 kW.

The incinerating plant operates discontinuously, waste is dosed into the furnace every 15 minutes with load of 60–65 kg. The input material is a classified as a biological and hospital waste. It is described with following codes according to waste catalogue: 180102, 180103, 180104, 200301, 150202, 150110 (European Waste Catalogue). The elemental characteristic of processed waste is in Table 1.

Table 1. Hospital waste characteristics

	Share of component, %	H_2O, %	Ash, %	Cl, %	F, %	S, %	Heating value, MJ kg^{-1}
Textile	29	6.6	14.2	13.2	1.8	9.5	15.1
Paper	24	5.8	5	0.5	-	4.2	15.4
Plastic	23	0.1	0.5	18	3	6.7	24.8
Biological component	14	32.1	18.6	5.3	2.1	12	11.4
Solvent, oil	10	0.6	0.8	16.1	1.3	21.3	39.6
Weighted average		**7.9**	**8.1**	**10.4**	**1.6**	**9.1**	**19.3**

Temperature in the furnace chamber is set at range 900–950 °C. Two natural gas burners automatically control temperature at required level. Pyrolysis gas forms by waste

carbonization in the furnace chamber that is subsequently mixed with oxygen and burned in thermo-reactor at the temperature 1,100–1,150 °C. Formed flue gas flows through a boiler where the temperature is reduced to 200–250 °C. Reduced temperature of flue gas allows to inject a sorbent into the system. Hence the device for sorbent addition is placed after the boiler. Flue gas followingly passes through 8 m long contactor-pipe labyrinth which enhance amount of collisions between sorbent and flue gas particles. Next, flue gas temperature is reduced to 130–135 °C in heat exchanger after which second 17 m long contactor-pipe labyrinth is placed. All solid particles involving hazardous compounds and sorbents injected into the system are captured on a tied filter subsequently. The technology diagram of the incinerating facility is given on the Fig. 1.

1 - Waste input   6 - Pipe labyrinth 1   11 - Ventilator
2 - Chamber furnace   7 - Heat exchanger   12 - Control unite
3 - Thermoreactor   8 - Sorbent injection – position B   13 - Stack
4 - Steam generator; boiler   9 - Pipe labyrinth 2
5 - Sorbent injection – position A   10 - Tied filter
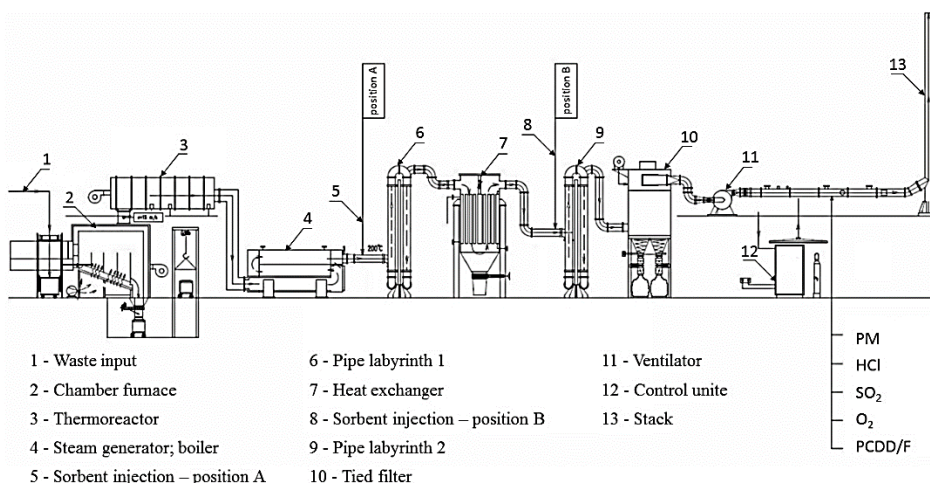
Figure 1. Facility technology diagram (Jirsa & Malaťák, 2017).

Measuring of emissions in flue gas was taken according to appropriate legislative (Act No. 201/2012 Coll.). The measuring point is placed at the horizontal flue pipe with diameter 355 mm after a ventilator according to ISO 9096 and EN 13284-1.

Within the experimental testing following properties and concentrations are determined according to international technical standards. It is specifically monitored: concentration of particulate matter (PM), hydrogen chloride (HCl), oxygen (O_2) and polychlorinated dibenzo-p-dioxins (PCDD) and dibenzofurans (PCDF) according to following technical standards:

- Gravimetric determination of the mass concentration of particulate matter (ISO 9096 EN 13284-1);
- Determining flow velocity and volume flow (ISO 10780);
- Determination of moisture in the gas pipeline (EN 14790);
- Paramagnetic determination of oxygen (EN 14789);
- Photometric determination of the mass concentrations in inorganic chloride compounds (EN 1911);
- Determination of the organic persistent substances mass, calculated from the measured values (PCDD/PCDF) (EN 1948, 1-4).

Methodology of PCDD/F determination according to EN 1948, 1-4

Equipment was rinsed with acetone and toluene before the samples were taken. PUF and glass filter were extracted with toluene and dried. PUF and glass filter was marked with sampling standards for yield determination and blinded test was done then.

PCDD/F samples were determined in the laboratory with addition of C^{13} internal standards (extraction and spraying standards) and determined on the GC-MS device. The yield of sampling standards was determined based on extraction standards. The results are given as an International toxicity equivalence factor I-TEF, see the Table 2.

Table 2. Toxic equivalency factor (Schecter et al., 2006)

Congener	I-TEF value	Congener	I-TEF value
Dibenzo-p-dioxins (PCDDs)		**Dibenzofurans (PCDFs)**	
2,3,7,8-TCDD	1	2,3,7,8-TCDF	0.1
1,2,3,7,8-PeCDD	0.5	1,2,3,7,8-PeCDF	0.05
		2,3,4,7,8-PeCDF	0.5
1,2,3,4,7,8-HxCDD	0.1	1,2,3,4,7,8-HxCDF	0.1
1,2,3,6,7,8-HxCDD	0.1	1,2,3,6,7,8-HxCDF	0.1
1,2,3,7,8,9-HxCDD	0.1	1,2,3,7,8,9-HxCDF	0.1
		2,3,4,6,7,8-HxCDF	0.1
1,2,3,4,6,7,8-HpCDD	0.01	1,2,3,4,6,7,8-HpCDF	0.01
		1,2,3,4,7,8,9-HpCDF	0.01
OCDD	0.001	OCDF	0.001

All volumes, weights of combustion air and emission concentration are given for normal conditions, i.e., at t = 0 °C, p = 101.325 kPa and the reference oxygen content in the flue gases $O_r = 11\%$.

Used carbon based sorbents

Chezacarb (CHZC) is commercial name for carbon based sorbent produced by Unipetrol a.s. It is produced during hydrogen production by partial oxidation of petroleum and petrochemical raw materials. Chezacarb is characterized by high level of specific surface area, above 1,000 m^2 g^{-1} with high capacity and high porosity, more than 3.5 cm^3 g^{-1}. It is effective in PCDD/F and PCB elimination. Small particles around 20 mm are able to cluster around pollutants and binding them irreversibly (Unipetrol, n.d.).

NORIT GL 50 is commercial name for carbon based sorbent produced by Cabot Corporation. It is a powdered steam activated carbon with an extra fine particle size that is suitable for the removal of dioxins, mercury and other contaminant traces from flue gases (Cabot Corporation, n.d.).

RESULTS AND DISCUSSION

Effect of chlorine in flue gas on PCDD/F and distribution of congeners

The dependence of PCDD/F formation on hydrogen chloride concentration in flue gas was observed. The characteristics of the biological waste meet the fuel quality requirements. An average calorific value corresponds to wood (Malaťák & Kučera, 2013) or vegetable matter (Malaťák & Bradna, 2014). The concentration of hydrogen

chloride was changed by mixing 100 kg of crushed PET bottles and 3 litres of 4.6% solution NaClO with incinerated waste before dosage to the burning chamber.

The measuring point was placed in front of the fabric filter. Flue gas temperature was 125–130 °C and volume of oxygen was 8.09–8.83%. The dependence of PCDD/F formation based on hydrogen chloride concentration in flue gas is shown in Figs 2, 3.
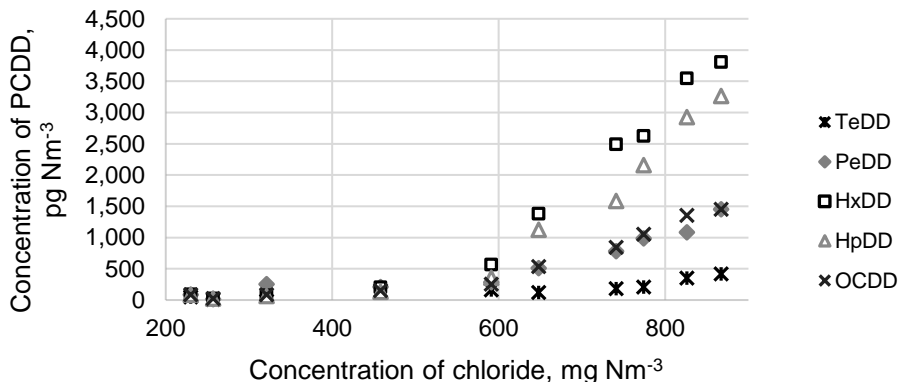
Figure 2. Dependence of PCDD individual congeneres concentration on chlorides concentration in flue gas.
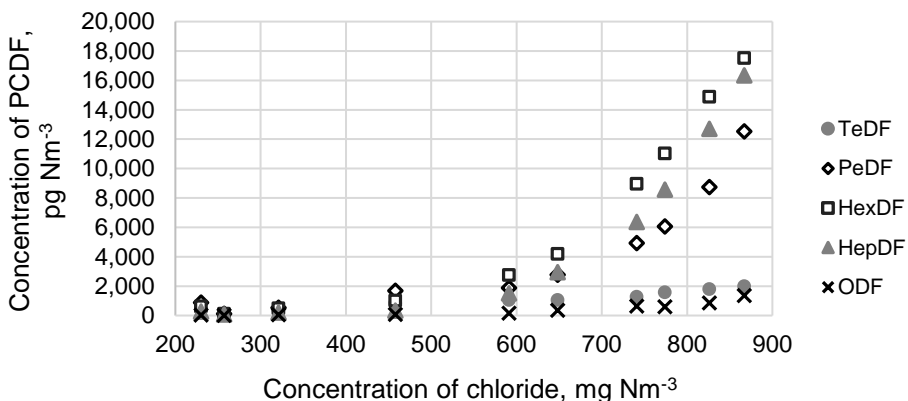
Figure 3. Dependence of PCDF individual congeneres concentration on chlorides concentration in flue gas.

The results show that the formation of both PCDD/F exponentially grows with the concentration of chlorides in the flue gas. However, the formation can vary based on type of congener. The distribution of concentration for different PCDD/F congeners are shown in Figs 4, 5.

It is obvious that the concentration of polychlorinated dibenzofurans is almost one order of magnitude higher that the concentration of polychlorinated dibenzodioxins. At chloride concentration of 458 mg Nm^{-3} formation of TeDD, PeDD, HxDD, HpDD and OCDD do not vary significantly. All the congeners formed at similar level between 150–200 pg Nm^{-3}. However, at chloride concentration of 867 mg Nm^{-3} formation of TeDD, PeDD, HxDD, HpDD and OCDD difers noticeably. Concentration of congener

with the lowest number of chlorine atoms, TeDD does not grow with increasing concentration of chlorides in flue gas. Concentration of PeDD and OCDD slightly increases with chlorides in flue gas. Concentration of HxDD and HpDD grows the most significantly with increasing concentration of chlorides in flue gas. The maximum concentration of is 3,811 pg Nm^{-3} for HxDD and 3,266 pg Nm^{-3} for HpDD at chloride concentration 867 mg Nm^{-3}.
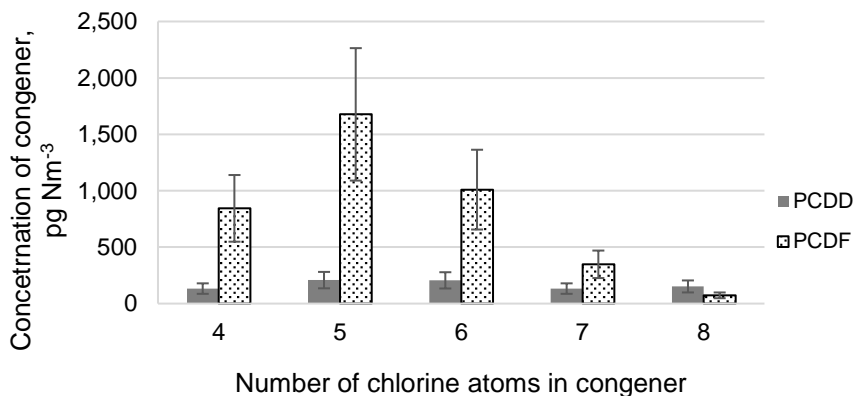
Figure 4. Concentration of persistent compounds in flue gases with content of chlorine equal to 458 mg Nm^{-3}.
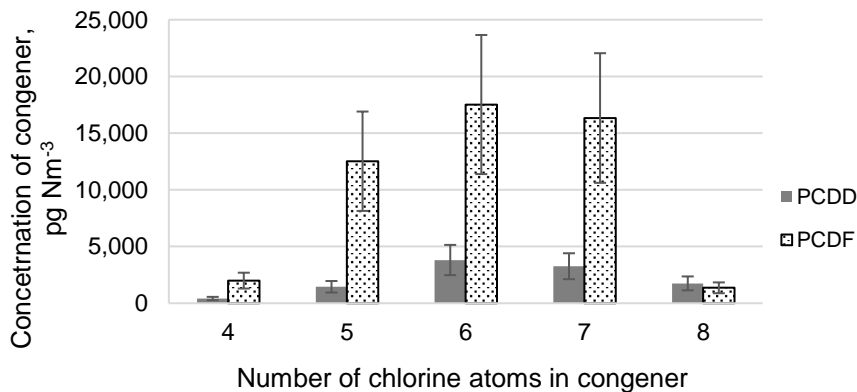
Figure 5. Concentration of persistent compounds in flue gases with content of chlorine equal to 867 mg Nm^{-3}.

Compared to that formation of polychlorinated dibenzofurans conducts differently. At chloride concentration of 458 mg Nm^{-3} TeDF, PeDF, HxDF form noticably more than HpDF and OCDF. The highest concentration 1,677 pg Nm^{-3} is masured for PeDF. However, concentration of OCDF is only 77 pg Nm^{-3}. With increasing concentration of chloride in flue gas congeners with 5, 6 and 7 chlorine atoms form the mostly. Maximum concentration of HxDF is 17,522 pg Nm^{-3} at chloride concentration of 867 mg Nm^{-3}. Similarly, concentration of the second most present congener, HpDF is 16,334 pg Nm^{-3} at the same level of chlorides in flue gas. On th other hand, concentration of TeDF and OCDF does not grow as signiciantly as concentration of PeDF, HxDF and HpDF with

increasing concentration of chlorides in flue gas, but still quite significantly compare to PCDD. The maximum concentration is 1,966 pg Nm^{-3} for TeDF and 1,361 pg Nm^{-3} for OCDF at chloride concentration of 867 mg Nm^{-3}. Very similar results were published for industrial incinerators (Chi et al., 2006) and for municipal waste incinerators (Kim et al. 2007).

Noticeable slope change of concentration fuction for individual congeners is around 600 mg Nm^{-3} of chlorides in flue gas when concentration of HxDD, HpDD and PeDF, HxDF, HpDF start growing dramatically compared to other PCDD and PCDF congeners. HxDF, HpDF have the major presence in flue gas.

Effect of Ca(OH)$_2$ on PCDD/F concentration reduction in flue gas

The influence of calcium hydroxide on concentration of PCDD/F in flue gas was measured. Calcium hydroxide was injected into the flue gas flow at rate of 5 kg per hour. The sorbent was dosed after a cooler where the temperature of flue gas was 225 ± 3 °C. The mean volume of flue gas was 3,296 $Nm^3\,h^{-1}$ and mean volume of O_2 was $10.3 \pm 0.95\%$. The concentration of hydrogen chloride decreased from original concentration of 458 mg Nm^{-3} to 230 mg Nm^{-3}. The reduction of individual congeners PCDD/F are shown in Table 3, 4.

Table 3. Effect of Ca(OH)$_2$ on PCDD concentration

PCDD	HCl	TeDD	PeDD	HxDD	HpDD	OCDD	Σ PCDD
I-TEF	mg Nm^{-3}	pg Nm^{-3}	pg Nm^{-3}	pg Nm^{-3}	pg Nm^{-3}	pg Nm^{-3}	pg Nm^{-3}
Initial concentration	458	133	208	206	133	152	832
Concentration when 5 kg Ca(OH)$_2$ dosed	230	51	86	94	85	87	403
Reduction of congener concentration		61.7%	58.7%	54.4%	36.1%	42.8%	51.6%

Individual congener reacts on calcium hydroxide addition to the system differently. The major reduction 61.7% was observed regarding TeDD. With growing order of chlorine atoms, the reduction slowly decreases. The mean decrease of all PCDD congeners is 51.6%.

Table 4. Effect of Ca(OH)$_2$ on PCDF concentration

PCDF	HCl	TeDF	PeDF	HexDF	HepDF	OCDF	Σ PCDF
I-TEF	mg Nm^{-3}	pg Nm^{-3}	pg Nm^{-3}	pg Nm^{-3}	pg Nm^{-3}	pg Nm^{-3}	pg Nm^{-3}
Initial concentration	458	844	1,677	1,010	348	73	3,952
Concentration when 5 kg Ca(OH)$_2$ dosed	230	406	883	612	263	33	2,197
Reduction of congener concentration		51.9%	47.3%	39.4%	24.4%	54.8%	44.4%

Similar effect was observed in regards with individual PCDF congeners as well. Maximum reduction 51.9% was seen with decreased concentration of TeDF. With increasing number of chlorine atoms in individual congener effect of Ca(OH)$_2$ on subsequent PCDF reduction descened. The mean decrease of all PCDF congeners is 44.4% and 45.7% for both PCDD and PCDF together. The result shows that calcium

hydroxide reduces the concentration of hydrogen chloride flue gas and subsequently reduces concentration of PCDD/F in flue gas.

Gunes similarly published that the lowest removal efficiency for particle phase was found to be 80% for TeDF while the highest removal efficiency found to be 100% for TeDD, PeDD and PeDF. Particle phase removal efficiencies for the rest of congeners were observed to range from 97–99% (Gunes et al., 2015). Lower chlorinated congeners have higher vapor pressures. So, they tend to go into gas phase and hence, have higher possibility of adsorption on activated carbon (Chi et al., 2006). On the other hand, higher chlorinated congeners tend to be present in particle phase due to their lower vapor pressures. These congeners are separated from gas stream after their adsorption onto activated carbon particles or their association with lime particles, consequently, filtration of the particles through bag house filter (Gunes et al., 2015).

Effect of activated carbon on PCDD/F concentration reduction in flue gas

Concentration of PCDD/F in flue gas can be decreased by calcium hydroxide that is usually used for reduction of acidic compounds in flue gas. However, the effect is not sufficient according to appropriate emission limits. Activated carbon is usually used for elimination of persistent organic pollutants in small incinerating facilities.

First measurement of PCCD/F concentration in flue gases was taken when neither sorbents nor active carbon was added into a system. It represents the reference point for evaluation. The volume of glue gas flow was 3,071 Nm^3 hr^{-1}.

Next 3.5 kg of calcium hydroxide per hour was injected into a flue gas stream after the heat exchanger (position A). The temperature of gases was 230 °C at dosing point. Calcium hydroxide can partially reduce concentration of PCDD/F by stabilizing chlorides in flue gas as it is shown in Table 4, 5. However, it cannot reduce PCDD/F at required level given by emission limits (Act No. 201/2012 Coll.).

Hence, activated carbon was examined on efficiency to diminish PCDD/F concentration to the acceptable level. There were two carbon based sorbents selected Chezacarb and NORIT, both crashed in high speed mill crusher to fine particles with size smaller than 5 μm. The dosing place had to be selected with regard to a flue gas temperature because there was a considerable content of oxygen. Dosing point was placed after a cooler (position B) where the temperature was 120 °C. Both sorbents Chezacarb and NORIT were dosed into the flue gas flow at rate of 300 g hr^{-1} and 400 g hr^{-1}. The results are shown in Table 5.

Table 5. Stabilization effect of activated carbon on PCDD/F concetration

	Reference emissions No sorbents added	$Ca(OH)_2$ 3.5 kg hr^{-1}	Chezacarb 300 g hr^{-1}	Chezacarb 400 g hr^{-1}	NORIT 300 g hr^{-1}	NORIT 400 g hr^{-1}
O_2	% vol. 8.58± 1.24	8.76± 1.28	8.45± 1.26	8.94± 1.48	8.65± 1.28	8.67 ± 1.30
Flue gas flow	Nm^3 hr^{-1} 3,071	3,208	3,710	4,100	3,890	4,020
Concentration of PCCD/DF	ng I-TEF Nm^{-3} 4.852	3.187	0.487	0.079	0.522	0.081

Result shows that both Chezacarb and NORIT are efficient to reduce concentration of persistent compounds in flue gases. Experiments were executed under the same conditions. All instruments and methodology were identical. Results are very similar, it is not possible to prefer one or the other sorbent based on sorption effectiveness. The results show that in order to satisfy emission limits for persistent compound approximately 0.1 g of activated carbon should be applied per 1 Nm^3 of flue gases with concentration 3–4 ng Nm^{-3} PCDD/F. Other researches published similar results. Abad stated that 92–96% removal efficiency can be achieved when 100 g Nm^{-3} of activated carbon is applied (Abad et al., 2003). Kim published that removal efficiency over 98% can be reached when 50 mg Nm^{-3} of activated carbon is injected into a system with dual bag filter, but 200 mg Nm^{-3} of activated carbon is necessary with a single filter applied (Kim et al., 2007).

CONCLUSIONS

The paper deals with formation and stabilization of PCDD/F during a process of biological and hospital waste thermal degradation. The experiments were conducted in a semi operation hospital waste incinerating plant with heating power 1.5 MW. Formation of PCDD/F exponentially grows with increasing concentration of chlorides in the flue gas, but formation varies based on type of congener. Concentration of PCDF is almost one order of magnitude higher that the concentration of PCDD. HxDF and HpDF reach the highest concentration 17,522 pg Nm^{-3} and 16,334 pg Nm^{-3} at chloride concentration 867 mg Nm^{-3}. However, concentration PCDD congeners does not exceed 4,000 pg Nm^{-3} at the same level of chlorides in flue gas. Calcium hydroxide dosed into the flue gas flow can decrease level of hydrogen chlorine and subsequently eliminate concentration of PCDD/F with the mean reduction of 45.7% at rate 5 kg h^{-1} of $Ca(OH)_2$ dosed into the flue gas flow. However, the effect of PCDD/F elimination by $Ca(OH)_2$ is not sufficient per emission limits. Activated carbon based sorbent is suitable to do so. Both examined carbon based sorbents commercially known as Chezacarb and NORIT achieve the same efficiency of PCDD/F stabilization in flue gas. It is not possible to prefer one or the other sorbent based only on sorption properties. In regards not to exceed emission limits of PCDD/F exposure, approximately 0.1 g of activated carbon must be applied per 1 Nm^3 of flue gases with total PCDD/F concentration of 3–4 ng Nm^{-3}. Carbon based sorbent is a vital supplement for PCDD/F elimination in dry sorption based refining technology in small scale waste incinerators.

REFERENCES

Abad, E., Caixach, J. & Rivera, J. 2003. Improvements in dioxin abatement strategies at a municipal waste management plant in Barcelona. *Chemosphere* **50**(9), 1175–1182.

Act No. 201/2012 Coll. Air Protection. Czech Republic. 2012.

Agency, E. (n.d.). Consolidated European Waste Catalogue. Retrieved from https://www.sepa.org.uk/media/139107/euro_waste_catalogue.pdf

Allen, R.W., Archer, E. & MacInnes, J. 2001. Adsorption by particles injected into a gas stream. *Chemical Engineering Journal* **83**(3), 165–174.

Cabot Corporation. (n.d.). Powdered Activated Carbon. Retrieved January 21, 2018, from http://www.cabotcorp.com/solutions/products-plus/activated-carbon/powdered

Cunill, F., Izquierdo, J.F., Martínez, J.C., Tejero, J. & Querol, J. 1991. Influence of different additives on the reaction between hydrated lime and sulfur dioxide. *Environmental Progress* **10**(4), 273–277.

Gunes, G., Saral, A., Yıldız, Ş. & Levent Kuzu, S. 2015. Determination of optimum dose of adsorbent for PCDD/F removal in the flue gas of a medical waste incineration plant. *Chemical Engineering Research and Design* **104**(2), 695–702.

Hisham, M.W.M. & Benson, S.W. 1995. Thermochemistry of the Deacon Process. *The Journal of Physical Chemistry* **99**(16), 6194–6198.

Chi, K.H., Chang, S.H., Huang, C.H., Huang, H.C. & Chang, M.B. 2006. Partitioning and removal of dioxin-like congeners in flue gases treated with activated carbon adsorption. *Chemosphere* **64**(9), 1489–1498.

Jirsa, P. & Malaťák, J. 2017. Dry sorption stabilization of flue gases in biological waste incinerating facility with heating power under 5 MW. *Agronomy Research* **15**(S1), 1024–1032.

Kim, B.H., Lee, S., Maken, S., Song, H.J., Park, J.W. & Min, B. 2007. Removal characteristics of PCDDs/Fs from municipal solid waste incinerator by dual bag filter (DBF) system. *Fuel* **86**(5–6).

Malaták, J. & Bradna, J. 2014. Use of waste material mixtures for energy purposes in small combustion devices. *Research in Agricultural Engineering* **60**(2), 50–59.

Malat'ák, J. & Kučera, M. 2013. Determination of some properties of solid biofuels from the pyrolysis technology. *Acta Facultatis Xylologiae* **55**(1), 119–127.

Phan, D.N.C., Jansson, S. & Boily, J.-F. 2014. Link between Fly Ash Properties and Polychlorinated Organic Pollutants Formed during Simulated Municipal Solid Waste Incineration. *Energy & Fuels* **28**(4), 2761–2769.

Schecter, A., Birnbaum, L., Ryan, J.J. & Constable, J.D. 2006. Dioxins: An overview. *Environmental Research* **101**(3), 419–428.

Stanmore, B. 2004. The formation of dioxins in combustion systems. *Combustion and Flame*, **136**(3), 398–427.

Unipetrol. (n.d.). Chezacarb for ecological use. Retrieved January 21, 2018, from http://www.unipetrolrpa.cz/en/OurProducts2/PetrochemicalProducts/CarbonBlackCHEZACARB/Pages/Chezacarb-for-ecological.aspx

Van Caneghem, J., Brems, A., Lievens, P., Block, C., Billen, P., Vermeulen, I., … & Vandecasteele, C. 2012. Fluidized bed waste incinerators: Design, operational and environmental issues. *Progress in Energy and Combustion Science* **38**(4), 551–582.

Wey, M.Y., Ou, W.Y., Liu, Z.S., Tseng, H.H., Yang, W.Y. & Chiang, B.C. 2001. Pollutants in incineration flue gas. *Journal of Hazardous Materials* **82**(3), 247–262.

Zhou, H., Meng, A., Long, Y., Li, Q. & Zhang, Y. 2015. A review of dioxin-related substances during municipal solid waste incineration. *Elsevier Ltd*, **36**,106–118.

Improving energy efficiency of biotechnical agricultural systems – scientific and organisational Issues

V. Karpov[1] and T. Kabanen[2,*]

[1]Saint-Petersburg state Agrarian University, Pushkin-1, Box No 1, RU196600 St.-Petersburg, Russia
[2]Tallinn University of Technology, Tartu College, Puiestee 78, EE51008 Tartu, Estonia
*Correspondence: toivokabanen@hot.ee

Abstract. The production process of an agricultural and industrial complex (AIC) includes processing of big areas of fertile soil that receive sun-generated electromagnetic energy. This is one of the peculiarities of the AIC, determined by the fact that the AIC produces primary (plant-based) food. The plants use part of the sun-generated energy to synthesise biological energy, which forms the nutrition value of the product and which is measured by a rational (relative) factor per unit of area. A plant community is a biological system where each plant is a biological element. The amount of fuel energy (which is anthropogenic unlike sun-generated energy) consumed by an AIC company to produce plant-based food is determined by the energy efficiency of the technical elements (fuel cells, both mobile and immobile) included in the consumer energy system (CES).Crops also supply food for livestock farming, which is the second biological branch of AIC and produces the second type of food, meat and poultry. Animals and poultry are raised using daily feed flow as the source of energy. As the energy consumption and the energy efficiency (expenses and return on investment, respectively) are determined by the technical part of the consumer energy system, it is necessary to find the dependence between the CES and biological systems (crop farming and animal farming) in the food production process.

Key words: energy saving, power consumption of production, criteria of energy efficiency, consumer power system.

INTRODUCTION

The concept of energy efficiency can be defined in various ways, the most popular of which is the relative decrease in energy consumption. Taking into account the overall aim of generating energy for the production of material goods and the fact that the material goods are the product of any enterprise, then product energy contents could be a relatively common unit of measurement, showing the amount of energy used to produce one piece of the final product. However, this value is applicable to similar plants producing similar products and is not suitable for evaluating the energy efficiency of a big corporation, region or state. As the sales markets and demand for products are the common evaluation factors of the units at this level, then the focus of analysis shifted from energy efficiency to gross regional product (GRP) and gross domestic product (GDP) energy contents, introducing a very specific indicator of energy contents of profit.

Even though this indicator shows efficiency indirectly (by means of demand),it does not impede the evaluation of energy-efficiency for the purposes of production development and for justifying the control methods of efficiency. International energy efficiency practices (Stasinopoulos et al., 2012), led to two important principles – integrated approach to system design and sustainable system development. Numerous instructive examples of energy consumption efficiency analysis in various production processes, cited in the book, use the efficiency factor (generally accepted non-dimensional parameter) as the means of evaluation. 'Efficient use of energy' (Karpov & Yuldashev, 2010), the concept of consumer energy system (CES) Fig. 1 – offers its own relative indicator to analyse the consumer energy efficiency.
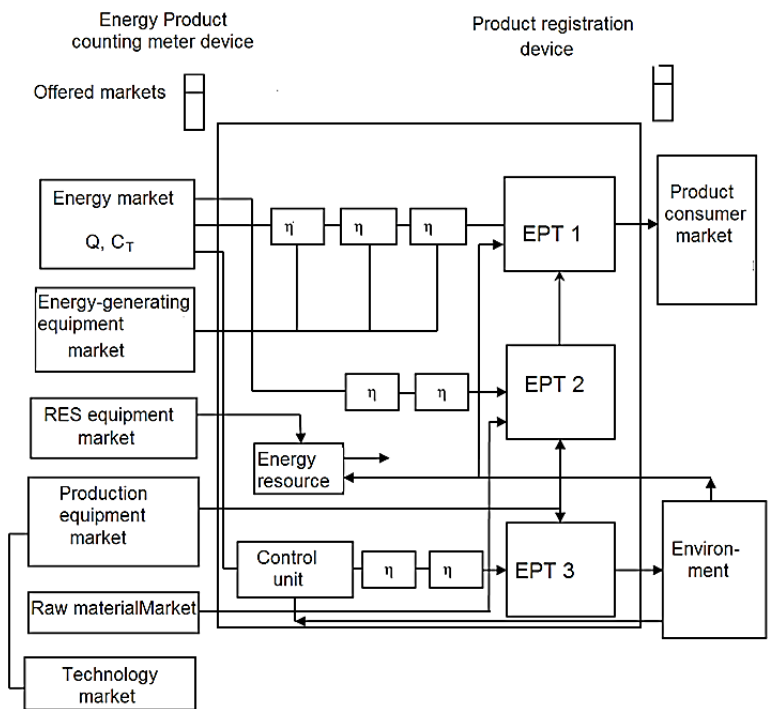
Figure 1. Energy scheme of the CES.

This indicator defines the relative energy contents Qe that is constantly moving through the technical element (TE) as the ratio between the input energy Qi (original measurable energy supplied to TE) and output energy Qo (measurable energy, leaving TE), i.e. $Qe = Qi / Qo$.

The introduction of the indicator makes it possible to analyse the efficiency of every individual TE as $Qe = 1 - \Delta Q/QQ$ (where $\Delta Q = Q_i - Q_k$ = energy losses in TE).and the efficiency of the energy transfer line connecting consecutive TEs, reveal the types of energy used by CES and efficiency of various types of products, simulate CES with a single TE that represents the total input energy and the sum of energy losses in the system.

Energy-technological processes (ETPs) that generate the result R by consuming the input energy are the key for CES energy efficiency. The value R is defined by the product manufacturing technology. The ETPs also determine the energy contents of the result R, where the energy contents is primary not only for the CES but also for the complete energy transfer system, from the energy generation point to the ETP.

MATERIALS AND METHODS

The basis of the research methods is made up of mathematical analysis of the energy efficiency criteria and suggestions to reduce energy waste. Therefore, the main and primary aim of the analysis of the biotechnical system (i.e. the conglomerate of the technical and biological systems within an AIC) is to define the specific role that the energy and technology processes of the technical system play in the efficiency of the biological system. Following our methodology, we first calculate the amount of consumed energy theoretically required (without losses) to receive R with the best achievable $Qe = 1$ (maximum efficiency), and then compare it to the measured amount of energy, actually consumed by ETP and exceeding the calculated net amount by the sum of various losses.

The share of the losses compared to the theoretical (minimum) energy consumption used to receive R defines both the reason (losses) and the value of the actual increment of the minimum Qe = 1 (at the minimum energy consumption). The advantage of the method to analyse the energy efficiency (using modern-type meters, PES and ETP with pre-defined R), offered by the Scientific School, entails the possibility to divide (differentiate) the consumed energy into two types: active energy and losses caused by the physical properties of various TEs.

Taking a multi-level hydroponic narrow-shelf greenhouse technology as an example (Kabanen, 2008), he proves that due to the design of the electric lamp it is not physically possible to arrange the shelves and the light flow within the greenhouse space to avoid the light losses. Moreover, this type of loss cannot be compensated even by increasing the power of the lamp and the energy consumption. The losses can be reduced or eliminated by using a light emitting diode instead of the traditional lamp.

Therefore, the Scientific School method allows defining and reducing in each of the CES energy lines the losses that increase the relative energy contents over *1*. The totalities of all the theoretical (calculated) amounts of energy in all energy lines on one hand and all losses on the other are the two complementary components of the amount of energy that CES used to make the product. The school suggests treating the first component as a system active energy and the second as a system loss. These two components determine the energy contents of the product, differentiated by the usage efficiency, not by a traditionally calculated statistical average one. We have to note that this differentiation is possible for energy consumer systems, but not for the energy transfer systems, which is why we can reasonably argue that any attempt to reduce the energy contents must begin with the energy audit of the consumer systems.

The possibility to control energy savings in technical consumer systems (i.e. in CES) has been experimentally verified in laboratory and real-life conditions, so we can claim that we are scientifically and methodologically ready to address this issue.

The extended CES layout including both fixed and mobile processes, land treatment and livestock-related processes describes the links between CES and the processes that support biological activities. Main focus was on basic energy flows to biological objects (plants, animals, poultry). Fig. 2 shows the results of the analysis of energy links between technical and biological objects.
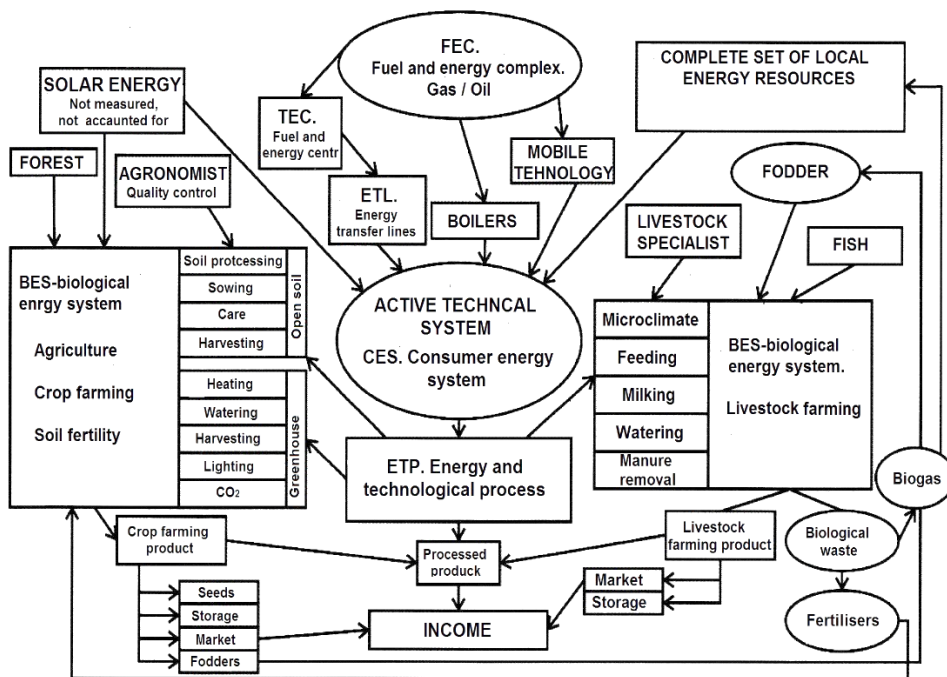
Figure 2. Energy links between CES, plant and animal farming.

The general industry-related energy layout reveals some important characteristics. Solar energy, transformed by plants into nutritional biological energy, and not anthropogenic (fuel) energy, is the source of nutritional biological energy contained in the basic agricultural plant products. The figure shows examples of fuel consumption in order to grow plants in open soil and in a greenhouse (left) and to keep animals (right). The 'fodder' line connecting the left and the right sides shows that the fodder of plant origin, containing biological energy and not fuel energy, is the main energy flow keeping the animals alive. This means that the energy contents of food production (both plant and animal) in the traditional meaning of the term is created by the technical system (PES), maintaining the plant and animal farming only, i.e. the energy contents of the farms fully depend on the energy efficiency of the power equipment used, on the plant farming technology and on the soil productivity.

As proven by the electric water heating experiments (Karpov et al., 2016), the technical equipment of the energy and technological process (ETP) can be considered a TE where energy is supplied and technological result R of the energy consumption is created and monitored. Meanwhile, the action (energy consumption) process is the only one of all the TE processes to register the energy losses that increase the energy contents of the product and reduce the energy use efficiency.

1065

This is presenting on the diagram of water heating at various ΔT (Fig. 3). The squares (non-hatched part) are the analytical foundation of the figure. These show the scales of the axis values in each quadrant as built according to the preliminary calculations. The first quadrant shows the amount of energy used to heat 20 litres of water by ΔT = 40 °C (Q = cmΔT, where Q = 3,352 KJ, time t = Q/P = 2,682 seconds and P – constant electric heater capacity).

The other two quadrants do not pose any questions. In the course of the experiment performed to verify the calculations, it turned out that the heating time determined by a straight line in the third quadrant and reflecting the ΔT value has increased by Δt. While the heater capacity remained constant, the amount of the consumed energy increased by up to 4,165 KJ pro rate the time. The energy losses are shown in the first quadrant as the increment of the calculated 3,352 KJ by 813 KJ. However, these are not actual losses, but the indirect result of its estimation at the heater input, i.e. this is the increment of the amount of energy supplied to ETP, not including the losses in the supply line within the enterprise.

Nevertheless, this increment allows evaluating the relative energy contents of the water heating process under certain conditions that are variables in the real-life environment (initial water temperature, ambient air temperature, presence / absence of air exchange, condition of the heater body thermal insulation, amount of the heated water, etc.). Considering that any direct measurement of the energy loss is not possible, that any PES contains a lot of ETPs, that these are of various duration (from daily to annual), and that farming takes place in various climates, it would be reasonable not to determine certain energy contents of a product but to find a certain acceptable minimum value and monitor and find reasons for deviations therefrom.
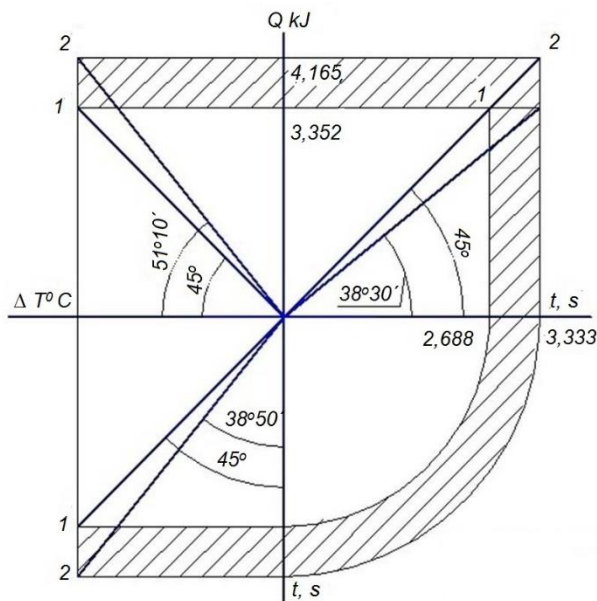
Figure 3. Energy diagram of water heating.

Taking into account the high relevance of the energy efficiency, high importance of technical consumer systems for methodological purposes and unique role of ETP energy within the systems as the means to determine the losses, we suggest distinguishing PES of plants as a separate class of active technical systems.

RESULTS AND DISCUSSION

This class may include the industrial technical systems that are supplied with energy in order to receive the result (product) of the system technology. These systems shall have the second (in addition to reliability) key indicator – high energy efficiency. It should be clear that any technical system which is reliable enough to keep operating, may do it with unacceptably high energy contents of the technological result, which in turn leads to unacceptably high energy contents of the final product, loss of competitive capacity and reduces the economic position of the whole plant. That is why informational support of the production process must be an indispensable part of any active technical system with the aim to determine the energy contents of the product and the system structure of the energy contents. The structure must be defined by the energy contents of all consumer system ETPs that are the result of the energy application and the primary indicator of the energy efficiency, as this indicator is obtained in the very end of the energy supply and usage chain. The closer the imaginary locus of the indicator is to its source (along the energy transfer line), the larger is its value due to increased losses of energy in the technical elements that form the energy transfer line. This is the reason why unbiased efficiency of energy usage cannot be determined in the energy transfer lines all the way to the consumer. This description of energy saving method allows postulating that this method makes CES a self-sufficient system indicator for the purposes of managing the energy contents of the final product. Inclusion of biological objects in the system means adding more ETPs and upgrading to a biotechnical energy system (Fig. 2), although the analysis of the energy efficiency of these processes remains basically the same, as the processes remain active processes and therefore the method of defining the energy contents of the biological products (fodder, food) does not change either. The only new factor is that the value of the product will be annually defined mainly by the productivity of the crop, soil fertility, and local climate, not by the amount of energy input in ETP. This is the reason for introducing innovative management of energy and biological processes at all stages of the crop vegetation in order to increase the specific (per unit of soil area) yield.

In terms of energy efficiency management, the multi-factor yield dependence may lead to using the soil for energy production, for instance, instead of biomass production. Therefore, the strict requirements of the energy efficiency make the agricultural energy (as a consumer energy system) management a multi-discipline occupation which in turn generates new requirements for professional training in agricultural schools.

CONCLUSIONS

Establishing the connections between the biological and technical systems will allow applying mathematical methods to determine and evaluate certain criteria of biological systems. For example, a unit of land area can be evaluated and controlled both in statics and dynamics and not only in terms of growth efficiency. We will be able to

evaluate the available area as a renewable energy resource (wind, sun, water flow) and offer the principles of using this resource. The treatment of biological waste as an additional source of energy will become more practical. The need to co-ordinate professional training curricula of biological, technical, and legal specialists employed by AICs will be evident, pressed by the competition in the sale of products. We should also highlight that the request for energy efficiency raises new scientific issues of agricultural production. The reason for these issues is the combination of determined and probability processes that form the energy contents of the monetary investments in the business. The research shows that mathematically, the calculation of the energy loss involves the differentiation of energy as a time function of complimentary elements with variable degree of smallness, i.e. the section of further mathematics, which is not included in the curriculum of the agricultural university. The possible multi-functional application of a square unit introduces a new field for the simplified numerical calculation of integral for the purposes of the agricultural energy management in addition to the standard units of time and length. This allows, in particular, comparing biological and non-biological technologies, considering energy-containing biological waste as a source of energy, and generating a unified approach to other biological objects in the country (e.g. forest or fish).Territorial differentiation of fertile soils creates new ways for using modern scientific and technical achievements (GPS, robots, drones, etc.) in precise land management.

REFERENCES

Stasinopoulos, P., Smith, M. & Hargrouvs, K. 2012. *Whole Systems design an integrated approach to sustainable engineering*. Eksmo, Moscow, 225 pp. (in Russia).

Kabanen, T. 2008. *Energy-saving lighting installations and equipment for multi-tier narrow bench greenhouse technologies.* Institut tehniki i tehnologi. St. Petersburg, 19 pp. (in Russia).

Karpov, V. & Yuldashev, Z. 2010. *Finite Ratio Method*. Energy Efficiency. St. Petersburg, 147 pp. (in Russia).

Karpov, V., Kabanen, T., Yuldashev, Z., Nemtsev, A. & Nemtsev, I. 2016. Basic theory and methods for managing energy efficiency in consumer systems (agricultural engineering). *Agronomy Research* **4**(5), 1619–1625.

Conceptual 'Cradle to Gate' analysis of GHG emissions from wood, agricultural plant and synthetic fibres

V. Kazulis[*], I. Muižniece and D. Blumberga

Riga Technical University, Faculty of Power and Electrical Engineering, Institute of Energy Systems and Environment, Azenes iela 12/1, LV-1048 Riga, Latvia
[*]Correspondence: valters.kazulis@rtu.lv

Abstract. Industrialization and fossil resource use has brought unprecedented anthropogenic carbon dioxide emissions. Use of synthetic fibre materials and unsustainable plant cultivation practices contribute to greenhouse gas emissions. The global market share of polyester fibre (synthetic fibre made from fossil resources) exceeded the share of cotton fibre (natural fibre) for the first time in 2000 and since then polyester has remained the most popular fibre. The demand for textiles keeps increasing. In Northern Europe locally made fibres from wood, hemp and flax could substitute fossil based fibres decreasing the global GHG emissions and helping local economies to prosper. Multi-criteria analysis method TOPSIS was used to carry out a conceptual research evaluating GHG emissions from wood, agricultural plant and synthetic fibre acquisition under two scenarios: fossil fuels are used as energy sources & industrial fertilizers are used; and renewable energy sources are used & industrial fertilizers are not used. Results show that wood and plant fibres have smaller GHG emissions than synthetic fibres in both scenarios. Factors affecting emission performance are analysed.

Key words: fibre, wood fibre, hemp fibre, flax fibre, synthetic fibre, carbon dioxide, multi-criteria analysis, TOPSIS.

INTRODUCTION

The data collected by Vlachogianni & Valavanidis (2013), International Energy Agency (2017) and British Petroleum (2017) reveal ever increasing reliance on fossil resources. Recently the only dip in the fossil resource consumption happened between 2008 and 2009, and was caused by the global financial crisis. Industrialization, urbanization, transportation, deforestation and energy production are driving the increase in the atmosphere's CO_2 concentration (Kumar et al., 2018). Since the late 19th century the CO_2 concentration has increased by approximately 50% from around 270 ppm to above 400 ppm (National Aeronautics and Space Administration, 2018). Recent anthropogenic rises in CO_2 levels have been more rapid than ever before the industrialization. The world annual average temperature rose by approximately a degree Celsius since the beginning of 20th Century.

Trackable amount of CO_2 emissions can be avoided by substituting products made from fossil resources by products made from sustainably acquired biomass – CO_2 emissions during the production process have to be smaller than the avoided CO_2

emissions (Kalnbalkite et al., 2017). Substitution of fossil source based products with products made from biomass is a step to be taken to mitigate emissions. Due to the significant forest covered areas Poland, Lithuania, Latvia, Estonia and other Northern European countries could find the end of fossil era opportune.

Nearly everyone around the globe is a customer of the global textile industry. The global market share of polyester fibre exceeded the share of cotton fibre for the first time in year of 2000 and this trend has continued (Palamutcu, 2017). Fibre demand is increasing and it reached 95.6 million tons in 2015. The increase of the world fibre market consumption was up to 99 million tons in 2016 and fossil source based synthetic fibres had the biggest share with 62.7%, cotton fibres took 24.3%, wood-based cellulose fibres around 6.6%, cellulosic and protein-based other fibres had 5.3% and wool around 1.1% (Lenzing Annual Report, 2016). Hemp, flax and wood fibres are advantageous and have suitable qualities to be cultivated in Northern Europe and cultivation is associated with low water, fertilizer and pesticide requirements (Zommere et al., 2013). The current global market share of hemp, linen and wood fibre textiles is multiple times smaller than the share of cotton textiles, however it is growing but growing demand for environmental friendly, skin friendly and bio-degradable textiles will be the key factor, expected to drive the market by 2020 (Palamutcu, 2017).

Cellulose content in hemp and flax is around 70%. Cellulose in wood constitute between 40-50%. Because cellulose extraction from wood involves a significant thermochemical phase therefore wood fibres are categorized as naturally derived synthetic fibres. Current technology advancements allow wood fibres to be produced via advanced 'closed loop' process minimizing impact on the environment. For example wood fibre lyocell which is a brand of rayon fibre production uses an amine oxide (a non-toxic solvent) which is continually recycled during the production process – 99% of solvent used in the cellulose extraction can be recovered (Shen & Patel, 2010).

Stockholm Environment Institute published research summarizing that use of fossil resources as a material for fibre production can have smaller impact on the environment than agricultural cultivation because agricultural cultivation involves use of pesticides and insecticides causing toxicological effect on the environment (Cherrett et al., 2005). The production and use of nitrogen containing fertilizers (such as HNO_3) generate considerable amounts of greenhouse gas (GHG) emissions and the global warming potential of N_2O for 100 year period is 310 times greater than CO_2. Soil emissions of N_2O were assumed to be linearly related to N fertiliser rate with 0.0157 kg N_2O per kg N from direct emissions; plus 0.0036 kg N_2O per kg N indirect emissions from leaching and 0.0015 kg N_2O per kg N from volatilisation, giving a total of 0.0208 kg N_2O per kg N, or 6.16 kg CO_2 equivalent per kg N; the average GHG emissions associated with the manufacture, packaging and transport of ammonium nitrate fertiliser were estimated to be 7.11 kg CO_2 equivalent per kg N (Kindred et al., 2008). Land cover change assuciated with deforestation directly affects the surface-atmosphere interactions changing moisture and further influence the atmospheric thermodynamic characteristics (Li et al., 2013).

Cotton crop cultivation and fibre production requires between 11,000 MJ and 32,000 MJ per ton and polyester 'cradle to gate' energy requirements are between 104,000 MJ and 126,000 MJ per ton, however synthetic fibre polyester manufacturing stages require very little if any water (Palamutcu, 2017).

Terinte et al. (2014) carried out 'cradle to gate' life cycle analysis (LCA) of undyed modal (wood cellulose fibre) – they found equivalent emissions to be 2.05 kg CO_2 emissions per kg of modal fabric. According to Walser et al. (2011) 'cradle to gate' analysis the equivalent emissions of 1 kg polyester t-shirts are 19.6 kg CO_2. According to Roos et al. (2015) 'cradle to gate' analysis of 1 kg polyster dress are 21 kg CO_2. Thomas et al. (2012) 'cradle to gate' analysis of different garments fibres results show that the average equivalent emissions of 1 kg flax /linen garments are 15 kg CO_2, 1 kg polysester garments are 21.3 kg CO_2 and average equivalent emissions of 1 kg cotton garments are 27.7 kg CO_2. Van der Velden et al. (2014) estimated the equivalent CO_2 emissions of 1 kg cotton fibre (cradle to gate) to be between 9 and 22,5 kg CO_2. Shen & Patel (2011) 'cradle to gate' analysis found that 1 kg lyocell equivalent emissions were 1.5–2.5 kg CO_2, pointing that the required land area for wood to produce lyocell can be 4 times smaller than the land required to produce equal amount of cotton fibre (Shen & Patel, 2010). Methodology details (handling of biogenic CO_2 emissions and soil carbon changes) are rarely clearly stated in the studied carbon footprint calculations (Roos et al., 2015).

Different locations require different amounts of fertilizers, insecticides and energy inputs. Similarly the available energy sources, production technologies, staff work-culture and logistics change from one location to another. Although there are differences in emission results for cotton, hemp and linen, it can assumed that the average CO_2 emissions from these fibres are similar and depend on the plant cultivation practices, fibre production technologies and energy sources. Use of industrial fertilizers and fossil resources are economically viable because the external costs such as GHG emissions are not internalized. GHG emissions are externalities and represent the biggest market failure the world has seen (Tsigaris & Wood, 2016).

This paper compares two scenarios of GHG emissions associated with fibre material acquisition for selected fibres – wood fibres, agricultural plant fibres and synthetic fibres. Raw material cultivation / extraction, base material production the material GHG emissions are analysed. The first scenario studies current industrial agriculture practices and the second scenario studies sustainable agricultural practices.

METHODOLOGY

This research evaluates GHG emissions of different fibres using multi criteria analysis (MCA) TOPSIS (*Technique for Order Preference by Similarity to Ideal Solution*) (Jahan et al., 2016). TOPSIS is performed by placing available alternatives (in this case fibre materials) and identified influencing factors (GHG emission sources of fibre acquisition process) in a matrix, identifying the relevant factors for a particular fibre and carrying out normalization calculations according to TOPSIS methodology. Upon completion of the calculations the most desirable alternative should have the shortest geometric distance from the ideal solution - whichever fibre acquisition is closer to 0 anthropogenic emissions is the most desirable alternative. The acquisition of the selected fibres were explored under two different scenarios:

1) fossil resources are used to power the production processes and industrially produced fertilizers are used;

2) renewable resources are used to power the production processes and agricultural practices are sustainable.

In both scenarios the alternative that is closest to the ideal situation is when the result is closest to 0 – no anthropogenic GHG emissions.

Literature review identified factors contributing to GHG emissions of fibre acquisition for three selected fibres: a derived synthetic fibre from wood, agricultural plant fibre (hemp /flax) and synthetic fibre polyester. Following possible GHG emission factors of fibre production were identified: use of industrial fertilizers; deforestation; extraction & fibre base material production; high energy intesity; and additional carbon introduction into atmosphere. The use of industrial fertilizers is mainly associated with agricultural plant fibre acquisition as trees do not have high soil nutrient requirements. Depending on the technologies agricultural plant cultivation as well as increased demand for wood fibres can be associated with deforestation. Extraction & base material production is associated with all three fibre acqusition. Possible CO_2 emissions from energy consumption to power processes is a significant factor – in the data matrix energy intesity represents the sum of average energy requirements of different production stages for each fibre which were found out in the literature review. The use of fossil sources generate additional CO_2 emissions and use of renewable energy sources is CO_2 neutral. The overall energy intesity still is an economic factor determining the choice of producing one good over another. Additional carbon introduction into the atmosphere is a factor showing whether the product is related with using the carbon already within biosphere or introducing carbon from the subterranean depths of earth into the biosphere which is not desirable considering the current the topicality of this paper.

A numerical weight was assigned to every factor (Table 1). The total sum of all assigned numerical weights is 1 – it can also be viewed as 100% however not all factors apply to each fibre. For example use of fertilisers is not related with acquisition of synthetic fibres. Weight of an individual factor is chosen relative to weights of other factors. The weights of factors were distributed accordingly: 0.15 is industrial fertilizer use, 0.15 is deforestation, 0.05 is extraction and & base material production (emissions from chemicals), 0.25 is energy intensity and 0.4 is additional CO_2 release into the atmosphere. Additional CO_2 release into the atmosphere was assigned the greatest numerical weight because the extraction of fossil resources add extra carbon to the carbon cycle eventually contributing towards increase in CO_2 emissions. If a fibre acquisition includes particular factor then in the matrix it is identified with '1', absence of factor is identified with '0'.

RESULTS AND DISCUSSION

The selected materials do not contain pure cellulose parts like cotton therefore extraction stage exists both for wood and agricultural plant fibres and here direct GHG emissions can be generated from energy source choice and indirect GHG emissions can come from the use of chemicals in extraction processes. The acquisition of fossil resources and base material production also involve direct GHG emissions that can be generated from energy source choice and indirect GHG emissions that can come from the use of chemicals in extraction processes. Literature review revealed significantly higher energy demand for wood and synthetic fibres in the thermochemical phases. The energy requirements for agricultural plants are lower because of the cellulose content in plants is higher and preparation for extraction is also less energy intensive. This study does not take into account the relatively long time that is needed for trees to grow.

The first alternative scenario explores GHG emissions from cultivation and production of the selected fibres using industrial fertilizers and fossil fuels. Table 1 shows the MCA TOPSIS data matrix. It was assumed that deforestation is caused by wood fibres, but not by agricultural fibre cultivation because the use of industrial fertilizers ensure greater yield per hectare.

Table 1. Multi criteria analysis matrix of GHG emissions from selected textiles. Scenario 1: fossil fuels and industrial fertilizers are used

Stage of life cycle (factors)	Wood fibres	Agricultural plant fibres	Synthetic fibres	Attributed weight
1 Use of fertilisers	0	1	0	0.15
2 Deforestation	1	0	0	0.15
3 Extraction & base material production	1	1	1	0.05
4 High energy intesity	1	0	1	0.25
5 Additional Carbon introduction into biosphere	0	0	1	0.4
Total TOPSIS analysis score	0.35	0.24	0.67	

Fig. 1 shows the results of the first scenario. The lowest GHG emissions results in this are from agricultural plant fibres resulting in 0.24 points. Fertilizer use is the most significant factor. The overall energy intensity in the agricultural plant fibre cultivation and production is low compared to other fibres. Wood fibres with 0.35 points do not need industrial fertilizers however the fibre production is energy intensive because the content of cellulose is smaller than in agricultural plant fibres, therefore wood fibres are the second best alternative. Synthetic fibres with 0.67 points are the least desirable alternative -they are made from fossil resources and the currently known production practices are energy intensive as well as the extraction and fibre base material production are associated with GHG emissions, however the use of fossil sources is not related with fertilizer use and deforestation. If the factor 'additional CO_2 release into atmosphere' would not be included then agricultural fibres would score 0.39 points, synthetic fibres would score 0.45 points and wood fibres would score 0.61 points.

Figure 1. Multi-criteria analysis results of GHG emissions from selected textiles. Scenario 1: fossil fuels and industrial fertilizers are used.

If in the first scenario it is assumed that wood fibres do not cause deforestation then wood fibres wood be the most desirable scenario scoring 0.28 points and agricultural fibres would be the second best alternative with 0.33 points. And if it is assumed that both wood and agricultural fibres cause deforestation agricultural fibres would score 0.30 points and wood fibre would score 0.33 points.

The second scenario (Table 2) assumes that renewable energy sources are used and agricultural plant cultivation is done sustainably without using industrial fertilizers - not causing additional anthropogenic CO_2 emissions. It is known that sustainable agriculture is associated with lower yields therefore assumption was made that agricultural fibre cultivation will cause deforestation. CO_2 emissions can be generated also from extraction and base material production for all three types of fibre and also additional CO_2 will be released into the atmosphere by the use of fossil sources as raw material for synthetic fibre production.

Table 2. Multi criteria analysis matrix of GHG emissions potential from different textiles. Scenario 2: fossil fuels and industrial fertilizers are not used

Stage of life cycle (factors)	Wood fibres	Agricultural plant fibres	Synthetic fibres	Attributed weight
1 Use of fertilisers	0	0	0	0.15
2 Deforestation	1	1	0	0.15
3 Extraction & base material production	1	1	1	0.05
4 High energy intesity	0	0	0	0.25
5 Additional Carbon introduction into biosphere	0	0	1	0.4
Total TOPSIS analysis score	0.18	0.44	0.56	

Fig. 2 illustrates the results of the second scenario. The lowest GHG emissions results are from wood fibres resulting in 0.18 points. Wood fibres generate GHG emissions from deforestation and extraction & fibre base material production stages. Agricultural plant fibres are second best alternative with 0.44 points. The negative side-effect of sustainable fertilizer use in agricultural plant fibre cultivation could be deforestation due to increased land requirements. Synthetic fibres with 0.56 points are the least desirable alternative.

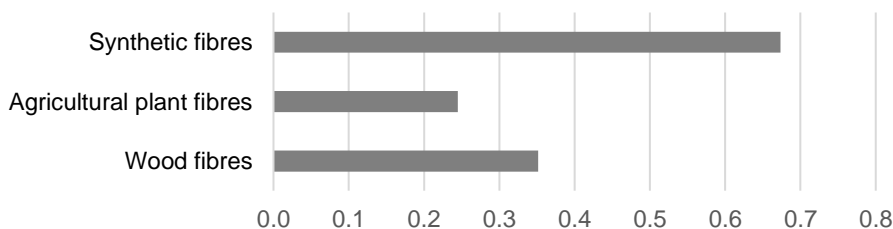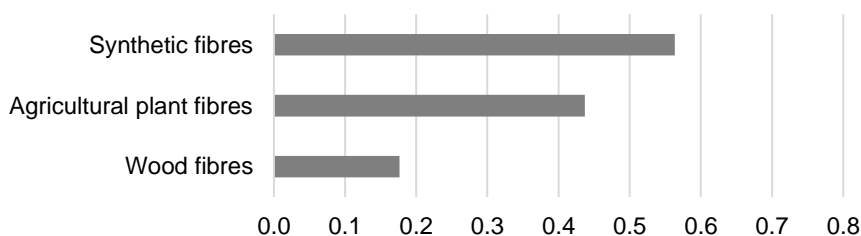**Figure 2.** Multi-criteria analysis results of GHG emissions from selected textiles. Scenario 2: fossil fuels and industrial fertilizers are not used.

If the factor 'additional CO_2 release into atmosphere would not be included' then the production synthetic fibres would be the most desirable with only extraction and base material production causing GHG emissions and wood fibres would be in the second place.

CONCLUSIONS

Multi-criteria analysis TOPSIS based on the data from literature review was carried out to estimate 'cradle to gate' GHG emissions from selected fibre materials: wood fibres, agricultural plant fibres and synthetic fibres. Two scenarios were explored:

1) fossil resources are used to power the production processes and industrially produced fertilizers are used;

2) renewable resources are used to power the production processes and agricultural practices are sustainable.

The results show that in first scenario agricultural plant fibres have the smallest GHG emissions followed by wood fibres and synthetic fibres have the highest GHG emissions. The reason for agricultural plans to be more attractive in this case is related with the high energy demand of fibre extraction from wood sources. Both wood fibre and synthetic fibre production technologies are energy intensive. Under sustainable management, if only renewable energy sources are used wood based fibres would have the smallest GHG emissions. Industrial fertilizer use for agricultural plant cultivation increases GHG emissions, however ensures greater yields per hectare. Sustainable agriculture cultivation could mean increased demand for land and lead to deforestation. It is important to note that proper technology of fiber acquisition can reduce or at least optimize water impact.

This research is conceptual therefore indicative and should be taken as a rough base for making real life decisions. Further researches about possibilities of locally producing sustainable fibres should be carried out.

REFERENCES

British Petroleum 2017. BP Statistical Review of World Energy.
https://www.bp.com/content/dam/bp/en/corporate/pdf/energy-economics/statistical-review-2017/bp-statistical-review-of-world-energy-2017-full-report.pdf Accessed 2.2.2018.

International Energy Agency. 2017. Key World Energy Statistics 2017.
https://www.iea.org/publications/freepublications/publication/key-world-energy-statistics.html Accessed 2.2.2018.

Cherrett, N., Barrett, J., Clemett, A., Chadwick, M. & Chadwick, M.J. 2005. *Ecological Footprint and Water Analysis of Cotton, Hemp and Polyester*. Stockholm Environment, 28 pp.

Jahan, A., Edwards, K. & Bahraminasab, M. 2016. *Multi-criteria Decision Analysis for Supporting the Selection of Engineering Materials in Product Design*. Butterworth-Heinemann, Elsevier, 252 pp.

Kalnbalkite, A., Zihare, L. & Blumberga, D. 2017. Methodology for estimation of carbon dioxide storage in bioproducts. *Energy Procedia* **128**, 533–538.

Kindred, D., Berry, P., Burch, O. & Sylverter-Bradley, R. 2008. Effects of nitrogen fertiliser use on greenhouse gas emissions and land use change. Aspects of Applied Biology 88, Effects of Climate Change on Plants: Implications for Agriculture 88.
http://citeseerx.ist.psu.edu/viewdoc/download?doi=10.1.1.516.3492&rep=rep1&type=pdf Accessed 2.2.2018.

Kumar, M., Sundaram, S., Gnansounou, E., Larroche, C. & Thakura, I.S. 2018. Carbon dioxide capture, storage and production of biofuel and biomaterials by bacteria: A review. *Bioresource Technology* **247**, 1059–1068 https://doi.org/10.1016/j.biortech.2017.09.050 Accessed 2.2.2018.

Lenzing Group Annual Report 2016. https://www.lenzing.com/fileadmin/content/PDF/07_Finanzen/Geschaeftsberichte/EN/GB _2016_EN.pdf Accessed 2.2.2018, pp 24.

Li, Z., Deng, Z., Shi, Q., Ke, X. & Liu, Y. 2013. Modeling the Impacts of Boreal Deforestation on the Near-Surface Temperature in European Russia. *Advances in Meteorology* 2013, Article ID 486962 https://www.hindawi.com/journals/amete/2013/486962/ Accessed 2.2.2018.

National Oceanic and Atmospheric Administration. Trends in atmospheric Carbon Dioxide. https://www.esrl.noaa.gov/gmd/ccgg/trends/full.html Accessed 10.04.2018.

Palamutcu, S. 2017. Sustainable Textile Technologies. In: *Textile Science and Clothing Technology. Textiles and Clothing Sustainability*. Springer pp. 2–21.

Roos, S., Posner, S., Jonsson, C. & Peters, G.M. 2015. Is unbleached cotton better than bleached? Exploring the limits of life cycle assessment in the textile sector. *Clothing and Textiles Research Journal* **33**(4), 231–247. http://journals.sagepub.com/doi/abs/10.1177/0887302X15576404 Accessed 2.2.2018.

Shen, L., Patel, M.K. 2010. Life Cycle Assessment of Man-made Cellulose Fibres. *Lenzinger Berichte* **88**, 1–59. http://www.proyectaryproducir.com.ar/public_html/Seminarios_Posgrado/Material_de_re ferencia/LIFE%20CYCLE%20ASSESSMENT%20OF%20MAN-MADE%20CELLULOSE%20FIBRES.pdf Accessed 2.2.2018.

Terinte, N., Manda, B.M.K., Taylor, J., Schuster, K.C. & Patel, M.K. 2014. Environmental assessment of coloured fabrics and opportunities for value creation: spin-dyeing versus conventional dyeing of modal fabrics. *Journal of Cleaner Production* **72**, 127–138. https://doi.org/10.1016/j.jclepro.2014.02.002 Accessed 2.2.2018.

Thomas, B., Fishwick, M., Joyce, J. & van Santen, A. 2012. A Carbon Footprint for UK Clothing and Opportunities for Savings. Final Report, 73 pp. http://www.wrap.org.uk/sites/files/wrap/Appendix%20IV%20-%20Carbon%20footprint%20report.pdf Accessed 2.2.2018.

Tsigaris, P. & Wood, J. 2016. A simple climate-Solow model for introducing the economics of climate change to undergraduate students. *International Review of Economics Education* **23**, 65–81 https://doi.org/10.1016/j.iree.2016.06.002 Accessed 2.2.2018.

Van der Velden, N.M., Patel, M.T. & Vogtlander, J.G. 2014. LCA benchmarking study on textiles made of cotton, polyester, nylon, acryl, or elastane. *International Journal of Life Cycle Assessment* **19**, 331–356 http://www.woodguide.org/files/2014/07/LCA-textiles.pdf Accessed 2.2.2018.

Vlachogianni, T. & Valavanidis, A. 2013. Energy and Environmental Impact on the Biosphere Energy Flow, Storage and Conversion in Human Civilization. *American Journal of Educational Research* **1**(3), 68–78. http://pubs.sciepub.com/education/1/3/2/ Accessed 2.2.2018.

Walser, T., Demou, E., Lang, D.J. & Hellweg, S. 2011. Prospective environmental life cycle assessment of nanosilver T-shirts. Envuironmental Science and Technnology **45**(10), 4570–4578. https://pubs.acs.org/doi/abs/10.1021/es2001248 Accessed 2.2.2018.

Zommere, G., Viļumsone, A., Kalniņa, D., Soliženko, R. & Stramkale, V. 2013. *Linu un kaņepju šķiedru uzbūves un celulozes satura salīdzinoša analīze (Flax and Hemp Fibre Property and Cellulose Comparitive Analysis)*. Materiālzinātne. Tekstila un apģērbu tehnoloģija **8**, 96–104 (in Latvian). http://org.daba.lv/LLZC/Zinatniska_darbiba/L-8387.pdf Accessed 2.2.2018.

Thermal properties of historic rural building materials in Czechia

P. Kic[1,*] and P. Neuberger[2]

[1]Czech University of Life Sciences Prague, Faculty of Engineering, Department of Technological Equipment of Buildings, Kamýcká 129, CZ165 21 Prague, Czech Republic
[2]Czech University of Life Sciences Prague, Faculty of Engineering, Department of Mechanical Engineering, Kamýcká 129, CZ165 21 Prague, Czech Republic
*Correspondence: kic@tf.czu.cz

Abstract. Due to the different natural conditions, various local natural building materials were used for the construction of rural residential and farm buildings in various locations in the Czech Republic. Currently, it is often a requirement for the modernization of relatively old buildings. The buildings were built with different technologies. Very often only locally available material was used. In many cases, the properties of old materials are not available in the literature. However, it is necessary to know the thermal properties of building materials for the preparation of a reconstruction design. Thermal properties of materials are the basis for determination of heat losses of buildings useful for design of heating systems. The aim of this paper is to compare the research results focused on the thermal conductivity of different old construction materials (stones and rocks) and to show examples of preserved historical agricultural buildings. The results presented in this paper are based on the measurements by the portable instrument Isomet 2104. Authors recognised significant differences between tested materials. The mean values of thermal conductivity λ_m of tested materials: gaize 1.49 W m^{-1} K^{-1}, artificial marble 1.80 W m^{-1} K^{-1}, gneiss 2.36 W m^{-1} K^{-1}, proterozoic shale 2.68 W m^{-1} K^{-1}, granite 3.66 W m^{-1} K^{-1} and quartz sandstone 6.15 W m^{-1} K^{-1}. Differences between thermal conductivity values of stones and rocks should be respected in calculation of heat balance of new or reconstructed buildings to avoid the problems of the formation of thermal bridges.

Key words: dynamic method, measurement, rocks, stones, thermal conductivity.

INTRODUCTION

Due to the different natural conditions, various local natural building materials were used for the construction of rural residential and farm buildings in various locations in the Czech Republic. Currently, it is often a requirement for the modernization of relatively old buildings. The buildings were built with different technologies. Very often only locally available material was used. The combination of different materials with not well known thermal properties can cause significant reduction of thermal insulation and the formation of thermal bridges.

In the world, there are many areas where timber (north of Europe, Scandinavia, mountainous areas of the Czech Republic, etc.) is predominantly used for constructions elsewhere clay was available therefore bricks were produced; in many areas stone and rocks are very common materials, which also have a large heat accumulation (e.g. Italy, central part of Czech Republic and others). The materials from which the buildings were built change their properties due to external climate and chemical changes of materials during the years of use.

In some cases, the properties of old materials are not available in the literature. However, it is necessary to know the thermal properties of building materials for the preparation of a reconstruction design. The diversity of building materials in old rural buildings can be explained mainly by efforts to reduce investment costs and availability of resources. That is why there are used mainly local resources. The building material is therefore also used repeatedly. It is no exception to dismantle the ruins of mansions or buildings damaged by fire and the use of those old materials for new construction.

Historical residential and church buildings around Prague include typical materials: Romanesque style (10th to 12th century) – marlstone, gothic (12th to 16th century) – sandstone, baroque (17th to 18th century) – marble, 19th century – granite. Agricultural structures are not so precisely defined in terms of time and material. Many authors, however, pay attention to building materials used for agricultural construction in their publications. In some cases, these are special constructions such as Conti et al. (2016a); Leso et al. (2017), sometimes using non-traditional material.

A very common problem is the reconstruction of buildings when using a combination of stone with other materials, such as brick masonry or blocks, as there may be a significant reduction in thermal insulation and the formation of thermal bridges (Kollmorgen, 1998; Ladener et al., 2001; Šubrt &Volf. 2003; Tywoniak, 2005).

Thermal conductivity is the most important parameter of thermal-technical properties of materials. It is used mainly in civil engineering. Its real value is a function several internal and external variables (density, moisture, temperature, porosity, chemical and mineralogical composition and phase composition, crystalline modification etc.). The attention is paid to the problems of insulation properties in different publications, e.g. (Muizniece et al., 2015; Kocova & Kic, 2016; Pleiksnis et al., 2016; Týbl & Kic, 2016; Valasek et al., 2016). The results of thermal conductivity measurements are discussed, e.g. in Conti et al. (2016b).

Thermal properties of building materials greatly affect the indoor environment, especially the indoor temperature of the building during winter and summer. This topic in agricultural constructions is solved, for example, by Kic (2017).

Thermal properties of materials are the basis for determination of heat losses of buildings useful for design of heating systems. Currently used tables of building materials do not include all locally used materials. For some of them, it provides a range of values Ražnjević (1984). Insufficient knowledge of exact values makes calculation of heat losses of buildings more difficult.

The aim of this research is to demonstrate the use of the dynamic method for measurement of a thermal conductivity for determination of thermal properties of materials used for buildings, especially of stone and rocks. It is important to show and confirm that there are significant differences between them. It should be also confirm the ability to obtain more accurate background data included in models used for heat losses calculation of older constructions.

MATERIALS AND METHODS

Five different materials were selected for this research work. The first material is artificial marble. This material is very popular and many companies are producing this material according to their patents. It is useful, to compare it with natural real materials. The artificial stone tested in this research was a marble imitation stone tile. The sample of tested material weighs 1 kg. The surface sensor was used to determine the thermal conductivity.

The second material is gneiss, which is available in many localities in the Czech Republic. A sample of this material was taken from a village in Southwest Bohemia. An example of the use of this local material is a set of buildings in this village of Fig. 1. It is a typical building for the folk architecture of Prácheňsko – the historical territory in the southwest of the Czech Republic. Fig. 1 shows the triangular stone shield of one of the buildings. This material is currently used as a buildings stone for different construction purposes. The sample of tested material weighs 1.95 kg. The surface sensor was used to determine the thermal conductivity.

Figure 1. Original folk architecture in the village Klínovice – stone triangular shield.

Quite frequently used for constructions is also the third tested material proterozoic rock (shale), which is easy to manipulate and prepare for different use in constructions. A tested sample of proterozoic shale was taken near the Prague – Suchdol district, where it is widely distributed. This material is used as a quarry stone. The sample of tested material weighs 1.6 kg. The surface sensor was used to determine the thermal conductivity.

The fourth tested material is granite. Granite is nearly always massive (lacking any internal structures), hard and tough, and therefore it has gained widespread use throughout human history as a construction stone. Granite tables are used extensively because of granite's rigidity, high dimensional stability, and excellent vibration characteristics. Granite – the tested material was a medium-grained grain pattern

gradient. The slab was used to build the house as a window sill. The material is currently also very often used for decorative purposes, memorials and paving. The sample of tested material weighs 10.2 kg. The surface sensor was used to determine the thermal conductivity.

The fifth material is gaize. Gaize is a sedimentary rock, a dusty species of marl. Gaize was formed from the finest particles settled on the seabed. It consists of clayey and dusty particles, it also contains limestone components and needles of sea mushrooms of microscopic dimensions (so-called sponges). The amount of these needles determines its strength and durability. In addition to these, there are also frequent remnants of dirconos. The common mineral admixture is glauconite. It has whitish to sandy yellowish-gray color. In Romanesque style, gaize was an important building material. As a building material, gaize were used mainly in Romanesque buildings. The presence of sponge needles increases the quality of stone for technical purposes, especially its strength. Family houses and farm buildings are constructed by use of this material which is available in several localities in the Czech Republic.

Gaize a tested sample of this material was taken in village Horoměřice (near Prague). The use of this material in construction is shown in Fig. 2. This is the original farmhouse in the village of Dušníky (currently part of Rudná near Prague). During its construction was used gaize from nearby quarries. The reason for its use was just its availability, perhaps even lightness and workability. From the quarries from the same area comes the stone of many Prague Romanesque monuments.

Figure 2. Reconstruction of a farmhouse in the village Dušníky.

This material is common in many areas of the Czech Republic (Marešová, 2006). According to additions its properties differ significantly. For example, quartz admixtures can be assumed in the test sample. The sample of tested material weighs 0.64 kg. The surface sensor was used to determine the thermal conductivity.

The sixth material is a quartz (quartz sandstone). It is a material whose component (quartz) is characterized by the highest values of the coefficient of thermal conductivity. The sample was taken near the village of Horoměřice. Quartz crystals prevailed in the sample. Near the village there is also gaize. As a building material, sandstone was used mainly in Gothic buildings. The sample of tested material weighs 3.15 kg. The surface sensor was used to determine the thermal conductivity.

For measurement of thermal conductivity the Isomet 2104 instrument (Applied Precision Ltd, Bratislava) with surface sensor was used. Isomet 2104 (Applied Precision Ltd., 2018) is a portable instrument controlled by microprocessor, to which the manufacturer supplies exchangeable needle and surface sensors of various ranges. The calibration constants are stored in the sensors memory.

This instrument measures the thermal conductivity, temperature and specific heat capacity of compact and loose materials. For the thermal conductivity is permissible measurement error 5% of reading + 0.003 W m^{-1} K^{-1}. The measured values can be stored in the internal memory of the instrument. The content of memory is accessible via display. Data can be transferred via RS-232 interface to a PC. The instrument can be powered from AC or battery.

To determine the thermal conductivity of the material is used unsteady method. This compared to stationary methods significantly reduces the time of measurement. The device analyses the time dependence of thermal responses to impulses of heat flux supplied to the material. The heat flux creates scattered electric output from the resistor located in the sensor. The sensor has a thermally conductive connection with the analysed material. Temperature resistance is sensed by a semiconductor sensor.

Temperature variation as a function of time is tested in discrete points. The obtained points are interleaved by regression polynomials using the method 'least squares'. The coefficients of the regression polynomials are used to calculate the thermo-physical parameters using analytical formulas.

Air temperatures and relative humidity were measured by sensor FHA 646–21 with operative range from -30 to +100 °C with accuracy ± 0.1 °C, and air humidity by capacitive sensor with operative range from 5 to 98% with accuracy ± 2% connected to the measuring instrument ALMEMO 2590–9 (Ahlborn GmbH, Germany).

There was used for the indirect measurement of material moisture the capacitive sensor FH A696–MF with operative range of mineral construction materials from 0 to 20% with accuracy 0.1%. The sensor was connected to the data logger ALMEMO 2690-8 (Ahlborn GmbH, Germany).

Ten measurements were carried out for each experimental material. Measurements were carried out under laboratory conditions by the air temperature of 25–26 °C and relative humidity 31–36%.

Each sample of the tested compact materials was measured ten times and, if possible, the surface sensor was attached to the sample at a suitable representative site to eliminate any potential differences in the structure. To improve the adhesion of the probe to the measured material, the contact surfaces were painted with thin layer silicone grease. Before each measurement, the sample was temperature-stabilized to ambient temperature. The surface for the probe was adjusted by grinding. The sample size of the material always exceeded the manufacturer's requirements. The probes were calibrated at the factory in 2017.

The obtained results of measurement were processed by Excel software and values of thermal conductivity were verified by statistical software Statistica 12 (*ANOVA and TUKEY HSD Test*). Different superscript letters (a, b, c, d) mean values in common are significantly different from each other in the row (*ANOVA; Tukey HSD Test; P ≤ 0.05*), e.g. if there are the same superscript letters in all the columns it means the differences between the values are not statistically significant at the significance level of 0.05.

RESULTS AND DISCUSSION

Main parameters of tested material samples which are density ρ_m and moisture w_m of materials, temperature t_a and relative humidity RH_a of air during the measurement are given in the Table 1. This table also contains statistical indicators of measured thermal conductivity λ_m. The data are the mean values ± SD (standard deviation). Different letters (a, b, c, d) in the superscript are the sign of high significant differences *(ANOVA; Tukey HSD Test; p ≤ 0.05).*

Table 1. Density ρ_m and moisture w_m of materials, temperature t_a and relative humidity RH_a of the air during the measurement and resulting values of thermal conductivity λ_m of tested materials. Different letters (a, b, c, d) in the superscript are the sign of high significant difference (*ANOVA; Tukey HSD Test; P ≤ 0.05*)

| Parameter | Material | | | | | |
	Artificial marble	Gneiss	Proterozoic shale	Granite	Gaize	Quartz sandstone
m, kg	1	1.95	1.6	10.2	0.64	3.15
ρ_m, kg m^{-3}	2,041.0	2,110.0	2,318.8	2,924.7	2,356.6	2,333.3
w_m ± SD, %	8.2 ± 0.2	5.8 ± 0.5	8.5 ± 1.4	7.2 ± 0.2	23.4 ± 0.5	4.6 ± 0.4
t_a ± SD, °C	25.9 ± 0.5	25.8 ± 0.4	25.1 ± 0.5	26.0 ± 0.2	23.3 ± 0.1	25.8 ± 0.5
RH_a ± SD, %	32.2 ± 1.0	32.7 ± 0.9	32.2 ± 0.8	31.9 ± 1.0	32.8 ± 1.4	32.4 ± 1.1
λ_m ± SD, W m^{-1} K^{-1}	1.80 ± 0.12[a]	2.36 ± 0.33[b]	2.68 ± 0.16[b]	3.66 ± 0.07[c]	1.49 ± 0.01[a]	6.15 ± 0.30[d]

SD – Standard deviation.

Table 1 shows that the lowest value of thermal conductivity $\lambda_m = 1.49$ W m^{-1} K^{-1} was measured on the sample of gaize. Very low, statistically not significantly different from gaize was the thermal conductivity $\lambda_m = 1.80$ W m^{-1} K^{-1} measured on the sample of artificial marble. It can be caused by the composition of ingredients and used for the production of this material. The composition provides artificial marble having a deep appearance characteristic of marble and having properties according to the composition. This material has also the lowest density 2,041 kg m^{-3}.

The differences between the thermal conductivity of gneiss $\lambda_m = 2.36$ W m^{-1} K^{-1} and proterozoic shale $\lambda_m = 2.68$ W m^{-1} K^{-1} were not statistically significant. Granite was the heaviest tested material and also its thermal conductivity $\lambda_m = 3.66$ W m^{-1} K^{-1} was bigger than previous materials.

Surprisingly the biggest values of thermal conductivity $\lambda_m = 6.15$ W m^{-1} K^{-1} were measured on the samples of quartz sandstone. This value is more than twice higher than gneiss or Proterozoic shale.

CONCLUSIONS

The results of measurements presented in this paper can be used for practical information useful for design and calculation of heat balance of new or reconstructed buildings. Significant differences of thermal conductivity of tested materials should be recognised and respected.

There are important differences between thermal conductivity values of stones and rocks used in the constructions. The thermal conductivity varies according to the tested materials from $\lambda_m = 1.80$ W m^{-1} K^{-1} to 6.15 W m^{-1} K^{-1}.

The results obtained by the dynamic unsteady method of measurements correspond to the thermal conductivity values mentioned in the literature (Ražnjević, 1984; Eppelbaum, 2014). A comparison of samples 5 and 6 shows that even materials occurring in one locality may have very different thermal properties. The use of the chosen method for determination of thermal conductivity of the material used for a particular historical building can significantly improve the determination of thermal losses of the building. The quartz contained in rocks significantly increases their thermal conductivity (sample 6).

A very common problem is the reconstruction of buildings when using a combination of stone with other materials, such as brick masonry or blocks, as there may be a significant reduction in thermal insulation and the formation of thermal bridges. The used instrument can detect locations of a perimeter construction with different thermal conductivity.

Portability and short duration of the tests make it ideal for the use outside the laboratory. It will be useful in real conditions for inspection and audit activities on already completed buildings. Described method can be used for this purpose as it is available and enough precise.

The presented method of measurement and obtained results can be suitably used in the preparation of laboratory exercises for university students of engineering study.

REFERENCES

Applied Precision Ltd.: https://www.appliedp.com/ (accessed on 16.1.2017).

Conti, L., Barbari, M. & Monti, M. 2016a. Design of sustainable agricultural buildings: A case study of a wine cellar in Tuscany, Italy. *Buildings* **6**(2), 1–8.

Conti, L., Barbari, M. & Monti, M. 2016b. Steady-State Thermal Properties of Rectangular Straw-Bales (RSB) for Building. *Buildings* **6**(4), 1–13.

Eppelbaum, L., Kutasov, I. & Pilchin, A. 2014. *Thermal Properties of Rocks and Density of Fluids.* In: Applied Geothermics. Lecture Notes in Earth System Sciences. Springer, Berlin, Heidelberg. DOI: 10.1007/978-3-642-34023-9_2

Kic, P. 2017. Effect of construction shape and materials on indoor microclimatic conditions inside the cowsheds in dairy farms. *Agronomy Research* **15**(2), 426–434.

Kocova, D. & Kic, P. 2016. Technical and economic aspects of thermal insulation of buildings. In: *15th International Scientific Conference Engineering for Rural Development*. Latvia University of Agriculture, Jelgava, 50–55.

Kollmorgen, U. 1998. *House insulation – a new energy savings*. Ikar, Praha, 127 pp. (in Czech).

Ladener, H., Fledhous, M., Gabriel, I., Gross, K., Janssen, M., Klima, M., Rath, U., Siepe, B., Strub, G., Braun, P.O., Conradi, G., Haefele, G., Kennedy, M., Kennedy, D., Nord, G. & Reinberg, G. 2001. *How to create from old building a low-energy house*. HEL, Ostrava, 213 pp. (in Czech).

Leso, L., Morshed, W., Conti, L. & Barbari, M. 2017. Evaluating thermal performance of experimental building solutions designed for livestock housing: The effect of greenery systems. *Agronomy Research* **15**(1), 239–248.

Marešová, L. 2006. *Degradation of the marlite on the set of the historical buildings.* Brno. Thesis. Masaryk University. Faculty of Science, 92 pp. (in Czech).

Muizniece, I, Vilcane, L. & Blumberga, D. 2015. Laboratory research of granulated heat insulation material from coniferous forestry residue. *Agronomy Research* **13**, 690–699.

Pleiksnis, S., Skujans, J., Visockis, E. & Pulkis, K. 2016. Increasing fire proofness of sapropel and hemp shive insulation material. In: *15th International Scientific Conference Engineering for Rural Development*. Latvia University of Agriculture, Jelgava, 403–408.

Ražnjević, K. 1984. *Thermodynamic tables.* Alfa, Bratislava, 336 pp. (in Slovak).

Šubrt, R. &Volf, M. 2003. *Construction details – Thermal bridges*. Grada Publishing, a.s., 152 pp. (in Czech).

Týbl, J. & Kic, P. 2016. Thermal properties and reduction of energy consumption of buildings. *Agronomy Research* **14**, 1222–1231.

Tywoniak, J. 2005. Low energy houses – principles and examples. Grada Publishing, a.s., 193 pp. (in Czech).

Valasek, P., Chocholous, P. & Muller, M. 2016. Mechanical properties of thermal insulating sandwich materials. In: *15th International Scientific Conference Engineering for Rural Development*. Latvia University of Agriculture, Jelgava, 324–328.

Plantograf V18 – new construction and properties

P. Koder[1], V. Novák[1,*], V. Ryzhenko[1], D. Hrubý[2], J. Volf[1] and D. Novák[3]

[1]Czech University of Life Sciences Prague, Faculty of Engineering, Department of Electrical and Automation, Kamýcká 129, CZ165 21 Prague, Czech Republic
[2]Slovak University of Agriculture in Nitra, Faculty of Engineering, Department of Electrical Engineering, Automation and Informatics, Tr. Andreja Hlinku 2, SK949 76 Nitra, Slovakia
[3]Matej Bel University, Faculty of Natural Sciences, Department of Technology, Tajovského 40, SK974 01 Banská Bystrica, Slovakia
*Correspondence: novakviktor@tf.czu.cz

Abstract. The article describes Plantograf V18, a planar tactile transducer, which converts the applied pressure into electric signal and enables a graphical presentation of the measured data; the new version V18 comes with some significant improvements and modifications. The device may be used everywhere where the pressure distribution between an object and surface is to be determined, e.g. in medicine or automotive industry. The article contains the detailed description of the transducer design and its electronic control circuits, as well as the yet unpublished measurements of pressure sensitivity with 3.5 mm electrodes.

Key words: transducer, pressure, sensor, conductive ink, FPGA.

INTRODUCTION

The described device represents a new development of the planar pressure converter Plantograf with some significantly enhanced features. The aim of the measuring system Plantograf is to measure the pressure distribution between an object and the surface; it was originally developed for medical purposes to measure the pressure under human feet; the later versions were also used for industrial applications, e.g. for designing car seats in the automotive industry.

The further development of this measuring system is justified by new requirements, which cannot be fulfilled using the preceding versions. The new development reflects besides other things the needs on the fields of:

- agricultural engineering – to enable to measure the soil compaction, i.e. the pressure within soil mass. The new version should have its own power supply and thus it will be independent on the availability of the power source, ready to use in 'field conditions';

- automotive industry – to enhance the accuracy of the pressure measurement under car tire patterns. The present resolution was insufficient; the new development should enhance both the resolution and the frame rate. This way it will be possible to measure fine pressure distribution under tire patterns, particularly with

dependency on the tire inflation, as well as dynamic processes when driving over a pad. For tractor tire patterns see example in Fig. 1;

- medical science – there were also requirements for improving both the resolution and the frame rate, to capture highly dynamic processes, e.g. athlete training.
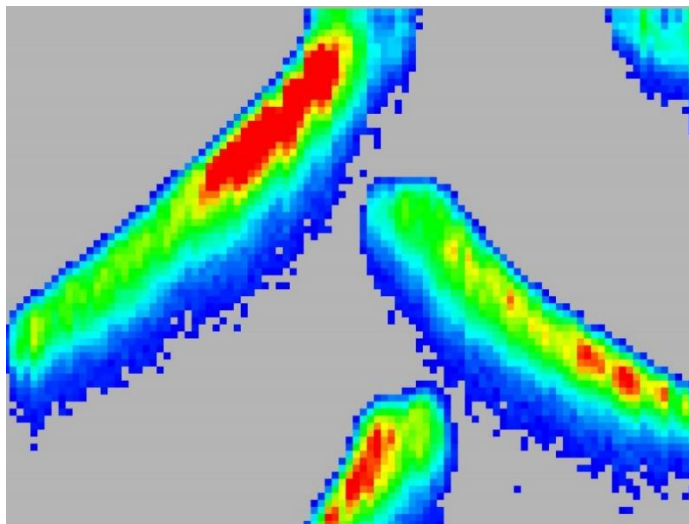
Figure 1. Pressure distribution under tractor tire pattern.

Compared to its predecessors, the new version should be capable with connection with new software and new material, i.e. conductive ink, to measure absolute pressure acting on the transducer, not only relative pressures on 8-bit scale. The main improvements concern the control electronic circuits, which enable to raise both the resolution and the frame rate, up to 500 fps on 128 x 128 matrix. The previous versions also exhibited too low sensitivity, caused by the impossibility of the gain change, which limited the width of measured pressure ranges. This issue will be also corrected with the new version, to extend the operation possibilities of the device. Given the number of 16,400 sensors (on a 500 x 500 mm matrix, 4 mm spacing and 2.5 mm or 3.5 mm electrode diameter) and the expected high scan speed, the described requirements yield some construction improvements and modifications, although the base principle stays the same; for additional information about principles of tactile sensing see Lee (2000); Weiss & Worn (2005); Dahiya & Valle (2008) and Fraden (2010).

Besides the named improvements, the new construction also supports wireless transmission of complete snapshots from the entire sensor. To enhance its 'field use' for measuring of e.g. soil compaction, it also allows battery power unlike its predecessors.

In the first stage, it was necessary to verify the appropriate material that would serve as a transducer between the applied pressure on the sensor and the measured electrical resistance. The main requirement is to measure a significant change of electrical resistance when pressure change occurs within the operating range of the sensor, and secondly that such dependence is linear or at last that it is possible to express by another simple mathematical function.

At this stage, the tried and tested DZT-3K conductive ink was used – for more details see our previous work in Volf et al. (2015) and Volf et al. (2016) – and the sensors were calibrated to verify the correct operation of the control electronics and of the individual sensors itself.

MATERIALS AND METHODS

Sensor overview and construction

From the physical point of view, the device is a transducer between the pressure and the magnitude of the measured electrical resistance, with the pressure being displayed with an 8-bit resolution, i.e. on a scale of 0–255. There are three main parts of the measuring system – a sensor field to capture the acting pressure, control electronic circuits and a connected computer running a service program and displaying the pressure distribution snapshots.

On the sensor field, the acting pressure causes the change of the electrical resistance of the material (here conductive ink DZT-3K), which is measured in real-time by electrical circuits. The calculation of the electrical resistance bases on the principle of a voltage divider, the scheme of which is shown in Fig. 2. The electrical resistance R_{INK} is calculated using the formula:

$$R_{INK} = \frac{R_{CONST} \cdot U_{INK}}{U_{NAP} - U_{INK}} \tag{1}$$

where R_{INK} – calculated electrical resistance of the ink; R_{CONST} – constant electrical resistance 10 kΩ; U_{INK} – measured voltage; U_{NAP} – stabilized supply voltage. The stabilized voltage 2 V is monitored on the output A1+, while the actual measured voltage on the voltage divider (ink layer) is measured on the output A2+, against reference zero (GND).
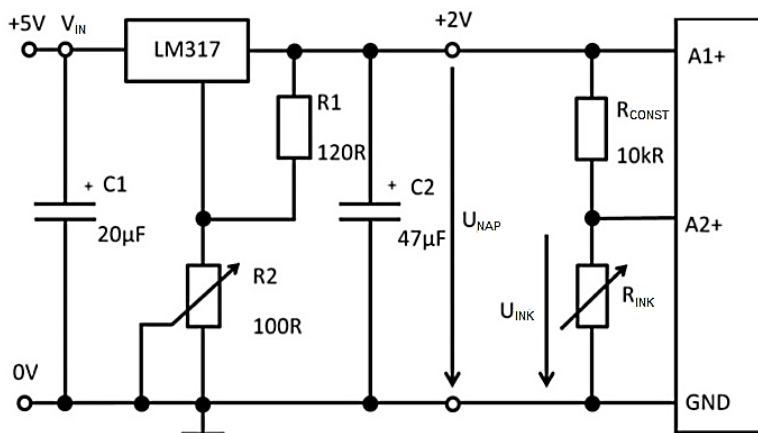
Figure 2. Circuit diagram of the voltage divider.

Fig. 3 shows a section through the entire sensor. The ink is attached to the electrodes on ink carrying layer, which is covered by cover layer that protects the entire sensor from mechanical harm and spreads the pressure on the electrodes. The electrodes

are placed on material called Cuflex that is supported by lower protective layer that protects the sensor from overloading. The passage of the electric current between the electrodes is indicated by a red arrow. The electric current flows from the outer electrode through the conductive ink layer which is deformed and which changes its electrical resistance under the applied pressure into the inner electrode. Further information about conversion of pressure using different materials is in Kim (2009); Astellanos (2010); Seminara (2013) and Volf et al. (2015).
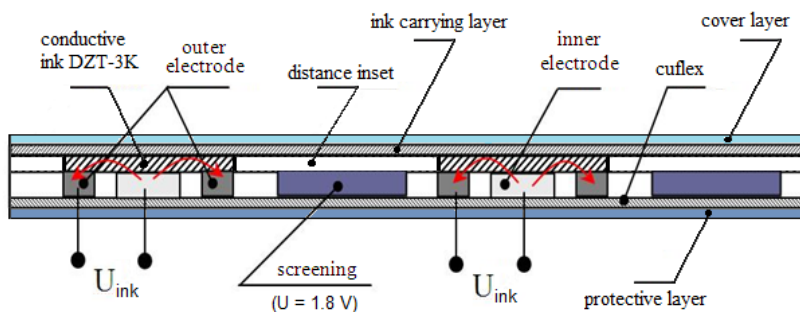
Figure 3. Section through the sensor with indicated current flow.

The new developed sensor matrix consists of individual electrodes with outer diameter of 3.5 mm or 2.5 mm, according to the size of the plate. The electrodes are arranged in an array of 128 x 128 electrodes. A section of the sensor matrix with individual electrodes is shown in Fig. 4.
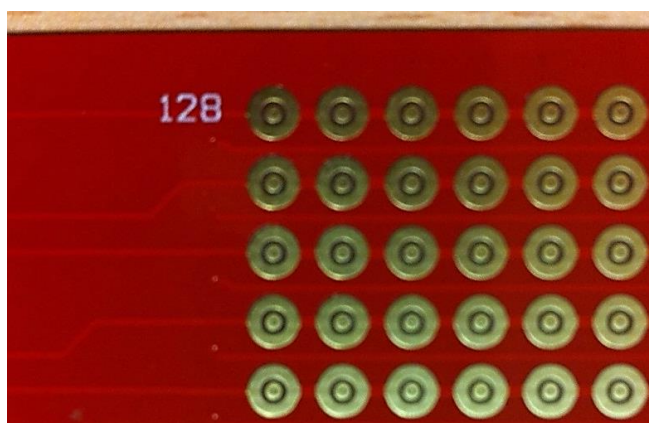
Figure 4. Section of the sensor matrix with individual electrodes.

The control electronics provide measuring of electrical resistance from each sensor of the matrix, which consists of total 16,384 (128 x 128) individual sensors. One image therefore consists of 16,384 scanned points, and given the resolution 8 bits per point (sensor), in represents 131,072 bits for one shot. Considering a frame rate of 500 fps, the processing and data transfer speed reaches up to approximately 8.2 MB/s. The block diagram of the entire system is shown in Fig. 5.
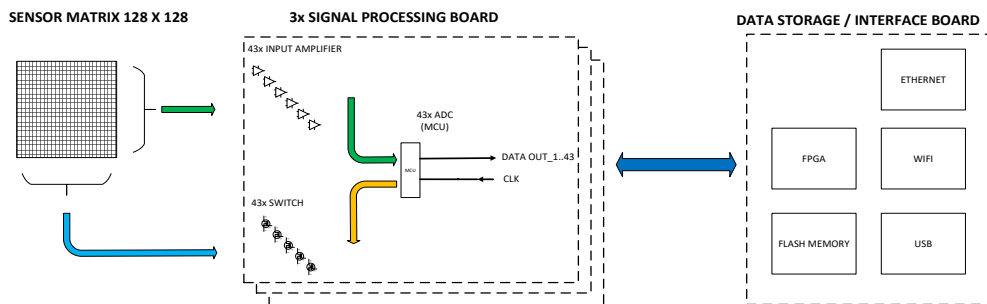
Figure 5. Block diagram of the pressure measuring system Plantograf V18.

The sensor matrix is divided into rows and columns. The columns are connected to voltage and the rows are read. The sensing and converting part of the electronics consists of three identical signal processing modules, each of which contains 43 (up to 45 possible) MOSFET switches that connect the selected column to the power supply. This board also contains 43 amplifiers that measure the sensor's electrical resistance. The signal from them is then led to the appropriate A/D converters. The digitized signal obtained this way is subsequently is fed into the memory and interface board (Field-programmable gate array – FPGA circuit), which provides full control of the Plantograf electronics. It collects the measured data and it provides their further transfer to the computer for further processing and visualization. The communication with the computer runs using USB or Ethernet interface, or wirelessly via Wi-Fi.

Signal processing

The first step in signal processing is provided by 128 (one for each matrix row) individual switches to select a column from the sensor matrix; this is implemented using MOSFET transistors to allow the current from selected column. The raw data is acquired using 128 individual circuits. The resistivity is incorporated into feedback of operating amplifiers, so the output voltage corresponds the resistance and thus the applied pressure onto the sensor. This voltage is led to the A/C conversion.

As the measured resistance of the material represents analogue signal, it has to be converted into digital (8 bit resolution) to allow further computer processing. This is controlled by 128 microprocessors, which also provide the communication with FPGA, set the Q-point of input circuits and control the sequential selection of column matrix. To obtain high sampling frequency, it is necessary to run the digitization parallel on more channels. Every microprocessor is connected with a datalink to superordinate control unit – the FPGA. The microprocessors also control the reference input voltage, to allow the change the Q-point (=working range) of the input circuits. This is used to adjust the measuring range, eliminate errors, calibrating, and for diagnostic purposes. The picture of the electrical control circuits is provided in Fig. 6.

For the function of the whole module, it is necessary to provide different supply voltages, as required by individual electronic circuits. In order to reduce the power loss of the system and the demands on the power supply, switched-mode power supplies are used. The base input supply voltage for the module is 5 V. This voltage is used to power the operational amplifiers and auxiliary sources. Other auxiliary sources provide 3.3 V supply, which is used for powering microprocessors and control logic unit. A negative

voltage of -1.8 V is used to power the amplifiers and as exciting voltage of the columns of the matrix. The supply and electric circuits meet the safety requirements for medical purposes.
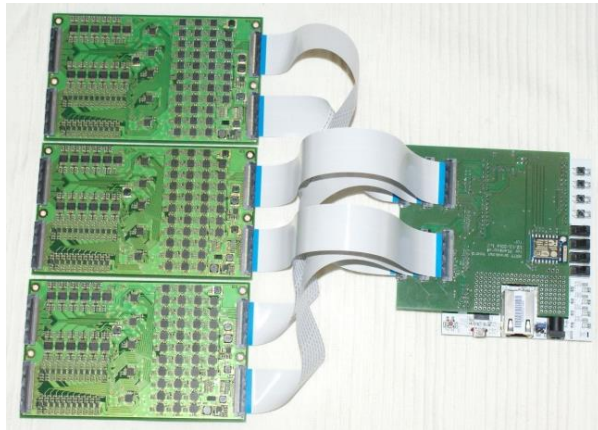
Figure 6. Electrical control unit of Plantograf V18. Three signal processing modules connected to FPGA circuit.

As the main control unit was selected the commercially available FPGA module Xilinx fitted with Artix 7 chip and basic peripherals. This unit also provides communication between the transducer and a connected computer, which runs the service program and displays the snapshots. According to the assignment, the module is besides usual connectivity options additionally fitted with a memory card cap to enable to capture highly dynamic processes as well as with a wireless Wi-Fi module.

RESULTS AND DISCUSSION

The measurement procedure is described in detail in Volf et al. (2016), as the measurement methodology stays the same; here we only summarise the most important facts: given the large number of measurements, the measurement was automatized using Turbo Scara SR60 robot. The applied force was measured by the Hottinger DF2S-3 strain gauge, and the output voltage was captured by the Almemo 2890-9 data logger. Each measurement for a given pressure was performed 10 times, and the measurement uncertainty was calculated from the results.

The testing was carried out on a matrix with 3.5 mm electrodes (outer diameter, labelled OB) placed on a printed board; the board contains conductors drawn from the rows and columns of the matrix, thus enabling the choice of a specific electrode. The following graphs in Figs 7–9 present the dependency of the measured electrical resistance on applied pressure for three ink layers of 6 μm, 17 μm and 26 μm. In the diagrams both the loading cycle and the unloading cycle are depicted and the total (combined) measurement uncertainty is calculated and graphically represented by respective intervals for each measured value.
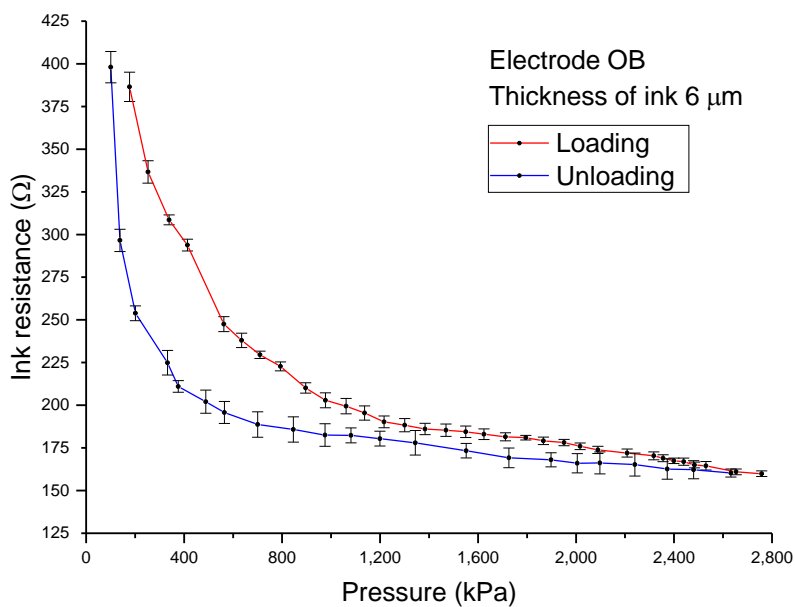
Figure 7. Dependence of measured electrical resistance of a 6 μm thick ink layer on the pressure (loading and unloading cycle).
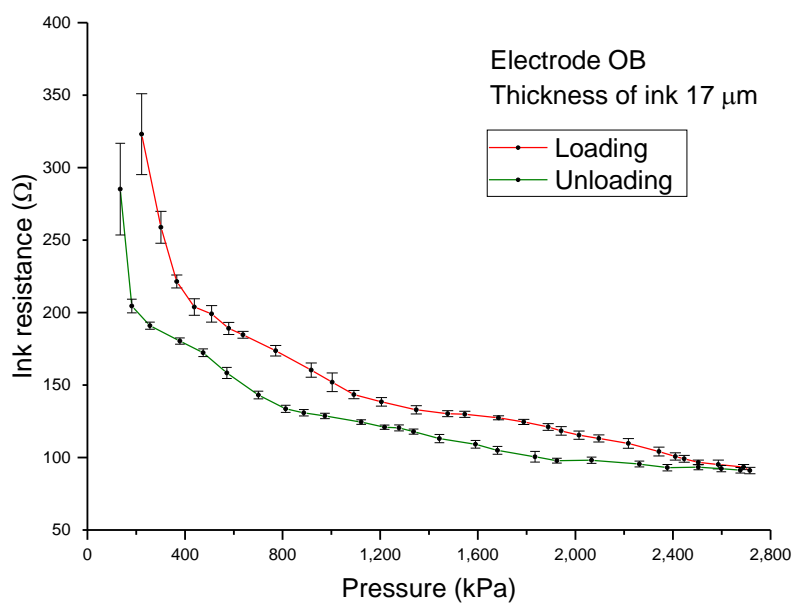
Figure 8. Dependence of measured electrical resistance of a 17 μm thick ink layer on the pressure (loading and unloading cycle).
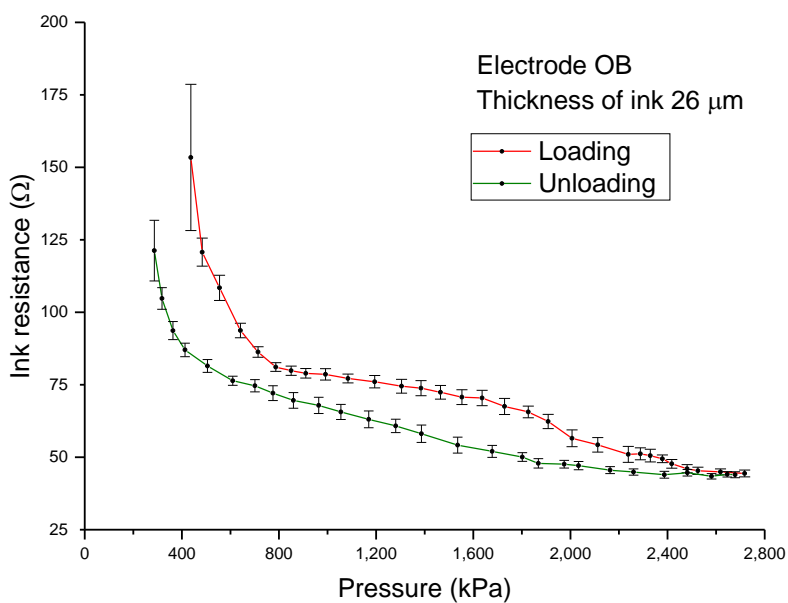
Figure 9. Dependence of measured electrical resistance of a 26 μm thick ink layer on the pressure (loading and unloading cycle).
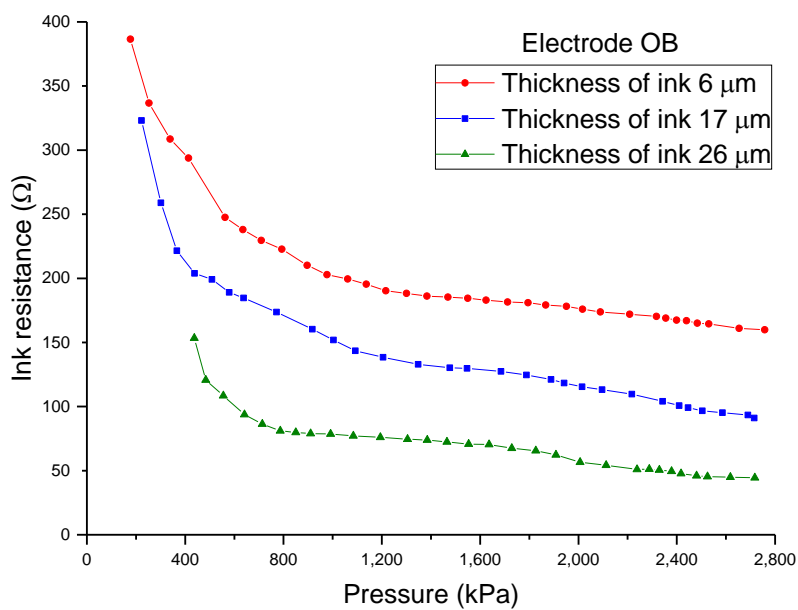
Figure 10. Dependence of measured electrical resistance for 6 μm, 17 μm and 26 μm thick ink layer on the pressure (summary).

All three diagrams exhibit appreciable hysteresis, i.e. a different shape of the curve in the loading and unloading cycle. This may be caused by relaxation of the ink and foil on which the ink is deposited; the hysteresis also limits the possibility to measure the absolute pressure acting on the sensor. From this point of view the 26 μm ink layer seems to be unsuitable due the very different courses of dependency.

By the 6 μm and 17 μm ink layers, the hysteresis is smaller and the lines are rather only vertically shifted unlike the 26 μm layer. Both setups exhibit nearly linear characteristics between 1,000 and 2,400 kPa that meet our initial requirements. It has to be also noted that when increasing the pressure on the measuring point, the C type uncertainty gradually decreases; thus the accuracy of the measurement is better at higher loads where the characteristic is not so steep. Following Fig. 10 summarizes the dependencies for all three ink layers in one graph.

From this graph it is apparent that all curves exhibit sufficient sensitivity in the range from 1,000 to 2,400 kPa, i.e. that the measured resistivity changes significantly with the applied pressure. From this point of view the most suitable seems to be the 17 μm ink layer with slightly steeper course and thus better sensitivity. Out of this range, the sensitivity decreases (above 2,400 kPa; mainly 17 μm and 26 μm layers), or the course does not exhibit the required linear character (cca. below 1,000 kPa, all curves).

We can conclude, that within a given pressure range (1,000–2,400 kPa) the 17 μm ink layer exhibits the best properties to act as converter between pressure and electrical resistance. The main limitations are persistent hysteresis and not entirely linear dependency of the electrical resistance on the pressure. These negatives can be, however, particularly eliminated by post-processing of the raw data using a dedicated computer program. The measurements of resistance with other materials and with other electrode types are discussed in Volf et al. (2012), Volf et al. (2015) and Volf et al. (2016).

CONCLUSIONS

The new developed planar pressure measuring system Plantograf V18 brings some new features and significant improvements: it is capable due to its high refresh rate to capture highly dynamics processes, which is essential e.g. in sports medicine or athlete training. The new developed electronic control circuits enable to change the gain, thus this transducer is capable to measure the pressure under human feet as well as car tyres. Due to its high sensor density and much wider pressure range, it is supposed to measure the pressure distribution under fine tire patterns on all agricultural machines, as well as other large transport means.

There are similar planar measurement systems in the world, for technical details see Texscan, Rsscan or Xsensor (2017). However, these systems have several limitations compared to Plantograf: limited resolution given the dimensions of the electrodes and their density, much lower frame rate and buffer size that limits the scanning time or inability to obtain raw data. Compared to those pressure transducers, this system processes a real-time signal from 16,400 sensors with a frame rate of 500 frames per second; in the future development, this should increase up to 1,000 frames per second. This is enabled by parallel processing of data from individual sensors. This makes this system much faster maintaining its incomparably high resolution due to its dense network.

The measurements with new OB electrode types with 3.5 mm diameter gave satisfactory results. As the transducer between applied pressure and output electrical resistance was selected conductive ink DZT-3K, deposited on a thin foil. Within the pressure range 1,000–2,400 kPa, the 17 µm ink layer exhibited nearly linear characteristic of dependency as required, as well as relatively small hysteresis and sufficient sensitivity, compared to other configurations with different ink layer thicknesses.

REFERENCES

Astellanos-Ramos, J. & Navas-Gonzáles, R. 2010. Tactile sensors based on conductive polymers. *Microsystem Technologies* **16**, 765–776.

Dahiya, R. & Valle, M. 2008. *Sensors: Focus on Tactile Force and Stress Sensors*.

Fraden, J. 2010. *Handbook of modern sensors: physics, designs, and applications*. New York, Springer, 2010, 663 pp. ISBN 978-1-4419-6465-6.

Kim, K. 2009. Polymer-based flexible tactile sensor up to 32×32 arrays integrated with interconnection terminals. *Sensors and Actuators A: Physical* **156**, 284–291.

Lee, M.H. 2000. Tactile sensing: New directions, new challenges. *The International Journal of Robotics Research* **19**, 636–643.

Seminara, L., Pinna, L., Valle, M., Basiricò, L., Loi, A., Cosseddu, P., Bonfiglio, A., Ascia, A., Biso, M., Ansaldo, A., Ricci, D. & Metta, G. 2013. Piezoelectric Polymer Transducer Arrays for Flexible Tactile Sensors. *IEEE Sensors Journal* **13**, 4022–4029.

Tekscan. *http://www.tekscan.com.* Accessed 10.12.2017.

Volf, J., Trinkl, A., Novák, M., Bílek, J., Prikner, P. & Neuberger, P. 2012. Plantograf V12 with Optimal Size Determination Sensor Electrodes and its Using for Pressure Distribution Between Tire and Road. In: *XX World Congress IMEKO*. IMEKO, Busan.

Volf, J., Novák, V. & Ryzhenko, V. 2015. Effect of conductive ink properties of tactile sensors. *Procedia Engineering* **120**, 200–205.

Volf, J., Svatoš, J., Koder, P., Novák, V., Papežová, S., Ryzhenko, V. & Hurtečák, J. 2015. Pressure Distribution Measurement System PLANTOGRAF V12 and its Electrodes Configuration. *Agronomy Research* **13**, 732–738.

Volf, J., Novák, V. & Ryzhenko, V. 2016. Effect of Conductive Ink on Transfer Characteristics of Pressure into Electric Signal for Tactile Sensors. *Agronomy Research* **14**, 1123–1129.

Weiss, K. & Worn, H. 2005. The working principle of resistive tactile sensor cells. In: *IEEE International Conference on Mechatronics and Automations*, 471–476.

Xsensor. *http://www.xsensor.com.* Accessed 10.12.2017.

Quality assessment of laser cladded HSS coatings with deep penetration into base material to obtain a smooth gradient of properties in coating-substrate interface

S. Ločs[1,2] and I. Boiko[1,*]

[1]Riga Technical University, Faculty of Mechanical Engineering, Transport and Aeronautics, Institute of Mechanical Engineering, Viskalu street 36A, LV-1006 Riga, Latvia
[2]Daugavpils University, Faculty of Natural Sciences and Mathematics, Parades street 1, LV-5401 Daugavpils, Latvia
[*]Correspondence: irina.boiko@rtu.lv

Abstract. The present research is dedicated to the study of influence of coaxial laser cladding (CLC) process parameters onto values of alloying components content in the coatings, morphology as well as the influence of post-cladding heat treatment on the quality and mechanical properties of coatings. The research is based on a hypothesis that applying of first layer of coatings onto steel substrate with keyhole in penetration allows achieving smooth gradient of properties of the coating-substrate system. As a result it may provide a smooth distribution of the internal residual stresses in interface as well as the better resistance to external stress during cyclic load in tool operation processes: metal forming, stamping etc. Experimental work was carried out using CLC system, which consists of industrial robot Kuka and 1 kW IPG Yb-fiber laser, integrated to the coaxial powder supplying cladding head. The regularities of formation of High Speed Steel AISI M2 cladding coatings created by different regimes were studied by deposition onto EN 41Cr4 and C80U steel substrates. The quality of achieved coatings has been evaluated by examination of morphology of transverse cross-sections, coatings geometrical features, elemental composition and microhardness distribution inside coatings. Additionally detailed assessment of coating thickness and content of alloying elements using statistical methods has been performed. As a result of the research done the degree of influence of chosen CLC process parameters onto quality characteristics were estimated. The most appropriate cladding regime for used method was proposed.

Key words: coaxial laser cladding, HSS coating, keyhole in penetration, quality.

INTRODUCTION

Shortage of material and energy resources aids development and application of progressive technologies, which help to ensure the maximal performance indicators of machines in balance with economic efficiency and the minimal harm to environment. At the same time, the introduction of the thermal coating technologies makes it possible to improve the ecological compatibility of production by replacing hazardous galvanic technologies (Ločs & Boiko, 2015).

Coaxial laser cladding (CLC) is a progressive method of applying coating, which is widely used for improvement of mechanical and exploitation properties of products. This method allows applying of functional and protective coatings with a strong metallurgical bound with base material by minimal thermal impact on the item (Schneider, 1998; Toyrserkani et al., 2005). Thanks to a range of advantages in comparison to thermal spraying and welding processes this method is widely used for hardfacing, refurbishment and even for building up (Additive Manufacturing) of expensive machine elements and tooling (turbine parts, engine components, metal forming tools etc.) (Tabernero et al., 2011; Weisheit et al., 2013).

Meanwhile, despite of process positive points, producing defect free coatings of tool steel materials is still problematic, because tool steels are hardly suitable for welding due to a high content of carbon and alloying elements. Frequent defects are pore and crack formations in clad layers (Pleterski et al., 2011; Kattire et al., 2015; Zeng et al., 2016).

The pores can appear primarily due to insufficient shielding of melted zone, due to the moisture from the powder, due to evaporation process in the molten pool during laser irradiation of metallic surface.

In its turn the phenomenon of cracking is associated with the fact that melting by high energy of laser beam causes high heating and cooling rate which create a rigid temperature regime in the near surface layers. Thus, a sharp thermal gradient combined with a high rate of solidification in the melting region causes formation of metastable phases and as a consequence cracking of coatings (Benyounis et al., 2009; Candel et al., 2013; Telasang et al., 2014; Cao et al., 2016). As a result, mechanical properties and fatigue strength of the components significantly decrease, which can lead to premature failure and breakdown of the product. That's why the laser cladding technology may have one of the limiting factors to introduction into the surfacing processes (Grigoryants et al., 2006; Luo et al., 2016).

Therefore, in order to obtain qualitative coatings with high mechanical properties and fatigue life, the enhancement of laser cladding technology is still an actual issue.

The aim of this research is to determine the degree of influence of CLC process parameters onto values of alloying components content in the coatings, morphology as well as the influence of post-cladding heat treatment on the quality and mechanical properties of coatings. The research is based on a hypothesis that applying of first layer of coatings onto steel substrate with keyhole in penetration ensures smooth gradient of properties both for the similar and for dissimilar material combinations in coating-substrate interface. As a result such a technique may provide a smooth distribution of the internal residual stresses as well as better resistance to external stress during cyclic load in tool operation processes: metal forming, stamping etc.

MATERIALS AND METHODS

High-speed steels (HSS) demonstrate high strength, hardness and wear resistance by application of appropriate heat treatment. Along with the application for cutting tools, these steels can also be used for producing of die tools. Thus, they are operated under especially severe conditions, at pressures in above of 2,000 MPa and heating to temperatures of 300–500 °C for mass and large-scale production, when it is necessary to ensure high durability of the die tooling (Adaskin, 2017).

The filler material used in this research was Tungsten-Molybdenum HSS powder AISI M2 of spherical shape with particle size 53–150 μm. For substrates high carbon steels EN 41Cr4 and C80U plates were used with dimensions of 100 x 100 x 10 mm. In total four plates (by two of each material) were processed. The work surfaces of plates were mechanically grinded before treatment. Chemical compositions of the materials are listed in the next (Table 1).

Table 1. Chemical composition of powder AISI M2 (1), substrate EN 41Cr4 (2) and C80U (3)

	Element content, wt% (Fe in balance)						
	C	Mn	Si	Mo	Cr	V	W
1	0.85–1.05	0.20–0.40	0.20–0.40	4.50–5.50	3.75–4.50	1.60–2.20	5.50–6.80
2	0.36–0.44	0.50–0.80	0.17–0.37	–	0.80–1.10	–	–
3	0.75–0.85	0.10–0.40	0.10–0.30	–	–	–	–

Experimental work was carried out using CLC system, which consists of industrial robot KR30HA (Kuka) with the integrated coaxial powder supplying cladding head WT03 (Permanova Lasersystem) and Yb-fiber laser YLR 1000 (IPG Laser) with 100 μm optical fiber and 1,000 W power supply. Optical system provides laser beam spot size in a focus plane of about 570 μm with a Gaussian intensity distribution. Powder mass feeding performed with the powder feeder TWIN-10-C (Sulzer Metco), where the argon was used as a carrier gas and as a shielding gas to prevent oxidation of the powder and a molten pool. The laser cladding equipment is presented in the next (Fig. 1).
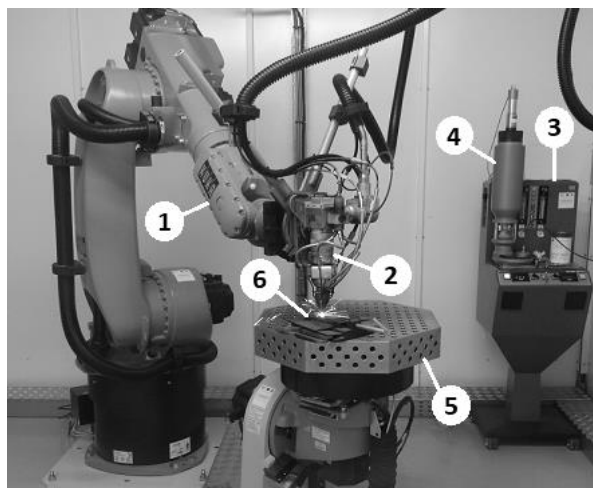
Figure 1. Laser cladding equipment: 1 – industrial robot KUKA; 2 – cladding tool; 3 – powder feeder; 4 – powder insert; 5 – table of positioner; 6 – workpiece.

Coatings during laser cladding were created by sequential overlapping of single cladding tracks. The cladding head all along process was located perpendicular to the surface being treated, directing laser beam toward the surface of the sample with stand-off distance 8 mm from the nozzle end. In order to establish interaction of three parameters with two values onto coating quality and properties the experimental research was carried out using experimental design (DOE) in form of two level full factorial

design 2^3 (Table 2). Thereafter 8 track coatings (approx. 8 mm wide) were deposited on each plate on the top surface of samples. For each coating 2 cross-sections were studied: produced coatings with prepared cut-off samples are displayed in the next (Fig. 2).

Table 2. Studied process factors and levels of variation

Factors	Designation	Levels		
		Upper (+1)	Nominal (0)	Lower (-1)
Overlap ratio, %	OR	50	40	30
Cladding speed, mm min^{-1}	V_C	1,500	1,200	900
Powder feed rate, g min^{-1}	F_P	10	7.5	5
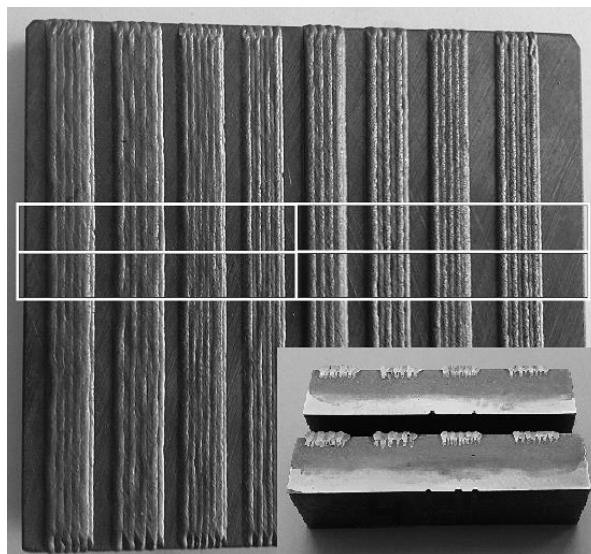
Figure 2. Laser cladded plate with cut-out scheme and produced specimens of experimental coatings cross-sections.

The experiment plan includes a combination of parameters such as the overlap ratio between adjacent cladding beads (50% and 30%), the cladding speed (900 mm min^{-1} and 1,500 mm min^{-1}) and the powder mass feed rate (5 g min^{-1} and 10 g min^{-1}). Disposition of the laser beam focal plane was 1 mm above the treatable surface (defocused beam), which was taken on the basis of the previous study of single bead formation (Ločs et al., 2017). The focus plane of the powder flow was coincided with laser beam focus. The following process parameters were fixed to operate: laser power 1,000 W; carrier gas flow (Ar) 5 L min^{-1}; shielding gas flow (Ar) 16 L min^{-1}. The samples were preheated to a temperature of 250 °C prior to treatment and the temperature regime was the same for each subsequent coating.

With aim to establish the influence of process parameters (overlap ratio, scanning speed and powder mass feed rate) on the coating characteristics predictive equations were created using regression analysis. For evaluating of statistical significance created models were tested by analysis of variance method (ANOVA). The relationship between CLC parameters and output responses were analysed and described in details. Therewith

the impact of appliance of post-cladding heat treatment was also obtained. By this reason one group of samples with produced coatings had post-cladding tempering (by plate heating in a furnace at 600 °C for 2 h and then cooling in air) (PCT), but the second group remained untempered. Plates with experimental coatings were transversely cross-sectioned, then polished and etched with Nital (4%). Examination of coatings transverse cross-sections was conducted by means of morphological observation using scanning electron microscope TESCAN-VEGA-LMU II (SEM). Elemental composition of the main alloying components in the microstructure was determined by energy dispersive spectrometry EDS analysis (EDS module INCAx-act Oxford Instruments). Microhardness profiles were measured along the transversal cross-section from the top of the coating to the substrate base using the Vickers hardness tester (Innovatest Nexus 4000). Measurements were performed under 200 g load and 10 s hold time on the each measurement point.

RESULTS AND DISCUSSION

The efficiency of a hardfaced coating primarily depends on its microstructure, which is defined by the chemical composition and solidification rate of coatings. Accordingly, the effect of processing parameters and their interactions should be controlled to optimize the properties.

During SEM analysis produced coatings were evaluated by measures of coatings thickness (H) and content of strong carbide-forming elements such as V, Cr, Mo, W in surface layer, which for analysis decided to express in the form of total amount of alloying elements mass fractions (A). According to this coating thickness deposited on 41Cr4 steel substrate designated as (H_1) and coating thickness for C80U (H_2) respectively. Similarly to this, sum of alloying elements in coating deposited on 41Cr4 steel substrate labelled as (A_1) and content of alloying elements in coating on C80U steel (A_2). The used matrix of DOE with mean results of measures (experimental responses) is presented in the Table 3.

Table 3. Experimental design matrix, thickness and sum of alloying elements V, Cr, Mo, V

Regime No.	OR, %	V_C, mm min^{-1}	F_P, g·min^{-1}	$\overline{H_1}$, µm	$\overline{H_2}$, µm	$\overline{A_1}$, wt%	$\overline{A_2}$, wt%
1	50	900	5	581	516	6.48	4.81
2	30	900	5	376	391	5.31	4.58
3	50	1,500	5	325	331	5.44	3.87
4	30	1,500	5	215	209	5.03	3.91
5	50	900	10	721	729	8.28	8.56
6	30	900	10	492	485	7.95	8.35
7	50	1,500	10	500	489	8.07	7.00
8	30	1,500	10	243	320	7.22	7.50

Morphology

In order to test the hypothesis of the current research, the coatings were created with significant penetration into substrate, which have keyhole geometry due to a high power density. As a result, depth of penetration was in range 1.8 to 2.4 mm (Fig. 3, a), which was determined as a sum of lengths ($D = D_1 + D_2$) of interfusion zone (IZ) and keyhole in penetration (KP).
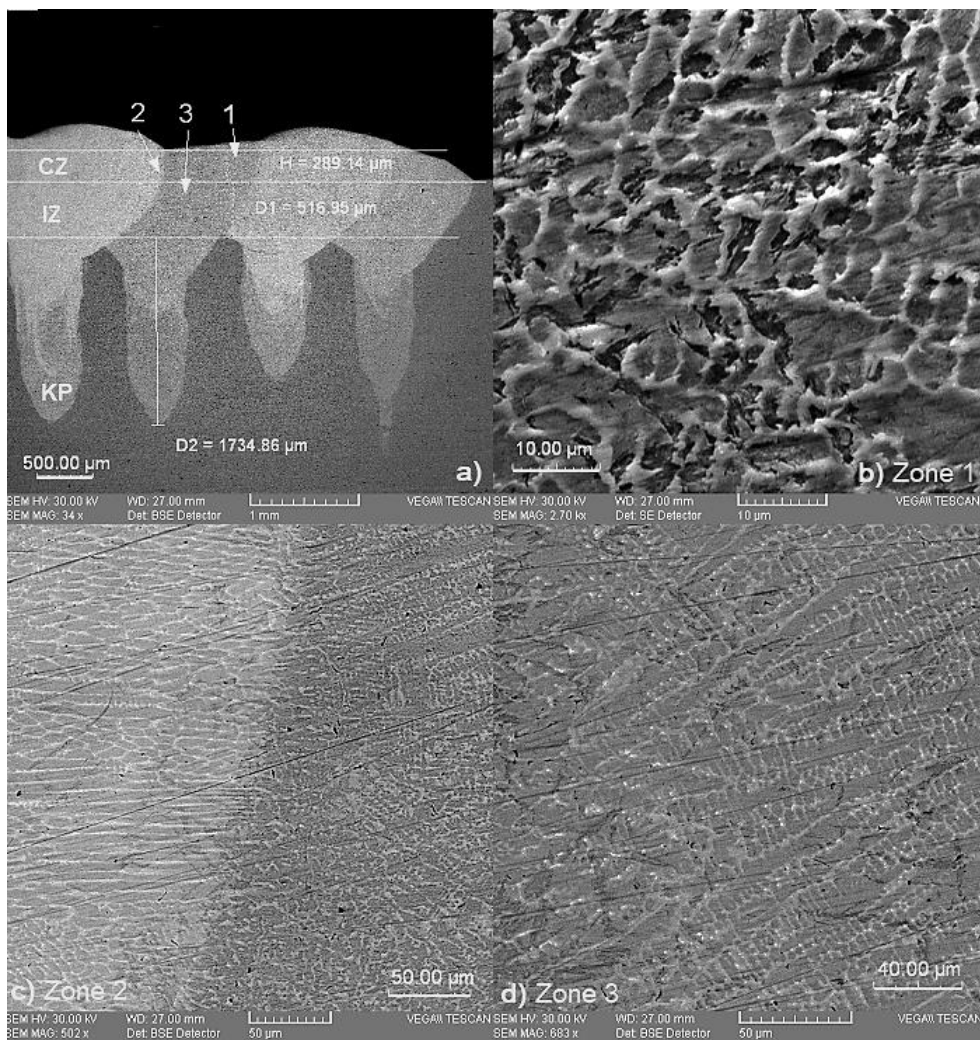
Figure 3. SEM images of cross-section of the laser cladding coating (a) deposited on 41Cr4 substrate according to regime No.2 with shown geometrical measures (CZ – clad zone; IZ – interfusion zone; KP – keyhole in penetration) and higher magnification electron images of denoted regions: 1 – zone near the surface (b); 2 – region between single tracks (c); 3 – the center zone of single track (d).

Detailed consideration of the SEM micrographs of the samples cross-sections was conducted to examine the morphology, geometrical parameters and defects of fabricated laser cladding (LC) coatings. The microstructure of M2 coatings on 41Cr4 and C80U substrates near the surface region was mostly equiaxed (Fig. 3, b), which could be attributed to a uniform heat flow in all the directions (Majumdar et al., 2005). The size of intercellular spacing ranged between 2–5 μm. However in the clad zone (CZ) and in IZ, i.e. in the middle part of a single clad bead and areas near the substrate had directionally solidified cellular-dendritic microstructure, growing almost perpendicularly from the fusion line (i.e. crystallization front between single tracks or with the base material) to the center zone of clad bead (Fig. 3, c, d). The micrograph of

zone with columnar dendrites structure is presented in the next (Fig. 3, d): dark regions attributed to dendritic regions, while interdendritic regions are white. As it's noted by (Navas et al., 2005; Candel et al., 2013) M2 LC coatings have fine cellular-dendritic structure consisted of martensite and carbide eutectic at grain boundaries of different kinds of M_nC_m (where M represents Cr, Mo, W, V). The improvement of the microstructure in HSS steels through solidification depends on the cooling rate and chemical composition of the alloy (Boccalini & Goldenstein, 2001; Benyounis et al., 2009).

The size of intercellular and primary dendritic spacing obtained in this study varied between 4–10 μm and secondary dendritic arm spacing in range between 2–4 μm respectively. Grains become finer by increasing cladding speed and by increasing distance between contiguous cladding tracks, which is referred to increasing cooling rate, due to reduction of heat input of the acting laser beam as well as influence of conducted heat of adjacently deposited cladding bead.

When comparing the quality of all produced coatings on both substrates it was found that most of the cracks contain coatings on C80U steel substrate. Furthermore appliance of post-cladding heat treatment insignificantly reduced this kind of defect. In this case by investigation of microstructure it was noticed that cracks had propagation along intergrain boundaries (Fig. 4, a, b), which could be characterized as solidification cracks also known as hot cracks. This may be an explanation of why the tempering didn't affect the decrease of crack formation.
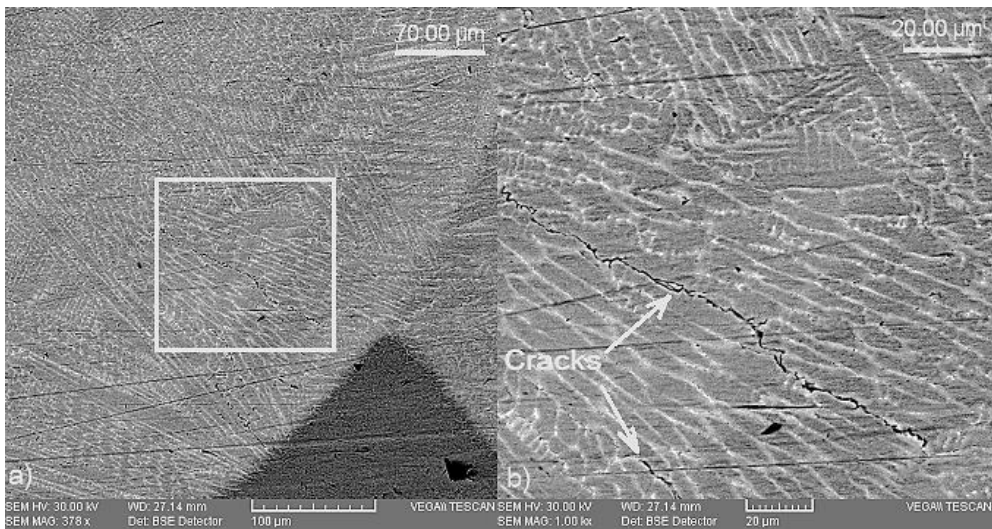
Figure 4. SEM images of the coating in interfusion zone (a) and higher magnification image of selected area (b) with microcracks at the grains boundaries.

It has to be pointed that the most of the cracks corresponded to 50% of clad tracks overlap, which contributes to the formation of a thicker coating. In this case, cracks can be formed due to a secondary remelting of previously deposited cladding track, which can cause formation of different interval of fragility during melt solidification. Concerning coatings produced on the base steel 41Cr4 there were also some cracks

detected, mainly on the thickest coatings produced. Consequently, to lower the formation of cracks, it is necessary to determine the optimal coating thickness.

The presence of pores of 100–300 μm was also found, mostly in the keyhole penetration. This phenomenon was described earlier in (Ločs et al., 2017), which related to the high power density of the acting laser beam, due to rapid evaporation of the molten material and producing air bubbles. Nevertheless the smallest content of pores pertained to coatings created at the higher cladding speed, which agrees well with (Katayama, 2010) study, where one of the confirmed action to prevent of the pore formation in the keyhole referred to increasing of the process speed.

Data analysis

In this study the influence of experimental factors was estimated by determining of mathematical models based on the measured parameters (thickness and sum of alloying elements in coatings) according to the design matrix. In order to confirm mathematical model coefficient of determination (R^2) was also calculated. Additionally ANOVA was completed for estimating of statistical significance of developed models by applying confidence level of 95% (*P*-value of 0.05).

Coating thickness

The range of thicknesses of produced coatings varied from 185 to 760 μm , the largest value as it has been expected corresponded to the largest amount of powder, the lowest scanning speed and for the highest value of overlap ratio (OR 50%). Fig. 5 depicts coatings thickness distribution relative to combination set of parameters.

As it can be seen this parameter shows practically identical distribution for both substrates. The decrease in thickness is accompanied by an increase in cladding speed and distance between adjacent cladding beads.
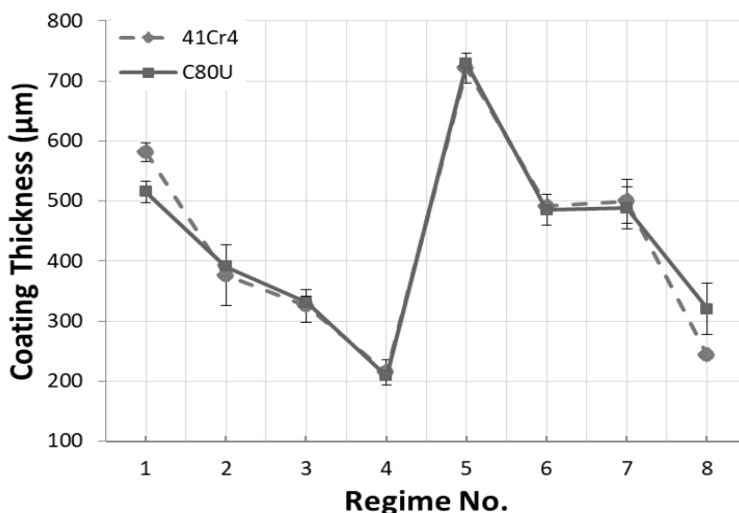
Figure 5. Variation of coatings thikness in relation to regimes.

Table 4 represents ANOVA for the coatings thickness. F-values of 42.41 for coatings produced on 41Cr4 steel substrate and of 45.52 for coatings on C80U steel substrate indicate the models are significant. P-values greatly less than 0.05 indicate that overlap ratio (OR), scanning speed (VC) and powder mass feed rate (FP) are all significant model terms. Especially the scanning speed turned out to be a dominant factor. Coefficients of determination (R^2) are very high and equal to 0.95 for both of H_1 and H_2 parameters and prove a high correlation between the experimental and the calculated results.

Table 4. ANOVA for the coatings height: DF – degree of freedom, SS – sum of squares, MS – mean squares

Source	DF	SS	MS	F	P
For 41Cr4 steel substrate					
Model	3	205,019	68,340	42.41	0.002
OR	1	80,400	80,400	49.89	0.002
V_C	1	98,513	98,513	61.13	0.001
F_P	1	26,106	26,106	16.20	0.016
Residual	4	6,446	1,612		
Total	7	211,465			
For C80U steel substrate					
Source	DF	SS	MS	F	P
Model	3	170,302	56,767	45.52	0.002
OR	1	54,182	54,182	43.45	0.003
V_C	1	74,522	74,522	59.76	0.002
F_P	1	41,598	41,598	33.36	0.004
Residual	4	4,988	1,247		
Total	7	175,290			

The mathematical models for coating thickness (H) and process parameters in terms of actual factors are given in the following expressions:

$$H_1 = 303.1 + 10.03 \ OR - 0.367 \ V_C + 22.85 \ F_P, \tag{1}$$

$$H_2 = 274.1 + 8.23 \ OR - 0.322 \ V_C + 28.84 \ F_P. \tag{2}$$

These equations (1 and 2) mirror of showed in Fig. 5 and demonstrate that powder feed rate has a positive effect onto coating thickness. The same effect presents OR parameter, namely by increasing percentage of overlap coating thickness enlarges. However, coating thickness decreases by increasing of cladding speed.

Elemental composition

In order to investigate relations between process parameters and content of the carbide-forming elements in clad zone (CZ) of coatings such as Cr, Mo, W, V elemental composition was measured on selected areas (Fig. 6, a) of all cross-sectioned coatings using EDS analysis (Fig. 6, b). The results of the generalized data for each regime are presented earlier in the (Table 3).
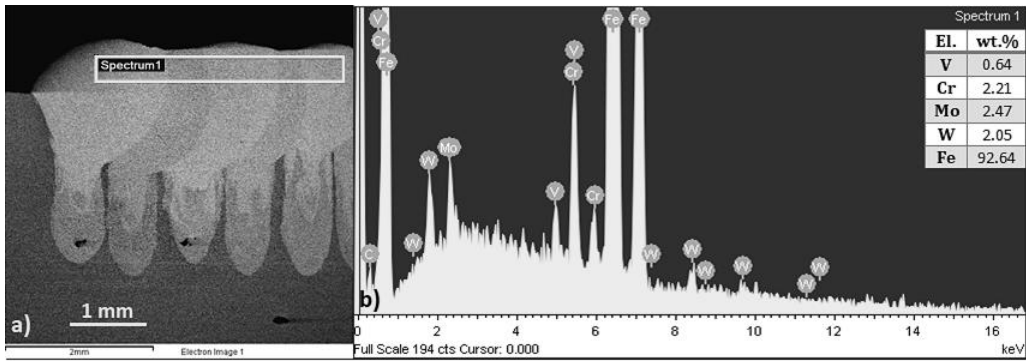
Figure 6. Cross-section SEM image of coating deposited by 1st regime (a) and spectra of X-ray emission for alloys present (b).

On the whole it was noticed that significant decrease of alloys after laser cladding is typical for all coatings achieved, which can be explained with the fact that by operating at a high power density quite huge intermixing occurs between melt and base and it causes ferrugination of cladded coatings. Iron consecration in upper layer of coatings correlates with observed parameter A_i (in form of the total amount of Cr, Mo, W, V), which was further used as the model's output response to determine the relationship with processing parameters. As it is shown below (Fig. 7), powder adding significantly increase content of alloys in the coatings. Maximal value corresponds to the 5th regime of DOE. Overall the plot of components distribution appeared very similar to previously presented by graph for coatings thickness. The coefficients of correlation (R) between two estimated parameters H_1 and A_1 as well as between H_2 and A_2 are equal to 0.65.
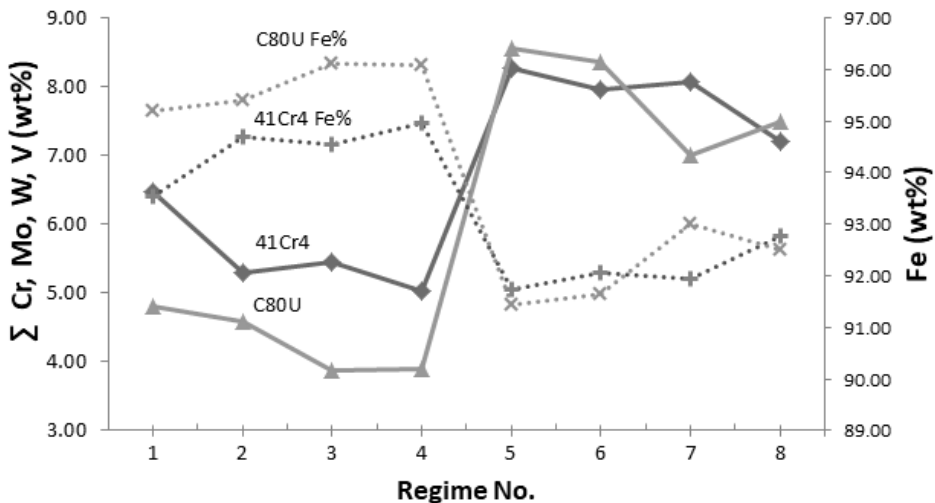
Figure 7. Variations of alloying elements content in coatings in relation to regimes.

Table 5 shows ANOVA for the total amount of alloy components. The models F-values of 65.17 for coatings on 41Cr4 steel substrate and 144.99 for coatings on C80U steel substrate represent high statistical significance. In this case powder feed rate (F_P) and cladding speed (V_C) are significant model terms. Therewith main effect showed powder feed rate. However overlap ratio (OR) showed significance only for processing on 41Cr4 steel substrate, but for C80U steel it didn't.

Table 5. ANOVA for the total amount of Cr, Mo, W, V: DF – degree of freedom, SS – sum of squares, MS – mean squares

For 41Cr4 steel substrate					
Source	DF	SS	MS	F	P
Model	3	12.304	4.101	65.17	0.001
OR	1	0.952	0.952	15.13	0.018
V_C	1	0.633	0.633	10.06	0.034
F_P	1	10.719	10.719	170.31	0.000
Residual	4	0.252	0.063		
Total	7	12.56			
For C80U steel substrate					
Source	DF	SS	MS	F	P
Model	3	27.356	9.119	144.99	0.000
OR	1	0.001	0.001	0.02	0.889
V_C	1	2.025	2.025	32.20	0.005
F_P	1	25.330	25.330	402.75	0.000
Residual	4	0.252	0.063		
Total	7	27.608			

The below given empirical relationships represent that the content of alloying elements increases by decreasing of cladding speed and by increasing of powder feed rate.

$$A_1 = 2.992 + 0.0345\ OR - 0.0009\ V_C + 0.4630\ F_P, \tag{3}$$

$$A_2 = 2.796 - 0.0013\ OR - 0.0017\ V_C + 0.7118\ F_P. \tag{4}$$

For these models R^2 has also very high indexes: values of 0.97 and 0.98 for coatings produced on 41Cr4 steel substrates and for coatings produced on C80U steel substrates respectevely. That denotes that the developed mathematical models are in a good agreement with the experimental data.

Mechanical properties
Fig. 8 demonstrates distribution profiles of Vickers microhardness along depth of transversal cross-sections in coating-substrate system. These profiles refer to the coatings created by the first four regimes of the DOE on both steel substrates (C80U and 41Cr4). The first approach includes the difference in overlap ratio (OR) of single cladding tracks and the difference in cladding speed (V_C) (solid lines); the second one corresponds to the similar area of regimes with applicable post-cladding tempering (+PCT) in addition (dash lines).

As it is seen the distribution of hardness values had consequent gradual decrease in depth. The hardness of clad zones of coatings varied in range of 830–500 HV0.2, depending on the combination of process parameters. Generally M2 coatings had 2–3 times highest values of hardness compared with substrates (~240–290 HV0.2, where the lowest value corresponds to 41Cr4 steel). Basically the highest hardness of clad zones corresponded to the coatings produced with OR50% and the lowest cladding speed concerning to both steel substrates (Fig. 8, a, b, c – profile 1). This outcome is well consistent with the previously obtained content of carbide-forming elements.
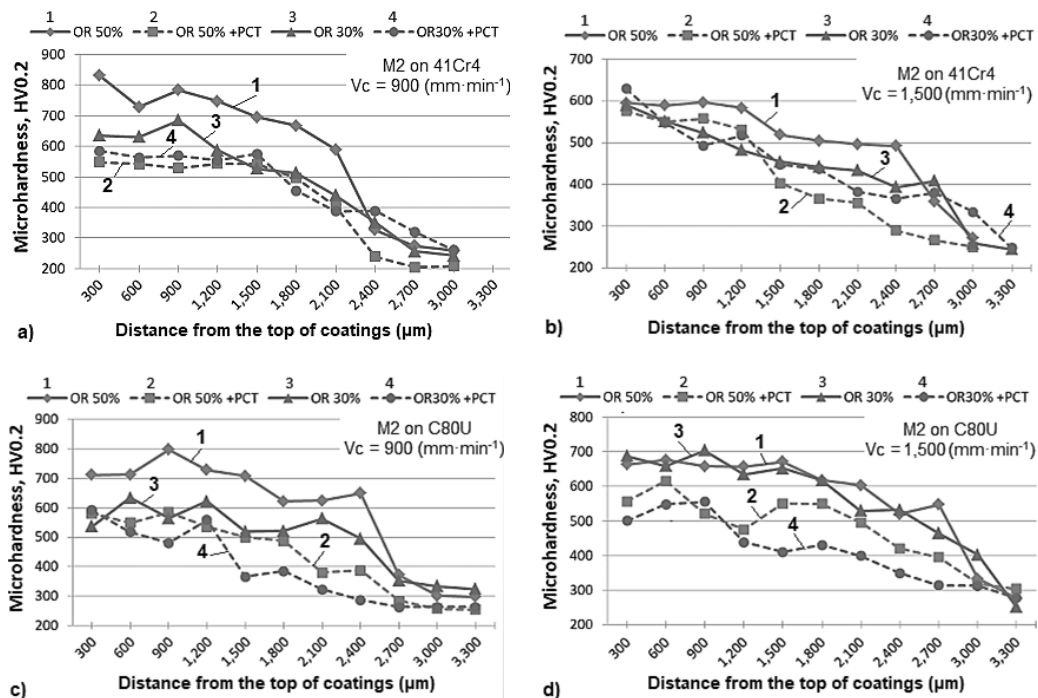
Figure 8. Vickers microhardness profiles on transverse cross-sections of coatings as function of depth: (a) M2 coatings deposited on 41Cr4 substrate: $V_C = 900$ mm min^{-1}; (b) M2 coatings deposited on 41Cr4 substrate: $V_C = 1,500$ mm min^{-1}; (c) M2 coating deposited on C80U substrate: $V_C = 900$ mm min^{-1}; (d) M2 coating deposited on C80U substrate: $V_C = 1,500$ mm min^{-1}.

As can be seen tempering mostly leads to a considerable decrease of hardness (profiles 2 and 4). However, on the other hand the profiles of post-clad tempering show more gradual variation of hardness towards the base material. Therewith, it was noticed, that hardness profiles of coatings produced with the lesser ratio of overlap (OR30% – profiles 3) demonstrate very close values to the PCT profiles, only excepting the case of C80U substrate and the highest cladding speed (Fig. 8, d – profiles 3). However this profile demonstrates a smoother transition of hardness towards the base, in comparison to profile 1, which in all cases showed abrupt transitions. That's why change of properties of this type could be the reason for fewer cracks in the coatings produced with 30% overlap.

Since the hardness index implicitly correlates to the strength of the material, this fact may be juxtaposed with the conditions for the distribution of residual stresses in the coating-substrate system. Based on the analysis of the hardness distribution, it may be assumed that coatings with keyhole in penetration affect the gradient of properties in depth. Thus, by controlling the size and shape of the penetration, by means of regulating the process parameters, it is possible to achieve a smooth redistribution of internal residual stresses, by reducing the stress in coating-substrate interface. Thereby applying such a technology may exclude the deposition of the buffer layer for hardfacing and cladding in surfacing applications. This method can also improve the fatigue strength of the coatings.

CONCLUSIONS

In current study laser cladding coatings were deposited using AISI M2 powder on EN 41Cr4 and C80U steel substrates. It was studied the influence of process parameters including overlap ratio between adjacent cladding beads, cladding speed and powder mass feed rate onto content of alloying elements and thickness of coatings and the influence of post-cladding tempering on the coatings quality. The quality of coatings has been evaluated by examination of morphology of transverse cross-sections, coatings geometrical features, elemental composition, mechanical properties (microhardness); additionally detailed assessment of coating thickness and content of alloying elements using statistical methods has been performed.

As a result the followings conclusions may be drawn:
− Coatings were created with significant penetration into substrate (1.8 to 2.4 mm), which have keyhole geometry due to a high power density;
− The microstructure of coatings was mostly equiaxed near the surface region (with grain size of 2–5 μm); in the middle part of a single clad bead and areas near the substrate region were cellular-dendritic structures (intercellular and primary dendritic spacing 4–10 μm, secondary dendritic arm spacing 2–4 μm);
− Grains become finer by increasing cladding speed and by increasing distance between contiguous cladding tracks;
− The presence of solidification cracks and gas pores was found. Cracks were mostly observed in coatings on C80U steel substrate and appliance of post-cladding heat treatment insignificantly reduced them. Reduction of overlap ratio and rise of cladding speed may lower the formation of cracks. Pores were most often located in keyhole penetration. Elimination of the pore formation is most likely to be achieved by increasing of cladding speed.
− Thickness of produced coatings varied from 185 to 760 μm. The largest value corresponded to the 5th regime of experimental design (OR 50%, $V_C = 900$ mm min^{-1}; $F_P = 10$ g min^{-1}). Maximal concentration of alloying carbide-forming elements (Cr, Mo, W, V) in the coating also corresponded to the 5th regime.
− ANOVA test of developed mathematical models for coating thickness indicated significant relationships between the process parameters and coating thickness. Results of the analysis demonstrated that scanning speed was a dominant factor, i.e. by increase of cladding speed coating thickness decreased. However both overlap ratio and powder feed rate had positive effect.

- Statistical analysis of alloying elements content showed adequacy of designed models, which represented that the content of them increases by decreasing of cladding speed and by increasing of powder feed rate. However overlap ratio showed significance only for processing on 41Cr4 steel substrate, but for C80U steel it didn't.
- Developed mathematical models can be used to predict coating thickness and content of alloying element in it within a confidence level more than 95%. According to this the optimal regime can be determined by relying onto created models.
- The analysis of microharndess distribution revealed that by producing coatings with 30% of overlap (i.e. larger distance between adjacent cladding beads) the smoother hardness profile was achieved. It was shown that coatings with keyhole in penetration may affect the gradient of properties in depth. Eventually it is assumed that by controlling size and shape of penetration, it is possible to achieve a smooth redistribution of internal residual stresses, by reducing the stress gradient in coating-substrate interface. Applying of this technology may exclude the deposition of the buffer layer for hardfacing and cladding in surfacing applications.
- As a result, in order to minimize the gradient of residual stresses in the coating it is preferable to perform laser cladding of the first layer of coating according to 8th regime (OR 30%, V_C = 1,500 mm min^{-1}; F_P = 10 g min^{-1}).

REFERENCES

Adaskin, A.M. 2017. *Tool materials in Mechanical Engineering*. Moscow, Infra-M, 319 pp. (in Russian).

Benyounis, K.Y., Fakron, O.M. & Abboud, J.H. 2009. Rapid solidification of M2 high-speed steel by laser melting. *Materials and Design* **30**, 674–678.

Boccalini, M. & Goldenstein, H. 2001. Solidification of high speed steels. *International Materials Reviews* **46**(2), 92–115.

Candel, J.J., Franconetti, P. & Amigó, V. 2013. Study of the solidification of M2 high speed steel Laser Cladding coatings. *Revista de Metalurgia* **49**(5), 369–377.

Cao, H.T., Dong, X.P., Pan, Z., Wu, X.W., Huang, Q.W. & Pei, Y.T. 2016. Surface alloying of high-vanadium high-speed steel on ductile iron using plasma transferred arc technique: Microstructure and wear properties. *Materials & Design* **100**, 223–234.

Grigoryants, A.G., Shiganov, I.N. & Misyurov, A.I. 2006. *Technological processes of laser processing*. Moscow, Bauman Moscow State Technical University, 664 pp. (in Russian).

Katayama, S. 2010. Understanding and improving process control in pulsed and continuous wave laser welding. In: *Advances in laser materials processing*. Woodhead Publishing Limited, Cambridge, pp. 181–210.

Kattire, P., Paul, S., Singh, R., Yan, W. 2015. Experimental characterization of laser cladding of CPM 9V on H13 tool steel for die repair applications. *Journal of Manufacturing Processes* **20**, 492–499.

Ločs, S. & Boiko, I. 2015. Investigation of Plasma Spray Deposition of Cermet Coatings. In*: 9th International Simposium on Powder Metallurgy, Surface Engineering, New Composite Materials, Welding*. Minsk, Belarus, pp. 122–125. (in Russian).

Ločs, S., Boiko, I., Drozdovs, P., Dovoreckis, J. & Devoyno, O. 2017. Investigation of coaxial laser cladding process parameters influence onto single pass clad geometry of tool steel. *Agronomy Research* **15**(4), 1659–1673.

Luo, K.Y., Jing, X., Sheng, J., Sun, G.F., Yan, Z. & Lu, J.Z. 2016. Characterization and analyses on micro-hardness, residual stress and microstructure in laser cladding coating of 316L stainless steel subjected to massive LSP treatment. *Journal of Alloys and Compounds* **673**, 158–169.

Majumdar, J.D., Pinkerton, A., Liu, Z., Manna, I. & Li, L. 2005. Microstructure characterisation and process optimization of laser assisted rapid fabrication of 316L stainless steel. *Applied Surface Science* **247**(1–4), 320–327.

Navas, C., Conde, A., Fernández, B.J., Zubiri, F. & de Damborenea, J. 2005. Laser coatings to improve wear resistance of mould steel. *Surface and Coatings Technology* **194**(1), 136–142.

Pleterski, M., Tusek, J., Muhic, T., Kosec, L. 2011. Laser cladding of cold-work tool steel by pulse shaping. *Journal of Materials Science and Technology* **27**(8), 707–713.

Schneider, M.F. 1998. *Laser cladding wth powder*. Twente (Netherlands), University, Dissetation, Enschede, 177 pp.

Tabernero, I., Lamikiz, A., Martínez, S., Ukar, E. & Figueras, J. 2011. Evaluation of the mechanical properties of Inconel 718 components built by laser cladding. *International Journal of Machine Tools and Manufacture* **51**(6), 465–470.

Telasang, G., Majumdar, J.D., Padmanabham, G., Tak, M. & Manna I. 2014. Effect of laser parameters on microstructure and hardness of laser clad and tempered AISI H13 tool steel. *Surface and Coatings Technology* **258**, 1108–1118.

Toyserkani, E., Khajepour, A. & Corbin, S. 2005. *Laser Cladding*. CRC Press LLC, New York, 263 pp.

Weisheit, A., Gasser, A., Backes, G., Jambor, T., Pirch, N. & Wissenbach, K. 2013. Direct Laser Cladding, Current Status and Future Scope of Application. In: *Laser-Assisted Fabrication of Materials*. In: Majumdar, J.D., Manna, I. (Eds.). Springer Heidelberg New York Dordrecht London, pp. 221–240.

Zeng, C., Tian, W., Liao, W.H., Hua, L. 2016. Microstructure and porosity evaluation in laser-cladding deposited Ni-based coatings. *Surface and Coatings Technology* **294**, 122–130.

Influence of the road profile in different geographical areas of the Czech Republic to the operational parameters of the electric vehicle

D. Marčev[*] and M. Kotek

Czech University of Life Science Prague, Faculty of Engineering, Department of Vehicles and Ground Transport, Kamýcká 129, CZ165 00 Prague, Czech Republic
[*]Correspondence: marcev@tf.czu.cz

Abstract. The aim of this paper is to compare the operating parameters of the full-electric vehicle VW e-up! operated in two significantly different geographic areas of the Czech Republic. The first tested area was the lowland area in the vicinity of municipality Mělník; the second area was a hilly area near the municipality of Ústí nad Labem with frequent and very sharp altitude changes. During measurement, the operating parameters of the battery (voltage, level) and electric motor (instantaneous voltage and current) were recorded. The results show a surprisingly small difference in vehicle tank range in both compared regions because the recuperation in the hilly area was used very often. It is possible to conclude that these electric vehicles can be used for everyday commuting under conditions of different geographical areas.

Key words: recuperation, real-world driving, altitude, vehicle range.

INTRODUCTION

For our global society, individual car transport is a key factor. Emissions, particularly emissions from road transport, have caused serious environmental pollution. With an emphasis on changing climate conditions, resource scarcity and population growth, vehicle manufacturers need to look for solutions that reduce the impact of individual car traffic on the environment. Road transport accounts for about one-fifth of total carbon dioxide emissions in the European Union. Furthermore, manufacturers are forced to comply with stricter emission standards (European Commission, 2010). The aim of the EU in the transport sector to reduce emissions by 60% until 2050. (European Commission, 2010).

A possible way to reduce emissions of internal combustion engine vehicles (ICEV) is to use biofuels. The disadvantage of biofuels is higher maintenance of the fuel system (especially removal of water from the system), lower engine performance and higher fuel consumption, based on the calorific values. In contrast, the advantage of using biofuels is the higher lubricity and very good biodegradability against diesel (Pexa & Mařík, 2014).

Another way to reduce car exhaust gases, is to replace ICEV with electric vehicles (EV). The worldwide trend is the ever increasing demand for EV (Mosquet et al., 2015). However, it is important to note that EVs do not produce any harmful emissions during operation, but the production of electricity itself and the other life cycle stages may have an impact on the environment (Li et al., 2016).

EV can contribute to sustainable road transport (Williams et al., 2012). However, the limited range represents a significant disadvantage of EV compared to ICEV. This disadvantage can discourage potential customers (Egbue & Long, 2012; Dimitropoulos et al., 2013) or lead them to purchase high-range EV, which are not cost-effective and even the most sustainable solution due to the environmental impact (McManus, 2012; Neubauer et al., 2012¸ Yuan et al., 2015).

For potential EV customers, the main parameter is a possible range. In order to get electric mobility, the main barrier is the range of EV (Franke et al., 2013). Range is affected by many factors. The first factor influencing the range is the construction of the vehicle and the other is the driver's impact on driving efficiency. In current EVs, the battery is the most expensive component. For this reason, it is advisable to focus on other vehicle design parameters, such as aerodynamic drag or a properly dimensioned electric motor. Driving style is critical for the EV range. Aggressive driving can significantly reduce range (Rimkus et al., 2012). It is also important in what conditions the EV works. A large altitude difference and extreme climatic conditions can significantly reduce the range of EV and therefore the use of EV in some areas seems to be ineffective.

The aim of this paper is to compare the operating parameters of the full-electric vehicle VW e-up! operated in two significantly different geographic areas of the Czech Republic and to show that even in such different locations, similar consumption can be achieved.

MATERIALS AND METHODS

The electric vehicle VW e-up! (Fig. 1) was used for this experiment. The e-up! is the electric version of Volkswagen up! city car. It is powered by a 60 kW electric motor which is powered by a 18.7 kWh lithium-ion battery pack integrated in the floor. Detailed technical parameters are shown in Table 1. Taking into account the vehicle properties and the 150 km range, the e-up! is ideal for city driving and for commuting purposes.

Figure 1. Volkswagen e-up!

Table 1. Technical parameters of VW e-up!

ENGINE	
Design	synchronous AC electric motor with permanent magnets
Power	60 kW
Torque	210 Nm at 0 rpm
Fuel system	electric plug-in
BATTERY	
Type	li-ion 323 V
Capacity	18.7 kWh
Number of cells	17 modules, 12 cells per module
Weight	230 kg
CAR BODY	
Service weight	1,185 kg
Manufacture year	2016
DRIVE PERFORMANCE	
Max. speed	130 km h^{-1}
Acceleration 0–100 km h^{-1}	12.4 s
Fuel consumption	11.7 kWh 100 km^{-1}
Tank range	150 km

The vehicle operating data (engine speed, load, vehicle speed, battery voltage and current, etc.) from the engine control unit were recorded via the OBD interface. Car diagnostic system VAG–COM was used for communication and record data from the OBD. The position and immediate speed and GPS coordinate were measured by Garmin GPS 18x USB with 1 Hz frequency.

The measurement was carried out on the two significantly different geographic areas of the Czech Republic (see Fig. 2). In both areas, extensive questionnaire surveys were conducted to identify the most frequent transport destinations of the population. In both locations there is a well-available fast-charging station within a distance of 20 km.
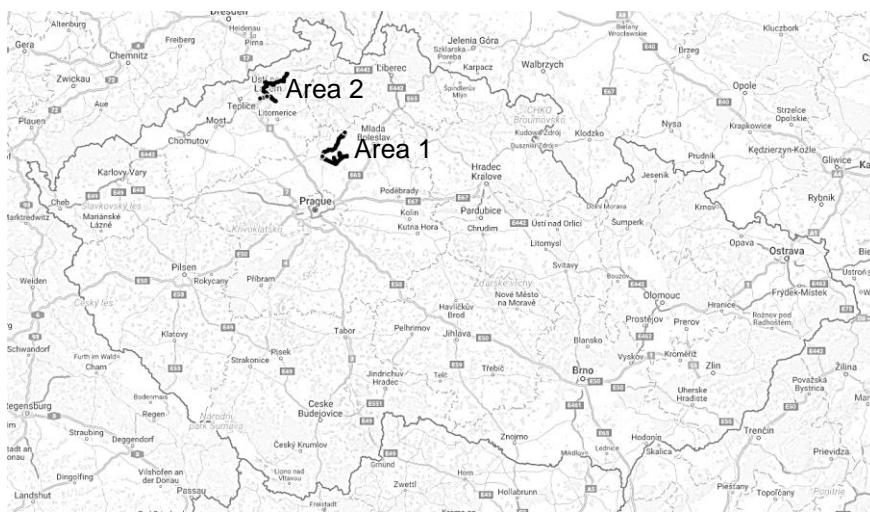
Figure 2. The map of tested areas with charging stations.

The first tested area was the lowland area in the vicinity of municipality Mělník which seems to be ideal for the use of an electric vehicle due to the appropriate terrain's properties. The first area is shown on the Fig. 3.

Figure 3. The map of area 1 – Mělník.

The second area (Fig. 4) was a hilly area near the municipality of Ústí nad Labem with frequent and very sharp altitude changes, which seems to be a very problematic altitude profile for an electric vehicle use because of on the first look this profile require much more power to overcome driving resistances, especially the gradient resistance.
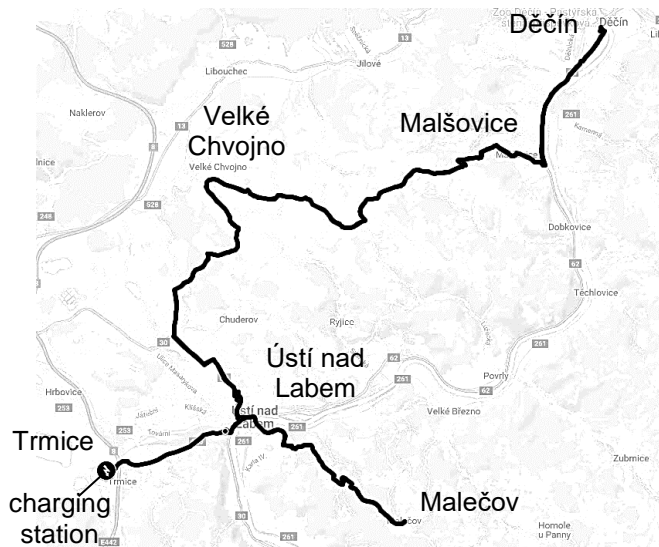
Figure 4. The map of area 2 – Ústí nad Labem.

The altitude road profile of both tested area is shown on Fig. 5. Table 2 provides summary of both areas with regard to time and track length spent with drive to uphill, downhill and along plane.
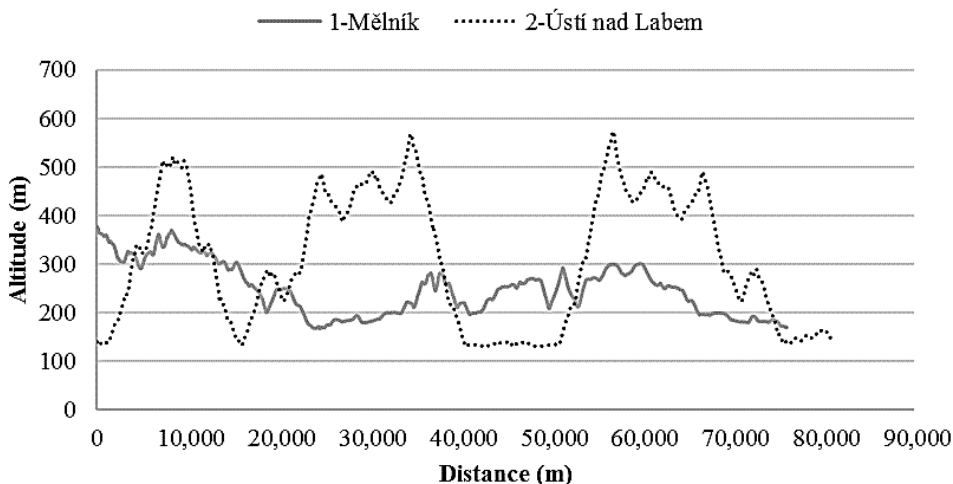
Figure 5. Altitude profile of tested areas.

Table 2. Tracks characteristics

	1 – Mělník	2 – Ústí n.L.
total track length (km)	75.92	80.77
total travel time (s)	6,187	7,239
avg. speed (km h^{-1})	44	40
abs. elevation difference (m)	210	442
PLANE		
time (s)	1,439	1,556
track length (km)	10.92	6.58
ASCENT		
time (s)	2,172	2,876
track length (km)	28.99	37.62
ascent (m)	0,796	1,953
avg. ascent (%)	2.75	5.19
DESCENT		
time (s)	2,576	2,807
track length (km)	36.01	36.57
descent (m)	1,004	1,943
avg. descent (%)	2.79	5.31

The experimental drives were conducted during weekdays at the time of morning and afternoon rush hour on 19–21 September 2017. The method floating car data (FCD) were used in the experiment. It means that the driver kept calm driving style and the drive is influenced by the immediate traffic situation. During the experiment, the outdoor temperature was around 12 °C, windless, partly cloudy, dry roads. In the vehicle the internal temperature was set to 20 °C and no additional electrical appliances were switched on.

RESULTS AND DISCUSSION

The main monitored parameter of the EV was the instantaneous consumed or recuperated current. Figs 6 and 7 show a selection of typical instantaneous power values from part of the test area. As can be seen from Fig. 6, in the lowland region of Mělník, the instantaneous value of peak power values reached maximum around 20 kW. Each deceleration is accompanied by a decrease in the current up to the negative values that signal the recuperation process. Compared with the second monitored area (Fig. 7), it is clear that maximum power values reaches up to double values. This phenomenon is mainly due to the course of the track altitude profile. The similar values of electric power distribution can be seen in (Fiori et al., 2016) where the EV was operated in driving cycle with higher vehicle speed, but without the influence of the gradient. The impact of gradient on energy consumption increases almost linearly with increasing absolute gradient (Liu et al., 2017).
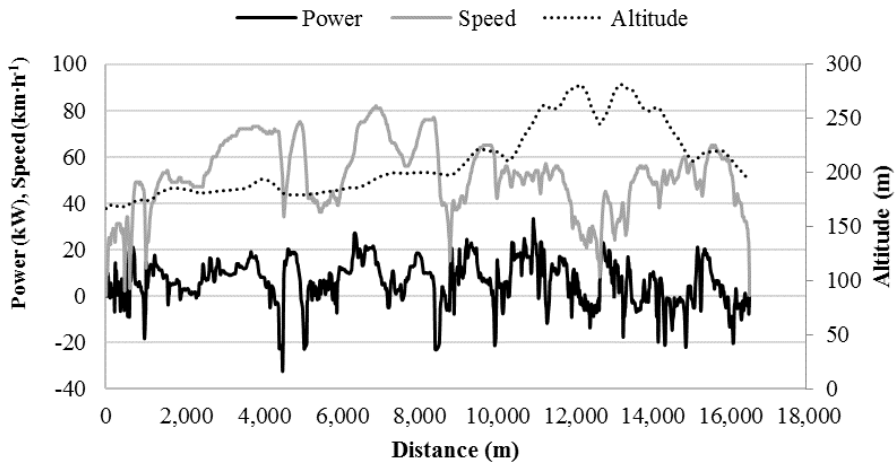
Figure 6. Example of typical instantaneous values of the electric power in the Mělník area.
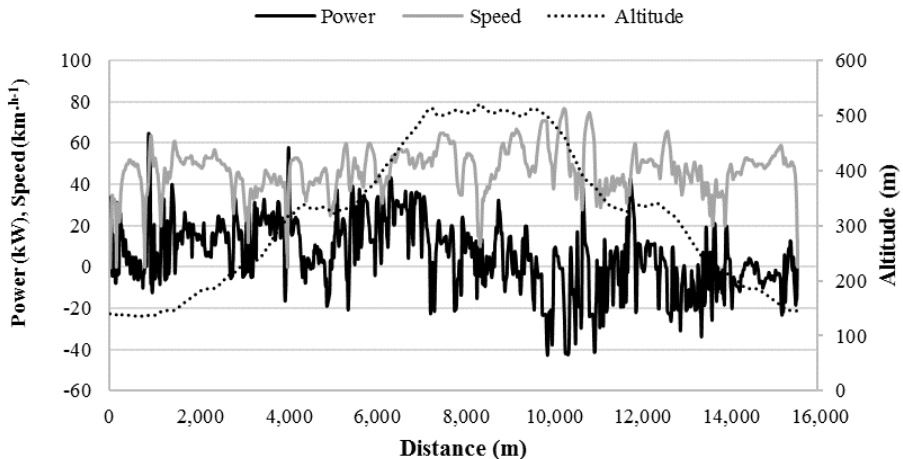
Figure 7. Example of typical instantaneous values of the electric power in the Ústí n.L. area.

Table 3 summarized total balance of EV current, power and consumption on both areas. It is obvious from the consumed battery level and avg. consumption that the hilly area around Ústí nad Labem can be expected to have higher electricity consumption, on the other hand, there is more often use of recuperation with higher avg. charging current thanks to which the average consumption increased by only 10%. The regenerative braking shows that EVs are more energy efficient than conventional fuel vehicles, especially in mountainous areas where conventional vehicles do not regenerate energy (Liu et al., 2017).

Table 3. Summary balance of current and power

	1 – Mělník	2 – Ústí n. L.
consumed battery level (% 100 km^{-1})	75.65	81.17
avg. consumption (kWh 100 km^{-1})	10.23	11.28
IDLING		
time (s)	608	979
CONSUMED		
time (s)	3,863	3,987
avg. current (A)	27.58	37.20
avg. power (kW)	10.33	13.90
RECUPERATED		
time (s)	1,717	2,274
avg. current (A)	18.36	26.16
avg. power (kW)	6.96	9.97

CONCLUSIONS

When choosing the appropriate route and riding style, energy consumption is not so fundamentally dependent on the location and altitude profile; in hilly area can be reached a similar consumption as in the lowland area. Of course, in the hilly area, it is necessary to expect a higher flow of electrical energy, which is necessary to overcome the driving resistances, especially the gradient resistance. On the other hand however on this area there is a potential to use recuperation abilities of EV. At the same time, it is necessary to take into account the battery state of charge, when at full charge there it is not possible to achieve maximum recuperation effect and hence the braking effect of the recuperation.

The experiment in form of real-world driving showed that small EV can be used for everyday commuting under conditions of different geographical areas especially when the each route not exceed the length of 70% real vehicle range.

REFERENCES

Dimitropoulos, A., Rietveld, P. & Van Ommeren, J.N. 2013. Consumer valuation of changes in driving range: A meta-analysis. *Transportation Research Part A: Policy and Practice* **55**, 27–45.

Egbue, O. & Long, S. 2012. Barriers to widespread adoption of electric vehicles: an analysis of consumer attitudes and perceptions. *Energy Policy* **48**, 717–729.

European Commission, 2010. Climate Action - 2050 low-carbon economy. http://www.ec.europa.eu/clima/policies/strategies/2050/index_en.htm, Accessed 28.10.2017.

European Commission, 2010. Climate Action - Reducing CO2 emissions from passenger cars. http://www.ec.europa.eu/clima/policies/transport/vehicles/cars/index_en.htm, Accessed 28.10.2017.

Fiori, Ch., Ahn, K. & Rakha, H.A. 2016. Power-based electric vehicle energy consumption model: Model development and validation. *Applied Energy* **168**, 257–268.

Franke, T., Neumann, I., Buhler, F., Cocoron, P. & Krems, J.F. 2012. Experiencing range in an electric vehicle: Understanding psychological barriers. *Applied Psychology* **61**, 368–391.

Li, W., Stanula, P., Egede, P., Kara, S. & Herrmann, Ch. 2016. Determining the Main Factors Influencing the Energy Consumption of Electric Vehicles in the Usage Phase. *Procedia CIPR* **48**, 352–357.

Liu, K., Yamamoto, T. & Morikawa, T. 2017. Impact of road gradient on energy consumption of electric vehicles. *Transportation Research Part D: Transport and Environment* **54**, 74–81.

McManus, M.C. 2012. Environmental consequences of the use of batteries in low carbon systems: the impact of battery production. *Applied Energy* **93**, 288–295.

Mosquet, X., Devineni, M., Mezger, T., Zablit, H., Dinger, A., Sticher, G., Gerrits, M. & Russo, M. 2011. Powering Autos to 2020. The Era of the Electric Car? *The Boston Consulting Group*. https://www.bcg.com/documents/file80920.pdf. Accessed 29.10.2017.

Neubauer, J., Broker, A. & Wood, E. 2012. Sensitivity of battery electric vehicle economics to drive patterns, vehicle range, and charge strategies. *Journal of Power Sources* **209**, 269–277.

Pexa, M. & Mařík, J. 2014. The impact of biofuels and technical engine condition to its smoke – Zetor 8641 Forterra. *Agronomy Research* **12**(2), 367–372.

Rimkus, A., Melaika, M., Pukalskas, S. & Nagurnas, S. 2012. Research of hydrogen influence for gas bus ecological and economic parameters. In: *16th International Conference Transport Means 2012*. Kaunas, 13–16.

Williams, J.H., DeBenedictis, A., Ghanadan, R., Mahone, A., Moore, J., Morrow III, W.R., Price, S. & Torn, M.S. 2012. The technology path to deep greenhouse gas emissions cuts by 2050: The pivotal role of electricity. *Science* **335**, 53–59.

Yuan, X., Li, L., Gou, H. & Dong, T. 2015. Energy and environmental impact of battery electric vehicle range in China. *Applied Energy* **157**, 75–84.

Extraction of oil from rapeseed using duo screw press

Č. Mizera[1,*], D. Herák[1], P. Hrabě[2] and A. Kabutey[1]

[1]Czech University of Life Sciences Prague, Faculty of Engineering, Department of Mechanical Engineering, Kamýcká 129, CZ165 21 Praha 6 Suchdol, Czech Republic
[2]Czech University of Life Sciences Prague, Faculty of Engineering, Department of Material Science and Manufacturing Technology, Kamýcká 129, CZ165 21 Praha 6 Suchdol, Czech Republic
*Correspondence: mizera@tf.czu.cz

Abstract. This study was focused on the analysis of optimize the pressing process of rapeseeds (*Brassica napus L.)* using screw press. For pressing of oil a screw press Farmer 20 – duo (Farmer 20, Farmet a.s., Ceska Skalice, Czech republic) was used. The screw rotation speed 10, 20, 30, 40, 55 and 65 rpm was used. Oil recovery efficiency and specific mechanical energy were decreased when the seed material troughput was increased. It has been found that the optimal operation point for screw press Farmer 20 – duo was at 20 kg h^{-1} rapeseed throughput. The specific mechanical energy at the optimal operation point was 0.61 kWh kg$_{oil}^{-1}$ Maximum oil recovery efficiency 82.6% was found at the lowest screw speed.

Key words: Farmer 20, oil recovery efficiency, pressing energy.

INTRODUCTION

Plant oil production plays an important role not only in the food industry. Mechanical pressing of oil seeds results in significantly lower oil yield compared to solvent extraction. However, health and environmental concerns related to the use of hazardous solvents as well as economic considerations regarding energy consumption and waste production have led to a revival of interest in mechanical pressing (Uitterhaegen & Evon, 2017). The original technology of pressing oil seeds was using a hydraulic press. This technology is characterized by the high efficiency of oil extraction, but it is non-continuous operation. That is why the oil extraction technology has been used for many years. In recent years, more and more scientific work has focused on extracting oil (Crowe et al., 2001; Zheng et al., 2003; Evon et al., 2013; Uitterhaegen & Evon, 2017). This process is ensured by means of a co-rotation twin screw press (Evon et al., 2013; Uitterhaegen & Evon, 2017) or screw press with a single screw of variable pitch and channel depth (Crowe et al., 2001; Zheng et al., 2003). Pressing the sunflower and coriander oils with a co-rotation twin screw press were investigated by Evon et al. (2009) and Uitterhaegen et al. (2015). In the second case, screw is slowly rotated in a cage type barrel and this ensures continuous operation (Isobe et al., 1992). Movement of the material through a press depends mainly on friction between the material and the barrel's inner surface and screw surface during screw rotation (Evon et al., 2013). In

practice, some parameters have been investigated that influence the pressing process. It was found that the moisture content of seeds affects performance screw press (Singh & Bargale, 1990; Singh et al., 2002). Lower seed moisture causes better oil yield, but also increases pressing temperature. Higher oil temperatures promote oxidation and degrade oil. Pressing rapeseeds dealt with a number of authors (Herak et al., 2015; Kabutey et al., 2017). Pressing of rapeseeds using the duo screw press (Farmer 20, Farmet a.s., Ceska Skalice, Czech republic) represents a very interesting option for small and medium – sized farmers. Regarding the optimization of oil extraction on the Farmer 20 screw press, other studies did not influence the different settings of the screw press. Therefore, the aim of this study was to analyze and optimize the pressing process at different screw rotation speed for rapeseeds pressing, focusing on optimizing the pressing process of the press Farmer 20.

MATERIALS AND METHODS

Sample
Rapeseeds (*Brassica napus L.*) obtained from the Ceska Skalice, Czech Republic were used for this experiment. The moisture content $M_c = 8.4 \pm 1.4\%$ (w.b.) of sample was determined using the standard oven method, ASAE method (ASAE S410.1 DEC97, ASAE, 1998). The procedure was that the initial mass of the sample before and after oven drying was weighed. For measuring of mass of each sample m_s *(g)* an electronic balance (Kern 440–35, Kern & Sohn GmbH, Balingen, Germany) was used. The test was repeated three times and result averaged.

Mechanical screw press Farmer 20 - DUO
The experiments were carried out on mechanical screw press Farmer 20 – duo (Farmer 20, Farmet a.s., Ceska Skalice, Czech republic). The duo screw press is powered by a 4.0 kW electric motor. Maximal capacity specified by the manufacturer in terms of seed throughput is 20 kg h^{-1}. The press is equipped with two screw head units (therefore the designation 'duo'). Each unit is equipped with a press cylinder with mesh size 1 mm. Nozzle diameter and screw speed were varied as the processing parameters. For measuring of parameters such as, rotation speed, torque, pressure, temperatures, mass of oil and mass of cake the different sensors were installed. Oil was collected into plastic containers. The schema screw press is shown in the Fig. 1.
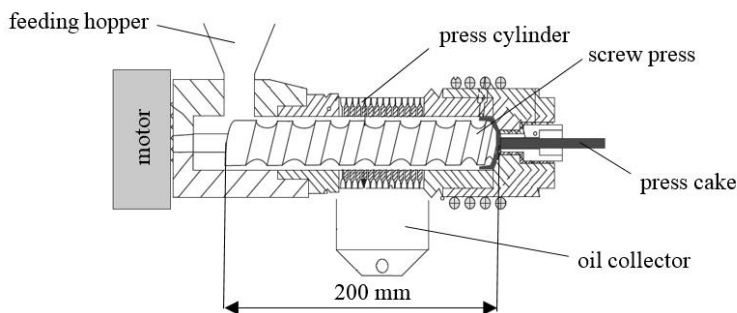
Figure 1. Scheme of mechanical screw press for oil extraction (Karaj & Müller, 2011).

Oil recovery efficiency was determined as the mass of pressed oil expressed as a percentage of the oil inside seeds. The oil content of the seeds was determined using the Soxhlet apparatus.

Processing of measured data

The measured values of pressing process were analysed with computer program Mathcad 14 (MathCAD 14, PTC Software, Needham, MA, USA), (Pritchard, 1998) uses Levenberg-Marquardt algorithm for data fitting (Marquardt 1963). The determined models of curves were statisticaly verified by using ANOVA.

RESULTS AND DISCUSSION

Fig. 2 shows the effect of screw rotation speed on electric power input of duo press and pressing time for 10 kg of rapeseeds. The graph shows 5 curves for different screw rotation speed in the range 10–65 rpm. Fig. 2 shows that, as expected, pressing time (for 10 kg rapeseeds) and power input decrease significantly as the screw rotation speed increases. This is due to a decrease in torque with increasing screw rotation. Higher speed means higher mechanical shear. This leads to self-heating of the material (*i.e.* higher material temperature) and thus to a lowering in material viscosity and in machine torque. (Karaj & Müller, 2011).
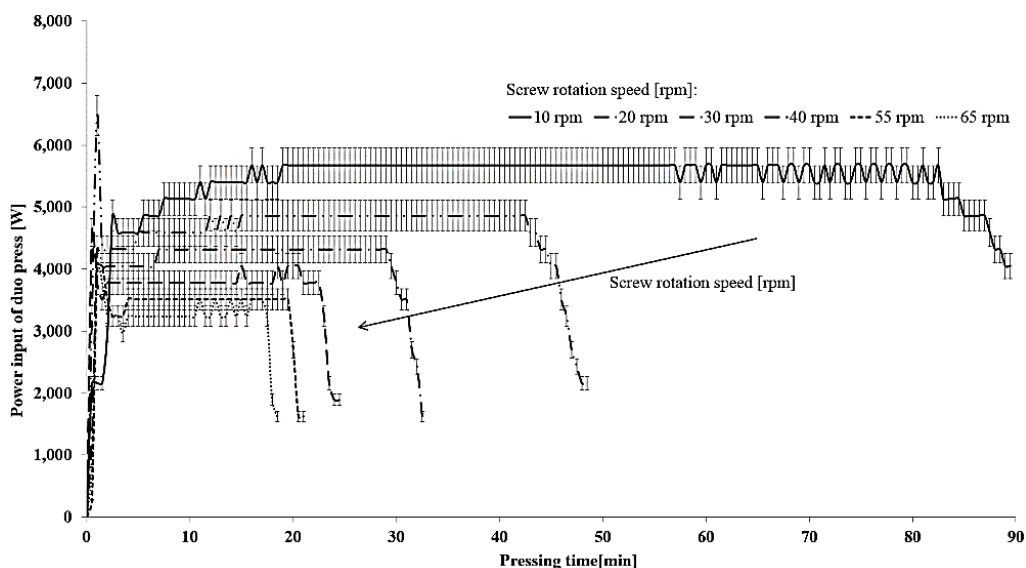
Figure 2. Effect of screw rotation speed on electric power input of duo press and pressing time for 10 kg of rapeseeds.

Fig. 3 shows the correlation of specific energy input and oil recovery efficiency versus material throughput. It is evident that specific energy (Es_{seed}) decreases as the troughput (TP) increases. The same dependence is also visible for specific energy for oil (Es_{oil}).

1120
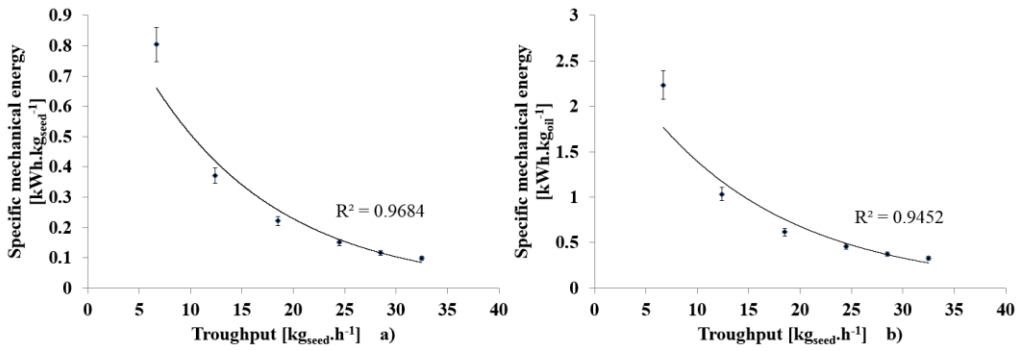
Figure 3. Dependence between seed material troughput and mechanical energy for a) pressing one kilogram of rapeseeds; b) obtaining one kilogram of oil.

The measured values of energy, depending on the troughput, decreases according to the exponential function and can be described using the Eq. 1 and Eq. 2

$$Es_{seed} = 1.1263 \cdot e^{-0.08 \cdot TP} \tag{1}$$

$$Es_{oil} = 2.8649 \cdot e^{-0.072 \cdot TP} \tag{2}$$

The model can be used only for the given troughput (5–35 kg h^{-1}) and mechanical screw press (Farmer 20). At an optimum troughput value 25 kg h^{-1}, the specific mechanical energy is about 0.5 kWh kg$_{oil}^{-1}$. Similar values were also found in linear pressing of bulk rapeseeds (Kabutey et al., 2017). Oil temperature 55 °C and press cake temperature 43 °C were measured at a troughput of 25 kg h^{-1}.

Fig. 4 shows the dependence between oil recovery efficiency (η_{oil}) and troughput (TP). Higher oil gain was achieved at lower troughput up to 20 kg h^{-1}.
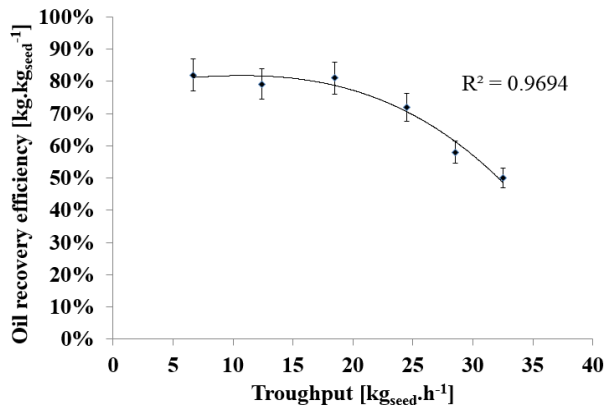
Figure 4. The effect of seed material troughput on oil obtained ratio.

Measured values of oil efficiency (η_{oil}) were fitted by exponential curve using Marguardt Levenberg algorithm and it is described by Eq. 3.

$$\eta_{oil} = 85.114 - 0.613 \cdot e^{\left(\frac{TP}{8.345}\right)} \tag{3}$$

The model can be also used only for the given troughput (5–35 kg h^{-1}) and mechanical screw press (Farmer 20).The oil recovery efficiency reached high values of around 85% for a troughput up to 20 kg h^{-1}. On the other hand there is an increase in specific energy at low values of troughput. For low screw rotation speeds, the energy value reaches about 2.3 kWh kg$_{oil}^{-1}$. Similar values of oil recovery were also determined for flax seeds (Zheng et al., 2005).

CONCLUSIONS

Power input of press was decreased when rotational speed of screw was higher. Oil recovery efficiency and specific mechanical energy were decreased when the seed material troughput was increased. Maximum oil recovery efficiency 82.6% was at the lowest screw speed. The optimal operation point for screw press Farmer 20 – duo was at 20 kg h^{-1} rapeseed throughput. The specific mechanical energy at the optimal operation point, which was determined by Eq. 2, was 0.61 kWh kg$_{oil}^{-1}$ and oil recovery efficiency 76.3%. The oil extraction efficiency was described and achieved the study objectives. Future studies should focus on analysing different press settings, nozzle diameter and physical properties of the input material as well as temperature influence on oil and press cake quality.

REFERENCES

ASAE S410.1 DEC97. 1998. Moisture measurement of peanut. In: ASAE standards, 45th edition. 560–561.

Crowe, T.W., Johnson, L.A. & Wang, T. 2001. Characterization of extruded-expelled soybean flours. *Journal of the American Oil Chemists' Society* **78**, 775–779.

Evon, P., Vandenbossche, V., Pontalier, P.Y. & Rigal, L. 2009. Aqueous extraction of residual oil from sunflower press cake using a twin-screw extruder: Feasibility study. *Industrial Crops and Products* **2**, 455–465.

Evon, P., Amalia Kartikac, I., Cerny, M. & Rigala, L. 2013. Extraction of oil from jatropha seeds using a twin-screw extruder: Feasibility study. *Industrial Crops and Products* **47**, 33–42.

Herak, D., Sleger, V., Mizera, C. & Sedlacek, A. 2015. Mechanical behaviour of bulk rapeseeds under quasi dynamic compression loading. *Engineering for Rural Development* **14**, 28–32.

Isobe, S., Zuber, F., Uemura, K. & Noguchi, A. 1992. A new twin-screw press design for oil extraction of dehulled sunflower seeds. *Journal of the American Oil Chemists' Society* **69**, 884–889.

Kabutey, A., Herak, D., Choteborsky, R., Dajbych, O., Sigalingging, R. & Akangbe, O.L. 2017. Compression behaviour of bulk rapeseed: Effects of heat treatment, force, and speed. *International Journal of Food Properties* **20**, 654–662.

Karaj, S. & Müller, J. 2011. Optimizing mechanical oil extraction of Jatropha curcas L. seeds with respect to press capacity, oil recovery and energy efficiency. *Industrial Crops and Products* **34**, 101–1016.

Marquardt, D.W. 1963. An Algorithm for Least-Squares Estimation of Nonlinear Parameters. *Journal of the Society for Industrial and Applied Mathematics* **11**, 431–441.

Pritchard, P.J. 1998. Mathcad: A tool for engineering problem solving. McGraw-Hill Science Engineering, New York, 336 pp.

Singh, J. & Bargale, P. 1990. Mechanical expression of oil from linseed (*Linum usitatissimum L*). *Journal of Oilseeds Research* **7**, 106–110.

Singh, K.K., Wiesenborn, D.P., Tostenson, K. & Kangas, N. 2002. Influence of moisture content and cooking on screw pressing of crambe seed. *Journal of the American Oil Chemists' Society* **79**, 165–170.

Uitterhaegen, E., Nguyen, Q.H., Sampaio, K.A., Stevens, C.V., Merah, O., Talou, T., Rigal, L. & Evon, P. 2015. Extraction of Coriander Oil Using Twin-Screw Extrusion: Feasibility Study and Potential Press Cake Applications. *Journal of the American Oil Chemists' Society* **92**, 1219–1233.

Uitterhaegen, E & Evon, P. 2017. Twin-screw extrusion technology for vegetable oil extraction: A review. *Journal of Food Engineering* **212**, 190–200.

Zheng, Y., Wiesenborn, D.P., Tostenson, K. & Kangas, N. 2003. Screw pressing of whole and dehulled flaxseed for organic oil. *Journal of the American Oil Chemists' Society* **80**, 1039–1045.

Zheng, Y., Wiesenborn, D.P., Tostenson, K. & Kangas, N. 2005. Energy analysis in the screw pressing of whole and dehulled flaxseed. *Journal of Food Engineering* **66**, 193–202.

Evaluation of reed biomass use for manufacturing products, taking into account environmental protection requirements

I. Muizniece[*], V. Kazulis, L. Zihare, L. Lupkina, K. Ivanovs and D. Blumberga

Riga Technical University, Institute of Energy Systems and Environment, Azenes iela 12/1, LV-1048 Riga, Latvia
[*]Correspondence: indra.muizniece@rtu.lv

Abstract. In many countries reed is considered as invasive or unnecessary plant, because it is spreading rapidly, causing decrease in biodiversity and creating unacceptable living conditions for many bird species in their natural habitats. Due to environmental considerations it is necessary to cut reed, to decrease their over exceeding growth. Reed burning or leaving for decomposition on fields, that has been practiced until now, creates additional carbon dioxide air pollution. Therefore, the question on what to do with cut reed has become vital from environmental protection perspective. In addition, this question applies to bioeconomy principles in compliance with their use in national economy, which makes it clear, that solutions for the use of reed biomass for production have to be found. But any production process can leave a negative effect on surrounding environment. Further to product production, economic motivation, possible market and availability of resources are primarily essential to see whether it is worth to produce the product at all. Therefore, reed biomass use possibilities in production have to be analysed as a complex question, taking into account environmental and climate, economic and technological aspects. In this study, solutions to perspective reed biomass use are evaluated, considering environmental protection requirements. For this task, multi-criteria analysis method TOPSIS is used, which includes 11 environmental and climate, economic and technological criteria. Evaluation includes both – already existing and new products that are divided in 3 sectors: power industry, construction and other products. Results of the research clearly state, which of reed biomass made products are perspective, taking into account not only traditional economic and technological aspects, but also environmental and climate aspects.

Key words: reed, multi-criteria analysis, TOPSIS, bioeconomy.

INTRODUCTION

Reed *(Phragmites)* is a perennial grasses herb that forms a dense and broad crops. Reed is found in wetlands, in standing water, in coastal areas and even as floating islands in the water. Reed is very adaptable to changes in the environment and can grow in many ecosystems and plant communities, including wetlands, coastal swamps, inland lakes and rivers, mountains, deserts and cities (Meyerson et al., 2016). In ecological succession water bodies and wetlands overgrow with reed and, when reed stands are gradually aging, they produce sufficient fertilizer and waste, draining the area with time and creating the possibility of developing bushes and trees in this environment. Reed is considered as one of the most invasive plant species in the world (Uddin et al., 2017).

Over the past 150 years, reed has grown exponentially and most reed stands form a dense monoculture because reed is monodominant (Dubrovskis & Adamovics, 2012). Reed provides cover for fish and invertebrates in lakes and rivers, produces oxygen, and is a nutrient for individual fish and other animals.

Changes in the chemical composition of the soil which are caused by human intervention (e.g. agriculture, livestock farming, industrialization, nutrient deposition, etc.) can create conditions that favor the introduction of reed in this ecosystem (Uddin & Robbinson, 2018). The expansion of invasive plant species can have dramatic effects on local ecosystems (Gordon, 1998). Changes in reed volume can also be considered as an indicator of the health of water bodies. Also the number of reduced reed can be related to water quality problems – pollution and herbicides. From 1,170,000 measurement sites in 33 European surveyed countries was determined that 35% of soil and groundwater pollution was made up of heavy metals (Panagos et al., 2013). Reed absorbs not only nutrients from the water body, but also polluting elements. The reed absorbs nitrogen (N) and phosphorus (N) which are dissolved in water, as well as heavy metals, therefore reed can be used to purify water bodies from these elements which increasingly come into water bodies as a result of human activities from agricultural land fertilization, waste, scum, overflows etc. (Cicero-Fernandez et al., 2017). Reed is intensified due to agricultural fertilizers that enter into the soil. Reed best absorbs nutrients up to 3-year age, because in this period reed are growing very fast (Adler et al., 2008). Reed indirectly affects the nitrogen cycle, because on the roots of reed certain denitrifying bacteria can grow. Reed promotes the sedimentation of suspended solids by reducing the rate of flow (Zhu et al., 2015), prevents erosion by stabilizing the soil (Horpilla et al., 2013). Although reed, on the one hand, competes with other plants, they can also contribute to the diversity of the biotope by increasing the wealth of fish and invertebrate taxonomy (Thomaz et al., 2007).

Reed can compete and occupy another plant site, as they have several benefit:
- reed can reach nutrients with rhizomes where they are not available to other plants;
- reed can reach nutrients with rhizomes where they are not available to other plants;
- they can change the soil by creating favorable conditions for them (Windham & Lathrop, 1999);
- reed genetically identical stalks can be interconnected with rhizomes, thus forming a single plant and it is not known how big and the old reed clone can develop. Stems that grow under unfavorable conditions can get nutrients from the rhizomes;
- reed can easier survive at rising water levels than other plants;
- increased levels of nitrogen contribute to reed reproduction;
- the rise of the CO_2 level in the atmosphere is promoted by plants such as reed with C3 photosynthesis pathway.

Up to now reed is mainly perceived as an invasive plant, whose further spread should be limited to preserve biodiversity. Rather than as a valuable, so far not fully used and undervalued bioresource which could be used to produce a variety of products, including high value added products. On the issue of reed management and utilization, its dual nature appears – on the one hand, the requirements of environmental protection, which restrict the area of reed, and, on the other, business interests, where the economic justification and long-term availability of the resource are the most important. Therefore, this issue needs to be seen as a complex system in which one process has an impact on

the other in order to find a compromise solution for the sustainable use of reed in the national economy, while respecting environmental protection requirements.

Currently, the use of reed in the national economy has the following positive aspects:

- do not have to be cultivated (no planting and fertilization required);
- grow in water bodies (places that are not suitable for the production of other crops and do not compete with the food industry);
- the use of reed in the national economy reduces the emissions of CO^2 and CH_4 in the atmosphere;
- clean up sediment of water bodies from nitrogen, phosphorus and the content of heavy metals if they are harvested.

By studying the distribution of reed, the possibility of using reed biomass in the national economy for the production of various products and its environmental impact, the dual nature of the investigated issue has been revealed:

1. it is necessary to restrict the spread of reed to prevent the overgrowth of the water bodies and to preserve the biodiversity what best to do in the summer when reed is green;

2. in order to use reed biomass as a raw material to production, entrepreneurs are primarily interested in the economic justification of this product, the long-term availability of the market and raw materials.

The first point is mainly for municipal and lake operators, while the second one is for entrepreneurs. In order to achieve a sustainable solution in the long term, it is necessary to find a compromise between these two sides, and only then will it be possible to ensure that the reed area does not uncontrolled increase and does not become an invasive plant that reduces biodiversity, while at the same time benefiting from its economic and social benefits.

Therefore, the research subject of this study is: Which products are prospective from reed to observe the environmental protection requirements?

By analyzing literature on the various products from reed biomass and from discussions with environmental protection requirements, it was concluded that in order to combine the interests of nature conservation and business, the most problematic issues are:

- **reed mowing time**

To reduce the area of reed, they need to be mowed in the summer when they are green, but for most products is required dry reed that is mowed in winter, because the transportation and drying of green reed is not economically viable. Till now there are no information about experience about possibility to mow reeds during the summer and then dry mowed reeds naturally in the field, as it is done with hay. But that would be possibility how to get and transport dry reed and also reduce its areas. If reed was only mowed in winter for product production, it would not affect the further spread of these areas, only reducing the size of the decomposition of reed biomass and pollution and emissions.

- **long-term stable and predictable reed biomass availability**

In order to start commercial production of a product using reed biomass, it will be essential for any entrepreneur to have the resources available in the required amount and in the long-term. At present, there are no research reports available to report developers that would clearly demonstrate the specific volumes of reed biomass that will be

available now and in the future in a specific area. In addition, starting the production, where the raw material is biomass of reed, the necessary amount should be available near the production site. Also, the diverse management of reed does not guarantee the availability of this resource. As a limiting factor, the seasonal nature of reed production should also be mentioned.

Therefore, the authors of this study came to the conclusion that for using reed biomass in the national economy is recommended to produce products for which:

- **reed biomass would be an alternative to the use of any other biomass in whole or in part**

If reed biomass could be used to produce products for which currently is used another biomass or replace part of another biomass, then the availability of resources would not be so significant. In this case, the use of reeds would depend solely on their relevance to the particular product and on the economic justification for their purchase and use, which might be even more advantageous in some cases if it is compared to other types of biomass. As well as the seasonal nature of reed extraction would no longer be decisive for them to not to be used when it is economically viable.

- **the moisture content of reed biomass is not significant**

In this case, there is a greater chance of getting raw material from the reed areas that are mown both in summer and winter. There will only be a difference between the cost of transportation of green and dry reed.

In addition, the principles of bioeconomy must also take into account in the economic development, which include the rational and efficient use of science-based local bioresources (European Commission, 2012; Blumberga et al., 2016). The use of reed for the production of products is absolutely in line with the principles of biotechonomy, because it has so far been incomplete used and undervalued resource, which was mostly considered to be cumbersome and associated with the extra costs of managing it. Although in this study is examined the possibility of using reed biomass for the production of various products, including products with low added value (direct energy combustion), it is clear that biomass of reed can also be used to produce products with higher added value (e.g., an extract that can be used in pharmaceutical industry and cosmetics).

The above-mentioned restrictive factors and many others have to be taken into account in order to determine the prospective use of reed biomass for the production of products in order to promote not only development of national economy and the use of a bioresource that is so far not fully exploited in accordance with the principles of bioeconomy but also to comply with environmental protection requirements.

Therefore, the aim of the study is to carry out a feasibility study on the use of reed in the national economy, observing environmental protection requirements. A multicriteria analysis method was used to achieve the goal, which allows for the consideration of different, mutually incomparable factors, also taking into account the importance of each of them in this case.

MATERIALS AND METHODS

In this study, the multi-criteria analysis (MCA) – TOPSIS (*Technique for Order Preference by Similarity to Ideal Solution*) method – was used (Jahan et al., 2016). It is a type of analysis that takes into account the influence of several factors. An analysis of

MCA TOPSIS provides an assessment of the situation as close as possible to the real situation. With this method it is possible to compare several alternatives and identify the best of the considered options, taking into account the various influencing criteria. In this study, alternatives are various products from reed biomass, which are not mutually compatible without an analytical approach. Multi-criteria analysis in the TOPSIS method evaluates the alternatives in relation to the ideal possible solution. The alternative which is closest to the ideal variant is considered as the best. The TOPSIS method is based on five calculation steps. The first step is to gather information about alternatives and selected criteria. In the second step of the calculation, these data are normalized. The next step is to normalize the data with the weight values and calculate the distance from the maximum and minimum values (distance from the ideal variant) (Lu et al., 2007; Doumpos & Grigoroudis, 2013; Ishizaka & Nemery, 2013).

To use this method (Fig. 1), information and data from scientific literature and other reliable sources of information (project reports, information which is provided by related industries, project data, etc.) were used to compare products from reed biomass. In the case of lack of data, an environmental engineering assessment, which is based on information on similar products, was taken into account.
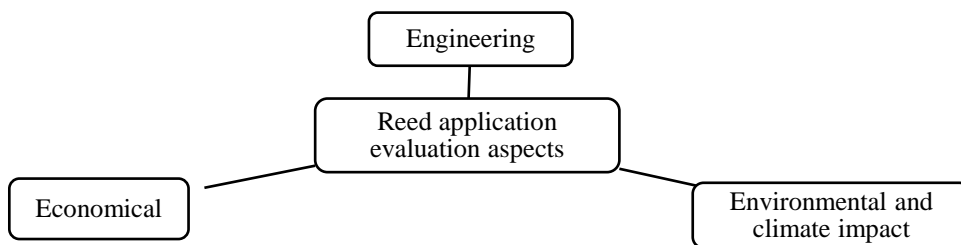
Figure 1. Grouping of evaluation aspects of reed application.

The used method – MCA TOPSIS – has proved itself in a similar study which was carried out by the Institute of Energy Systems and Environment of RTU 'Forest biomass – new products and technologies' in 2016 where was analyzed the potential for commercialization in Latvia of various innovative products that can be made from low-value forest biomass (RTU, 2017).

In this study, in order to determine the most promising products from reeds in the TOPSIS method in accordance with the requirements of environmental protection, the main factors, which are affecting the research issue, were defined as 11 indicators (Table 1).

To determine the significance or weight of each of the raised factors, the assessment of nature conservation experts was used. Using this method to evaluate the product, the subjectivity of the evaluators is reduced because it is based on reasonable numbers or expert judgment.

Table 1. Indicators which are included in the multi-criteria analysis

Indicators of engineering index	Indicators of the climate and environmental impacts	Economic Indicators
• The stage of manufacture of the product; • used amount of reed resources (%) in the final product; • the complexity of the technological process; • the possibility to replace other biomass with reed biomass which so far is used to produce the particular product	• The amount of CO_2 emissions which is arisen in the production process of product; • the consumption of resources (energy, water, chemicals) in the production process of the product; • the impact of raw material extraction and production processes on the environment (air, water, soil, living organisms); • the impact of the product on human health	• product outlet market; the necessary investments for launching the product; • product added value

RESULTS AND DISCUSSION

Within the framework of this study, using the TOPSIS multi-criteria analysis, 11 products were analyzed in order to identify the most promising products from reed, observing environmental protection requirements: thermal insulation panel of reed, sound insulation panel of reed, roofing of reed, fuel from reed for direct combustion, reed composite material (with clay), reed composite material (binder of fossil origin), biogas, extract, bioethanol, activated carbon, paper and cardboard. First of all, the selected products were evaluated in terms of sectors: construction, energy and other products that are not relevant to the two sectors which are mentioned above.

The weight which is given by experts in the field of nature protection to the included indicators in the multi-criteria analysis is summarized in Table 2. The weight of all indicators should be 100. As it can be seen, according to experts, the most significant indicator is the impact of the raw material extraction and production process on the environment (air, water, soil, living organisms) and the consumption of resources (energy, water, chemicals) in the production process of the product.

Table 2. Results of determining the weight of multi-criteria analysis indicators

Criterion	Weight
The stage of manufacture of the product	11
Used amount of reed resources (%) in the final product	6
Outlet market of product	11
The complexity of the technological process	8
The amount of CO_2 emissions which is arisen in the production process of product	5
The consumption of resources (energy, water, chemicals) in the production process of the product	12
The impact of raw material extraction and production processes on the environment (air, water, soil, living organisms)	17
The impact of the product on human health	9

The possibility to replace other biomass with reed biomass which so far is used to produce the particular product	7
The necessary investments for launching the product	8
Product added value	6

The results of the multi-criteria analysis are summarized in Table 3.

For the construction industry, five products were analyzed, from which sound or thermal insulation panels of reed were equally well and promising, and the most ancient and most commonly used type of reed – the product – roofing of reed. The production of reed composite material with binder of fossil origin is definitely not supported because the production of this product does not match the requirements of environmental protection.

Table 3. Results of the evaluation of the product from reed using a multi-criteria analysis

Product	Result of Multi-Criteria Analysis	Place
Thermal insulation panel of reed	0.826	1
Sound insulation panel of reed	0.826	2
Roofing of reed	0.789	3
Direct combustion	0.685	4
Reed composite material (with clay)	0.628	5
Biogas	0.578	6
Extract	0.559	7
Bioethanol	0.538	8
Reed composite material (binder of fossil origin)	0.469	9
Activated carbon	0.393	10
Paper and cardboard	0.343	11

For the energy sector, three products were analyzed, of which the best result was fuel from reed for direct combustion. This is mainly due to the fact that the launch of this product requires relatively less investment because the production process is simpler.

In the 'other products' category were included only three products. Of the analyzed, the greatest potential has extract from reed. In this case, for reed extract production, extraction in water technology without any chemical adding is used. So it is environment friendly production process. It should be noted that this product has the highest added value of all analyzed, since it can be used in pharmaceutical and cosmetic production, and its production corresponds to the principles of bioeconomy.

By comparing all of the eleven analyzed products from reed, the most promising products, in compliance with environmental protection requirements, are reed panels for thermal insulation and sound insulation and roofs from reed (Table 3). The first three products with the highest ratings in the multi-criteria analysis are products from the construction industry. These are not products with the highest added value, but in any case, from the environmental and climate point of view, are better than products for energy sector, as they can replace the products which are made from fossil fuels and temporarily store carbon so that it does not enter the environment and does not contribute to climate change.

The results which are obtained in this study are considered as a feasibility study in order to have a clear direction for future research. In order to more fully assess the compliance of the most promising products with the requirements of environmental

protection, it would be necessary to make and compare their life cycle analysis to determine their long-term impact on climate and environment. From a business perspective, for the most promising products is also required detailed economic and market analysis.

The results show that, in view of environmental protection requirements, the most promising products are those whose production is required dry, winter-mown reed. Which, in turn, does not coincide with the interests of managers of reed areas who want to reduce these areas and therefore mowing is done in the summer when the reeds are green. In order to find a solution to this controversial situation, planed and well-considered management of reed area is needed, which would include those areas where it is necessary to eliminate reed stands, mow in summer, and the rest in winter, in order to ensure availability of the resource in the long term.

CONCLUSIONS

Reed is a widespread invasive plant, the management and control of reed is complex and resource-intensive. From an environmental point of view, reed areas should be reduced. But from the point of view of the bioeconomy and sustainable use of resources, reed is little used and undervalued bioresource that could be used to produce products and get economic benefits. There is a number of inconsistencies between the two sides in terms of availability and quality of resources, which is why it is best to use reed as an alternative to other bioresources for the production of products.

A multi-criteria analysis has been conducted to determine which products can be promising from reed biomass with respect to environmental protection requirements. The obtained results show that the most promising are products related to the construction industry – thermal insulation and sound insulation panels and roofing from reed. However, for the production of these products is required dry, winter-mown reed, the harvest of which would not affect the spread of reed areas. Therefore, for the management of reed areas is required planned and prudent management that would include areas where it is necessary to eliminate reed stands, mow in summer, and the rest in winter, in order to ensure the availability of reed biomass resources for long-term production of products and to prevent uncontrolled reed areas.

REFERENCES

Adler, A., Karacic, A. & Weih, M. 2008. Biomass allocation and nutrient use in fast-growing woody and herbaceous perennials used for phytoremediation. *Plant Soil* **305**, 189–206.

Blumberga, D., Barisa, A., Kubule, A., Kļaviņa, K., Lauka, D., Muizniece, I., Blumberga, A. & Timma, L. 2016. *Biotehonomika*. Rīga, RTU Izdevniecība, 338 pp. (in Latvian).

Cicero-Fernandez, D., Peña-Fernández, M., Expósito-Camargo, J.A. & Antizar-Ladislao, B. 2017. Long-term (two annual cycles) phytoremediation of heavy metal-contaminated estuarine sediments by Phragmites australis. *New Biotechnology* **38**(B), 56–64.

Doumpos, M. & Grigoroudis, E. 2013. *Multicriteria Decision Aid and Artificial Intelligence: Links, Theory and Applications.* USA, Wiley-Blackwell, 368 pp.

Dubrovskis, V. & Adamovics, A. 2012. *Bioenerģētikas horizonti.* Jelgava, 352 pp. (in Latvian)

European Commission. 2012. *Innovating for Sustainable Growth: A Bioeconomy for Europe.* 9 pp.

Gordon, D.R. 1998. Effects of Invasive, Non-indigenous Plant Species on Ecosystem Processes: Lessons from Florida. *Ecological Applications. Ecological Society of America* **8(4)**, 975–989.

Horpilla, J., Kaitaranta, J., Joensuu, L. & Nurminen, L. 2013. Influence of emergent macrophyte (Phragmites australis) density on water turbulence and erosion of organic-rich sediment. *Journal of Hydrodynamics* **25**(2), 288–293 pp.

Lu, J., Zhang, G. & Ruan, D. 2007. *Multi-Objective Group Decision Making: Methods Software and Applications with Fuzzy Set Techniques*. SGP, Imperial College Press, 408 pp.

Meyerson, L.A., Cronin, J.T. & Pyšek, P. 2016. Phragmites Australis as a Model Organism for Studying Plant Invasions. *Biological Invasions* **18**(9), 2421–2431.

Ishizaka, A. & Nemery, P. 2013. *Multi-criteria Decision Analysis: Methods and Software.* USA, Wiley, 310 pp.

Jahan, A., Edwards, K. & Bahraminasab, M. 2016. *Multi-criteria Decision Analysis for Supporting the Selection of Engineering Materials in Product Design*. Butterworth-Heinemann, Elsevier, 252 pp.

Panagos, P., Liedekerke, M.V., Yigin,I, Y. & Montanarella, L. 2013. Contaminated Sites in Europe: Review of the Current Situation Based on Data Collected through a European Network. *Journal of Environmental and Public Health*, 11 pp.

RTU Vides aizsardzības un siltuma sistēmu institūts. 2017. *Meža biomasa - jauni produkti un tehnoloģijas*, Research Report, 212 pp. (in Latvian)

Thomaz, S., Dibble, E.D., Evangelista, L.R., Higuti, J. & Bini, L.M. 2007. Influence of aquatic macrophyte habitat complexity on invertebrate abundance and richness in tropical lagoons. *Freshwater Biology* **53**, 358–367.

Uddin, N. & Robinson, R.W. 2018. Can Nutrient Enrichment Influence the Invasion of Phragmites Australis? *Science of The Total Environment* **613-614**, 1449–1458.

Uddin, N., Rrobinson, R.W., Buultjens, A., Harun, A.Y. & Shampa, S.H. 2017. Role of Allelopathy of Phragmites Australis in its Invasion Processes. *Journal of Experimental Marine Biology and Ecology* **486**, 237–244.

Windham, L. & Lathrop, R.G. 1999. Effects of Phragmites Australis (Common Reed) Invasion on Aboveground Biomass and Soil Properties in Brackish Tidal Marsh of the Mullica River, New Jersey. *Estuaries* **22**, 927–935.

Zhu, M., Zhu, G, Nurminen, L., Wu, T., Deng, J., Zhang, Y. Qin, B. & Ventela, A.M. 2015. The Influence of Macrophytes on Sediment Resuspension and the Effect of Associated Nutrients in a Shallow and Large Lake (Lake Taihu, China). *PLoS One* **10**(6):e0127915.

Diagnostics of hydraulic fluids used in aviation

M. Obergruber[1], V. Hönig[1,*], P. Procházka[2] and J. Táborský[1]

[1]Czech University of Life Sciences Prague, Faculty of Agrobiology, Food and Natural Resources, Department of Chemistry, Kamýcká 129, CZ16521 Prague 6, Czech Republic
[2]Czech University of Life Sciences Prague, Faculty of Economics and Management, Department of Economics, Kamýcká 129, CZ16521 Prague 6, Czech Republic
*Correspondence: honig@af.czu.cz

Abstract. Diagnostics is a maintenance industry that monitors performance, parameters, and follow–up. Diagnosing hydraulic fluids means comparing the parameters of the used hydraulic fluid sample to the parameters of the clean fluid. It is also essential to monitor the limit values either by the aircraft manufacturer or by the manufacturer of the hydraulic fluid. This means that the manufacturer recommends the limitations of the liquid parameters. The measurements of the fluid samples give an overview of the liquid quality. Most businesses focus on so–called proactive maintenance. The main senses and objectives of proactive maintenance are: lubricant sample analysis, lubricant status, machine status, next step recommendation, database saving and trend analysis. This article focuses on the quality of hydraulic fluid focused in aviation. The aim of the article was to determine the properties of the hydraulic fluid used in the A320 aircraft family, determine the interval of its exchange. Monitoring the state of the hydraulic fluid could contribute to the timely detection of the problem, thus avoiding a failure of the device or the system as a whole. The tracking proposal is an integral part of this article.

Key words: particle analysis, control interval, kinematic viscosity, hydraulic fluid, cleanliness code.

INTRODUCTION

Airbus A320 is built by using of Hi–Tech materials such as composites composed of carbon fiber or kevlar or glass fiber and titanium. Due to the light components, the aircraft is as light as possible. The first flight of the A320 took place on February 22, 1987. Certification and supplies began some days later. Air France and British Airways started commercial flights with the A320 in May 1987. The A320–100 had the range of 3,500 km. The range of up to 5,500 km was extended for versions A320–200 after structural modifications and placing the winglets wing ends. Winglets reduce tensile stress, reduce induced resistance and fuel consumption. After the winglets were installed, the A320–100 production was completed and the production of the A320–200 continued (Airbus S.A.S, 2008; Planes.CZ, 2017).

The extended version of the A320, the A321 has been designed. The body of the aircraft is longer being 6.93 meters than A320. The flaps were modified and the chassis was reinforced. The new version was capable to accommodate 176 passengers. The

airplane was equipped with two extra emergency exits. The first flight was made on March 11, 1993 (Airbus S.A.S 2008, Planes.CZ).

Another version of the A320 is a smaller A319. This version combined A320 and A321 drives. It is 3.73 meters shorter than the A320 and accommodates only 130 passengers. The range is 5,000 km. The airplane is also compiled in Hamburg by DASA. The airplane was first presented in Farnborough in 1993.

Table 1 lists the parameters of the entire A320 Family Airbus S.A.S 2008

Table 1. A320 Family Specifications (Airbus S.A.S, 2008)

Type	A318	A319	A320	A321
Length	31.44 m	33.84 m	37.57 m	44.51 m
Wing span	34.09 m	33.91 m	34.09 m	34.09 m
Drive units	2 Pratt & Whitney PW–6000 or CFM International CF56–5	98 CFM International CFM56–5A or International Aero Engines IAE V2500–A5s	CFM International CFM56–5A1 or CFM56–5A3	International Aero Engines V–2530–A5 or CFM International CFM–56–5B1
Maximum range	2,780 km	3,391 km	4,843 km	4,907 km

The life of the aircraft is 20 years – approximately 48,000 flights, the average duration of the flight being one hour and twenty–five minutes. The airplane is approved for 24,000 flights with a threshold for the first inspection of the state of construction after 20,000 flights. The design criterion for the chassis is 60,000 cycles.

The booster system operates at a pressure of 0.555 MPa (8.06 PSI). The pressure relief valve is set at 0.579 MPa (8.40 PSI). The maximum fuel volume in the configuration of the two main tanks is 15,609 liters. The configuration with three fuel tanks is 23,859 liters with 2% reserve for thermal expansion (Planes.CZ). The aircraft is equipped with three continuous hydraulic systems: Green, Yellow and Blue. Each is supplied from its own tank. The normal system pressure is 20.68 MPa (3,000PSI) (Airbus S.A.S 2008).

The **green system** controls: chassis opening and closing including bow chassis control, normal braking system, engine thrust reversing no.1 (left side), flight control elements, power transmission unit, side damper (in–flight stability), take–off and landing flaps, moving leading edges (slots).

The **blue system** controls: flight control elements, Constant Speed Motor/ Generator, take–off and landing flaps and floating leading edges (slots).

The **yellow system** controls: cargo doors, backup brakes and parking brakes, engine thrust reversing no.2 (right side), flight control elements, power transmission unit, side air damper (in–flight stability), take–off and landing flaps (Airbus S.A.S, 2008; Lufthansa Training Manual, 2017).

Green system (System 1) is powered by a pump located on the engine number 1. Blue system (System 2) is powered by an electric drive pump. Yellow system (System 3) is powered by a pump located on motor number 2. This system can also be powered by an electric drive pump which allows ground manipulation when the engines 1 and 2 are switched off.

Diagnostics is a maintenance industry that monitors performance, parameters, and follow–up. Diagnosing hydraulic fluids means comparing the parameters of the sample taken with the clean fluid parameters. Monitoring of limit values is essential. The manufacturer recommends the limitations of the liquid parameters. The analysis obtains an overview of the liquid state and determines the wear and tear (Veselá et al., 2014; Hönig, 2015). Proactive maintenance is currently the most common. The objective is to analyze the lubricant sample, determine the condition of the lubricant and determine the state of the machine. The aim is also to recommend the next procedure and store the result in the database, make the trend analysis, and do the maintenance quickly and accurately. The method is very effective and reduces the cost of downtime, spare parts, operational substances and maintenance work (Aleš et al., 2012; Aleš et al., 2016; Hönig & Orsák, 2016).

It is necessary to know the construction materials for monitoring the condition of the machine. Oil is a medium bearing wear particles (Hönig & Hromádko, 2014; Hönig et al., 2014a). The change in the fluid properties may indicate damage of the machine (Hönig et al., 2014b). The kinematic viscosity at 40 °C is an important parameter as well as the cleanliness codes according to NAS 1638, ISO 4406 and ISO 4407. The hydraulic liquid is phosphate–ester base and is designed for commercial airliners. The liquid has higher thermal stability, lower density and more of anti–corrosive effects than previous types of hydraulic fluids. The EXXON HyJet IV A–plus meets all the requirements of aircraft manufacturers. EXXON HyJet IV A–plus is used as a refill for hydraulic systems of transport aircraft, where the former–ester base is recommended (ExxonMobil).

Table 2. Basic parameters of pure liquid specified by the manufacturer (Airbus S.A.S, 2008)

Parameter	Standard	EXXON HyJet IV	Limit
Kinematic viscosity at 40 °C, $mm^2\ s^{-1}$	ASTM D445	10.55	± 20% 8.44–12.66
Density at 25 °C, $kg\ m^{-3}$	ASTM D4052	996	99–1,005
Acid number, mg KOH g^{-1}	ASTM D974	0.4	1.5 max.
Water content, %	ASTM D6304	0.1	0.2 max.
Cleanliness Code NAS 1638	–	4	9 max.
El. Conductivity, microSiem cm^{-1}		1.4	0.5 min.

The basic control intervals are:

Pre–Flight and Flight check: performed before each flight, no more than two hours before scheduled departure. Tasks may alternatively be performed by the flight crew as part of the approved pre–flight checklist (Planes.CZ, 2017).

Daily check: performed daily, time may not exceed 36 hours from the previous one. **Weekly check:** every 8 days.

A check level A
1A every 600 flight hours or 100 days;
2A every 1,200 flight hours;
4A every 2,400 flight hours.

C check level C
1C every 20 month/6,000 flight hours/4,500 flight cycles;
2C very 40 month/12,000 flight hours/9,000 flight cycles;
3C every 60 month/18,000 flight hours/13,500 flight cycles;
4C every 80 month/24,000 flight hours/18,000 flight cycles;
IL check: structure review every 5 years
D check: structure review every 12 years
5–year check: additional check every 5 years
10–year check: additional check every 10 years
The main fatigue threshold is set to 24,000 flight cycles or 42,000 flight hours (Airbus S.A.S 2008; Lufthansa Training Manual, 2017).

The aim of the article was to determine the quality of the hydraulic fluid used in the A320 aircraft family, determine the interval of its exchange and create a measurement methodology. The quality of the EXXON HyJet IV A–plus liquid (Table 2) was monitored.

MATERIALS AND METHODS

Samples are routinely taken at C Check and sent to German Lufthansa Laboratory. The C Check has large intervals, so A Check has been selected (600 flight hours). Using the A Check, the interval is shorter and more samples can be taken than when using the C Check. The A Check can be defined as performing a functional check of the aircraft and its systems. It mainly focuses on checking features that are not routinely tested (backup systems, state–of–the–art signaling, etc.). The overview of analyzed aircraft and their age is shown in Table 3.

Sampling was performed within 1 year according to Lufthansa's subscription and analysis procedures. In the sampling, the contamination of the sample should be avoided. The sampling is done either in clean glass containers or in plastic containers. The aircraft was connected to a source and the hydraulic systems where activated for sampling.

The following tests were performed:

- Acid number according to ASTM D974
- Kinematic viscosity at 40 °C according to EN ISO 3104
- Density at 25 °C according to EN ISO 3675
- Cleanliness code according to NAS 1638 a ISO 4406 (Parker.com, 2018).

Table 3. Overview of the analyzed Airbus A320 Family of Airline company

Age, year	Type
11	A321
	A321
6	A320
	A320
2	A320
	A320
	A320

An automated evaluation of the cleanliness code is based on the microscopic analysis of the pollutant solids contained in the hydraulic fluid. The principle is to sum the amount of particles on a membrane filter with known area after the known volume of hydraulic fluid has been filtered through the membrane.

The result is a computerized code indicating the amount of solid impurities according to standards NAS1638 and ISO 4406. The Lambda DN 45 microscope with color CCD camera connected to Lambdasoft 2000 was used (Fig. 1 and Fig. 5).

Three measurements were made to determine the acid number, kinematic viscosity and density. The result is always the arithmetic mean of all measurements. For the determination of solid impurities and NAS 1638 10 images were scored vertically and 10 images horizontally on each filter.

Based on the measured results, Lambdasoft software was used and the software results are a completed statistical evaluation according to NAS 1638.

Figure 1. Lambda DN 45 microscope.

RESULTS AND DISCUSSION

The pure liquid had a purple color and the color darkened due to wear. The used liquid was brown. The NSA307110 standard introduces the word transparent. Lufthansa has the parameter marked as 'pure' according to NSA307110.

The clean liquid should have an acid number smaller than 0.15 mg KOH g^{-1}. The calculated average acid value was 0.41 mg KOH g^{-1}.

Fig. 2 shows that the acid number was reduced by refilling of the liquid. The acid number increases gradually. The limitation was satisfactory.
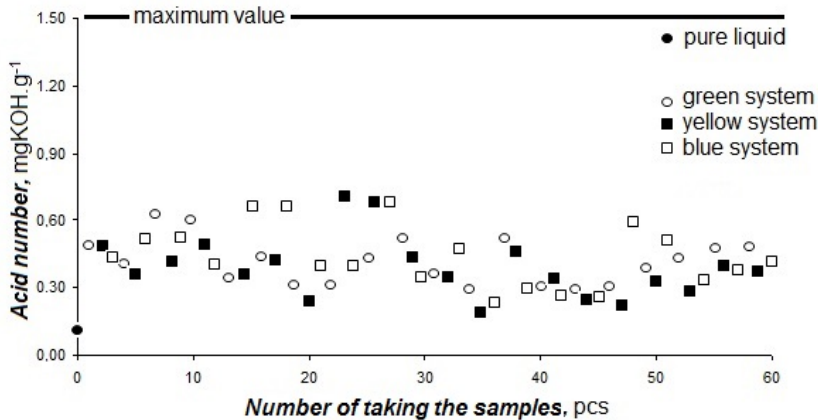
Figure 2. The trend of the acid number.

The results of the kinematic viscosity fluctuated slightly (Fig. 3). This may be caused by an admixture of another liquid or increased water content. The average of viscosity value was 6.67 mm^2 s^{-1}.

The values of kinematic viscosities where close to the lower limit. The results of the kinematic viscosity measurements guaranteed that the fluid is easy to pump, has low resistance to system startup and ensures good tightness and sufficient lubrication.
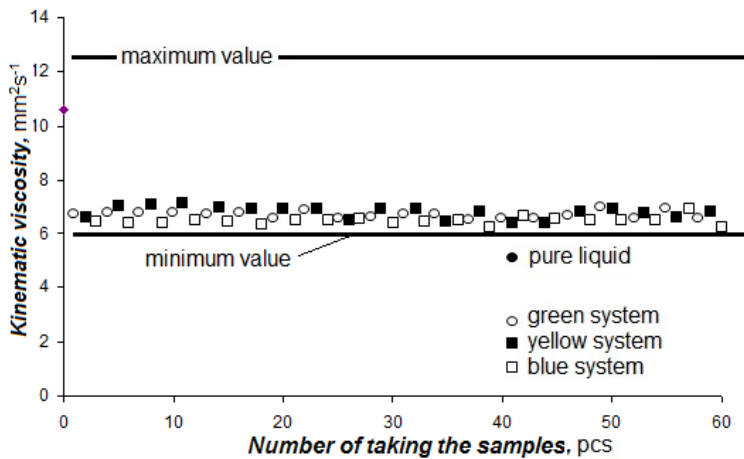
Figure 3. The trend of kinematic viscosity at 40 °C.

Fig. 4 shows that it would be advisable to adjust the maximum density value. The value is based on the Lufthansa Training Manual. Pure liquid has a tolerance field in the range 993 to 1,066 kg m^{-3}. The range of 990 to 1,020 kg m^{-3} would be preferable.

The most important parameter of the hydraulic fluid is the cleanliness code. Proper selection of the sampler is also important. The sampler should be made of glass or plastic. Plastic are used most often. Glass containers are more suitable for the cleanliness code. By friction of wall fluid, some metal particles can form grooves (Mihalčová & Hekmat, 2008).
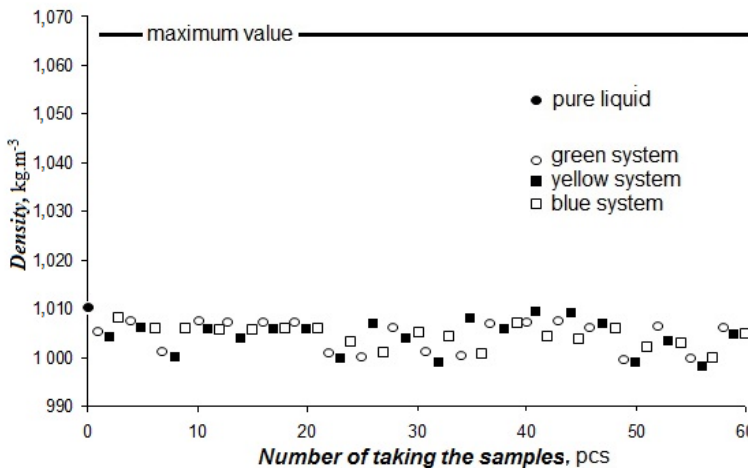
Figure 4. The trend of density at 25 °C.

In addition to NAS 1638, ISO 4406 is also used. The difference between them is that NAS 1638 refers to 100 mL of sample, ISO 4406 converts the particles to one milliliter.

1138

The fluid system is continuously refilled and the hydraulic system is always properly controlled. The first replacement is therefore appropriate after the complete dismantling of the aircraft and replacing end–of–life parts with new ones (IL Check – every 5 years).
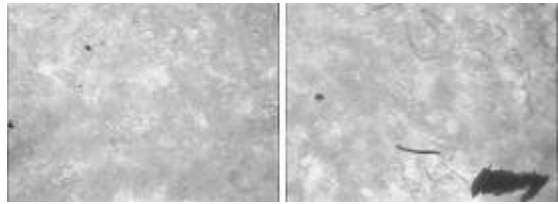
Figure. 5. Images from the Lambda microscope.

Two samples of the hydraulic fluid of the blue system exceeded the permitted values determined by the chemical analysis. It is necessary to make an immediate exchange regardless of the exchange interval (Fig. 6).
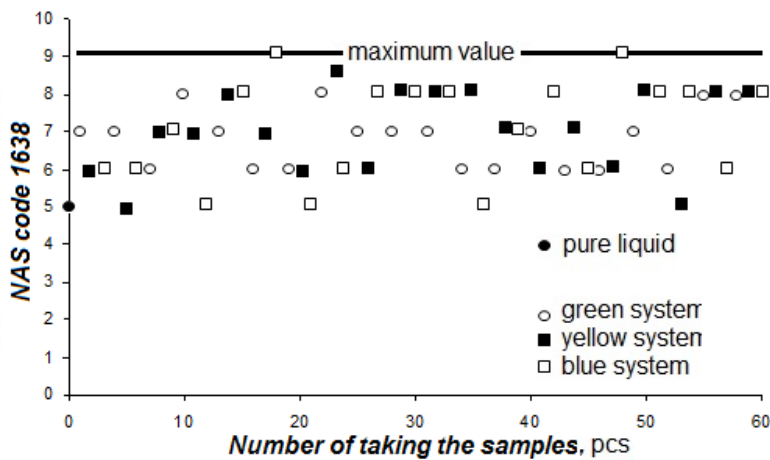
Figure 6. The trend of the cleanliness code.

It is important to analyze how much hydraulic fluids are added. The volume of the hydraulic fluid of the aircraft will be replaced in 13 months with the addition of 4 liters of liquid per month.

This may be one of the reasons why the fluid does not change. It is important to monitor and record the amount of liquid supplied. The analysis should be performed at least once every 6 months.

For economic evaluation, it is necessary first to quantify the price of filling of all hydraulic systems of the aircraft. The cost of one tank (0.946 liter) is 7.68 EUR. The total volume of fluid is shown in Table 4.

For a capacity of 53 liters, 56 tanks of a total value of EUR 430 are needed. The basic lack of control is that the costs of each fill are not recorded and the exchange date is not determined. For this reason, it is not possible to calculate the exact cost savings associated with the exchange. Replacement of filter inserts is also important. Increased replacement means increased wear and therefore

Table 4. The total volume of hydraulic fluid in A320

volume of the green system	23 L
volume of the yellow system	20 L
volume of the blue system	10 L
total volume	**53 L**

increased costs (Pexa et al., 2015; Pavlů et al., 2016). Another factor is downtime. By increasing the maintenance reliability, the back–ups to other lines can be used and downtime is shortened and costs will be saved. The measurement result can determine what is more cost–effective: changing the hydraulic fluid or introduces system monitoring and analysis. As a final consequence, the worst is the loss of prestige if the aircraft is shut down (Zhang et al., 2017).

CONCLUSIONS

Airlines have to take care of their fleet of transport aircraft at a very high level and take the highest safety.

Important factors in air transport are safety and reliability. Reliability is clearly the highest priority and costs are subject to this requirement. The measured values were evaluated and the procedure and interval of the hydraulic fluid change was designed. The exchange interval was set at 5 years. The limit of particle size was also identified. Immediate fluid exchange is required in this case.

The aim of the article was to determine the properties of the hydraulic fluid used in the A320 aircraft family, determine the interval of its exchange and create measurement methodology. The parameters analyzed where acid number, kinematic viscosity at 40 °C, density at 25 °C and cleanliness code. Based on the results, the following could be concluded. The average acid number was 0.41 mg KOH g^{-1}. The acid number increases by exploitation of the liquid and decreases by the fluid supply. The acid number limits are satisfactory. The average kinematic viscosity value was 6.67 $mm^2 s^{-1}$. Different liquids or higher water content influences kinematic viscosity. The standard limit of the kinematic viscosity can be reduced to 12 $mm^2 s^{-1}$ and optimal operation will still be ensured. Adjusting maximum density is also possible. According to the measured values, the interval may range from 990 to 1,020 kg m^{-3}.

Two samples of the hydraulic fluid from the blue system exceeded the allowed values determined by the chemical analysis and it is necessary to make an immediate exchange regardless of the exchange interval.

REFERENCES

Airbus S.A.S 2008 [online], [cit.2017–12–11]. Available at: http://www.airbus.com/en/aircraftfamilies/a320/
Aleš, Z., Pavlů, J., Svobodová, J. & Pexa, M. 2016. Use of Microscopy for Morphology Analysis of Wear Particles Generated in the Fuel Systems of Internal Combustion Engine, *Manufacturing Technology* **16**(5), 849–853.
Aleš.Z, Pexa, M. & Pavlů, J. 2012. *Tribotechnical diagnostics of agricultural machines*, Engineering for Rural Development conference Jelgava, 24.–25.05.2012, [online]. [cit.2014–05.01] Available at www: http://www. http://tf.llu.lv.
ASTM D974 Standard Test Method for Acid and Base Number by Color-Indicator Titration [online], [cit.2018–12–02]. Available at: http://www.ns-aria.com/wp-content/uploads/2015/09/ASTM-D974.pdf

EN ISO 3104 Petroleum products–Transparent and opaque liquids–Determination of kinematic viscosity and calculation of dynamic viscosity [online], [cit.2018–12–02]. Available at: https://www.iso.org/obp/ui/#iso:std:iso:3104:ed-2:v1:en

EN ISO 3675:1998 Crude petroleum and liquid petroleum products–Laboratory determination of density–Hydrometer method [online], [cit.2018–12–02]. Available at: https://www.iso.org/standard/26326.html

ExxonMobil [online], [cit.2017–12–11]. Available at: https://www.exxonmobil. com/english–US/Aviation/pds/GLXXHyJet–IVA–plus

Hönig, V. 2015. Morphological Classification of Nonferrous Wear Particles in Engine Oil Using Pherrographical Method. *Manufacturing Technology* **15**(4), 530–534.

Hönig, V. & Hromádko, J. 2014. Possibilities of using vegetable oil to power diesel engines as well as their impact on engine oil. *Agronomy Research* **12**(8), 323–332.

Hönig, V., Miholová, D. & Orsák, M. 2014a. Measurement of Wear Metals in Engine Oils by Atomic Absorption Spektrometry Method. *Manufacturing Technology* **14**(3), 317–322.

Hönig, V. & Orsák, M. 2016. Wear of Engine Oils Using Gaseous Fuels. *Manufacturing Technology* **16**(5), 923–927.

Hönig, V., Smrčka, L. & Horníčková, Š. 2014b. Application of discriminant analysis in monitoring the wear particles in the engine oil. *Manufacturing Technology* **14**(3), 322–326.

Lufthansa Training Manual: ATA 29 Hydraulic Power [online], [cit.2017–12–11]. Available at: https://www.metabunk.org/attachments/docslide–us_a–320–engine–pdf.16733/

Mihalčová, J. & Hekmat, H. 2008. Tribotechnical Diagnostics in Waste Oil Operation I. Methods of Evaluation of Wear Particles in Oils, *Chemické listy* **102**, 358–362 (In Czech).

Parker.com [online], [cit.2018–12–02]. Available at: http://www.parker.com/Literature/ EMHFF/ConMon/Guide%20to%20Contamination%20Standards.pdf

Pavlů, J., Hönig, V., Aleš, Z. & Chotěborský, R. 2016. Tribodiagnostic Analysis of Motor oil after Failure of Turbocharger of Combustion Engine. *Manufacturing Technology* **16**(5), 1115–1122.

Pexa, M., Aleš, Z., Pavlů, J. & Čedík, J. 2015. Analysis of Wear Particles Morphology of Machine Parts Based on Aluminium. *Manufacturing Technology* **15**(4), 664–670.

Planes.CZ, [online], [cit.2017–12–11]. Available at: http://www.planes.cz

Veselá, K., Pexa, M. & Mařík, J. 2014. The effect of biofuels on the quality and purity of engine oil. *Agronomy Research* **12**(2), 425–430.

Zhang, C.R., Xie, F.R., Huang, K., Wu, T. & Liang, Z. 2017. MIP models and a hybrid method for the capacitated air-cargo network planning and scheduling problems. *Transportation Research Part E–Logistics and Transportation Review* **103**, pp. 158–173.

Sapropel processing approaches towards high added-value products

V. Obuka[1], M. Boroduskis[2], A. Ramata-Stunda[2], L. Klavins[1] and M. Klavins[1,*]

[1]University of Latvia, Department of Environmental Science, Raina Blvd. 19, LV-1586 Riga, Latvia
[2]University of Latvia, Faculty of Biology, Raina Blvd. 19, LV-1586 Riga, Latvia
*Correspondence: maris.klavins@lu.lv

Abstract. Sapropel is an organic sediment from fresh water bodies that is widely distributed in the northern regions of the world. The distribution and unique properties of sapropel make it an important natural resource that can be used in agriculture, horticulture, forestry and farming directly as obtained. The aim of this study was to investigate the extraction possibilities of sapropel and potential applications of its extracts. Humic substances constitute an important ingredient of sapropel, and they can be extracted by mild alkaline extraction. Humic substances from peaty sapropel have significant differences in composition and properties, thus demonstrating the impact of precursor biological materials on the properties of humic substances formed in the humification process.

Key words: sapropel, extraction, agriculture, humic substances, biological activity.

INTRODUCTION

Sapropel (gyttja) is the bottom deposits of fresh water bodies. It contains more than 15% organic matter and, thus, is a partially renewable geological resource found in inland waters or under bogs. Sapropel is formed from the residues of algae, plankton and benthic organisms, although terrestrial vegetation can also contribute to its development (Niessen & Sturm, 1987). Depending on the composition and properties of sapropel and the availability of resources, it can be used in a number of areas, such as agriculture, medicine, veterinary medicine, construction, livestock farming, balneology and cosmetic applications.

Sapropel consists of three main components that interact with each other: organic and mineral elements as well as living organisms. The average elemental composition of the organic matter of sapropel (%) is: C 60.0, H 6.0, N 2.5, O 35.0 (Poznyak & Rakovskiy, 1962). The nitrogen content of sapropel is not directly related to its mineralisation degree (Braksh, 1971); in different types of sapropel, it ranges from 2.7% to 6% of organic substances and 0.5% to 4.0% of dry weight (Ponomareva, 2002).

Sapropel contains various groups of chemical compounds (Poznyak & Rakovskiy, 1962): a) bitumens, b) water-soluble substances, c) easily hydrolysable substances (including humic and fulvic acids), d) cellulose, e) non-hydrolysable substances.

Comparing the groups of chemical compounds in sapropel, it was established that the groups of substances (humic acids, non-hydrolysable substances, etc.), according to their chemical nature from different sites, are not identical and depend on the properties of sapropel-forming organisms (plankton, vascular plants, humic substances) and their transformation conditions (Braksh, 1971). Bitumens (lipids) are organic substances that are extracted from sapropel with a variety of organic solvents. The composition of bitumen is characterised by fatty acids, steroids, carotenoids, paraffin, wax and glycerol content (Orlov et al., 1996).

The bitumen components of sapropel attract particular attention, because they have a high bactericidal, bacteriostatic and antioxidant activity. Several studies have focused on the easy and efficient methods to obtain these substances from sapropel (Kireycheva & Khokhlova, 2000; Shinkarev et al.,2000). The bitumen content in sapropel is 2–7% of the organic mass (Lopotko et al., 1992). Moreover, when using a gasoline and alcohol-benzene mixture for extraction, even ~10% of bitumens were obtained (Poznyak & Rakovskiy, 1962).

Sapropel is characterised by low carbohydrate content, because active decomposition of carbohydrates to carbon dioxide and humification (formation of humic substances in the reactions of amino acid condensation) take place during the formation of sapropel. The average content of hemicellulose in the organic matter of sapropel is 6–25%, of cellulose – 1–8% (Pidoplichko & Grishchuk, 1962). The components of sapropel contain an average of 1–2% cellulose. The carbohydrate complex of sapropel, in turn, consists of $\geq 80\%$ of hemicellulose (Lopotko et al., 1992).

The water-soluble vitamins have also been found in sapropel, including ascorbic acid (C) and B group vitamins: thiamine (B1), riboflavin (B2), pantothenic acid (B5), pyridoxine (B6), folic acid (B9) and cyanocobalamin (B12). Large quantities of fat-soluble vitamins – tocopherol (E) and vitamins D and P – have also been found (Shtin, 2005).

The composition and properties of humic substances in sapropel are determined by its key features like biological activity, biochemical stability, binding ability, etc. They contain humic acids, fulvic acids and humine. The humic substances in sapropel differ from those in soil. The former have a higher carbon/hydrogen ratio and have no saturated aromatic rings (Orlov et al., 1996). They are also more reduced and possess a greater activity than the humic substances in soil.

Humic substances are commonly extracted from the minerals and organic compounds in sapropel following the classical scheme of Tyurin, which he used for soils (Orlov et al., 1996). Humic acids make the largest group of organic substances, and they are usually extracted from sediments with alkaline solvents and precipitated into an acid environment (pH 1–2).

Although this method is simple in use, it does not provide for a complete extraction of all low-molecular-weight components (carbohydrates, alcohols, amino acids); therefore, depending on the investigated material and purposes, this scheme is often modified (Karpukhin, 1998; Kireycheva & Khokhlova, 2000).

The aim of this study is to investigate the extraction possibilities of sapropel in respect to the potential applications of sapropel extracts.

MATERIALS AND METHODS

Sapropel samples were taken from Lake Pilvelis in Latgale region, Latvia. The samples were obtained with an Eckman drag and stored at 4 °C until analysis. Identification of the type sapropel and its biological analysis were done by a microscope (400–1,000 magnification), using known methods (Bellinger & Sigee, 2011). The loss-on-ignition was determined by heating sapropel samples at 550 °C and 950 °C (Heiri et al., 2001).

Preparation of the extracts of sapropel

A 5.00 g sample of dried (at 105 °C to constant weight) sapropel in a 120 mL flask was extracted for 24 hrs on a shaker (Bio San PSU-20, Latvia) with NaOH and KOH solutions at the concentrations of 0.1%, 0.5%, 1%, 2%, 4% and 8%. After treatment, the extracts were filtered, and sorption at 410 nm was measured (Hach Lange DR 2800). The extract was acidified with conc. HCl to pH 2 and filtered after 24 hrs to estimate the concentrations of humic acids (precipitate) and fulvic acids (soluble phase). A calibration graph was accordingly drawn, using the reference humic and fulvic acids. The ratio of the humic and fulvic acid yield was calculated as a dry weight (in mg) ratio. Treatment with ultrasound was done using 0.27 kW and 3 kW ultrasound baths, respectively.

Characterisation of sapropel extracts

The Fourier transform infrared spectra (FTIR) were obtained on a Nicolet AVATAR 330. The elemental composition (C, H, N, S) of humic substances in sapropel was determined using an Elemental Analyzer Model EA-11008. The concentration of total polyphenolics was determined by the Folin-Ciocalteau colorimetric method (Siriwoharn et al., 2004). The radical scavenging activity was determined using 2,2-diphenyl-1-picrylhydrazyl (DPPH) (Aldrich). The mixture was incubated for 20 minutes in a dark place at room temperature. The absorption was measured in a quartz cuvette (d=1 cm) with a spectrophotometer (Hach-Lange DR 2800) at a 517 nm wavelength. Three parallel measurements were made. The radical scavenging activity was expressed in millimoles of Trolox equivalent in respect to 1 gram of dry extract mass (mM Trolox eq/g) (Siriwoharn et al., 2004). The metal-binding capacity of the sapropel extracts was estimated potentiometrically using a Cu^{2+} ion selective electrode (Shi et al., 2018). 5 mg samples of the humic substances of sapropel and a 20 mL solution containing 1–100 mg L^{-1} Cu^{2+} were added into a 50 mL centrifuge tube and shaken at 200 rpm overnight. The concentrations of Cu^{2+} in the solutions were measured by a ion-selective electrode, and the absorption capacities were calculated as differences between the initial and equilibrium concentrations of metal ions per gram of humic acid.

RESULTS AND DISCUSSION

According to the pollen analysis, the studied samples of sapropel are rich in *Betula* (up to 42%), *Pinus* (26%) and *Picea* pollens. The share of cultivated plants, such as *Secale cereale*, in the area reach about 1.5%. The dominant species of macrofossils include *Potamogeton natans, Nymphaea alba* and *Characeae. Daphnia* and *Bryozoa* occurred in small quantities. The organic matter of gyttja in Lake Pilvelis is characterised

by low content of carbon (45%) and high content of oxygen (48%), nitrogen (2.5%) and hydrogen (5.3%). According to sediment types, the studied samples belong to peaty sapropel. The loss-on-ignition analysis indicates that the organic matter in sapropel makes 82.86%, mineral matter – 15.94%, and carbonates – 1.18% (on dry matter basis). The pH of sapropel samples is nearly neutral – 7.19.

Humic substances belong to the group of substances that influence the application possibilities of sapropel extracts. Alkali metal hydroxides have traditionally been used for the extraction of these substances. As demonstrated in Fig. 1, extraction with KOH gives significantly higher yields in comparison with NaOH.
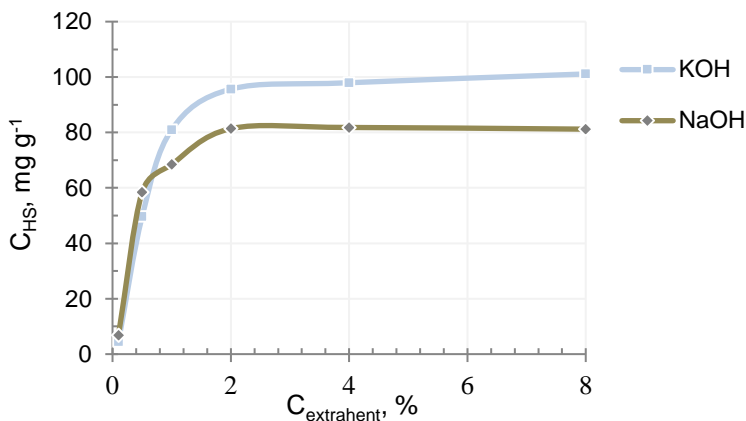
Figure 1. Yields of humic substances obtained from sapropel depending on the type and concentration of an extrahent.

An important parameter influencing the properties of sapropel is the relation (ratio) between humic and fulvic acids (Fig. 2). Humic acids dominate in the studied sapropel samples. However, when the extraction is done with concentrated alkali solutions, the HA/FA ratio is likely to decrease as a result of destruction of humic acids and reduction in their molecular mass (transformation of humic acids into fulvic acids).
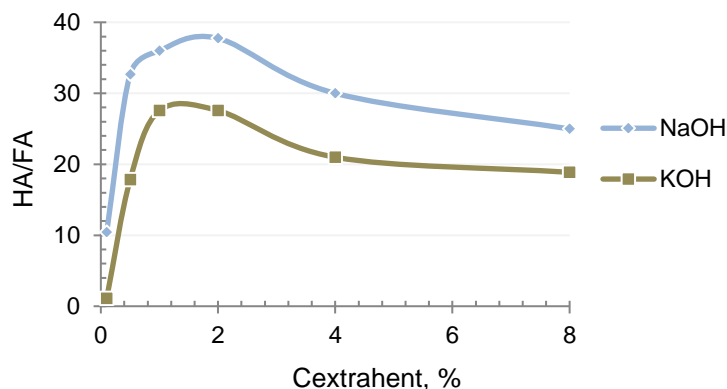
Figure 2. Changes in the humic acid/fulvic acid ratio depending on the extrahent concentration and type.

An important parameter influencing the properties of sapropel is the relation (ratio) between humic and fulvic acids (Fig. 2). Humic acids dominate in the studied sapropel samples. However, when the extraction is done with concentrated alkali solutions, the HA/FA ratio is likely to decrease as a result of destruction of humic acids and reduction in their molecular mass (transformation of humic acids into fulvic acids).

A major factor influencing the extraction efficiency is the intensity of treatment during the extraction process. While maceration gives low yields of extracts, intensive treatment with ultrasound, especially at a high power and additional heating, gives high yields. Notably, in the latter case, a possibly major factor contributing to the solubilisation of sapropel is the chemical and mechanochemical destruction of its detrital particles (Fig. 3). At the same time, the intensive extraction methods provide for high yields of extracts for diverse applications.
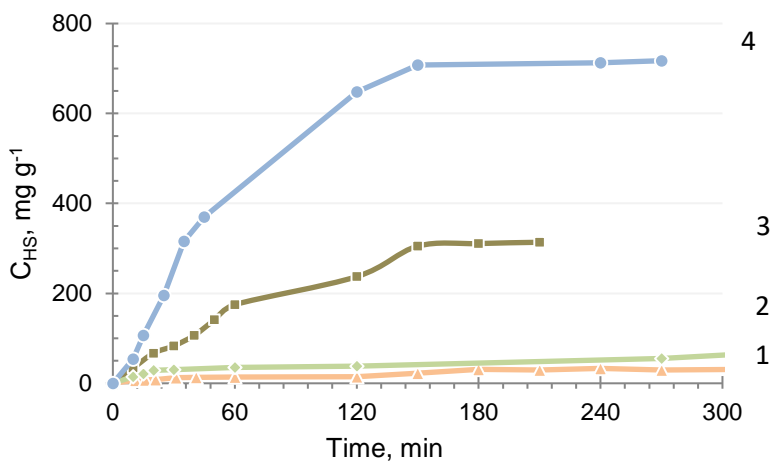
Figure 3. The impact of extraction methods on the yield of humic substances. 1 – maceration; 2 – shaking (140 rpm); 3 – treatment with ultrasound (0.27 kW); 4 – treatment with ultrasound (3 kW) and heating (80 °C).

The obtained extracts were characterised by their elemental composition: C 54.02–54.87%, N 2.01–4.07%, H 4.87–6.54%, O 38.10–42.48%, S traces. The loss-on-ignition analysis shows that the obtained sapropel extracts fully consist of organic matter (98.72%). The concentration of nitrogen in the sapropel extracts can be considered as high and might support the application of such extracts in agriculture.

The FTIR spectra of humic and fulvic acids in sapropel can be split by regions, depending on the informativity and the presence of important functional groups. The absorption bands in the spectral region of $3,600–2,800\ cm^{-1}$ are very broad. The absorbance in this spectral region is determined by the presence of -OH groups. Sorption at the wavelengths of $2,950$ and $2,850\ cm^{-1}$ identifies the presence of CH_3- and CH_2-groups. Typical intensive sorption lines are common for the region around $1,700\ cm^{-1}$ $(1,725–1,700\ cm^{-1})$, which is characteristic for carbonyl groups in aldehydes, ketones and carbonic acids. The actual sorption maximum greatly depends on the conjugation degree, presence of substituents, and hydrogen bonding. In the spectral region of $1,690–1,500\ cm^{-1}$, it is possible to identify the sorption maximum of amide bonds (1,620–

1,640 cm^{-1} and 1,550–1,540 cm^{-1}). In the region of 1,625–1,610 cm^{-1}, the sorption indicates the presence of aromatic C = C and carbonyl groups, and hinones. At the wavelengths of 1,470–1,370 cm^{-1}, there are bands typical for C-H and O-H bonding and sorption maximums typical for C-O. For wavelengths below 1,000 cm^{-1}, fingerprint patterns are evident. The sorption in this spectral region provides information about a possible role of the share of carbohydrates in the structure of humic molecules. Sorption at 1,080 cm^{-1} shows the OH deformation or C-O stretch of phenol and alcohol OH groups, and 1,040 cm^{-1} indicates the C-O stretch of polysaccharide components. The major differences between humic and fulvic acids are visible at the signals of 1,590–1,700 cm^{-1} and 1,125–1,045 cm^{-1} and are related to the differences in the number of carboxylic groups and organic amides, as well as carbohydrates. The FTIR spectra demonstrate the presence of a high number of different oxygen-containing functional groups.
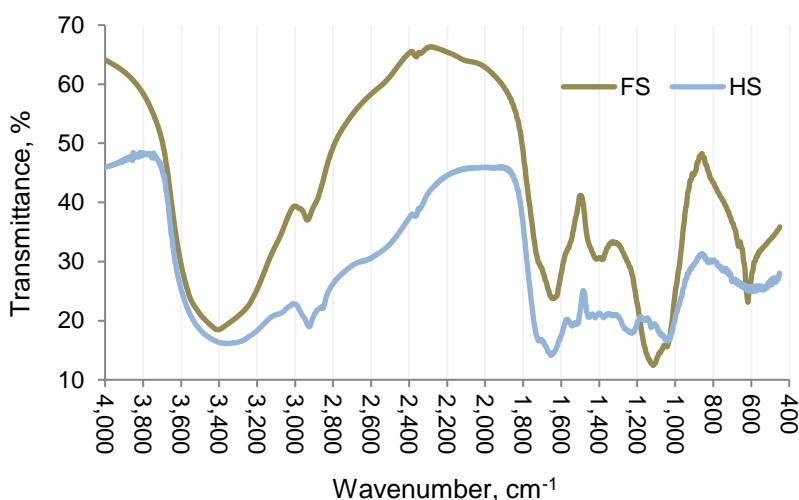
Figure 4. The Fourier transform infrared spectra of the humic (HS) and fulvic (FS) acids in sapropel.

An important characteristic of the extracts of sapropel is their ability to scavenge free radicals. For the analysis of the radical scavenging activity, we used the stable free radical DPPH, which has an intense purple colour that can be measured spectrophotometrically. In the presence of compounds that are capable of either transferring an electron, or donating hydrogen, DPPH will become discoloured. In this fashion, the change in DPPH absorbance after the addition of a test material is often used as an indicator of the antioxidant capacity of the material. The extracts of sapropel have a relatively high radical scavenging activity (7.17–13.20 mM Trolox eq g^{-1}). The detected radical scavenging activity of the extracts of sapropel can be compared with that of ascorbic acid (Vitamin C, a well-known antioxidant): 13.9 ± 0.7 7.17–13.20 mM Trolox eq g^{-1}; cranberry extracts: 15.5 ± 0.8 7.17–13.20 mM Trolox eq g^{-1}. The radical scavenging activity of sapropel extracts is much higher than the activity of humic substances extracted from peat (0.2–3.1 mM Trolox eq g^{-1}) or soil

(1.8–2.2 mM Trolox eq g^{-1}), indicating a possible field of application of sapropel extracts as antioxidants in cosmetics and biopharmacy. The total concentration of polyphenolics in sapropel extracts is between 0.67 and 1.03 mg gallic acid equivalent/g of extract and so can be considered as high, at least compared to peat humic acids, where the concentration of polyphenolics is significantly lower (0.02 mg gallic acid equivalent g^{-1}).

An important parameter characterising humic substances is their metal-binding capacity (Evangelou et al., 2002; Shi et al., 2018). The maximum metal-binding capacity of humic substances in sapropel is 9.48 ± 0.12; and for fulvic acids – 12.21 ± 0.08 mM of Cu^{2+} g^{-1} humic substances. The metal-binding capacity for humic substances in sapropel detected in our study is higher than the values found in the literature describing the humic substances of other origins. The studied metal-binding properties of humic acids in sapropel indicate their application potential for detoxification (metal binding). Other potential contributions could be for the use of sapropel extracts in agriculture (possibilities of use in metal-contaminated soils), cosmetics and biopharmacy (metal binding).

CONCLUSIONS

Sapropel is an organic sediment from fresh water bodies and is widely distributed in the northern regions of the world. The aim of the study was to investigate the extraction possibilities of sapropel and potential applications of its extracts. An important ingredient of sapropel is humic substances, and they can be extracted by mild alkaline extraction. The humic substances from peaty sapropel demonstrate significant differences in composition and properties from the humic substances of other origins (peat, soil, etc.), thus indicating the impact of precursor biological material on the properties of humic substances formed during the humification process. The alkali extracts of sapropel samples from a Latvian lake were studied. The solution of potassium hydroxide at a concentration not exceeding 2 wt% extracted the coloured humic substances more completely than the solution of sodium hydroxide. The maximum extraction was determined as 100 mg g^{-1}. Treatment with ultrasound (at 3 kW) and heating (at 80 °C) enhanced the extraction up to 700 mg/g. The scavenging activity of the prepared extracts was determined as the reaction of inhibition of the generation of radicals by DPPH. The humic substances in sapropel have a significant radical scavenging activity and a distinct metal-binding capacity. Therefore, the extraction of sapropel can contribute to the development of high added-value products with diverse application possibilities.

REFERENCES

Bellinger, E.G. & Sigee, D.C. 2011. Freshwater Algae: Identification and Use as Bioindicators. Chichester: Wiley, 265 pp.

Braksh, N. 1971. *Sapropel sediments and application possibilities*. Zinatne, Riga, 282 pp. (in Russian).

Evangelou, V.P., Marsi, M., Chappell, M.A. 2002. Potentiometric-spectroscopic evaluation of metal-ion complexes by humic fractions extracted from corn tissue. *Spectrochimica Acta PtA* **58**, 2159–2175.

Heiri, O., Lotter, A.F. & Lemcke, G. 2001. Loss on ignition as a method for estimating organic and carbonate content in sediments: reproducibility and comparability of results. *Journal of Paleolimnology* **25**, 101–110.

Karpukhin, A. 1998. Complex Compounds of Humic Substances with heavy Metals. *Eurasian Soil Science* **31**(7), 764–771.

Kireycheva, L. & Khokhlova, O. 2000. The elemental composition of sapropel humic substances. *Soil Science* **9**, 1–376 (in Russian).

Lopotko, M., Yevdokimova, G. & Kuzmitskiy, P. 1992. *Sapropelits in agriculture*. Science and Technology, Minsk, 1–215 (in Russian).

Niessen, F. & Sturm, M. 1987. Die Sedimente des Baldeggersees (Schweiz): Ablagerungsraum und Eutrophierungsentwicklung der letzten 100 Jahre. *Archiv für Hydrobiologie* **108**, 365–378.

Orlov, D., Biryukova, O. & Sukhanova, N. 1996. Soil organic matter of the Russian Federation. *Soil Science* **2**, 197–207 (in Russian).

Pidoplichko, A.P. & Grishchuk, R.I. 1962. Certain Results of research of Belarussian SSR sapropel deposits. *Chemistry and genesis of peat and sapropel*, 258–274. (in Russian).

Ponomareva, M.A. 2002. *Chemical composition and application of sapropel in Tatarstan.* Doctoral Thesis. Tula State Pedagogical University, Tula, 245 pp. (in Russian).

Poznyak, V. & Rakovskiy, V. 1962. The chemical composition of the organic mass of Byelorussian SSR sapropel. *Chemistry and genesis of peat and sapropel,* 298–308. (in Russian).

Shinkarev, A., Lyutakhina, N. & Gnevashov, S. 2000. Separation of the Groups of Humic Substances Upon Recurrent Treatment with Solvents. *Eurasian Soil Science* **33**(7), 709–712.

Siriwoharn, T., Wrolstad, R.E., Finn, C.E. & Pereira, C.B. 2004. Influence of cultivar, maturity, and sampling on blackberry (*Rubus* L. Hybrids) anthocyanins, polyphenolics, and antioxidant properties. *Journal of Agricultural and Food Chemistry* **52**(26), 8021–8030.

Shi, W., Lu, C., He, J., En, H., Gao, M., Zhao, B., Zhou, B., Zhou, H., Liu, H. & Zhang, Y. 2018. Nature differences of humic acids fractions induced by extracted sequence as explanatory factors for binding characteristics of heavy metals. *Ecotoxicology and Environmental Safety* **154**, 59–68

Shtin, S.M. 2005. *Lake sapropel and their complex development.* MSMU, Moscow, 373 pp. (in Russian).

Comparison of predicted and real parameters of PV systems in the Czech Republic and Spain

T. Olšan[1], B.M. Soucase[2] and M. Libra[1]

[1]Czech University of Life Science, Kamycka 129, CZ16521 Prague, the Czech Republic
[2]Universitat Politecnica de Valencia, Camino de Vera, Applied Physics, ES46022 Valencia, Spain
*Correspondence: tolsan@email.cz

Abstract. This paper compares predicted performance by a simulation software for a given new constructed PV system of crystalline silicon technology located in Prague with 10 kWp peak power and a similar system in Spain. Simulation software used for the sake of this paper was publicly available PVGIS from the website of its creators, parameters were set to be the same like in the real PV system. The difference between the predicted and the real data was calculated and then discussed in the result section of this paper. Suggestion how to increase the accuracy of the prediction by the simulation software is in the discussion part of this paper.

Key words: PV systems, PVGIS, PV simulation, predicted and real data comparison.

INTRODUCTION

The European Union wants to have 20% of their energy demand covered by the renewable sources by the year 2020. This plan was proposed in 2008. Different countries have different goals, for the Czech Republic that goal is 13% of renewables by the year 2020 and for the Spain that goal is 20% by the same year.

To reach this goal, several countries in EU started subsidy policy on renewables to increase the demand for renewable sources, so renewable sources will be more affordable. This resulted in solar and wind industry boom in those countries with this policy, including both Spain and the Czech Republic. Thanks to this, the Czech Republic already fulfilled its goal in 2014 when renewables covered 13.4% of energy demand. But this subsidy policy was later cancelled in both the Czech Republic and Spain.

In the case of the Czech Republic, the return of investment into photovoltaic (PV) systems was around 7 years when the subsidy policy of government guaranteed the higher price for an electricity generated and then distributed to a grid by a renewable source. Subsidy policy ended in the Czech Republic on 1.1. 2011 and ever since new PV systems were mainly small rooftop installations.

With some of the advance in PV technology, increased lifespan and especially increased the efficiency of PV cells, solar panels will be again interesting technology to invest in on a big scale as far north as the Czech Republic even without subsidy from the government. Therefore, it is helpful to have a software to predict a performance of a PV system and so return of investment.

There are more PV simulations available online for free, namely PVGIS, RETSCreen, and PVWatts. Tho PVGIS design is plain and it can appear difficult for the beginners to use, it provides the best yearly estimate (Psomopoulos et al., 2015). These simulations can be used to predict the performance of the PV systems in the long run, one way how to predict weather pattern in a short term is described in (Rezk et al., 2015).

Such a prediction can be not only useful to help reach certain environmental goals but it is also important for developing countries who struggle to supply electricity in the remote areas to see if its economically viable to build off grid solar power plants in these areas (Ajan et al., 2003). A case study of a PV system in Ivory Coast is done in (Guaita-Pradas, Soucase & Aka 2015). A comparison of PV system cost and payback time in India and Pakistan is in (Guaita-Pradas, Ullah & Soucase, 2015). Comparison of return of investment of the PV power plants in Germany, Spain and Morocco is in (Guaita-Pradas & Soucase, 2014a), due to the subsidy policy in Spain and low cost of electrical energy in Morocco it is actually Spain with the shortest return of investment, also called the internal rate of return.

MATERIALS AND METHODS

PVGIS software used for comparison of real and predicted data is available for free on the website: http://re.jrc.ec.europa.eu/pvgis/apps4/pvest.php?lang=en&map=europe.

This website provides several options for calculations: PV estimation, monthly radiation, daily radiation and stand-alone estimation. This paper focuses on PV performance estimation given by PVGIS software and its deviation from real PV systems with same parameters. PVGIS software can give the prediction for the area of Europe, Asia, and Africa.

PVGIS software can generate a lot of useful information for potential investor given some necessary information about intended project such as installed peak PV power, used PV technology (the most common one is crystalline silicon), estimated losses, radiation database (there are 2 options, one based on ground measurement and other based on satellite data), inclination and orientation of PV system. This paper deals only with PV estimation option from above-mentioned website.

PVGIS software takes into the account losses of the PV system. Estimating losses due to the soiling, aging and degradation of materials are given in (Thevenard & Pelland, 2011). Estimating losses thanks to the shading are given in (Nguyen & Pearce, 2012). Accuracy of the old and new solar irradiance database available in the PVGIS software is discussed in (Huld et al., 2012).

PV systems from two sites were chosen for the comparison, one in Prague in the Czech Republic and one near Valencia in Spain. In both cases we calculate the electricity production by using PVGIS software and then this output is compared with actual production data measured in situ.

PV SYSTEM IN THE CZECH REPUBLIC

The first PV system is located in Prague in the Czech Republic. PV system in Prague is located on the campus of CULS university in the roof of Engineering faculty in the northwest part of Prague. It is facing the southeast. Installation of this free-standing polycrystalline PV system is showed on Fig. 1.

Figure 1. PV system in Prague.

It's installed peak power is 10 kWp, the inclination is 35° and its technology is crystalline silicon. This installation cost around 11,000 €s. The maintenance costs 12,960 czk per year or around 480 €s per year. All these parameters are showed on Fig. 2 along with interface of PVGIS online tool. Losses were set to 0% because it is a brand new PV installation, total losses were 11%. The position of this installation is 50°7′42′′ latitude and 14°22′26′′ longitude.
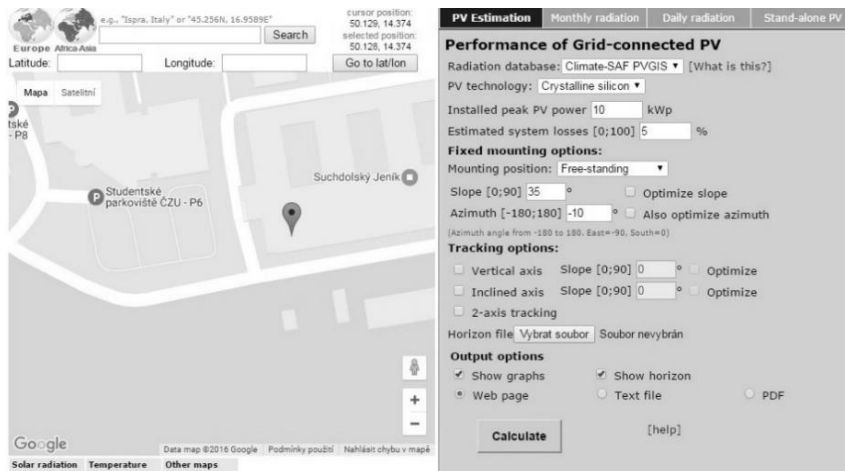
Figure 2. GUI of PVGIS with parameters for PV installation in Prague.

The output of PVGIS is in the form of pdf file or as a web page, it will generate the PV estimate in kWh per month, irradiation estimate in kWh sqm^{-1} per month and graph of horizon height in the summer and the winter solstice. The graph with the PV estimation is showed on Fig. 3. Total electricity production was estimated to 10,700 kWh. Currently, the price for 1 kWh generated by renewable resource on the market is same as for any other source, 3,4 czk for 1 kWh, that is around 13 € cents. According to this estimation, one year would yield the income of 1,445 €, the cost of the whole PV installation without the cost of maintenance would be pay off after less than 7 years and 8 months. However, data from the PV installation for the first year actually shows that electricity production was 11,881 kWh, therefore first year yields around 1,533 € of income and whole installation without the cost of maintenance will be payed off in 7 years and 3 months. If we consider the cost of the maintenance for 480 € per year (plus 3% inflation rate), than the whole PV system in Prague with the maintenance will be pay off in 10 years but that is only if the revenue will be each year the same (plus 3% of inflation rate).
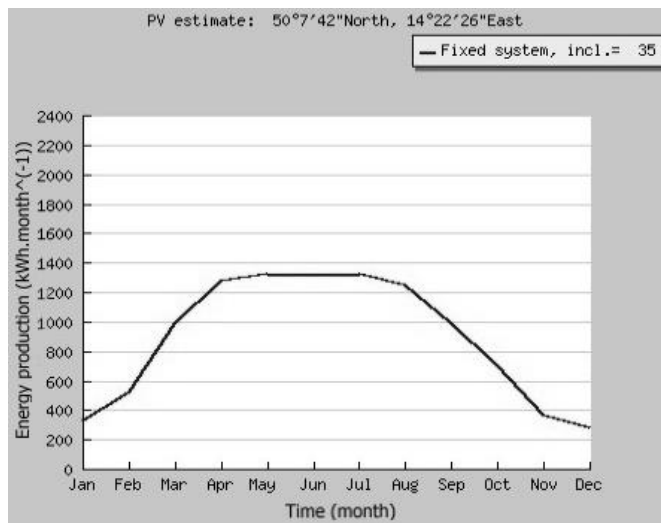
Figure 3. PV estimate for installation in Prague on the CULS campus.

The estimated irradiation is showed on Fig. 4. PVGIS can also calculate the horizon of the selected place but that is not important for this article. The irradiation is based on a database and currently an user of PVGIS can choose between older database which was based on a data collected in a ground stations between 1981–1990 or a new database that uses data from Meteosat satellites.

These calculations are compared with real data from PV installation in the northwest Prague in the CULS (Czech University of Life Sciences) campus.
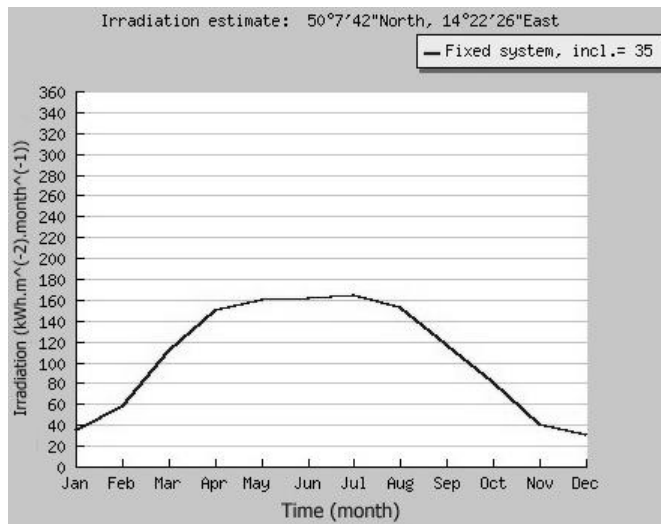
Figure 4. Irradiation estimate for Prague.

All predicted values by PVGIS in kWh per month are in the Table 1 along with the available real data.

Table 1. Generated electricity in kWh and estimate for each month

	Prague – estimated Em (kWh)	Prague – real Em (kWh)	Difference (%)
Jan.	343	358	-4.2
Feb.	551	559	-1.4
Marc.	1,030	873	17.9
Apr.	1,350	1,250	8
May	1,400	1,575	-11.1
Jun.	1,390	1,461	-4.9
Jul.	1,380	1,499	-8
Aug.	1,310	1,493	-12.3
Sep.	1,040	1,323	-21.4
Oct.	741	542	36,7
Nov.	382	554	-31
Dec.	294	394	-25.4
Aveg.	935	990	-5.6
Sum	11,200	11,881	-5.7

PV SYSTEM IN SPAIN

The second PV system is located in Spain in a moderate size city Ontinyent with 100,000 inhabitants located about 80 km south of Valencia. This PV system with polycrystalline technology was connected to grid in November 2011 when there was a governmental subsidy policy in Spain similar to that one in the Czech Republic where the owner of PV system has a guaranteed price for 1 kWh over a long time. In the case of Spain, the prime for the energy production was set at 0.28 € kWh^{-1} and this price will remain fixed for the next 25 years.

The PV system is facing directly towards the south and has the inclination of 35°. This PV system is divided into 4 parts across the whole city with total installed power of 255.3 kW. Because it was built earlier, the price for 1 installed Watt was around 1.8 € (Standard prices in 2011). The cost of this whole PV system was then about 459,540 €. One part of it has an 115.92 kW installed power and its located on the roof of Colegio Público Rafael Juan Vidal. The satellite picture of this place is on Fig. 5.
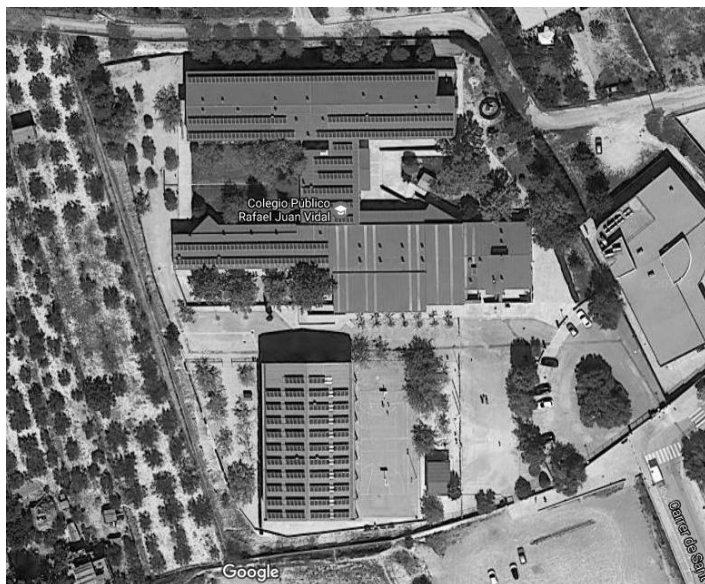
Figure 5. Picture of the PV system in Ontinyent from Google Maps.

Because the system was connected to the grid at the end of 2011 and the year 2017 is not over yet, all calculations are cumulative for five consecutive years from 2012 till 2016. In Table 2 is data from these five years along with estimate from PVGIS, the difference between the two and also losses that were set in PVGIS.

Table 2. Yearly yield of PV system in Ontinyent and estimate by PVGIS with losses

Year	Estimated Em (kWh)	Real Em (kWh)	Differ. (%)	Losses (%)
2012	392,000	392,542.02	-0.14	14.50
2013	392,000	392,731.00	-0.19	14.50
2014	388 000	388,363.00	-0.09	15.50
2015	381,000	380,902.00	0.03	17.00
2016	372,000	371,337.30	0.19	19.00

This PV system was built when the Spanish government was subsiding the renewables and so it has the guaranteed price of 0.28 € for 1 kWh for 25 years. The policy of Spanish government changed since then and the prefeairibility of the investment into PV power plants after the change of the subsidy policy is discussed in (Guaita-Pradas & Soucase, 2014b). In last two months of 2011 when this PV system was operational, the revenue was 8,452 €. For each year the calculation assumes 3% inflation rate and also 9% of revenue will go for the insurance and the maintenance. The cost of

the whole PV system was about 459,540 € and for two months of 2011 and five years between 2012–2016 the net revenue of this PV system was 513,357 € while according to the PVGIS it should be a little smaller at 512,896 €, the difference is less than 0.05%. So the PV system is Spain was already payed off in 4 years and 8 months. As can be seen from Table 2 PVGIS is quite good at predicting the revenue from a given PV power plant over whole year but not for each month which was the case of Prague. The difference for one month varied widely over the year in the case of Prague, between – 25% to + 37%. But in the case of Ontinyent in Spain, the estimate only varied less than 0.2%. In Table 3 there are some parameters for both PV system in Prague and Ontinyent.

Table 3. Production data related to both PV installations

PV installation	PV peak power (kW)	Energy produced (kWh year^{-1})	Energy production/ Peak Power (kWh kW^{-1})	Irradiation (kWh m^{-2})	Income/ kWh (€ kwh^{-1})	Payback time (months)
Prague	10	11,881	1,188.1	1,250	0.13	120
Ontinyent	255.3	331,337.3	1,297.84	2,010	0.28	56

RESULTS AND DISCUSSION

As can be seen from Table 3, the PV system in Ontinyent performs better than the PV system in Prague as well its return of investment is much shorter. This can be due to several factors. Mainly orientation of the panels and the geographical position and thus the irradiation received by the panels of the PV power plant are two main factors for the energy production. In Table 4 there are data from the site in Ontinyent about energy production and open data from AEMET about rainfall in Xativa, a site that it's closest to this city in this open access database for possible influence on the energy production.

Table 4. Rainfall in Xativa near Ontinyent and energy production 2012–2016 in Ontinyent

Year	Energy produced (kWh year^{-1})	Yearly difference (%)	Rainfall (mm)	Yearly difference (%)
2012	392,542.02	-	415.8	-
2013	392,731.00	+ 0.05	307.6	-26.03
2014	388,363.00	-1.11	199.2	-35.25
2015	380,902.00	-1.93	355.4	+ 43.96
2016	371,337.30	-2.52	515.8	+ 45.13

Firstly, Ontinyent is in a souther position than Prague, Pragues has a latitude of 50°7′ while Valencia has a latitude of 39°28′, the difference is over ten degress. Prague also has a typical central European climate, in 2016 Prague had 590 mm of rainfall which was on 91% of a longterm average (Český hydrometeorologický ústav, 2017). While Ontinyent is less than 50 km away from the Mediterranean Sea and thus it has a weather close to that of a coastal cities. Valencia and Ontinyent also has on average less rainfall during a year, there was 67 rainy days with 518 mm of rainfall in 2016 in Valencia while there was 68 rainy days with only 404 mm of rainfall in 2015 in Valencia (AEMET OpenData, 2017). Less precipitation with a southern position in turn means more average yearly sun irradiation as can be seen from Table 3. In Table 4 there is a sum of energy

produced in a whole year for a period of time 2012–2016 in Ontinyent with data about rainfall in each year to see if the rainfall affects the production at this site. From 2013 onwards the production was dropping annually by 1–2% which is an average annually drop in the energy production for the PV panels thanks to aging or soiling of the panels. In this site, the PV panels are using polycrystalline technology which is less sensitive to the cloudy weather because these panels can easier absorpt the diffused solar radiation from clouds. Also, more rain occurs during winter months when the production is smaller than during summer months. Moreover, rain cleanes the panels from the dust and their production improves. The change in the rainfall doesn't affect the 1–2% drop in the production.

CONCLUSIONS

The PVGIS is good at predicting the revenue from a given PV power plant over whole year but not for each month which was the case of Prague. The difference for one month varied widely over the year in the case of Prague, between -37% to + 18%. But in the case of Ontinyent in Spain, the estimate only varied less than 0.2%.

The renewable energies are the main hope in substituting the current fossil based economy and their ecological impact is much lower than that of fossil energies. According to (Castro et al., 2013) the global electric power available from the solar energy in the 21st century can be around 2–4 TW while in the year 2013 there was only 0.008 TW of net average solar power production. Especially the countries with a lot of hours of sunshine during a year, like Spain, should be interested the most in the solar energy.

Both countries have a different conditions whenever it's a subsidy policy that supports the investments into the renewable energy sources or amount of irradiation received by a year in that country. However, in both cases, the PV power plant is actually profitable in a matter of few years.

The PVGIS can be used to produce estimate accurate enough for the investors who want to invest into PV power plants.

REFERENCES

AEMET OpenData [online]. 2017 [cit. 2017-06-14]. Available from: https://opendata.aemet.es/centrodedescargas/inicio

Ajan, Ch.W., Ahmed, S.S., Ahmad, H.B., Taha, F. & Zind, A.A.B.M. 2003. On the policy of photovoltaic and diesel generation mix for an off-grid site: East Malaysian perspectives. *Solar Energy* **74**, 453–467.

Castro, C. de, Mediavilla, M., Miguel, L.J. & Frechoso, F. 2013. Global solar electric potential: A review of their technical and sustainable limits. *Renewable and Sustainable Energy Reviews* **28**, 824–835.

Guaita-Pradas, I. & Marí Soucase, B. 2014a. Endorse of Renewable Energy Plants, Still An Alternative Investment in Spain? *SOP Transactions on economic research* **1**(2), 10.

Guaita-Pradas, I. & Marí Soucase, B. 2014b. Energy production in PV plants regarded as economic investments. An assessment for PV investments in Germany, Spain and Morroco. *Proceedings of Renewable and Sustainable Energy Conference* (IRSEC), 37–41.

Guaita-Pradas, I., Marí Soucase, B. & Aka, B. 2015. Energy production and financial analysis of photovoltaic energy plants in Ivory coast. *Africa science* **11**(2), 24–34.

Guaita-Pradas, I., Ullah, S. & Marí Soucase, B. 2015. Sustainable Development with Renewable Energy in India and Pakistan. *International Journal of Renewable Energy Research* **5**(2), 575–580.

Huld, T., Müller, R. & Gambardella, A. 2012. A new solar radiation database for estimating PV performance in Europe and Africa. *Solar Energy* **86**, 1803–1815.

Nguyen, H.T. & Pearce, J.M. 2012. Incorporating shading losses in solar photovoltaic potential assessment at the municipal scale. *Solar Energy* **86**, 1245–1260.

Psomopoulos, C.S., Ioannidis, G.Ch., Kaminaris, S.D., Mardikis, K.D. & Katsikas, N.G. 2015. A Comparative Evaluation of Photovoltaic Electricity Production Assessment Software (PVGIS, PVWatts and RETScreen). *Environmental Pro*cesses **2**(S1), 175–189. DOI: 10.1007/s40710-015-0092-4. ISSN 2198–7491. Available from: http://link.springer.com/10.1007/s40710-015-0092-4

Rezk, H., Tyukhov, I. & Raupov, A. 2015. Experimental implementation of meteorological data and photovoltaic solar radiation monitoring system. *International Transactions on Electrical Energy Systems* **25**, 3573–3585.

Renewable Energy Directice – European Commission. European Commission [online]. 2017 [cit. 2017-06-07]. Available from: https://ec.europa.eu/energy/en/topics/renewable-energy/renewable-energy-directive

Thevenard, D. & Pelland, S. 2013. Estimating the uncertainty in long-term photovoltaic yield prediction. *Solar Energy* **91**, 432–445.

Territorial precipitation in 2016. Český hydrometeorologický ústav [online]. Prague, 2017 [cit. 2017-06-07]. Available from: http://portal.chmi.cz/historicka-data/pocasi/uzemni-srazky

Exhaust particle size distributions of a non-road diesel engine in an endurance test

T. Ovaska[1,*], S. Niemi[1], T. Katila[2] and O. Nilsson[1]

[1]University of Vaasa, School of Technology and Innovations, P.O. Box 700, FI-65101 Vaasa, Finland
[2]AGCO Power Oy, Linnavuorentie 8–10, FI37240 Linnavuori, Nokia, Finland
*Correspondence: teemu.ovaska@uva.fi

Abstract. The main objective of this study was to find out how the non-road diesel engine running period of 500 hours affects the exhaust particle size distribution. By means of an engine exhaust particle sizer (EEPS), particle number was measured before the endurance test and after 250 and 500 hours of engine operation. The size distributions were determined at full and 75% loads both at rated and at intermediate speeds. The soot, gaseous emissions and the basic engine performance were also determined and lubricating oil was analysed a few times during the running period. A blend of low-sulphur fossil diesel and soybean methyl ester (B20) was used as fuel in the 4-cylinder, turbocharged, intercooled engine which was equipped with a diesel oxidation catalyst (DOC) and a selective catalytic reduction (SCR) system. All emissions were measured downstream the catalysts. During the 500 hours of operation, the particle number increased considerably within an approximate size range of 7 to 30 nm. Between the initial and final measurements, no notable differences were observed in the particle number emissions within a particle size range of 50 to 200 nm. The copper content of lubricating oil also increased significantly during the 500 hours' experiment. One possible reason for the substantial increase in the nucleation mode particle number was assumed to be copper, which is one of the metallic elements originating from engine wear. The engine efficiency was almost equal, and the differences both in smoke and hydrocarbon emission were negligible throughout the 500 hours' experiment.

Key words: particle number, exhaust aftertreatment, B20, blend fuel, soybean methyl ester.

INTRODUCTION

Some of the combustion products of diesel engines have long been recognized as harmful pollutant emissions that affect the air quality, human health, and climate change. Both the gaseous and particulate emissions are regulated worldwide.

The emission legislation has been met by exploiting different engine design, aftertreatment system, and fuel technologies. All these technologies are needed gradually during 2019–2020 when the new emission stage (Stage V), regulated by the European Commission and the Council, comes into force. The regulation also limits the particle number (PN) emissions of the non-road diesel engines. (EU Regulation 2016/1628). The new PN limitation enforces the usage of diesel particulate filters (DPF) along with the possible catalyst devices in the near future.

Diesel engine exhaust contains non-volatile particles which form the size distribution with two distinctive particle modes; soot mode and core (nucleation) mode. (Kittelson, 1998; Rönkkö et al., 2006; Filippo & Maricq, 2008; Lähde et al., 2010). The formation of the core mode particles is considered to initiate in the cylinder. Soot particles are formed in the cylinder, when either the fuel or the remnants of lubricating oil do not burn completely during combustion. The particle mean diameters in nucleation mode are under 40 nm, whereas the mean diameter range in soot mode is 20–100 nm.

The particles with mean diameters of less than 2.5 µm or 10 µm are often reported to be adverse to human health. In addition, the concentrations of black carbon and nanosized particles < 100 nm may cause health risks. (Oberdörster et al., 2005; Janssen et al., 2011). The smallest particles can deposit onto the lungs and may penetrate into the cardiovascular and even cerebrovascular system via respiratory organs. (Anderson et al., 2012; Oravisjärvi et al., 2014).

Reliable operation of a diesel engine is ensured when the engine is capable of running without failures. When the engine is run with the same fuel in the constant ambient conditions, one can assume that heterogeneous air/fuel mixture preparation during the ignition delay, fuel ignition quality, residence time at different combustion temperatures, and expansion duration are equal. Therefore, the emission formation mechanisms and the resultant concentrations of the different emission species in the exhaust will be the same.

However, mechanical wear of the engine also affects the non-volatile particle number of diesel exhaust in long-term use. The wear metals, such as Fe, Al, Cu, Zn, Co, and Ni, are found among the exhaust particle ash content. (Agarwal, 2005; Dwivedi et al., 2006; Sarvi et al., 2011; Sharma & Murugan, 2017).

This study examined how the non-road diesel engine running period of 500 hours affects the exhaust particle size distribution. A blend of low-sulphur fossil diesel and soybean methyl ester (B20) was used as fuel in the high-speed non-road engine which was equipped with a diesel oxidation catalyst (DOC) and a selective catalytic reduction (SCR) system. The particle number were measured before the endurance test and after 250 and 500 hours of engine operation at full and 75% loads both at rated and at intermediate speeds. The soot, gaseous emissions and the basic engine performance were determined as well. During the experiments, the engine control parameters were kept constant.

MATERIALS AND METHODS

The experimental measurements were performed by the University of Vaasa (UV) at the internal combustion engine (ICE) laboratory of the Technobothnia Research Centre in Vaasa, Finland.

Engine
The test engine was a 4-cylinder non-road diesel engine equipped with a common-rail injection system. The new, turbocharged, intercooled engine was equipped with a DOC and a urea-based SCR system. During all the measurements, emissions were recorded downstream the catalysts.

The test engine was installed in a test bed and loaded by means of an eddy-current dynamometer of model Horiba WT300. The main engine specification is given in Table 1.

Fuel and lubricating oil

Fuel used during the endurance test was a blend of low-sulphur fossil diesel and soybean methyl ester (B20). The fuel consisted of 20 vol.-% soybean methyl ester (SME) and of 80 vol.-% commercial low-sulphur diesel fuel oil (DFO).

Table 1. Main engine specification

Engine	AGCO POWER 49 AWI
Cylinder number	4
Bore (mm)	108
Stroke (mm)	134
Swept volume (dm^3)	4.9
Rated speed (rpm)	2,100
Rated power (kW)	103
Maximum torque with rated speed (Nm)	462*
Maximum torque with 1,500 rpm (Nm)	583*

*conformable to measured torques obtained with B20 fuel.

The commercially available Valtra Engine CR-4, 10W-40 (ACEA E9, API CJ-4) was used as lubricating oil in the engine. Lubricating oil was analysed after the operating hours of 0, 207, 357 and 553. The analysing results of the lubricating oil have been reported earlier by Sirviö et al. (2016).

Analytical instruments

The adopted measurement instruments are listed in Table 2. Before the measurements, the analysers were calibrated manually once a day according to the instructions of the instrument manufacturers. The arrangement of the test bench and measurement devices is seen in Fig. 1 in which temperature sensors are abbreviated to TS.

During the measurements, the particles from a size range of 5.6 to 560 nm were recorded by using the engine exhaust particle sizer (EEPS), for which the sample flow rate was adjusted at 5.0 L min^{-1}. The 'SOOT' inversion was applied in the EEPS data processing. The exhaust sample was first diluted with ambient air by means of a rotating disc diluter (RDD) (model MD19-E3, Matter Engineering AG). The dilution ratio used in the RDD was constant 60 during the measurements. The exhaust aerosol sample was conducted to the RDD and a dilution air was kept at 150 °C. The diluted sample (5 L min^{-1}) was further diluted by purified air with a dilution ratio of 2. Thus, the total dilution ratio used in particle size distribution measurements was 120. In this way, mainly the non-volatile particle fraction 150°C is measured by the EEPS.

Three-minute stable time intervals were chosen for the results recordings of the particle number (PN) and particle size distributions. The average values, calculated from the recordings, were multiplied by the dilution ratio of the exhaust sample.

The recorded smoke value was the average of three consecutively measured smoke numbers.

Table 2. Measuring equipment

Parameter	Device	Technology
Particle number and size distribution	TSI EEPS 3090	spectrometer
Hydrocarbons	J.U.M. VE7	HFID
Smoke	AVL 415 S	optical filter
NO_x	Eco Physics CLD 822 M h	chemiluminescence
NO_x, λ	WDO UniNO$_x$ sensors	ZrO_2-based multilayer
O_2	Siemens Oxymat 61	paramagnetic
Air mass flow rate	ABB Sensyflow P	thermal mass

The sensor data were collected by means of software, made in the LabVIEW system-design platform. In addition to the gaseous emissions, the systems recorded the temperatures of cooling water, intake air and exhaust gas plus the pressures of the intake air and exhaust gas. The engine control parameters were followed via WinEEM4 engine management software, provided by the engine manufacturer.
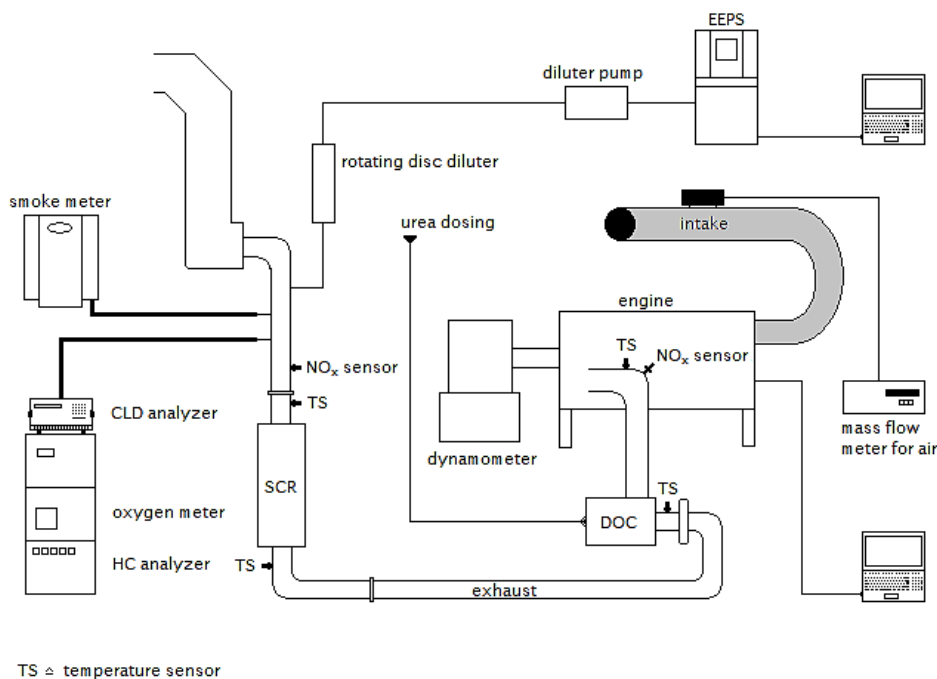
Figure 1. Experimental set-up.

Based on the measured hydrocarbon (HC) concentrations, the brake specific emissions of HC were calculated according to the ISO 8178 standard.

Experimental matrix and running procedure

Before the endurance test of 500 running hours, the baseline performance and emissions measurements were performed with a new engine installation. Thereafter, the engine was daily operated according to a defined running procedure consisting of sequential load points which were supposed to represent the actual use of the engine as

accurately as possible. After 250 hours of engine operation, the performance and emissions measurements were repeated, as they were after 500 hours.

The measurements were conducted at full and 75% loads both at rated and at intermediate speeds. The rated engine speed was 2,100 rpm and the intermediate speed 1,500 rpm.

Before the measurements, the intake air temperature was adjusted at 50 °C downstream the charge air cooler when the engine was run at full load at rated speed. The temperature was controlled manually by regulating cooling water flow to the heat exchanger. After this initial adjustment, the temperature was allowed to change with engine load and speed.

During the measurements, the engine was run with urea dosing, the alpha ratio being 0.95.

Before the recordings at each load point, it was waited that the engine had stabilized, the criteria being that the temperatures of coolant water, intake air and exhaust were stable. The length of the measurement period was not tied to a certain time.

All measurement values were recorded once at each load point.

Daily operation

The daily running cycle between the measurements is given in Table 3. The engine was run by an autopilot-system which was implemented into the LabVIEW platform. The autopilot system made it possible to regulate the dynamometer automatically.

Table 3. Daily cycle of the endurance test

Point	Speed (rpm)	Load (%)	Torque (Nm)	Duration (min)
1	1,000	0	0	15
2	1,300	14	75	15
3	1,600	21	123	15
4	1,800	29	175	30
5	2,000	40	214	15
6	2,100	51	236	15
7	1,900	60	346	15
8	1,700	49	293	15
9	1,500	30	175	30
10	1,200	25	127	15

RESULTS AND DISCUSSION

Particle size distributions

Generally, the PN increased considerably within an approximate size range of 7 to 30 nm during the 500 hours of engine operation. Between the initial and final measurements, no notable differences were, however, observed in the PN emissions within a particle size range of 50 to 200 nm.

Fig. 2 shows the particle size distributions at full and 75% loads both at rated and intermediate speeds. For both speeds and loads, a bimodal shape was detected for the distributions. One peak was detected at a particle size of ca. 10 nm and the other at ca. 32–60 nm. At the initial measurements, the lowest quantity of particles was observed within the size ranges of 7–15 nm and 24–86 nm regardless of the engine speed or load.
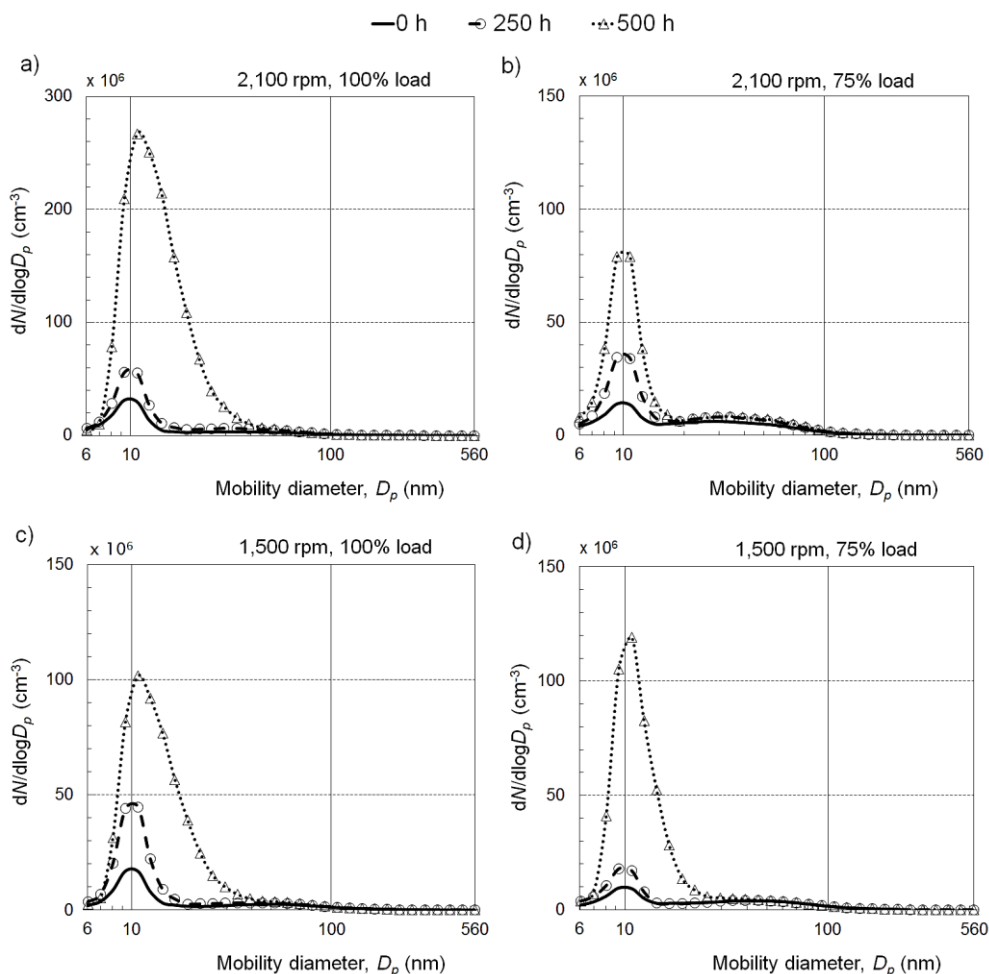
Figure 2. Effect of running period of 500 hours on the exhaust particle size distribution a) at full and b) 75% load at rated speed, and c) at full and d) 75% load at intermediate speed.

After 250 hours' operation, the number of particles under 154 nm increased compared to the baseline apart from at intermediate speed at 75% load where the PN between 86–200 nm decreased. The greatest PN was detected at the size category of 10 nm. At rated speed, the PN was here 1.9-fold at full load and 2.5-fold at 75% load compared to the baseline. At intermediate speed at full and 75% load, the PN was 2.7-fold and 1.8-fold, respectively, at this size category.

After the 500 hours' operation, the PN increased within the size range of 7–200 nm compared to baseline. The highest particle numbers of this study were recorded within the size range of 8–42 nm. The PN peaked again at the size category of 10 nm. Now, at rated speed, the PN was 9.0-fold at full load and 5.9-fold at 75% load compared to the baseline. At intermediate speed at full and 75% load, the PN was 6.1-fold and 13-fold, respectively.

Usually, the initiation of the nucleation is assumed to be sulphur driven. First, when sulphur from fuel and lubricating oil burn in the cylinder, sulphur dioxide is formed. In

the oxidation catalyst, sulphur dioxide of exhaust gas can be converted to sulphur trioxide under high exhaust temperatures. (Giechaskiel et al., 2007) Thus, the nucleation mode of particles downstream the SCR catalyst may be caused by sulphuric acid originating from reaction between sulphur trioxide and water vapor (Vaaraslahti et al., 2004; Arnold et al., 2006; Rönkkö et al.,2007; Biswas et al., 2008). However, the sulphur content of fuel or lubricating oil were not observed to change during the study.

Sirviö et al. (2016) observed that the copper concentration in lubricating oil increased significantly from 49 to 420 ppm between the oil analysis hours of 357 and 553. Copper is one of the metallic elements originating from engine wear. However, the contents of other wear metals, such as lead, did not increase, as would have been probable in the case of damage in bearings or other engine parts (Sirviö et al. 2016).

Schumacher et al. (2005) fuelled an on-road truck diesel engine with the different blends of hydrogenated soybean ethyl-ester. During the first 50,000 miles of operation, 2–3 lubrication oil samples were taken. The samples contained the high levels of copper which were suggested to originate from a copper oil cooler.

For this paper, one possible reason for the substantial increase in the nucleation mode particle number was assumed to be copper which originated from the break-in of a new oil cooler.

Fig. 3 illustrates the effect of the operation time on the measured total particle number (TPN, from 6 to 560 nm), where linear interdependences are presented by using the PN data from each load point.
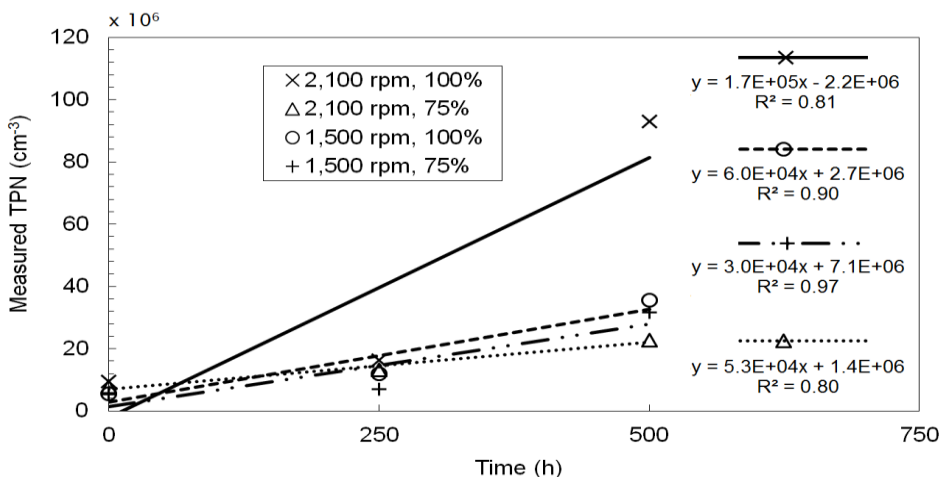
Figure 3. Measured TPN as a function of the operation time.

All correlations were positive irrespective of the engine speed or load. For the presented interdependences, the values of squared correlation factors were between 0.80–0.97.

In general, the total particle numbers were the smallest at the initial measurement and far the highest after 500 hours of engine operation. The least TPN were detected always at intermediate speed at 75% load, whereas the highest TPN were recorded every time at rated power.

HC emissions and smoke

The brake specific HC emission was minor throughout the 500 hours of engine operation, Fig. 4. At rated speed, the HC emission varied from 0.01 to 0.02 g kWh^{-1}, and at intermediate speed from 0.006 to 0.009 g kWh^{-1}. The engine was equipped with a DOC, which reduce the HC concentration of exhaust by promoting the chemical oxidation of HC. Therefore, the HC emission was almost negligible at both loads and speeds.
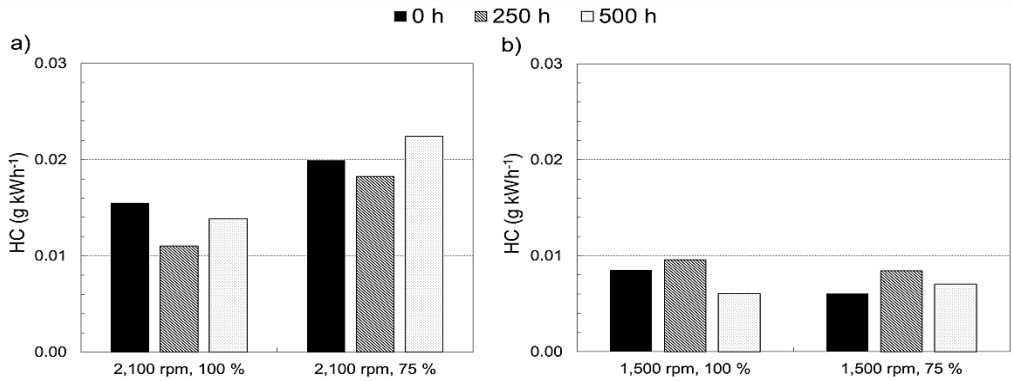
Figure 4. Brake specific HC emissions a) at full and 75% load at rated speed, and b) at full and 75% load at intermediate speed.

Fig. 5 depicts the smoke emissions. Both at rated and at intermediate speed, the smoke was very low, the FSN readings varying from 0.020 to 0.064. No reliable conclusion can be drawn from the smoke emission.
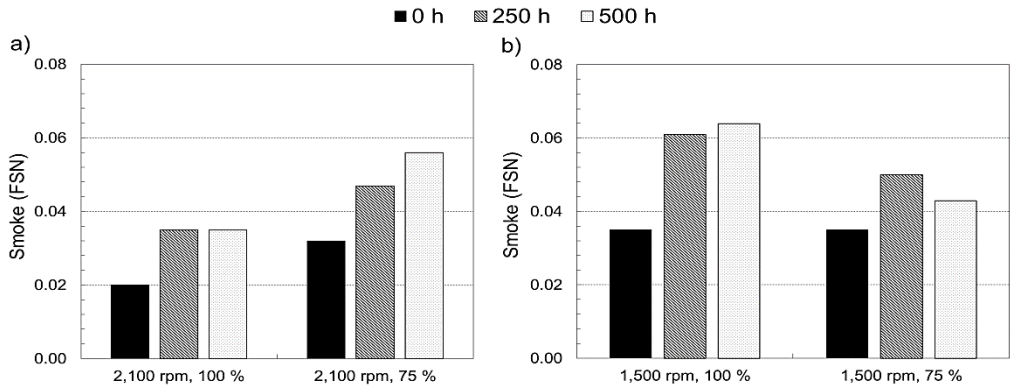
Figure 5. Exhaust smoke a) at full and 75% load at rated speed, and b) at full and 75% load at intermediate speed.

When comparing either the HC or smoke emissions, the differences were negligible, and no clear trend was detected during the 500 hours' operation. The notable increase of PN within an approximate size range of 7 to 30 nm during the 500 hours of engine operation cannot be explained by means of the HC or the smoke emissions.

Performance

The engine efficiency was almost constant at all loads, Fig. 6. At different load points, the efficiencies varied only by 0 to 0.3 percentage points.
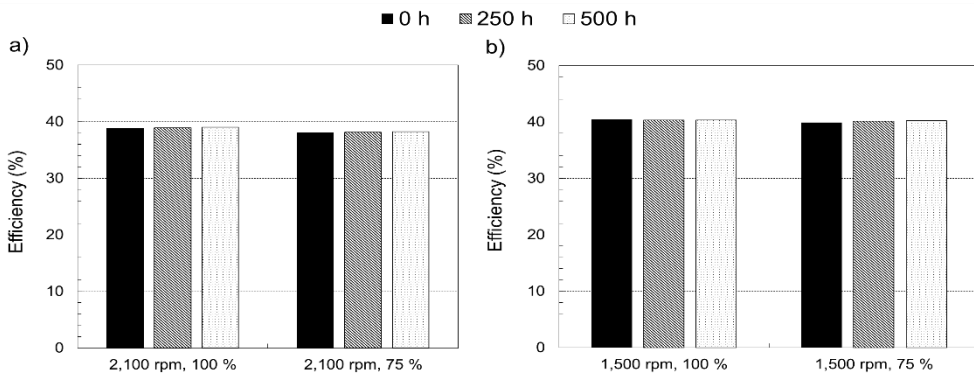
Figure 6. Engine fuel conversion efficiency a) at full and 75% load at rated speed, and b) at full and 75% load at intermediate speed.

CONCLUSIONS

1. During the 500 hours of engine operation, the particle number increased considerably within an approximate size range of 7 to 30 nm

2. No notable differences were observed in the particle number emissions within a particle size range of 50 to 200 nm

3. The correlations between the measured TPN and operation time were positive irrespective of the engine speed or load

4. The engine efficiency remained almost constant, and the changes both in smoke and hydrocarbon emissions were negligible.

The regular change interval for the lubricating oil filter of the non-road diesel engine used in the current study is 500 hours. As a next study, the experiment period could be extended to 1000 hours. Then, the main interest would be the effect of the extended period on the particle number and size distribution, after the oil filter change.

REFERENCES

Agarwal, A.K. 2005. Experimental investigations of the effect of biodiesel utilization on lubricating oil tribology in diesel engines. *Proc. Inst. Mech. Eng. Part D: J. Automobile Eng.* **219**(5), 703–713.

Anderson, J.O., Thundiyil, J.G. & Stolbach, A. 2012. Clearing the air: a review of the effects of particulate matter air pollution on human health. *J. Med. Toxicol.* **8**(2), 166–175.

Arnold, F., Pirjola, L., Aufmhoff, H., Schuck, T., Lähde, T. & Hämeri, K. 2006. First gaseous sulphuric acid measurements in automobile exhaust: Implications for volatile nanoparticle formation. *Atmos. Environ* **40**(37), 7079–7105.

Biswas, S., Hu, S., Verma, V., Herner, J.D., Robertson, W.H., Ayala, A. & Sioutas, C. 2008. Physical properties of particulate matter (PM) from late model heavy-duty diesel vehicles operating with advanced PM and NO_x emission control technologies. *Atmos. Environ.* **42**(22), 5622–5634.

Dwivedi, D., Agarwal, A.K. & Sharma, M. 2006. Particulate emission characterization of a biodiesel vs diesel-fuelled compression ignition transport engine: A comparative study. *Atmos. Environ* **40**(29), 5586–5595.

EU Regulation 2016/1628. 2016. Regulation of the European Parliament and of the Council on requirements relating to gaseous and particulate pollutant emission limits and type-approval for internal combustion engines for non-road mobile machinery. Accessed 26.1.2018.

Filippo, A.D. & Maricq, M.M. 2008. Diesel nucleation mode particles: Semivolatile or solid?. *Environ. Sci. Technol.* **42**(21), 7957–7962.

Giechaskiel, B., Ntziachristos, L., Samaras, Z., Casati, R., Scheer, V. & Vogt, R. 2007. Effect of speed and speed-transition on the formation of nucleation mode particles from a light duty diesel vehicle. *SAE Tech. Pap.* 2007-01-1110.

Janssen, N.A., Hoek, G., Simic-Lawson, M., Fischer, P., Van Bree, L., Ten Brink, H., Keuken, M., Atkinson, R.W., Anderson, H.R., Brunekreef, B. & Cassee, F.R. 2011. Black carbon as an additional indicator of the adverse health effects of airborne particles compared with PM10 and PM2. 5. *Environ. Health Perspect.* **119**(12), 1691.

Kittelson, D.B. 1998. Engines and nanoparticles: a review. *J. Aerosol Sci.* **29**(5–6), 575–588.

Lähde, T., Rönkkö, T., Virtanen, A., Solla, A., Kytö, M., Söderström, C. & Keskinen, J. 2010. Dependence between nonvolatile nucleation mode particle and soot number concentrations in an EGR equipped heavy-duty diesel engine exhaust. *Environ. Sci. Technol.* **44**(8), 3175–3180.

Oberdörster, G., Oberdörster, E. & Oberdörster, J. 2005. Nanotoxicology: an emerging discipline evolving from studies of ultrafine particles. *Environ. Health Perspect.* **113**(7), 823.

Oravisjärvi, K., Pietikäinen, M., Ruuskanen, J., Niemi, S., Laurén, M., Voutilainen, A., Keiski, R.L. & Rautio, A. 2014. Diesel particle composition after exhaust after-treatment of an off-road diesel engine and modeling of deposition into the human lung. *J. Aerosol Sci.* **69**, 32–47.

Rönkkö, T., Virtanen, A., Vaaraslahti, K., Keskinen, J., Pirjola, L. & Lappi, M. 2006. Effect of dilution conditions and driving parameters on nucleation mode particles in diesel exhaust: Laboratory and on-road study. *Atmos. Environ* **40**(16), 2893–2901.

Rönkkö, T., Virtanen, A., Kannosto, J., Keskinen, J., Lappi, M. & Pirjola, L. 2007. Nucleation mode particles with a nonvolatile core in the exhaust of a heavy duty diesel vehicle. *Environ. Sci. Technol.* **41**(18), 6384–6389.

Sarvi, A., Lyyränen, J., Jokiniemi, J. & Zevenhoven, R. 2011. Particulate emissions from large-scale medium-speed diesel engines: 2. Chemical composition. *Fuel Process. Technol.* **92**(10), 2116–2122.

Schumacher, L.G., Peterson, C.L. & Van Gerpen, J. 2005. Engine oil analysis of biodiesel-fueled engines. *Appl. Eng. Agric.* **21**(2), 153–158.

Sharma, A. & Murugan, S. 2017. Durability analysis of a single cylinder DI diesel engine operating with a non-petroleum fuel. *Fuel* **191**, 393–402.

Sirviö, K., Niemi, S., Katila, T., Ovaska, T., Nilsson, O. & Hiltunen, E. 2016. B20 fuel effects on engine lubricating oil properties. In: *The 28th CIMAC World Congress on Combustion Engine Technology* Helsinki, Finland, Paper No.: 025, pp. 1–8.

Vaaraslahti, K., Virtanen, A., Ristimäki, J. & Keskinen, J. 2004. Nucleation mode formation in heavy-duty diesel exhaust with and without a particulate filter. *Environ. Sci. Technol.* **38**(18), 4884–4890.

Capacitive frost depth indicator

V. Papez[1] and S. Papezova[2,*]

[1]Czech Technical University in Prague, Faculty of Electrical Engineering, Department of Electrotechnology, Technicka 2, CZ166 27 Pague 6, Czech Republic
[2]Czech University of Life Sciences in Prague, Faculty of Engineering, Department of Electrical Engineering and Automation, Kamycka 129, CZ165 21 Prague 6 - Suchdol, Czech Republic
*Correspondence: papezovas@tf.czu.cz

Abstract. The depth of soil freezing, i.e., the depth at which water is frozen, is a significant factor in meteorology, as it affects many processes in agriculture, building, etc. Soil frost penetration is an important factor for overwintering organisms, but also for physical and chemical processes in soil, particularly for its mechanical properties. The depth of freezing is normally determined directly, i.e. mechanically, using a special soil freezing meter, i.e., frost-depth indicator, according to the process of water freezing in the probe. Another method lies in determining the soil temperature by the interpolation of the curves from the graph, as measured by soil thermometers according to the change in the resistivity of soil or water, when frozen. The principle of the frost-depth indicator function is to evaluate the temperature dependence of water permittivity, which decreases, when water is frozen, from $\varepsilon_r \sim 87$ at 1 °C to $\varepsilon_r \sim 3.2$ at -1 °C, typical for ice. The water permittivity is evaluated by a measuring capacitor, which is adapted into the shape of the frost depth indicator probe, whose dielectric is deionized water. During freezing, the capacity is reduced in this area. The capacity of the partially frozen probe is directly proportional to the length of its non-frozen section. The measuring capacitor is a part of the resonant circuit of the oscillator. The frequency of the oscillator varies with the capacity of the probe and is further evaluated. The achievable measurement accuracy is approximately 2% for the probe of a 1m length and in direct evaluation by an autonomous counter. For the computer evaluation, with the possibility to compensate the probe non-linearity, the measurement accuracy is approximately 0.5%.

Key words: depth of soil freezing, capacity measurement, water permittivity.

INTRODUCTION

The depth of soil freezing is currently measured in many ways. The easiest method is to use a mechanical indicator, which is a hose filled in with distilled water. The hose is inserted into a plastic pipe that is permanently embedded in the soil. The depth of soil freezing is evaluated by the operator´s palpation of the hose after a couple of hours after inserting the probe into the soil. The non-frozen section appears soft, while the frozen section is hardened, which indicates the presence of ice (Pokladníková et al., 2005). Similarly, the freezing depth is evaluated by means of a soil monolith. Here, a soil

sample is used as a probe medium, whose state is again evaluated by the operator (Střelcová & Škvarenina, 2005)

Other methods evaluate the depth of freezing according to soil temperature. In the methods using thermometers, temperature readings from the thermometers, which are embedded at different depths in soil, are evaluated. According to the temperature course samples, the position of the temperature function passing through zero is then approximated and a freezing depth is assigned to this position.

More advanced designs use temperature indications for substance, whose colour considerably varies with certain temperatures. The frost depth indicator is a probe containing a substance that significantly changes its colour around 0 °C. The frost depth indicator is inserted into soil. After temperature stabilization and subsequent removal of the probe, the depth of soil freezing is evaluated according to the position of the colour transition in the probe. Electrical measurements exploit the changes in resistivity of soil or water, when frozen. The resistivity of frozen water and soil is by several orders higher than the resistivity of non-frozen water and soil.

Frost depth indicators evaluating the soil-freezing depth according to the soil resistivity use the probe, made of the insulator with separated electrodes on the surface. Electrical resistance is then measured in between them. The probe is inserted into soil and the depth of freezing is determined by the position of the electrodes, where the resistance sharply increases (Bagal, 2010a, Bagal, 2010b).

The methods employing the change in water resistivity during freezing work in a similar way, with the only difference that the water filling and the electrodes are enclosed inside the probe, inserted into the soil.

A mechanical procedure is the most used procedure for its simplicity and reliability. Its disadvantage, the same as at other non-electrical processes, is the need for the operator´s manipulation with the device at the measuring station, which excludes a remote measuring of the depth of freezing. On the other hand, electrical procedures usually allow remote measurements. However, their disadvantage is the undesirable influence of conductivity measurements of the non-frozen electrolyte or soil between the electrodes and the surface states of the electrodes, on which the evaluated resistance strongly depends. These phenomena then complicate the evaluation of the measurement, which is complex and may be unreliable.

The capacitive frost depth indicator, described below, works on the principle of the evaluation of water permittivity, which decreases at the high-frequency range from $\varepsilon_r \sim$ 87 (at 1 °C) to $\varepsilon_r \sim$3.2 (at -1 °C), at the temperature typical for ice (Chaplin, 2017).

Water permittivity is evaluated by a measuring capacitor that is adapted into the shape of the frost depth indicator, vertically embedded into soil. When the part of the probe freezes, the capacity of the measuring capacitor is reduced in this area and the total capacity of the probe decreases. The total probe capacity varies between the minimum value, corresponding to the fully frozen probe, and the maximum value, corresponding to the non-freezing probe.

In order to achieve high measurement accuracy, both the probe construction and the capacity evaluation method are optimized with respect to the parasitic capacity parameters of the measuring capacitor and the frequency dependence of the complex water permittivity (Artemov & Volkov, 2014).

MATERIALS AND METHODS

The measuring probe is principally designed as a plate capacitor, whose dielectric is distilled water, or ice and other suitable solid and flexible dielectric (Papež, 2013). An example of a possible design of the probe is shown in Fig. 1, in a sectional view, perpendicular to the longitudinal axis of the probe.
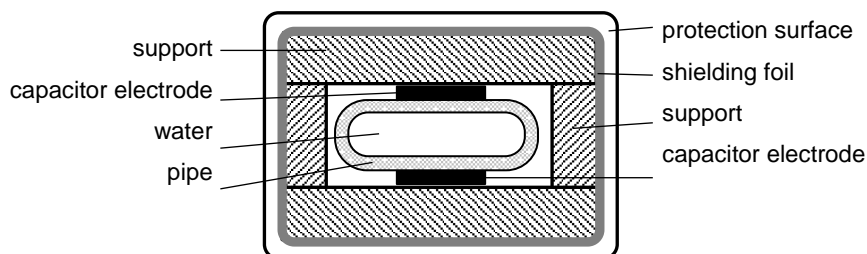
Figure 1. Example of a measuring probe design.

The basis of the probe design is formed by two strips thin conductive metallic foils, serving as measuring capacitor electrodes which are glued and attached to two rigid plates made of high-quality solid dielectrics. Both plates are mechanically interconnected and fixed by means of two rigid dielectric rectangular constructions. In this way a rectangular hollow is formed along the whole length of the probe between the plates and dielectric construction, on whose opposed walls are located the electrodes of the measuring capacitor. A flexible tube, made of low-loss dielectric, is inserted into the hollow along the full length of the probe. The tube is filled in, under moderate overpressure, with airless distilled water and hermetically sealed. The tube has, in terms of the probe function, three important functions:

a) reduces the impact of a large increase in permittivity; and, if need be, of a water loss factor during de-freezing, on the properties of the measuring capacitor;

b) allows suppressing the occurrence of any electrochemical processes on the surface of the electrodes placed in water by separating the water filling from the electrodes by an inert dielectric layer;

c) prevents the mechanical construction of the probe from degradation and damage, caused by the increase in volume of the water filling during freezing. The change in volume of water is hereby compensated by the compression of the flexible material of the tube, in which the water filling is closed.

From the outside, the probe is shielded with a thin metallic foil, which is glued on the outer sides of the plates, or is mounted on the sides of the probe, and it is connected to the film on the outside of the dielectric plates. The protection against the external influence/impact is ensured by coating the probe with a plastic tube, resembling a hose. The capacity frequency dependencies of the probe sample and its loss factor ($D = 1/Q$) are shown for a non-frozen probe (Fig. 2), and a frozen probe (Fig. 3). Length of a probe sample was selected at 1 m. As a material for the tube, a silicone rubber with a wall thickness of 1 mm was used. The width of measuring capacitor plates was 6 mm and water channel height was 4 mm.
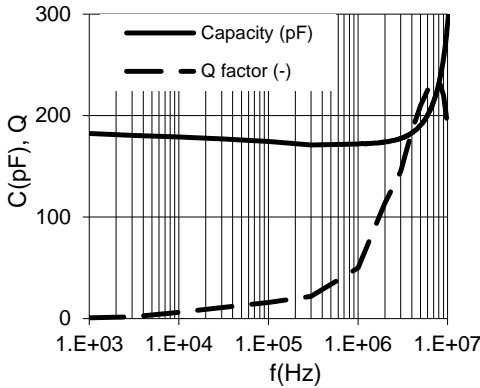
Figure 2. The capacity frequency dependence and Q factor for a non-frozen probe.
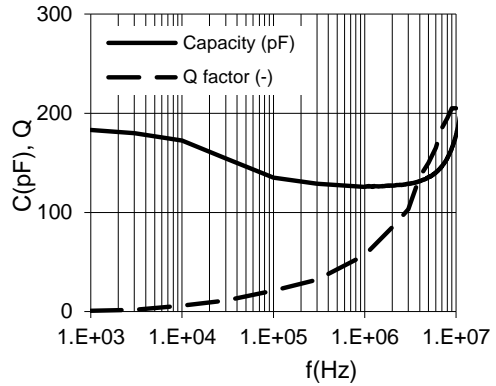
Figure 3. The capacity frequency dependence and Q factor for a frozen probe.

The change in capacity of the probe, when frozen, is best seen in the frequency range of 0.3–3 MHz, where the capacity of a non-frozen probe (with the leads) is 181 pF and the capacity of a frozen probe is 135 pF. At frequencies lower than 30 kHz (Artemov & Volkov, 2014), the capacity of the frozen probe is significantly influenced by the polarization of ice at temperatures around -1 °C. A sharp rise in its permittivity to the values corresponding to liquid water, also results in the increase in the capacity of a frozen probe, in the low frequency range, to the values, corresponding to the frozen probe. At the same time, at low frequencies, the loss factor of the capacitor, representing the probe, increases significantly. These phenomena exclude the possibility of using of conventional commercial capacity meters, operating in the low frequency range at frequencies from 100 Hz to 100 kHz for capacity measurement.

At higher frequencies, the capacity of the non-frozen probe is influenced by its internal inductance and inductance of the leads. Reactance of the serial inductance reduces capacitor reactance at high frequencies, resulting in a fictitious increase in its capacitance and an increase in its loss factor. Assuming the frost depth evaluation according to the capacity ratio of the frozen and partially frozen probes, the phenomenon also complicates the measurement because the indicated ratio of fictitious capacity reactance does not correspond to the desired ratio of real capacity reactance

$$\frac{X_{C1} - X_L}{X_{C2} - X_L} \neq \frac{X_{C1}}{X_{C2}} \tag{1}$$

where X_{C1} – reactance of a non-frozen probe; X_{C2} – reactance of a frozen probe; X_L – reactance of probe inductance.

To achieve the accuracy in measuring the probe capacitance, it is best to use the frequencies around 3 MHz, where the capacitor has low losses, the quality factor $Q > 100$ and the influence of the probe inductance still remains very small.

Since only commercially available high-performance measuring instruments, such as HP 4291, Agilent 4285, or Keysight E4991, allow measuring in this frequency range, a special device for evaluating the probe capacity has been designed and implemented.

The probe capacity is evaluated by the frequency of an RF oscillator, in whose resonant circuit the measuring capacitor is inserted. The principal diagram of the oscillator is shown in Fig. 4. The resonance frequency of the control circuit, which is depends on the probe freezing length is determined by Eq. (2)

$$f = \frac{1}{2\pi} \frac{1}{\sqrt{L(C_0 + C_k) - L\Delta Cl}}, \tag{2}$$

where L – inductance of a resonant circuit; C_0 – total capacity of a non-frozen probe, including leads; ΔC – proportional drop in capacity of the probe, when frozen; C_k – capacitance of a calibration capacitor; l – the ratio of the length of the probe frozen section to the total length of the probe measuring section, $0 \le l \le 1$.
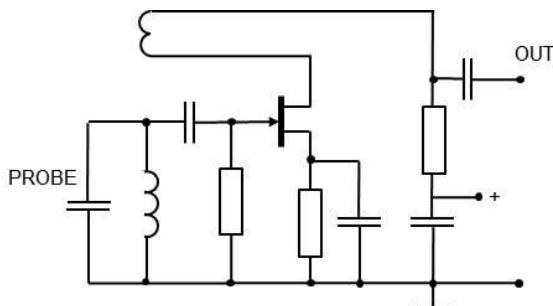
Figure 4. Principal diagram of the oscillator.

Considering the fact that, for a non-frozen probe, $l=0$, the resonance frequency is f_0, for small changes in frequency, using the approximation $(1+x)^{-0.5} \approx 1-x/2$, f can be exactly (2) or approximately, expressed by Eq. (3).

$$f = f_0 \frac{1}{\sqrt{1 - \frac{\Delta C}{(C_0 + C_k)} l}} \approx f_0 (1 + \frac{\Delta C}{2(C_0 + C_k)} l) \tag{3}$$

According to the approximating formula, the length of the frozen section of the probe, depending on the resonant frequency f, can be expressed by a simple linear function

$$l = (\frac{f}{f_0} - 1) \frac{2(C_0 + C_k)}{\Delta C}. \tag{4}$$

The error caused by the inaccuracy of the approximation is small for small values of the ratio $\Delta C/(C_0 + C_k)$, or for the ratio f_i/f_0 of the oscillation frequencies with a frozen and non-frozen probe. The error increases with the increasing value of these ratios. The size of the maximum error, resulting from the approximation can be, according to the fore mentioned ratio $\alpha = f_i/f_0$, expressed by

$$MAX(l - l_A) \le \frac{\frac{\sqrt{2}\alpha}{\sqrt{a^2 + 1}} - \frac{\alpha}{2} - \frac{1}{2}}{\alpha - 1}. \tag{5}$$

In contrast, the measurement error, resulting from the frequency instability of the measuring oscillator and its temperature dependence with the increasing ratio of α,

decreases and the resulting error in determining the relative freezing time reaches approx. $\delta f/(\alpha-1)$, depending on relative frequency deviation δf. Both these dependencies are shown in the graph in Fig. 5.
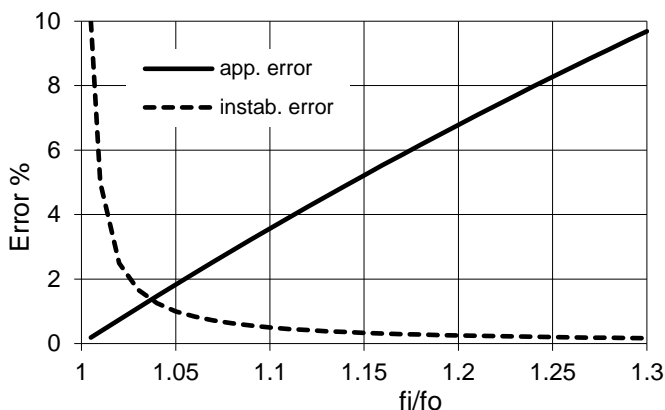
Figure 5. Error dependence caused by the approximation and the error caused by frequency instability at $\alpha = f_i/f_0$.

Function (4), expressing the length of the frozen section, depending on the frequency of the measuring oscillator signal, is evaluated by a counter, whose input signal is a measuring oscillator signal. In the counter operation algorithm, the coefficient $C_0/\Delta C$ can be set by selecting the counting time, and the differential operation is realized by resetting the counter in its overflow. The counter module M and the counting time T are selected so that, in processing the signal f_0 with the non-frozen probe, the counter should overflow at least once during the counting period and the number indicated after the counting should equal zero (6).

$$T = \frac{Mn}{f_0} = \frac{Mn + A}{f_i} . \qquad (6)$$

When the water has been frozen, the indicated number corresponds to the difference between the just generated frequency f_j, and the frequency f_0, with a non-frozen probe. If the ratio of f_j/f_0 and the counter module are suitably chosen, using (5), both the counting time and the number of counter overflows during the counting period n can be determined such that the number indicated at the counter output directly corresponds to the length A of the probe freezing. A is expressed in appropriate length units $(A \leq M - 1)$.

RESULTS AND DISCUSSION

Following the results of the above mentioned analysis, a sample of a frost depth indicator with a direct indication of the depth of freezing has been designed. A probe of a 1m length, having the capacity of 135 pF in a frozen state and 181 pF in a non-frozen state has been applied. The construction of the oscillator is based on the principle diagram shown in Fig. 4.

A principal diagram of the frost depth indicator is shown in Fig. 6. The resonant circuit of the oscillator is completed by an adjustable capacitor C_A. An inductor L of the resonant circuit has an adjustable inductance.
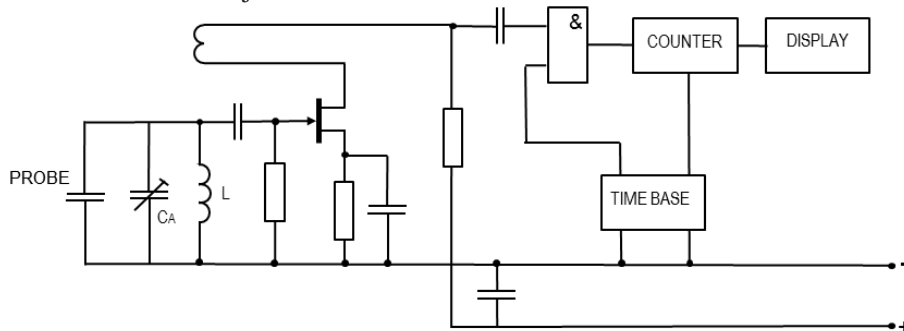
Figure 6. Principal diagram of the frost depth indicator.

By adjusting the adjustable elements, the oscillator operating frequencies f_0 and f_i are set to the appropriate selected values, corresponding to the applied counter algorithm, as specified by (Chaplin, 2017). The frequency of the measuring oscillator is evaluated by a counter, whose resulting state is displayed on the display, after the counting has been finished. The counting period and counter timing are controlled by the time base circuit.

For the sample of the frost depth indicator were selected $f_0 = 3.2$ MHz and $f_i = 3.4$ MHz, and the module 1,600 (16*100). The counter overflows at the moment, when the counting time reaches 500 µs at a non-frozen probe. When the probe of a 1 m length freezes, the counter enables direct indication of freezing in the value range of 0–100. The values correspond to the freezing length in centimeters. The realized frost depth indicator is shown in Fig. 7.

Figure 7. Realized frost depth indicator.

When the measurement is evaluated by a computer, a digital signal depicting the indicated frequency is sent to a computer, where the length of freezing is either computed according to exact mathematical relations or is read from the conversion table. The data for the conversion table can be most easily obtained by calibrating the sensor. In this way, it is possible to consider all the phenomena that influence the measurement without any further errors.

Measurement accuracy can be further increased by introducing a correction of the temperature dependence of the oscillator on its operating temperature. The method is suitable for long-distance evaluation of measurements from many sensors through the

measurement center because the sensors are simple and the signal can be transmitted over a long distance.

The frost depth indicator was tested in a mode close to its real use in practice. The probe was partially inserted into a space with a temperature of approx. -5 °C and the device together with the second part of the probe were placed in a heated box, whose temperature was maintained at about 5 °C. The probe was slipped through the hollow and fixed in such a way to let freeze only its selected length. The readings of the values were carried out in a steady state, i.e., 8–16 hours after the last manipulation with the device. Comparative measurements were carried out after the probe was partially inserted into a heated box with the temperature of 5 °C, and the device together with the second part of the probe were inserted into the space with the temperature of -5 °C.

The results of the test are shown in Fig. 8 and Fig. 9. A measurement error of 1.6% of the maximum value was detected in the middle of the measuring range. The error resulted from the simplification of the evaluation algorithm by a linear approximation. The shift by 10 °C of the operating temperature of the measuring device causes an error of the indicated value by approximately 1%.
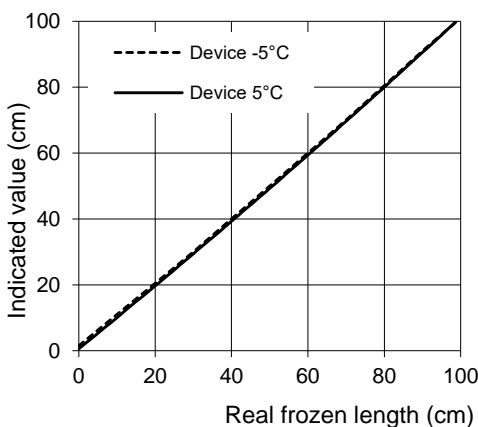
Figure 8. Dependence of the indicated value on the actual length of a frozen part.
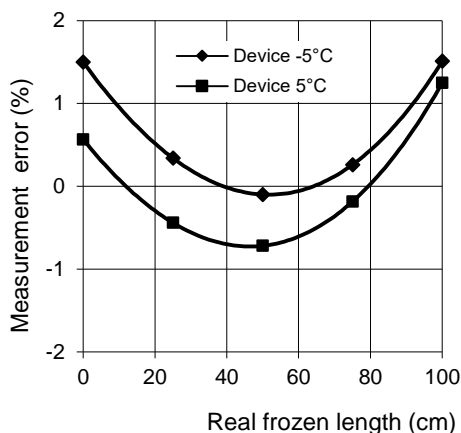
Figure 9. Dependence of the measurement error the length a frozen part.

CONCLUSIONS

The capacity probe for the soil freezing depth evaluation has been designed to achieve the maximum mechanical and electrochemical stability of the probe. The analysis of the frequency dependence of the probe complex impedance has been carried out. Based on its results, the method of the probe capacity evaluation has been determined, which allows to achieve the highest accuracy of the measurement.

With respect to the loss factor and parasitic inductance of the capacitor representing the probe, the optimum frequency range of 2–3 MHz was determined to evaluate the probe capacity. The principle of its evaluation is to monitor the resonance frequency of the resonant circuit, whose part is also the probe. The resonant circuit serves, at the same time, as an oscillator control circuit, whose operating frequency enables the evaluation of the requested capacity.

When the frequency is directly evaluated by the counter, the accuracy of the freezing depth measurement is approximately 2%. When the frequency is evaluated by the microcomputer, the accuracy can be improved to approx. 0.5%, when using the compensation of parasitic influences.

REFERENCES

Artemov, V.G. & Volkov, A.A. 2014. Water and Ice Dielectric Spectra Scaling at 0 °C. *Ferroelectrics* **466**, 158–165.

Bagal, Z. 2010a. Electronic soil freeze meter. Patent. Office of Industrial Property. Patent document 2010–286 (in Czech).

Bagal, Z. 2010b. Electronic soil freeze meter. Utility design. Office of Industrial Property. Patent document 2010-22559 number of registration 21177 (in Czech).

Chaplin, M. 2017. Water and Microwaves. *Water structure and science*. *http://www1.lsbu.ac.uk water/microwave_water.html.* Accessed 30.12.2017.

Papež, V. 2013. Soil freeze meter. Patent. Office of Industrial Property. Patent document 304000. 2013-06-26. (in Czech).

Pokladníková, H., Rožnovský, J. & Dufková, V. 2005. Soil freezing at the station Bystrice nad Perstejnem, In: *Bioclimatology of present and future,* Krtiny, ISBN 80-86 690-31-08 (in Czech).

Střelcová, K. & Škvarenina, J. 2005. *Bioclimatology a meteorology*. Technical University in Zvolen, 138 pp. (in Slovak).

Battery capacity drop during operation

S. Papezova[1,*] and V. Papez[2]

[1]Czech University of Life Sciences in Prague, Faculty of Engineering, Department of Electrical Engineering and Automation, Kamycka 129, CZ165 21 Prague 6 - Suchdol, Czech Republic
[2]Czech Technical University in Prague, Faculty of Electrical Engineering, Department of Electrotechnology, Technicka 2, CZ166 27 Pague 6, Czech Republic
*Correspondence: papezovas@tf.czu.cz

Abstract. A lithium-iron-phosphate ($LiFePO_4$) battery is nowadays considered one of the best types of batteries. The paper deals with the evaluation of the drop in their capacity during operation. Based on the physical analysis of charging and discharging processes, a mathematical model of the battery capacity has been developed during its lifetime. The decrease in capacity during battery operation is evaluated according to the loss of active material, which gradually diminishes due to a number of different processes. The analysis of the loss of the active material is carried out, in particular, according to the depth of discharge, battery temperature, charging and discharging time, including the time when the battery is out of service. The tests were performed on the Winston Battery, Calb, Thunder Sky and Sinopoly batteries by cyclic discharging and charging at the 50%, 90% or 100% depth of discharge. Their real parameters were determined, compared to the model parameters and the parameters specified by the manufacturers and suppliers. Two automated systems were used for testing. During the test, in the tested battery with several cells, charging and discharging by a constant current were carried out automatically. Operating parameters of the tested battery were continuously scanned, recorded and evaluated by the control computer. The capacity curves during the battery operation, determined by the type of models, were compared with the results of long-term real battery tests.

Key words: $LiFePO_4$ battery, lifespan, capacity drop, depth of discharge.

INTRODUCTION

A lithium-iron-phosphate ($LiFePO_4$) battery is now considered one of the best battery types. Although their purchase price is several times higher than that of other types of batteries, manufacturers and suppliers report that the $LiFePO_4$ battery has much longer lifetime and shows much lower cost of electrical energy storage than other batteries. For example, when comparing the cost of the accumulators for a standard stationary battery for cyclical energy storage of several kWh, the lowest purchase price can be found at the Pb battery of a traction type (Trojan, 2018). Approximately twice higher purchase price is at a NiCd battery (Saft-Ferak, 2018) and a $LiFePO_4$ battery (Winston, 2018). To ensure reliable operation, the $LiFePO_4$ battery needs to be supplemented with the battery management system, which increases the cost of the

LiFePO$_4$ system to approximately three times in comparison to the Pb battery price. If battery maintenance costs and the price of energy, dissipated due to the efficiency of the charging and discharging processes, is neglected the cost of electrical energy storage in the battery is decisively determined by its lifetime. Since the lifetime of NiCd battery is approximately the same as the lifetime of the traction Pb battery under the same operating conditions, its cost of electrical energy storage is approximately twice than that of the Pb battery. The LiFePO$_4$ battery, if its lifetime is, at minimum, three times higher than the Pb battery, shows even lower costs of electrical energy storage.

Determining a specific lifetime of LiFePO$_4$ batteries is very problematic. Whereas the values of the other batteries reported by most manufacturers are nearly the same; i.e., 600–800 cycles for the capacity drop to 80% of the nominal value for Pb and NiCd batteries with the capacity of several hundred Ah and with 80% discharge depth (DOD), the LiFePO$_4$ battery capacity reported by different manufacturers often differ more than three times. The stated capacities of the same products reported by the manufacturers and distributors differ by up to twofold; see Fig. 1. The unreliable determination of the battery lifetimes then becomes one of the barriers to their wide-range use in practice.
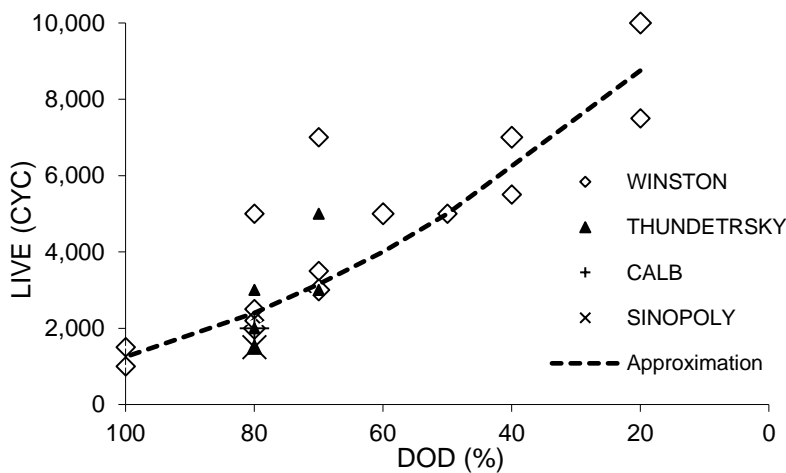
Figure 1. Dependence of the lifetime of the batteries from different manufacturers on DOD (Calb, 2018; Instruction, 2018; Lithium, 2018; Sinopoly, 2018).

The problem can then be solved only by the experimental verification of the real lifetime of the batteries and by providing at least an approximate description of the drop in the battery capacity during its operation. The lifetime also depends on other operating parameters, especially on the depth of battery discharge, its temperature, the charging and discharging currents with respect to time, including the time when the battery is out of service.

MATERIALS AND METHODS

The capacity exploitable in the battery operation is determined by the amount of active material on the battery electrodes that can react in electrochemical reactions in the process of discharging and charging.

The capacity drop during the battery operation is caused by the loss of active material that gradually diminishes due to a number of different processes. In general, these phenomena can be described as discrete cyclic and continuous processes. A discrete process is based on a defined initial state that proceeds according to a given algorithm and results in a final state. Individual cyclical processes of the same type take place one after another, whereas the final state of the nth process is the initial state of the $n+1$ process.

To maintain a long battery lifetime, it is necessary to minimize the degradation of the battery structure during the cyclic process, i.e., to minimize the loss of active material between the initial and final states of the process. Continuous degradation processes are characterized by the rate of the loss of active material in the structure. For a known rate, it is possible to determine the loss of the active material over arbitrary time. It is also possible to express the result of the process over selected time and evaluate the continuous degradation process as a sequence of corresponding discrete processes.

A typical cyclic degradation process in the battery is the process of its discharging and recharging. By discharging, an active material is converted to another that is converted by charging back to the initial constituent. Since the reverse conversion efficiency is always less than 1, an active material on the battery electrodes is gradually diminishing and the capacity of the battery decreases. The loss of an active material, and thus the battery capacity during one cycle (discharge and subsequent charge) can be described by (1)

$$Q_{n+1} = Q_n(1 - \Delta) \tag{1}$$

where Q_n – the capacity of the battery in cycle n, proportional to the amount of active material; Δ – degeneration factor; $(1-\Delta)$ – the efficiency of an active material regeneration during the cycle.

The process of an active material loss during the sequence m of the identical cyclic degradation processes can be then described by a geometric progression, whose quotient is $(1-\Delta)$, as

$$Q_{n+m} = Q_n(1 - \Delta)^m \tag{2}$$

Eq. (2) can be written in the form

$$Q_{n+m} \approx Q_n e^{-\Delta m} \tag{3}$$

This form of approximation is often used to describe the battery lifetime parameters. An argument of the function may be also continuous, which is usually time. This approach leads to modeling battery lifetime parameters by means of an analogy to the electrical signals during transient processes in RC circuits (Dalal, 2011)

$$Q(t) = Q(0)\, e^{-\frac{t}{\tau}} \tag{4}$$

where $Q(t)$ – an instantaneous value of the battery capacity at time t; $\tau = RC$ is a time constant of a simple RC circuit.

The problem with the models is to determine the relation of the model parameters (time constants) to the physical reality of the battery operation. Mathematical methods can determine very accurate values of the model parameters, valid for the set of measurements without specifying a more general dependence of these values on the battery operation parameters.

Analysis of the loss of an active material due to spontaneous discharges

A typical continuous degradation process of the battery is the process its aging, which can be, in the extreme case, approximated by the degradation of an active material of the battery when stored in a charged state in the store.

To approximate the process, the Arrhenius approximation of the rate of the active material degradation using an exponential function (Hu et al., 2016) is currently applied. The approximation is based on the idea that in order to initiate the degradation reaction, the particle must be supplied with a certain activation energy required to the transfer of chemical bonds. The probability that this condition will occur grows exponentially with the temperature.

$$k(T) = Ae^{-\frac{E_a}{RT}}, \tag{5}$$

here $k(T)$ – represents a product degradation rate; A – the frequency factor; E_a – the activation energy; R – denotes the ideal gas constant (8.314 J mol^{-1}.K^{-1}); T – absolute temperature with the unit of K.

According to the above mentioned approximations, the process of losing both an active material and capacity during the battery operation, when it is degraded by N-cyclic degradation processes at time t, can be expressed by

$$Q(N, t) = Q_0 e^{-\Delta N} \left(1 - t. k_{ef}(T) \right). \tag{6}$$

The change in the battery capacity in the order of units of percent can also be expressed in the form of (7).

$$Q(N, t) = Q_0 e^{-\Delta N - \frac{t}{\tau_{ef}}}, \tag{7}$$

where k_{ef} (T) – the effective value of the product degradation rate; $\tau_{ef}(T)$ – the time constant of the thermal battery degradation (8).

$$\tau_{ef}(T) = \frac{1}{k_{ef}(T)} = \hat{A} e^{\frac{E_a}{RT}} \tag{8}$$

The constants Δ and τ_{ef} (T) primarily depend on the quality of the monitored products, and for one sample on the battery operating parameters.

Analysis of an active material loss of the battery due to DOD

The efficiency of an active material regeneration (1 - Δ) depends primarily on the depth of discharge (DOD) in the cycle. For a deeply discharged cell, the efficiency of an active material regeneration is significantly less than that of the cell that has been discharged with a small value of DOD only.

This phenomenon is caused by the dependence of a relative amount of active material, which is regenerated in the discharging and charging processes, on the depth inside the body with an active material, where the active material is being regenerated. For a simple approximation, it can be assumed that the ratio between the amount of m_l of the active material, non-regenerated at a certain depth, to the amount of an active material m_0, entering the regeneration, can be approximated by a linear function

$$\frac{m_l}{m_0} = a + bx \tag{9}$$

where x – the depth from the surface of the body with an active material; a, b – constants. Then the total amount of non-regenerated material from the surface to the maximum regeneration depth x_{max} can be expressed by the integral (10)

$$m_L = m_0 \int_0^{x_{max}} (a+bx)dx = m_0(a.x_{max} + \frac{b}{2}x_{max}^2) . \tag{10}$$

Considering the stoichiometric conception of electrochemical reactions in the battery, the amount of charge being regenerated is proportional to the amount of a regenerated active material. Since, for one sample of the battery, the size of the regenerated charge is proportional to the discharge depth (DOD), and the maximum depth of regeneration is again proportional to the amount of a regenerated active material, the amount of non-regenerated material, depending on DOD, can be expressed as

$$\frac{m_L}{m_0} = \Delta = a'(DOD) + b'(DOD)^2 . \tag{11}$$

Analysis of the loss of an active material due to thermal cell degradation
The time constant of a spontaneous thermal cell degradation τ_{ef} (T) depends both on the cell temperature and on the activation energy of the degradation processes in the cell. Searching for a time constant is complicated by the fact that the number of degradation processes can be higher, and the experimental monitoring of the cell ageing is highly time-consuming.

A normal aging of the cells at a normal temperature, which is reflected by a 4–8% drop of capacity per year, corresponds to the activation energy E_a of the most significant degradation process in the range of 45,000–51,000 J mol^{-1} that corresponds to the values 36,000–53,000 J mol^{-1} reported by Smith et al. (2014).

The temperature of the cell, however, need not be determined by the ambient temperature itself. The temperature increases due to the power losses in the cell at high currents, especially during the cell installation into the batteries or in poor cell cooling.

The power dissipated in the cell, when current I passes through, is determined by the equivalent cell DC internal resistance R_i

$$P_D = I^2(R_i) . \tag{12}$$

The equivalent cell DC internal resistance R_i depends on the cell capacity. The cells with large capacity have an equivalent DC resistance significantly lower than the cells with low capacity. The dependence of the resistance on the cell capacity Q can be

approximated, e.g., by Eq. (13). The approximation deviation, e.g., for cell series with capacity 40–1,000 AH is less than 10%.

$$R_i = \frac{0.02}{|Q|^{2/3}} . \tag{13}$$

The dissipated power for the cell capacity Q can then be approximated by (14). If the cell is loaded with a commonly considered current, whose size corresponds to the ampere-hour cell capacity, the dissipated power can be expressed by (15).

$$P_D = \frac{0.02\, I^2}{|Q|^{2/3}} , \tag{14}$$

$$P_D = 0.02\, |Q|^{4/3} . \tag{15}$$

For the known dissipated power, the resulting temperature rise ΔT in a steady state of the cell is determined by its thermal resistance R_{th} in the process of cooling. This can be determined for a free-standing cell as a reciprocal of the product of its surface S and a heat transfer coefficient α on its surface (16).

$$\Delta T = P_D . R_{th} = \frac{P_D}{\alpha\, S} . \tag{16}$$

The dependence of the stabilized temperature rise on the passing current for the cells with the capacity of 40–1,000 AH is shown in Fig. 2.
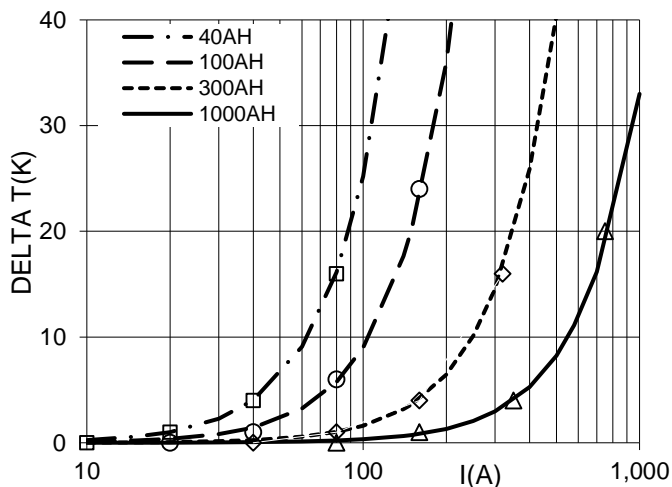
Figure 2. Dependence of the temperature rise of the cells with different capacity on the passing current.

The current, whose size corresponds to the ampere-hour cell capacity, will cause the temperature rise from 4 to 33 K. Minor temperature rise is exhibited by the cells with low capacity, because they have a larger surface area, with regard to the capacity, and hence a lower thermal resistance.

In case the cell is cyclically discharged and charged with the identical current during the test, the power dissipation of this level will be dissipated in the cell practically permanently and will cause the same cell temperature rise both during charging and discharging. This can lead to a significant reduction in the cell lifetime in long-term processes. The phenomenon is manifested, e.g., by the decrease in the cell lifetime during charging and discharging by large currents comparable with the numerical value of the ampere-hour cell capacity. As an example can serve the change in the battery WB-LYP 1000 AHA lifetime caused by the operation under high current 0.5 C or C; see Fig. 3.
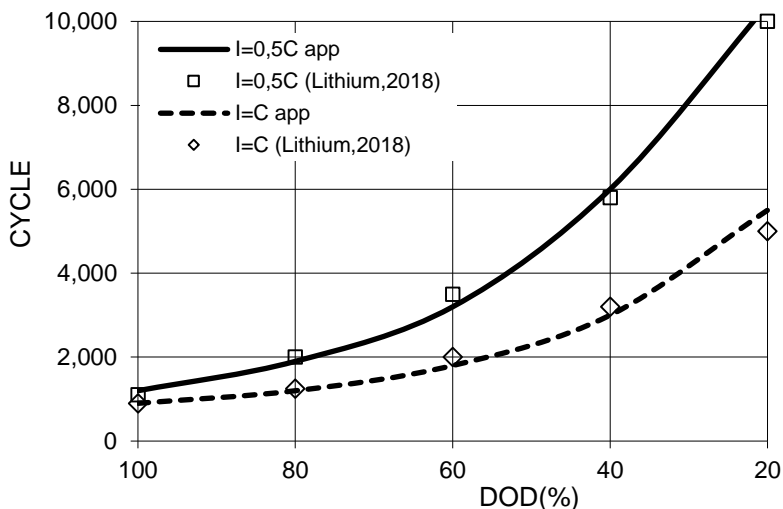
Figure 3. Comparison of the cell lifetime approximation with stated values (Lithium, 2018).

The temperature of the cell, which is charging or discharging by the current corresponding to the C-rate, is 25 to 30 K higher than the temperature of the cell, which is charging or discharging with a 0.5 C-rate current. Increasing the temperature causes about five times the increase in cell aging rate. Since the time corresponding to the time of charge and discharge of the cell is also inversely proportional to the load current, the time corresponding to the lifetime of the cell is also inversely proportional to the load current.

Effect of increasing the speed of the aging of the article is consequently smaller than would correspond to its absolute value; a double increase in the load current will cause cell life to decrease (for DOD < 80%) by approximately half.

The cell temperature rise sharply drops when the current passing through the cell decreases because the power dissipated in the cell, when the current passes through, is proportional to the square root of this current. For the current, corresponding to one quarter of the ampere-hour cell capacity, the influence of this charging and discharging current level on the lifetime of a well-cooled cell can usually be neglected. Another situation occurs when the cells are stacked into batteries. Such a composed body will have several times higher dissipated power related to its surface than the free-standing cell, hence it will have multiple times higher temperature rise. Typically, for a 4-cell

battery (12 V LiFePO$_4$), the temperature rise on the surface of the external cells is about 2.5 times higher and 4 times higher at the central cells in comparison to the situation if they were placed separately. A state of a 4-cell battery with 40 Ah capacity, operated at a 10 A current is shown in Fig. 4 (Papezova & Papez, 2017).
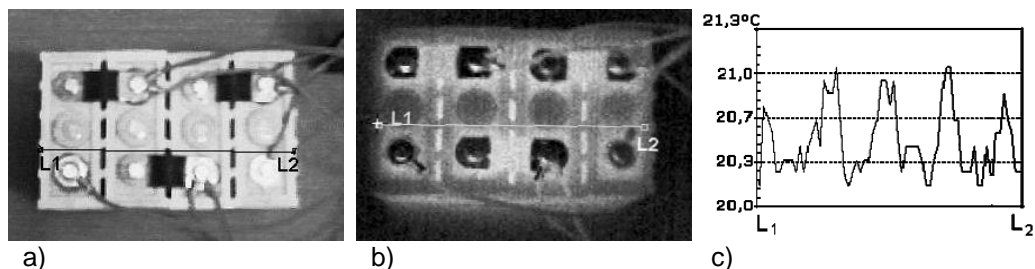
Figure 4. Temperature of the cells; a) real photo, b) infra photo, c) a distribution of temperature on the cells.

To solve the battery temperature rise in a dynamic mode, it is possible to simply connect thermal capacity and thermal resistance in parallel. The time constant of this integration network is 2,000–3,000 s for small cells and 4,000–5,000 s for large cells. The battery thermal response to fast current changes, too short for these time constants, can be solved according to the current RMS value. For slow current changes, the temperature rise must be solved as the integrator response to the pulse excitation signal.

Further increase in the rate of spontaneous degradation may also be caused by a number of other effects, e.g., by electrolyte contamination or by mechanical interaction in the cell electrode system.

RESULTS AND DISCUSSION

The initial analysis was performed for 8 batteries compiled from Winston Battery, Calb, Thunder Sky, and Sinopoly. The batteries have been tested continuously for almost 4 years by cyclic discharging and charging at a depth of the discharge 30–100%, as well as maintained at rest without operation. On the basis of the experiments, the parameters of the above mentioned model were determined to be the parameters for the batteries of individual manufacturers.

Two automatic systems (Papezova & Papez, 2017) were used for testing. In the tested 4-cell battery, the charging and discharging processes under the selected constant current were run automatically. Individual cells were equipped with balancing and protective circuits that prevented from exceeding the maximum voltage during charging, as well as the voltage drop under the minimum level during the discharge. The operating parameters of the tested battery were continuously scanned, recorded and evaluated by the control computer.

Examples of the measured values are given in Tables 1 and 2.

Table 1. Test results of 4 cellsWB-LYP40AHA Winston Battery with DOD = 100%

After	Time (h)	Dischar. voltage (V)	Charg. voltage (V)	Full dischar. (Ah)	Full dischar. (%)	Full charge (Ah)	Charg. Effic. (%)	Capac. drop (Ah)
0 c.	0	11.94	15.8	45.	112.5	45.6	97.7	
100 c.	900	11.94	15.9	43.7	109.3	44	99.4	1.3
200 c.	1,900	11.93	15.86	42.33	105.8	42.8	98.9	2.7
300 c.	2,800	11.87	15.85	41.3	103.3	41.7	99.1	3.7
400 c.	5,800	11.88	15.83	39.6	99.0	40	99.0	5.4
500 c.	10,000	11.89	15.8	37.2	93.0	37.9	98.1	7.8
600 c.	10,900	11.88	15.9	35.8	89.5	36.2	98.9	9.2
700 c.	11,800	11.87	15.86	35.	87.5	35.4	98.9	10
800 c.	12,700	11.87	15.85	33.8	84.5	34.3	98.5	11.2
900 c.	13,600	11.86	15.85	32.6	82.5	33.3	98.8	12.1
1,000 c.	14,500	11.86	15.84	32.1	80.25	32.5	98.8	12.9

Table2. Test results of 4 cellsWB-LYP40AHA Winston Battery with DOD = 50%

After	Time (h)	Dischar. voltage (V)	Charg. voltage (V)	Full dischar. (Ah)	Full dischar. (%)	Full charge (Ah)	Charg. Effic. (%)	Capac. drop (Ah)
0 c.	0	12.87	15.24	45.00	112.5	45.5	98.90	
200 c.	435	12.87	15.28	44.1	110.25	44.6	98.81	0.9
400 c.	870	12.86	15.26	43.3	108.25	43.7	98.98	1.7
600 c.	1,305	12.85	15.13	42.5	106.25	42.9	99	2.5
800 c.	1,740	12.86	15.20	41.7	104.25	42.0	99.3	3.3
1,000 c.	2,175	12.86	15.18	41	102.5	41.3	99.3	4
1,200 c.	2,610	12.87	15.22	40.4	101	40.7	99	4.6
1,400 c.	3,045	12.87	15.15	39.8	99.5	40.2	99.0	5.2
1,600 c.	3,480	12.86	15.15	39.2	98	39.6	98.72	5.8
1,800 c.	3,915	12.87	15.09	38.5	96.75	39.0	98.7	6.5
2,000 c.	4,350	12.86	15.10	37.9	94.75	38.4	98.7	7.1
2,200 c.	4,785	12.86	15.13	37.1	92.75	37.5	98.93	7.9
2,400 c.	5,220	12.87	15.15	36.3	90.75	36.8	98.64	8.7
2,600 c.	5,622	12.86	15.18	35.6	89	36	98.9	9.4
2,800 c.	5,655	12.86	15.19	35	87.5	35.4	98.87	10
3,000 c.	6,090	12.87	15.15	34.5	86.25	35	98.6	10.5
3,200 c.	6,525	12.86	15.2	33.9	84.75	34.4	98.5	11.1
3,400 c.	6,960	12.86	15.14	33.3	83.25	33.7	98.8	11.7
3,600 c.	7,395	12.86	15.16	32.7	81.75	33.1	98.8	12.3
3,800 c.	7,830	12.87	15.18	32	80	32.3	99.1	13
4,000 c.	8,265	12.86	15.18	31.6	79	32	98.8	13.4

CONCLUSIONS

The curves approximated by the model were further compared with the real measured values of the batteries from individual manufacturers. The parameters of the batteries from various manufacturers were also compared mutually. Dependences of the cell capacity of different manufacturers on the number of working cycles are displayed in Fig. 5.
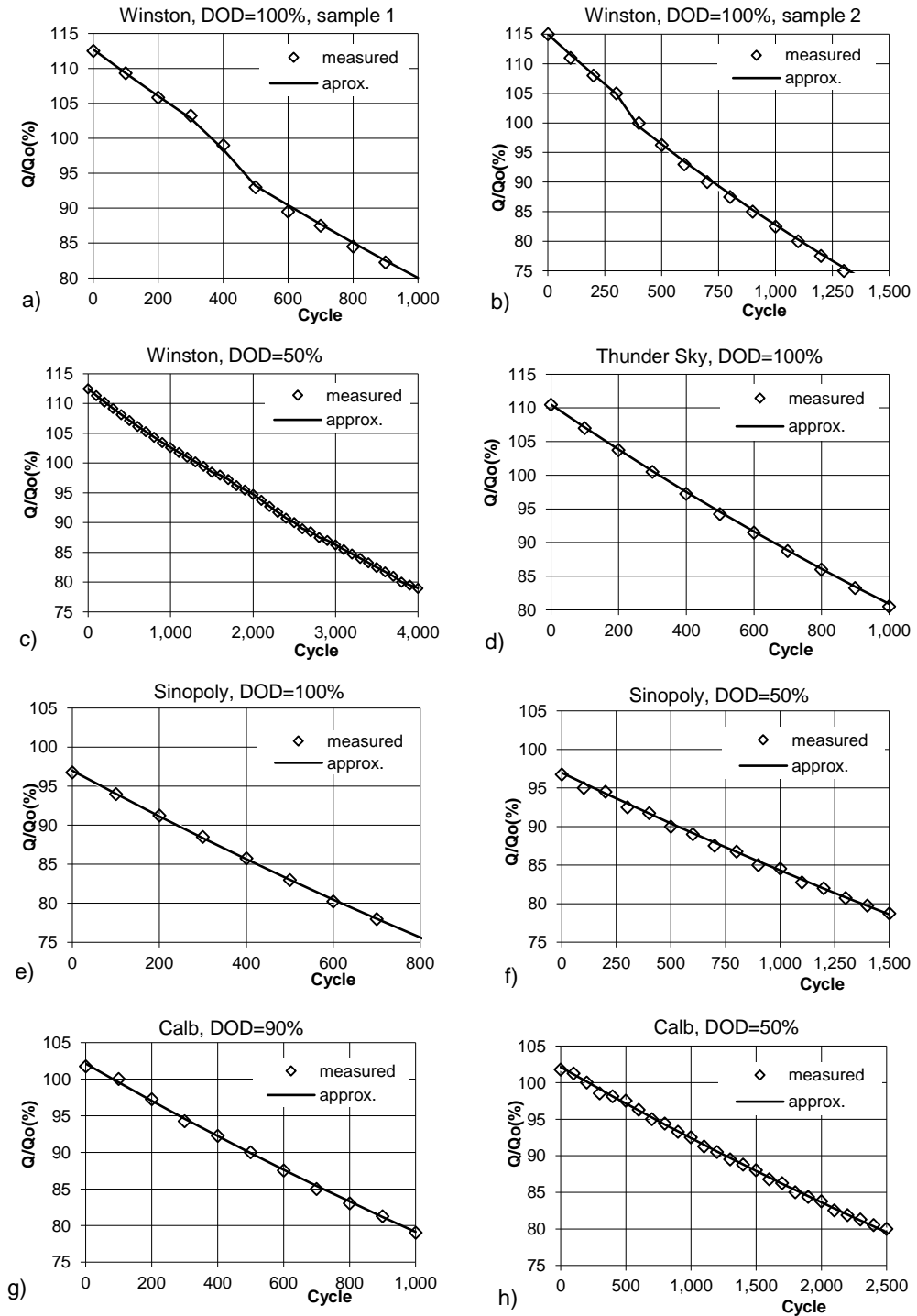
Figure 5. Dependence of the cell capacity of different manufacturers on the number of working cycles.

Mean square deviation approximations, optimized for all batteries, are 0.2–0.3%. The deviation can be reduced to a maximum value of 0.15% by fitting to individual manufacturers. The lifetime of the tested batteries of all manufacturers is approximately 1,000 cycles (for the drop in capacity to 80% of the nominal value), for the deep discharge with 90–100% DOD and the test lasting approximately 1 year.

The smallest lifetime, with only 800 cycles, was set for the Sinopoly batteries, which also had the largest capacity drop during storage. For the discharge with 50% DOD and for the test lasting approximately 2 years, the highest lifetime of approximately 4,000 cycles was set for Winston batteries. The lifetime is less than that stated by the manufacturer. The deviation is probably caused by the aging of the battery during the test. For the test lasting approximately 1 year, the battery lifetime would be by 1,000 cycles higher.

The lifetime of Calb batteries was approximately 2,500 cycles and the lifetime of Sinopoly batteries was only about 1,500 cycles in this mode; among others, due to the highest capacity drop in time, approximately 8% per year. The indicated time constant of the battery aging ranged from 10^5 hours (Sinopoly) to 1.7×10^5 hours (Thunder Sky). The cyclic degradation constant for DOD = 50% ranged from 5×10^{-5} (Calb) to 7×10^{-5} (Sinopoly); for DOD = 100% ranged from 22×10^{-5} (Sinopoly) to 26×10^{-5} (Thunder Sky).

To ensure the claimed lifetime, the manufacturers, mostly probably, assemble the cells with a larger initial capacity than they declare on the labels, e.g., at the Winston batteries by about 15%, at the Thunder Sky batteries even by 20%.

REFERENCES

Calb lithium-ion cells and modules. *http://www.calbusainc.com/calb-ca-series/*. Accessed 18.1.2018.

Dalal, M., Ma, J. & He, D. 2011. Lithium-ion battery life prognostic health management system using particle filtering framework, *Proc. IMechE*. Vol. **225** Part O: *J. Risk and Reliability*, pp.81–90.

Hu, M.,Wang, J., Fu, Ch., Qin, D. & Xie, S. 2016. Study on Cycle-Life Prediction Model of Lithium-Ion Battery for Electric Vehicles, *International Journal of Electrochemical Science Int. J. Electrochem. Sci*. **11**, 577–589.

Instruction Manual. *http://www.thunderstruck-ev.com/Manuals/Thundersky%20Product%20-Manual.pdf*. Accessed 18.1.2018.

Lithium & solar power LiFePO$_4$. *http://gwl-power.tumblr.com/tagged/WinstonBattery*. Access-ed 18.1.2018.

Lithium-ion Power Battery. *http://en.winston-battery.com/index.php/products/power-battery*. Accessed 18.1.2018.

Papezova, S. & Papez, V. 2017. Endurance LiFePO$_4$ battery testing. *Agronomy Research* **15**(S1), 1152–1161.

Saft-Ferak Rada KPH/KPM/KPL. *http://www.saft-ferak.cz/cz/ada-kphkpmkpl*. Accessed 18.1.2018.

Sinopoly battery products. *http://www.sinopolybattery.com/en/products.aspx?cid=10*. Accessed 18.1.2018.

Smith, K., Wood, E, Santhanagopalan, S. Kim, G., Neubauer, J. & Pesaran, A. 2014. Models for Battery Reliability and Lifetime, Conference Paper NREL/CP-5400-57746. https://www.nrel.gov/docs/fy14osti/57746.pdf

Trojan TRAKCNI BLOKOVE GiS. *https://www.battery-expert.cz/trakcni-blokove-gis--trojan/*. Accessed 18.1.2018.

Winston – lithium batteries of new generation. *https://www.battery.cz/lithiove-trakcni-baterie/*. Access-ed 18.1.2018. (in Czech).

The operational parameters and emissions of portable generator after long-term operation on n-butanol

M. Pexa, J. Čedík[*], B. Peterka and M. Holůbek

Czech University of Life Sciences Prague, Faculty of Engineering, Department for Quality and Dependability of Machines, Kamýcká 129, CZ165 21 Prague 6, Czech Republic
[*]Correspondence: cedikj@tf.czu.cz

Abstract. The utilization of biofuels in spark ignition and compression ignition engines is the trend of the recent time. The great expectations are inserted into n-butanol as a fuel, especially for spark ignition engines. The short time use of n-butanol in the SI (spark ignition) combustion engine does not make a big problem (start of the cold engine, change of the air-fuel ratio). The purpose of this contribution is the effect of long-term use of n-butanol as a fuel for SI engine. For this purpose the small portable generator was used. The harmful emissions, fuel consumption and power of the generator was measured then the generator was operated for 300 hours on 100% n-butanol with 80% of nominal load and the measurement was repeated. The generator was loaded with adjustable electrical resistance. As a reference fuel the petrol BA 95 with no bio-component was used. During the operation on n-butanol no technical problems occurred with the generator. After 300 hours of operation on n-butanol the performance parameters slightly decreased with little impact on production of harmful emissions components.

Key words: biofuel, petrol, emission, fuel consumption, spark ignition.

INTRODUCTION

In the present time, combustion of conventional fossil fuels such as petrol and diesel fuel represents more than half of the world's primary energy consumption. The use of the biofuels helps to reduce the consumption of fossil fuels and amount of greenhouse gasses released into atmosphere and also helps to ensure the energy security (Awad et al., 2018).

The alcohol based biofuels are the most widely used for SI engines. Ethanol, the most used biofuel for SI engines, has many disadvantages such as its affinity to the water, aggression to the most of rubber and plastic sealing elements, low calorific value etc. (Čedík et al., 2014a; 2014b; Gailis & Pirs, 2017).

N-butanol could be used as an alternative to ethanol as alcohol-based biofuel. The n-butanol is the second generation biofuel. In many studies the utilization of n-butanol in CI (compression ignition) as a fuel admixture is studied. In CI engines the n-butanol is usually utilized to decrease the viscosity of the fuel blends with higher concentrations of biodiesel or vegetable oil (Rakopoulos et al., 2010; Yilmaz et al., 2014; Atmanli et al., 2015; Čedík et al., 2015; Pexa et al., 2016; Babu et al., 2017; Peterka et al., 2017).

The n-butanol can be produced similarly to ethanol, by fermentation or in petrochemical way (Ezeji et al., 2003; Ndaba et al., 2015; Rocha–Meneses et al., 2017). Compared with ethanol the properties of n-butanol are closer to petrol due to the longer hydrocarbon chain. However, similarly to ethanol, the use of 100% n-butanol in spark ignition engines also requires the modification of the air-fuel mixing ratio, due to lower stoichiometric ratio of n-butanol. In comparison with the ethanol, the n-butanol has several advantages, such as a lower ignition temperature and higher calorific value. Also, compared with ethanol, the n-butanol has better mixing properties with hydrocarbon fuels and due to lower oxygen content the stoichiometric ratio is more similar to petrol. Therefore, the higher concentrations of n-butanol in petrol without engine modification can be used. The n-butanol is also less corrosive due to lower affinity to water than ethanol (Qureshi & Ezeji, 2008; Shapovalov & Ashkinazi, 2008; Andersen et al., 2010; Harvey & Meylemans, 2011; Swana et al., 2011; Gu et al., 2012; Serras-Pereira et al., 2013; Hönig et al., 2015a; 2015b; Yusri et al., 2016; Peterka et al., 2017). Petrol blended with n-butanol was studied in the various range of mixing ratios up to 100% of n-butanol (Wallner et al., 2009; Williams et al., 2009; Yang et al., 2009; Dernotte et al., 2010; Wigg et al., 2011; Gu et al., 2012; Feng et al., 2013; Elfasakhany, 2014; Yusri et al., 2016; Peterka et al., 2017; Yusoff, et al., 2017). The results of these studies show that, in comparison with petrol, fuel blended with n-butanol reduces the emissions of carbon monoxide and unburned hydrocarbons, emissions of carbon dioxide and nitrogen oxides could be decreased or increased (Peterka et al. 2017). Due to the lower calorific value compared with petrol the specific fuel consumption is higher and the torque and power are lower. Better combustion efficiency can be achieved due to better anti-detonation characteristics of n-butanol compared with petrol and higher oxygen content. Yusri et al. (2016) found that the addition of n-butanol into the petrol in concentration up to 15% decreases the cylinder pressure, emissions of CO, NO_X and exhaust gas temperature. Some sources indicate the increased torque and reduced energy consumption at 35% concentration of n-butanol in petrol (Feng et al., 2013). Other sources state that the performance parameters of the engine are maintained the same in concentration range from 10% (Kukharonak et al., 2017) to 20% (Yang et al., 2009) of n-butanol in the petrol. Peterka et al. (2017) found increased emissions of NO_X, especially at low and moderate engine load, decreased emissions o CO and HC, slightly increased emissions of CO_2, especially in lower engine load, and increased fuel consumption.

Most of the above mentioned studies were carried out in short term measurement and does not take into account the effect of long term operation of the engine.

The aim of the paper is to compare the emission production and fuel consumption of the generator when operating on n-butanol and petrol BA 95 after 300 operating hours with approx. 80% of nominal load. The harmful emissions components (CO – carbon monoxide, CO_2 – carbon dioxide, NO_X – nitrogen oxides, HC – hydrocarbons and PM – particulate matter) and fuel consumption are monitored and compared with the results, obtained after 5 operating hours.

MATERIALS AND METHODS

The two mobile generators ProMax 3500A (Fig. 1, Table 1). The combustion engine, connected to the alternator is suitable for long-time tests since the engine can be

easily loaded and the electrical output power of the generator is equivalent to the engine load.

Figure 1. Mobile generator ProMax 3500A powered by small Briggs and Stratton engine type Vanguard 6.5HP.

The measurement is focused on the comparison of fuel consumption and emissions production of the combustion engine of the generator before and after its long time operation on petrol BA 95 and n-butanol. Two generators were used in the study, one for each fuel. Before the test the generators were new. The measurement was carried out after 5 operating hours and after 300 operating hours of the engine with 80% of nominal load of the generator.

During loading of the combustion engine the frequency, electrical current and voltage of the output of the generator are measured using the electrometer ZPA ED310 equipped with an RS 485 (accuracy of 0.05%). Simultaneously with the measurement of electrical parameters fuel mass flow rate using Vibra AJ 6200 standard precision scale (accuracy 0.1 g) is also measured. In order to monitor the operating parameters of the engine during measurements, the oil temperature sensor, fuel temperature sensor and intake air temperature sensor was mounted on the engine. BrainBee emission analyser and EEPS particle analyser are used as testing devices of emissions (Table 2). All data are stored to the PC memory using

Table 1. Basic specification of the used generators

Electrical parameters	
Parameter	**Specification**
Manufacturer	Briggs and Stratton
Type	ProMax 3500A
Rated power	2,700 W
Maximum power	3,400 kVA
Output voltage	220 V
Output frequency	50 Hz
Output current	11.2 A
Engine parameters	
Parameter	**Specification**
Manufacturer	Briggs and Stratton
Type	Vanguard 6.5HP
Rated power	4.8 kW at 3,600 min^{-1}
Max. torque	13.3 Nm at 3,000 min
Engine type	4-stroke, spark ignitio
Displacement	205 cm^3
Cooling	Air cooled
Bore X Stroke	68.3 X 55.9 mm
Compression ratio	8.3:1
Valves	2
Valve mechanism	OHV
Lubrication	Splash
Crankshaft orientanion	Horizontal

Table 2. Parameters of the emission analyser BrainBee

Component	Resolution	Accuracy
CO	0.01% vol.	0.03% vol. or 5% read value
CO_2	0.1% vol.	0.5% vol. or 5% read value
HC	1 ppm vol.	10 ppm vol. or 5% read value
O_2	0.01% vol.	0.1% vol. or 5% read value
NO	1 ppm	10 ppm vol. or 5% read value
Opacity	0.1%	2%
Temperature	1 °C	2.5 °C

RS482 to RS232 interface and for this purposes software application was developed in LabView.

The values of emissions production are measured in volumetric concentrations and, based on the amount of the intake air, they are recalculated into mass production.

The principle of the measurement is similar to that used by Peterka et al. (2017). The combustion engine of the generator works at the rotation speed of 3000 min^{-1} (electrical output frequency of 50 Hz). In this rotation speed the engine is gradually loaded by electrical resistance to the power of approx. 660, 1,320, 1950 and 2,560 W. Under these loads, which corresponds to 25, 50, 75 and 100% of the nominal power of the generator, the measurements are performed with petrol BA 95 (with no ethanol) and with 100% n-butanol (BUT). The basic parameters of the fuels are listed in Table 3.

Table 3. Basic properties of used fuels (Feng et al., 2015; Elfasakhany & Mahrous, 2016)

Property	n-Butanol	Petrol
Chemical formula	C_4H_9OH	$C_4–C_{12}$
Molecular weight (g mol^{-1})	74	100–105
Density (kg m^{-3})	810	720–760
Carbon content (%)	65	86
Hydrogen content (%)	13.5	14
Oxygen content (%)	21.6	–
Auto ignition temperature (°C)	343	257
Calorific value (MJ kg^{-1})	33.1	42.9
Latent heat of vaporization (KJ kg^{-1})	716	380–500
Stoichiometric air-fuel ratio	11.21	14.7
Octane number	96	86–94
Boiling temperature (°C)	117.7	25–275
Adiabatic flame temperature (K)	2,340	2,370
Saturation pressure at 38 °C (kPa)	2.27	31.01

Transmission losses and the change in viscosity of engine oil are not considered. The measurement is performed at an operating temperature, which is dependent on the load from 90 °C to 110 °C of the engine oil temperature.

The air–fuel ratio (AFR) was monitored within the measurement. Then, the AFR was modified using the fuel choke. AFR for petrol BA 95 is 14.7:1 and 11.2:1 for n-butanol (Elfasakhany & Mahrous, 2016).

RESULTS AND DISCUSSION

The result values of emission components, fuel consumption, rotation speed and engine load are the mean values from two minutes record with frequency of 1 Hz. The emissions of particulate matter were excluded from the data evaluation. The concentration of particulate matter in the exhaust gas of the spark ignition engine is very low and from the viewpoint of measurement device it is at the limit of detection.

In the Table 4 the volumetric concentrations of emission components in the exhaust gas of combustion engine of the generator after 5 operating hours are shown. The grey areas in the tables highlights the lower value of harmful emissions production or fuel consumption in comparison between the used fuels. The volumetric concentrations of

emission components in the exhaust gas after 300 operating hours are shown in the Table 5.

Table 4. Fuel consumption and volumetric concentrations of the emissions components in the exhaust gas of the combustion engine after 5 operating hours for BA 95 and BUT fuels. (FC – fuel consumption; SFC – specific fuel consumption) (Peterka et al., 2017)

	Engine speed	Output power	NO_X	CO	CO_2	HC	FC	SFC
	min^{-1}	W	ppm	%	%	ppm	$g\ h^{-1}$	$g\ kWh^{-1}$
BA 95	3,142.95	656.10	88.86	3.82	7.91	104.06	600.12	914.67
	3,121.01	1,331.87	175.90	3.92	7.74	120.48	789.39	592.70
	3,101.91	1,939.89	363.21	4.09	8.61	129.40	960.29	495.02
	2,989.63	2,566.52	660.79	4.68	10.56	137.27	1,162.49	452.94
BUT	3,141.04	656.65	155.19	0.77	9.65	44.32	665.77	1,013.89
	3,122.16	1,330.26	361.20	1.59	9.35	56.11	882.97	663.76
	3,091.03	1,941.19	714.57	2.08	9.82	77.86	1,106.60	570.06
	2,915.82	2,591.58	818.34	3.35	11.26	90.86	1,408.77	543.59

From the Table 4 and 5 it is evident that after 300 operating hours the BUT fuel reached better values in terms of emissions of nitrogen oxides and carbon dioxide. On the other hand, the fuel BA 95 reached better results in emissions of carbon monoxide and unburned hydrocarbons. The fuel consumption was increased for both tested fuels, n-butanol and petrol, but for the n-butanol the fuel consumption increase is more significant.

Table 5. Fuel consumption and volumetric concentrations of the emissions components in the exhaust gas of the combustion engine after 300 operating hours for BA 95 and BUT fuels. (FC – fuel consumption, SFC – specific fuel consumption)

	Engine speed	Output power	NO_X	CO	CO_2	HC	FC	SFC
	min^{-1}	W	ppm	%	%	ppm	$g\ h^{-1}$	$g\ kWh^{-1}$
BA 95	3,124.45	681.28	82.41	2.56	6.37	76.21	884.4	1,298.14
	3,122.32	1,333.46	129.83	3.2	6.74	90.03	825.6	619.14
	3,041.81	1,949.28	255.98	3.1	7.29	98.82	972	498.65
	2,862.39	2,605.51	611.55	3.12	8.93	98.17	1,203.6	461.94
BUT	3,138.58	680.26	40.14	3.57	6.27	118.97	807.6	1,187.2
	3,117.1	1,333.1	44.58	4.43	5.94	132.98	1,094.4	820.95
	3,009.68	1,958.33	30.97	6.45	5.68	211.14	1,423.08	726.68
	2,941.71	2,298.51	84.35	5.1	6.81	178.72	1,399.5	608.87

Also, it may be noted that the maximum electric output power of the generator decreased by approx. 11% after 300 operating hours on n-butanol.

The mass production of the harmful emissions components is shown in the Table 6 (after 5 operating hours) and in the Table 7 (after 300 operating hours). The mass production of emissions components was calculated based on fuel consumption and AFR ratio.

Table 6. Mass production of the emissions components in the exhaust gas of the combustion engine after 5 operating hours for BA 95 and BUT fuels. (FC – fuel consumption, SFC – specific fuel consumption) (Peterka et al., 2017)

	Engine speed	Output power	NO_X	CO	CO_2	HC
	min^{-1}	W	$g\ h^{-1}$	$g\ h^{-1}$	$g\ h^{-1}$	$g\ h^{-1}$
BA 95	3,142.95	656.1	0.8	0.032	1,040.34	1.37
	3,121.01	1,331.87	2.08	0.043	1,340.4	2.09
	3,101.91	1,939.89	5.21	0.055	1,813.84	2.73
	2,989.63	2,566.52	11.48	0.076	2,690.74	3.51
BUT	3,141.04	656.65	1.26	0.006	1,150.4	0.53
	3,122.16	1,330.26	3.89	0.016	1,477.1	0.89
	3,091.03	1,941.19	9.65	0.026	1,945.88	1.55
	2,915.82	2,591.58	14.07	0.054	2,838.27	2.3

Table 7. Mass production of the emissions components in the exhaust gas of the combustion engine after 300 operating hours for BA 95 and BUT fuels. (FC – fuel consumption, SFC – specific fuel consumption)

	Engine speed	Output power	NO_X	CO	CO_2	HC
	min^{-1}	W	$g\ h^{-1}$	$g\ h^{-1}$	$g\ h^{-1}$	$g\ h^{-1}$
BA 95	3,124.45	681.28	1.6	0.032	1,234.76	1.48
	3,122.32	1,333.46	2.35	0.037	1,220.86	1.63
	3,041.81	1,949.28	5.46	0.042	1,554.08	2.11
	2,862.39	2,605.51	16.14	0.052	2,357.28	2.6
BUT	3,138.58	680.26	0.58	0.033	905.89	1.72
	3,117.1	1,333.1	0.87	0.055	1,163.03	2.61
	3,009.68	1,958.33	0.79	0.105	1,447.42	5.39
	2,941.71	2,298.51	2.11	0.081	1,704.86	4.49

Table 8. The percentage comparison of mass emissions production and fuel consumption after 5 operating hours (100%) and after 300 operating hours for BA 95 and BUT fuels. (FC – fuel consumption, SFC – specific fuel consumption)

	No.	Engine speed	Output power	NO_X	CO	CO_2	HC	FC	SFC
	-	%	%	%	%	%	%	%	%
BA 95	1	99.41	103.84	200.47	98.81	118.69	107.93	147.37	141.92
	2	100.04	100.12	113.23	85.52	91.08	78.16	104.59	104.46
	3	98.06	100.48	104.64	76.69	85.68	77.30	101.22	100.73
	4	95.74	101.52	140.55	69.08	87.61	74.05	103.54	101.99
BUT	5	99.92	103.59	46.03	563.49	78.75	325.62	121.30	117.09
	6	99.84	100.21	22.44	345.47	78.74	293.74	123.95	123.68
	7	97.37	100.88	8.18	399.20	74.38	348.74	128.60	127.47
	8	100.89	88.69	15.02	151.31	60.07	195.41	99.34	112.01

The percentage comparison of the mass production of harmful emissions and fuel consumption of the engine after 5 operating hours (100%) and after 300 operating hours is shown in the Table 8. Also, the decrease of the maximum output power of the generator to the value of 2.3 kW in the case of n-butanol has to be taken into account. The value, measured after 5 operating hours (2.6 kW), was not reached. This point has number 8 in the Table 8. From the comparison of the engine speed and output power it

is evident that the very similar operating condition were reached. The highest deviation of speed is approx. 4% and the highest deviation of output power is 11% (at point no. 8). At other points the deviation of output power did not exceed 4%, as in the case of the engine speed.
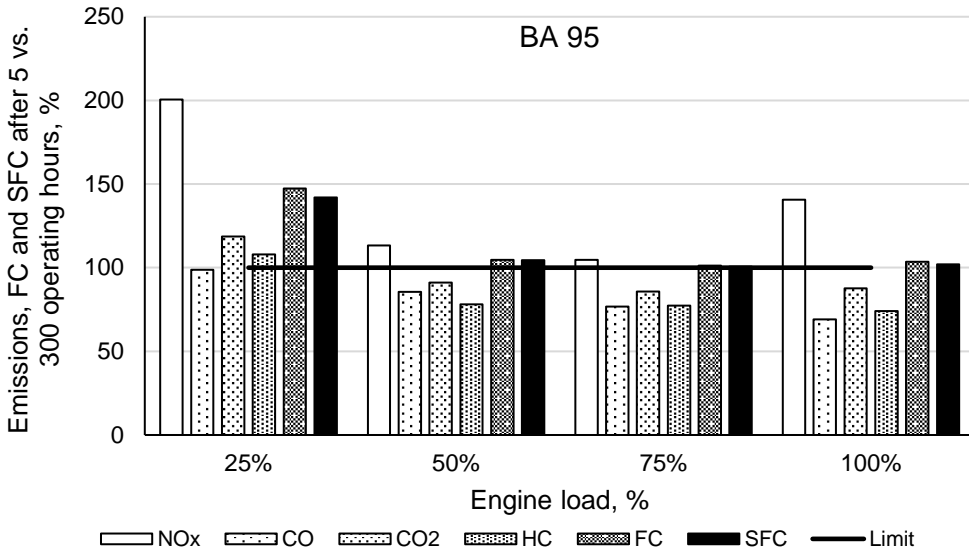
Figure 2. Percentage comparison of emissions production and fuel consumption of the generator oprerating on petrol (BA 95) after 5 operating hours (100%) and 300 operating hours. (FC – fuel consumption, SFC – specific fuel consumption)
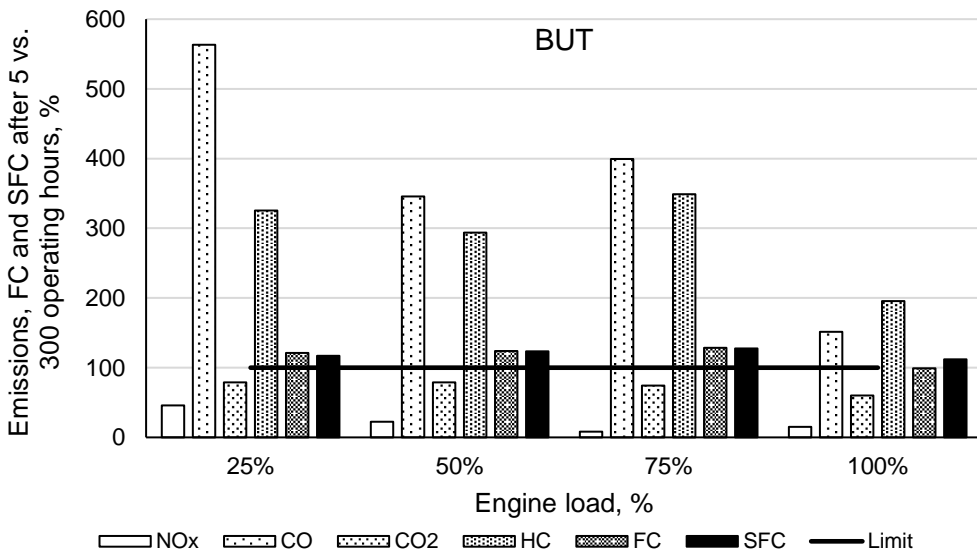
Figure 3. Percentage comparison of emissions production and fuel consumption of the generator oprerating on n-butanol (BUT) after 5 operating hours (100%) and 300 operating hours. (FC – fuel consumption, SFC – specific fuel consumption).

The result values of the percentage comparison, are also shown in graphical form in the Fig. 2 (BA 95) and Fig. 3 (BUT). In more detail, it can be stated that after 300 operating hours in all measured points the increase of the fuel consumption was reached with both fuels, BA 95 and BUT. After 300 hours of operation on BA 95 all of the monitored emission components, except CO, were increased at approx. 25% engine load (point no. 1). At other engine loads (approx. 50%, 75% and 100% – points 2, 3 and 4 in Table 8) the emissions of HC, CO_2 and CO were decreased and the emissions of NO_X were increased in comparison with the results, obtained after 5 operating hours.

After 300 operating hours on BUT fuel the emissions of NO_X and CO_2 were reduced and the the emissions of CO and HC were increased at all engine loads. The emissions of NO_X were reduced by up to 91.8% (at 75% load – point no. 7 in Table 8), however, the emissions of CO were increased on average 3.6 times and emissions of HC on average 2.9 times in comparison with the results, obtained after 5 operating hours. Increased emissions of CO and HC and decreased emissions of CO_2 indicates worsened combustion efficiency. Also, the decreased NO_X emissions indicates lower combustion temperature. This result could be explained by the aggressiveness of n-butanol to rubber sealing elements and plastic parts in the carburettor and therefore worsened mixture preparation.

CONCLUSIONS

The contributions provides a new information about the long-term operation of the combustion engine on n-butanol on its operational parameters. The measurements, focused on comparison of fuel consumption and emissions production (CO_2, CO, NO_X, HC) of combustion engine fuelled by carburettor (generator) during its operation on BA 95 and n-butanol (BUT) after 300 operating hours, reached following results:

- The fuel consumption was increased after 300 operating hours on both fuels BA 95 (on average by 14%) and BUT (on average by 18%).
- By use of BA 95 fuel the decrease of emissions production of HC (on average by approx. 15%), CO_2 (on average by approx. 4%) and CO (on average by approx. 17%) and the increase of NO_X emissions production (on average by approx. 40%) was reached at engine loads approx. 50%, 75% and 100% after 300 operating hours.
- By use of BUT fuel the decrease of emissions production of NO_X (on average by approx. 75%) and CO_2 (on average by approx. 25%) and increase of emissions production of CO (on average 3.6 times) and HC (on average 2.9 times) was reached at all measured engine loads (approx. 25%, 50%, 75% and 100%) after 300 operating hours.

In comparison with the results, obtained after 5 operating hours of generators the BUT fuel reached the higher fuel consumption (by approx. 25%), higher production of CO (by approx. 67%) and HC (by approx. 80%) after 300 operating hours. BA 95 fuel reached the higher production of NO_X (by approx. 70%) and CO_2 (by approx. 12% after 300 operating hours.

REFERENCES

Andersen, V.F., Anderson, J.E., Wallington, T.J., Mueller, S.A. & Nielsen, O.J. 2010. Distillation curves for alcohol-gasoline blends. *Energy and Fuels* **24**(4), 2683–2691.

Atmanli, A., Ileri, E. & Yüksel, B. 2015. Effects of higher ratios of n-butanol addition to diesel-vegetable oil blends on performance and exhaust emissions of a diesel engine. *Journal of the Energy Institute* **88**(3), 209–220.

Awad, O.I., Mamat, R., Ali, O.M., Sidik, N.A.C., Yusaf, T., Kadirgama, K. & Kettner, M. 2017. Alcohol and ether as alternative fuels in spark ignition engine: A review. *Renewable and Sustainable Energy Reviews* **82**, 2586–2605.

Babu, V., Murthy, M. & Rao, A.P. 2017. Butanol and pentanol: The promising biofuels for CI engines – A review. *Renewable and Sustainable Energy Reviews* **78**, 1068–1088.

Čedík, J., Pexa, M., Kotek, M. & Hromádko, J. 2014a. Effect of E85 Fuel on Harmful Emissions -Škoda Fabia 1.2 HTP. *Agronomy Research* **12**(2), 315–322.

Čedík, J., Pexa, M., Kotek, M. & Hromádko, J. 2014b. Effect of E85 fuel on performance parameters. fuel consumption and engine efficiency - Škoda Fabia 1.2 HTP. *Agronomy Research* **12**(2), 37–314.

Čedík, J., Pexa, M., Mařík, J., Hönig, V., Horníčková, & Kubín, K. 2015. Influence of butanol and FAME blends on operational characteristics of compression ignition engine. *Agronomy Research* **13**(2), 541–549.

Dernotte, J., Mounaim-Rousselle, C., Halter, F. & Seers, P. 2010. Evaluation of butanol-gasoline blends in a port fuel-injection. spark-ignition engine. *Oil and Gas Science and Technology* **65**(2), 345–351.

Elfasakhany, A. 2014. Experimental study on emissions and performance of an internal combustion engine fueled with gasoline and gasoline/n-butanol blends. *Energy Conversion and Management* **88**, 277–283.

Elfasakhany, A. & Mahrous, A.-F. 2016. Performance and emissions assessment of n-butanol–methanol–gasoline blends as a fuel in spark-ignition engines', *Alexandria Engineering Journal* **55**(3), 3015–3024.

Ezeji, T.C., Qureshi, N. & Blaschek, H.P. 2003. Production of acetone. butanol and ethanol by Clostridium beijerinckii BA101 and in situ recovery by gas stripping. *World Journal of Microbiology Biotechnology* **19**, 595–603.

Feng, R., Fu, J., Yang, J., Wang, Y., Li, Y., Deng, B. Zhang, D. 2015. Combustion and emissions study on motorcycle engine fueled with butanol-gasoline blend. Renewable Energy **81**, 113–122.

Feng, R., Yang, J., Zhang, D., Deng, B., Fu, J., Liu, J. & Liu, X. 2013. Experimental study on SI engine fuelled with butanol-gasoline blend and H_2O addition. *Energy Conversion and Management* **74**, 192–200.

Gailis, M. & Pirs, V. 2017. Experimental analysis of combustion process in SI Engine using ethanol and ethanol-gasoline blend. *Agronomy Research* **15**(S1), 981–998.

Gu, X., Huang, Z., Cai, J., Gong, J., Wu, X. & Lee, C-f. 2012. Emission characteristics of a spark ignition engine fuelled with gasoline-n-butanol blends in combination with EGR. *Fuel* **93**, 611–7.

Harvey, B.G. & Meylemans, H.A. 2011. The role of butanol in the development of sustainable fuel technologies. *Journal of Chemical Technology and Biotechnology* **86**, 2–9.

Hönig, V., Smrčka, L., Ilves, R. & Küüt, A. 2015a. Adding biobutanol to diesel fuel and impact on fuel blend parametres. *Agronomy Research* **13**(5), 1227–1233

Hönig, V., Orsák, M., Pexa, M. & Linhart, Z. 2015b. The distillation characteristics of automotive gasoline containing biobutanol, bioethanol and the influence of the oxygenates. *Agronomy Research* **13**(2), 558–567.

Kukharonak, H., Ivashko, V., Pukalskas, S., Rimkus, A. & Matijošius, J. 2017. ScienceDirect Operation of a Spark-Ignition Engine on Mixtures of Petrol and N-Butanol. *Procedia Engineering* **187**, 588–598.

Ndaba, B., Chiyanzu, I. & Marx, S. 2015. n-Butanol derived from biochemical and chemical routes: A review. *Biotechnology Reports* **8**, 1–9.

Peterka, B., Pexa, M., Čedík, J., Mader, D. & Kotek, M. 2017. Comparison of exhaust emissions and fuel consumption of small combustion engine of portable generator operated on petrol and biobutanol. *Agronomy Research* **15**(S1), 1162–1169.

Pexa, M., Čedík, J. & Pražan, R. 2016. Smoke and NO_X emissions of combustion engine using biofuels. *Agronomy Research* **14**(2), 547–555.

Qureshi, N. & Ezeji, T.C. 2008. Butanol, a superior biofuel production from agricultural residues (renewable biomass): recent progress in technology. *Biofuels Bioprod Bioref*. **2**, 319–330.

Rakopoulos, C.D., Dimaratos, A.M., Giakoumis, E.G. & Rakopoulos, D.C. 2010. Investigating the emissions during acceleration of a turbocharged diesel engine operating with bio-diesel or n-butanol diesel fuel blends. *Energy* **35**(12), 5173–5184.

Rocha–Meneses, L., Raud, M., Orupõld, K. & Kikas, T. 2017. Second-generation bioethanol production: A review of strategies for waste valorisation. *Agronomy Research* **15**(3), 830–847.

Serras-Pereira, J., Aleiferis, P.G., Walmsley, H.L., Davies, T.J. & Cracknell, R.F. 2013. Heat flux characteristics of spray wall impingement with ethanol. butanol. iso-octane. gasoline and E10 fuels. *International Journal of Heat and Fluid Flow* **44**, 662–683.

Shapovalov, O.I. & Ashkinazi, L.A. 2008. Biobutanol: Biofuel of second generation. *Russian Journal of Applied Chemistry* **81**(12), 2232–2236.

Swana, J., Yang, Y., Behnam, M. & Thompson, R. 2011. An analysis of net energy production and feedstock availability for biobutanol and bioethanol. *Bioresource Technology* **102**(2), 2112–2117.

Wallner, T., Miers, S.A. & McConnell, S. 2009. A comparison of ethanol and butanol as oxygenates using a direct-injection. spark-ignition engine. *Journal of Engineering for Gas Turbines and Power* **131**, 1–9.

Wigg, B.R., Coverdill, R.E., Lee, C.F. & Kyritsis, D.C. 2011. Emissions characteristics of neat butanol fuel using a port fuel-injected. spark-ignition engine. *SAE*, 1–902.

Williams, J., Goodfellow, C., Lance, D., Ota, A., Nakata, K. & Kawatake, K. 2009. Impact of butanol and other bio-components on the thermal efficiency of prototype and conventional engines. *SAE,* 1–1908.

Yang, J., Yang, X.L., Liu, J.P., Han, Z.Y. & Zhong, Z.H. 2009. Dyno test investigations of gasoline engine fueled with butanol–gasoline blends. *SAE,* 1–1891.

Yilmaz, N., Vigil, F.M., Benalil, K., Davis, S.M. & Calva, A. 2014. Effect of biodiesel–butanol fuel blends on emissions and performance characteristics of a diesel engine. *Fuel* **135**, 46–50.

Yusri, I.M., Mamat, R., Azmi, W.H., Najafi, G., Sidik, N.A.C. & Awad, O.I. 2016. Experimental investigation of combustion, emissions and thermal balance of secondary butyl alcohol-gasoline blends in a spark ignition engine. *Energy Convers Manag.* **123**, 1–14.

Yusoff, M.N.A.M., Zulkifli, N.W.M., Masjuki, H.H., Harith, M.H., Syahir, A.Z., Kalam, M.A., Mansor, M.F., Azham, A. & Khuong, L.S. 2017. Performance and emission characteristics of a spark ignition engine fuelled with butanol isomer-gasoline blends. *Transportation Research Part D* **57**, 23–38.

Determination of conversion relations for the use of small hydrodynamic pumps in reverse turbine operation

M. Polák

Czech University of Life Sciences in Prague, Faculty of Engineering, Kamýcká 129, CZ16521, Praha 6, Czech Republic
Correspondence: karel@tf.czu.cz

Abstract. In small-scale hydropower, hydrodynamic pumps used in reverse mode are an important economical alternative to conventional water turbines. Efficient utilisation of these devices however requires taking into account all the specifics of the reverse pump operation and optimise the pump design for maximum utilisation of the hydro-technical potential of the deployment site. The article compares existing conversion models, describes initial theoretical assumptions and determines new conversion relations for the design of pumps as turbines (PAT) for the lowest power and specific speed category. The validity of the conversion relations is experimentally verified on a hydraulic test circuit with a radial centrifugal pump tested in both pump and turbine operation modes. The results of the verification of the new conversion relations proved better correspondence to reality within this category of machines than that reported by the previously used conversion models.

Key words: pump as turbine (PAT), conversion relations, specific speed, head, flowrate.

INTRODUCTION

Standard centrifugal pumps may be operated in reverse mode as water turbines. They are often cheaper than specifically designed turbines, especially in case of devices of less than 100 kW (micro-hydro). The first pump turbine had been set at a remote farm in the Yorkshire Dales of the North England in 1930. This scheme has been working for a five year testing time, after which its reliability was confirmed before being transferred to other countries. (Williams, 1994) Especially in developing countries, small and micro hydropower plants are very effective source for electricity generation with energy pay-back time less than other conventional electricity generation systems. Using pump as turbine (PAT) is an attractive, significant and cost-effective alternative. Pump manufacturers do not normally provide the characteristic curves of their pumps working as turbines. (Naeimi, et al., 2017) However, in order to use a pump in a micro-hydro scheme, the turbine performance must be found either by testing or by calculation. Several methods have been suggested for predicting the turbine performance based on the data for pump performance at best efficiency, but they produce a wide range of results. (Williams, 1994; Bláha et al., 2011) In this paper, nine such methods are compared using an analysis of the effects of poor turbine prediction on the operation of a pump as turbine at a typical micro hydro site. None of these methods gives an accurate

prediction, especially for the smallest pumps. This was the cause for searching such conversion relations that would better reflect reality, especially for machines with the lowest power and specific speed. Data from experimental measurements of the performance characteristics of ten radial centrifugal pumps were used for the purpose of determining the conversion relations. Three of them were verified at the author's workplace (No. 1, 2 a 3 – see Table 1 a Table 2), others were taken from (Singh, 2005; Singh, 2011).

MATERIALS AND METHODS

Determination of pump performance parameters in turbine operation

The methodology for the conversion of the parameters was verified on radial single stage centrifugal pumps in the range of power $P = 0.1 \div 9$ kW and specific speed $N_{qT} = 15 \div 70$ rpm. A typical representative in this category is a META series pump, manufactured in the Czech Republic by ISH PUMPS Olomouc, a.s. which was verified at the author's workplace. The pump's scheme, including its parameters as provided by the manufacturer is shown in Fig. 1.
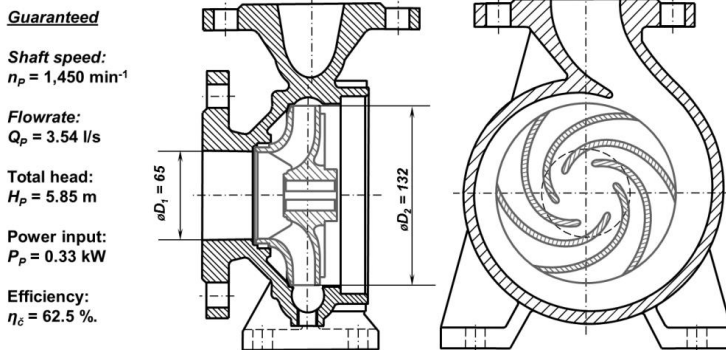
Figure 1. Centrifugal pump for experimental tests and original pump parameters (Source: Polák, 2017).

Verification tests were conducted on a hydraulic circuit in the Fluid Mechanics laboratory at the Faculty of Engineering, Czech University of Life Sciences Prague. The circuit diagram is shown in Fig. 2. Characteristics of the pump and its modifications in the turbine mode were measured in the first stage. Subsequently the effect of the modifications in the pump operation was verified.

The testing circuit consisted of a set of two reservoirs with pipes and control and measuring elements. With this setting the tested pump (T-P) was measured in turbine mode – by closing valve V2 while regulating valve V1, the water flows in the direction of dashed arrows, while the feeding pump (FP) creates the hydro-technical potential for the turbine. After rearranging the valves V1 and V2, the machine (T-P) was tested in the pumping operation on the same circuit – by closing the valve V1 and controlling valve V2 the water flows in the direction of grey arrows. The dynamometer (M) with continuous revolutions control allows operation in motor and braking mode. The dynamometer has cylindrical stator. It is placed on a bed allowing a slight rotation, which

enables a measurement of the reaction torque at load. Dynamometer is a DC machine connected to continuous resistance load control unit. The water flow was measured using an ultrasonic flowmeter Siemens SITRANS FUP1010. The turbine shaft speed was measured using an infrared sensor TESTO 465 (Polák, 2017, ČSN EN ISO 9906).
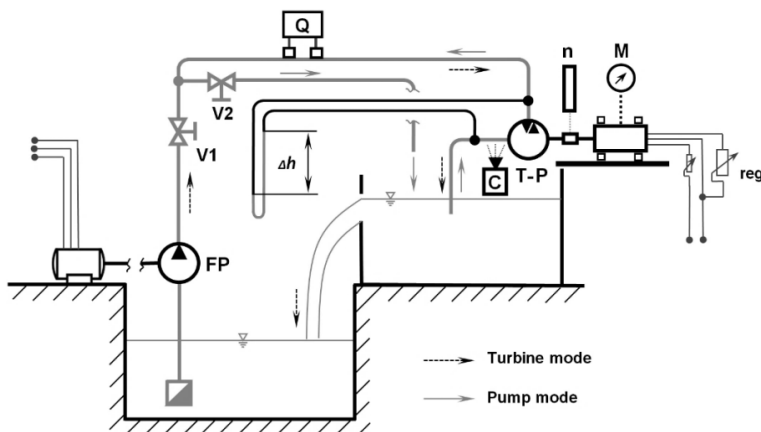
Figure 2. Hydraulic circuit scheme for testing turbines/pumps. Q – flowmeter, FP – feed pump (for turbine mode), T–P tested pump/turbine, V1, V2 – control valves, M – dynamometer, n – revolution counter, reg – load/drive control of the turbine/pump (Source: Polák, 2017).

The characteristics of the pump and consequently the turbine operation were experimentally determined on the test circuit for all ten monitored pumps. Then the parameters corresponding to optimum operation at best efficiency point (BEP) were determined from the characteristics, i.e. flow, total head, efficiency and shaft speed. An overview of the performance parameters of each machine in pump mode is given in Table 1. An overview of the performance parameters of the same machines in turbine mode is in Table 2.

Table 1. Overview of performance parameters in pump mode (Source: author; Singh, 2005)

Pump No.	1	2	3	4	5	6	7	8	9	10
Impeller diameter: D_1, mm	96	132	132	258	206	174	264	200	139	224
Total head: H_P, m	2.27	5.7	6.5	21.5	15.8	8.38	19.8	10.5	5.6	10.6
Flowrate: Q_P, L s^{-1}	0.76	3.8	3.8	26.5	25.4	15.3	65.9	33	13.5	103
Shaft speed: N_P, rpm	1,450	1,450	1,450	1,500	1,500	1,450	1,450	1,450	1,450	1,450
Efficiency: η_P, %	0.44	0.7	0.73	0.78	0.79	0.74	0.85	0.80	0.76	0.84
Specific speed: N_{qP}, rpm	22	24	22	25	35	36	40	45	46	79

Table 2. Overview of performance parameters in turbine mode (Source: author; Singh, 2005)

Pump No.	1	2	3	4	5	6	7	8	9	10
Impeller diameter: D_1, mm	96	132	132	258	206	174	264	200	139	224
Total head: H_T, m	14.6	13.5	13.8	17.1	15.5	13.4	16	13.7	10.6	10
Flowrate: Q_T, L s^{-1}	3.0	6.0	5.5	30.1	28.6	22.7	67.5	43.9	19.7	108
Shaft speed: N_T, rpm	1,450	1,450	1,450	900	1,300	1,400	1,100	1,400	1,600	1,200
Efficiency: η_T, %	0.2	0.48	0.55	0.77	0.81	0.72	0.84	0.8	0.76	0.76
Specific speed: N_{qT}, rpm	15	16	15	19	28	30	36	41	38	70
Power output: P_T, W	86	381	410	3,863	3,523	2,134	8,847	4.691	1,557	7,992

Verification of the conformity of existing conversion relations

On the basis of the experimentally obtained data, the validity of the existing conversion relations was verified according to various authors (Frosina et al., 2017; Derakhshan & Nourbakhsh, 2008; Nautiyal et al., 2010). An overview of existing conversion relations is in Table 3.

Table 3. Conversion relations according to various authors

Author	Source, Year	Head ratio H_T/H_P	Flowrate ratio Q_T/Q_P	Remarks
Stepanoff	(Stepanoff, 1957)	$\dfrac{1}{\eta_P}$	$\dfrac{1}{\sqrt{\eta_P}}$	Accurate for $Ns = 40 \div 60$
Childs	(Childs, 1962)	$\dfrac{1}{\eta_P}$	$\dfrac{1}{\eta_P}$	-
Hancock	(Hancock, 1963)	$\dfrac{1}{\eta_T}$	$\dfrac{1}{\eta_T}$	-
Grover	(Grover, 1980)	$2.693 - 0.0229 N_{sT}$	$2.379 - 0.0264 N_{sT}$	Applied for $Ns = 10 \div 50$
Hergt	(Lewinsky, 1987)	$1.3 - \dfrac{6}{N_{qT} - 3}$	$1.3 - \dfrac{1.6}{N_{qT} - 5}$	-
Sharma	(Sharma, 1985)	$\dfrac{1}{\eta_P^{1.2}}$	$\dfrac{1}{\eta_P^{0.8}}$	Accurate for $Ns = 40 \div 60$
Schmiedl	(Schmiedl, 1988)	$-1.4 + \dfrac{2.5}{\eta_P}$	$-1.5 + \dfrac{2.4}{\eta_P^2}$	-
Alatorre-Frenk	(Alatorre-Frenk, 1994)	$\dfrac{1}{0.85\eta_P^5 + 0.385}$	$\dfrac{0.85\eta_P^5 + 0.385}{2\eta_P^{9.5} + 0.205}$	-
Güllich-volute	(Güllich, 2008)	$\dfrac{2.4}{\eta_P^2} - 1.5$	$\dfrac{2.5}{\eta_P} - 1.4$	-

The parameters of the pump mode from Table 1 were used in order to verify the validity of the above mentioned conversion relations. Conversion results, i.e. flows and gradients for turbine mode, were then compared with the real values recorded in the laboratory (Table 1). Fig. 3 and Fig. 4 shows an example of a comparison of the results for two pumps of the same specific speeds, but different sizes and power. The figures show differences between conversion results and reality for pump No. 3 ($D_1 = 132$ mm, $N_{qT} = 22$ rpm, $P_T = 410$ W) and pump No. 4 ($D_1 = 258$ mm, $N_{qT} = 25$ rpm, $P_T = 3.9$ kW). Results of the calculations according to all nine authors listed in Table 3 are lined up on the horizontal axis. Fig. 3 show the relative differences of the turbine head ΔH_T calculated according to:

$$\Delta H_T = 100 \cdot \frac{H_{T*} - H_T}{H_T} \ [\%] \tag{1}$$

where H_T is the real turbine head measured on the test circuit, and H_{T*} is the turbine head calculated according to the respective author.
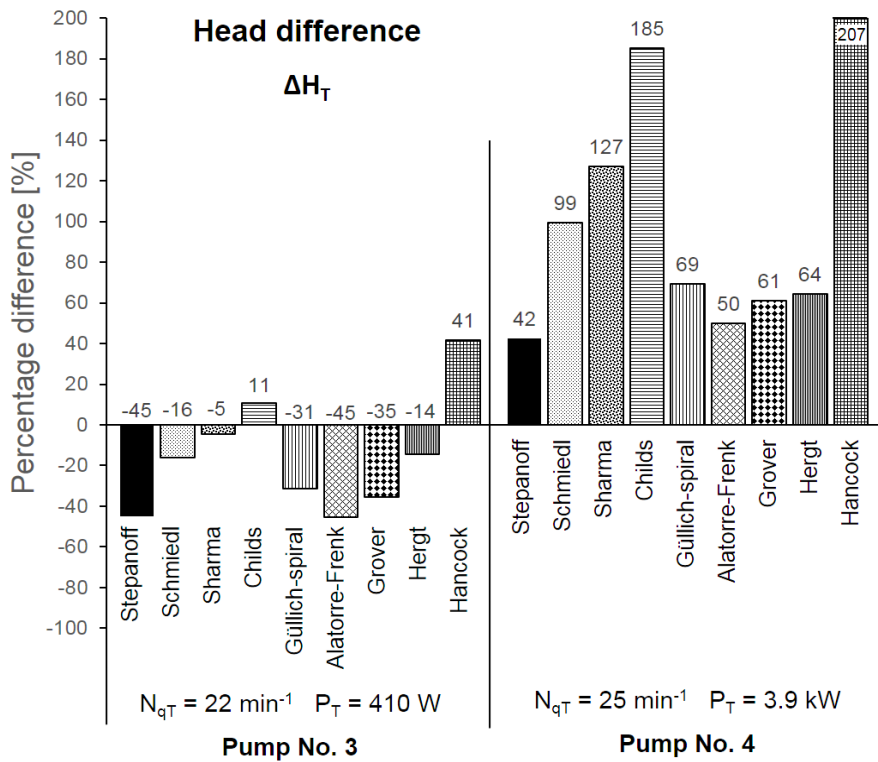
Figure 3. Comparison of turbine head calculation results according to various authors.
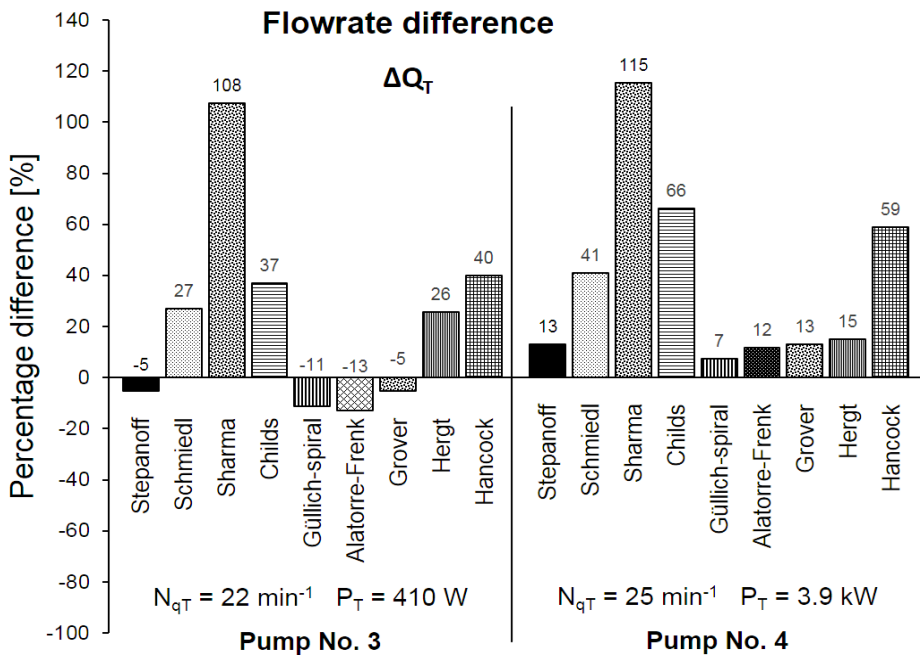
Figure 4. Comparison of turbine flowrate calculation results according to various authors.

Fig. 4 show the relative differences of the turbine flowrate ΔQ_T according to:

$$\Delta Q_T = 100 \cdot \frac{Q_{T*} - Q_T}{Q_T} \ [\%] \tag{2}$$

where Q_T is the real turbine flowrate recorded on the test circuit and Q_{T*} is the value of the turbine flowrate calculated according to the respective author.

It is apparent from comparison of the graphs in Fig. 3 and Fig. 4 that the best results (the smallest differences) are presented by the conversion model according to Stepanoff. The following Fig. 5 shows the comparison of the differences of the conversion for all tested pumps only according to Stepanoff. On the x-axis, the pumps are arranged according to the revolutions N_{qT} (horizontal x-axis numbers) and power P (vertical x-axis numbers). On the y-axis, the relative values of the deviation of the real values from the calculated flowrate ΔQ_T, as well as from the ΔH_T) are presented (horizontal numbers above the x-axis.
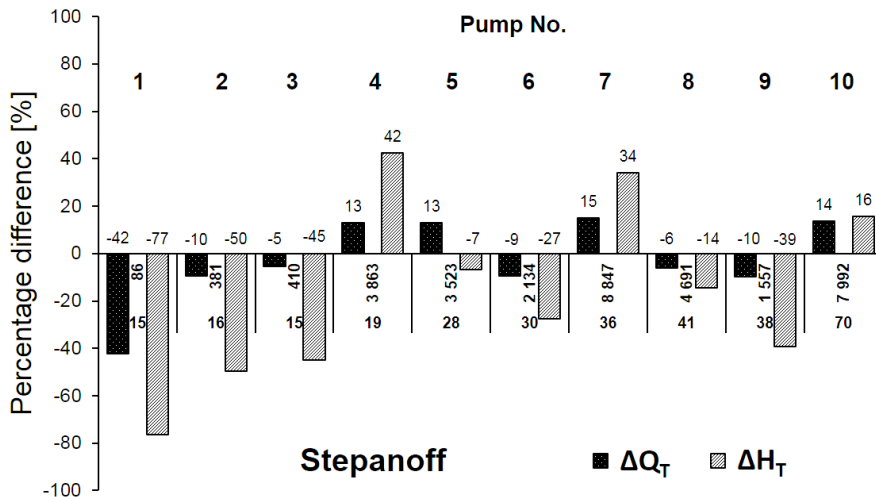
Figure 5. Comparison of conversion calculations according to Stepanoff.

Determination of the conversion relations for the lowest power category
The conversion of parameters according to Stepanoff is based solely on the efficiency of the pump. It assumes that the efficiency is the same both in the pump and turbine mode. However, this does not apply generally. The efficiency is lower in the turbine mode particularly for machines with the lowest specific speed and power. In these cases, it is necessary to take into account the reduction in efficiency and include it in the conversions. Furthermore, it shows that the coefficients in the conversion relations for small pumps cannot be considered as constant. This implies the necessity of coefficients variability along with the definition of the area of their use. These circumstances led to the search for such conversion relations that would meet these assumptions.

It is apparent from the comparison in Fig. 5 that the greatest difference between the calculated values and the reality is for the five pumps with the lowest power where the differences exceeded 40% (especially in the turbine head). It concerned specifically

1205

pumps No. 1, 2, 3, 6 and 9. These pumps were focused on with the aim to find such conversion relations, which would better reflect the reality.

The test results from the laboratory tests were used to determine more appropriate conversion relations. A prerequisite for their derivation was the hypothesis that the efficiency of small pumps in the turbine mode changes in a similar relation as the specific speed does. This relation can be expressed by equation (3):

$$\Delta\eta = \Delta N_q \tag{3}$$

where:

$$\Delta\eta = \frac{\eta_P - \eta_T}{\eta_P} \tag{4}$$

and

$$\Delta N_q = \frac{N_{qP} - N_{qT}}{N_{qP}} \tag{5}$$

where η_P, η_T is pump or turbine efficiency, and N_{qP}, N_{qT} is specific speed by the flowrate in pump or turbine mode. Specific speed is defined by a generally known relation (Munson 2006; Melichar et at. 1998):

$$N_q = N \cdot \frac{Q^{\frac{1}{2}}}{H^{\frac{3}{4}}} \tag{6}$$

where N is shaft speed, Q pump or turbine flowrate and H pump or turbine head. Based on an analysis of the results of the experimental verification, the conversion relations were expressed. The turbine flowrate Q_T and the head H_T is determined from the known hydrotechnical potential of the deployment site. The pump flow rate Q_P is determined from these values using the conversion relation (7):

$$Q_P = Q_T \cdot \eta_P{}^x \tag{7}$$

and respective pump head H_P:

$$H_P = H_T \cdot \eta_P{}^y \tag{8}$$

where x and y are constants. Their values are in range of $x = 1 \div 1.6$ and $y = 2 \div 2.6$ and they depend on specific speed and size of the pump. The values H_P and Q_P are then used to select a specific pump from the manufacturer's catalogue using the H-Q characteristics. Conversion rates for turbine mode depending on the original pump parameters can be expressed from formulas (7) and (8) as $Q_T = Q_P/\eta_p{}^x$ and $H_T = H_P/\eta_p{}^x$.

RESULTS AND DISCUSSION

An overview of the results comparison of the conversion model according to equations (3) to (8) proposed by the author of the article is given in Fig. 6. The calculation differences of the five smallest pumps No. 1, 2, 3, 6 and 9 are presented here, for which the calculation was designed. The results showed that, compared to Stepanoff's model (difference above 40%), the authors' conversion model achieved significantly better conformity with the reality (differences up to 5% or 15%). Higher difference occurred only at turbine head calculation for pump No. 6. The probable cause of this is

generally higher sensitivity of the turbine head calculation to the equation constants used. It is also similar for Stepanoff's model (see ΔH_T on Fig. 5). Another reason can be also exceeding the interval defining the optimum use of the conversion relations. This implies the need for correction of the conversion model, which is the subject of further research.
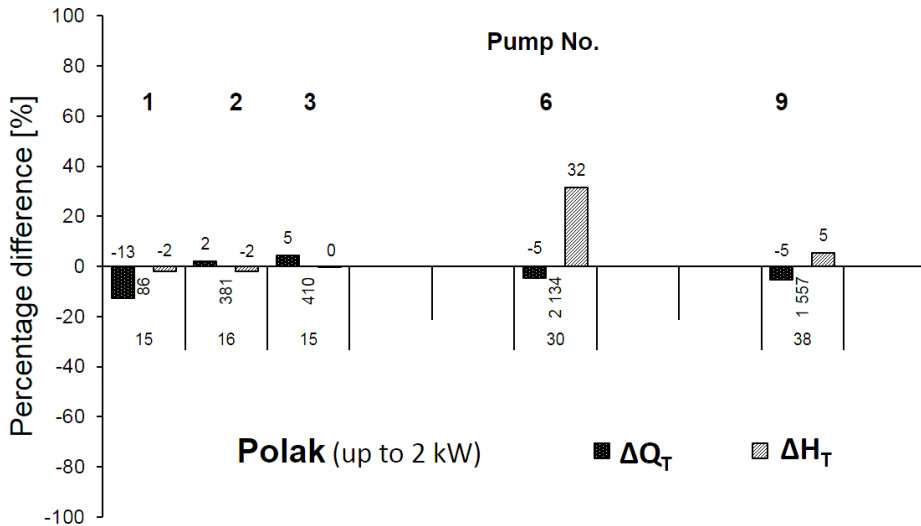
Figure 6. Comparison of conversion calculations according to author

CONCLUSIONS

The conversion relations for the radial centrifugal pump parameters for turbine mode were verified in this study. The results of experimental verification of ten radial single stage centrifugal pumps in the range of specific speed $N_{qT} = 15 \div 70$ rpm and power $P = 0.1 \div 9$ kW were used for this purpose. By comparing the conversion results according to nine different authors, it was found that Stepanoff's model was the most conforming. However, it failed for pumps with the smallest power and specific speed, where deviations exceeded 40%. The probable cause is the changing efficiency of the pump in turbine mode, which is not considered by Stepanoff's model. The author of this study took into account changing efficiency and included it in his own conversion relations. With these new relations, the results for pumps with the smallest power differ from reality by less than 5 or 15%. The conversion was subsequently verified on the remaining five larger pumps. It appeared that the difference between the calculation results and the reality increased with increasing power and specific speed. Therefore, the author's proposed conversion model is suitable for small pumps with power output of up to 2 kW and specific speed up to 40 rpm for which it was primarily designed.

REFERENCES

Alatorre-Frenk, C. 1994. Cost minimization in micro hydro systems using pumps-asturbines, *Ph.D. Thesis.* University of Warwick, 1994.

Bláha, J., Melichar, J. & Mosler, P. 2011. Contribution to the use of hydrodynamic pumps as turbines. *Energetika* **5**, 1–5. (in Czech)

Childs, S.M. 1962. Convert pumps to turbines and recover HP. *Hydro Carbon Processing and Petroleum Refiner* **41**(10), 173–4.

ČSN EN ISO 9906: Hydrodynamic pumps – Acceptance tests of hydraulic performance parameters – Degrees accuracy of 1, 2 and 3, ČSNI. (in Czech)

Derakhshan, S. & Nourbakhsh, A. 2008. Experimental study of characteristic curves of centrifugal pumps working as turbines in different specific speeds. *Experimental thermal and fluid science* **32**(3), 800–807.

Frosina, E., Buono, D. & Senatore, A. 2017. A performance prediction method for pumps as turbines (PAT) using a computational fluid dynamics (CFD) modeling approach. *Energies* **10**(1), 103.

Grover, K.M. 1980. Conversion of pumps to turbines. Katonah, New York: GSA Inter Corp, pp. 125– 38.

Gülich, J.F. 2008. *Centrifugal pumps, 3rd Edition*. Berlin: Springer, ISBN 978-3-642-40113-8.

Hancock, J.W. 1663. Centrifugal pump or water turbine. *Pipe Line News* 1963, 25–7.

Lewinsky-Keslitz, H.P. 1987. Pumpen als Turbinen fur Kleinkraftwerke. *Wasserwirtschaft* 1987; **77**(10), 531–7.

Melichar, J., Vojtek, J. & Bláha, J. 1998. *Small hydro turbines, construction and operation*. ČVUT, Praha. pp 296. (in Czech)

Munson, B.R., Zouny, D.F. & Okishii, T.H. 2006. *Fundamentals of Fluid Mechanics, Fifth edition*, John Wiley & Sons, Inc., New York, 770 pp., ISBN 0-471-67582-2.

Naeimi, H., Shahabi, M.N. & Mohammadi, S. 2017. A Comparison of Prediction Methods for Design of Pump as Turbine for Small Hydro Plant: Implemented Plant. In: *IOP Conference Series: Earth and Environmental Science.* IOP Publishing.

Nautiyal, H. & Kumar, V. 2010. Reverse running pumps analytical, experimental and computational study: A review. Renewable and Sustainable Energy Reviews, 2010, 14.7: 2059–2067.

Polák, M. 2017. Experimental evaluation of hydraulic design modifications of radial centrifugal pumps. *Agronomy Research* **15**(S I), 1189–1197.

Schmiedl, E. 1988. Serien-Kreiselpumpen im Turbinenbetrieb. Pumpentagung Karlsruhe, 357 pp. (in German).

Sharma, K. 1985. Small hydroelectric project-use of centrifugal pumps as turbines. *Technical report*. Bangalore, India: Kirloskar Electric Co, pp. 14–6.

Singh, P. 2005. Optimization of internal hydraulics system design for pumps as turbine with Field Implementation and Evaluation. *PhD thesis*, Universität Fridericiana, Karlsruhe.

Singh, P. & Nestmann, F. 2011. Internal hydraulic analysis of impeller rounding in centrifugal pumps as turbines. *Experimental Thermal and Fluid Science* **35**, 121–134.

Stepanoff, A.J. 1957. *Centrifugal and axial flow pumps, design and applications*, John Willy and Sons, Inc., New York 1957, 462 pp.

Williams, AA. 1994. The turbine performance of centrifugal pumps: a comparison of prediction methods. *Proceedings of the IMechE Part A Journal of Power and Energy* 1994, **208**, 59–66.

Preliminary conclusions on application of ultrasonic sensors in evaluation of distribution and depth of ruts in forest thinning

K. Pužuls, T. Štāls, A. Zimelis and A. Lazdiņš[*]

Latvian State forest Research Institute 'Silava', Rīgas street 111, LV-2169 Salaspils, Latvia
[*]Correspondence: andis.lazdins@silava.lv

Abstract. The scope of the study is to elaborate equipment for measurement of ruts during log forwarding. The system is supposed to be used in practical forestry to replace manual measurement of length of deep ruts and to provide spatially explicated information on soil bearing capacity, which can be used in planning of forest operations.

A set of 4 pairs of ultrasonic sensors were installed on front and rear bunks to measure distance to the ground at 90º angle (in front and behind the wheels in each side of forwarder) and at certain angle to measure distance to the ground outside strip-road. Measurement data are sent to the logger, where they are stored in .csv files. Wired connection between the sensors and the logger was used in earlier version, but later replaced with wireless connection. Depth of rut is calculated using formula for calculation of length of cathetus of a right-angled triangle. Data processing in spreadsheet includes initial identification of error values and calculation of depth of ruts. Further spatial data analysis is done in GIS software.

According to the study results ultrasonic sensors provides sufficient accuracy to characterize depth of ruts in 1...5 m long segments of strip-roads, including dynamic data on depth and length of ruts after each pass. However, the accuracy is insufficient to compare measurements from sensors mounted on front and rear bunks, as well as on left and right side of machine, therefore it is enough to have 2 pairs on sensors on rear bunks.

Key words: ultrasonic sensors, rut depth, harvesting.

INTRODUCTION

Harvesting in forest can cause soil disturbance through compaction, rut formation and mixing of soil layers (Prindulis et al., 2016). Harmful effect can be also observed on water regime, if forwarding roads interferes with water streams. These impacts affect the soil functions and forest productivity. Soil compaction may result in an increased bulk density and decreased porosity, water permeability and aeration. Deep ruts, particularly in thinnings of coniferous stands, are associated with distribution of root rot, deterioration of moisture regime, and increase of output of methyl-mercury into water bodies (Eklöf et al., 2014). These issues will become more important in the future since harvesting operations on unfrozen soils are getting more common due to the anticipated climate warming and increasing area of forest stands on soils with low bearing capacity requiring thinning.

The ultrasound frequency exceeds 20 kHz (Panda et al., 2016). Nowadays ultrasound is used in many different fields because of its characteristics. Its physical properties in different environments is similar to the normal (audible) sound. Ultrasound can spread in gases, liquids and solids (Maghsoudi et al., 2015). Ultrasound can be divided in two groups, according to field of application:

- active ultrasound – ultrasound of a very high frequency is used to create a physical or chemical reaction. It is used in surface cleaning, welding, drilling etc. (Koval et al., 2016);
- passive ultrasound – low frequency ultrasound is used. It is used to determine a distance, to measure density and detect damages in different materials, detection of gas and liquid flow, as well as in medicine (Koval et al., 2016).

An ultrasonic sensor sends impulses of ultrasound waves towards an object and receives echo signals that are reflected back. The distance between the device and the surface of an object is calculated according to the time period from sending the ultrasound waves and receiving an echo (Gudra et al., 2017). The main advantage of ultrasound emitters is their ability to measure distance, level, contours of an object and position from a distance. Ultrasonic sensors can perform successfully in difficult conditions – measurements are relatively accurate regardless of the impact of light, dust, fog and the material (Koval et al., 2016). It is possible to measure any material that can reflect sound, regardless of its colour and transparency. The growing popularity of ultrasonic sensors demands millimetre range of operation. The main factor that influences measurements is change in the speed of sound, which is influenced by several environmental factors: temperature, relative air humidity, air pressure, CO_2 levels in air and altitude above sea level. However, it was found during latest studies that influence of CO_2 is insignificant. Environmental errors in measurements can be minimized by adjustment procedures (Panda et al., 2016).

Ultrasonic sensors have been used in practice for a relatively long time. In agriculture ultrasonic sensors have been used for more than 40 years to automate and facilitate crop harvesting, to dose pesticides and fertilizers and to detect weeds in crops (Schumann & Zaman, 2005; Escolà et al., 2011; Andújar et al., 2012; Chang et al., 2017).

Several studies describe the operation of ultrasonic sensors. Escolà in his research encountered accuracy problems during measuring distance to apple trees. When measuring trees with thinner foliage, the ultrasound impulse can reflect deeper in the canopy, where the surface of reflection is larger. The distance from the sensor and the shape of the tree crown also affects accuracy of measurements (Escolà et al., 2011). Andújar et al. in their research on weed monitoring in growing food crops found possibility to identify weeds acccording on difference in height between the crops and weeds (Andújar et al., 2012).

Due to device's ability to work under difficult conditions, where high accuracy is not crucial, it can be used to detect the level in different storage tanks. Nowadays waste management in cities is becoming more problematic, therefore it is proposed to install specified sensor blocks in garbage bins, which would consist of an ultrasonic sensor, a gas sensor, a humidity sensor and a GSM modem. These sensors would be used for measuring garbage level as a part of organization of waste management system (Lokhande, 2016).

Ultrasonic sensors can be used as individual elements or grouped in arrays. Ultrasonic sensor arrays are widely used to perform different inspections. Sensor arrays provide increased quality and reduce the amount of time required for inspection, however the main advantage over traditional single element transducers is to perform a number of functions simultaneously. It is possible to place sensors so that they can perform continuous scanning, focused scanning and scanning at a specific angle. Using the ultrasonic sensor array it is possible to carry out measurements and obtain immediate images of the research object (Drinkwater & Wilcox, 2006).

When sensors located nearby are working simultaneously, interference has to be taken into account. It is recommended to divide sensors into groups in order to avoid inaccurate readings due to overlapping of reflected waves. However this method is ineffective, as data collection time increases and quality of data declines, and not suitable for data collection, when the sensors are located on a moving object (Escolà et al., 2011).

Nowadays ultrasonic sensors are also used in road maintenance, in order to detect ruts. Rut depth is measured with a specialized arrays of ultrasonic sensors. The amount of individual elements and their position in the array can vary. All the arrays work simultaneously and periodically to avoid overlapping of signals (Serigos, 2012). Sensor arrays with 3 or 5 elements can detect only depth of ruts that have been formed on the road. Along with increasing the number of elements per array, accuracy of measurements of road surface increases.

During logging significant soil disruptions can occur – tearing of topsoil and compaction and mixing of different soil layers (Prindulis et al., 2016). Soil damage can has negatively influence both, on chemical and physical properties, thereby negatively affecting development of the forest stand. The degree of soil damage depends on a number of factors, e.g., soil moisture, topography, logging type, machines used, drive count and whether logging residues have been put in strip roads (Laffan, Jordan, & Duhig, 2001).

Within the scope of this study an automatic ultrasonic rut measurement system was developed and tested. The aim of the study was to create an automatic rut measuring system, which can be used both, in practice and research. In practice it can be used as a control and monitoring tool to minimize the impact of logging on the remaining trees and soil. In research it can be used to automate soil impact measurement and to obtain more detailed data on distribution and depth of ruts. In this article preliminary results of field trials are presented.

METHODS

Description of the device. Rut measurement system consists of the central block, which reads and stores data, and several attachable blocks – global navigation system antenna, which guarantees accuracy of measurements up to 1 meter, sensors of cabin microclimate and vibrations of operator seat, sensors of engine speed and fuel consumption, as well as 2 distance measuring blocks, which are equipped with ultrasonic distance sensors (HRXL MaxSonar WRMT). Obtained data are stored in the SD card in the central block and the storage period is up to half of a year. The central block collects measurements of each component every second, when it is provided with power supply.

Each distance measuring block consists of two ultrasonic sensors, where one sensor (turned at a 90° angle towards ground) measures distance to the ground behind tractor whereas the other one – at a 67° or 66° angle outside the strip road.

The software developed within the scope of the project includes an option to connect to the central block in real-time, establishing a connection through *Bluetooth* wireless module. Telemetric data and data on measurable parameters from all the attached blocks can be observed online, whereas stored data can be converted to CSV (comma separated value) format for further processing and analysis in external tools.

Methods applied in field tests. Testing of the rut measuring system was carried out in forest thinning. The system was mounted on John Deere 810E forwarder. Forwarder worked in 'business as usual' conditions, without any special requirements in relation to the ruts' measurement.

During the field tests the central block was placed in the operator cabin with continuous access to power source. Both distance measuring blocks and global navigation system antenna were attached in order to test the system during experimental drives. Distance measuring blocks were mounted on the rear bunks of the forwarder in order not to disturb the operator and not to be damaged. Distance measuring block was placed so that the ultrasonic sensor (directed towards ground at an angle of 90°) is positioned in the middle of a rut.

Spatial data processing. When carrying out spatial data analysis, it is possible to observe the motion of the forwarder in the felling site. With spatial data processing it is possible to select strip roads and distribution by segments. Before processing spatial data the initial quality assurance was done to exclude outliers from the analysis.

Data spatial processing was carried out in QGIS software environment. After data input strip road was randomly selected for further processing. Trial was conducted in thinning, where the GPS signal is inaccurate, therefore the selected road was divided in 10 m wide segments. After dividing the road into segments, obtained data were processed using Microsoft Excel to calculate depth of ruts. In future it is planned to do all calculations within the QGIS environment providing powerful tools for spatial and geometry analysis.

Data filtering. Qualitative data selection was carried out by filtering measurements of ultrasonic sensors in Microsoft Excel. In order to filter errors, the maximum (5,000 mm) and the minimum (300 mm) value was set for each sensor. Maximum values in output data indicate that the ultrasound impulse in a 5 m distance has not reached a lock point and the sensor cannot receive the reflected wave from the object locater further away, whereas the minimum value indicates that in a 0.30 m distance from the sensor met an obstacle, e.g., a branch. Values between 300 and 5,000 mm were considered qualitative data.

Calculation of rut depth. In order to calculate rut depth measurements from side sensors were taken into account. Before starting the field tests the distance to soil surface should be measured to calibrate the calculation (Fig. 1). Angle of horizontal position of the machine is considered in the calculation and outlying values are filtered out.
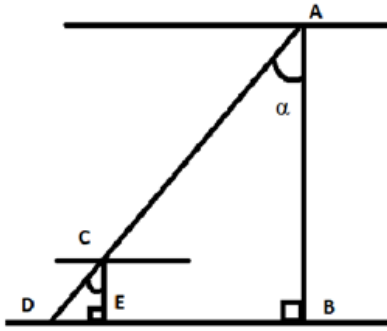
Figure 1. AD – measurement of the sensor pointed sideways; AB – measurement of the sensor pointing downwards; AC – distance between the sensor and ground surface; CE – footprint of a tractor in soil.

Footprints left by the forwarder on the soil can be calculated by subtracting the distance to the ground surface from the measured distance during the drive and carrying out trigonometric adjustments (1).

$$CE = (AD - AC) \times \cos \alpha \qquad (1)$$

RESULTS AND DISCUSSION

Spatial data. The obtained spatial data were of high quality and it was possible to process them. Because of the high accuracy of GPS coordinates it was possible to distinguish strip roads and select them to process data further.

GPS signal in thinnings was less accurate, as it was influenced by remaining trees. The selected strip road was divided into segments, each 10 m long. The length of the selected road was 108 m and it was divided in 11 segments of the same size (Fig 2). Depending from quality of rut depth measurement data the length of segments can be increased or decreased to obtain statistically representative data set for each segment.
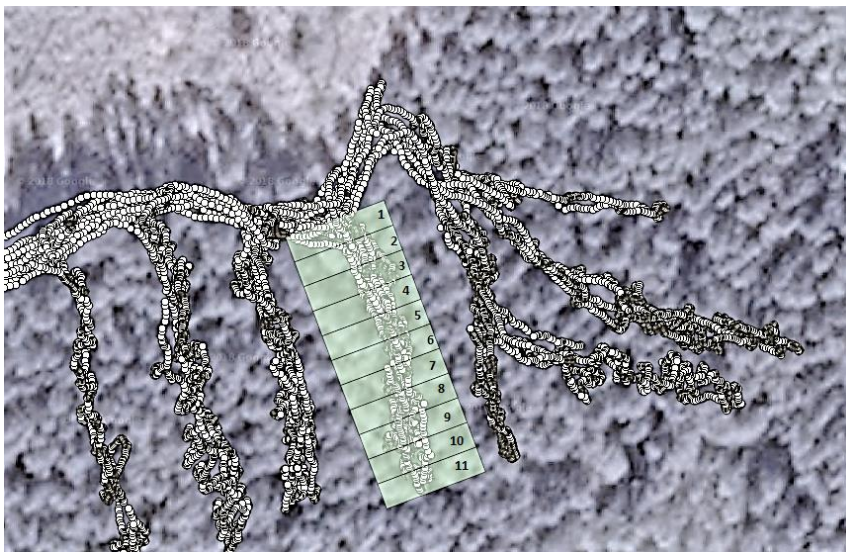
Figure 2. The selected strip road, divided into segments.

The first segment was not used for further data processing in order to avoid measurements that were carried out on the main road. The segments 10 and 11 also were excluded, because it was difficult to precisely distinguish forwarder passes in these segments. It is planned to use average vector direction to identify possible turning points to distinguish the passes.

Geometry analysis. After selection of the strip road and its division in sectors it was possible to distinguish number of passes and time spent in each sector. The total time spent in the selected strip road was 50 min 43 s. In order to haul all logs, 4 passes were required. During the first pass forwarder didn't drive beyond the segment 2, therefore this drive was not taken into account in calculations. During each pass, forwarder crossed each segment 2 times, while driving in and out from the felling site. The rut's measurement data show how the status of the strip road changes after each pass. Taking into account that the forwarder does not always move using the same track, drives cannot be compared completely impartial. It is possible to observe similar tendencies between different drives in the same sectors. It can be assumed that during those drives the forwarder has taken a similar trajectory.

It has to be taken into account that the surface from which the ultrasound wave reflects is very variable. Deviations from the trajectory of the previous drive can significantly impact the measurements. As a result the location, where the ultrasound wave has reflected in the previous drive, and the reflected angle have changed. It would not be correct to compare results from sensors of both sides, as the amount of successful measurement from both sides is small. Therefore data from each sensor was analysed separately (Figs 3 and 4).
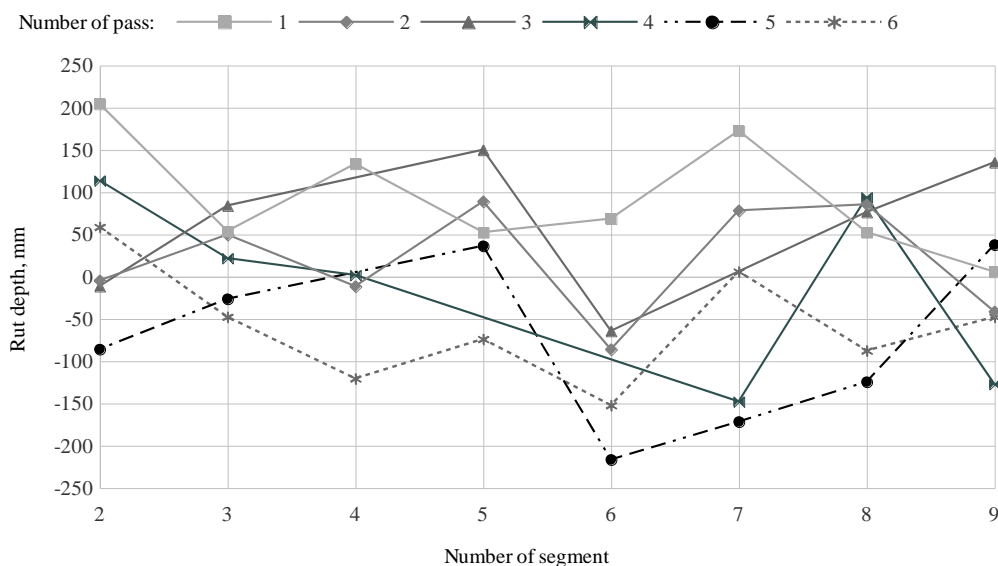
Figure 3. Measurements from the ultrasonic sensor of the left side.
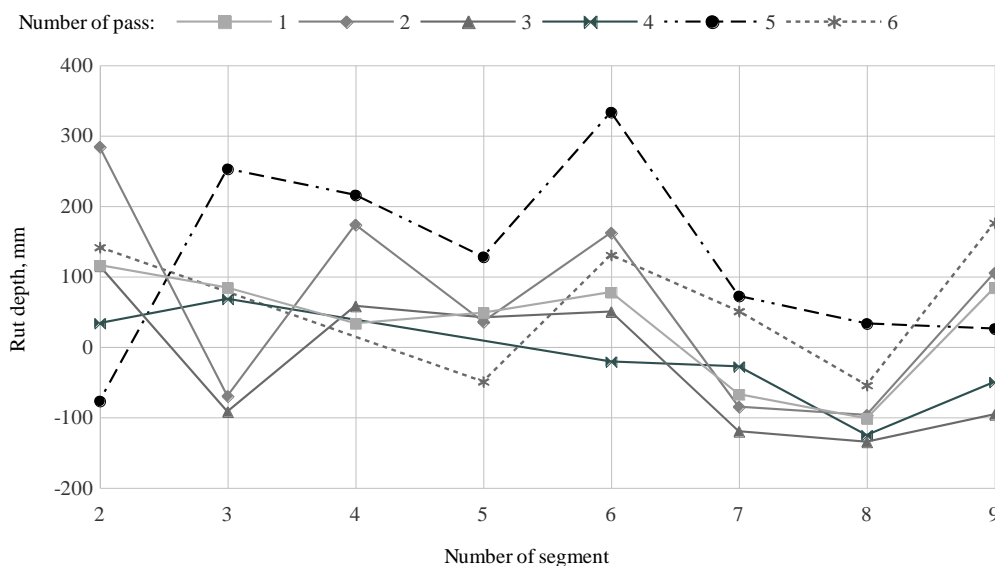
Figure 4. Measurements from the ultrasonic sensor of the right side.

A 10 m long segment provides sufficient quantitative information on soil impact and rut formation during forwarding; however, it is too long to provide information on rut formation demanded for the formal quality assurance. Additional benefit of the elaborated system is detailed representation of number of passes, driving speed, productivity, soil bearing capacity, fuel consumption and other technical information, which can be utilized to improve the forwarding performance, as well as to plan further forest management activities in a particular stand. The amount of valid data has to be increased in future to reduce length of the segments and to improve accuracy of the measurements.

Comparing the tendencies during following passes the rut depth in the forest can be characterized. Results from the sensor of the right side show that significant footprints in soil could have occurred in segments 7 and 8 (Fig. 4). None of the footprints exceeded the depth of 20 cm, therefore they cannot be considered as ruts according to formal quality requirements.

In field test harvesting residues were placed on strip roads. In result, forwarder was driving above actual ground level, which explains positive values. If the results from both side ultrasonic sensors are either positive or negative it possible to say if there is or is not any ruts. Taking into account, that results shows average values from segments, it is hard to say if in these segments are obstacles which impair movement of forwarder. To see obstacles on strip roads closer investigation in all segments needs to be done.

It can be observed that the amplitude between the measurements from the sensors of the left side is larger and it is more complicate to observe certain patterns. The tilt of the forwarder was not taken into account, when taking measurements, therefore it is difficult to assess, if changes in results are due to tilting of the forwarder or due to the chosen driving trajectory. The tilting is associated with use of harvesting residues in

strip-roads to improve forwarding conditions, therefore forwarder is driving over a kind of embankment until it is completely compacted and mixed with topsoil.

Comparing results from sensors of both sides, an opposite change in results is observed. It can be assumed that changes are proportional to the tilt of the forwarder. However the tilt of the forwarder was not taken into account in calculations, therefore in this case clear connections cannot be drawn. Tilt of the forwarder should be taken into account when carrying out further research on rut formation, using ultrasonic sensors. Additional forwarder tilt sensor can be added to system to determine forwarder horizontal and vertical tilt. It is also important to consider that forwarder can use different tracks during different passes to avoid ruts' formation, therefore for the quality assurance purpose the deepest ruts in a particular segment should be used Instead of ruts depth during the last pass.

Future trials should be carried out in final felling sites, where harvesting residues are not placed in strip roads, in order to investigate dynamics of ruts formation more precisely and to avoid impact of logging residues. In order to evaluate the system more effectively, felling sites with flat terrain should be selected.

REFERENCES

Andújar, D., Weis, M. & Gerhards, R. 2012. An Ultrasonic System for Weed Detection in Cereal Crops. *Sensors* **12**(12), 17343–17357. https://doi.org/10.3390/s121217343

Chang, Y.K., Zaman, Q.U., Rehman, T.U., Farooque, A.A., Esau, T. & Jameel, M.W. 2017. A real-time ultrasonic system to measure wild blueberry plant height during harvesting. *Biosystems Engineering* **157**, 35–44. https://doi.org/10.1016/j.biosystemseng.2017.02.004

Drinkwater, B.W. & Wilcox, P.D. 2006. Ultrasonic arrays for non-destructive evaluation: A review. *NDT & E International* **39**(7), 525–541.
https://doi.org/10.1016/j.ndteint.2006.03.006

Eklöf, K., Schelker, J., Sørensen, R., Meili, M., Laudon, H., von Brömssen, C. & Bishop, K. 2014. Impact of Forestry on Total and Methyl-Mercury in Surface Waters: Distinguishing Effects of Logging and Site Preparation. *Environmental Science & Technology* **48**(9), 4690–4698. https://doi.org/10.1021/es404879p

Escolà, A., Planas, S., Rosell, J.R., Pomar, J., Camp, F., Solanelles, F., … & Gil, E. 2011. Performance of an Ultrasonic Ranging Sensor in Apple Tree Canopies. *Sensors* **11**(12), 2459–2477. https://doi.org/10.3390/s110302459

Gudra, T., Banasiak, D., Herman, K. & Opieliński, K. 2017. Comparative analysis of the results of snowfall level measurements performed using ultrasonic aerolocation method in real conditions in different climatic areas. *Applied Acoustics* **125**, 71–79. https://doi.org/10.1016/j.apacoust.2017.04.011

Koval, L., Vaňuš, J. & Bilík, P. 2016. Distance Measuring by Ultrasonic Sensor. *IFAC-PapersOnLine* **49**(25), 153–158. https://doi.org/10.1016/j.ifacol.2016.12.026

Laffan, M., Jordan, G. & Duhig, N. 2001. Impacts on soils from cable-logging steep slopes in northeastern Tasmania, Australia. *Forest Ecology and Management* **144**(1–3), 91–99. https://doi.org/10.1016/S0378-1127(00)00360-1

Lokhande, P. 2016. Garbage Collection Management System. *International Journal of Engineering And Computer Science*. https://doi.org/10.18535/ijecs/v5i11.14

Maghsoudi, H., Minaei, S., Ghobadian, B. & Masoudi, H. 2015. Ultrasonic sensing of pistachio canopy for low-volume precision spraying. *Computers and Electronics in Agriculture* **112**, 149–160. https://doi.org/10.1016/j.compag.2014.12.015

Panda, K.G., Agrawal, D., Nshimiyimana, A. & Hossain, A. 2016. Effects of environment on accuracy of ultrasonic sensor operates in millimetre range. *Perspectives in Science* **8**, 574–576. https://doi.org/10.1016/j.pisc.2016.06.024

Prindulis, U., Kalēja, S. & Lazdiņš, A. 2016. Soil compaction in young stands during mechanized logging of biofuel and roundwood assortments. In *Research for Rural Development* (Vol. **2**, pp. 69–76).

Schumann, A.W. & Zaman, Q.U. 2005. Software development for real-time ultrasonic mapping of tree canopy size. *Computers and Electronics in Agriculture* **47**(1), 25–40. https://doi.org/10.1016/j.compag.2004.10.002

Serigos, P.A. 2012. *Field evaluation and analysis of automated rut measurement systems data for Texas conditions* (thesis). Retrieved from https://repositories.lib.utexas.edu/handle/2152/ETD-UT-2012-05-572

Flash points of gasoline from Kukersite oil shale: Prediction from vapor pressure

R. Rannaveski and M. Listak[*]

Tallinn University of Technology, School of Engineering, Department of Energy Technology, Ehitajate tee 5, EE19086 Tallinn, Estonia
[*]Correspondence: madis.listak@ttu.ee

Abstract. The flash point of liquid fuels, especially of light distillates such as gasoline or naphtha, is an important parameter for the handling of such materials. In this work, flash points and volatility characteristics (vapor pressure, boiling point) of a number of shale gasoline samples with different volatilities were measured. The shale gasoline fractions were produced from Kukersite oil shale using solid heat carrier retorting technology. Several existing correlations for calculating flash points of hydrocarbons and petroleum fractions are evaluated, and the absolute average deviations were found to be between 1.1 to 20.9 °C. New, easy-to-use correlations are proposed for estimating flash points for oil shale based gasolines from volatility characteristic that are readily available. The correlation proposed in this work are based on the vapor pressure at 20 or 37.8 °C (100 °F), Reid vapor pressure (37.8 °C) or boiling point. The average absolute deviations for these correlations were 0.82 to 0.93 °C, meaning they are comparable to or better than existing methods developed for petroleum oils, which mostly use boiling point as the input parameter, when applied to gasoline from Kukersite oil shale.

Key words: oil shale, gasoline, flash point, closed cup, correlations, vapor pressure, Reid vapor pressure, boiling point, alternative fuel, mineral oil.

INTRODUCTION

Oil shale (a solid fossil fuel) has the potential to be an important source of liquid fuel due to the large amount of oil shale resources available worldwide (Oja & Suuberg, 2012). The world's oil shale resources are estimated to be equivalent to more than 2.9 trillion barrels of oil (1 barrel = 0.159 m³) (Dyni, 2003). Shale oil is obtained by thermally processing kerogen, the insoluble crosslinked organic matter in oil shale (Savest et al., 2007; Hruljova et al., 2013). This is performed in an oxygen free environment in a process termed pyrolysis (also known by the industrial term 'retorting'). The process results in a so called 'synthetic crude oil', which, similarly to tars/oils from coal or biomass pyrolytic thermochemical conversions (Suuberg & Oja, 1997; Oja & Suuberg, 1998), has a wide distribution of properties/constituents (for kukersite oil shale derived shale oils see Oja, 2005; Oja, 2015; Oja, 2015a; Järvik & Oja, 2017). Therefore, in industry commonly the 'synthetic crude oil' is divided into 'straight-run fractions' as products (Qian, 2010). Often one of these products is a shale gasoline fraction with a boiling range up to about 200 °C (Oja, 2007; Qian, 2010). As with

petroleum based gasoline, the handling of shale gasoline depends on several parameters, one of which is the flash point. Knowledge of a flammable liquid's flash point is an important factor in the production, processing, handling and transport of these liquids because it describes the fire and explosion potential of a material (Hristova & Tchaoushev, 2006; Skrinska et al., 2015). Fuels with low flash points have a higher fire hazard. The flash point is also a key parameter for the classification of flammable liquids, and is an important parameter included on material safety data sheets (MSDS). The flash point is defined as the lowest temperature at which there is enough vapor to ignite a mixture of air and these vapors. Therefore, in addition to technical constraints (experimental methods/procedures (Phoon et al., 2014)), the flash point value depends in large measure on vapor pressure of a substance, but also somewhat on its composition/structure. There are various prediction methods available for flash points, varying from simple empirical methods with one input parameter to more sophisticated methods (Hristova & Tchaoushev, 2006; Valenzuela et al., 2011; Phoon et al., 2014). However, for oils and oil fractions (ill-defined mixtures that can contain from hundreds to thousands of components) mostly one input parameter based empirical methods are of practical interest (see Table 1).

In this paper the practical interest is in evaluating the close cup flash points of the 'straight run' gasoline fraction (ill-defined mixture) from Kukersite shale oil. For this particular shale oil, produced by solid heat carrier (SHC) retorting technology from Kukersite oil shale, about 20% of the shale oil is taken as the gasoline fraction, which has a boiling range below 200 °C. The shale gasoline consists mainly of paraffins and olefins (67%). It also contains compounds containing heteromatoms, such as sulphur or oxygen, as the content of heteroatoms is about 2–4% (Gubergrits et al., 1989; Qian, 2010). Some background information on thermodynamic properties of shale oil gasolines can be found from (Kollerov, 1951; Qian, 2010; Baird & Oja, 2016). The aim of this work was to provide convenient predictive correlations for determining the flash point of this shale gasoline from its vapor pressure at a certain temperature (vapor pressure at 20 °C or Reid vapor pressure at 100 °F) or its atmospheric boiling point. In addition to proposing new correlations, we also test the applicability of existing flash point correlations that have been proposed for hydrocarbons or petroleum fractions. The correlations tested are given in Table 1. A more detailed description of some of these correlations, and several other correlations that use different input parameters than what we tested in this work, can be found in (Alqaheem et al., 2017).

EXPERIMENTAL

Materials
The shale gasoline fractions used in this study were obtained from the whole shale oil (Kollerov, 1951; Baird et al., 2015; Oja et al., 2016) produced using a solid heat carrier process (Golubev, 2003; Elenurm et al., 2008) at Eesti Energia's Narva Oil Plant (Narva, Estonia). This plant uses Kukersite oil shale (Estonia) as the raw material. Two different gasoline fractions were used, which were produced at different times. The gasoline fractions are henceforth identified as Sample 1 (specific gravity (SG) of 0.751, atomic hydrogen-carbon ratio (H/C) of 1.82) and Sample 2 (SG 0.77, H/C 1.81). From these, different shale gasoline samples with varying volatility were prepared by evaporating part of the sample in a simple batch distillation system (similar to the setup

for an Engler distillation (ASTM D86). In total 8 samples were prepared for further analysis, with 7 to 38% of the gasoline being evaporated. These samples were used for vapor pressure and flash point measurements. The flash points of the initial shale gasoline fractions (Sample 1 and Sample 2) were ≤ -38 °C.

Closed cup flash point measurements

The flash points were measured according to the ASTM D6450 closed cup flash point standard. Measurements were carried out using an Eralytics Eraflash Flash Point Tester. It was found that due to the limitations of our Eraflash flash point tester measurements for samples with flash points below -10 °C were less accurate than measurements for the other samples. The standard deviation for samples with flash points greater than -10 °C was below 1 °C. However, for samples with flash points lower than -10 °C, the standard deviation was found to be up to 2.1 °C. Therefore, more measurements had to be carried out to get a more accurate average flash point and the flash points reported in this study are average values of five measurements. The performance of the setup was tested using dodecane and benzene (Sigma-Aldrich, purity > 99%). Using the Eraflash Flash Point Tester the flash point of dodecane was found to be 78.5 ± 0.5 °C, which is comparable to the flash point found in the literature (81–83 °C (Hughes et al., 1996; Li et al., 2014)); the flash point benzene was found to be -0.8 ± 0.5 °C, which is comparable to the flash point found in literature (-13 to -9 °C (Mack, 1923; Choe, 1988)); the flash point of toluene was found to be 8.2 ± 0.5 °C, which is comparable to the flash point found in literature (7.2 °C (Liaw et al., 2010)).

Vapor pressure measurements

The vapor pressure curves covering the temperature range from room temperature to 100 °C were measured using a commercial Eralytics Eravap Vapor Pressure Tester according to the ASTM D6378 Standard. Performance tests for the device can be found in (Siitsman & Oja, 2015). Some earlier vapor pressure data also exist for Kukersite shale gasoline fractions with narrow boiling ranges (Siitsman & Oja, 2015), which were measured using the DSC technique (Siitsman et al., 2014; Siitsman & Oja, 2016).

RESULTS AND DISCUSSION

Because the aim of this work was to derive/propose easy-to-use correlations for the determination of the flash point from a convenient volatility characteristic (such as the vapor pressure at a specific temperature or the boiling point), the vapor pressures of the shale gasoline samples were measured. For the 8 samples the exact evaporation percentages and vapor pressure data are given in (Table 2).

Table 1. Overview of existing flash point (TF) correlations, containing either boiling point (TB) or vapor pressure (pvap) as input parameters, tested in this work

Corre-lation	Authors	Equation	Range	Ref
1	Butler et al.	$T_F(°K) = 255.752T_B(°K) - 119$	$366.2 \leq T_B \leq 644.2°K$	(Butler et al., 1956)
2	Riazi-Daubert	$\dfrac{1}{T_F 0.556(°K)} = -1.4568 * 10^{-2} + \dfrac{2.84947}{0.556T_{B(°K)}} - 1.057 * 10^{-3} lnT_B(°K)$	$338.2 \leq T_B \leq 866.2 °K$	(Riazi & Daubert, 1987)
3	Walsh-Mortimer	$T_F(K) = 231.2 - 40\log(p^{vap}(310.93\ °K))\ (bar)$	N/A	(Walsh & Mortimer, 1971)
4	Patil	$T_F(K) = 4.656 + 0.844T_B - 2.34 * 10^{-3}T_B^2$	$248.15 \leq T_F \leq 381.48°K$	(Patil, 1988)
5	Satyanarayana-Kakati	$T_F(°K) = -83.3362 + 273.73T_B(°K) + 0.1118 * \dfrac{10^{-3}}{274.15T_B(°C)} + 38.734SG$	$293.2 \leq T_B \leq 613.2\ K$	(Satyanarayana & Kakati, 1991)
6	Satyanarayana-Rao (hydrocarbons)	$T_F(K) = 225.1 + \dfrac{537.6\left(\dfrac{2217}{T_B(K)}\right)^2 e^{-\frac{2217}{T_B}}}{\left(1 - e^{-\frac{2217}{T_B}}\right)^2}$	N/A	(Satyanarayana & Rao, 1992)
7	Satyanarayana-Rao (petroleum fractions)	$T_F(K) = 237.9 + \dfrac{334.4\left(\dfrac{1807}{T_B(K)}\right)^2 e^{-\frac{1807}{T_B}}}{\left(1 - e^{-\frac{1807}{T_B}}\right)^2}$	N/A	(Satyanarayana & Rao, 1992)
8	Hshieh (Organic)	$T_F(°K) = -54.5377 + 273.7383T_B(°K) + 0.00022T_B^2$	$263.2 \leq T_B \leq 648.2\ K$	(Hshieh, 1997)
9	Hshieh (Organosilicon)	$T_F(°K) = -51.2385 + 273.6494T_B(°K) + 0.00047T_B^2$	$263.2 \leq T_B \leq 648.2\ K$	(Hshieh, 1997)
10	Alqaheem-Riazi (Hydrocarbons)	$T_F(K) = 0.71T_B(K)$	$393.0 \leq T_B \leq 707.0\ K$	(Alqaheem & Riazi, 2017)
11	Alqaheem-Riazi (Petroleum Fractions)	$T_F(K) = 0.69T_B(K)$	$393.0 \leq T_B \leq 707.0\ K$	(Alqaheem & Riazi, 2017)
12	Wang-Sun	$T_F(K) = 33.176 + 0.67465T_B(K)$	N/A	(Wang & Sun, 2001)

SG stands for the specific gravity.

Table 2. Vapor pressure data for initial Sample 1, initial Sample 2 and the samples obtained from evaporating different percentages of these initial shale gasoline samples

T, °C	Sample 1 VP, kPa	Vaporized from Sample 1					Sample 2 VP, kPa	Vaporized from Sample 2		
		7.1% VP, kPa	12.0% VP, kPa	16.6% VP, kPa	24.8% VP, kPa	37.8% VP, kPa		13.6% VP, kPa	19.2% VP, kPa	23.6% VP, kPa
20	18.9	10.9	8.2	–	–	–	18.1	–	–	–
30	25.9	15.4	12.1	11.0	9.5	–	25.2	9.8	7.2	6.5
37.8	32.9	20.1	16.0	14.7	12.8	9.2	32.2	13.1	9.8	8.9
40	35.2	21.7	17.3	15.9	13.9	10.3	34.5	14.3	10.8	9.7
50	46.7	29.9	24.4	22.5	19.7	15.3	46.1	20.2	15.4	13.9
60	61.2	40.6	33.6	31.3	27.5	21.7	60.5	28.0	21.7	19.6
70	78.9	54.3	45.7	42.6	37.6	30.3	70.8	38.2	30.0	27.1
80	100.5	71.5	61.0	57.2	50.7	41.5	99.0	51.1	40.7	36.9
90	126.8	93.1	80.5	75.8	67.5	56.2	124.3	67.5	54.4	49.5
100	158.5	119.8	104.7	99.0	88.8	74.8	154.6	87.8	71.8	65.7

The calculated volatility characteristics (vapor pressures at 20 and 37.8 °C (100 °F), Reid vapor pressure at 100 °F and the atmospheric boiling point) and measured flash points for the samples are given in (Table 3). These four volatility characteristics were chosen because they are the most common volatility parameters given in gasoline safety data sheets. Vapor pressures at each temperature and atmospheric boiling points were calculated using the data given in (Table 2). For this the dataset corresponding for different evaporation percentages were fitted by an integrated Calusius-Clapeyron equation. Reid Vapor Pressure was calculated from the vapor pressure at 37.8 °C using the following equation (1) from ´ASTM D6377´:

$$RVP = 0.915VP37.8 \text{ °C} \qquad (1)$$

where RVP is the Reid vapor pressure and VP37.8 °C is the measured vapor pressure at 37.8 °C.

The measured flash points were used along with the selected volatility characteristics in Table 3 to develop correlations. Here it is also worth mentioning that when extrapolating to calculate the vapor pressure at the flash point temperature it was found that for shale gasoline the vapor pressure at the flash point was between 1.5 to 2.5 kPa. This is in the range of lower and upper flammability limits ($0.01 < $ Pvap (atm) < 0.08) proposed by ´Algunaibet et al., 2016´.

Table 3. Flash points (T_F) and selected vaporization characteristics of the different samples, obtained from evaporating different percentages of these initial shale gasoline samples. The vaporization characteristics are vapor pressure at 20 °C ($VP_{20 \text{ °C}}$), vapor pressure at 37.8 °C or 100 °F $_{(VP100 \text{ °F})}$, Reid vapor pressure (RVP) and boiling point (T_B)

	Based on the initial Sample 1					Based on the initial Sample 2		
Evaporated, %	7.1	12.0	16.6	24.8	37.8	13.6	19.2	23.6
T_F, °C	-14.0	-10.3	-7.7	-4.7	0.5	-6.7	0.5	2.2
$VP_{20 \text{ °C}}$, kPa	10.7	8.1	7.3	6.3	4.4	6.5	4.8	4.3
$VP_{100 \text{ °F}}$, kPa	20.2	16.1	14.7	12.8	9.4	13.1	9.8	8.9
RVP, kPa	18.5	14.7	13.4	11.7	8.6	12.0	9.0	8.1
T_B, °C	93.5	98.9	101.3	105.8	111.1	105.5	113.5	117.5

The aim of developing correlations using these different input parameters was to make it possible to estimate flash points for shale gasoline from a wider range of available data (either from vapor pressure at 20 or 37.8 °C, the Reid vapor pressure at 100 °F or the atmospheric boiling point). As an illustrative example, Fig. 1 illustrates the relation between flash point and vapor pressure at 20 °C for the shale gasoline fractions studied in this work. As seen from Fig. 1, the flash point-vapor pressure dependency for shale gasoline fractions derived from vaporizing portions of either Sample 1 or Sample 2 show a similar trend.

As seen from Fig. 1, a linear equation can be used to describe the relationship between the flash point and the vapor pressure at 20 °C. This is also the case for other pairs. The following are the linear Eqs (2, 3, 4) correlating the flash point with vapor pressures at 20 and 37.8 °C and the Reid vapor pressure:

$$T_F \text{ (°C)} = -2.6547VP_{20 \text{ °C}}(kPa) + 12.14 \qquad (2)$$

$$T_F \text{ (°C)} = -1.4948VP_{100 \text{ °F}}(kPa) + 14.337 \qquad (3)$$

$$T_F\ (°C) = -1.6337\,RVP(kPa) + 14.337 \tag{4}$$

The correlation between the flash point and the boiling points of shale gasoline turned out to be similar to the one proposed by 'Alqaheem and Riazi, 2017' in Eq. 5:

$$T_F(K) = 0.7068\,T_B(K) \tag{5}$$
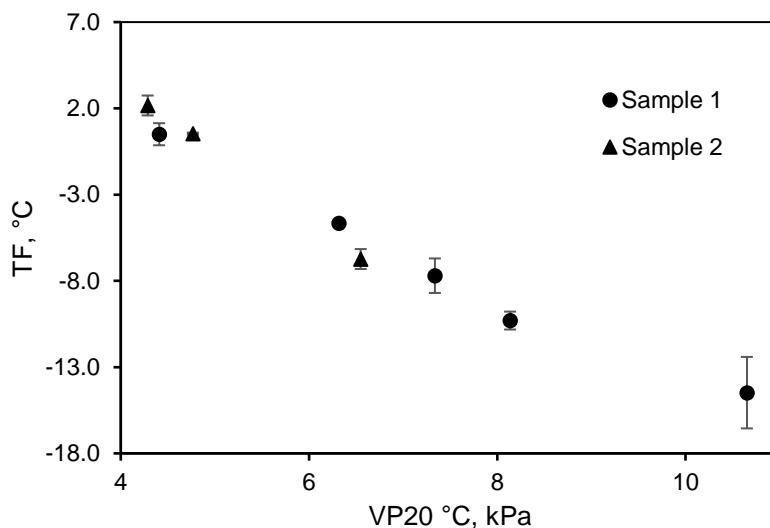
Figure 1. Graphical representation of the relationship between the flash point (T_F) and the vapor pressure at 20 °C ($VP_{20\ °C}$). Error bars represent the standard deviation of the experiments.

Table 4 summarizes an evaluation of the performance of flash point correlations given in Table 1 when applied to the shale gasoline fractions of this study, and also includes the correlations proposed in this work. The evaluation is based on the average deviation (AD) and absolute average deviation (ADD) of the values predicted by the correlations:

Table 4. Average deviation (AD) and absolute average deviation (ADD) of the calculated flash points, using the correlations from Table 1, when compared to experimental values of this work

	Correlations from Table 1											
	1	2	3	4	5	6	7	8	9	10	11	12
AD, °C	-5.8	-6.2	0.8	6.4	-13.7	-10.6	-22.4	-15.5	-12.2	-1.2	6.4	-21.0
AAD, °C	5.8	6.1	1.1	10.2	13.7	10.6	21.7	15.5	12.2	1.3	6.4	20.9

Deviation = Experimental – Calculated.

Results presented in Table 4 and Table 5 show that Correlations 3 and 10 (from Table 1) and the ones proposed in this work are the most accurate when estimating the flash points of shale gasoline. All these correlations have AADs around 1 °C. On the other hand, Correlations 7 and 12 gave AADs of over 20 °C. Correlations developed specifically for petroleum fractions were also less accurate than their counterparts that were developed for pure hydrocarbons (Correlations 6 vs 7 and 10 vs 11).

Table 5. Average deviation (AD) and absolute average deviation (ADD) of the calculated flash points, using the correlation derived in this study, when compared to experimental values of this work

	Correlations in this work			
	T_B	$VP_{20\,°C}$	$VP_{100°F}$	RVP
AD, °C	0	0	0	-0.2
AAD, °C	0.87	0.93	0.82	0.90

Deviation = Experimental – Calculated.

CONCLUSION

The aim of this work was to propose correlations for estimating the close cup flash point for shale gasoline fraction produced from Kukersite oil shale. These correlations can be used in risk assessment calculations related to handling and transporting these fuels. The work was based on experimentally measured closed cup flash points and vapor pressure curves. Based on the vapor pressure data the desired volatility properties (vapor pressures at 20 and 37.8 °C (100 °F), Reid vapor pressure at 100 °F and the atmospheric boiling point) were determined for 8 gasoline samples with different volatilities. Using this data, convenient correlations were developed or selected from the literature that allow the flash point of Kukersite shale gasoline to be estimated with an AADs of around 1 °C.

REFERENCES

Algunaibet, I.M., Voice, A.K, Kalghatgi, G.T. & Babiker, H. 2016. Flammability and volatility attributes of binary mixtures of some practical multi-component fuels. *Fuel* **172**, 273–283.

Alqaheem, S.S. & Riazi, M.R. 2017. Flash Points of Hydrocarbons and Petroleum Products: Prediction and Evaluation of Methods. *Energy Fuels* **31**(4), 3578–3584.

ASTM D86-12. Standard Test Method for Distillation of Petroleum Products at Atmospheric Pressure, West Conshohocken, PA: ASTM International, 2012.ASTM D86

Baird, Z.S., Oja, V. & Järvik, O. 2015. Distribution of hydroxyl groups in Kukersite shale oil: quantitative determination by Fourier transform infrared (FTIR) spectroscopy. *Applied Spectroscopy* **68** (5), 555−562.

Baird, Z.S. & Oja, V. 2016. Predicting fuel properties using chemometrics: a review and an extension to temperature dependent physical properties by using infrared spectroscopy to predict density. *Chemometrics and Intelligent Laboratory Systems* **158**, 41–47.

Butler, R.M., Cooke, G.M., Lukk, G.G. & Jameson, B.G. 1956. Prediction of Flash Points of Middle Distillates. *Ind. Eng. Chem.* **48**, 808.

Choe, M.-H. 1988. Experimentelle und theoretische Untersuchungen zur Flammpunktbestimmung von Flüssigkeitsgemischen. Thesis.

Dyni, J.R. 2003. Geology and Resources of Some World Oil-Shale Deposits. *Oil Shale* **20**(3), 193–252.

Elenurm, A., Oja, V., Tali, E., Tearo, E. & Yanchilin, A. 2008. Thermal Processing of Dictyonema Agrillite and Kukersite Oil Shale: Transformation and Distribution of Sulfur Compounds in Pilot-Scale Galoter Process. *Oil Shale* **25**(3), 328−333.

Golubev N. 2003. Solid oil shale heat carrier technology for oil shale retorting. *Oil Shale* **20**(3), 324–332.

Gubergrits, M.J., Rohtla, I., Elenurm, A. & Myasoyedov, A.M. 1989. Comparison of light oil products from oil shale retorting in solid heat carrier units UTT-3000 and UTT-500. *Oil Shale* **6**(2), 189–194. (in Russian).

Hristova, M & Tchaoushev, S. 2006. Calculation of Flash Points and Flammability Limits of Substances and Mixtures. *J. Chem. Technol. Metall*. **41**(3), 291–296.

Hruljova, J., Savest, N., Oja, V. & Suuberg, M.E. 2013. Kukersite oil shale kerogen solvent swelling in binary mixtures. *Fuel* **105**, 77−82.

Hshieh, F.Y. 1997. Correlation of closed cup flash points with normal boiling points for silicone and general organic compounds. *Fire Mater*. **21**, 277−282.

Hughes, J.M., Hardy, D.R. & Beal, E.J. 1996. Flash Point Value for n-Dodecane Based on the Manual Pensky-Martens Closed Cup Method (ASTM D-93). *Energy & Fuels* **10**, 1276–1277.

Järvik, O. & Oja, V. 2017. Molecular Weight Distributions and Average Molecular Weights of Pyrolysis Oils from Oil Shales: Literature Data and Measurements by Size Exclusion Chromatography (SEC) and Atmospheric Solids Analysis Probe Mass Spectroscopy (ASAP MS) for Oils from Four Different Deposits. *Energy & Fuels* **31**(1), 328−339.

Kollerov, D.K. 1951. Physicochemical properties of oil shale and coal liquids (Fiziko-khimicheskie svojstva zhidkikh slantsevykh i kamenougol'nykh produktov). Moscow, 245 pp. (in Russian).

Li, X., Duan, P.P., Sun, K.N. & Yan, X. 2014. Prediction of the Flash Point of Binary and Ternary Straight-Chain Alkane Mixtures. *Advances in Materials Science and Engineering* **2014**, 5 pp.

Liaw, H-J., Gerbaud, V. & Chiu, C-Y. 2010. Flash Point for Ternary Partially Miscible Mixtures of Flammable Solvents. *J. Chem. Eng. Data* **55**, 134–14.

Mack, E., Boord, C.E & Barham, H.N. 1923. Calculation of Flash Points for Pure Organic Substances. *Industrial and Engineering Chemistry* 963–965.

Oja, V. & Suuberg, E.M. 1998. Measurements of the Vapor Pressures of Coal Tars Using the Nonisothermal Knudsen Effusion Method. *Energy & Fuels* **12**(6), 1313−1321.

Oja, V 2005. Characterization of tars from Estonian Kukersite oil shale based on their volatility. *Journal of Analytical and Applied Pyrolysis* **74**, 55−60.

Oja, V. 2007. Is it time to improve the status of oil shale science? *Oil Shale* **24**(2), 97−100.

Oja, V. & Suuberg, E.M. 2012. Oil Shale Processing, Chemistry and Technology. In: R. A. Mayer (Editors). *Encyclopedia of Sustainability Science and Technology* (7457−7491). Springer.

Oja, V. 2015. Examination of molecular weight distributions of primary pyrolysis oils from three different oil shales via direct pyrolysis Field Ionization Spectrometry. *Fuel* **159**, 759−765.

Oja, V. 2015a. Vaporization parameters of primary pyrolysis oil from Kukersite oil shale. *Oil Shale* **32**(2), 124−133.

Oja, V., Rooleht, R. & Baird, S.Z. 2016. Physical and thermodynamic properties of Kukersite pyrolysis shale oil: literature review. *Oil Shale* **33**(2), 184–197.

Patil, G.S. 1988. Estimation of flash point. *Fire Mater*. **12**, 127−131.

Phoon, L.Y., Mustaffa, A.A., Hashim, H. & Mat, R.A. 2014. Review of Flash Point Prediction Models for Flammable Liquid Mixtures. *Ind. Eng. Chem. Res.* **53**, 12553−12565.

Qian, J. 2010. *Oil Shale – Petroleum Alternative*. China Petrochemical Press, Beijing, 619 pp.

Riazi, M.R. & Daubert, T.E. 1987. Predicting flash point and pour points. *Hydrocarbon Process* **66**, 81−83.

Satyanarayana, K. & Kakati, M.C. 1991. Correlation of flash points. *Fire Mater*. **15**, 97−100.

Satyanarayana, K. & Rao, P.G. 1992. Improved equation to estimate flash points of organic compounds. *J. Hazard. Mater*. **32**, 81−85.

Savest, N., Oja, V., Kaevand, T. & Lille, Ü. 2007. Interaction of Estonian kukersite with organic solvents: A volumetric swelling and molecular simulation study. *Fuel* **86** (1–2), 17–21.

Siitsman, C., Kamenev, I. & Oja, V. 2014. Vapour pressure data of nicotine, anabasine and cotinine using Differential Scanning Calorimetry. *Thermochimica Acta* **595**, 35−42.

Siitsman, C. & Oja, V. 2015. Extension of the DSC method to measuring vapor pressures of narrow boiling range oil cuts. *Thermochimica Acta* **622,** 31–37.

Siitsman, C. & Oja, V. 2016. Application of a DSC based vapor pressure method for examining the extent of ideality in associating binary mixtures with narrow boiling range oil cuts as a mixture component. *Thermochimica Acta* **637**, 24−30.

Skrinska, M., Skrinsky, J., Dolnicek, P., Lukesova, P. & Marek, J. 2015. Flash-Point Prediction for Industrial Applications. In: *Proceedings – 2014 International Conference on Mathematics and Computers in Sciences and in Industry*, MCSI 2014, 86–88.

Suuberg, E.M. & Oja, V. 1997. Vapor pressures and heats of vaporization of primary coal tars, Technical Report, US Department of Energy, United States. doi:10.2172/774960. http://www.osti.gov/scitech/servlets/purl/774960.

Valenzuela, E.M., Vázquez-Román, R., Patel, S. & Mannan, S.M. 2011. Prediction models for the flash point of pure components. *Journal of Loss Prevention in the Process Industries* **24**, 753–757.

Walsh, R.E & Mortimer, J.V. 1971. New Way to Test Product Quality. *Hydrocarbon Processing* **50**(9), 153–158.

Wang, K.Q & Sun, X.Z. 2001. Correlation and calculation of the flash points of organic compounds. *Computational Applied Chemistry* **18**, 581–584.

Factors influencing use of fuelwood and its environmental impacts in Tapanuli Utara regency, North Sumatra

H. Roubík[1], J. Mazancová[1,*], A. Brunerová[2] and D. Herák[3]

[1]Department of Sustainable Technologies, Faculty of Tropical AgriSciences, Czech University of Life Sciences Prague, Kamýcká 129, CZ165 00 Prague, Czech Republic
[2]Department of Material Science and Manufacturing, Faculty of Engineering, Czech University of Life Sciences Prague, Kamýcká 129, CZ165 00 Prague, Czech Republic
[3]Department of Mechanical Engineering, Faculty of Engineering, Czech University of Life Sciences Prague, Kamýcká 129, CZ165 00 Prague, Czech Republic
*Correspondence: mazan@ftz.czu.cz

Abstract. Deforestation and forest degradation, after burning of fossil fuels, is considered as the second leading cause of anthropogenic greenhouse emissions (accounting for over 17% of global carbon dioxide emissions) and has become an important issue concerning climate change mitigation. The provision of wood energy is generally thought to be a major contributor to forest loss. In Indonesia, more than half of the rainforest there, the third-largest swath in the world, has been felled in just a few years. Furthermore, permission has been granted to convert the majority of what remains into palm or acacia plantations. The logging and burning of forests to clear land for cultivation has made Indonesia one of the largest emitters of greenhouse gases. Therefore, the objective of this study was to assess the current level and influencing factors of the use of fuelwood among the rural population as well as the consequent environmental impacts in the target area in North Sumatra. The questionnaire survey using randomly selected households (n = 196) was administered in Tapanuli Utara regency from July to August 2014; followed by several field visits from August to September 2016. Obtained data were analysed with descriptive statistics and cross tabulation. The results indicate that fuelwood is a significant source of energy in the target area. For 31% of respondents it is the major energy source and for 64% it is a supplementary source. The high rate of use of wood as fuel corresponds to the poor financial situation of respondents and the easy accessibility of wood, but only from the surrounding area (own garden or adjacent land). Wood resources are often very distant (on average over 1,000 metres) as a consequence of high deforestation. This study reveals that there is a non-sustainable trend of forest conversion resulting in high land degradation in Tapanuli Utara regency.

Key words: rural household; energy sources; Indonesia; Developing countries.

INTRODUCTION

In the developing world, biofuel is widely applied for energy production (Barnes et al., 2005; Demirbas, 2009) and has the potential to secure the planet's future energy needs (Demirbas, 2009). The increase in population and income levels combined with increased per capita energy consumption requires energy production to keep pace with economic growth (Reddy, 2016).

Indonesia itself houses the most extensive rainforest cover in all of Asia; however its future is unsecure, as there is rapid transformation of these lands in order to accommodate increasing population and growing economy. Ensuring sufficient energy resources is a future issue that requires the attention of all the world's countries, because the well-being of humans in modern times is closely linked to the quantity, availability and quality of energy used (Hasan et al., 2012; Kimaro & Lulandala, 2013). In the case of Indonesia, the largest economy in Southeast Asia (Gunningham, 2013), sufficient energy supply is a very important factor in promoting further development (Hasan et al., 2012). The strong economic and population growth of the country and the development of the industrial sector are causing an ever-increasing demand for energy. From 1980 to 2010, total energy production rose 2.8 times, while consumption rose almost fivefold (Mujiyanto & Tiess, 2013). In 2010, approximately 96% of Indonesia's total energy consumption was covered by non-renewable energy sources – fossil fuels. Renewable resources, in particular geothermal and hydroelectric power, constituted about four percent; a very small proportion compared to other countries (Hasan et al., 2012). Given the fact that Indonesia is still energy dependent on the use of fossil fuels, with current oil and gas supplies estimated at 23 years and 52 years (MEMR, 2010), it is in the national interest to diversify the share of energy towards new and renewable sources which ensure energy self-sufficiency and autonomy (Ibrahim et al., 2010). It must be highlighted that the use of traditional biomass energy sources, which are used extensively in Indonesia, has many negative effects (Gurung & Oh, 2013), both social and environmental (Kimaro & Lulandala, 2013; Gunningham, 2013). Because the collection of fuelwood is time and labour intensive, and is mostly carried out by women (Grassi et al., 2015), it is also associated with gender equity issues (Gurung & Oh, 2013). Such consequences of women´s time allocation due to the fuelwood collection have already been discussed in the work of Kumar and Hotchkiss (1988).

Deforestation and forest degradation is considered as the second leading cause of anthropogenic greenhouse emissions after the burning of fossil fuels (van der Werf, 2009) (accounting for over 17% of global carbon dioxide emissions) and has become an important issue concerning climate change mitigation (Ter-Mikaelian et al., 2015). The provision of wood energy is generally thought to be a major contributor to forest loss (Ter-Mikaelian et al., 2015). In Indonesia, more than half of the rainforest there, the third-largest swath in the world, has been felled in a few years. Furthermore, permission has been granted to convert the majority of what remains into palm or acacia plantations (Vidal, 2013). The logging and burning of forests to clear land for cultivation has made Indonesia one of the largest emitters of greenhouse gases (Harrison et al., 2009). Therefore, the objective of this study is to assess the current level and influencing factors of fuelwood use among the rural population as well as the consequent environmental impacts in the target area in North Sumatra.

MATERIALS AND METHODS

Description of the study area

The survey was conducted in the province of North Sumatra, Tapanuli Utara regency (Fig. 1). The population of North Sumatra consists of over 13.9 million inhabitants, which constitutes around 5.4% of the population of Indonesia (currently 255,461,700 inhabitants; the prediction for 2035 is around 305,652,000 inhabitants [BPS, 2015]). North Sumatra is the fourth most populous province in the country. The population of Tapanuli Utara regency, according to the latest data from 2014, is over 290,000.
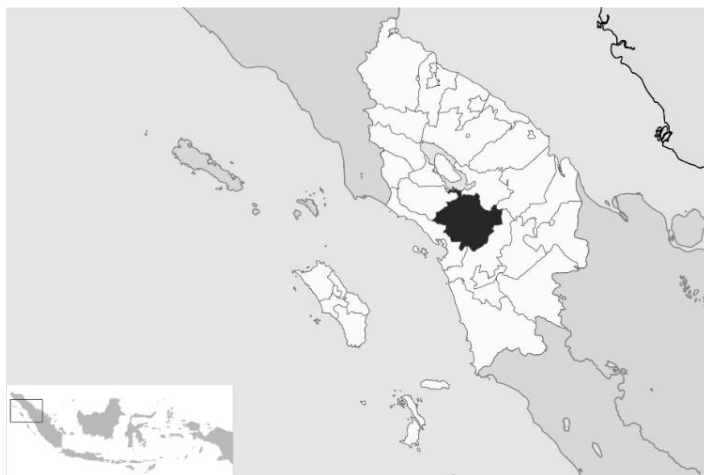
Figure 1. Target area (Tapanuli Utara regency) of North Sumatra (Adjusted from: Wikimedia Commons).

Data collection and analysis

The survey was conducted using randomly selected households (n = 196) (with a confidence level of 95% giving a margin of error of less than 7%) from July to August 2014 and followed by several field visits from August to September 2016. The methods of data collection consisted of one-hour questionnaire. The questionnaire included different types of questions such as open, closed, semi-open, evaluation and multiple-choice questions. The questionnaire was subject to pilot testing and was subsequently adjusted and translated into the Indonesia language before final distribution. Main categories of the questionnaire are given in Table 1. Data obtained in the survey were analysed with descriptive statistics and cross tabulation.

Table 1. Main categories of the questionnaire

Category	Type of questions
Socio-economic characteristics of respondents related par	District, village, sex, role in household, size of family, education, occupation, income, farm size, crops, equipment in household.
Usage of energy sources related part	Use of energy sources, main and additional cooking fuels, LPG consumption, availability of LPG, cooking time, fuelwood collection and related factors.

RESULTS AND DISCUSSION

Energy sources used for cooking and their relationship to household incomes

The target area is relatively well electrified, as one of the main electrification networks of Sumatra (GENI, 2014) passes through this area. However, as in many areas of Indonesia, several-hour electricity breakdowns still occur almost every day. Among the respondents, 88% had access to the electricity network and 19% of the farms (farm buildings). Therefore, the most widespread source of energy for daily usage in the area is electricity, followed by LPG and fuelwood, which is mainly due to low incomes and the relatively easy availability of fuel. Kerosene was not included in the research because the target region was converted during 2010–2011 (World Bank, 2013) as part of the national kerosene replacement programme for LPG. The main and secondary sources of energy used for cooking were identified in the research, and their distribution is shown in Fig. 2. The respondents were given three fuel type options to be determined as the main (only one option possible) and the secondary fuel (max. two options possible). In many cases, however, respondents had a problem with determining the main fuel, especially those who used LPG and electricity in a balanced ratio. From Fig. 2, we can see the percentage of secondary fuels (n = 135), expressed as a percentage of 150%, which was due to the fact that 45 respondents out of 90 chose two fuels as secondary. The remaining 45 respondents (50%) used only one major fuel and the other as a supplementary fuel.
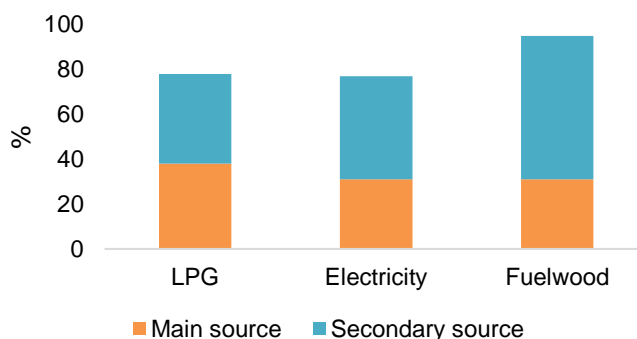
Figure 2. Used energy sources for cooking in the target area.

Respondents did not only use the three main fuels under investigation for cooking for their own use, but also for preparing feed for livestock (39%) and coffee roasting (8%).

According to Fig. 2, there is a balanced share between LPG users and electricity. Both of these sources provide high quality energy and, above all, suitable user conditions in terms of air cleanliness and kitchen accessories, and efficiency and time savings. Due to frequent power outages, LPG is a suitable source of energy, which may be one of the main reasons for the balanced combination of use of these two energy sources in the target area. Therefore, biogas from a biogas plant has the potential to be an appropriate energy source. According to the research developed for Hivos (a Dutch organization for development), which assessed the impact of the national IDBP (Indonesia Domestic

Biogas Programme) programme among new users of biogas plants, LPG consumption decreased from 76% to 27% (JRI Research, 2011). This result confirms the assumption that biogas is a suitable substitute for LPG. The same study also demonstrates that LPG is a suitable complementary fuel when a biogas plants user owns only one biogas burner that does not cover their daily needs and/or there is reduced or insufficient biogas production in the biogas plant.

Other research indicates that the choice of the selected energy source is evaluated on the basis of the functional relationship between household incomes and relative prices of available fuels or energy sources (Barnes et al., 2005) resulting in the so called 'energy ladder model', which is given in three phases. The first phase is the absolute dependence on traditional biomass sources. In the second phase, the transition to kerosene, coal and charcoal is linked to higher income, deforestation and urbanization. The third phase is the transition to LPG, natural gas, electricity, biogas and other renewable energy sources. It is only a simplified model; in practice, there is usually no complete transition to a new energy source, but a partial substitution (Andadari et al., 2014). A similar trend was also observed during our research. Even households from higher income groups use fuelwood as fuel as well as electricity and LPG as a supportive energy source.

LPG consumption, availability and costs

According to the study by Budya & Arofat (2011) – which presents the results of a survey of a private research organization in collaboration with Frontier which evaluated the satisfaction of LPG users who received the LPG Initiative Package under the Indonesian National Program – the following data was found: on average, respondents used 3 kg of LPG bottles for 10.58 days and 1.92 hours of cooking each day. This means that the average monthly consumption was approximately three bottles of LPG, 9 kg. The price for filling 3 kg of LPG bottle was 13,800 IDR (1.38 USD). Hence, the respondents spent on average 41,400 IDR (4.14 USD) monthly.

Based on the results of our study, the average cooking time was 1.84 hours (on average two to three meals a day). The monthly average household consumption was 9.48 kg of LPG, which also corresponds to the consumption of approximately three 3 kg LPG bottles per month. The LPG price was significantly higher in the target area of research. The price of a 3 kg LPG bottle (subsidized by state subsidies) was around 19,000 IDR (1.84 USD). The higher price was probably due to the relative remoteness from the nearest cities Siborongborong and Tarutung, where the price was about 4,000 IDR lower. The LPG bottles were delivered to the stores in the target area by intermediaries or imported by sellers themselves, which was probably the reason for the higher prices. In the target area, 12 kg of LPG bottles that were not subsidized by the state were also used, and the price was around 90,000 IDR (8.74 USD). However, most respondents reported the use of 3 kg LPG bottles, as they are subsidized (World Bank, 2013). In addition, there are 6 kg and 50 kg LPG bottles available in Indonesia that are not subsidized.

To determine the availability of LPG, a scale rating ranging from 1 (easy accessibility) to 5 (difficult accessibility) was used. The response rates for each grade are as follows: 1 (3%), 2 (38%), 3 (34%), 4 (13%), 5 (12%). This question was addressed to all respondents, not only to LPG users, so it is possible to assume that grades four and five were mainly chosen by non-LPG users. Based on observations from the target area, it was not physical LPG availability that was the issue but rather financial, in particular

due to the relatively high value of LPG from local dealers and low household incomes. The key figure is the LPG cost as a percentage share of total household income. The average revenue in the target area amounted to 132.38 USD and the average percentage share of LPG expenditure of total revenue was 6.78%, i.e. 8.97 USD. Research results from Andadari et al. (2014), which examined similar parameters in the Central Java region in two rural areas (Semarang Regency), two suburban and one urban area (the city of Salatiga), indicate the following results. The average household income was 134.43 USD and LPG cost as a percentage of total household income was 2.91%, or 3.91 USD. Given the similarity between the average household income and the fact that 91.1% of respondents used LPG, we can assume that the lower percentage of LPG expenditure in the comparative research was due to lower LPG use compared to the target area of our research as well as lower LPG consumption per household. In a comparative study, the average number of household members was 3.42 compared to 6 members in our target area, which is significant if we assume a direct ratio between the growing number of household members and the increasing consumption of LPG. The lower LPG price in the comparative research could be due to a more developed LPG distribution network and also the shorter distance from Saltiga to the rural areas: 7 and 9 km, compared to the distance from the target research area (Pagar Batu) to Siboronborong – 14.2 km – and Tarutung – 13.3 km. The reason for this was also the better accessibility of rural areas in Java compared to other areas of Indonesia, as is also reported by Andadari et al. (2014). According to the authors, the target area of the research is quite remote from the surrounding cities, mainly due to the undeveloped road infrastructure. The area is situated on the Sipoholon plateau where it is not possible to transit larger trucks and the overall transport of the area is not very optimized, which increases the price of imported goods.

Factors influencing the use of wood as a fuel and its environmental impacts
Fuelwood is a significant source of energy in the target area. According to Fig. 2, wood was the main source of energy used by 31% of respondents and 64% of respondents as supplementary fuel. The main reason for the high rate of use of wood as fuel is mainly its easy physical and financial availability in rural areas (World Bank, 2013; Andadari et al., 2014). Based on observations and interviews in the target area, wood was freely available from surrounding forests or own gardens or adjacent plots, i.e. completely free of charge. However, a high level of deforestation was seen on the landscape profile, which is one of the main warning signals in the area that needs to be addressed. Unexpected knowledge was the presence of frequent and extensive forest fires. After interviewing the employees of the agricultural training centre Agroihutan, it was apparent there was not a well-founded reason for these fires, but according to their claims, they were intentionally started to entertain a certain group of locals. Such practices are not, to the best of our knowledge, cited in any scientific sources. In addition to these fires, the burning of already leached forests or shrubs was recorded for the purpose of setting up new agricultural parcels (see Fig. 3, a and b).

Figure 3. Burning of forests to clear land for cultivation.

Important information is provided in Table 2, which lists the main factors and data on the collection of wood in the target area. The data in the table shows that wood resources are often very distant, which is one of the impacts of high deforestation; on the other hand, the low value of distance demonstrates the easy availability of wood fuel from their own garden or adjacent land.

Table 2. Fuelwood collection factors in the target area

	N	Average	St.Dev.	Min	Max
Age of fuelwood pickers (men)	60	34.1	11.8	18	67
Age of fuelwood pickers (women)	32	35.9	11.5	19	64
Age of fuelwood pickers (children)	33	12.6	2.8	5	17
Distance to the source of fuelwood (metres)	86	1,013.8	-	10	5,000
Length of the path to the source of fuelwood (minutes)	86	46.1	-	1	180
Time of fuelwood collection (hours/week)	86	4.8	-	1	36
Frequency of fuelwood collection (times/week)	76	2.1	1.2	1	7

It is clear from the results of our research that the persistently high rate of use of wood as fuel is due in particular to the poor financial situation of respondents and the easy accessibility of wood from the surrounding area. The results of Andadari et al. (2014), who assessed the effects of the kerosene replacement programme for LPG, demonstrate that in the surveyed rural areas covered by research there was only a slight decrease in the consumption of wood as fuel from 50.3% to 49.7% for those who had the main wood source. The results of the study (World Bank, 2013) show that even a LPG-subsidized state is financially inaccessible to many households. The same source states that 40% of LPG comes from imports, which, as a result of price increases on the international market, may lead to the inability to maintain the same subsidy rate. Such a situation would lead to an increase in LPG sale prices, which would likely lead to an even higher rate of use of wood and biomass. In the future, therefore, this trend can be anticipated in rural areas especially, where the consequences may include increased deforestation, soil degradation and increased greenhouse gas emissions and, above all, air pollution – not only outdoors but especially in the home, leading to increased health problems and reduced life expectancy and comfort. One of the appropriate solutions may

be the adoption of effective biomass stoves, the extension of which belongs to one of the three main national initiatives for 'access to clean cooking'. These stoves greatly increase the efficiency of combustion and reduce the amount of air pollution. Another solution is the installation of a biogas plant, which significantly reduces the negative aspects of the use of wood as a fuel and increases comfort. Research findings from southern Sri Lanka showed an 86% decrease in fuel consumption after biogas plant implementation (de Alwis, 2002); therefore, this could be a very suitable option for the target area (Roubík et al., 2016; Ginting 2017).

Other benefits included, for example, more time for gainful activities, rest and social participation, more time for children, better study conditions, and a reduced risk of eye inflammation and respiratory diseases (JRI Research, 2011). With sufficient production, biogas surpluses could be used to light gas lamps or generate electricity after installing additional accessories.

CONCLUSIONS

Currently, the majority of respondents use 3 kg LPG bottles, as they are subsidized, but once the subsidies stop some rural households are likely to face difficulties to ensure their energy consumption by LPG of higher price. Furthermore, the results demonstrate that fuelwood is a significant source of energy in the target area. For 31% of respondents it is the major energy source and for 64% of respondents it is a supplementary source. The high rate of the use of wood as fuel corresponds to the poor financial situation of respondents and the easy accessibility of wood, but only from the surrounding area (own garden or adjacent land). Wood resources are often very distant (on average over 1,000 metres) as a consequence of high deforestation. Our study reveals that there is a non-sustainable trend of forest conversion, resulting in high land degradation in Tapanuli Utara regency.

REFERENCES

Andadari, R.K., Mulder, P. & Rietveld, P. 2014. Energy poverty reduction by fuel switching. Impact evaluation of the LPG conversion program in Indonesia. *Energy Policy* **66**, 436–449.

Barnes, D.F., Krutilla, K. & Hyde, W. 2005. The Urban Household Energy Transition. Energy, Poverty and the Environment in the Developing World., Washington, DC. World Bank Publications, 131 pp.

Budya, H. & Arofat, M.Y. 2011. Providing cleaner energy access in Indonesia through the megaproject of kerosene conversion to LPG. *Energy Policy* **39**(12), 7575–7586.

De Alwis, A. 2002. Biogas – A review of Sri Lanka´s performance with a renewable energy technology. *Energy for Sustainable Development* **6**(1), 30–37.

Demirbas, A. 2009. Biofuels securing the planet's future energy needs. *Energy Conversion and Management* **50**(9), 2239–2249.

GENI. 2014. National energy grid Sumatra. Available at:
http://www.geni.org/globalenergy/library/national_energy_grid/sumatra/index.shtml

Ginting, N. 2017. Substitution of pig feed preparation using firewood with biogas in Samosir Island: transforming an environmental catastrophe into environmental, social, economic benefits. IOP Conference Series: Materials Science and Engineering **309**, 1–5.

Grassi, F., Landberg, L. & Huyer, S. 2015. Running out of time: The reduction of women´s work burden in agricultural production. *Food and Agriculture Organization of the United Nations*. ISBN 978-92-5-108810-4

Gunningham, N. 2013. Managing the energy trilemma: The case of Indonesia. *Energy Policy* **54**, 184–193.

Gurung, A. & Oh, S.E. 2013. Conversion of traditional biomass into modern bioenergy systems: A review in context to improve the energy situation in Nepal. *Renewable Energy* **50**, 206–213.

Harrison, M.E., Page, S.E. & Limin, S.H. 2009. The global impact of Indonesian forest fires. *Biologist* **56**(3), 156–163.

Hasan, M.H., Mahlia, T.M.I. & Hadi, N. 2012. A review on energy scenario and Sustainable energy in Indonesia. *Renewable and Sustainable Energy Reviews* **16**(4), 2316–2328.

Ibrahim, H.D., Thaib, N.M. & Wahid, L.M.A. 2010. Indonesian Energy Scenario to 2050: Projection of Consumption, Supply Options and Primary Energy Mix Scenarios. Jakarta, Indonesia, 2010, 1–12. Available at: http://www.snvworld.org/en/sectors/renewable-energy/publications/biogas-user-surveyindonesia-2011

JRI Research. 2011. Biogas User Survey Indonesia. Available at: http://www.snvworld.org/en/sectors/renewable-energy/publications/biogas-user-surveyindonesia-2011.

Kimaro, J. & Lulandala, L. 2013. Contribution of non-timber forest products to poverty alleviation and forest conservation in Rufiji District – Tanzania. *Livestock Research for Rural Development* **25**(5).

Kumar, S.K. & Kotchkiss, D. 1988. Consequences of deforestation for women´s time allocation, agricultural production, and nutrition in hill areas of Nepal. *International Food Policy Research Institute* **69**, 72 pp.

MEMR. 2010. Handbook of energy and economic statistic of Indonesia. Jakarta, Indonesia: Ministry of Energy and Mineral Resources.

Mercer, D.E. & Soussan, J. 1992. "Fuelwood problems and solutions." Available online: https://www.researchgate.net/profile/Daniel_Mercer/publication/255614937_Fuelwood_Problems_and_Solutions/links/0deec53ad71656210a000000.pdf

Mujiyanto, S & Tiess, G. 2013. Secure energy supply in 2025: Indonesia's need for an energy policy strategy. *Energy Policy* **61**, 31–41.

Reddy, B.S. 2016. India's energy system transition – Survival of the greenest. *Renewable Energy* **92**, 293–302.

Roubík, H., Mazancová, J., Heller, T., Brunerová, A. & Herák, D. 2016. Biogas as a promising energy source for Sumatra (review). *6th International Conference on Trends in Agricultural Engineering*, pp. 537–544.

Ter-Mikaelian, M.T., Colombo, S.J. & Chen, J. 2015. The Burning Question: Does Forest Bioenergy Reduce Carbon Emissions? A Review of Common Misconceptions about Forest Carbon Accounting. *Journal of Forestry* **113**(1), 57–68.

Van der Werf, G.R., Morton, D.C., DeFries, R.S., Olivier, J.G.J., Kasibhatla, P.S., Jackson, R.B., Collatz, G.J. & Randerson, J.T., 2009. CO_2 emissions from forest loss. *Nature Geoscience* **2**, 737–738.

Vidal, J. 2013. The Sumatran Rainforest Will Mostly Disappear Within 20 Years. *The Observer*, Guardian News & Media Ltd 2013. Available at: https://www.theguardian.com/world/2013/may/26/sumatra-borneo-deforestation-tigers-palm-oil

World Bank. 2013. Indonesia: Toward Universal Access to Clean Cooking. Available at: https://openknowledge.worldbank.org/handle/10986/16068.

Properties of local produced animal-fat based biodiesel and its blend with fossil fuel

K. Sirviö[*], S. Heikkilä, R. Help, S. Niemi and E. Hiltunen

University of Vaasa, Faculty of Technology, PL 700, FIN-65101 Vaasa, Finland
[*]Correspondence: katriina.sirvio@uva.fi

Abstract. In the near future, more emphasis must be put on reducing greenhouse gas (GHG) emissions in road transportation, house heating, agricultural activities, marine transport etc. This study concentrated on the use of alternative fuels in engine-driven applications of non-road machineries and decentralized energy production. Today, the engines are mainly designed for crude oil derived fuels and liquid renewable fuels are blended with crude oil based fuels to fulfill the requirements of renewable energy usage. Due to the environmental reasons on one hand and to the agricultural needs, on the other hand, different blends of bio- and fossil fuels are becoming more popular. In Europe, the maximum FAME content in diesel fuel is 7 vol% according to the EN 590:2013 but higher percentages are also available and targeted around the world. For example in the United States, the 20% blend fraction is becoming more common. For these reasons, B20 fuels were chosen to be investigated in this study. Special emphasis was put on improving blending issues since fuel blending may cause some operating risks. The main aim was to research widely the properties of animal-fat based methyl ester (AFME) and B20 fuel blend produced from it. AFME is a waste based fuel and produced in Ostrobothnia region, Finland. The aim was to find out in which engine applications the fuels are feasible and investigate if the fuels fit in the quality of automotive fuel Standards. According to the results, AFME is a feasible option to increase self-sufficient energy production in Ostrobothnia.

Key words: Biofuel, blending, FAME, AFME, diesel fuel, B20.

INTRODUCTION

In the near future, more emphasis must be put on reducing greenhouse gas (GHG) emissions in road transportation, house heating, agricultural activities, etc. There is an increasing demand to put alternative fuels into operation for engine usage to replace the conventional fossil fuels. Alternative fuel has to be technologically feasible, economic, ecologically beneficial and easily accessible. For diesel engines, biodiesel, produced from vegetable, animal or waste oils, is one of the alternative fuel sources (Bae & Kim, 2016). Today, the engines are mainly designed for crude oil derived fuels and liquid renewable fuels are blended with crude oil based fuels to fulfill the requirements of renewable energy usage. The amount of renewable energy is then increased but the dependency on crude oil is remained.

Decentralized energy production is one way to decrease the dependence on import energy. It would also have benefits for the environment through reduced transportation. In countryside, there may also be possibilities to utilize own yield of oils and fats as

biodiesel fuel through transesterification and this could be financially beneficial for the farmers. In rural areas, there is an increasing need for cheap, both fossil and renewable, fuels in agricultural engine applications. Due to the environmental reasons on one hand and to the agricultural needs, on the other hand, different blends of bio- and fossil fuels are becoming more popular.

Now, 95% of biodiesels are produced from edible vegetable oils. The use of edible oils is problematic because the use of them causes environmental problems, increases the edible oil prices and consumes food resources. Waste, recycled and non-edible oils would be much better options as raw materials. Nevertheless, the share of them is minor, only 2% of total biodiesel production. (Sajjadi et al., 2016) Waste animal-fats are still becoming more common feedstock as raw material for biofuel production. Veal and beef tallow, lard, chicken and goose fat have been successfully studied as raw material for esterification process. Together with feedstock the presence of impurities highly influences the quality of biodiesel. This makes the manufacturing process laborious because the fat needs to be purified before the esterification process (Sander et al.,2018). Further, the esterification processes in animal fat based biodiesel production have not always been successful due to the high free fatty acid contents. It is still possible to optimize the manufacturing process and achieve the ester content above 96.5 m-% which is the lowest limit set in EN 14214 (Encinar et al., 2011). The study of waste based fuels is important because recycling of potential energy raw materials is still one step forward in increasing the suitable and more sustainable options.

Fur farming is one industry which produces animal fat as a residue and waste. The quantity of animal-fat based biodiesel manufactured as a by-product in fur farming is marginal but still it can have a notable regional impact on the energy efficiency and power production. Animal fats as well as vegetable oils and residues can also be utilized in production of synthetic, paraffinic diesel, also called as renewable diesel. This kind of fuel is, though, not studied in this paper.

In Europe, the maximum FAME content in diesel fuel is 7 vol% according to the EN 590:2013 (SFS-EN 590:2013, 2013) but higher percentages are also available and targeted around the world. For example in the United States, the 20% blend fraction is becoming more common. B20 and B30 fuels do even have their own Standard, EN 16709, which specifies the quality of those fuels with a high biodiesel content (SFS-EN 16709:2016, 2016). That is why B20 fuels were chosen to be investigated in this study.

Fuel blending may, however, cause operating risks. The fuels need to be stable and compatible with engine and other blended fuels. Several studies have been made to figure out how biodiesels and their blends affect the lifetime of the engines. A review of short run tests reports that biofuels can replace conventional diesel fuel but a long run analysis is needed for assessment of the engine life. Problems that may occur are carbon deposition, lubricating oil dilution, piston ring sticking and injector nozzle choking (Patel et al., 2016).

This study determined the properties of animal-fat based methyl ester (AFME) and B20 fuel produced from it. AFME is a waste based fuel and produced in Ostrobothnia region, Finland. This fuel has earlier been studied in terms of its required antioxidant content (Sirviö et al., 2014). The other properties of AFME have not been studied and published this detailed elsewhere. As the manufacturing process of this AFME is uniquely planned for the certain type of animal fat waste (Feora, 2011), it is well-

grounded to measure the properties of AFME and compare them to fuel Standards. For the FAME type fuels, the bottleneck in the fuel quality has been the cold properties and oxidation and storage stability. If the fuel is not feasible in automotive engine applications, it is possible to utilize it in power generation or as heating oil and still promote the self-sufficient energy production.

The B20 fuel sample was prepared by mixing 20 vol% AFME biodiesel and 80 vol% fossil diesel fuel oil (DFO). The question was, whether the fuels fulfill the requirements set in Standards EN 14214, EN 16709 and EN 590, and if not, what enhancements are needed to improve the fuel quality.

In the current study, the parameters were investigated that correlate with the quality of the fuel blends. The analysed properties were density, kinematic viscosity, oxidation stability, water content, flash point, acid number, Sulphur content, cetane number, distillation curve and cold properties. The aim was to figure out how the fuels fulfill the requirements of the Standards in terms of the measured properties.

MATERIALS AND METHODS

The AFME was Feora Ecofuel, a product of Ab Feora which is located in Uusikaarlepyy, Finland. The capacity of batch processing line is 2,400 tons per year. The set-up consists of front-end acid esterification for converting free fatty acids (FFAs) into biodiesel with minimal yield loss, and a two-step alkali-transesterification in which triglyserides are turned into biodiesel. After that biodiesel is refined using neutralization (Feora, 2011).

The DFO was a product of Neste, Finland. It was low-sulphuric (7.2 mg kg^{-1}) fuel, which fulfilled the requirements of Standard EN 590.

All the analyses results, except for distillation, were measured at least twice and the results are presented as arithmetic means of at least two replicate measurements. The distillation curve was measured once for each sample.

Acid number

The acid number of the blends was analysed by a titrator Metrohm Titrando 888. The method is a potentiometric titration method. The sample is diluted with iso-propanol and titrated by potassium hydroxide. The measurement was produced according to Standard EN 14104:2003 (SFS-EN 14104, 2003).

Cetane number

The cetane number describes the ignition quality of the fuel. The cetane numbers were analysed by the IQT according to Standard EN15195. In this analysis, the ignition delay, ID, is measured. (SFS EN 15195:2014)

Cold flow properties

The cold flow properties were evaluated by three different methods: cloud point (according to ASTMD 7689), pour point (ASTMD 7346), and cold filter plugging point (CFPP) (EN 116), (ASTMD 7689, 2011; ASTMD 7346, 2015; EN 116, 2015).

Concentration of elements

The concentration of elements (S, Na, K, Mg, Ca, P, Cu, Fe, Zn) was measured by a Perkin Elmer ICP OES spectrometer 7000DV. In this method, a weight sample is diluted with kerosene in a weight ratio of 1:1. The solution is injected to spectrometers plasma. Calibration was made by the known concentrations of the standards. The defined standards (emission intensities in known concentrations) and the presence and concentration of the element are evaluated by comparing the intensity of the light to these standards. The analysis is an in-house method carried out according to the standards SFS-EN 14538 and SFS-EN 14107, as well as to the manufacturer's advices. The quality assurance is secured by using an internal standard (SFS-EN 14538, 2007; SFS-EN 14107; 2003).

Distillation curve

The distillation curve was produced according to Standard EN ISO 3405 (EN ISO 3405, 2011).

Ester content

The ester content was measured by a Perkin Elmer gas chromatograph Clarus 580. Methyl heptadecanoate is used as an internal standard for this method. It is suitable for biodiesels containing methyl esters between C14 and C24 and when the ester content is higher than 90 m-%.

Flash point

The flash points were measured according to Standard ASTM D93-A (ASTM D93, 2002).

Oxidation stability

The oxidation stability was measured by a Biodiesel Rancimat 873 instrument. The method describes the accelerated oxidation stability of biodiesel. The sample is heated and air flow is conducted through it. The vaporizing compounds of the sample drift with air into water and the conductivity of the water is measured. The end point is achieved when the conductivity increase is at its highest. The method is described in Standard EN 15751:2014 and according this Standard the maximum induction period is 48 hours (SFS-EN 15751, 2014).

Viscosity and density

The viscosities were measured by a Stabinger SVM 3000 rotational viscometer. The measurement is based on torque and speed measurements. The device calculates the dynamic viscosity from the rotor speed. The device also has a density measuring cell that employs an oscillating U-tube principle. The kinematic viscosity is calculated automatically based on these measurements (Anton Paar, 2012).

Water content

The water content was measured utilizing a Mettler Toledo C30 Coulometric KF Titrator. The method was coulometric Karl Fischer titration method according to Standard EN ISO 12937. (EN 12937, 2000)

RESULTS AND DISCUSSION

The analysed results and limitations of fuel Standards are presented in Table 1.

Table 1. The analysed properties of AFME and B20 fuel

Property	Method	AFME	B20	Unit	EN 590	EN 14214	EN 16709 (B20)
Density @15°C	ASTM D7042	880	843	kg m^{-3}	820–845	860–900	820–860
Viscosity @40°C	ASTM D7042	4.46	3.80	mm^2 s^{-1}	2.00–4.50	3.50–5.00	2.00–4.62
Oxidation stability	EN 14112/EN 15751	2.2	8.9	h	> 20	> 8	> 20
Water content	EN ISO 12937/ manufacturer's device	537	-	ppm	< 200	< 500	< 260
Flash point	EN 2719	> 120	84	°C	> 55	> 101	> 55
Sulphur content	EN 14538/ EN 14107/ manufacturer's device	30	10	ppm	< 10	< 10	< 10
Cetane number	EN 15195	64	62		> 51	> 51	> 51
Cloud point	ASTMD7689	5.4	0.3	°C	< -10 (arctic climates)	< -3	
Pour point	ASTMD7346	6	-18	°C			
CFPP	EN116	2	-5	°C	< -20 (arctic climates)	< -10	< -20
Acid number	EN 14104	0.30	0.09	mgKOH g^{-1}		< 0.50	
Ester content	EN 14103	94.2	-	m-%		> 96.5	
Na+K	EN 14538/ EN 14107/ manufacturer's device	< 2	<2	ppm		< 5	
Ca+Mg	'	< 2	< 2	ppm		< 5	
P	'	< 1	< 1	ppm		< 4	
Cu	'	< 1	< 1	ppm			
Fe	'	< 1	< 1	ppm			
Zn	'	< 1	< 1	ppm			

The relative standard deviations are: density and kinematic viscosity 1%, acid number 7.9%, ester content 1%, flash point 3.0% and OSI 4.5%. These had been determined for the analysis methods earlier.

Density, kinematic viscosity and oxidation stability

The density of AFME was relatively high, 880 kg m^{-3}. Due to AFMEs high density, the density of B20 was also high, 843 kg m^{-3} but the result was within the limits of EN 590 and EN 16709 where the maximum values of densities are 845 kg m^{-3} and 860 kg m^{-3}, respectively. The kinematic viscosities of both fuels, AFME and B20, were within the limits of all Standards. The result of AFME was 4.46 mm^2 s^{-1} and of B20, 3.80 mm^2 s^{-1}.

The oxidation stability results of both AFME and B20 were poor. Neat AFME showed an OSI result of 2.2 hours. According to the FAME standard, EN14214, the result should be above 8 hours. B20 fuel's oxidation stability was 8.9 hours, which is still far off from the target, the minimum of 20 hours. The fuels studied here were not stabilized by antioxidant addition.

Flash point, water and Sulphur contents

The water content of AFME was 537 ppm (mass based), which is clearly above 200 ppm, the limit of Standard EN590, and 260 ppm, the limit of Standard EN 16709. The water content of B20 was not measured. It can be approximated that when the AFME contained water 537 ppm, B20 contains one fifth of it (108 ppm) plus the content from neat fossil diesel (approx. 100 ppm). The limit of 200 ppm might be exceeded.

The flash point of AFME was high, above 120 °C. The flash point of B20 also fulfilled the requirements set in EN 590 and EN 16709 as the result, 84 °C, was clearly above 55 °C.

The Sulphur content of AFME was relatively high and above the maximum limit of all Standards, being 30 ppm. The fossil diesel used for blending was low sulphuric and the Sulphur content of B20 was 10 ppm, which almost fulfilled the target (< 10 ppm) set in Standards EN 590 and EN 16709.

Cold properties

The allowed cold properties of diesel fuel may vary depending on the season. Here, the results are compared to the arctic limits in the winter time. What needs to be taken account is that the limitation is not as strict in the summer time.

According to Standard EN 590, the CFPP maximum in temperate climates is at its highest +5 °C, but in arctic climates the cloud point must be below -20 °C. Neither B20 nor AFME reached the arctic limitation, the CFPPs being -5 and +2 °C, respectively. The cloud point in arctic areas should be at its highest -10 °C according the EN 590. For AFME, it was 5.4 °C and for B20 0.3 °C. Thus, the requirement set in Standard was not reached for neither of them. No limit is set for the pour point in the Standards. The pour point of AFME was 6° and of B20 -18 °C.

Acid number, ester content and concentration of elements

The acid number of AFME and B20 were 0.30 mg KOH g^{-1} and 0.09 mg KOH g^{-1}, respectively. The highest Standard limit set for FAMEs is 0.50 mg KOH g^{-1} and AFME fulfilled the acid number requirement.

The ester content of AFME was slightly lower (94.2 m-%) than the target set in EN 14214 (min. 96.5 m-%).

No significant amounts of trace elements were found.

Distillation

The shape of the distillation curve of both neat AFME and B20 is rather straight. The shape of fossil diesel fuel's distillation curve is usually 'S' shaped. In Standards EN 590 and EN 16709, the limits are that below 250 °C, no more than 65% is allowed to distillate, at least 85% must be recovered by 350 °C, and at 360 °C, at least 95% has to be distilled. Fig. 1 shows that both neat AFME and B20 fulfilled these requirements. At 250 °C, less than 20% of B20 and 0% of AFME had distillated. At 350 °C, the

recovery percentage of both samples was slightly below 95%. The distillation of both samples was completed at 360 °C.
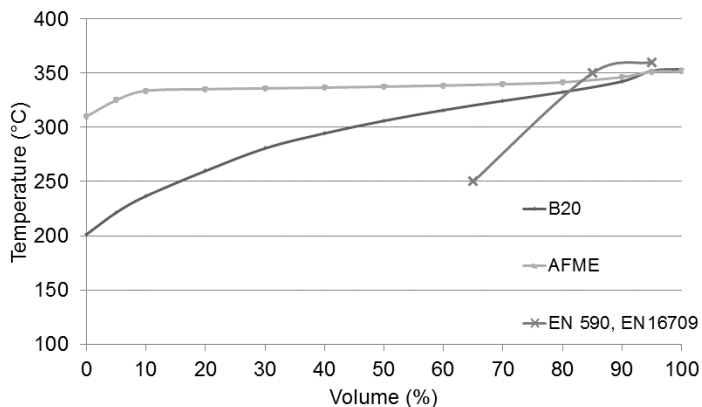

Figure 1. Distillation curves of AFME and B20 compared to the requirements set in Standards EN 90 and EN 16709.

Altogether, the quality of AFME and B20 fuels was fair. Neat AFME does not fulfill all the requirements of an automotive standard but there are other applications for its usage, e.g. power generation. In the Standard EN 16709, it is mentioned that FAME used for blending should fulfill the requirements set in EN 14214. The AFME researched in this study, is therefore not suitable for the EN 16709 blends. Though, the characteristics of the fuels could be enhanced by the following measures and the quality level set in Standards be achieved.

The FAME yield (ester content), being slightly under the target, could probably be increased by optimizing the chemical equilibrium in the manufacturing process.

The oxidation stability of both neat AFME and the blend needs to be enhanced. Several articles have been published related to biodiesel stability and relatively high concentrations of antioxidants were found to be required to fulfil the requirements set for the fuels stability (Das et al., 2009; Yang et al., 2017).

FAMEs are likely to bond water molecules. The water content of neat AFME (537 ppm) was above the allowed limit, 500 ppm. The moisture is dried in manufacturing process, but the drying process may be improved for lowering the water content. High water content, together with air exposure, are important factors affecting the degradation of biodiesel (Sorate & Bhale, 2015).

A correlation might exist between the poor oxidation stability and high water content. Karavalakis et al. (2011) have found that the oxidation stability behaviour of biodiesel blends is a very complicated process. The most important factors affecting the blends' oxidation are the biodiesel composition and used antioxidants, in other words stability improving additives. No antioxidants were used in the production of AFME in this study. The effect of suitable antioxidant depends on the raw material used for biodiesel production. As an example, butylated hydroxytoluene (BHT) is said to work well with animal fat based biodiesels (Varatharajan & Pushparani, 2018).

Another weakness was the fuels' cold properties. The cold properties were compared to requirements set for the arctic regions because AFME was produced in Finland. In cold weather, the saturated biodiesel compounds crystallize. In engines, these crystals will clog fuel lines and filters. The higher the amount of saturated compounds is, the higher the cloud and pour points are. Moreover, a fuel suitable for a low ambient temperature must have favorable cold flow properties (Sorate & Bhale, 2015). Generally, neither AFME nor other FAMEs, which consist of large fractions of saturated compounds, are suitable for arctic areas without proper improvements.

In arctic conditions, the cold performance of AFME may be challenging but B20 (e.g. CFPP -5 °C) fuel may be feasible in Finland outside of December, January and February. In these months, the average temperatures have been below -5 °C, according to the statistics of 1981–2010. (Finnish Meteorological Institute, 2017, 1) The annual average temperature has though risen 0.2–0.4 °C per decade in last 40 years, though the annual variation is extensive. (Finnish Meteorological Institute, 2017, 2) This may broaden the feasible season range of FAMEs at least in blends in Scandinavia in coming decades.

Seames et al. (2010) have proposed a production method, which may lead to improved biodiesel that has better cloud and pour points and better oxidation stability. The suggested thermal batch cracking resulted in the enrichment of the final product by C_7-C_{16} fractions and in converting the unsaturated esters into saturated ones. However, the reaction temperature was quite high being 440 °C. For a waste based fuel, this may be too expensive a way to enhance the quality of the fuel. A more economical way to use the fuel is to confine the usage outside the coldest seasons of the year.

Another option for improving the cold properties are additives (cold flow improvers). In the case of vegetable oil based methyl esters, just blending biodiesel with other fuels than DFO, like kerosene, can sufficiently improve the cold properties (Bhale et al., 2009; Sirviö et al., 2018). However, kerosene is rather expensive and kerosene-FAME blends may not be the most profitable options for the engine applications studied in this paper.

CONCLUSIONS

In this study, the aim was to research the properties of animal-fat based methyl ester (AFME) and B20 fuel produced from it and fossil diesel fuel. The B20 fuel sample was prepared by mixing 20 vol% biodiesel and 80 vol% fossil diesel. The question was, whether the fuels fulfill the requirements set in Standards EN 14214, EN 16709 and EN 590 and, if not, what are the enhancements needed to improve the fuel quality.

The parameters were investigated that correlate with the quality of the fuel blends. The properties analysed for both the samples were density, kinematic viscosity, oxidation stability, water content, flash point, acid number, Sulphur content, cetane number, distillation curve and cold properties. The aim was to figure out how the fuels fulfill the requirements of the Standards in terms of the measured properties.

Based on the study, the following conclusions could be drawn:

• Neat AFME did not fulfill all the requirements of an automotive standard but there are other applications for its usage, e.g. power generation or heating.

• The restricting quality parameters of AFME were the low ester content, high water content, low oxidation stability and poor cold flow properties. These properties can though be enhanced.

• The high water content and low ester content can be enhanced by optimizing the manufacturing process.

• B20 did not completely fulfill the requirements set for B20 fuel in Standard EN 16709. The restricting parameters were the same as for the neat AFME; low oxidation stability and poor cold flow properties.

• The oxidation stability of AFME and B20 fuel could be enhanced by adding suitable antioxidant straight after manufacturing.

• The cold properties of AFME and B20 fuel could be improved by adding suitable cold flow improver as an additive. Blending AFME with kerosene should also be studied further.

REFERENCES

ASTM D93-02. 2002. *Standard Test Methods for Flash Point by Pensky-Martens Closed Cup Tester,* ASTM International.

ASTMD7346-15. 2015. *Standard Test Method for No Flow Point and Pour Point of Petroleum Products and Liquid Fuels.* ASTM International.

ASTMD7689-11. 2011. *Standard Test Method for Cloud Point of Petroleum Products (Mini Method),* ASTM International.

Bae, C. & Kim, J. 2016. Alternative fuels for internal combustion engines. *Proceedings of the Combustion Institute*, 1–25.

Bhale, P.V., Deshpande, N.V. & Thombre, S.B. 2009. Improving the low temperature properties of biodiesel fuel. *Renewable Energy* **34**, 794–800.

Das, L.M., Bora, D.K., Pradhan, S., Naik, M.K. & Naik, S.N. 2009. Long-term storage stability of biodiesel produced from Karanja oil. *Fuel* **88**, 2315–2318.

Encinar, J.M., Sánchez, N., Martínez, G. & García, L. 2011. Study of biodiesel production from animal fats with free fatty acid content. *Bioresource Technology* **102**, 10907–10914.

EN 116:2015. 2015. *Diesel and domestic heating fuels. Determination of cold filter plugging point. Stepwise cooling bath method,* Finnish Petroleum and Biofuels Association.

EN 14103:2003. 2003. *Fat and oil derivatives. Fatty Acid Methyl Esters (FAME). Determination of ester and linolenic acid methyl ester contents.* Finnish Standards Association SFS.

EN 14104:2003. 2003. *Fat and oil derivatives. Fatty acid methyl esters (FAME). Determination of acid value.* Finnish Standards Association SFS.

EN 14107:2003. 2003. *Fat and oil derivatives- Fatty Acid Methyl Esters (FAME) -Determination of phosphorus content by inductively coupled plasma (ICP) emission spectrometry.* Finnish Standards Association SFS.

EN 14112. 2003. *Fat and oil derivatives. Fatty acid methyl esters (FAME). Determination of oxidation stability (accelerated oxidation test).* Finnish Standards Association SFS.

EN 14214:2012+A1:2014. 2014. *Liquid petroleum products - Fatty acid methyl esters (FAME) for use in diesel engines and heating applications - Requirements and test method.* Finnish Petroleum Federation.

EN 14538:2007. 2007. *Fat and oil derivatives. Fatty acid methyl ester (FAME). Determination of Ca, K, Mg and Na content by optical emission spectral analysis with inductively coupled plasma (ICP OES).* Finnish Standards Association SFS.

EN 15195:2014. 2014. *Liquid petroleum products. Determination of ignition delay and derived cetane number (DCN) of middle distillate fuels by combustion in a constant volume chamber,* Finnish Petroleum and Biofuels Association.

EN 15751:2014. 2014. *Automotive fuels. Fatty acid methyl ester (FAME) fuel and blends with diesel fuel. Determination of oxidation stability by accelerated oxidation method.* Finnish Petroleum Federation.

EN ISO 3405:2011. 2011. *Petroleum products. Determination of distillation characteristics at atmospheric pressure,* Finnish Petroleum and Biofuels Association.

EN ISO 12937: 2000. 2000. *Petroleum products. Determination of water. Coulometric Karl Fischer titration method.* Finnish Petroleum and Biofuels Association. P. 18.

Feora. 2011. Alfa Laval case story online: *http://www.feora.fi/documents/alfalaval_artikel11.pdf* Accessed 27.9.2017.

Finnish Meteorological Institute, 2017.1. *http://ilmatieteenlaitos.fi/kuukausitilastot.* Accessed 26.9.2017. In Finnish.

Finnish Meteorological Institute, 2017.2. Climate change. *http://ilmatieteenlaitos.fi/ilmastonmuutoskysymyksia* Accessed 27.9.2017. In Finnish.

Karavalakis, G., Hilari, D., Givalou, L., Karonis, D. & Stournas, S. 2011. Storage stability and ageing effect of biodiesel blends treated with different antioxidants. *Energy* **36**, 369–374.

Patel, P.D., Lakdawala, A., Chourasia, S. & Patel, R.N. 2016. Bio fuels for compression ignition engine: A review on engine performance, emission and life cycle analysis. *Renewable and Sustainable Energy Reviews* **65**, 24–43.

Sajjadi, B., Raman, A.A.A. & Arandiyan, H. 2016. A comprehensive review on properties of edible and non-edible vegetable oil-based biodiesel: Composition, specifications and prediction models. *Renewable and Sustainable Energy Reviews* **63**, 62–92.

Sander, A., Košćak, M.A., Kosir, D., Milosavljević, N., Vuković, J.P. & Magić, L. 2018. The influence of animal fat type and purification conditions on biodiesel quality. *Renewable Energy* **118**,752–760.

Seames, W., Luo, Y., Ahmed, I., Aulich, T., Kubatova, A., Stavova, J. & Kozliak, E. 2010. The thermal cracking of canola and soybean methyl esters: Improvement of cold flow properties. *Biomass and bioenergy* **34**, 939–946.

SFS-EN 16709:2016. 2016. *Automotive Fuels - High Fame Diesel Fuel (B20 and B30) - Requirements and Test Methods*. Finnish Petroleum Federation. P. 5.

SFS-EN 590:2013. 2013. *Automotive fuels. Diesel. Requirements and test methods.* Finnish Petroleum Federation. 1+13 pp.

Sirviö, K., Niemi, S., Vauhkonen, V. & Hiltunen, E. 2014. Antioxidant studies for animal-based fat methyl ester. *Agronomy Research* **2**, 407–416.

Sirviö, K., Niemi, S., Heikkilä, S., Kiijärvi, J., Hissa, M. & Hiltunen, E. 2018. Feasibility of new liquid fuel blends for medium-speed engines. *Submitted to Fuel 03/2018*.

Sorate, K.A. & Bhale, B.V. 2015. Biodiesel properties and automotive system compatibility issues. *Renewable and Sustainable Energy Reviews* **41**, 777–798.

SVM 3000 Stabinger Viscometer -brochure. 2012, Anton Paar 1/10. C18IP007EN-K. 8 pp.

Varatharajan, K. & Pushparani, D.S. 2018. Screening of antioxidant additives for biodiesel fuels. *Renewable and Sustainable Energy Reviews* **82**, 2017–2028.

Yang, J., He, Q.S., Corscadden, K. & Caldwell, C. 2017. Improvement on oxidation and storage stability of biodiesel derived from an emerging feedstock camelina. *Fuel Processing Technology* **157**, 90–98.

Kinematic viscosity studies for medium-speed CI engine fuel blends

K. Sirviö[*], S. Niemi, R. Help, S. Heikkilä and E. Hiltunen

University of Vaasa, Faculty of Technology, PL 700, FIN-65101 Vaasa, Finland
[*]Correspondence: katriina.sirvio@uva.fi

Abstract. Engine-driven power plants, run by diesel fuel or gas, will be needed for peaking power to keep the electricity grids stable when the production of renewable electricity, e.g. utilizing wind or solar power, is increased.

The choice of the alternative, renewable fuels for engine-driven power plants and marine applications is at the moment quite narrow. The amount of renewables of all liquid fuels is at present less than 2%. Biodiesels, FAMEs, have been studied for long time and apparently, despite of the problems they may have, they are still in the great interest. One important increment to the category of alternatives is fuels that are produced from e.g. oil wastes, i.e., recycled fuels. They are not renewable, but recycling of potential energy raw materials is still one step forward in increasing the suitable and more sustainable options.

To utilize the blends in medium-speed engines for power production, accurate knowledge of the physical and chemical properties of fuel blends is very important for the optimization of engine performance. The determination of the fuel kinematic viscosity is needed to create proper fuel atomization. The injection viscosity affects directly the combustion efficiency and the engine power. Consequently, this study focused on measuring kinematic viscosity curves for seven fuel blends, as well as the neat fuels used for blending. The temperature range was 10–90 °C. The fuels used for blending were rapeseed methyl ester, animal-fat based methyl ester, hydro-treated vegetable oil, light fuel oil and marine gas oil produced from recycled lubricating oils.

Key words: Fuel viscosity, viscosity curve, alternative fuels, fuel blends, power plant, renewable energy.

INTRODUCTION

In future energy systems, an increasing amount of renewable energy production, e.g. wind or solar power, will be installed. Due to the intermittent electricity production of those new plants, more emphasis should be put on peaking power to keep the electricity grids stable all the time. Hydro power is the best way to adjust the electricity supply so that the frequency and voltage of the electricity grid remain at a required level. Hydro power is not, though, obtainable everywhere.

Engine-driven power plants, run by liquid fuel or gas, will also be needed for peaking and regulation power generation. They are particularly suitable for this purpose because the plants can be started, loaded and stopped very quickl. (Franck & Hägglund, 2013). They can also be feasible to ensure energy security in rural areas. To increase the share of renewable energy, new liquid and gaseous fuels produced from biomass,

residues or waste should, however, be found for engine-driven power plants. These alternative fuels are also needed for marine applications. Together with energy production, in marine industry, the need for cleaner fuels is the most prompt. In 2012, marine sector was responsible for approximately 2% of global emissions, when total greenhouse gas or CO_2 emissions were considered (European Parliament, 2015). Shipping is also one of the most important sources of black carbon in the Arctic sea areas (Quinn et al. 2011). Also the emission legislation in maritime is becoming stricter. Many ship operators cannot yet meet these new regulations. The possibilities they have to meet the limitations, is installing exhaust after treatment equipment or switching to low-sulphur diesel or residual, or other alternative fuels (Lahtinen, 2106). The alternative fuels may reduce engine emissions below mandated limits. For these reasons, the alternative fuels industry has grown dramatically for both liquid and gaseous fuels. (McGill et al. 2013)

By now, the price of the alternative fuel options has not been competitive with cheap fossil fuels. Still, alternative, local and cost-effective fuels are needed in many regions around the world to increase the self-sufficiency of the energy generation. The independence of imported energy will be emphasized during the coming decades, especially in the countryside. Gases form one option, but the availability of gas is varying and in some areas it is very limited. In the future, thus, various liquid fuel options will play an important role in flexible power generation as well as in marine and heavy-duty applications.

Biodiesels, FAMEs, have been studied for long time and apparently, despite of the problems they may have, they are still in the great interest. However, the FAMEs are not the only option in the category of alternatives (Bae & Kim, 2016). One important increment to the category is fuels that are produced from e.g. oil wastes, i.e., recycled fuels. They are not renewable, but recycling of potential energy raw materials is still one step forward in increasing the suitable and more sustainable options. This fuel category has been paid attention to in the latest years. Still, even larger amount of waste oils should be collected and utilized as fuel or other recycling products (Maceiras et al., 2017). Waste oils are hazardous to health because they contain Sulphur, oxidized compounds, hydrocarbons, metals (Cr, Pb) as toxicants (Nerín et al., 2000). For this reason, it is important to upgrade the waste oils and remove these toxicants at the same process.

Renewable diesels, like hydrotreated vegetable oils, HVOs, are produced from triglycerides through hydro processing. The raw material for these fuels can also be something else than vegetable oils, e.g. animal fats or forest residues, and for this reason the name renewable diesel fuel is said to be more suitable. HVOs are used for all kind of engine applications but in Finland these fuels are good-quality fuels and they fulfill the standard requirements set for automotive use. In addition, HVOs are practically Sulphur free and they reduce both greenhouse gas emissions and local emissions, such as NOx and particles (Laurikko et al., 2014; Niemi et al., 2016). Only exception may be the density, which is usually slightly lower than the lower limit of the Standard EN 590. The outcome of the high quality is that they are rather expensive.

Currently, the commercial choice of the alternative, renewable fuels is quite narrow. There are several alternatives but the price and volumes are limiting the distribution. Worldwide, the amount of renewables in all liquid fuels is at present less than 2%. One realistic way to improve the amount of renewables, to fulfill the 27% target set in the EU climate & energy framework, is to blend renewables with fossil fuels. The

renewables should still be produced in a sustainable way and the best options for biofuel production are non-edible oils and fats as well as residues and wastes. FAME is commonly blended into petroleum diesel before use, e.g. from 2 V-% (B2) to 20 V-% concentration (B20). The blend fraction of 20 V-% is becoming more common as the targets set for increasing renewable energy are aspired. The other blend options have also proven to be feasible. Lapuerta et al. have studied the properties of HVO together with low-Sulphuric fossil diesel (Lapuerta et al., 2011). MGO-FAME blend seems also be a good option for marine application based on its analysis results (Sirviö et al., 2018).

To utilize the blends in medium-speed engines for power production, accurate knowledge of the physical and chemical properties, such as kinematic viscosity, of fuel blends is very important, especially for the optimization of the engine performance. Fuel blending may inflict operating complications. The fuel blend needs to be stable and compatible with engine, lubricant and other fuels. In CI engines, fuel blending may cause, e.g., carbon deposition, lubricating oil dilution, piston ring sticking and injector nozzle choking (Patel et al., 2016).

The viscosity affects directly the combustion efficiency and engine power. The fuel kinematic viscosity is an important factor when targeting at proper fuel atomization. The atomization of the fuel into droplets ensures large surface area which again ensures the sufficient evaporation after fuel injection on the combustion chamber. In case the injection strategy of an engine is not optimum in terms of the kinematic viscosity, insufficient evaporation causes unburned hydrocarbon emissions (Heywood, 1988). The changes in viscosity cause instant changes in engine operation also in other parts except combustion chamber. Too viscous fuel increases pumping losses in the injection system and the injection pressure at the pump end may increase when conventional in-line pumps are adopted. All this may cause disruptions in the combustion process and poor combustion leads to e.g. increased hydrocarbon and soot emissions. On the other hand, a too low viscosity may cause the injection pump to seize. Too low viscosity may also produce leakage at the injection pump and injector tips. This affects the pressure and delivered volume at the injector and may cause fuel leakage into the cylinder late during expansion (Guibet, 1999; Kalghatgi, 2014). High viscosity can also increase emissions, mainly unburned hydrocarbons, by increasing the droplet size from the nozzle, which again affects the combustion process (Neste Oil, 2007).

This study concentrated on the determination of the kinematic viscosity curves for seven fuel blends, as well as the neat fuels used for blending, at a temperature range of 10–90 °C. The fuels used for blending were rapeseed methyl ester, animal-fat based methyl ester, hydrotreated vegetable oil, light fuel oil and marine gas oil produced from recycled lubricating oils. The animal-fat based methyl ester was also produced from residue, originating from fur industry. The aim was to examine the differences in kinematic viscosity of the studied blends. This study produces useful basic information for the engine injection designers in terms of engines fuel flexibility as the optimum injection temperature will be adjusted based on the viscosity curve.

MATERIALS AND METHODS

In the current study, several fuel blends were prepared for the viscosity measurements. The fuels used for blends were the following.

Rapeseed methyl ester (RME) was a product of ASG Analytik-Service Gesellschaft mbH, Germany. It contained 1,000 mg kg^{-1} of butylated hydroxytoluene (BHT) as antioxidant and it was delivered to the University of Vaasa (UV) in January, 2017. RME fulfilled the requirements of Standard EN 14214:2012 (EN 14214, 2012).

Hydrotreated vegetable oil (HVO) was a product of UPM Biofuels, Finland. It is renewable diesel based on wood and forest residues namely tall oil. HVO was delivered to the UV in February 2017.

Animal fat methyl ester (AFME) was Feora Ecofuel, a product of Ab Feora, which is located in Uusikaarlepyy, Finland. AFME was delivered to the UV in March 2017.

Light fuel oil (LFO) was a product of Oy Teboil Ab, Finland. It was low sulphuric, winter grade diesel, delivered to the UV in September 2016. LFO fulfilled the requirements of Standard EN 590:2013 (EN590, 2013).

Marine gas oil (MGO) was a product of STR Tecoil, Finland. It was marine fuel produced from recycled lubricating oils. It was delivered to the UV in September 2016.

Seven different fuel blends were prepared: RME-LFO 20:80, HVO-LFO 20:80, AFME-LFO 20:80, RME-HVO 20:80, RME-MGO 20:80, HVO-MGO 20:80, AFME-MGO 20:80. Table 1 lists the fuel blends and their blending ratios. The blends were prepared in the Fuel laboratory at the University of Vaasa.

Table 1. Fuel blends and their blending ratios.

Sample	RME (V-%)	LFO (V-%)	HVO (V-%)	AFME (V-%)	MGO (V-%)
RME-LFO	20	80			
HVO-LFO		80	20		
AFME-LFO		80		20	
RME-HVO	20		80		
RME-MGO	20				80
HVO-MGO			20		80
AFME-MGO				20	80

Kinematic viscosity

The kinematic viscosity was measured by a Stabinger SVM 3000 rotational viscometer. The measurement is based on a torque and speed measurements. The device calculates the dynamic viscosity, η (mPas), from the rotor speed by Eq. 1

$$\eta = \frac{K}{\left(n_2 / n_1 - 1\right)} \tag{1}$$

where K is constant; n_1 is speed of the measuring rotor (mm s^{-1}); n_2 is speed of the measuring tube (mm s^{-1}).

The device also has a density measuring cell that employs an oscillating U-tube principle. The kinematic viscosity, KV (mm^2 s^{-1}), was calculated automatically based on these measurements according to Eq. 2

$$KV = \frac{\eta}{\rho} \tag{2}$$

where η is dynamic viscosity (mPas); ρ is density (g cm^{-3}) (Novotny-Farkas et al., 2010).

The kinematic viscosity was measured as a function of temperature for all the seven blends and for all the neat fuels used for blending. The measurements were carried out

according the Standard ASTM D7042 (Anton Paar, 2012; ASTM D7042, 2016). The uncertainty was ± 0.30% for the kinematic viscosity. The dynamic viscosity was also measured, as it is a necessity to measure the kinematic viscosity. The uncertainty was ± 0.30% for the dynamic viscosity.

The device also has a density measuring cell that employs an oscillating U-tube principle. The densities were also recorded. For the density, the uncertainty was ± 0.05%.

The limitation of kinematic viscosity set in automotive fuel Standard EN 590 is 2.00–4.50 mm^2 s^{-1} and the limitation of density is 820–845 kg m^{-3} (EN 590, 2013). The limitation of kinematic viscosity set for methyl esters in EN14214 is 3.50–5.00 mm^2 s^{-1} and the limitation of density is 860–900 kg m^{-3} (EN 14214:2012, 2012). In marine fuel Standard (DMA grade) the limitation of density is maximum 890 kg m^{-3} and the limitation of kinematic viscosity is 2.00–6.00 mm^2 s^{-1}. (ISO 8217:2017, 2017)

RESULTS AND DISCUSSION

The dynamic viscosity (40 °C), kinematic viscosity (40 °C) and density (15 °C) results are presented in Table 2. The kinematic viscosities are also shown as a function of temperature in Fig. 1 for neat fuels, in Fig. 2 for the blends made of LFO, FAMEs and HVO, and in Fig. 3 for the blends made of MGO, FAMEs and HVO. The temperature range is 10–90 °C. All the obtained results are arithmetic means of at least two replicate measurements. The results of dynamic viscosity are not though examined as detailed as kinematic viscosity and density because the dynamic viscosity is not standardized property and therefore cannot be compared to the Standards.

Table 2 shows that LFO met the requirements of kinematic viscosity (2.00–4.50 mm^2 s^{-1}) and density (820–845 kg m^{-3}) set in automotive fuel Standard EN590 (EN590, 2013).

Table 2. Dynamic viscosity (40 °C), kinematic viscosity (40 °C) and density (15 °C) results for the blends and neat fuels

Sample	Dynamic viscosity, 40 °C (mPas)	Kinematic viscosity, 40 °C (mm^2 s^{-1})	Density, 15 °C (kg m^{-3})
RME-LFO	2.62	3.15	849
HVO-LFO	2.34	2.86	836
AFME-LFO	2.59	3.12	849
RME-HVO	2.49	3.08	826
RME-MGO	5.73	6.85	853
HVO-MGO	5.34	6.49	839
AFME-MGO	5.71	6.84	852
LFO	2.38	2.89	841
RME	3.92	4.48	883
AFME	3.86	4.47	880
HVO	2.28	2.87	813
MGO	6.36	7.70	843

Both FAMEs also met the limitations set for methyl esters in EN14214, which are 3.50–5.00 mm^2 s^{-1} and 860–900 kg m^{-3} (EN 14214:2012, 2012).

MGO was compared to marine fuel Standard and it met the limitation of density, as it is maximum 890 kg m^{-3} but the kinematic viscosity of MGO was above the allowed 6.00 mm^2 s^{-1} being 7.70 mm^2 s^{-1} (ISO 8217:2017, 2017).

The blends RME-LFO, AFME-LFO and RME-HVO fulfilled the requirements set for B20 in EN 16709, the standard for B20 and B30 fuels. The limitation of kinematic viscosity is 2.00–4.62 mm^2 s^{-1} and density 820–860 kg m^{-3} (EN 16709:2016).

The blend LFO-HVO can be compared to EN590 and it fulfilled the requirements set for these properties.

None of the blends, which contained MGO, fitted in the limits of kinematic viscosity set for marine fuels in Standard ISO 8217. The densities of these blends were, though, within the limits.

The kinematic viscosity of MGO was the highest within the entire temperature range. FAMEs had almost equal viscosities; the curves cannot be separated from each other in Fig. 1. LFO and HVO had the lowest viscosities and showed very similar results throughout the whole 10 to 90 °C range.
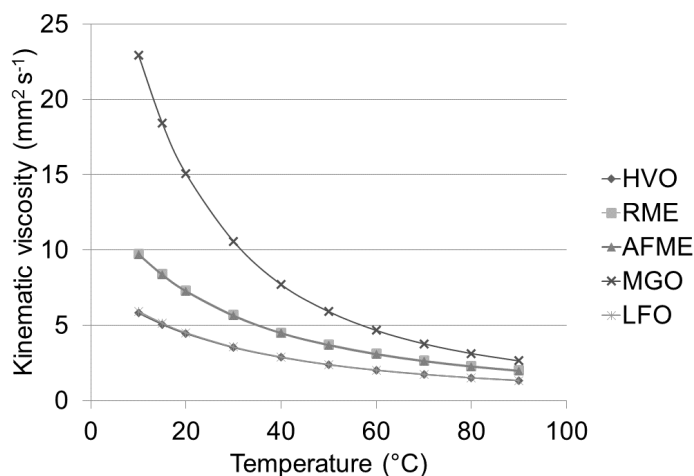

Figure 1. Kinematic viscosity as the function of temperature for the neat fuels.

The kinematic viscosities of the blends made of LFO, FAMEs and HVO were at an almost similar level throughout the temperature range, approximately from 1.3 to 6.5 mm^2 s^{-1}. The curve of HVO-LFO was slightly below the curves of FAME containing blends, as could be expected from the results of neat fuels.

The kinematic viscosity curves of the MGO blends, Fig. 3, differed from those of other blends, presented in Fig. 2. The viscosities of MGO blends varied approximately between 2.5–23 mm^2 s^{-1}. The viscosities of other blends varied from 1.3 to 6.5 mm^2 s^{-1}. As neat, the viscosity of MGO was the highest at 40 °C (7.70 mm^2 s^{-1}), and the phenomenon was the same for the MGO blends. Their viscosity was higher within the whole temperature range than it was for the other blends.
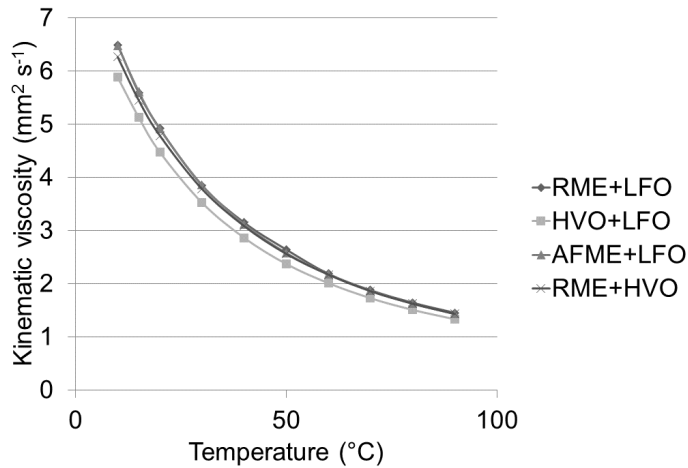
Figure 2. Kinematic viscosity as the function of temperature for the made of LFO, FAMEs and HVO.
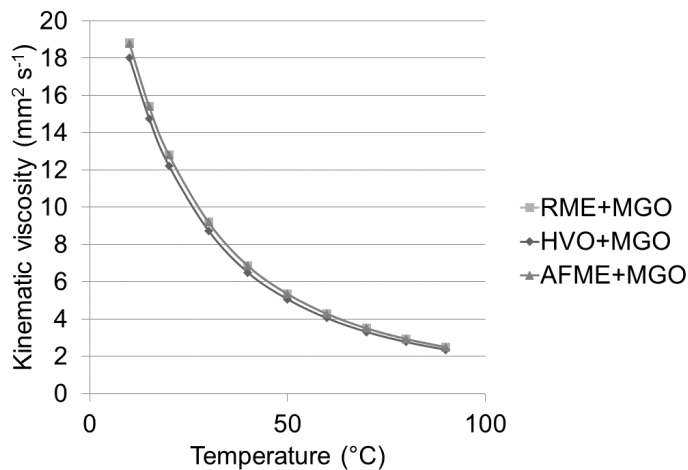

Figure 3. Kinematic viscosity as the function of temperature for the MGO blends.

Gabiña et al. have studied a technical suitability of an alternative marine fuel, produced from automotive lubricating oil. In their study, the kinematic viscosity at 40 °C of the fuel was 20.8 $mm^2 s^{-1}$ and the density 850.3 $kg m^{-3}$ at 15 °C. They state that the fuel must be warmed up to adjust the viscosity at the level, the injection system requires (Gabiña et al. 2016). The quality of their lubricant based fuel differs from the MGO studied here in terms of the viscosity. The kinematic viscosity curve was not measured in Gabiña et al. study. Neither were there other published results found in terms of MGO's kinematic viscosity as function of temperature.

Lapuerta et al. studied the HVO blends kinematic viscosity as a function of blends HVO content. In their study, the neat HVO had a kinematic viscosity of 2.65 $mm^2 s^{-1}$ and a density of 775.8 $kg m^{-3}$. The LFO they used for blending, had 2.24 $mm^2 s^{-1}$ as kinematic viscosity and 843.8 $kg m^{-3}$ as density. (Lapuerta et al., 2011) Compared to the

HVO and LFO studied in this paper, the fuels of Lapuerta et al. resulted in lower viscosities. Apparently, the fuels in the Lapuerta et al. study would also lead to lower kinematic viscosity curves than the fuels studied in this research work.

According to Fig. 1, the viscosity behavour of LFO and HVO were very similar during the whole 10 to 90 °C range, varying approximately from 1.3 to 6 mm^2 s^{-1}. In terms of viscosity, these fuels are acting similarly as a function of temperature. Gong et al. had studied the suitability of HVO as a single fuel for currently available fuel injection systems. They found out that LFO and HVO fuels displayed very similar spray tip penetrations and droplet sizes. (Gong et al., 2010) Even though there are several factors affecting the injection system, the similarity in viscosity behavior is one of the most important ones. The study of Gong et al. proved the same phenomenon as the present study. The quality of HVO fuel is almost equivalent to LFO.

Corach et al. (2017) studied kinematic viscosity of soybean biodiesel and its blends with fossil diesel fuel. Their measurement temperature range was 25–45 °C. Within this range, none of the fuels from B0 to B100 resulted in above 6 mm^2 s^{-1}. This is similar to the results of FAME blends in the present study. Ramírez-Verduzco et al. (2011) studied the densities and viscosities of biodiesel blends to develop predicting models for the viscosity measurements. They measured kinematic viscosities at temperatures of 20–100 °C. The biodiesel they used was made of a mixture of vegetable oils. At 40 °C, the neat biodiesel had a kinematic viscosity of 7.03 mm^2 s^{-1} and B20 showed 3.30 mm^2 s^{-1} (Ramírez-Verduzco et al., 2011).

The biodiesels studied here had lower viscosities at the temperature of 40 °C as did the biodiesel of the Ramírez-Verduzco et al. (2011) study: AFME 4.47 and B20 of AFME, 3.12 mm^2 s^{-1}, and RME 4.48 and B20 of RME, 3.15 mm^2 s^{-1}. Even though the FAMEs studied in this study were manufactured from different raw materials, they gave similar results in the measurements. The study of Ramírez-Verduzco et al. (2011) showed that this is not the case with all FAMEs and the blends prepared from them. Yoon et al. (2008) studied the properties of soybean oil biodiesel. In their study, only B100 and B80 fuel reached the kinematic viscosity of 10 mm^2 s^{-1}. The temperature was then below 10 °C. (Yoon et al., 2008)

What needs to be taken into account is that biodiesels and HVO are mainly used in other engine applications than marine or power plant engines. According to the results of this study, all the studied blends are, however, also feasible for marine and power plant applications. As the viscosities vary or are rather low, there is need for more detailed engine design in terms of the fuel injection. The properties and feasibility of all kind of alternative fuels must be studied detailed to reach the ambitious targets for emissions reduction. One way to control the emissions is to optimize the fuel injection to ensure proper combustion in the cylinder. The fuel kinematic viscosity is an important factor when targeting at proper fuel atomization; the viscosity affects combustion. Poor atomization leads to poor combustion and higher hydrocarbon and soot emissions. Fuel flexibility is the future in engine design. It means that even if the fuel properties change, the engine will be flexible and able to run on different fuel options. The optimum injection temperature will be adjusted based on the viscosity curve. For the engine designers and operators, this study produced useful fundamental information about the behavior of fuel and fuel blends. This study also proved that there are cleaner options available for energy production and marine industry.

CONCLUSIONS

The aim of this study was to measure kinematic viscosity curves for seven fuel blends, as well as the neat fuels used for blending, within a temperature range of 10–90 °C. The fuels used for blending were rapeseed methyl ester, animal-fat based methyl ester, hydrotreated vegetable oil, light fuel oil, and marine gas oil produced from recycled lubricating oils. Based on the results, the following conclusions could be drawn:

• For MGO and the MGO blends the kinematic viscosities varied between 2.5–23 mm^2 s^{-1} at temperatures from 10 to 90 °C.

• For the blends containing LFO, FAME and HVO the kinematic viscosities varied from 1.3 to 6.5 mm^2 s^{-1} at temperatures from 10 to 90 °C.

• Even though the methyl esters studied here were produced from different raw materials, animal fat and rapeseed oil, they both and their blends with LFO behaved almost identically in the kinematic viscosity measurements.

• The studied HVO fuel showed viscosity results almost equal to LFO.

• All the studied blends proved to be feasible options for medium-speed and other CI engine fuels. The fuel injection system must only be optimized properly for different kinematic viscosities.

REFERENCES

ASTM D7042-16e3. 2016. Standard Test Method for Dynamic Viscosity and Density of Liquids by Stabinger Viscometer (and the Calculation of Kinematic Viscosity), ASTM International, 13 pp.

Bae, C. & Kim, J. 2016. Alternative fuels for internal combustion engines. *Proceedings of the Combustion Institute*, 1–25.

Corach, J., Colman, M., Sorichetti, P.A. & Romano, S.D. 2017. Kinematic viscosity of soybean biodiesel and diesel fossil fuel blends: Estimation from permittivity and temperature. *Fuel* **207**, 488–492.

EN 14214:2012+A1:2014. 2014. *Liquid petroleum products – Fatty acid methyl esters (FAME) for use in diesel engines and heating applications – Requirements and test method.* Finnish Petroleum Federation. P. 22.

EN 590:2013. 2013. *Automotive fuels. Diesel. Requirements and test methods.* Finnish Petroleum Federation. 1+13 pp.

European Parliament. 2015. Emission Reduction Targets for International Aviation and Shipping. Study for the ENVI Committee, pp. 52.

Franck, T. & Hägglund, T. 2013. Emphasising flexible power generation. Wärtsilä Technical Journal 02. *https://www.smartpowergeneration.com/content-center/articles/emphasising-flexible-power-generation,* p. 9–11 Accessed 28.3.2018.

Gabiña, G., Martin, L., Basurko, O.C., Clemente, M., Aldekoa, S. & Uriondo, Z. 2016. Waste oil-based alternative fuels for marine diesel engines. *Fuel Processing Technology* **153**, 28–36.

Gong, Y., Kaario, O., Tilli, A., Larmi, M. & Tanner, F. 2010, A computational investigation of hydrotreated vegetable oil sprays using RANS and a modified version of the RNG k-epsilon model in OpenFOAM. *SAE Paper*. p. 11.

Guibet, J.C. 1999. *Fuels and Engines.* Éditions Technip, Paris, France, 771 pp.

Heywood, J.B. 1988. *Internal ombustion Engine Fundamentals*. McGraw-Hill Book Company, 930 pp.

ISO 8217:2017. 2017. Petroleum products. Fuels (class F). Specifications of marine fuels, International Organization for Standardization.

Kalghatgi, G. 2014. *Fuel/Engine Interactions.* SAE International, Warrendale, Pennsylvania, USA, 255 pp.

Lahtinen, J.M. 2016. Closed-loop exhaust gas scrubber onboard a mechant ship. *Acta Wasaensia* 342. pp. 143.

Lapuerta, M., Villajos, M., Agudelo, J.R. & Boehman, A.L. 2011. Key properties and blending strategies of hydrotreated vegetable oil as biofuel for diesel engines. *Fuel Processing Technology* **92**, 2406–2411.

Laurikko, J.K., Nylund, N.-O., Aakko-Saksa, P., Mannonen, S., Vauhkonen, V. & Roslund, P. 2014. Crude Tall Oil-Based Renewable Diesel in Passenger Car Field Test. *SAE Technical Paper 2014-01-2774*, doi:10.4271/2014-01-2774. P. 9.

Maceiras, R., Alfonsín, V. & Morales, F.J. 2017. Recycling of waste engine oil for diesel production. *Waste Management* **60**, 351–356.

McGill, R., Remley, W. & Winther, K. 2013. *Alternative Fuels for Marine Applications. Annex 41.* A Report from the IEA Advanced Motor Fuels Implementing Agreement. pp. 108.

Nerín, C., Domeño, C., Moliner, R., Lázaro, M.J., Suelves, I. & Valderrama, J. 2000. Behaviour of different industrial waste oils in a pyrolysis process: metals distribution and valuable products. *Journal of Analytical and Applied Pyrolysis* **55**, 171–183.

Neste Oil. 2007. *Diesel fuel guide*, P. 46, Espoo. In Finnish.

Niemi, S., Vauhkonen, V., Mannonen, S., Ovaska, T., Nilsson, O., Sirviö, K., Heikkilä, S. & Kiijärvi, J. 2016. Effects of wood-based renewable diesel fuel blends on the performance and emission of a non-road diesel engine. *Fuel* **186**, 1–10.

Novotny-Farkas, F., Böhme, W., Stabinger, H. & Belitsch, W. 2010. The stabinger viscometer: a new and unique instrument for oil service laboratories. *Customer Portrait, Anton Paar*. pp. 4.

Patel, P.D., Lakdawala, A., Chourasia, S. & Patel, R.N. 2016. Bio fuels for compression ignition engine: A review on engine performance, emission and life cycle analysis. *Renewable and Sustainable Energy Reviews* **65**, 24–43.

Quinn, P.K., Stohl, A., Arneth, A., Berntsen, T., Burkhart, J.F., Christensen, J., Flanner, M., Kupiainen, K., Lihavainen, H., Shepherd, M., Shevchenko, V., Skov, H. & Vestreng, V. 2011. *The Impact of Black Carbon on Artic Climate.* AMAP Technical Report No. 4. P. 74.

Ramírez-Verduzco, L.F., García-Flores, B.E., Rodríguez-Rodríguez, J.E. & Jaramillo-Jaboc, A.R. 2011. Prediction of the density and viscosity in biodiesel blends at various temperatures. *Fuel* **90**, 1751–1761.

SFS-EN 16709:2016. 2016. *Automotive Fuels – High Fame Diesel Fuel (B20 and B30) – Requirements and Test Methods*. Finnish Petroleum Federation. pp. 5.

SFS-EN 590:2013. 2013. *Automotive fuels. Diesel. Requirements and test methods.* Finnish Petroleum Federation. 1+13 pp.

Sirviö, K., Niemi, S., Heikkilä, S., Kiijärvi, J. Hissa, M. & Hiltunen, E. 2018. Feasibility of new liquid fuel blends for medium-speed engines. *Submitted to Fuel 03/2018*, pp. 13

SVM 3000 Stabinger Viscometer -brochure. 2012. Anton Paar 1/10. C18IP007EN-K, 8 pp.

Yoon, S.H., Park, S.H. & Lee, C.S. 2008. Experimental Investigation on the Fuel Properties of Biodiesel and Its Blends at Various Temperatures. *Energy & Fuels* **22**, 652–656.

Effect of rubber powder from waste tyre rubbers on mechanical properties of one-component polyurethane putty

M. Tichý[1,*], M. Müller[1], P. Valášek[1] and I. Miturska[2]

[1]Czech University of Life Sciences, Faculty of Engineering, Department of Material Science and Manufacturing Technology, Faculty of Engineering, Kamýcká 129, CZ165 21 Prague, Czech Republic
[2]Lublin University of Technology, Department of Production Engineering, Mechanical Engineering Faculty, Nadbystrzycka 36, PL20 618 Lublin, Poland
*Correspondence: xticm001@studenti.czu.cz

Abstract. The utilization of adhesives in technical practice is varied. Adhesives serve for a creation of strength bonds on the one hand, and on the other hand e.g. for cementing. The aim of the research is a modification of one-component polyurethane putty RPS 45 used in automotive industry to increase strength properties in an adhesive bond. An interaction between a filler in the form of rubber powder micro-particles and one-component polyurethane adhesive was investigated by means of SEM analysis. Sealing is a primary property of this putty. Sealing putties usually reach very small strength which can be increased by an admixture of the filler. In order to keep elastic properties, micro-particles of the rubber powder gained from tyre recycling process were used as the filler. An aspect of a loading speed of the adhesive bond is essential at the practical application at which the adhesive bond can be failed in adhesive or cohesive layers. The adhesive bond can be perceived in terms of its function as a complex of three layers, i.e. an adhesive bonded material, the interaction between the adhesive and the adhesive bonded material and the adhesive layer itself. There are often states in the practices when the adhesive bonds are exposed to the loading which can be either a static or a dynamic one. That is why the research is focused not only on the evaluation of the influence of the modification of the one-component polyurethane adhesive, but also on the influence of the loading speed of the adhesive bond. Tested speeds set on a universal testing machine Zwick/Roell Z150 were 2, 50 and 100 mm min^{-1}. The results of mechanical tests proved a positive influence of the filler on the strength σ_m higher by $42.68 \pm 6.96\%$ and the elongation at break ε_b higher by $12.2 \pm 20.95\%$. On the contrary, the stress at yield σ_y was decreased.

Key words: Loading speed, particle filler, strength, stress at yield, elongation, SEM, recycling.

INTRODUCTION

The technology of adhesives is constantly in high demand. It enables bonding of diverse materials, creating light structures and complex constructions (Pohlit et al., 2008). Adhesive bonds are often applied in industries such as aircraft industry, car manufacturing and electric industry to decrease weight, the concentration of voltage and to facilitate manufacturing (Mancusi & Ascione, 2013).

For the matrix we used a polyurethane putty, which is used in the automotive industry and has excellent shock-absorbing properties. Polyurethanes belong to the group of polyesteramides. The experiment featured soft polyurethanes, which solidify thanks to air humidity on being expressed from a hermetically sealed tube (Ducháček, 2015). Putties in general have good elastic properties. However, they reach very small strengths. The subject of study is increasing the strength of polyurethane putty with a filler made from rubber powder extracted from tyres trough the recycling process.

Rubber granules can be used as fillers in composite materials with various matrix basis (Sienkiewicz et al., 2017). It is assumed that the rubber particle acts as an absorbing 'toughening' processes (Mona, et al., 2015).

The dynamic increase of used tyre waste is a serious environmental issue. Recent news points to a significant progress in tyre recycling. This means that tyres no longer pose a threat as hazardous waste but an environmentally friendly source where the extracted granulation product can be used to make new polymeric composites. (Sienkiewicz et al., 2017).

In order to preserve the elasticity, the rubber powder is a suitable modifier (Quan et al., 2018). Polymers are basic materials for creating the matrix for composites. Resilience and toughness of the polymeric matrix depends on the orientation of nanofibers in the polymer (Ekrem & Avci, 2018). As reinforcing stiffeners, the composites use continuous fibres but also various kinds of short reinforcement elements (Cho et al., 2006). In the course of research, the polyurethane matrix used rubber powder from recycled tyres as a reinforcing particle element.

The properties of the composite with reinforcement particle elements depend on the material but also on the volume ratio of the particle filler, the size of the particles and the homogeneousness of particle distribution in the volume and the adhesive properties between the matrix and the particles (Míšek, 2003). To understand the effect of particle size in the composite, the mechanical properties of the composite must be established (Cho et al., 2006). They are the tensile strength, stress at yield, and strain at strength. The relation between particle size and mechanical properties was studied by many authors (Knapníčková et al., 2014; Valášek & Müller, 2014; Müller, 2015). Studies showed that tensile strength of the polyester composite with glass balls increases with the decreasing size of the glass balls (Cho et al., 2006). The polymer matrix is generally of a lower rigidity than the inorganic particles, however, the toughness depends on the tension transfer between individual particles and the polymeric matrix (Shao-Yun et al., 2008).

The limiting factors for the strength of adhesive bonds are defects in adhesive caused by production process, air bubbles, foreign bodies, grease and dirt as well as generally insufficient preparation of the glued surfaces (Ribeiro et al., 2016). To ensure the strength of the adhesive bond, it is most important to treat the surface by e.g. sandblasting for bonding steel, titanium, titanium alloys, aluminium alloys, the polymer and the composite (Rudawska et al., 2016).

The aim of this research was to establish the kind of interaction between the filler in the form of rubber powder and the polyurethane putty and how this interaction affects the mechanical properties of the adhesive. Also, the relations between the filler particle size, the filler volume ratio, and the mechanical properties were the focus of this study.

MATERIALS AND METHODS

The subject of study was the modification of a single-component polyurethane putty RPS 45 with a filler of rubber powder from recycled tyres. The modification of the single-component polyurethane putty was studied while changing the concentration and grain size of the filler. Rubber powder was chosen to establish the relation between the microparticle size of the reinforcing elements and the mechanical properties. The rubber powder with maximum dimensions of 0–400 μm is labelled as AGP4 and the powder with maximum dimensions of 0–800 μm is labelled as AGP8.

The filler concentration in the polyurethane putty was 5, 10 and 15 wt.%. Adding the rubber microparticles created a composite adhesive with polyurethane basis. The effectiveness of tension transfer between microparticles was measured by SEM analysis and observing the tension curve during mechanical tension tests.

Adhesive bonds were created in accordance with ČSN EN 1465 (the equivalent of BS 1465), which describes testing the single-lap adhesive bonds. To examine the strength of the adhesive bond we used carbon steel S235J0 of thickness 1.5 ± 0.1 mm. The bonded material consisted of two test bodies with dimensions of 100 x 25 mm and the modified putty was applied creating a single-lap adhesive bond at length of approx. 12.5 ± 0.25 mm. The single-lap bond was immediately weighted right after bonding for 12 hours to allow the glue to harden and solidify. The surface of test bodies was treated by sandblasting by Garnet MESH 80 (ČSN ISO 8501-1) and degreased in an acetone bath. Roughness parameters were measured with a portable profilometer Mitutoyo Surftest 301. A limit wavelength of the cut-off was set as 0.8 mm. The surface roughness at the grit blasted adhesive bonded material, i.e. structural carbon steel S235J0 was Ra = 1.76 ± 0.18 μm, Rz 11.22 ± 0.84 μm.

To establish the mechanical properties of the modified polyurethane putty, three factors were studied. They were the strength (σm), stress at yield (σy) and strain at strength (εb) with filler concentrations of 5, 10 and 15 wt.%. To find out about the relation of mechanical properties depending on the loading speed, these factors were measured at the speeds 2, 50 and 100 mm min^{-1}.

Adhesive bonds were tested by a static tensile test. Next, we evaluated the influence of concentration and grain size of the filler on the properties of the modified single-component polyurethane putty RPS 45. Mechanical tests (according to DIN EN 1465) were carried out on a universal measuring device for tensile testing Zwick/Roell Z150 with evaluation software testXpert II. The samples were tested in individual series. The types of disruptions of adhesive bonds were assessed according to ISO 10365.

To follow the interaction between the single-component polyurethane putty and the filler powder made from recycled tyres, was used a scanning electron microscope TESCAN MIRA 3 GMX (SEM), which examined the break surfaces and the interaction of the adhesive bond. The preparation of the test sample was done by gold-plating on the machine Quarum Q150R ES in argon vacuum. The samples were measured with a microscope TESCAN MIRA 3 GMX in nitrogen vacuum and the images were taken with acceleration voltage (HV) of 5.0 kV at a distance of approx. 15 mm.

The recorded values were processed by means of statistical analysis. To compare the recorded data statistically, we used Anova (Analysis Of Variance). By means of the Anova F-test we established p-values, which will make it possible to compare the

differences of tested sets. The null hypothesis H_0 was set to a state when there is no statistically significant difference between the median values of the data sets being compared: $p > 0.05$

RESULTS AND DISCUSSION

The result of statistical testing is evident from Table 1. Filler concentration i.e. microparticles of rubber granulate, had significant influence on the strength and strain at strength of adhesive bonds. The strength of the adhesive bond was increased by adding filler up to $42.68 \pm 6.96\%$. There was an increase on the strain at strength up to $12.2 \pm 20.95\%$. The hypothesis H_0 was not confirmed i.e. is statistically significant difference between the strength and strain at strength of adhesive bond according to adhesive bonds with filler and without filler (matrix). Similar statistical results were obtained on stress at yield of tested variants AGP4−50 mm min^{-1}, AGP4−100 mm min^{-1}, AGP8-2 mm min^{-1} and AGP8-100 mm min^{-1} i.e. a significant influence of stress at yield was determined, depending on adhesive bonds with filler and without filler.

The stress at yield for adhesive bonds AGP4−2 mm min^{-1} and AGP8−50 mm min^{-1}, there was not statistically significant difference between adhesive bonds with filler and without filler i.e. the hypothesis H_0 was confirmed.

Table 1. The results of statistical testing for mechanical properties – parameter p (comparison of adhesive bond with no filler (matrix) and adhesive bond with filler concentrations 5−15 wt. % rubber powder)

Filler	Loading speed (mm min^{-1})	Strength σ_m (MPa)	Stress at yield σ_y (MPa)	Strain at strength ε_b (%)
AGP4	2	0.0000	0.5577	0.0000
	50	0.0000	0.0000	0.0000
	100	0.0004	0.0000	0.0000
AGP8	2	0.0000	0.0141	0.0000
	50	0.0002	0.0822	0.0001
	100	0.0015	0.0202	0.0000

Effect of the modification on the tensile strength is shown in Fig. 1 by the percentage difference between the strength of the adhesive bond without filler and adhesive bond with filler concentrations 5, 10 and 15 wt.% at loading speeds 2, 50 and 100 mm min^{-1}. The Fig. 1 shows that the highest increase in the tensile strength is found on adhesive bond with the filler concentration 10 wt.% AGP4 at loading speed 2 mm min^{-1} up to $42.68 \pm 6.96\%$. The course of the stress points that tensile strength is horizontal at the filler concentration 5 and 10 w.% and decreases at the filler concentration 15 wt.%. From this it can be concluded that the filler concentration 15 wt.% of adhesive bond is approaching the critical volume concentration (Míšek, 2003).

The Fig. 1 shows that modification of adhesive has positive influence on the tensile strength with the filler concentrations 5, 10 and 15 wt.% AGP4 at loading speeds 2 and 50 mm min^{-1} and with the filler concentration 5 wt.% AGP4 at loading speed 100 mm min^{-1}. Positive influence with the filler concentrations 5, 10 and 15 wt. % AGP8 at loading speed 2 mm min^{-1} and with the filler concentrations 5, 10 wt.% AGP8 at

loading speed 50 mm min^{-1}. This implies that the particle size affects the tensile strength i.e. decreasing filler particles increase the tensile strength. The influence on the increase in strength has a particle size filler 400 μm (AGP4) compared to a particle size filler 800 μm (AGP8). At loading speed 100 mm min^{-1} is a large drop in concentration 10 wt.% AGP8 – 17.17 ± 10.08% i.e. there is not significant increase at modification of adhesive bonds for loading speed 100 mm min^{-1} with filler AGP8.
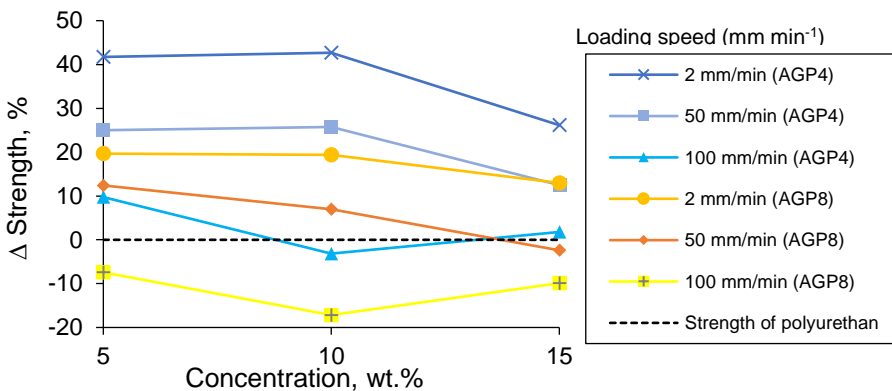

Figure 1. Percentage difference between strength of adhesive with no filler and strength of adhesive with 5, 10 and 15 wt.% concentration of filler AGP4, AGP8 on loading speed 2, 50 and 100 mm min^{-1}.
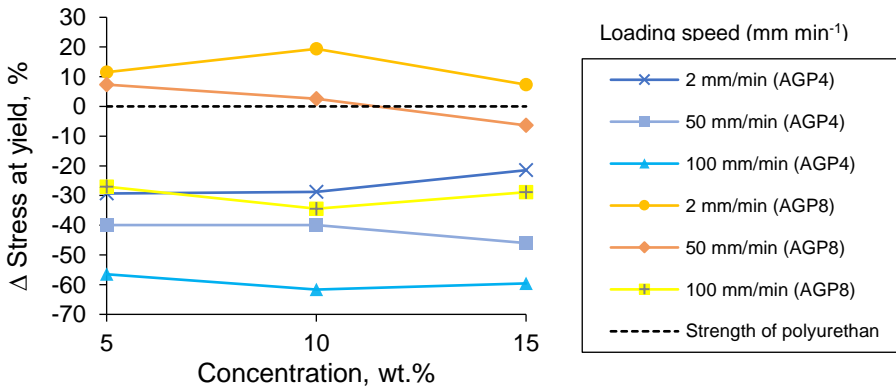

Figure 2. Percentage difference between stress at yield of adhesive with no filler and stress at yield of adhesive with 5, 10 and 15 wt.% concentration of filler AGP4, AGP8 on loading speed 2, 50 and 100 mm min^{-1}.

Effect of the modification on the stress at yield is shown on Fig. 2 by the percentage difference between the stress at yield of the adhesive bond without filler and adhesive bond with the filler concentrations 5, 10 and 15 wt.% at loading speeds 2, 50 and 100 mm min^{-1}. In general, modification of adhesive bond with filler AGP4 has negative influence on the stress at yield. The biggest drop on the stress at yield – 61.65 ± 6.99% is with the filler concentration 10 wt.% AGP4 at loading speed 100 mm min^{-1}. The stress at yield was increased with the filler concentrations 5, 10 and 15 wt.% AGP8 at loading

speed 2 mm min^{-1} in maximum up to $19.37 \pm 5.70\%$. This implies that particle size 0.8 mm (AGP8) has biggest influence on tress at yield at loading speed 2 mm min^{-1}.

Effect of modification on strain at strength is shown on Fig. 3 by the difference between strain at strength of adhesive bond without filler and adhesive bond with the filler concentrations 5, 10 and 15 wt.% at loading speeds 2, 50 and 100 mm min^{-1}. Fig. 3 shows that influence on strain at strength at filler AGP8 is without significant difference between concentrations. The influence on strain at strength has filler AGP8 with concentration 15 wt.% at loading speed 2 mm min^{-1} up to $3.3 \pm 16.95\%$. The influence on strain at strength has filler AGP4 at loading speed 2 mm min^{-1} with concentration 15 wt.% at maximum increase up to $12.2 \pm 20.95\%$. Particle size 400 μm (AGP4) will stay better in the matrix which increase strain at strength (Fig. 3.). Increase strain at strength is also given by flexibility segments of adhesive bond.
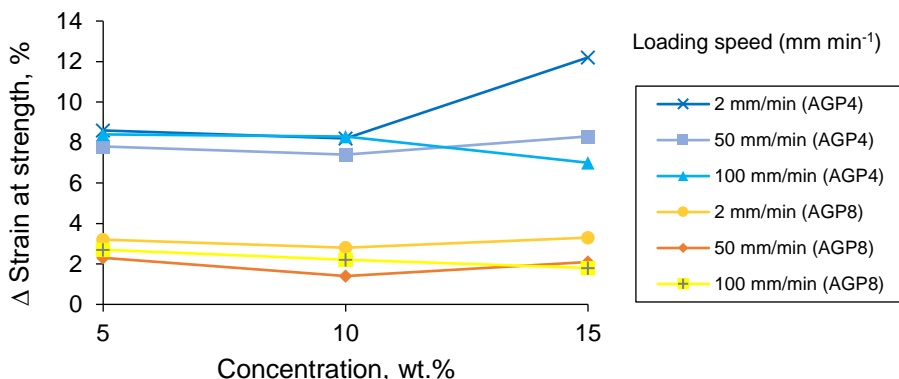

Figure 3. Percentage difference between strain at strength with no filler and strain at strength of adhesive with 5, 10 and 15 wt.% concentration of filler AGP4, AGP8 on loading speed 2, 50 and 100 mm min^{-1}.

After tensile test on fracture surface is possible to determine interaction between filler and polyurethane matrix with SEM analysis (Fig. 4, A, B). Fig. 4 Shows location with good wettability of particle filler and matrix i.e. polyurethane putty.
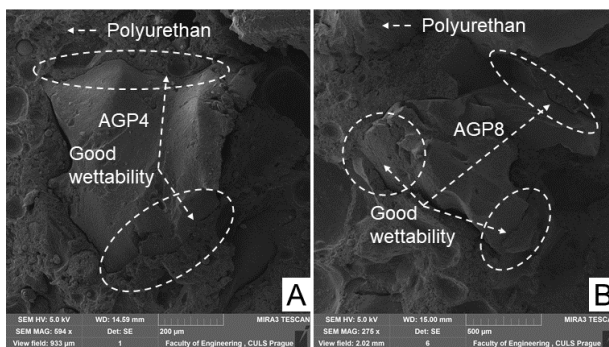

Figure 4. SEM images of fracture surface after strength test of adhesive bonds with filler AGP4 (secondary electrons): A: filler AGP4 (size of particle 0,4 mm) (MAG 594 x), B: filler AGP8 (size of particle 800 μm) (MAG 510 x).

This low interaction of wettability at the microparticle AGP and polyurethane (matrix) interface is not visible throughout the perimeter (Figs 5 and 6). It can be assumed that this is not a lower microparticle AGP wettability, but rather the deformation of the elastomeric microparticle AGP and delamination from polyurethane (matrix). Microparticle AGP and matrix have delamination in some locations i.e. producing of low interaction. If there was bad wettability, it would be low interaction around the perimeter at microparticle AGP and matrix.

Fig. 5 and Fig. 6 shows different distribution of AGP in matrix depending on the concentration of filler. Fig. 5C, Fig. 6C shows contacting the microparticles AGP with concentration 15 wt.% i.e. microparticle are not fully separated by the matrix. At concentration 10 wt.% (Fig. 5, C; Fig. 6, C.) is visible, that microparticle are fully separated by the matrix.
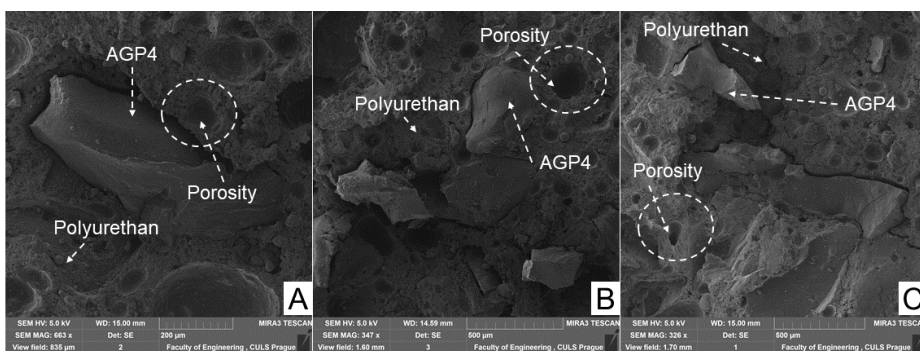

Figure 5. SEM images of fracture surface after tensile strength test of adhesive bonds (secondary electrons): A: Concentration 5 wt.% of filler AGP4 (MAG 663 x), B: Concentration 10 wt.% of filler AGP4 (MAG 347), C: Concentration 15 wt.% of filler AGP4 (MAG 326 x).
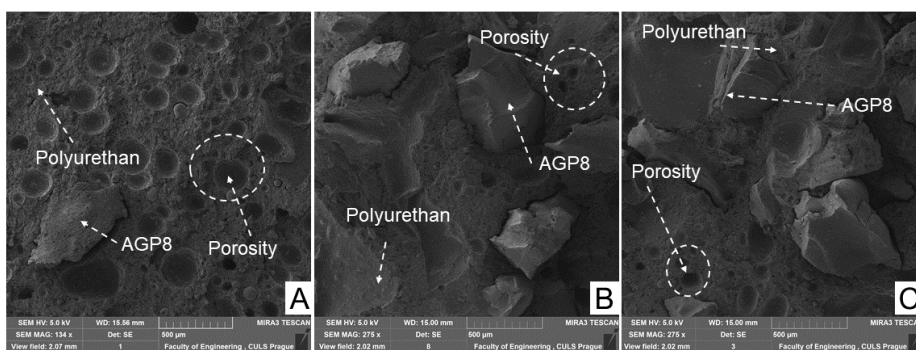

Figure 6. SEM images of fracture surface after tensile strength test of adhesive bonds (secondary electrons): A: Concentration 5 wt.% of filler AGP8 (MAG 134 x), B: Concentration 10 wt.% of filler AGP8 (MAG 275 x), C: Concentration 15 wt.% of filler AGP8 (MAG 275 x).

The research shows that increasing the loading speed increases strength, stress at yield and strain at strength. Maximal strength of adhesive bond is 2.129 ± 0.125 MPa with concentration 5 wt.% AGP4 at loading speed 100 mm min^{-1}. Maximal stress at yield is 0.49 ± 0.18 MPa without filler at loading speed 100 mm min^{-1}. Maximal strain at

strength is $14.8\% \pm 20.9\%$ with concentration 15 wt.% AGP4 at loading speed 100 mm min^{-1}. This implies that the highest value achieves the adhesive bond at loading speed 100 mm min^{-1}.

The most significant influence of modification on strength is up to $42.68 \pm 6.96\%$ with concentration 10% AGP4 at loading speed 2 mm min^{-1}. The stress at yield is most influenced by modification up to $19.37 \pm 5.70\%$ with concentration 10 wt.% AGP8 at loading speed 2 mm min^{-1}. The strain at strength is most influenced by modification up to $12.2 \pm 20.95\%$ with concentration 15 wt.% AGP4 at loading speed 2 mm min^{-1}. This implies that modification of one-component polyurethane putty has most influence at loading speed 2 mm min^{-1} with concentrations 10 and 15 wt.%. It can be agreed with the statement that waste tire rubbers are attractive group of materials due to their preparation only from rubber wastes what means sustainable and clean recycling (Sienkiewicz, 2017).

In the statistical results was confirmed the influence of filler on strength and strain at strength i.e. is statistically significant difference between the median values of strength and strain at strength, parameter: $p < 0.05$. Statistically significant difference was not confirmed on stress at yield with concentration AGP4–2 mm min^{-1}, parameter: $p = 0,5577$ and AGP8–50 mm min^{-1}, parameter: $p = 0,0822$. At rest variants is statistically significant difference on stress at yield, parameter: $p < 0.05$.

CONCLUSIONS

The modification of the single-component polyurethane putty in the form of a rubber powder is highly beneficial in terms of the strength and strain at strength. The highest increase of the strength is by $42.68 \pm 6.96\%$ at AGP4 filler with concentration 10 wt.% at the loading speed 2 mm min^{-1}. The strain at strength increased by $12.2 \pm 20.95\%$ at AGP4 concentration 15 wt.% at the loading speed 2 mm min^{-1}. The modification has its strongest impact on RPS 45 polyurethane putty at the loading speed 2 mm min^{-1}.

Fracture surface of the adhesive bond switched from the cohesive one to the adhesive one, which shows in the thin boarder layers between the bonded material and adhesive with the AGP4, AGP8 fillers. The results of the experiment proved a positive impact of adding the rubber AGP particles in the adhesive. That is why the following research will have to concentrate on the border between the bonded material and the adhesive to remove this thin boarder layer, i.e. for the adhesive bond not to show any adhesive type of damage.

The use of the rubber filler coming from recycled tyres has a positive impact on the environment. The research shows a way how to recycle the used tyres and thus how to relieve the environment of the burden. There is also the economical factor at play where using the recycled material decreases the price of the adhesive.

REFERENCES

Cho, J., Joshi, M.S. & Sun, C.T. 2006. Effect of inclusion size on mechanical properties of polymeric composites with micro and nano particles. *Composites Science and Technology* **66**(13), 1941−1952.

ČSN ISO 8501-1. 1998. *Preparation of steel substrates before application of paints and related products. Visual assessment of surface cleanliness. Part 1: Rust grades and preparation grades of uncoated steel substrates and of steel substrates after overall removal of previous coatings.* Prague: Czech Standards Institute. (in Prague).

ČSN ISO 10365. 1995. *Adhesives. Designation of main failure patterns.* Prague: Czech Standards Institute (in Prague).

DIN EN 1465. 2009-07. *Adhesives - Determination of tensile lap-shear strength of bonded assemblies.* Berlin: German Institute for Standardisation (in Berlin).

Ducháček, V. 2015. *Polymers: production, properties, processing, application.* 3rd edition. Prague: University of chemistry and technology, 276 pp. (in Prague).

Ekrem, M. & Avci, A. 2018. Effects of polyvinyl alcohol nanofiber mats on the adhesion strength and fracture toughness of epoxy adhesive joints. *Composites Part B: Engineering* **138**, 256−264.

Knapčíková, L, Monka, P. & Hloch, S. 2014. Composite Materials Reinforced with Fabric from Used Tyres. *Journal of Manufacturing and Industrial Engineering* **12**, 20−24.

Mancusi, G. & Ascione, F. 2013. Performance at collapse of adhesive bonding. *Compos Struct* **96**, 256−261.

Míšek, B. 2003. *Kompozity*. Technický dozorčí spolek Brno, 81 pp. (in Brno)

Mona, A. Ahmed, Usama, F. Kandil, Neviene, O. Shaker, Ahmed, I. Hashem. 2015. The overall effect of reactive rubber nanoparticles and nano clay on the mechanical properties of epoxy resin. *Journal of Radiation Research and Aplied Sciences* **8**(4), 549−61.

Müller, M. 2015. Hybrid composite materials on basis of reactoplastic matrix reinforced with textile fibres from process of tyres recyclation. *Agronomy Research* **13**(3), 700−708.

Pohlit, D.J., Dillard, D.A., Jacob, G.C. & Starbuck, J.M. 2008. Evaluating the rate-dependent fracture toughness of an automotive adhesive. *Journal of Adhesion* **84**(2), 143−163.

Quan, D., Carolan, D., Rouge, C., Murphy, N. & Ivankovic, A. 2018. Mechanical and fracture properties of epoxy adhesives modified with graphene nanoplatelets and rubber particles. *International Journal of Adhesion and Adhesives* **81**, 21−29.

Ribeiro, F.M.F., Campilho, R.D.S.G., Carbas, R.J.C. & da Silva, L.F.M. 2016. Strength and damage growth in composite bonded joints with defects. *Composites Part B: Engineering* **100**, pp. 91−100.

Rudawska, A., Danczak, I., Müller, M. & Valasek, P. 2016. The effect of sandblasting on surface properties for adhesion. *International Journal of Adhesion and Adhesives* **70**, 176−190.

Shao-Yun, F., Xi−Qiao, F., Bernd, L. & Yiu−Wing, M. 2008. Effects of particle size, particle/matrix interface adhesion and particle loading on mechanical properties of particulate–polymer composites. *Composites Part B: Engineering* **39**(6), 933−961.

Sienkiewicz, M., Janik, H., Borzędowska−Labuda, K. & Kucińska−Lipka, J. 2017. Environmentally friendly polymer-rubber composites obtained from waste tyres: A review. *Journal of Cleaner Production* **147**, 560−571.

Valášek, P. & Müller, M. 2014. EPDM rubber material utilization in epoxy composite systems. *Agronomy Research* **12**, 291−298.

Lake blue clay - sapropel - flax shive briquettes for water absorption and desorption

R. Tretjakova[*], A. Martinovs, M. Avisane and G. Kolcs

Rezekne Academy of Technologies, Faculty of Engineering, Atbrīvošanas aleja 115/K-4, LV-4601 Rēzekne, Latvia
[*]Correspondence: rasma.tretjakova@rta.lv

Abstract. Latvian lakes are rich in sapropel sediments and below the sapropel layer there is another valuable natural resource, namely blue clay. Flax shives are formed in large quantities as a waste in flax processing factories. The problem involves processing and rational use of these resources. The paper studies the obtaining of briquettes from flax shives using sapropel and lake clay as a binding material. Briquettes are intended for use in cases when problems with regular plant watering occur. For example, provision of plants with water in greenhouses, indoor spaces for a long period of time without human presence. Briquettes are placed into the soil next to the plant roots. Briquettes are initially moistened and absorb a significant amount of water (moisture content to be expressed in comparison to the sample's dry weight 250–380%). The presence of clay in them contributes to slow drying of briquettes and provides a long lasting supply of moisture to the plant roots. The paper deals with the issues of the optimal composition of components and the amount of pressure for the production of briquettes, as well as water absorption and desorption properties of briquettes. The aim of the study is to develop a production method of clay – sapropel – flax shive briquettes with good water absorption and desorption properties.

Key words: clay, sapropel, flax shives, briquettes.

INTRODUCTION

Latvia has 2256 lakes with the total area of 1,001 km^2. Most lakes and bogs contain sapropel deposits. Overall resources of sapropel in Latvia comprise approximately 2 billion m^3 (Stankevica & Kļavins, 2013). The sapropel is a renewable and natural resource. Numerous studies have shown the possibility of the effective use of sapropel in building, bio-energy, food, chemical industry, agriculture, veterinary medicine, cattle-breeding, forestry, medicine and cosmetics (Kireicheva & Khokhlova, 1998; Shinkarev et al., 2000; Schepetkin et al., 2002; Nikolaeva et al., 2009; Obuka et al., 2013; Ostrovskij, 2014; Platonov et al., 2014; Tsukanov et al., 2014). A sufficient number of studies has been done to determine the sapropel presence in Latvia, its use in solid soap, glue and composite material manufacturing, as well as its humus impact on hydroponics (Research of modification possibilities and properties of peat, sapropel and clays, 2015).

Clay is one of the most common and most accessible minerals in Latvia. Latvia is rich in clay and it has the largest amount of clay resources in Europe. Most of Latvia's clay resources are used in manufacturing building ceramics, however, the potential of local clay is not sufficiently used (Stinkule, 2014). In the world clays have a tremendous number of miscellaneous uses. The use of clays as soaps, absorbents and construction material has been reported since ancient times. Clays are used in the manufacture of porcelain, whiteware, refractories, bricks, tiles, stoneware, glazed products, catalysts, in preparation of muds for drilling oil wells, as effective barriers to isolate radioactive wastes, and may absorb various pollutants including organic compounds and inorganic trace metals (Kodama & Grim, 2018). The effectiveness of clay in the pharmaceutical industry, in medicine and cosmetology has been proved (Lopez-Galindo et al., 2007; Ray & Ferrell, 2008; Carretero & Pozo, 2009; Ghiaci et al., 2009; Williams & Haydel, 2010; Abdel-Motelib et al., 2011; Matike et al., 2011). The structure, composition and formation of clay deposites is very variable. The lake blue clay is located below the sapropel layer and is considered to be the recent sediment. The natural composition of clay has admixtures of various dispersions - quartz, calcite, dolomite, feldspar, organic compounds etc. (Stinkule, 2014), therefore the use of clay minerals in composites requires pre-treatment of clay, namely release from coarse-grained admixtures. The lake blue clay is free of coarse-grained admixtures.

Since ancient times the flax has always taken a significant place in the agriculture of Latvia (Ivanovs & Stramkale, 2001). Flax fibre (shives) is considered to be waste product remaining after the cellulose fibre removal from flax straw. The core flax shive is generally composed of ~46% cellulose, ~26% hemicellulose, ~23% lignin and ~2% ash (Stemergy renewable bio-fibre, 2018). For every tonne of flax fibre there can be produced 2.5 tonnes of shive (Cox et al., 1999). Flax shives are an industrial and agricultural by-product and it is important to find a solution for its rational use.

The aim of the research is to develop environmentally friendly, biodegradable briquettes with good water absorption and desorption properties using local resources such as lake clay, sapropel and industrial by-product, namely flax shive, and offer a method for their production. The briquettes, which accumulate water in large quantities and slowly return it providing soil with additional water reserves for a long period of time, are intended for use in agriculture. They are placed into the soil where it is necessary to provide water for extended period of time or in areas where the access to water is limited, for example, provision of plants with water in greenhouses or indoor spaces for a long period of time without human presence. Briquettes will gradually provide the soil with water and plants will absorb from it. In the study the mixture of sapropel and blue lake clay is used in briquettes as binders. There are indications that the clay mineral surface (surface charge) and the organic component form a chemical bond (Švinka et al., 2016). Sapropel has an adhesive and hydrophobic quality (Stankeviča & Kļaviņš, 2013; Obuka et al., 2015). Clay in briquettes also serves as water absorbent. Clay materials contain water in several forms. The water may be held in pores and may be removed by drying under ambient conditions. Water may also be adsorbed on the surface of clay mineral structures (Kodama & Grim, 2018). Flax shive performs the function of filler and water absorbent in briquettes. The core flask shive has a porous structure making it very absorbent (Stemergy renewable bio-fibre, 2018).

MATERIALS AND METHODS

In the study briquettes with different composition of mass of sapropel, flax shive and clay are used (Table 1). Separate tests are carried out on a binder of briquettes, specifically dried solid sapropel.

Table 1. Composition and mechanical properties of briquettes used in the research

Type of briquettes	1	2	3	4	5	6	7	8	9
Composition in mass %; sapropel : flax shive : clay	80: 10:10	80: 15:5	80: 5:15	75: 10:15	75: 15:10	75: 20:5	70: 15:15	85: 7.5:7.5	85: 10:5
Hardness, Shore A	30 ± 16	52 ± 12	58 ± 17	40 ± 10	40 ± 24	51 ± 11	40 ± 14	41 ± 13	52 ± 29
Compressive strength 10% relative deformation; MPa; measurement error 1.6%	0.051	0.104	0.038	0.040	0.124	0.103	0.061	0.061	0.063
Density, kg m^{-3}; measurement error 2.0%	232	196	202	195	207	205	199	209	184

Blue clay and sapropel were collected from the lake Plusons (Latvia). Sapropel colour is black–grey; odour – weak, wet soil; consistency – plastic, soft, easily applied and adhesive; moisture 90.53%, dry matter – 9.47%; pH 7.51; contains Na, Mg, K, Ca, Fe, Cr, Mn, Co, Ni, Cu, Zn, Cd, Pb, Al, Ag, Ba. Blue clay has a colloid composition, sludge odour, grey colour, plastic, soft, smooth consistency, moisture 80.16%, dry matter – 19.84%, pH 7.74., which contains Na, Mg, K, Ca, Fe, Cr, Mn, Co, Ni, Cu, Zn, Cd, Pb, Al, Ag, Ba (Tretjakova et al., 2017).

Drying of sapropel samples (until the mass is left unchanged) is carried out in a laboratory room at the temperature of 20 ± 1 °C with a relative air humidity of 31 ± 3% and in a drying oven Memmert UNE 400 at a high temperature (80, 100, 140, 1,600 °C). Shore D Hardness Tester is used to measure the hardness of dried sapropel.

Sapropel, flax shives and clay are mixed to uniform consistency, filled in cubic shapes having dimensions of 50 x 50 x 50 mm and dried in a laboratory room in still air (temperature 20 ± 1 °C, relative humidity of air 31 ± 3%)(Fig. 1).

Figure 1. Sapropel, flax shives and clay briquettes.

The obtained briquettes are tested for water content:

$$u = \frac{m_w}{m_{dry}} \cdot 100\% \,, \qquad (1)$$

where m_{dry} – dry mass of the material (oven-dried material), m_w – the mass of water in the material; $m_w = m - m_{dry}$; m – the mass of wet material.

Dry mass of dried briquettes is determined m_{dry}. Then the briquettes are completely immersed in water at a temperature of 20 °C for 1 hour. In the beginning when the briquettes are removed from water the water content (time t = 0) is determined. Then the drying process of briquettes in the soil is studied. A flat bath (length-500 mm, width-400 mm, depth-80 mm), which is fully filled with soil is used. The initial moisture of soil is 21%. Water-impregnated briquettes are placed in the soil at least 50 mm from each other. The samples are kept in a room with a temperature of 20 ± 1 °C, relative humidity of air is 31 ±%. From time to time briquettes are removed out of soil, carefully cleaned of soil particles, weighed (wet mass m is determined) and placed back into the soil. Their water content is calculated. The process of measurement continues until the briquettes have completely released the water to the soil (until the mass of the briquettes remains unchanged).

Using universal tensile machine Zwick / Roell Z-150 (Fig. 2), briquettes are subjected to pressure testing; strain rate-10mm min^{-1}; maximum compression load of 2kN; temperature 20 °C. The compressive strength is determined from the compression coefficients at a relative deformation of 10%. Shore A Hardness Tester is used to measure hardness of briquettes.
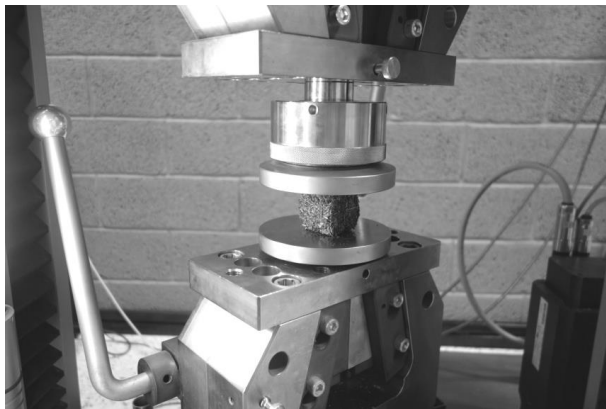

Figure 2. Briquette pressure testing using Zwick / Roell Z-150 universal testing machine.

RESULTS AND DISCUSSION

It is important to accelerate the technological process of manufacturing briquettes. The greatest amount of time it consumes is due to drying of the sapropel, clay and flax shive briquettes. The drying process can be accelerated by raising the temperature in the dryer and providing an intense flow of dry air and discharge of the wet one. It is important (especially during transportation) that the mechanical resistance of the briquettes is as high as possible. Sapropel serves as a binder in briquettes, so the

mechanical properties of sapropel greatly affect the mechanical resistance of briquettes. In order to determine the optimum temperature during drying, the hardness of the dried sapropel is used initially as an indicator. It has been identified that with increasing drying temperature the hardness decreases (Fig. 3). For example, the sapropel just dried at 20 °C according to Shore D is 66 ± 3.7, but the hardness of freshly dried sapropel at 160 °C is only 49 ± 6. Hardness increases over time after complete drying of the sapropel, for example, within 1 week (samples are located in a room with a temperature of 20 ± 1 °C and a relative humidity of $31 \pm 3\%$) after drying out the sapropel, the Shore D hardness increases from 66 ± 3.7 to 74 ± 3 (if the drying temperature was 20 °C), 49 ± 6 to 63 ± 4.5 (if the drying temperature was 160 °C). The explanation may be related to the hydration processes during sapropel drying (similar to the way it occurs during hardening of the concrete), which result in the formation of hydrosilicates, hydroaluminates, and calcium hydroferrates. The probability may be proven by the presence of silicon, calcium, iron, aluminium and oxygen in the content of sapropel (Martinovs et al., 2017; Pleiksnis et al., 2017). This means that drying must be done slowly (for a long time without forced ventilation) at a temperature of 20 °C to obtain more resistant material. In this case, sapropel is dried to have the highest degree of hardness. The briquettes must be kept at least 1 week in a warehouse after drying. During this time the hardness of sapropel increases by 12% (if the drying is at 20 °C, Fig. 3). Only then briquettes can be transported. This means that accelerating the production technological process at the expense of drying time is problematic, therefore additional research is still needed. Consequently, it must be taken into consideration that briquette manufacturing requires large areas for drying and storing products.
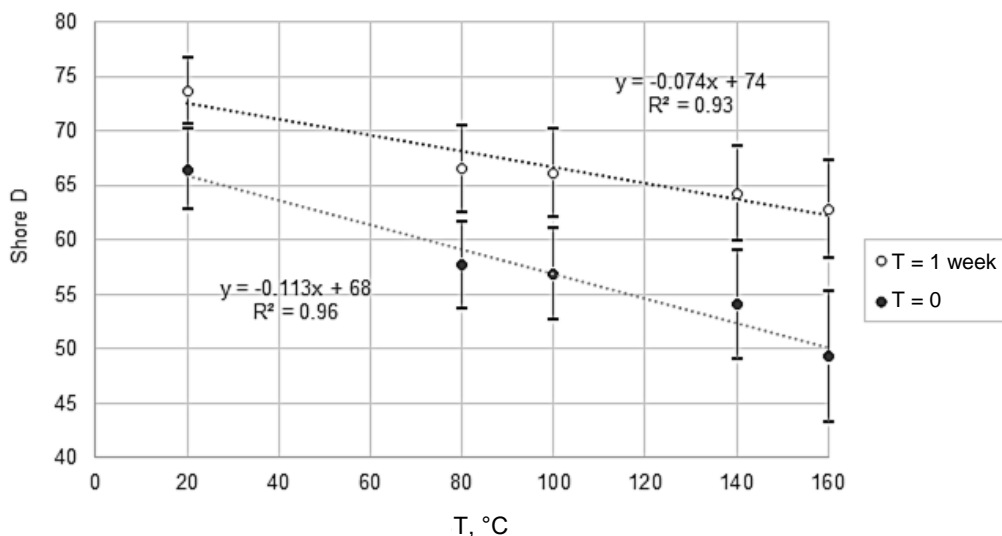

Figure 3. Sapropel hardness (Shore D) depending on the drying temperature (T) and the time(t) after sapropel has been completely dried (t = 0-freshly dried sapropel; t = 1 week-solid sapropel which has been kept in a warehouse for one week).

The press test charts for all types of briquettes are given in Fig. 4. It shows that the briquette type No.5 deforms the least in the result of pressure (maximum load for all samples 2kN). Composition, hardness, compressive strength at 10% relative deformation and density for various types of briquettes are given in Table 1. These results (compressive strength, density) are close to sapropel and hemp shives thermal insulation material (Pleiksnis et al.,2017). It has been proven that hemp shives are especially strong and flexible (Adamovics et al., 2013). This means that it would be possible to use hemp shives or other fillers, such as sawdust, wood chips or their blends instead of flax shives. In Table 2 there are given the results of the drying process of water-impregnated briquettes. It shows the changes in water content % in different types of briquettes over some period of time. Figures for the characterization of the composition of the briquettes mean the proportion of the mass of sapropel-shives- blue clay, for example, 80:10:10 means that 80% of briquettes contain sapropel, 10% of flax shives and 10% of blue clay. The data in Table 2 shows that the best water desorption properties are in briquettes with composition 75:15:10 (briquette type No. 5).
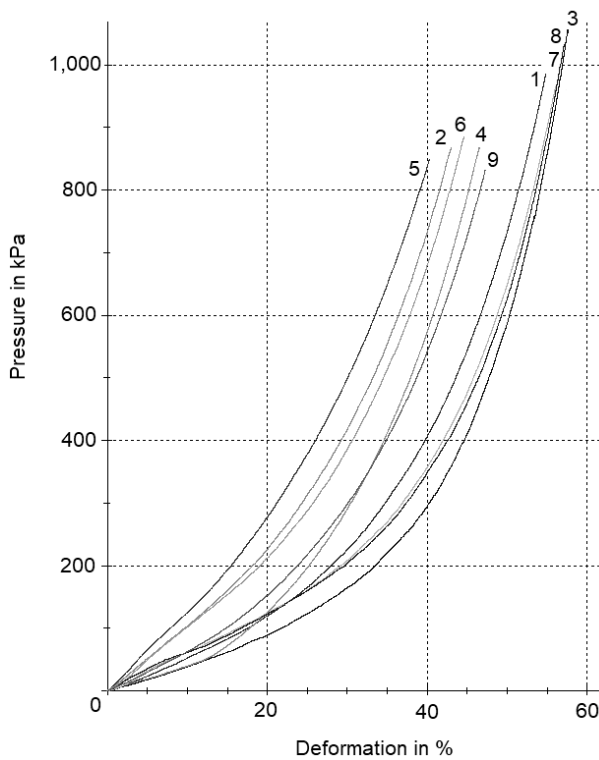

Figure 4. Briquette press characteristic curves in the range up to 2kN of compressive force.

Table 2. Changes in absolute water content (u) (%) of briquettes during a period of time t (when they are drying in soil)

t, day	Type of briquettes								
	1	2	3	4	5	6	7	8	9
0	320	317	289	297	243	290	316	329	320
1	191	205	178	194	185	211	207	197	202
2	161	167	148	157	161	180	171	168	174
3	141	148	131	136	142	154	148	146	146
4	125	131	102	116	124	133	124	125	126
7	74	71	52	77	90	71	73	80	77
8	61	59	32	61	78	59	58	60	61
9	49	50	20	47	66	50	45	46	50
10	38	40	9	32	55	40	33	30	37
11	26	29		22	44	29	20	17	24
14	12	12			22	17	12	11	11
15					19				

Briquettes have low mechanical resistance and they can easily be damaged during transportation. To solve this problem, a briquetting machine (Fig. 5) is offered. The certain proportions of sapropel, flax shive and clay are mixed to uniform consistency and put in a briquetting machine. Briquettes have a cubic shape with dimensions of 50 x 50 x 50 mm. For forming, drying, storing and transportation of briquettes, thermoplastic forms that have been manufactured using a plastic vacuum forming method are used. The prepared form is placed in the molding machine. Constructively the briquetting equipment consists of a rack (made of steel tubes), a table surface (on which there are placed linear movement knobs, namely linear rails, electric drive), the feed hopper and a rammer roller to tamp the mixture in a mold. The mixture gets into the shapes after the shutter with pneumatic drive built in the feed hopper is opened. The amount of mixture in forms can be adjusted by changing the speed of the hopper and the roller. This can be done by adjusting the speed of the electric drive motor with a variable frequency drive. When the hopper reaches the end position, the end switch is actuated, the shutter is closed, the electric drive is reversed and the hopper gets to the starting position. A new briquetting cycle can be started after inserting a new shape and pressing the start button done by the machine operator.

Traditionally, sapropel is used as a soil improver or supplementary fertilizer (Stankeviča & Kļaviņš, 2013). Thus, briquettes will simultaneously promote soil regeneration both in water return process and in the process of decay by returning minerals and organic matter to the soil. Sapropel in composition of fertilizers participates as physiologically active binder of the base having high ion exchange and sorption properties. It is also an additional supplier of humic substances, amino acids, including aspartic, glutamic, as well as glycine, alanine and histidine, into nutrient medium of plants (Agafonova et al., 2015). The plants need macro elements such as H, C, O, N, Mg, K, Ca, P, microelements Cl, B, Fe, Mn, Co, Ni, Zn, Cu, Mo (Mohr & Schopfer, 1995). There is lack of Cu in the soil of Latvia. The elemental analysis on sapropel showed that lake sediments in comparison with peat have a higher N concentration. Higher concentrations in organic lake sediments are common for metals of natural origin such as Ca, Fe and Mg. Heavy metal concentration compared to its maximum permissible concentration in soil showed that the sapropelic sediments are not

contaminated (Stankevica et al., 2012). The Plusons lake sapropel has a high concentration of such elements as K, Fe, Co, Ni, Zn, Cu that are important to a plant, but in comparison with sapropel the lake clay contains significantly more Mg, Ca, Mn and less heavy metals such as Cd, Zn, Cu (Tretjakova et al., 2017). Additional additives can be added in briquettes to adapt them to different soils.
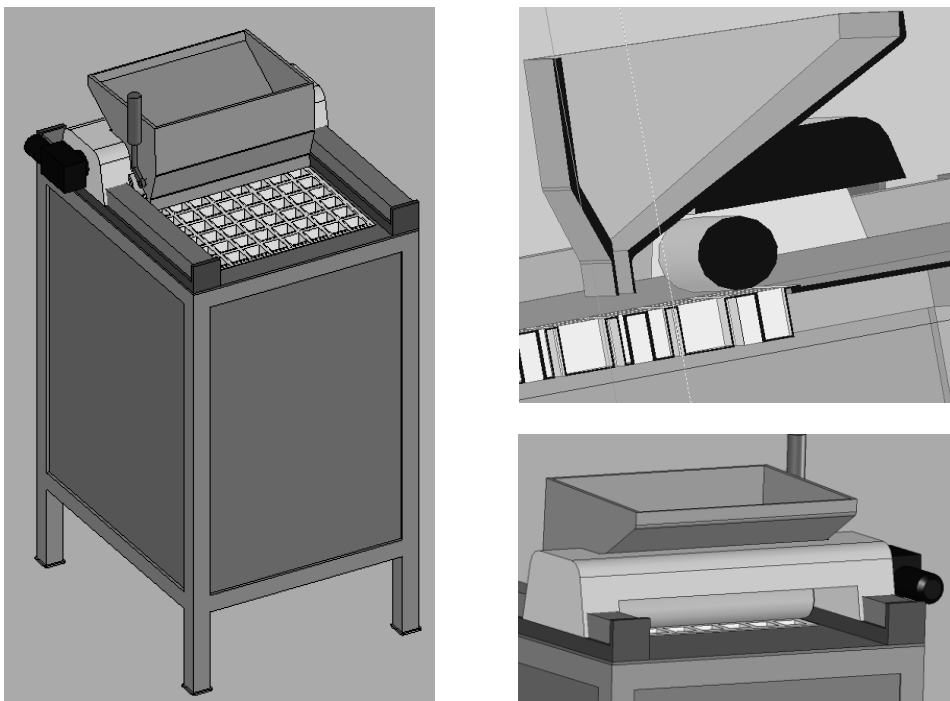

Figure 5. 3D model of briquetting equipment from different views.

Both sapropel and clay are microbiologically active and form an appropriate environment for microorganisms, while some clays have antibacterial properties, therefore microbiological stability of briquettes is important. Clay and sapropel contamination with microorganisms must be controlled, given that both can originate diseases or damage the product when it is stored. Results of the microbiological testing of the Plusons lake blue clays show that the presence of *Candida albicans, Pseudomonas aeruginosa, Staphilacoccus aureus has* not been stated. The number of mesophyll aerobic microorganisms varied < 1 to 3.6 X 10 CFU 0.1 g^{-1} (Tretjakova et al., 2017). *C. albicans, P. aeruginosa, S. aureus* have not been found in the sapropel of the Plusons lake. The number of mesophyll aerobic microorganisms varied from 3.6 x 10 to 5.0 x 10^2 CFU 0.1 g^{-1} (unpublished). Platonov et al. (2014) have demonstrated sapropel protective antibiotic activity against *Escherichia coli, S.aureus, C.diphterie* and fungi Candida. Strus et al. (2014) studies have shown a slight antibacterial activity of sapropel against selected test cultures (*E. coli, P. aeruginosa, Bacillus subtilis, Proteus vulgaris, C. albicans*). Sapropel has antimicrobial activity on *S. aureus* reference culture (Tretjakova et al., 2015). Fungus and actinomycetes synthesize antibiotics and sulfanilamides in sapropel (Stankeviča & Kļaviņš, 2013). Clay has antibacterial and

antifungal properties. Clay shows antibacterial effect against *E. coli*, *S. aureus, P. aeruginosa* (Williams & Haydel, 2010; Parolo et al., 2011; Lafi & Al-Dulaimy, 2011). Antimicrobial testing of two clays proved that while one clay promotes bacterial growth, the other one eliminates bacteria or significantly inhibits its growth (Williams et al., 2008). The research results showed that some natural clay samples were devoid of antimicrobial and antifungal activity (Nikolajeva et al., 2013). The biological effects of clay minerals are influenced by their mineral composition and particle size (World Health Organization), therefore in-depth studies on the microbial resistance of the briquettes are needed.

Macroporous sapropel support seemed to be promising for adhesion of various microorganisms in order to prepare commercially attractive whole-cell biocatalysts (Kovalenko et al., 2016). In Žvagiņa et al. (2015) studies the clay was tested for the immobilization of bacteria. Muter et al. (2011), Muter et al. (2012), Nikolajeva et al. (2012) concluded in their studies that ceramic materials can be used for immobilization of microorganisms. Griba (2011) has compared in her study the clay extracted in Russia and Latvia and has come to conclusion that bacteria is more adhesive in clays extracted in Latvia. Thus, briquettes could be the material for the immobilization of such genera of bacteria as Azotobacter, Bacillus, Rhizobium and Streptomyces that promote the growth of plants. Further research is also needed in this area.

CONCLUSIONS

Briquettes containing 75% sapropel, 15% flax shive and 10% blue clay have the best mechanical and water desorption properties.

To obtain more durable briquettes, they should be dried slowly (for a long time without forced ventilation) at 20 °C.

After drying the briquettes must be places in a warehouse for at least 1 week. During this time sapropel hardness increases by 12%, then the briquettes can be transported.

Forming, drying, storing and transportation of briquettes should be done in the thermoplastic forms or other materials (ideally, a biodegradable material).

It is recommended to carry out further studies on the microbial activity of the briquettes and the possibilities of immobilization of bacteria that furthers the growth of plants.

NACIONĀLAIS ATTĪSTĪBAS PLĀNS 2020

EIROPAS SAVIENĪBA
Eiropas Reģionālās attīstības fonds

PostDoc Latvia

IEGULDĪJUMS TAVĀ NĀKOTNĒ

REFERENCES

Abdel-Motelib, A., Kader, Z.A., Ragab, Y.A. & Mosalamy, M. 2011. Suitability of a Miocene bentonite from North Western Desert of Egypt for pharmaceutical use. *Applied Clay Science* **52**, 140–144.

Adamovics, A., Kakitis, A. & Platace, R. 2013. Industrial Hemp Productivity and Tensile Endurance Determine of Hemp Fiber. In *Proceedings of the sixth international scientific conference Rural development* **6**(2), Lithuania, pp.11–16.

Agafonova, L., Alsina, I., Sokolov, G., Kovrik, S., Bambalov, N., Apse, J. & Rak, M. 2015. New Kinds of Sapropel and Peat Based Fertilizers. In: *Environment. Technology. Resources, Rezekne, Latvia Proceedings of the 10th International Scientific and Practical Conference.* Volume **II**, pp. 20–26.

Carretero, M.I. & Pozo, M. 2009. Clay and non-clay minerals in the pharmaceutical industry. Part I. Excipients and medical applications. *Applied Clay Science* **46**, 73–80.

Cox, M., El-Shafey, E., Pichugin, A.A. & Appleton, Q. 1999. Preparation and characterization of a carbon adsorbent from flax shives by dehydration with sulfuric acid. *Journal of Chemical Technology and Biotechnology* **74**, 1019–1029.

Ghiaci, M., Aghaei, H., Soleimanian, S. & Sedaghat, S. 2009. Enzyme immobilization: 1. Modified bentonite as a new and efficient support for immobilization of Candida rugosa lipase. *Applied Clay Science* **43**(3–4), 289–295.

Giba, T. 2011. *Research of the interaction of clay, ceramic granules and bacteria.* Bachelor thesis. University of Latvia, Riga, 33 pp. (in Latvian).

Ivanovs, S. & Stramkale, V. 2001. *Flax cultivation and harvesting technology.* Jelgava. 191 pp. (In Latvian).

Kireicheva, L.V. & Khokhlova, O.B. 1998. *Sapropels: composition, properties, applications.* Moscow, pp. 124 (In Russian).

Kodama, H. & Grim, R.E. 2018. Clay mineral. Encyclopedia Britannica. Accessed 21.1.2018. *https://www.britannica.com/science/clay-mineral/Chemical-and-physical-properties.*

Kovalenko, G.A., Perminova, L.V., Rudina, N.A., Maksimova, Yu.G. & Maksimov, A.Yu. 2016. Sapropel-based supports as novel macroporous carbon-mineral adsorbents for enzymatic active substances. *Resource-Efficient Technologies* **2**, 159–167.

Lafi, S.A. & Al-Dulaimy, M.R. 2011. Antibacterial effect of some mineral clays in vitro. *Egypt. Acad. J. Biolog. Sci.* **3**(1), 75–81.

Lopez-Galindo, A., Viseras, C. & Cerezo, P. 2007. Compositional, technical and safety specifications of clays to be used as pharmaceutical and cosmetic products. *Applied Clay Science* **36**(1–3), 51–63.

Martinovs, A., Tretjakova, R., Castro, R., Solovyev, V., Timmerberg, J., Cvetkov, A., Gango, S., Borkenstein, A., Beckmann, P., Schütte, H., Puchkov, N., Trifonov, S. 2017. Effect of Heat Treatment on Electrical and Mechanical Properties of the Solid Sapropel. In: *Proceedings of the 11th International Scientific and Practical Conference 'Environment. Technology. Resources'* Rezekne, Latvia, **III**, pp. 200–206.

Matike, D.M.E., Ekosse, G.I.E. & Ngole, M.V. 2011. Physico-chemical properties od clayley soils used traditionally for cosmetics in Eastern Cape, South Africa. *Phys. Sci.* **6**(33), 7557–7566.

Muter, O., Berzins, A., Potapova, K., Strikauska, S. & Stelmahere, S. 2011. Bacteria immobilization on ceramic beads for soil remediation technologies. *Journal of International Scientific Publications: Ecology & Safety* **5**, 152–162.

Muter, O., Potapova, K., Nikolajeva, V., Petriņa, Z., Griba, T., Patmalnieks, A., Švinka, R. & Švinka, V. 2012. Comparative study on bacteria colonization onto ceramic beads originated from two Devonian clay deposits in Latvia. *Scientific Journal of RTU: Material Science and Applied Chemistry* **26**, 134–139.

Mohr, H. & Schopfer, P. 1995. *Plant Physiology*. Berlin, Springer-Verlag, 629 pp.

Nikolajeva, V., Griba, T. & Petriņa, Z. 2012. Factors influencing adhesion of *Pseudomonas putida* on porous clay ceramic granules. *Environmental and Experimental Biology* **10**, 77–80.

Nikolajeva, V., Griba, T., Petriņa, Z. & Karasa, J. 2013. Antimicrobial Activity of Natural and Treated Clays. *Material Science and Applied Chemistry* **29**, 142–147.

Nikolaeva, L.A., Latyshev, V.G. & Burenina, O.N. 2009. Fuel Briquettes from Brown Coals of Yakutia. *Solid Fuel Chemistry* **43**(2), 109–112.

Obuka, V., Korjakins, A., Brencis, R., Preikšs, I., Purmalis, O., Stankeviča, K. & Kļaviņš, M. 2013. Sapropel/Peat-Wood Chip Insulation Materials and Their Properties. *Materials Sciences and Applied Chemistry* **29**, 127–136.

Obuka, V., Šinka, M., Kļaviņš, M., Stankeviča, K. & Korjakins, A. 2015. Sapropel as a Binder: Properties and Application Possibilities for Composite Materials. *IOP Conference Series: Materials Science and Engineering* **96**(1), 1–10.

Ostrovskij, M.V. 2014. Testing HUMIN PLUS Microfertilizer. *European Agrophysical Journal* **1**(2), 77–83.

Parolo, M.E., Fernandez, L.G., Zajonkovsky, I., Sánchez, M.P. & Baschini, M. 2011. Antibacterial activity of materials synthesized from clay minerals. Science against microbial pathogens: Communicating current research and technological advances. Spain: Formatex Research Center **1**, 144–151.

Platonov, V.V., Khadartsev, A.A., Chunosov, S.N. & Fridzon, K.Y. 2014. The biological effect of sapropel. *Fundamental research* **9**(11), 474–2480 (In Russian).

Platonov, V.V., Khadartsev, A.A., Chunosov, S.N. & Fridzon, K.Y. 2014. The biological effect of sapropel. *Fundamental research* **9**(11), 2474–2480 (In Russian).

Pleiksnis, S., Sinka, M. & Sahmenko, G. 2017. Experimental justification for sapropel and hemp shives use as a thermal insulation in Latvia. In: *Proceedings of the 11th International Scientific and Practical Conference 'Environment. Technology. Resources'* Rezekne, Latvia, **I**, pp. 175–181.

Ray, E. & Ferrell, J.R. 2008. Medicinal clay and spiritual healing. *Clays and Clay Minerals* **56**(6), 751–760.

Research of modification possibilities and properties of peat, sapropel and clays 2015. Accessed 23.11.2017. *http://www.lu.lv/vpp/zemes-dzilu-resursu-izpete-jauni-produkti-un-tehnologijas-zeme/5-apaksprojekts/projekta-rezultati/sapropelis/*.

Schepetkin, I., Khlebnikov, A. & Kwon, B.S. 2002. Medical drugs from humus matter: Focus on mumie. *Drug Development Research* **57**(3), 140–159.

Shinkarev, A., Lyutakhina, N. & Gnevashov, S. 2000. Separation of the groups of humic substances upon recurrent treatment with Solvents. *Eurasian Soil Science* **33**(7), 709–712.

Stankevica, K., Klavins, M. & Rutina, L. 2012. Accumulation of Metals in Sapropel. *Material Science and Applied Chemistry* **26**, 99–105.

Stankeviča, K. & Kļaviņš, M. 2013. Sapropel and its application possibilities. *Materials Sciences and Applied Chemistry* **29**, 109–126 (in Latvian).

Stemergy renewable bio-fibre 2018. *http://www.stemergy.com/products/flaxfibre/flaxshives/*. Accessed 4.1.2018.

Stinkule, A. 2014. *Clay in depths of the earth of Latvia.* Riga, RTU, 121 pp. (In Latvian).

Strus, O.E., Polovko, N.P., Maloshtan, L.M. & Solodchenko, T.P. 2014. The study of the properties of sapropel deposits of Pribich. *Problems of ecological and medical genetics and clinical immunology* **3**(123).

Švinka, V., Švinka, R., Timma, I., Lindiņa, L., Cimmers, A. 2016. Non-traditional usage of clay in Latvia. In: *Abstract book I International Interdisciplinary symposium Clays and ceramics,* Riga, Latvia, pp. 64–65 (in Latvian).

Tretjakova, R., Grebeža, J. & Martinovs, A. 2015. Research into biological characterictics of dried sapropel. In: *Proceedings of the X International Scientific and Practical Conference 'Environment. Technology. Resources'* **I**, Rezekne, Latvia, pp. 223–227.

Tsukanov, S.V., Owayski, F., Zeidan, I., Zeidan, A., Uptis, I., Apse, J. & Ostrovskij, M.V. 2014. Application of Organic Fertilizers Based on Sapropel and Peat in Countries of Middle East. *European Agrophysical Journal* **1**(3), 118–128.

Williams, L.B. & Haydel, S.E. 2010. Evaluation of the medicinal use of clay minerals as antibacterial agents. *Geol Rev.* **52**(7/8), 745–770.

Williams, L.B., Haydel S.E., Giese, R.F.Jr. & Eberl, D.D. 2008. Chemical and mineralogical characteristics of french green clays used for healing. *Clays and Clay Minerals* **56**(4), 437–452.

World Health Organization: Bentonite, kaolin and selected clay minerals. Environmental Health. Criteria 231. http://www.inchem.org/documents/ehc/ehc/ehc231.htm. Accessed: 03.01.2018.

Žvagiņa, S., Petriņa, Z., Nikolajeva, V. & Lielpētere, A. 2015. Immobilization and Survival of Root Nodule Bacterium *Rhizobium leguminosarum* Biovar *viciae Material Science and Applied Chemistry* **32**, 75–79.

Technical design of complex vision-tactile navigation system for using of blind persons navigation

J. Volf, F. Škeřík and V. Novák[*]

Czech University of Life Sciences Prague, Faculty of Engineering, Department of Electrical and Automation, Kamýcká 129, CZ165 21 Prague, Czech Republic
[*]Correspondence: novakviktor@tf.czu.cz

Abstract. This article presents the system used for navigation and orientation of blind persons in an unknown terrain. This system called 'Tactile Navigation System' constitutes a compensation instrument for blind persons. It is composed from three basic elements: a camera, a control unit and a tactile activator. The tactile navigation system converts the image from the camera to the tactile information and it transfers this information to the blind person. The blind person can recognize by vibration of the tactile activator placed on the antebrachium whether he comes on an impediment or if he can continue free walking. The main advantage of this system is the possibility of detecting any individual impediment earlier than using other common compensation tools, such as a simple blind stick, which is not a competitor with this device, but a helper. This way the system facilitates the orientation of a blind person an in an unknown terrain. The article describes in detail the overall composition and functionality of the system as well as the principle and function of its individual elements.

Key words: tactile systems, pattern processing, edge operator, blind persons, navigation, tactile activator.

INTRODUCTION

The need of navigation of blind persons is still a challenge. The white stick accompanies them for centuries, even in the electronic age. This article is a small contribution in this branch. The aim of the projected device is to enable the orientation of blind persons in the space. The design and the individual components have undergone some changes during the development, as the technology of individual elements developed. But the basic idea has not changed. The described tactile navigation system includes a camera, pattern processing system, a control unit, a tactile activator and a power supply, with detailed description of the edge detection system and the behaviour of tactile actuators. This navigation system has been designed basing on tactile perception of a picture from a camera. There are also other system using visuo-auditory based navigation (e.g. Auvray et al., 2007), however, we did not follow this way because the tactile sensing does not burden the audio sensing of the blind person and does not distract its attention this way.

MATERIALS AND METHODS

Overview of present systems

For the better awareness in this issue, we will present some already developed and experimentally verified navigation systems for blind persons.

One of the used systems is the Tyflosonar (2017), which represents a multi-functional electronic device. It uses ultrasound for the distance measurement. In addition to the obstacle detection it includes also a sound beacon and a sound indicator of light intensity. Additional functionalities are the obstacle distance measurement and the accumulator test. The blind person wears the device usually on the chest.

The navigation system Dinasys is intended for orientation of visually handicapped persons in an unfamiliar environment of buildings, corridors, closed outside areas or other closed rooms. This navigation system is not intended for orientation in streets or in open space. The navigation system consists of two components – a modified white stick and very strong permanent magnets. The magnets are put into or glued onto the ground to mark the proper path. The magnet can be placed under a carpet or embedded into soil up to 5 cm deep. There are also being developed another, particularly acoustic navigation systems by the company (Diansys, 2017).

Other system is called Tongue Display Unit (TDU, under the commertional name (Brainport®) (Kaczmarek, 2011). The TDU has been designed at the University of Madison. The system consists of a camera that scans the surroundings. The processed signal from the camera gets to a 12 x 12 matrix, which is located on an elastic foil. The foil is put on the tongue. The tactile cells of the tongue are stimulated by electrical impulses in individual points of the matrix. The letter T was tested in various positions. After a short practice, very good results in its recognition were achieved. The simultaneous brain examination has proved that while using the TDU, the picture processing centres of the brain are stimulated. It even holds true for persons that are blind from birth and that have never used the brain view centres.

An interesting solution of orientation of blind persons is called ActiveBelt (2017). The device is a vibration belt, which is equipped with eight vibration motors evenly placed at the belt´s perimeter. The belt is connected with a GPS module with a pre-set address. The direction of the motion towards an obstacle of the blind person is determinated by the vibrations of the corresponding vibration motor.

The last non-invasive system is a blind person camera. This camera has got no LCD but a Braille display (A camera For the Blind, 2017), which is capable to display the picture in 3D-mode. It enables the user to sense a picture by means of the touch. This way can the blind persons perceive their surroundings by means of visual information by way of the touch.

Recently, with the advance of the neurosurgery and the optical surgery, invasive solutions start to be implemented, e.g. an implant of the artificial retina or a picture taken by a camera, which is after modulation transmitted into the brain view centre. As the article is focused on non-invasive methods, further information of the invasive solutions can be found in Margalit et al. (2002) and Volf & Škeřík (2014). Psychological aspects of blind persons' perception and comparison of blind and blindfolded control groups are stated in Segond et al. (2013).

Means of the information gain about the surroundings

As mentioned above, the described tactile navigation system is intended for the orienntation of blind persons in an unfamiliar or a partly familiar environment. A block diagram of the entire system is shown in Fig. 1.
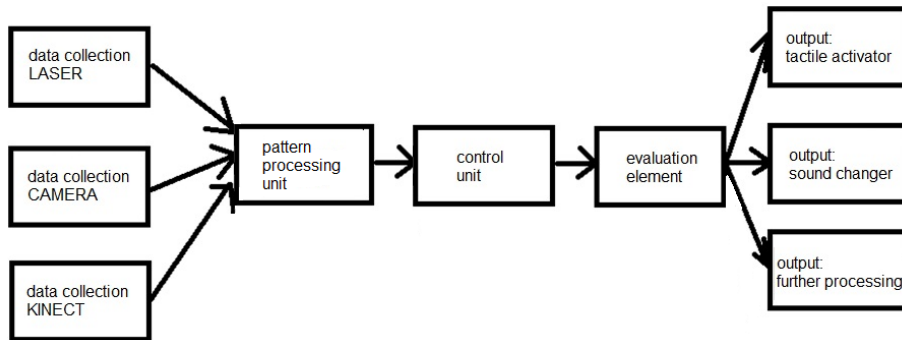

Figure 1. Block diagram of the tactile navigation system.

The tactile navigation system enables to collect information from various sources, not only from a camera or from a laser distance measuring system, but also from other supportive systems, e.g. the Kinect. The pattern processing unit processes signal from camera and reduces these data (by signal processor) to form, that can be processed by control unit. The control unit and the evaluation element process individual signals, convert them into requested form and transmit them to other components of the system, which mediate the information to the blind person by diverse ways. The system described in this article passes the information on via a tactile activator, which by means of vibrations of motors transfers this information through skin receptors at the forearm (Králíček, 2011; Silbernagl & Despopoulos, 2004; Volf et al., 2015).

Another way of use is a sound changer that should by means of speech synthesis speak the transmitted information, and so warn the blind person acoustically about the situation in front of it or in its surroundings. An alternative is use of acoustic signal with variable frequency. The designed tactile system is controlled by a microprocessor; it has to work with minimal energy in real time, so there are high demands on the simplicity of the recognition system.

A camera CMUcam3 (2017) was used to record the environment. The camera is placed on the head of the blind person and it records the area in the direction of the head´s turn, so the space of the view and the likely walk is scanned. According to the configuration of the processor, the camera can make a video record or individual snapshots by pre-set instructions that depend mainly on the recording and processing speed.

Individual pictures are passed on the control unit, which by means of SW detects edges and converts the resulting picture into information that can be transmitted to the blind person. The edge detection can be carried out by means of various software tools and methods; we have used the Hough Transformation. A closer description is in the part about the picture processing. To get the information about the obstacle distance, we need to use either two cameras or a rangefinder.

Other system that complexly solves the gaining of information about the environment is the game console Kinect by Microsoft. It combines a RGB camera, deep sensor, broad scale microphones and a separate control processor. Kinect can follow the motion in 3D mode, react to instructions and orders and it can even recognize a change of emotions or voice timbre. Today, there are being performed tests of a tactile navigation system that uses the sensor Kinect. The blind person will obtain exact information about the surroundings in that it can move safely.

Picture processing

A very important part of working with pictures and searching for specific objects is the pre-processing of the picture, further information can be found in Volf (1994), Šonka et al. (2014), Burger & Burge (2009) and Prajer (2009). The colour picture loaded by the camera is initially converted into a grey-scale and then its contrast is modified.

Based on neurophysiological and psychological research, it turns out that by image perception plays a very important role places with a significant change in brightness. These places are called edges. It is simply possible to prove the ability of the human brain to abstracted on the edge only the overall image perception – an example can be a drawing.

An edge in the image can be distinguished basing on pixel values, depending on the values of the surrounding pixels. This is caused by a sudden change in the value of the $f(x, y)$ image function. Changing the value of the function of the two variables can be quite easily determined using a partial derivative.

Change the function value is given by its gradient ∇, which is a vector variable that determines the direction of the greatest increment of the function in the given direction and the slope of this growth (gradient module). Pixels with a large gradient module are detected as edges. Gradient size $|\nabla f(x, y)|$ and its direction φ – represent the angle between the coordinate axis x and the radius vector to the point of coordinates [x, y]. This is for a continuous function given by the following Eqs (1), (2):

$$|\nabla f(x, y)| = \sqrt{\left(\frac{\partial f}{\partial x}\right)^2 + \left(\frac{\partial f}{\partial y}\right)^2} \tag{1}$$

$$\varphi = arg\left(\frac{\partial f}{\partial x}, \frac{\partial f}{\partial y}\right) \tag{2}$$

The best of the edge detectors for our purpose appears to be the Canny edge detector, the today's advanced edge detector. It bases on the idea that the jumping edge (in 2D we can imagine it as a step) can be searched for by a filter. The design of this filter is conceived as a rotation variable. The detector is optimal for jump edges with respect to the three criteria (Šonka et al., 2014):

1. *The detection criterion* requires that significant edges are not overlooked and that multiple edges are not present on one edge.

2. *The localization criterion* requires that the difference between the actual and the found edge position is minimal.

3. *One response criterion* ensures that the detector does not respond multiple times to one edge of the image. This expectation is already partly secured by the first criterion. This requirement is especially focused on dull and non-smooth edges, which are not provided by the first requirement.

First, the edge detector was formulated for the 1D signal and the first two optimization criteria. Using the calculus of variations and symbolic derivation program, an explicit solution was found. After adding the *One response criterion*, it was necessary to look for the most appropriate filter response by numeric optimization. The resulting filter can be approximated by Gaussian filtration with an error of less than 20%. After generalizing into 2D, the edge is given by its position, orientation and size (it can be imagined as the height of the stairs). The edge thickness (magnitude of the intensity gradient *f*) is calculated according to the Eq. (3):

$$|G_n \cdot f| = |\nabla(G \cdot f)| \tag{3}$$

Since convolution and derivation are associative operations, we can first realize the convolution of the image *f* with Gaussian *G* in the Eq. (3) and then compute the directional second derivative using the estimation in the direction *n* according to Eq. (4):

$$n = \frac{\nabla(G \cdot f)}{|\nabla(G \cdot f)|} \tag{4}$$

The position of the edge (the local maximum of the convolution *f* with the operator G_n), depending on 2D Gaussian *G*, is obtained by substitution from the equation for its first derivative *G″* (5):

$$G_n = \frac{\partial G}{\partial n} = n.\nabla G \quad => \quad \frac{\partial G_n}{\partial n} \cdot f = \frac{\partial^2 G}{\partial n^2} \cdot f = 0 \tag{5}$$

Image filtering is one part of the preparation of real-image scanning and its processing by a microprocessor or signal processor; here it is necessary to point out that today there are also CCD cameras with an inbuilt microprocessor allowing to filter directly and simplifying the device.

The distances of the obstacle could be determined using 'higher' image processing tasks. First, it is necessary to identify the object in the image and determine its dimensions. Then it is examined, based on its shape, how far it is from the observer. However, such real-time calculations are very hardware demanding. The simplier way to determine the distance is to use a laser or ultrasonic measuring device. The acquired distance information can be converted to a sound sensation – the closer the obstacle, the higher the frequency of signal intervals. It is not advisable to generate steady sound signals, because a blind person also uses hearing for the orientation in the space, and such steady signals could be rather confusing.

Tactile activator
There are demonstrated two possible tactile activator solutions to inform a blind person about the surroundings. The first one uses stimulation by alternating current and the second one bases on mechanical principle – transmission of information by vibration.

Due to the principle of irritation with AC electrical stimulation, the tip of the electric pulse must be able to transmit the electric impulses to the surface of the skin, which results in a number of requirements: the spikes must be rigid in order not to bend and their attachment in the matrix must be firm, to maintain their position. On the other hand, the entire matrix with spikes should be compliant to copy the shape of the surface of the human body where it is attached to adhere sufficiently to it. For the human body it were experimentally determined optimal values of frequencies around 200–250 Hz,

voltage and the current must meet safety limits, voltage up to 12 V and current up to 3.5 mA.

As can be seen, some requirements are in direct contrast: the stiffness of the matrix and spikes can be met, but the positional stiffness of the spikes, to copy the shape of the human body is hard to match. A possible compromise is use of a thin fastening system and short spikes, which also lowers total activator height. Spikes are made from titanium, chirurgical steel, with combination with other conductive materials such as gilded tips. For our experimental use we created an array of 10 x 16 pin connectors with a 2.45 mm pitch embedded in silicone forming; see illustrative image in Fig. 2.

Another alternative is the use of cross-linked joints formed on thin printed circuit board, such as Teflon film with double-sided copper layer with the trade name Cuflex. This material is very flexible and replicates very well the shape of the arm.

The use of so-called 'smart' textiles is also very promising, a relatively new and progressive branch in the textile industry. Thin conductors forming points (conductive connections) or conductive paths (buses) are inserted into the outline of the fabric at selected locations. This way, it is possible to create e.g. a numeric keypad; or it is even possible to directly integrate circuits to the created busses or to connect the solar cells for the power supply.

In the other case, an activator with vibrating elements was used to transmit environmental information. The tactile activator is a box (see Fig. 3) that consists of 9 miniature electro motors, their control units and the control unit of the entire tactile navigation system. The signals from the camera or from the control unit of the system are brought by cable into the tactile activator and then are converted into information for the blind person by means of control units and a multiplexor. The information is created by an electro motor. The shaft of the motor is equipped with an eccentric mechanism that creates vibrations by its irregular shape after the spin-off of the motor. The electro motors are set into a 3 x 3 matrix, that will be extended to 5 x 5 matrix of motors in the future, in order to ensure the highest possible accuracy of the system. To transmit the vibration to the blind person, the electro motor is equipped with a small plastic plate that is placed in the opening of the plastic deck of the tactile activator. The electro motor is embedded in a rubber wrap in order to distinguish the vibration of the motor and not to influence other parts of the activator. Vibrating electro motors by the company Maxon (2017) were used, specifically the motor 30200 EC 10 lat, power 0.2 W.
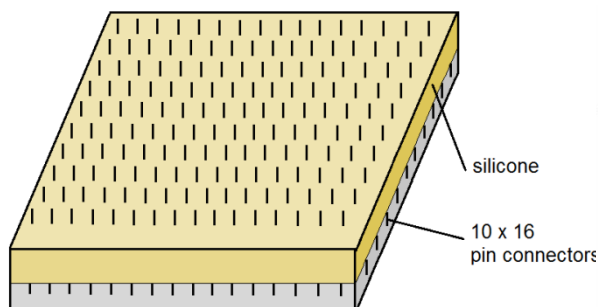

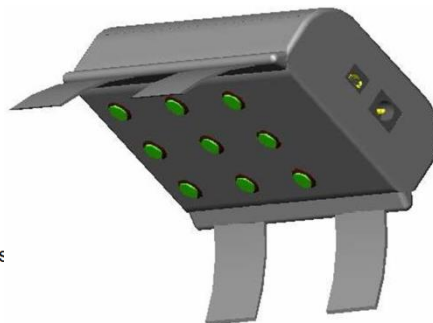**Figure 2.** Pin connector matrix.

Figure 3. Tactile activator.

The activator itself is placed on the forearm and it is fixed by two belts that ensure its right position and that prevent shifting or slipping from this position. The belts are wide enough to minimize the pressure onto the arm and to ensure that the wearing will not be unpleasant.

By this prototype, the power supply of the entire system is realized by means of a battery that is placed in a bag at the waist. The entire system is designed to help with the orientation as much and to limit as little as possible. As the control unit the 1-Q-EC Amplifier DEC Module 24/2 was used. The unit is connected with the tactile activator with a 17-pin connector.

RESULTS AND DISCUSSION

Edge detection
In following we present the results of edge detection by using the Canny detector on two pictures. First Fig. 4 represents the scene from the interior, the second Fig. 5 the exterior scene; namely the entrance to Ládví metro line C in Prague. The interior was photographed from a distance of 1.8 m, exterior from a distance of 10 m.
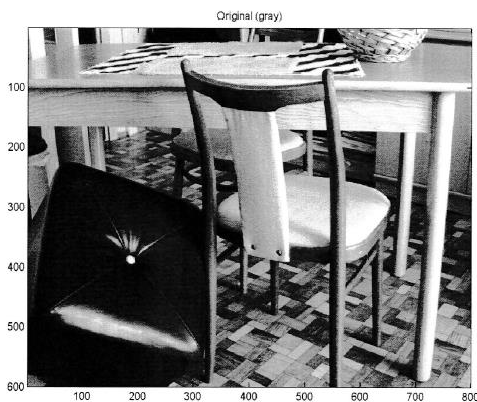

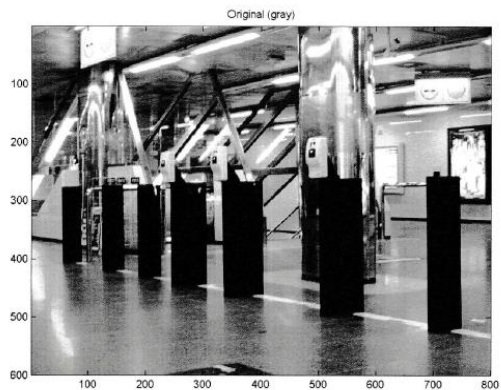**Figure 4.** Interior image.

Figure 5. Exterior image.

For filtering, a 5 point and 9 point Laplace operator, Robinson operator and Kirsch operator were used. Laplace operator is invariant respective to turn. It only indicates the size of the edge, not its direction. It represents a second derivative. Increasing the pixel weight of that closer to the representative point of the mask, it loses its invariance respective to rotation. Both Robinson and Kirsch operators approximate the first derivative; both are not directionally invariant. Robinson operator estimates the gradient for the neighborhood of 3 x 3. The x-axis and y-axis directions were used for image filtering, see expresions (6):

$$h_1 = \begin{bmatrix} 1 & 1 & 1 \\ 1 & -2 & 1 \\ -1 & -1 & -1 \end{bmatrix} ; \ h_2 = \begin{bmatrix} 1 & 1 & 1 \\ -1 & -2 & 1 \\ -1 & -1 & 1 \end{bmatrix} ; \ h_3 = \begin{bmatrix} -1 & 1 & 1 \\ -1 & -2 & 1 \\ -1 & 1 & 1 \end{bmatrix} \qquad (6)$$

Figs 6 and 7 show the result of the operation using the Robinson operator, which achieves comparable results with Kirsch operator; Laplace operator has generated worse results.
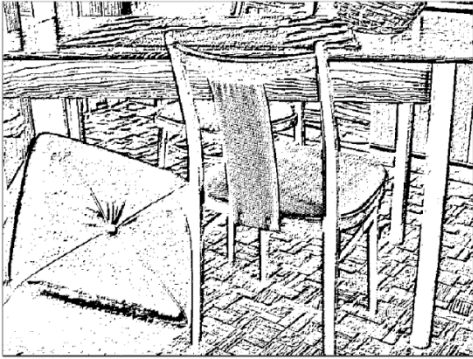
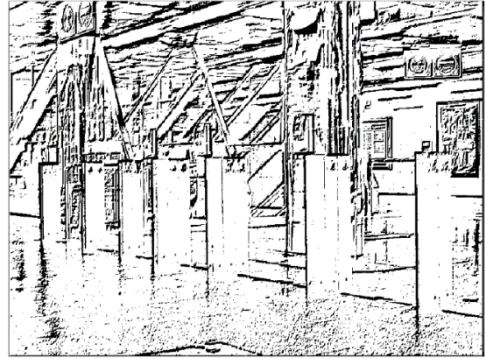**Figure 6.** Results after using Robinson operator for interior scene.

Figure 7. Results after using Robinson operator for exterior scene.

Tactile activator

During the realization and testing of pin connector matrix, it turned out that it is not advisable for the spikes to protrude too far from the silicone body. The touch experience was greater than the perception of electrical pulses. Pulses were tested with both constant voltage and superposed alternate component. By adding a conductive gel between the skin and the actuator, pulse perception improved.

It appeared that using dynamic irritation, by renewing pulses by rows with a certain period; it will be possible to achieve better results than with simple static irritation. Another possible modification to improve sensitivity is modifying the ground electrode: instead of existing antistatic bracelets, grounding electrodes may be placed just on the edges of the actuator, or grounding fibres may be inserted between the electrodes, which is exacting on the precise placement.

To address the spikes to the output of the multiplexer, it can be used the direct principle, i.e. to connect all the wires from the spikes (demanding on the number of M x N outputs), or the matrix selection principle addressing (M + N outputs only).

Finally, the spike resolution was tested on the actuator. First, the point on the left edge was switched and the distance to the next switched point gradually shortened. The smallest distance which can be distinguished with respect to the spike pitch of 2.54 mm is about its double, i.e. 5 mm. At less distances, perception was ambiguous.

The next paragraphs describe the function of tactile activators; in Figs 8 and 9 is demonstrated the behaviour of the electro motors of the tactile activator while passaging through a door frame or

Figure 8. Experimental door frame.

through a narrowed space. The camera records the picture and converts it into data for the microprocessor. It calculates two vertical edges that don´t adjoin with each other,

because their distance is sufficient. The data processing matrix evaluates the distance as high and passes the information on the specified control units that get going the electro motors at the sides of the activator. If the blind person approaches the frames, the picture will not change, so the same electro motors will be working. The transmitted information would change only by deviation of the camera´s direction. Red marked vibrating motors that warn the blind person about the door in front of it. Vibrating motors warn about an obstacle, non-vibrating motors guarantee a free pass. But the disadvantage of the 3 x 3 arrangement is clearly visible. With the 5 x 5 layout it would be possible to better specify the position of the door frame. However, since the primordial functionality of the system is tested, an actuator with lower resolution has been used. This is only capable to 'display' simple images, such as door frames or stairs. Complicated scenarios (such as in Figs 4–7) is not possible to process in this stage, it would be necessary to use an actuator with significantly more points; the scenes should demonstrate the capabilities of the edge detection. Real behaviour has been tested using following simple experimental scenes.
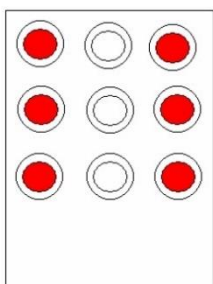
Figure 9. Visualization of the motors warning about the door.

Figure 10. Experimental stairs.

While passing stairs (Fig. 10), the system detects a group of horizontal edges. The stairs are announced by vibrations for a specific time of the first row, then of the second and finally of the third, see Fig. 11. This way the blind person can be warned about rising stairs. Stairs represent a backward moving edge, that is indicated this way using the software to distinguish it from e.g. a fence, where all the actuator motors would be activated simultaneously. The electro motors continue working until the blind person is in the space in front of the stairs or until walking the stairs. As soon as the recorded space in front of the camera changes, the work of the electro motors changes correspondingly. While
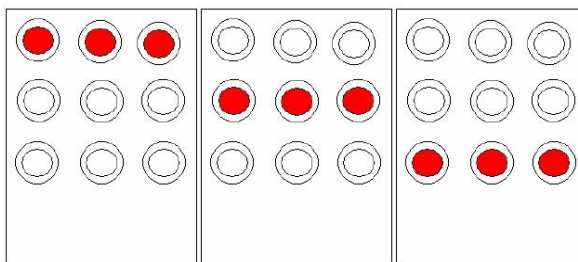
Figure 11. Visualization of the motors warning about the stairs.

going down the stairs, there is a problem with the appropriate detection of the edges; however, after their detection (i.e. falling stairs) the electro motors will work in a reversed order than by rising stairs to distinguish them.

CONCLUSIONS

The designed technical solution presents a contribution to the issue of the orientation of blind persons in a familiar and unfamiliar environment. The capabilities of various edge detection algorithms were tested; Robinson operator and Kirsch operator edge detection methods gave satisfactory results under both indoor and outdoor conditions. Further, two tactile activators were tested to enable the orientation in unknown space – a pin connector matrix and an array of 3 x 3 vibrating motors. The pin connector array sends small electrical impulses to the skin that warns the blind person about an obstacle. Better results were obtained using dynamic irritation by renewing pulses compared with static irritation, the resolution was limited to cca. 5 mm distance of corresponding pins. Next, the tactile activator with an array of 3 x 3 vibrating motors has been tested by detection of simple shapes, such as door frame of stairs. The detection and function of the activator is satisfactory, the main issue is the limited resolution of the 3x3 matrix; the resolution can be increased during the further research, to obtain more precise perception of the surroundings; however, even this simplified prototype demonstrated its designed capability. The system is designed for blind persons in the first way, but by its extension and by usage of additional supporting systems it can be used in every branch. The aim of the project is to design a functional system and to put it into practice in order to contribute to a simplification of the workflows. It can be also pointed out new possibilities of game consoles like the Kintec that can be used in support systems for disabled people.

REFERENCES

A Camera For the Blind. *http://content.time.com/time/specials/packages/article/0,28804,1852747_1854195_1854193,00.html*. Accessed 8.4.2018.

ActiveBelt. *http://www.mobiquitous.com/active-belt-e.html*. Accessed 15.12.2017.

Auvray, M., Hanneton, S. & O'Regan, J.K. 2007. Learning to perceive with a visuo-auditory substitution system: Localisation and object recognition with 'The vOICe' *Perception* **36**, 416–430.

Burger, W. & Burge, J. 2009. *Principles of Digital Image Processing*. Springer-Verlag London Limited, London, 369 pp.

CMUcam3. *http://www.robotstorehk.com/sensors/doc/CMUcam3_datasheet.pdf*. Accessed 17.12.2017.

Diansys. *http://www.dinasys.cz/produkty.html.* Accessed 8.4.2018.

Kaczmarek, K.A. 2011. The tongue display unit (TDU) for electrotactile spatiotemporal pattern presentation. *Scientia Iranica* **18**, 1476–1485.

Králíček, P. 2011. *Introduction into special neurophysiology*. Galén, Praha, 235 pp. (in Czech).

Margalit, E., Maia, M., Weiland, J.D., Greenberg, R.J., Fujii, G.Y., Torres, G., Piyathaisere, D.V., O'Hearn, T.M., Liu, W., Lazzi, G., Dagnelie, G., Scribner, D.A., de Juan, E.Jr. & Humayun, M.S. 2002. Retinal Prosthesis for the Blind. *Survey of ophthalmology* **47**, 335–356.

Maxon Motors. *http:// http://www.maxonmotor.com/maxon/view/content/Index*. Accessed 17.12.2017.

Prajer, I. 2009. *Visual Information Scanning and Processing in Biomedicine*. Diploma Thesis, Faculty of Mechanical Engineering of Czech Technical University in Prague, Prague, 102 pp. (in Czech).

Segond, H., Weiss, D., Kawalec, M. & Sampaio, E. 2013. Perceiving space and optical cues via a visuo-tactile sensory substitution system: A methodological approach for training of blind subjects for navigation. *Perception* **42**, 508–528.

Silbernagl, S. & Despopoulos, A. 2004. *Atlas of Human Physiology*. Grada, Praha, 448 pp. (in Czech).

Šonka, M., Hlaváč, V. & Boyle, R. 2014. *Image Processing, Analysis and Machine Vision*. Thomson, 870 pp.

Tyflosonar. *http://www.volny.cz/vladimir.zaza/tyfloson.html.* Accessed 15.12.2017.

Volf, J. 1994. Methods of Processing Tactile Information-Based on the Solution of Helmholtz-Equation, *Eurosensors VII. Sensors and Actuators A-Physical* **41**, 174–179.

Volf, J. & Škeřík, F. 2014. Tactile Navigation System for Blind Persons. *Jemná mechanika a optika* **59**, 276–280. (in Czech).

Volf, J., Škeřík, F. & Novák, V. 2015. Tactile Navigation System for Navigation of Blind Persons. In: *World Congress IMEKO 2015 Prague 2015*, pp. 1742–1745.

Production and characterization of Al-BN composite materials using by powder metallurgy

A. Yonetken[1,*] and A. Erol[2]

[1]University of Afyon Kocatepe, Faculty of Engineering, Department of Electrical Engineering, ANS campus, TR03200 Afyonkarahisar, Turkey
[2]University of Afyon Kocatepe, Faculty of Technology, Department of Metallurgy and Materials Engineering, ANS campus, TR03200 Afyonkarahisar, Turkey
*Correspondence: yonetken@aku.edu.tr

Abstract. Aluminum matrix composites containing 3, 6, 9, 12 and15% BN has been fabricated by conventional microwave sintering at 550 °C temperature. Compounds formation between Al and BN powders is observed after sintering under Ar shroud. XRD, SEM (Scanning Electron Microscope), mechanical testing and measurements were employed to characterize the properties of Al + BN composite. Experimental results suggest that the best properties as hardness 42, 62 HV were obtained for Al+12% BN composite.

Key words: Powder metallurgy, Sintering, Ceramic-Metal Composites.

INTRODUCTION

Al matrix composites produced by powder metallurgy (PM) have been receiving more attention than conventional melting-casting methods in aerospace, military and car industries, due to the improved physical, chemical and mechanical properties (Harding, M.D et al., 2015). Boron nitride (BN) is a synthetically refractory material, which is widely applied due to its fascinating physical and chemical properties (Guo et al., 2005; Zhang et al., 2005; Yang et al., 2005). It has key properties such as high thermal conductivity, low thermal expansion, good, high electrical resistance, low dielectric constant, nontoxic, easily machined-nonabrasive and lubricious (Chen et al., 2004; Chen et al., 2005; Lin et al., 2007). Hexagonal boron nitride, either in its pure form or as a composite, is an extremely suitable material for special applications at high temperatures. Gas seals for oxygen sensors, parts for high-temperature furnaces (Kalaiselvan et al., 2011). Metals are very useful in making different components and their properties can be improved by adding reinforcement like B_4C and BN e.t.c. Aluminium matrix composites (AMCs) are the competent material in the industrial world (Yuan et al., 2009). These composite materials also offer outstanding properties such as high strength to- weight ratio, good corrosion resistance and versatility to the designer. Two major processing techniques that have been found suitable for these composites are powder metallurgy and solidification processing (Yang et al., 2003). The hardness is affected not only by the uniformity of distribution of particles in the matrix but also by the strength of the particle-matrix boundary and the mechanical properties of

the matrix (Maiti et al., 2008). Various reinforcement particles such as boron carbide (B_4C), titanium carbide (TiC), have been incorporated in aluminum matrix composites by direct melt reaction or by a combined method of self-propagating reaction and casting, ball-milling and reactive sintering and hot extrusion, cold isostatic press and hot extrusion, wet milling, cold isostatic pressing and hot extrusion (Chawla et al., 1987; Li et al., 2007).

The metal matrix composites derive good demand for their use in automobile and aerospace applications (Kennedy et al., 2001). However, the application of these materials is often limited by their poor ductility which is generally associated with in homogeneous size and distribution of the reinforcing particles (Kennedy et al., 2001).

BN particles have not good wettability in liquid aluminium and strong interfacial bonding with Aluminium matrix even though inmate metal- ceramic contact is not too easily achieved in composites fabricated from metal powders Albitera et al., 2003; Karantzalis et al., 2009).

In the present work, Composites work Al-%3BN, Al-%6BN, Al-%9BN. Al-%12BN and Al-%15BN were fabricated, microstructure were characterized and mechanical properties such as hardness and density were studied. It was observed that the best properties as hardness 42, 65 HV were obtained for Al+12% BN composite.

MATERIALS AND METHODS

Starting powders employed in this study were as follows: the purity of 99.8% for Al powders with a particle size lower than 70 µm, the purity of 99.9% for BN ceramic powders a particle size lower than 75 µm The composition of -%3BN, Al-%6BN, Al-%9BN. Al-%12BN and Al-%15BN, powders specimens were prepared in 10g square prism compressed pre-form. They were mixed homogenously for 24 hours in a mixer following the weighing. The mixture was shaped by single axis cold hydraulic pressing using high strength steel die. A pressure of 200 Bar was used for the compacting all the powder mixtures. The cold pressed samples underwent for a sintering at 550 °C for 2 hours in a traditional tube furnace using Argon gas atmosphere. The specimens were cooled in the furnace after sintering and their micro hardness and shear strengths measurements were carried out using METTEST-HT (Vickers) micro hardness tester machine, respectively.

LEO 1430 VP model Scanning Electron Microscope fitted with Oxford EDX analyzer was used for micro structural and EDX compositional analysis.

The volumetric changes of -%3BN, Al-%6BN, Al-%9BN. Al-%12BN and Al-%15BN, composites material after sintering were calculated by using (d = m/V) formula (Fig. 1). The volume of post-sintered samples was measured with Archimedes principle. All the percentages and ratios are given in weight percent unless stated otherwise.

Experimental Results and Discussion
Characterization of specimens
In the study, the samples prepared and shape were sintered at 550 °C in conventional furnace and made ready for physical, mechanical and metallographic analyses. Density-composition change curve is shown in Fig. 1. The highest sintered density was achieved at Al-%3BN composition as 2,975 g cm^{-3}.
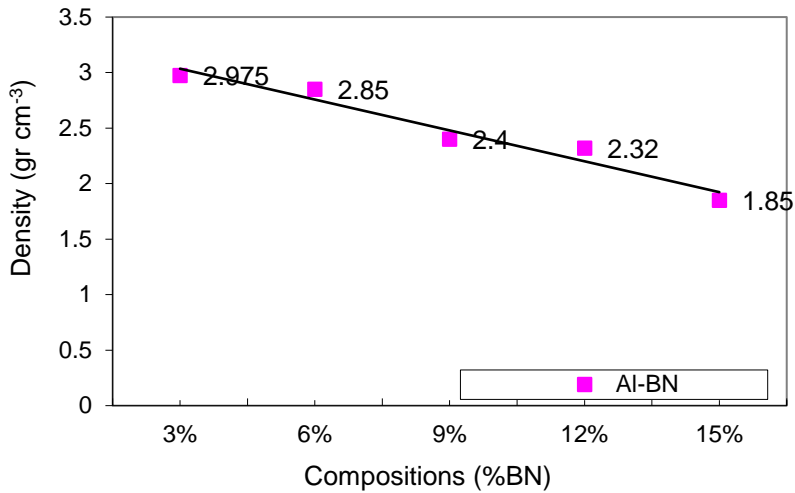
Figure 1. The density change with respect to composition at 550 °C.

The micro hardness-temperature change diagram is shown in Fig. 2. The micro hardness values of the composite samples produced using conventional sintering technique within the temperature at 550 °C. According to this, the highest microhardness value in the composite samples fabricated using powder metallurgy method was observed to be 42.65HV at composition of Al-%12BN composites.
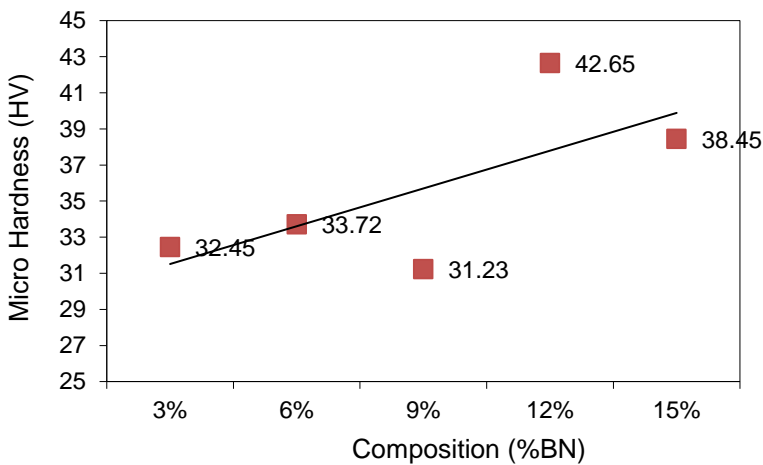

Figure 2. The micro hardness tests results from sintered specimens treated at different compositions.

Metallographic Analysis

The SEM analysis result of the metal matrix composite specimen obtained from Al-%3BN powders sintered at 550 °C is shown in Fig. 3. Grain growth is observed and a homogeneous structure and grain boundaries can be seen that the pores very smaller. This density and hardness values are confirmed.
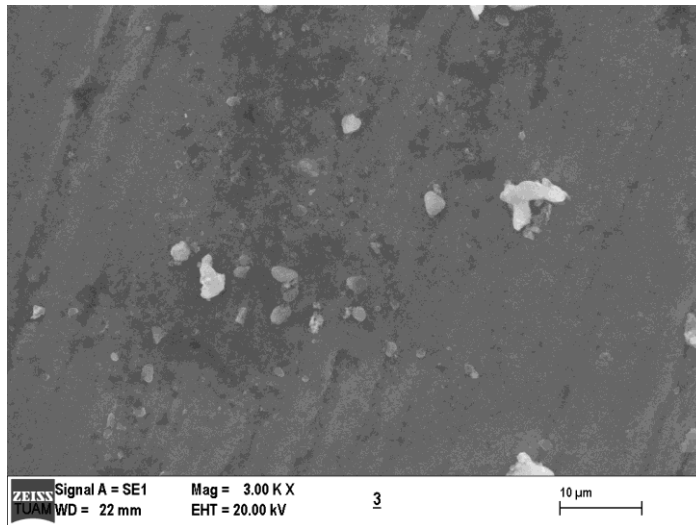
Figure 3. SEM view of Al-%3BN composite 550 °C.

The SEM analysis result of the metal matrix composite specimen obtained from Al-%15BN powders sintered at 550 °C is shown in Fig. 4. grain growth is observed. It is not a homogeneous structure and grain boundaries can be seen that the very pores. This density and hardness values are confirmed.
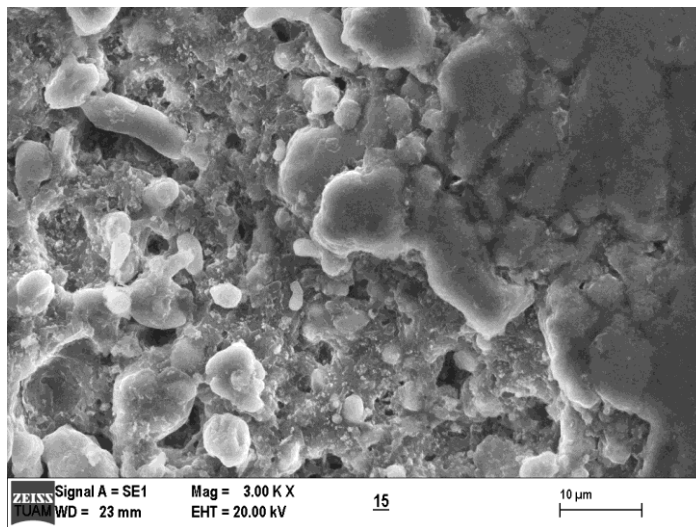

Figure 4. SEM view of Al-%15BN composite 550 °C.

The Al and BN phases, which was the main addition in the composite, has evidently the highest peak intensity over the other phases present in the XRD analysis in the Al-%3BN composites. Fig. 5 which shows the presence of Al and BN phases in the fabricated ceramic-metal composites
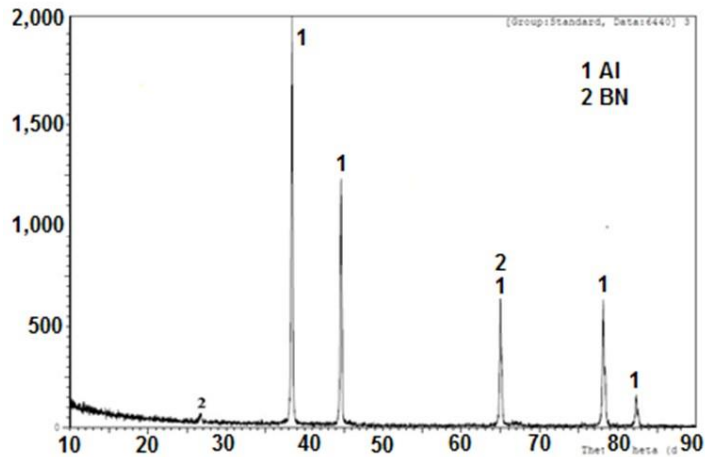
Figure 5. Present the XRD analysis results of Al-%3BN composites at 550 °C.

Fig. 6 present the XRD analysis results of Al-%15BN composites at 550 °C. The Al and BN phases, which was the main addition in the composite, has evidently the highest peak intensity over the other phases present in the XRD analysis in the Al-%15BN composites. Fig. 4 which shows the presence of Al and BN phases in the fabricated ceramic-metal composites.
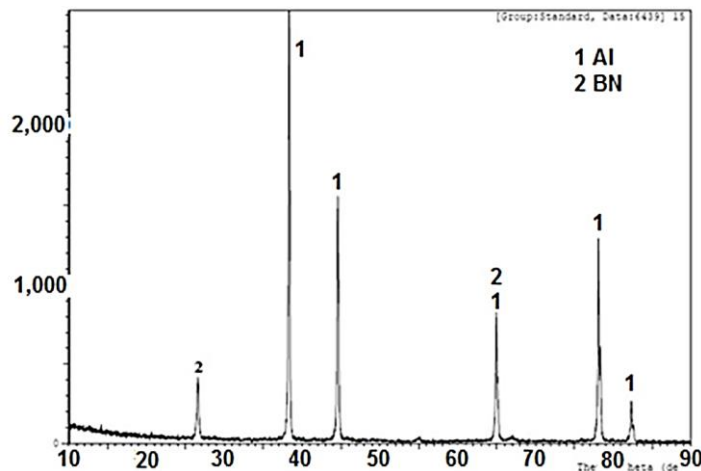

Figure 6. Present the XRD analysis results of Al-%15BN composites at 550 °C.

RESULTS AND DISCUSSION

The following results were concluded from the experimental findings
- The highest density in composite made from Al-%3BN, Al-%6BN, Al-%9BN, Al-%12BN and Al-%15BN powders sintered at 550°C temperatures was obtained as 550 °C The highest density sample was found as 2, 975gr cm^{-3} at 550 °C.

- The highest micro hardness in Al-%12BN composite samples fabricated using powder metallurgy method was found as 42.65HV at 550 °C.
- It was also found out for composition Al-%12BN at 550 °C suggest that the best properties. As the composition ratio of BN in aluminium increases, the porosity increases. A decrease in hardness was observed due to porosity.

REFERENCES

Albitera, A., Contrerasa, A., Bedollab, E. & Pereza, R. 2003. Structural and chemical characterization of precipitates in Al-2024/TiC composites. Compos. Part A **34**, 17–24.

Chen, L.Y., Huang, M.X., Luo, T., Gu, Y.L., Shi, L., Yang, Z.H. & Qian, Y.T., 2004. *Mater. Lett.* **58**, 3634–3636.

Chen, L.Y., Gu, Y.L., Li, Z.F., Qian, Y.T., Yang, Z.H. & Ma, J.H. 2005. *J. Cryst. Growth* **273**, 646–650.

Guo, Q.X., Xie, Y., Yi, C.Q, L. Zhu, P. Gao, J. 2005. *Solid State Chem*. **178**, 1925–19281.

Harding, M.D., Donaldson, I.W., Hexemer, R.L. Jr., Gharghouri, M.A., Bishop, D.P. 2015. Characterization of the microstructure, mechanical properties, and shot peening, response of an industry processed Al–Zn–Mg–Cu PM alloy, *J. Mater. Process. Technol*. **221**, 31–39.

Jens Eichler, E. & Christoph Lesniak, C. Boron nitride (BN) and BN composites for high-temperature applications. *Journal of the European Ceramic Society* **28**, 1105–1109.

Kalaiselvan, K., Murugan, N., Parameswaran, S. 2007. Production and characterization of AA6061–B_4C stir cast composite. *Materials and Design* **32**, (2011) 4004–4009.

Karantzalis, A.E., Lekatou, A.E., Poulas, G.V. & Mavros, H. 2009. Microstructural observations in a cast Al-Si- Cu/TiC composite. *J. Mater. Eng. Perform*. **19**, 585–590.

Kennedy, A.R. & Wyatt, S.M. 2001. Characterising particle–matrix interfacial bonding in particulate Al–TiC MMCs produced by different methods. Compos. Part A **32**, 555–559.

Li, G., Zhao, Y., Dai, Q., Zhang, H. & Wang, H. 2007. In-situ Fabrication of Particulate Reinforced Aluminum Matrix Composites under High-frequency Pulsed Electromagnetic Field. *Journal of University of Science and Technology Beijing, Mineral, Metallurgy, Materia* **14**(5), 460–463.

Lin, L.X., Y. Zheng, Y. & Wei, K.M. 2007. Facile synthesis of hexagonal boron nitride fibres and flowers. *Mater. Lett*. **61**, 1735–1737.

Maiti, R. & Chakraborty, M. 2008. Synthesis and Characterization of Molybdenum Aluminide Nanoparticles Reinforced Aluminium Matrix Composites. *Journal of Alloys and Compounds* **458**(1–2), 450–456.

Nukami T. 2004. The growth of TiC particles in an Al matrix. *J. Mater. Sci.* Lett. **17**, 267–269.

Yang, H.S., Iwamoto, C., Yoshid T.A. 2005. Thin Solid Films 483 (2005) 218–221.

Yang, Q., Senda, T., Ohmori A. 2003. Effect of carbide grain size on microstructure and sliding wear behavior of HVOF-sprayed WC–12% Co coatings, *Wear* **254**, 23–34.

Yuan, Q., Zheng, Y. & Yu, H. 2009. Mechanism of synthesizing nanocrystalline TiC in different milling atmosphere. *J. Refractory Metals & Hard Materials* **27**, 696–700.

Xialiang Shi, Sheng Wang, Hua Yang, Xinglong Duan, Xuebin Dong, 2008. Fabrication and characterization of hexagonal boron nitride powder by spray drying and calcining– nitriding technology. *Journal of Solid State Chemistry* **181**, 2274–2278.

Zhang X.W., Boyen H.G., Yin H., Ziemann P., Banhart F. 2005. *Diam. Relat. Mater*. **14**, 1474–1481.

INSTRUCTIONS TO AUTHORS

Papers must be in English (British spelling). English will be revised by a proofreader, but authors are strongly urged to have their manuscripts reviewed linguistically prior to submission. Contributions should be sent electronically. Papers are considered by referees before acceptance. The manuscript should follow the instructions below.

Structure: Title, Authors (initials & surname; an asterisk indicates the corresponding author), Authors' affiliation with postal address (each on a separate line) and e-mail of the corresponding author, Abstract (up to 250 words), Key words (not repeating words in the title), Introduction, Materials and methods, Results and discussion, Conclusions, Acknowledgements (optional), References.

Layout, page size and font
- Use preferably the latest version of **Microsoft Word**, doc., docx. format.
- Set page size to **B5 Envelope or ISO B5 (17.6 x 25 cm)**, all margins at 2 cm.
- Use single line spacing and justify the text. Do not use page numbering. Use indent 0.8 cm (do not use tab or spaces instead).
- Use font Times New Roman, point size for the title of article **14 (Bold)**, author's names 12, core text 11; Abstract, Key words, Acknowledgements, References, tables and figure captions 10.
- Use *italics* for Latin biological names, mathematical variables and statistical terms.
- Use single ('…') instead of double quotation marks ("…").

Tables
- All tables must be referred to in the text (Table 1; Tables 1, 3; Tables 2–3).
- Use font Times New Roman, regular, 10 pt. Insert tables by Word's 'Insert' menu.
- Do not use vertical lines as dividers; only horizontal lines (1/2 pt) are allowed. Primary column and row headings should start with an initial capital.

Figures
- All figures must be referred to in the text (Fig. 1; Fig. 1 A; Figs 1, 3; Figs 1–3). Use only black and white or greyscale for figures. Avoid 3D charts, background shading, gridlines and excessive symbols. Use font **Arial** within the figures. Make sure that thickness of the lines is greater than 0.3 pt.
- Do not put caption in the frame of the figure.
- The preferred graphic format is EPS; for half-tones please use TIFF. MS Office files are also acceptable. Please include these files in your submission.
- Check and double-check spelling in figures and graphs. Proof-readers may not be able to change mistakes in a different program.

References

- **Within the text**

In case of two authors, use '&', if more than two authors, provide first author 'et al.':
   Smith & Jones (1996); (Smith & Jones, 1996);
   Brown et al. (1997); (Brown et al., 1997)

When referring to more than one publication, arrange them by following keys: 1. year of publication (ascending), 2. alphabetical order for the same year of publication:

(Smith & Jones, 1996; Brown et al., 1997; Adams, 1998; Smith, 1998)

- **For whole books**

Name(s) and initials of the author(s). Year of publication. *Title of the book* (*in italics*). Publisher, place of publication, number of pages.

Shiyatov, S.G. 1986. *Dendrochronology of the upper timberline in the Urals*. Nauka, Moscow, 350 pp. (in Russian).

- **For articles in a journal**

Name(s) and initials of the author(s). Year of publication. Title of the article. *Abbreviated journal title* (*in italic*) volume (in bold), page numbers.

Titles of papers published in languages other than English, German, French, Italian, Spanish, and Portuguese should be replaced by an English translation, with an explanatory note at the end, e.g., (in Russian, English abstr.).

Karube, I. & Tamiyra, M.Y. 1987. Biosensors for environmental control. *Pure Appl. Chem.* **59**, 545–554.

Frey, R. 1958. Zur Kenntnis der Diptera brachycera p.p. der Kapverdischen Inseln. *Commentat.Biol.* **18**(4), 1–61.

Danielyan, S.G. & Nabaldiyan, K.M. 1971. The causal agents of meloids in bees. *Veterinariya* **8**, 64–65 (in Russian).

- **For articles in collections:**

Name(s) and initials of the author(s). Year of publication. Title of the article. Name(s) and initials of the editor(s) (preceded by In:) *Title of the collection (in italics)*, publisher, place of publication, page numbers.

Yurtsev, B.A., Tolmachev, A.I. & Rebristaya, O.V. 1978. The floristic delimitation and subdivisions of the Arctic. In: Yurtsev, B. A. (ed.) *The Arctic Floristic Region*. Nauka, Leningrad, pp. 9–104 (in Russian).

- **For conference proceedings:**

Name(s) and initials of the author(s). Year of publication. Name(s) and initials of the editor(s) (preceded by In:) *Proceedings name (in italics)*, publisher, place of publishing, page numbers.

Ritchie, M.E. & Olff, H. 1999. Herbivore diversity and plant dynamics: compensatory and additive effects. In: Olff, H., Brown, V.K. & Drent R.H. (eds) *Herbivores between plants and predators. Proc. Int. Conf. The 38th Symposium of the British Ecological Society*, Blackwell Science, Oxford, UK, pp. 175–204.

Please note
- Use '.' (not ',') for decimal point: 0.6 ± 0.2; Use ',' for thousands – 1,230.4;
- Use '–' (not '-') and without space: pp. 27–36, 1998–2000, 4–6 min, 3–5 kg
- With spaces: 5 h, 5 kg, 5 m, 5°C, C : D = 0.6 ± 0.2; $p < 0.001$
- Without space: 55°, 5% (not 55 °, 5 %)
- Use 'kg ha^{-1}' (not 'kg/ha');
- Use degree sign ' ° ' : 5 °C (not 5 ^{O} C).